Volume 2

5 CHARACTERISATION OF A TIMETAL 834 BILLET

5.1 Introduction

This chapter concerns work that was carried out to investigate and characterise microstructure, microtexture and global textures in the Timet supplied billet of Timetal 834. Several titanium alloys including Timetal 834 have been reported to contain regions with strong local textures referred to as macrozones. To date, there has been little work published on whether these macrozones are present throughout a billet and how they may vary depending on location. In particular, since the scale of the macrozones tends to be large, there have been few statistically representative measurements made of the macrotexture, which would reveal whether the macrozones themselves have preferred orientations. Therefore, the main focus of this work was to study the effect of location on the macrozones in terms of their size, shape, texture intensity and crystallographic orientation and to see if any differences could be related to the primary working process. This was accomplished using a combination of optical microscopy, EBSD and neutron texture analysis to study a cross-sectional slice from the billet.

5.2 Results

5.2.1 Characterisation at the Scale of the α_p Grains

The microstructure at the scale of the α_p grains was investigated using optical microscopy, scanning electron microscopy and high resolution EBSD. The microstructure showed differences between the centre and the edge of the billet but no obvious angular dependence. Representative micrographs from the centre and edge of the billet in the longitudinal and transverse planes are shown in Fig. 5.1 and 5.2. The billet had a bimodal microstructure with a high volume fraction of α_p grains and the remainder consisting of coarse lamellar α_s colonies. The average α_p volume fraction varied from approximately 90% in the centre to 70% at the edge. The edges of the α_p grains were frequently feathery in appearance due to epitaxial growth of the α_p grains into the surrounding β phase. This 'feathery α' was more extensive in the centre of the billet, which accounted for the higher α_p volume fraction there and also contributed to a slightly larger α_p grain size (the mean linear intercept α_p grain size varied from 18 μm in the centre to 15 μm at the edge). The α_p grains were shaped like plates, with the longest axis of these plates strongly aligned with the billet axis. α_p grain aspect ratios were higher in the centre of the billet compared to the edge. In the billet centre, the grains had a thickness of about 15 μm and lengths which varied from around 15 to 80 μm.

Scanning electron microscopy was used to examine the microstructure at higher magnification, which showed that throughout the billet there were thin continuous layers of β phase between the α_s lamellae in the α_s colonies, and at the boundaries between feathery α_p grains (Fig. 5.3).

To provide microtexture information, two high resolution EBSD maps (0.25μm step size) were acquired from specimen 2 (centre) and 1 (edge) in the transverse plane. A band contrast map and an IPF map for each phase, α and β, is shown in Figs. 5.4 and 5.5 for the centre and edge respectively. It can be seen that in these maps, which only cover a relatively small area, there does not appear to be strong microtexture in the α phase, with the α_p grains and α_s colonies showing a range of crystallographic orientations. Within the α_p grains themselves, substructure in the form of low angle grain boundaries can be seen. In the centre of the billet (Fig. 5.4), the thickness of the regions of retained β phase is greater compared to the edge. This meant that good β phase Kikuchi patterns could be obtained more reliably, resulting in better indexing of the β phase in the centre. In the β phase maps, it can be seen that there is a common β orientation for each α_s colony and that between α_p grains, a common β orientation often extends for lengths comparable to the α_p grains but no further.

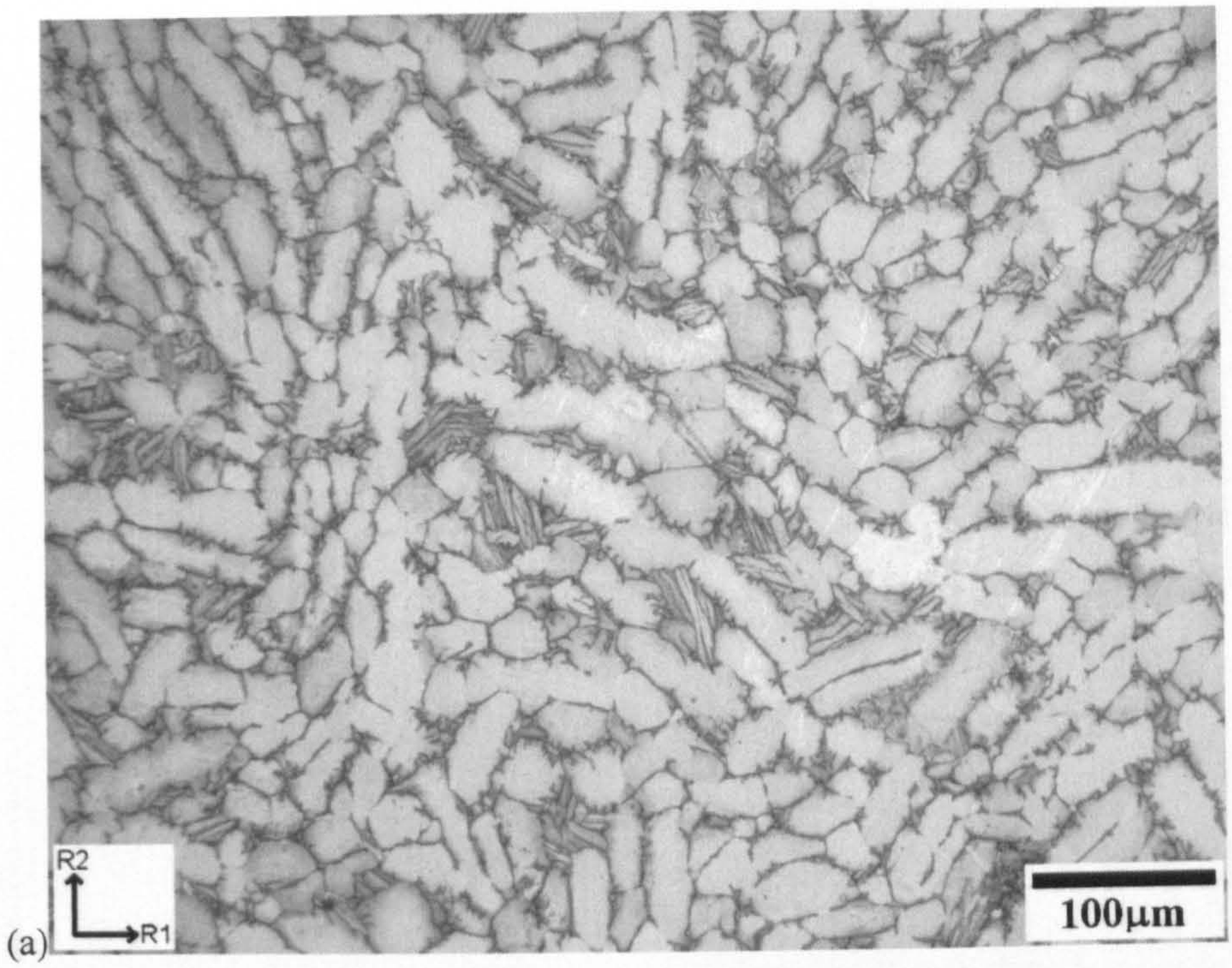

(a)

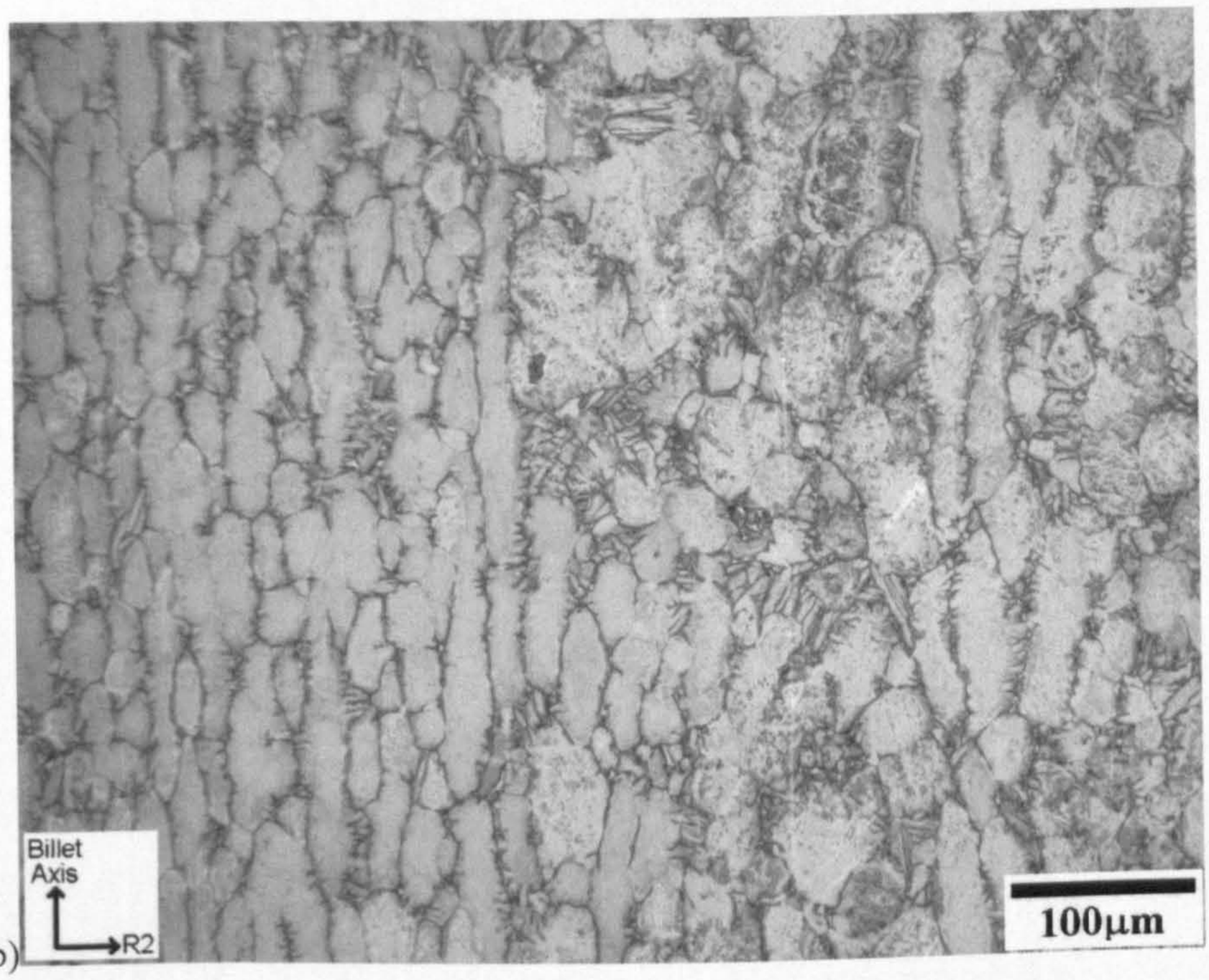

(b)

Fig. 5.1 Optical micrographs from the centre of the billet. (a) transverse section, (b) longitudinal section.

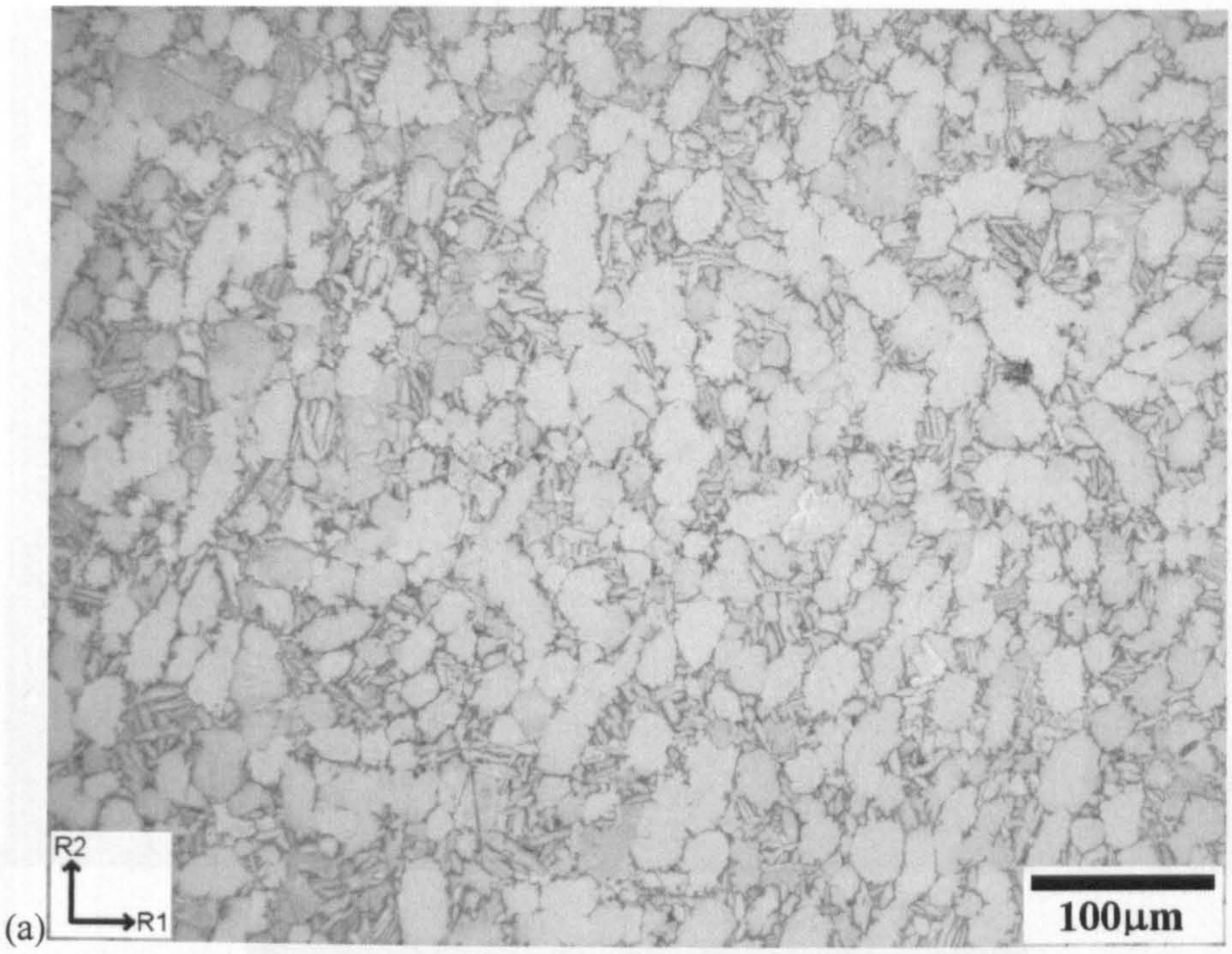

(a)

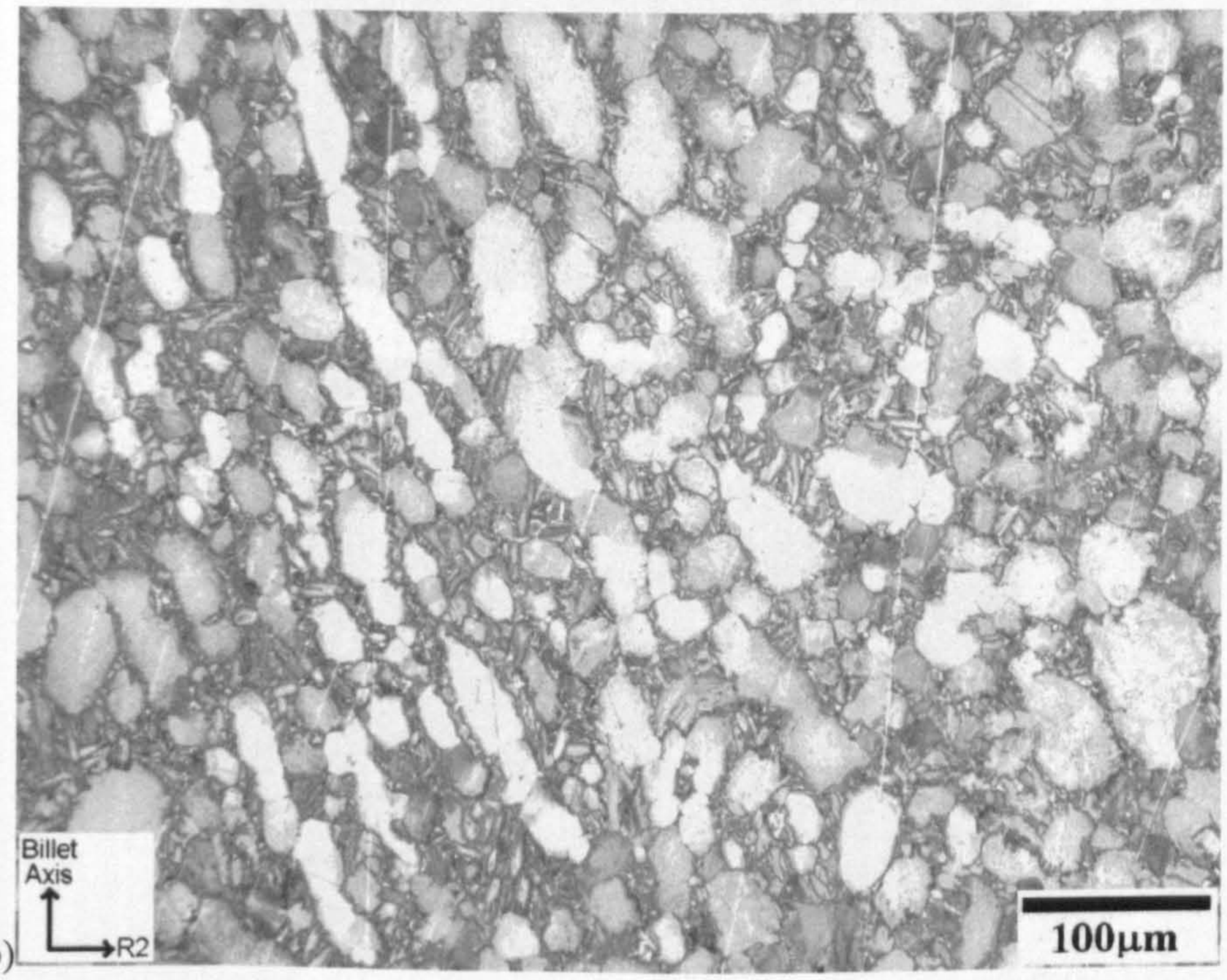

(b)

Fig. 5.2 Optical micrographs from the edge of the billet. (a) transverse section, (b) longitudinal section.

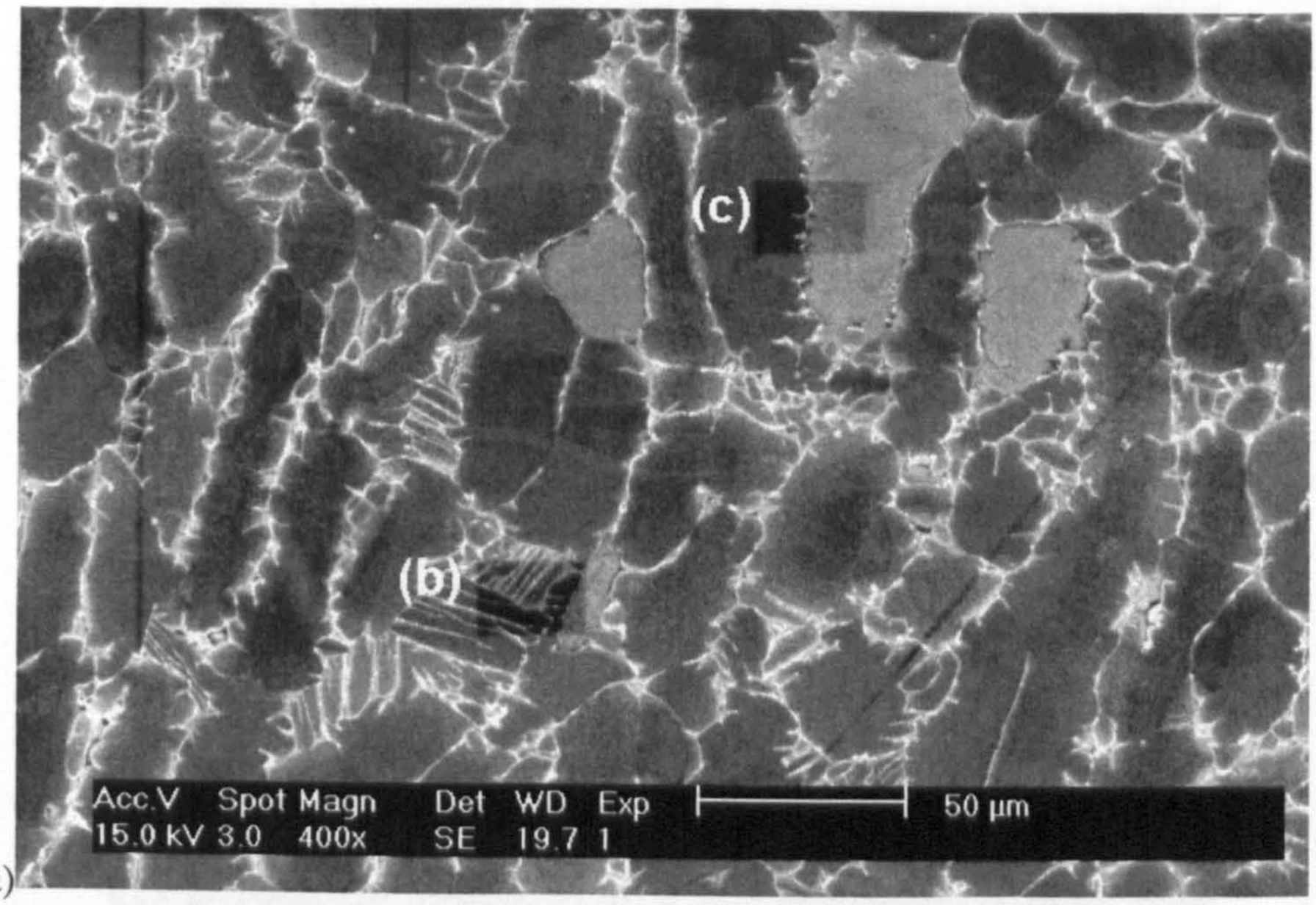

(a)

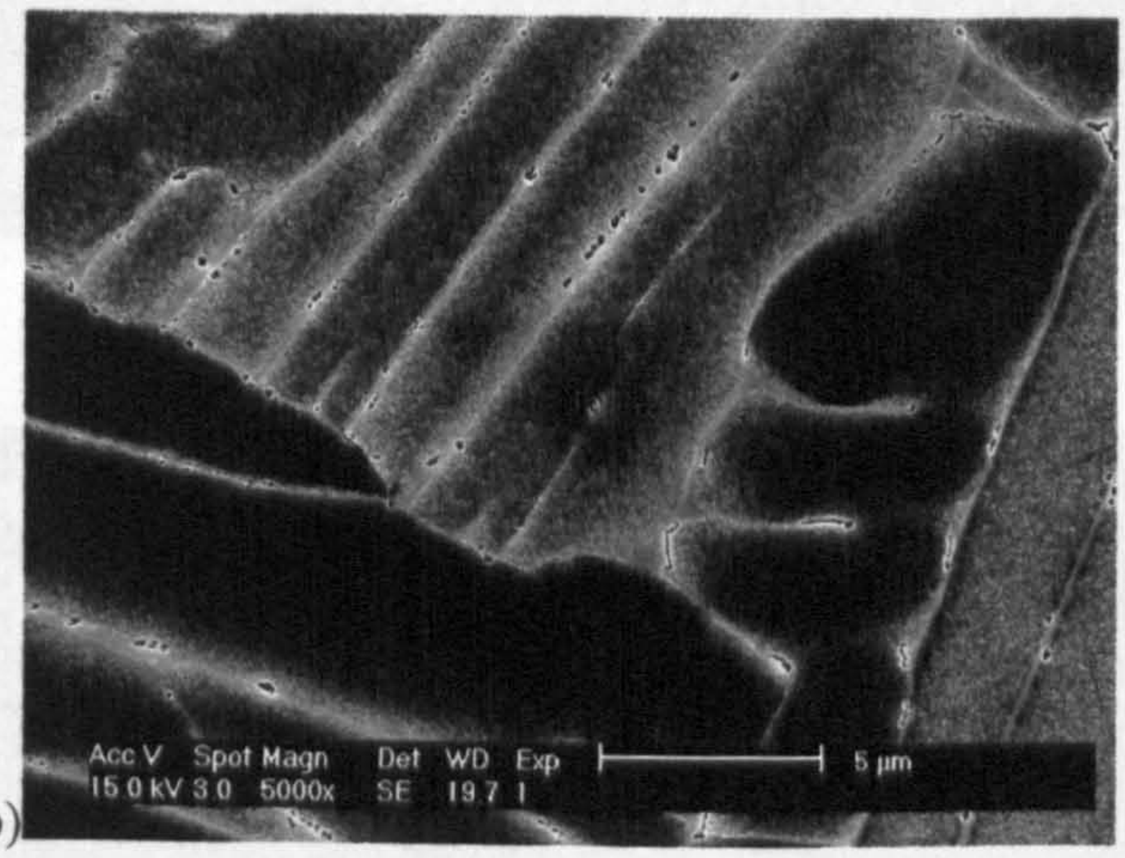

(b)

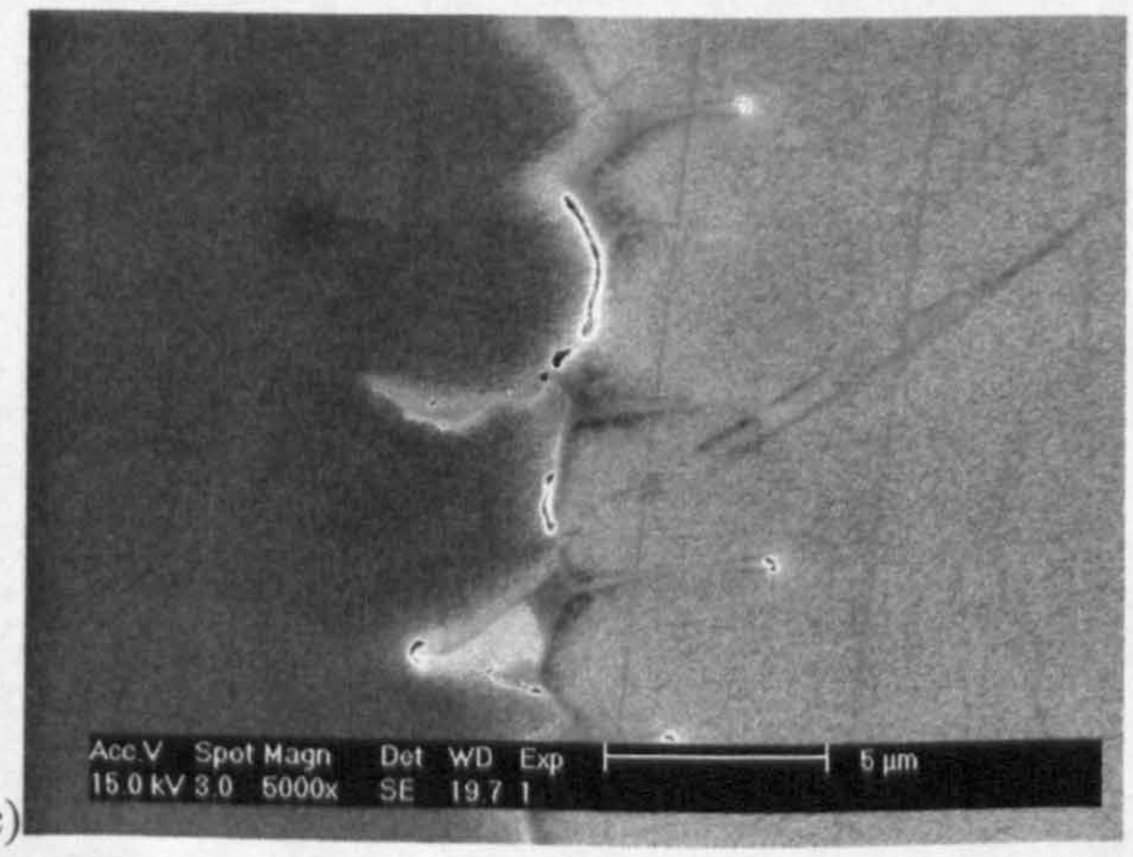

(c)

Fig. 5.3 Secondary electron images from an etched billet specimen. (a) low magnification image showing position of images (b) and (c): (b) α_s colony showing thin β phase layers between α_s lamellae, (c) thin β phase layer between feathery α_p grains.

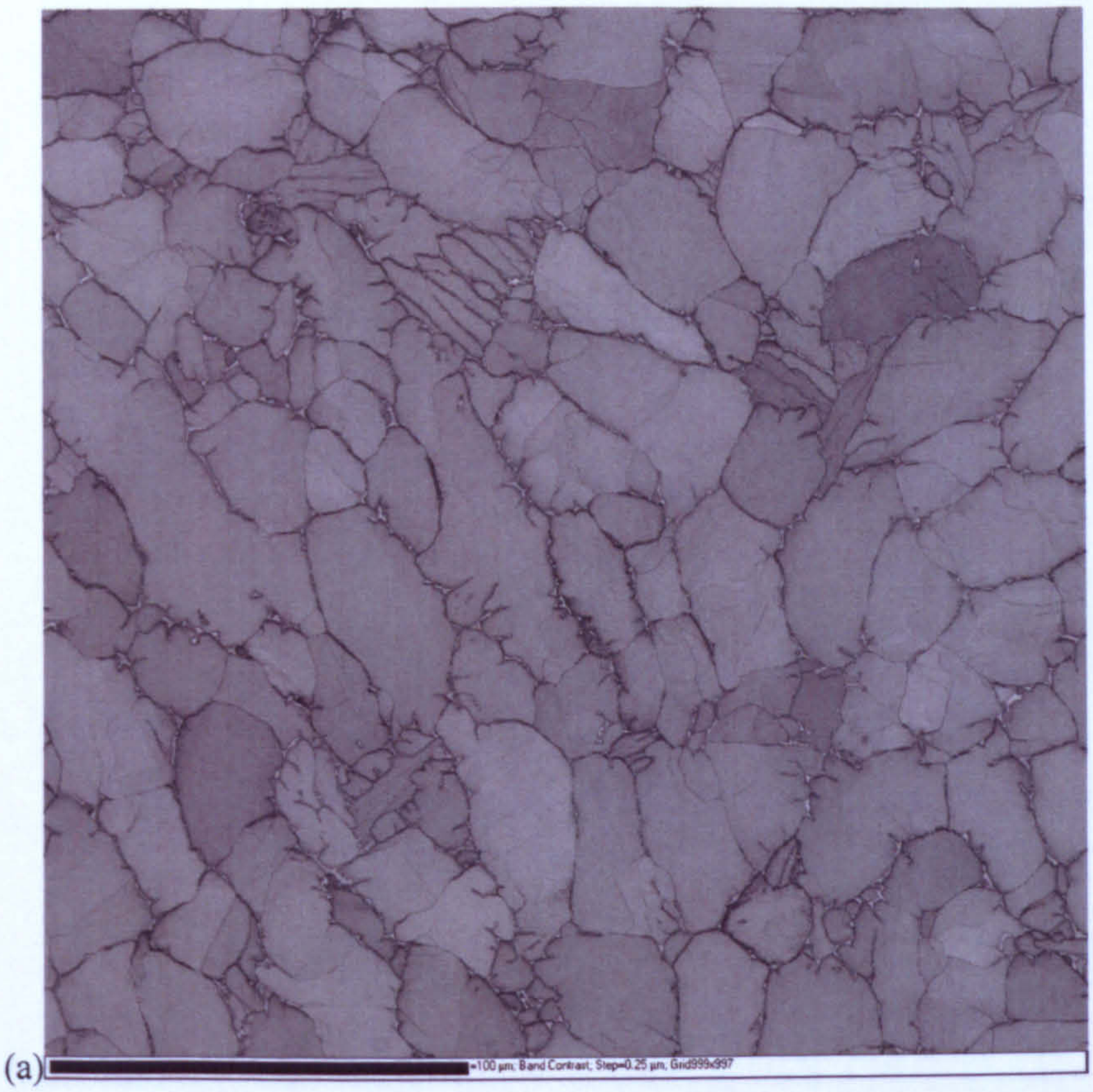
=100 µm; Band Contrast; Step=0.25 µm; Grid999x997

(a)

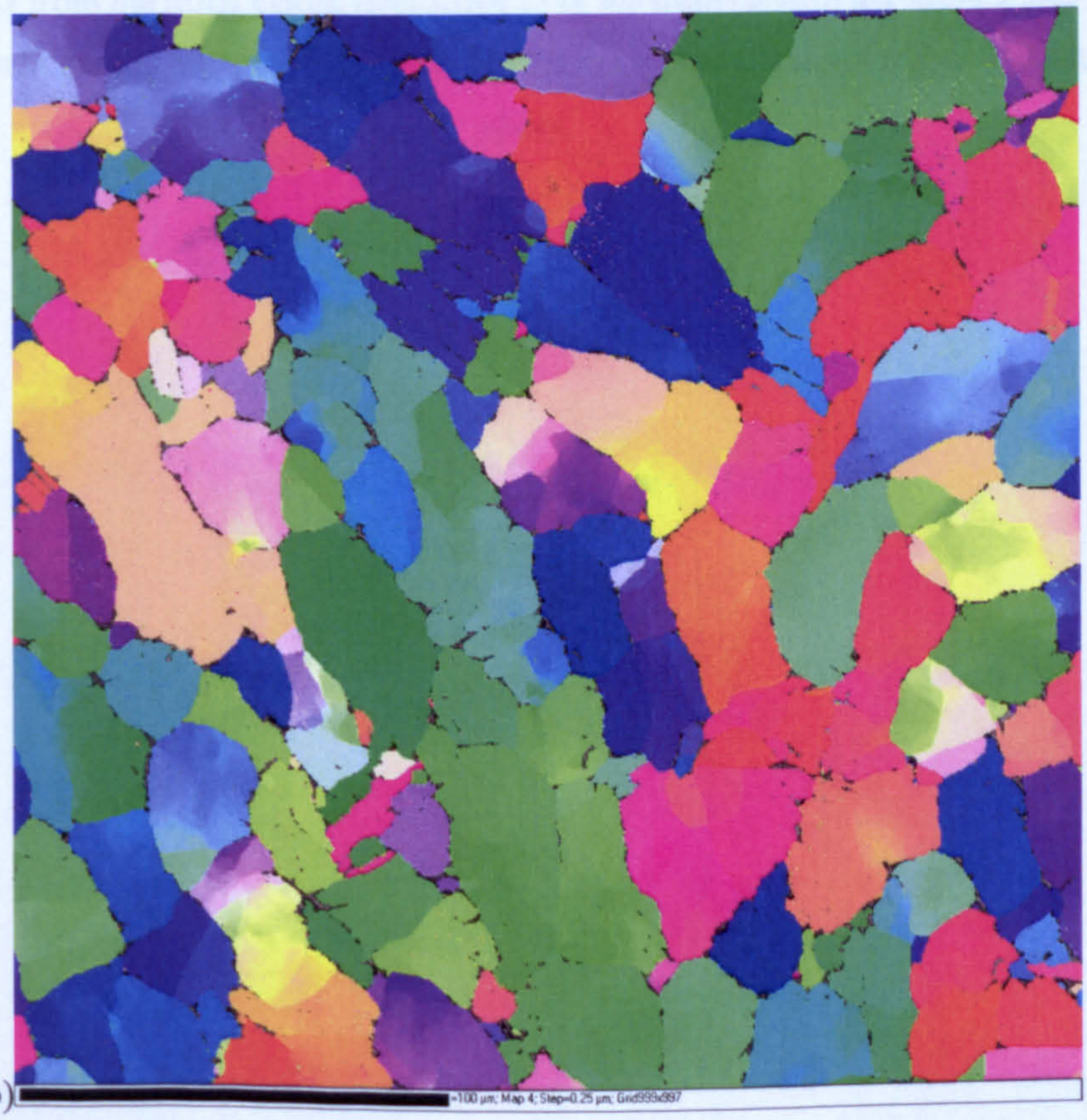
=100 µm; Map 4; Step=0.25 µm; Grid999x997

(b)

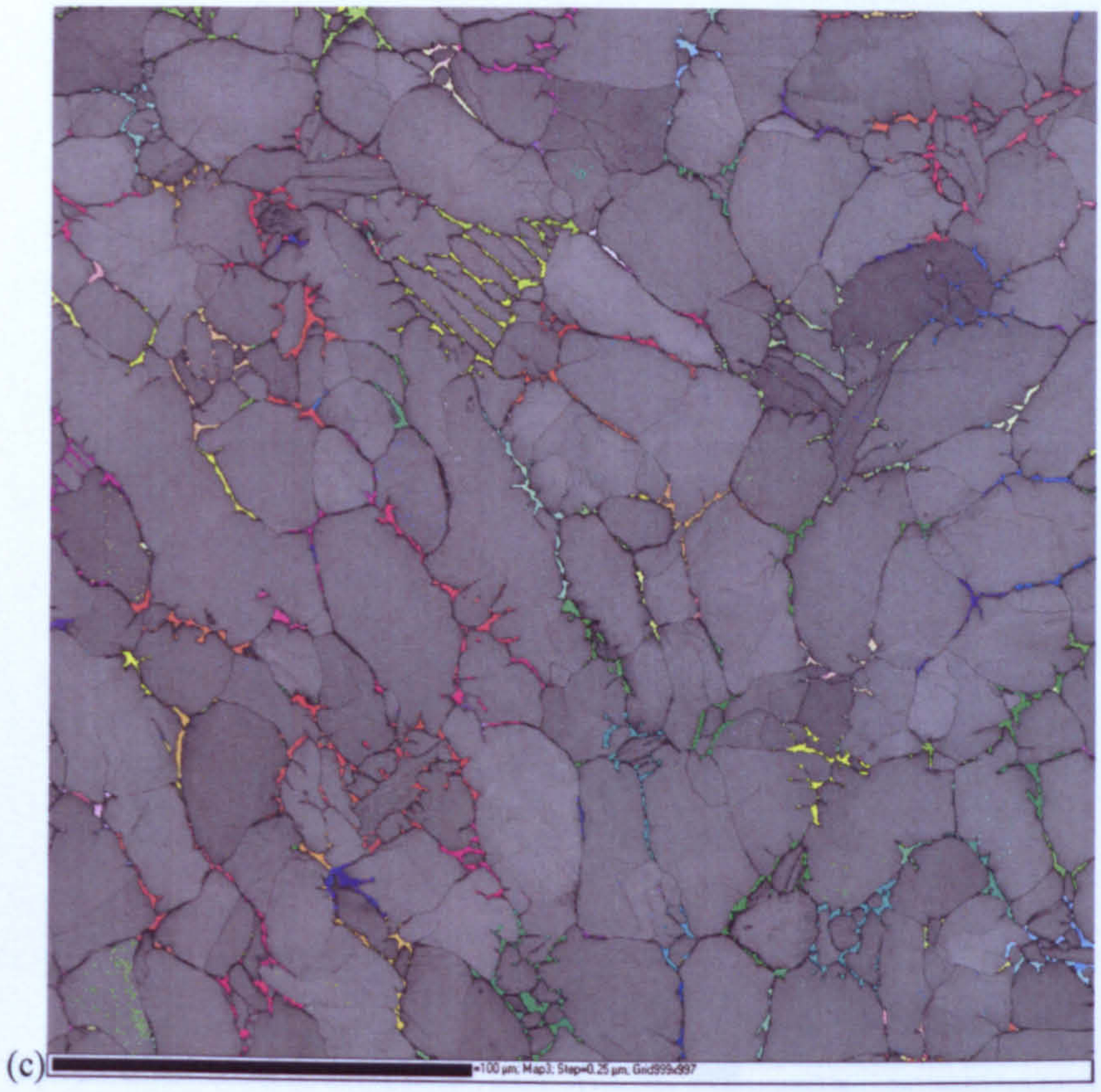

Fig. 5.4 EBSD from the billet centre (specimen 2) in the transverse plane using a step size of 0.25 µm. (a) band contrast map, (b) IPF colouring for the α phase, and (c) IPF colouring for the β phase.

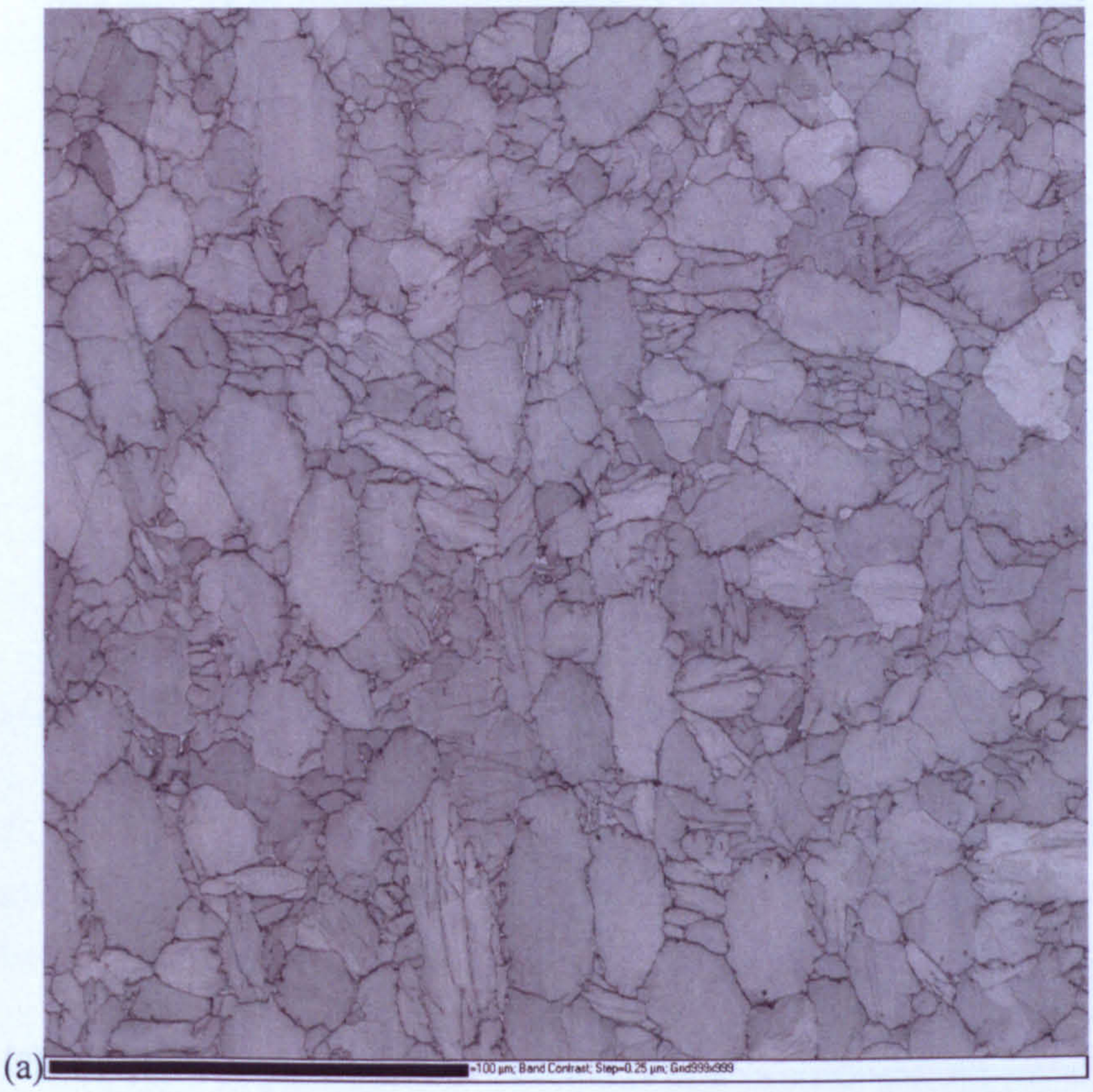
=100 µm; Band Contrast; Step=0.25 µm; Grid999x999

(a)


=100 µm; Map 4; Step=0.25 µm; Grid999x999

(b)

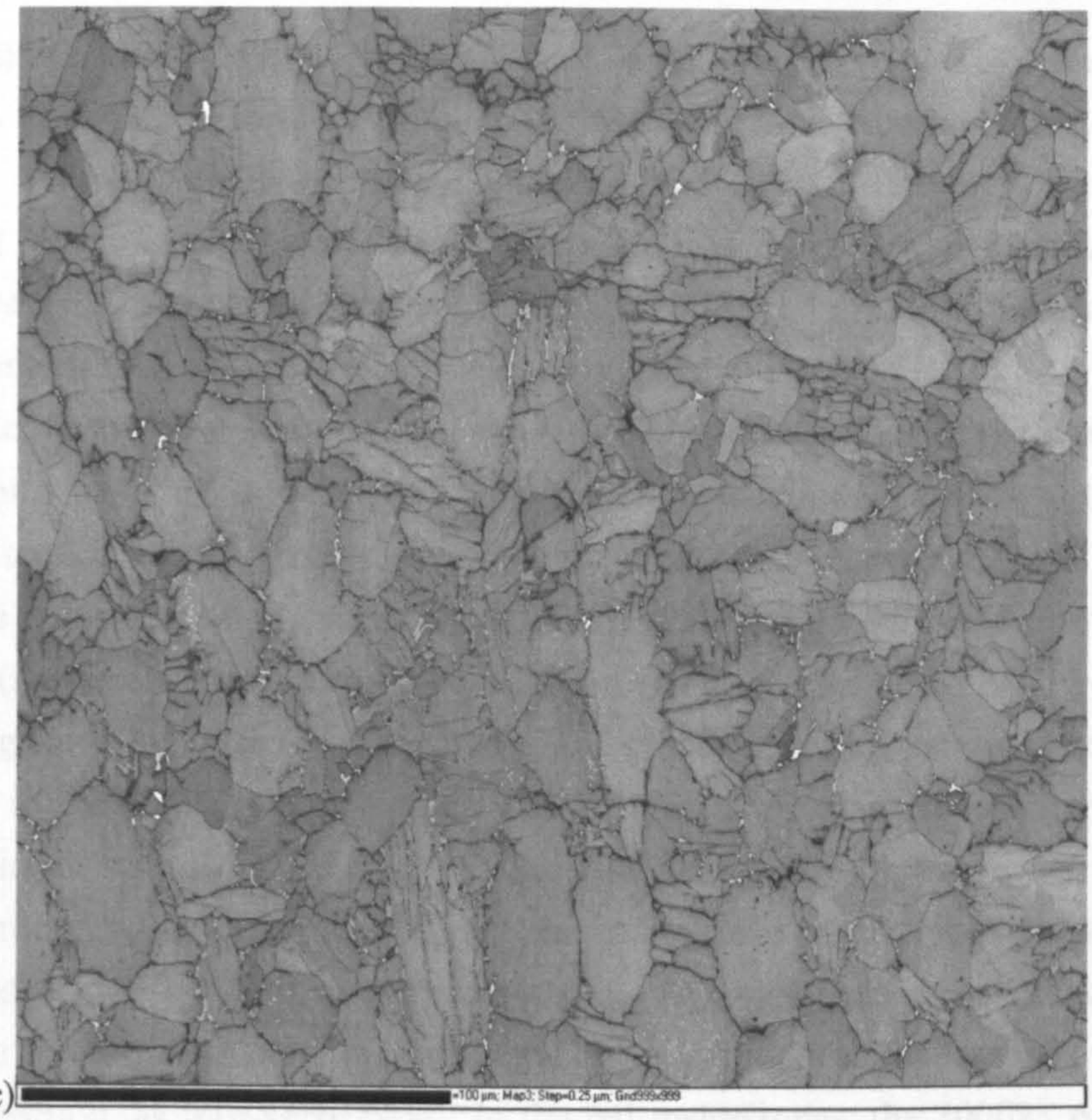

Fig. 5.5 EBSD from the billet edge (specimen 1) in the transverse plane using a step size of 0.25 µm. (a) band contrast map, (b) IPF colouring for the α phase, and (c) IPF colouring for the β phase.

5.2.2 Characterisation at the Scale of the Macrozones

Optical microscopy at lower magnification showed that the billet contained regions of aligned α_p grains. These aligned regions were more prominent in the centre of the billet compared to the edge. Fig. 5.6 is a micrograph taken in a longitudinal section in the centre of the billet, which clearly shows these aligned regions. The aligned regions were in the form of long columnar shapes, with their major axis aligned with the billet axis. As well as grain alignment, there also appeared to be slight differences in the α_p volume fraction, α_p grain size and α_p aspect ratio, which gave further distinction between neighbouring groups of aligned grains.

To provide information on the crystallographic orientation of the α phase in the aligned regions, an EBSD map was acquired from the centre of the billet in the longitudinal plane using a step size of 3µm. The map is displayed in Fig. 5.7 using Euler colouring and Fig. 5.8 using inverse pole figure (IPF) colouring (note that the IPF colouring is with respect to the billet axis instead of the map normal, which means that the colours show

which crystallographic planes of the α phase lie in the transverse plane of the billet). It can be seen that the regions of aligned grains also share common crystallographic orientations. This demonstrates that regions of aligned α_p grains are in fact macrozones, regions with strong local textures. In the longitudinal section, the macrozones have thicknesses ranging from approximately 100 to 1000 μm and are up to several thousand microns in length.

To provide more information on the crystallographic orientations of the α phase in the aligned regions, two EBSD maps were acquired from specimen 2 (centre) and 1 (edge) using a step size of 3 μm. These maps were acquired in the transverse plane in order to maximise the number of aligned regions contained in the maps. The map from the centre of the billet (specimen 2) is shown in Fig. 5.9 using a combination of band contrast and IPF colouring to reveal microstructure as well as orientation information. It can be seen that viewed in the transverse plane, the macrozones are much more equiaxed. The macrozones in the map from the centre of the billet are mainly blue or red in colour. In the blue macrozones, the prismatic $\{10\bar{1}0\}$ planes lie in the transverse plane of the billet, which means that the c-axis must also lie in the transverse plane in a direction perpendicular to the billet axis. We can therefore describe these macrozones in terms of the c-axis direction, as transverse type. In the red macrozones, the {0002} planes lie in the transverse plane, which means the c-axis is aligned with the billet axis. In terms of the c-axis direction, these macrozones can be described as axial type. More diffuse groups of green grains are also present. These are also transverse type but in this case, the $\{11\bar{2}0\}$ planes lies in the transverse plane. The blue transverse macrozones tend to be larger and occupy a greater portion of the scanned region compared to the red axial macrozones. It should be noted that an IPF colour does not define a unique orientation because planes sharing the same colour may be rotated differently about the IPF reference direction. For example, the apparently very large blue macrozone in the top right corner of Fig. 5.9 is actually composed of several regions with different c-axis directions in the transverse plane. In this particular example, shown in greater detail in Fig. 5.10, the main c-axis directions appear to have formed via platelet bending and kinking of a single prior colony of α lamellae. Fig. 5.11 shows a typical example of a blue transverse macrozone in greater detail, together with a pole figure and pole figure contour plot of the measured orientations in the selected macrozone. It can be seen from the figure that almost every α_p grain in the macrozone has a similar crystallographic orientation, which results in an extremely strong local texture. For the blue transverse macrozones, there was a very strong tendency for the c-axis of the crystal to be in the same direction as the direction of grain alignment in the transverse plane. The misorientation map (Fig. 5.11(b)), shows the misorientations between adjacent α grains because the thin layers of β phase between the α grains was not indexed. The clear lack of boundaries within the blue transverse macrozone shows that most of the grains within the macrozone are misorientated from

their neighbours by less than 15°. Fig. 5.12 shows a typical example of a red axial macrozone in greater detail. It can be seen from the pole figure that there is a larger spread in the grain orientations compared to the blue transverse macrozone, which results in a weaker local texture. The misorientation map shows that most of the grains within a red axial macrozone are misorientated from their neighbours by more than 15°.

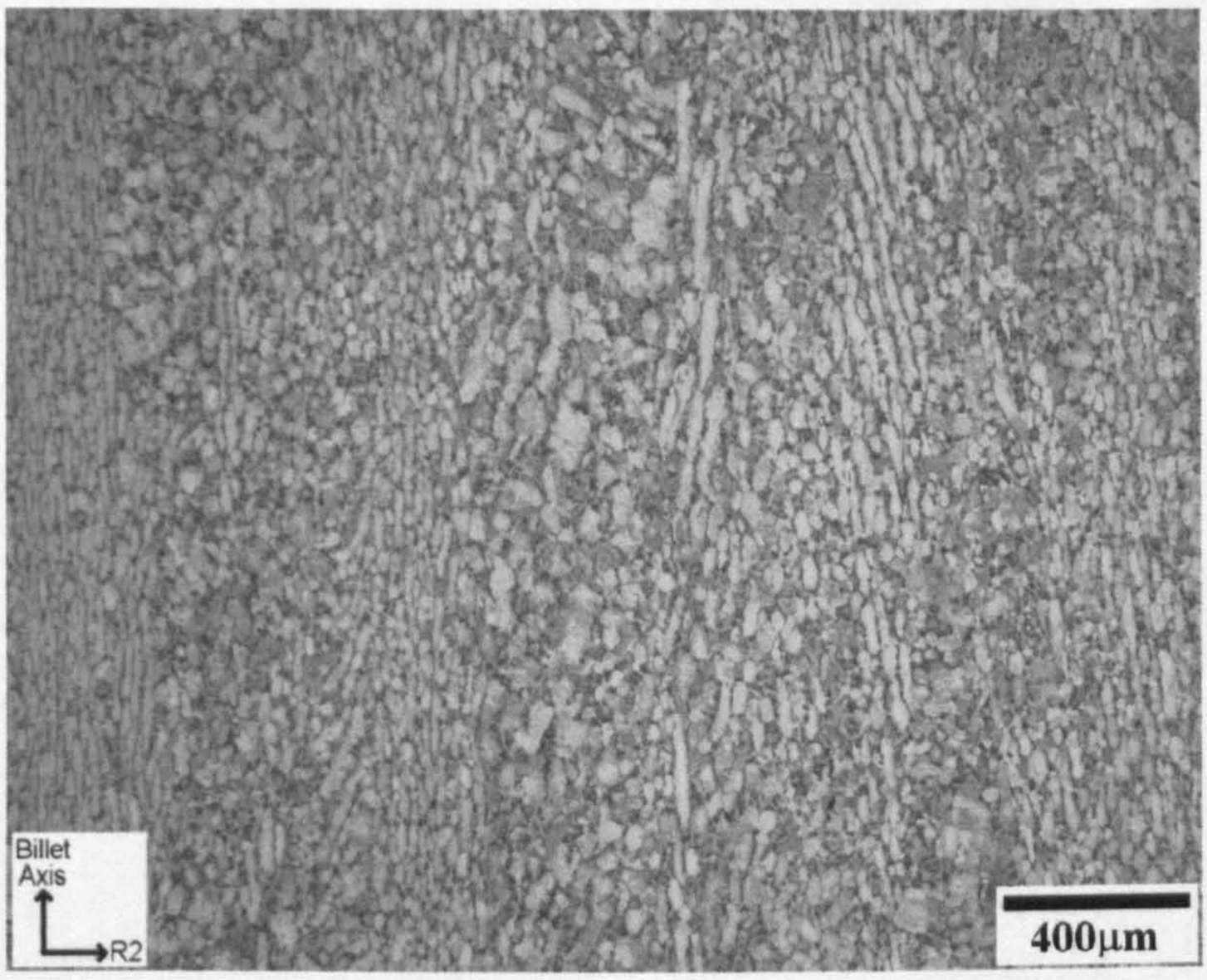

Fig. 5.6 Longitudinal section showing columnar shaped groupings of aligned α_p grains. Both the groupings and the α_p grains themselves are predominantly aligned with the billet axis.

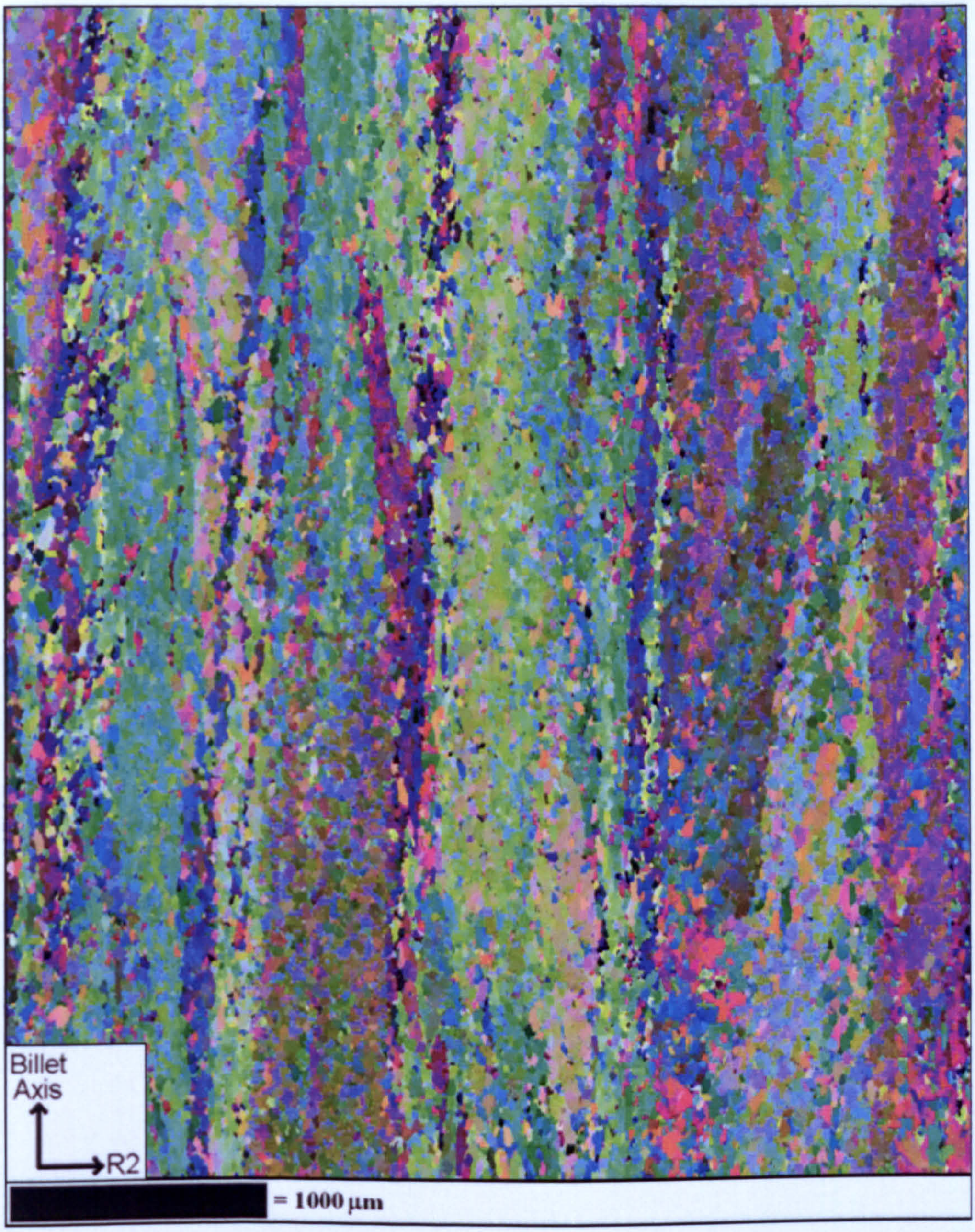

Fig. 5.7 EBSD map of the α phase in a longitudinal section from the centre of the billet (specimen 2). Euler colouring.

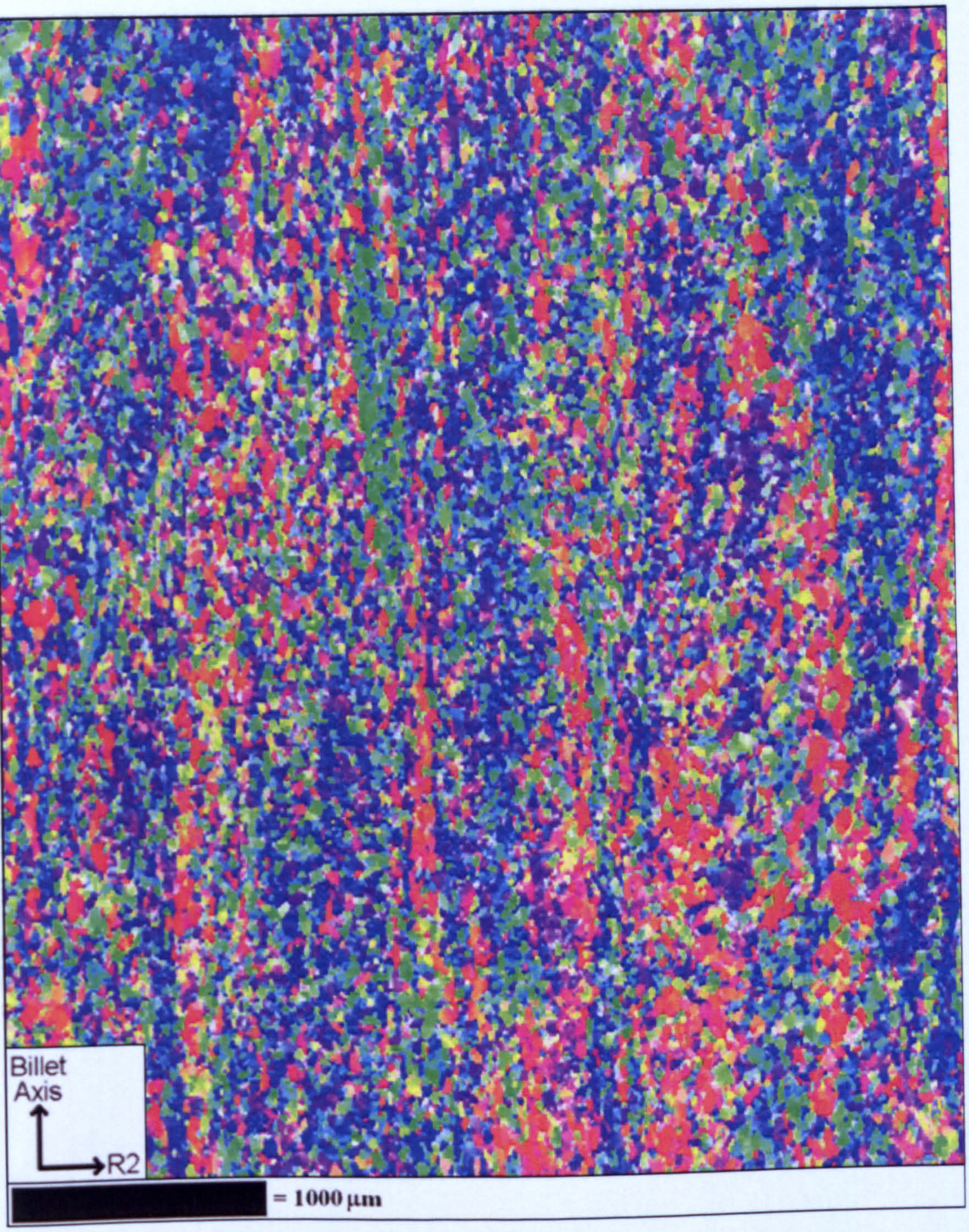

Fig. 5.8 EBSD map of the α phase in a longitudinal section from the centre of the billet (specimen 2). Same area as Fig. 5.7 using IPF colouring with respect to the billet axis (i.e. not the map normal).

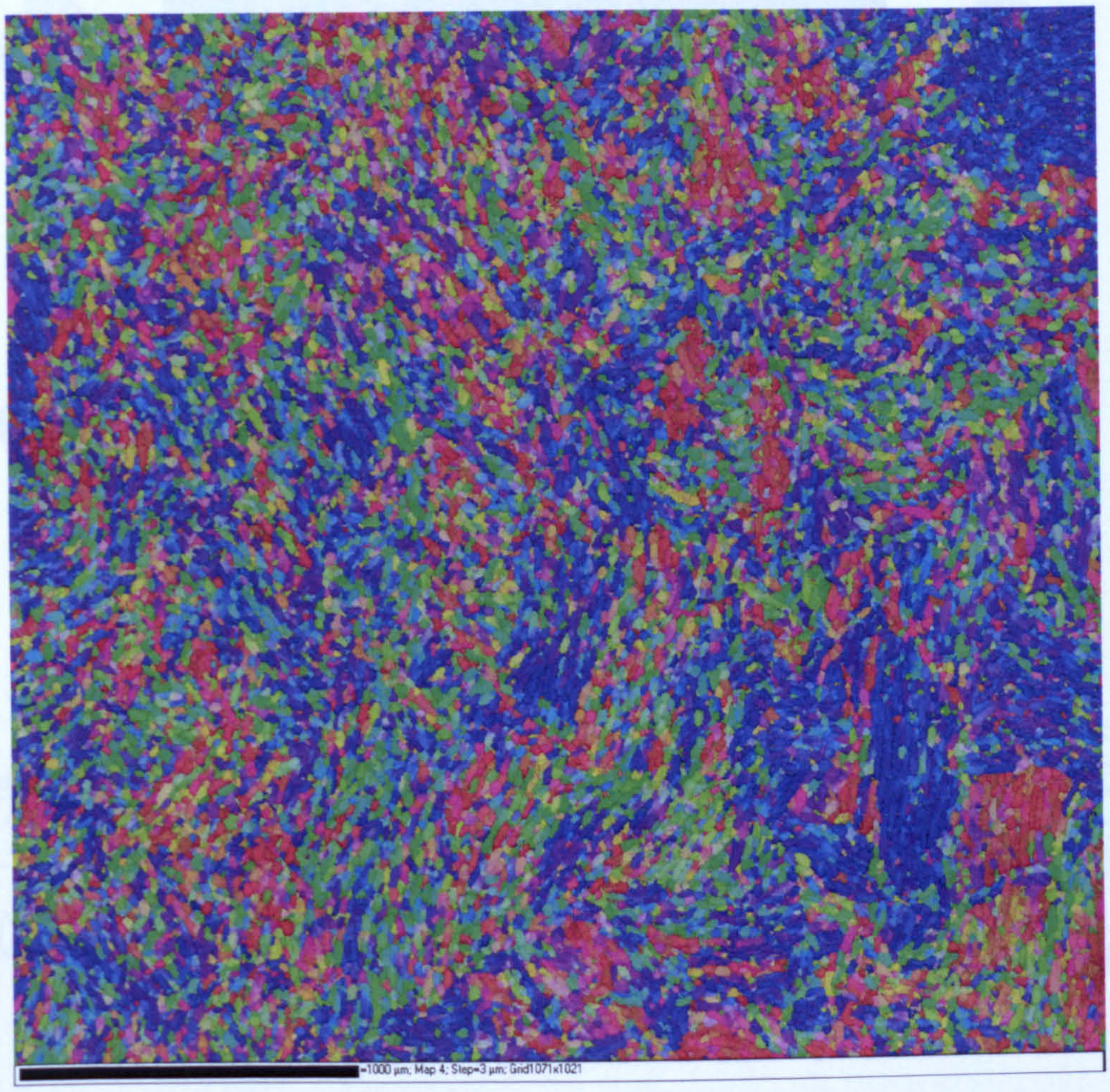

Fig. 5.9 EBSD map of the α phase in a transverse section (perpendicular to billet axis) from the centre of the billet (specimen 2). IPF colouring + band contrast.

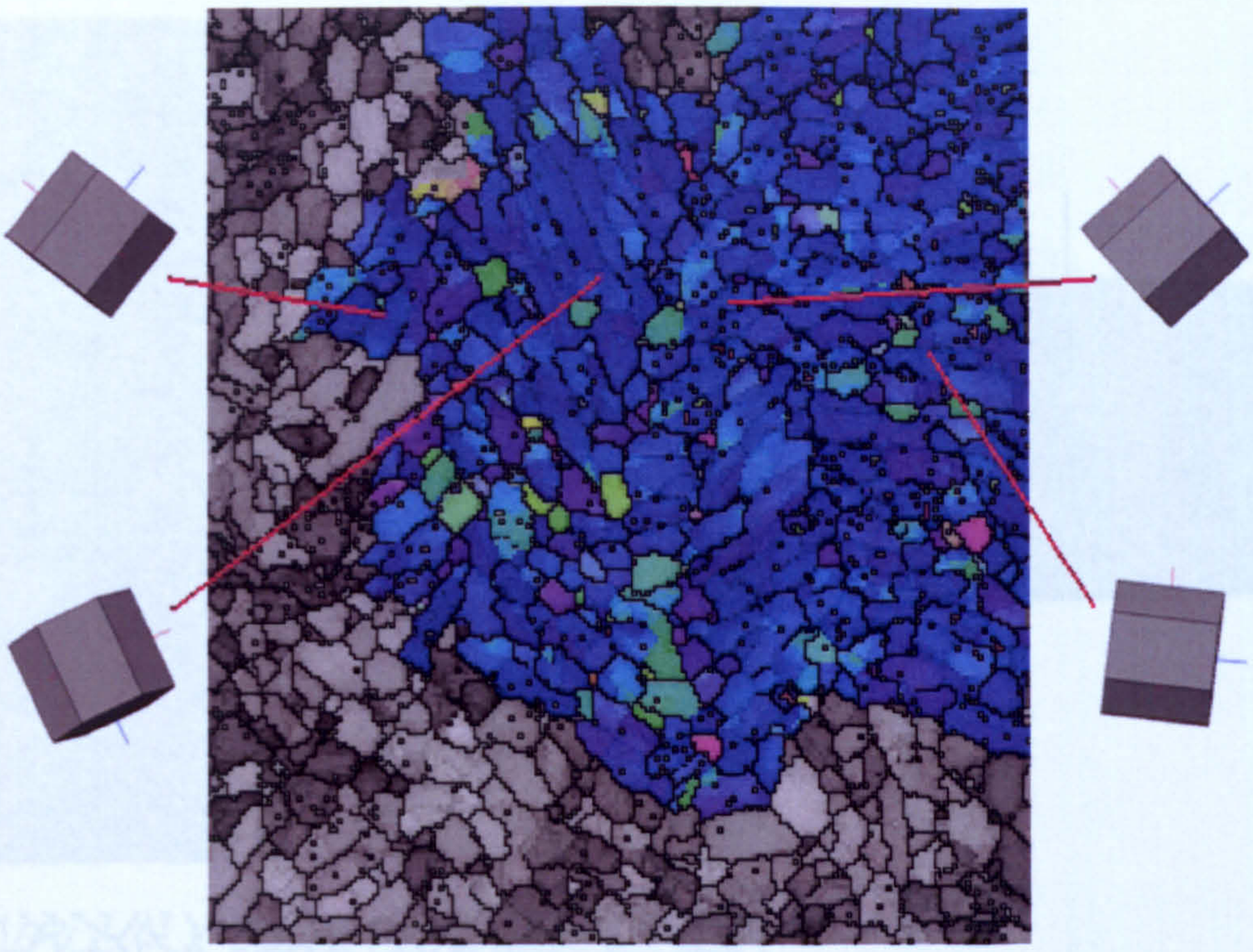

(a)

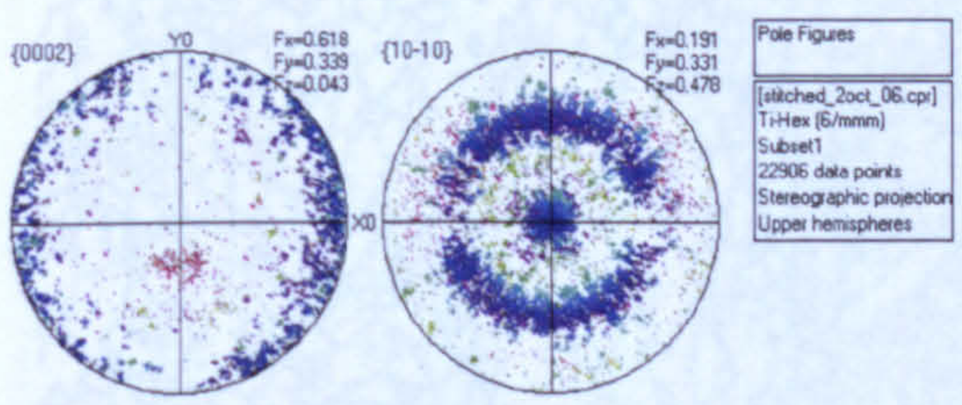

(b)

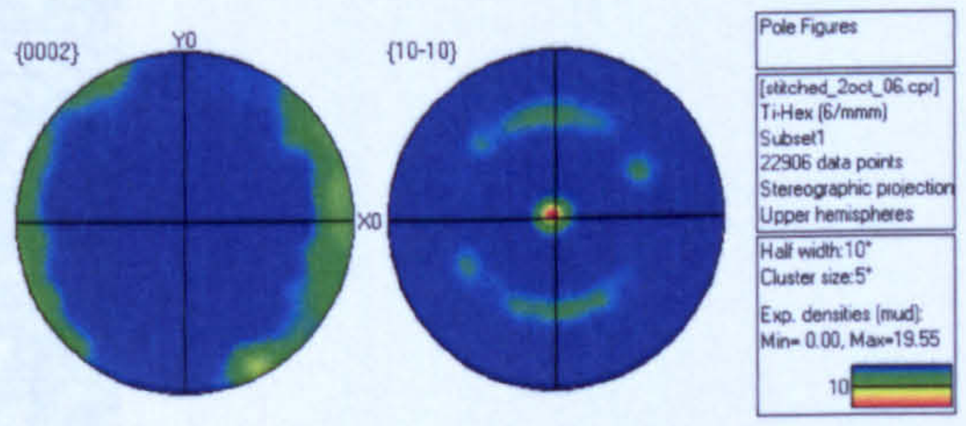

(c)

Fig. 5.10 An apparently large macrozone that shares common $\{10\,\bar{1}\,0\}$ planes but actually has a range of c-axis directions. This example shows evidence of large scale platelet bending and kinking of single prior colony of α lamellae.

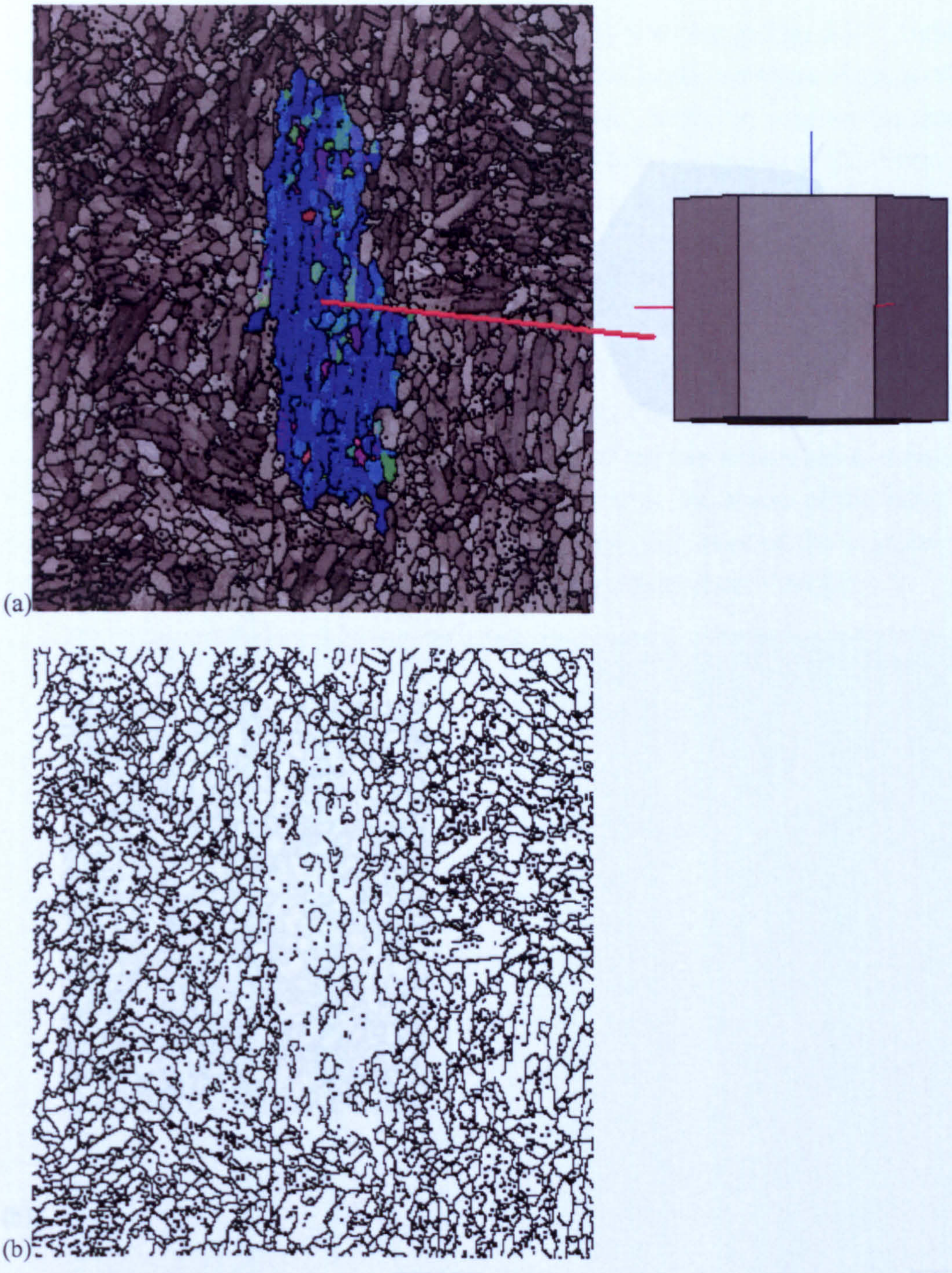

Fig. 5.11 Typical example of a blue, transverse macrozone from the centre of the billet.
(a) IPF of selected macrozone, (b) 15° misorientations, (c) pole figures, (d) contour plots.

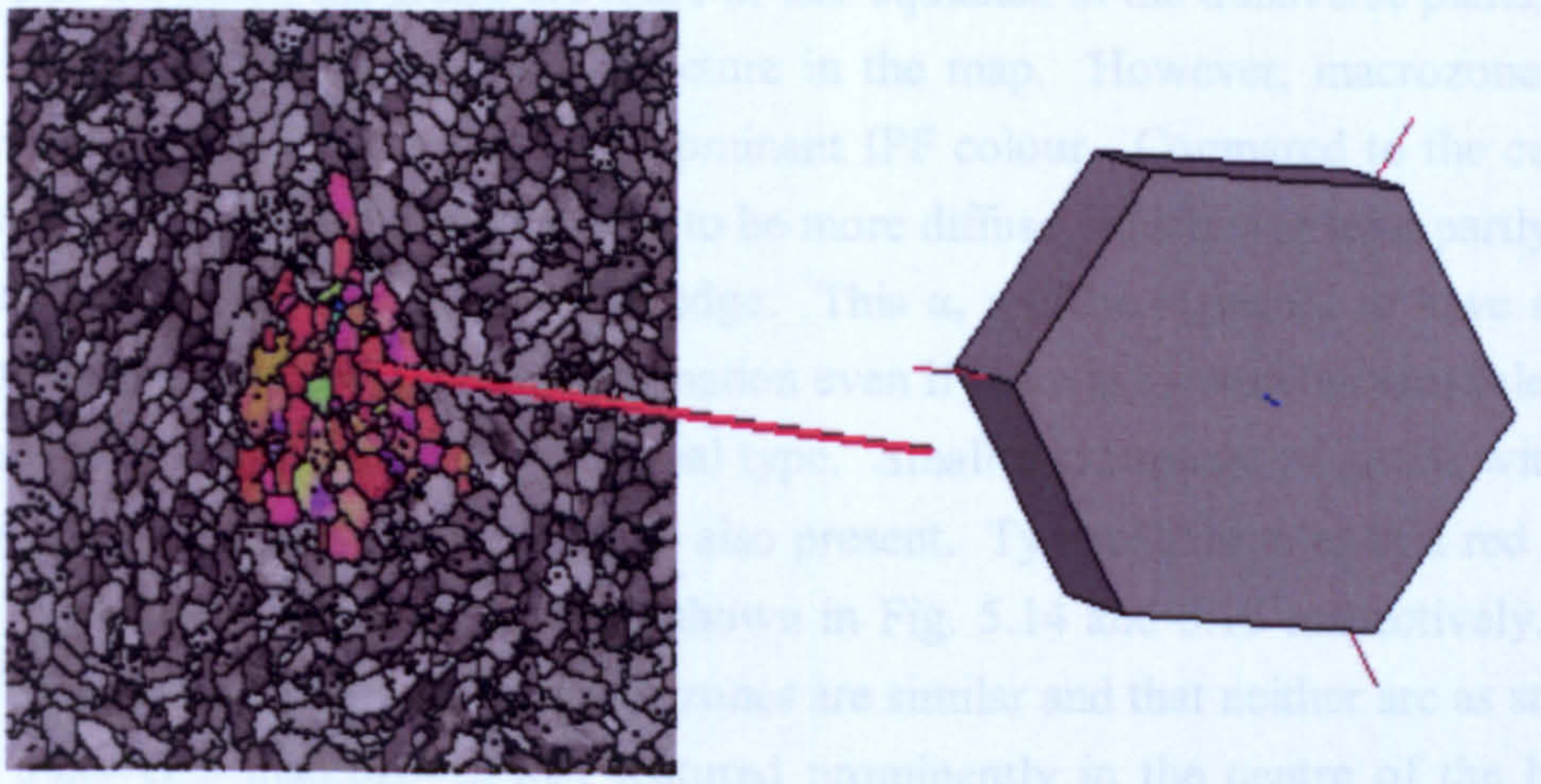

(a)

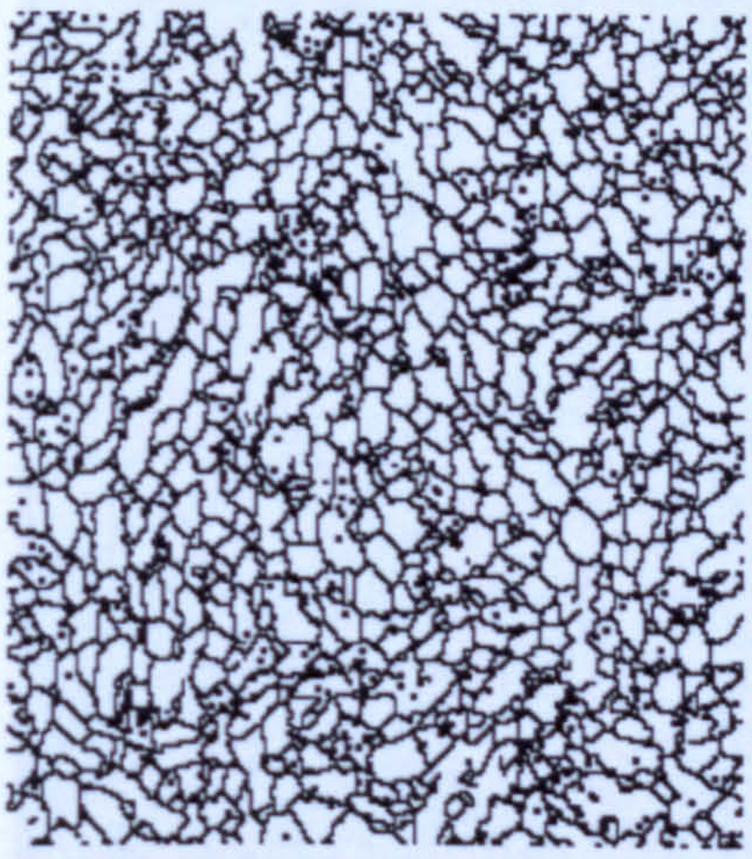

(b)

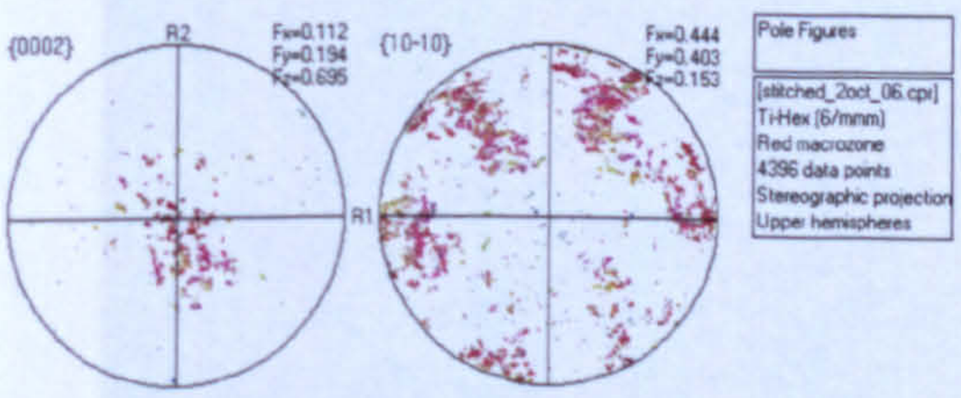

(c)

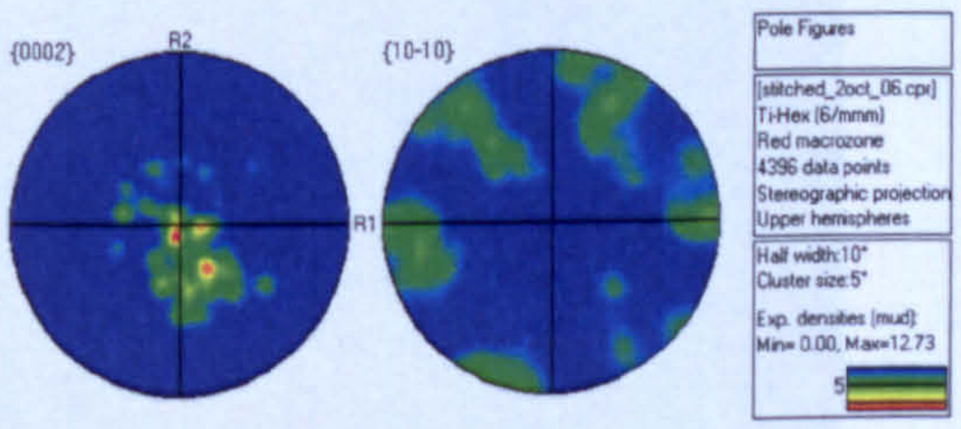

(d)

Fig. 5.12 Typical example of a red axial macrozone from the centre of the billet.
(a) IPF of selected macrozone, (b) 15° misorientations, (c) pole figures, (d) contour plots.

The map from the edge of the billet (specimen 1) is shown in Fig. 5.13. Unlike the centre of the billet, the grains are more or less equiaxed in the transverse plane, so there is no clear alignment of the grain structure in the map. However, macrozones can once again be identified as areas with a dominant IPF colour. Compared to the centre of the billet, macrozones at the edge appear to be more diffuse, which is at least partly due to the higher volume fraction of α_s at the edge. This α_s will be expected to have a spread of orientations due to the $\beta \rightarrow \alpha$ transformation even if there is a strong variant selection. The largest macrozones are of the red axial type. Smaller groupings of grains with blue and green transverse type orientations are also present. Typical examples of a red axial and a blue transverse type macrozone are shown in Fig. 5.14 and 5.15 respectively. It can be seen that the strengths of these macrozones are similar and that neither are as strong as the blue transverse macrozones that featured prominently in the centre of the billet. The boundary maps for the macrozones at the edge show that most of the α grains in the macrozones are misorientated from their neighbour grains by more than 15°.

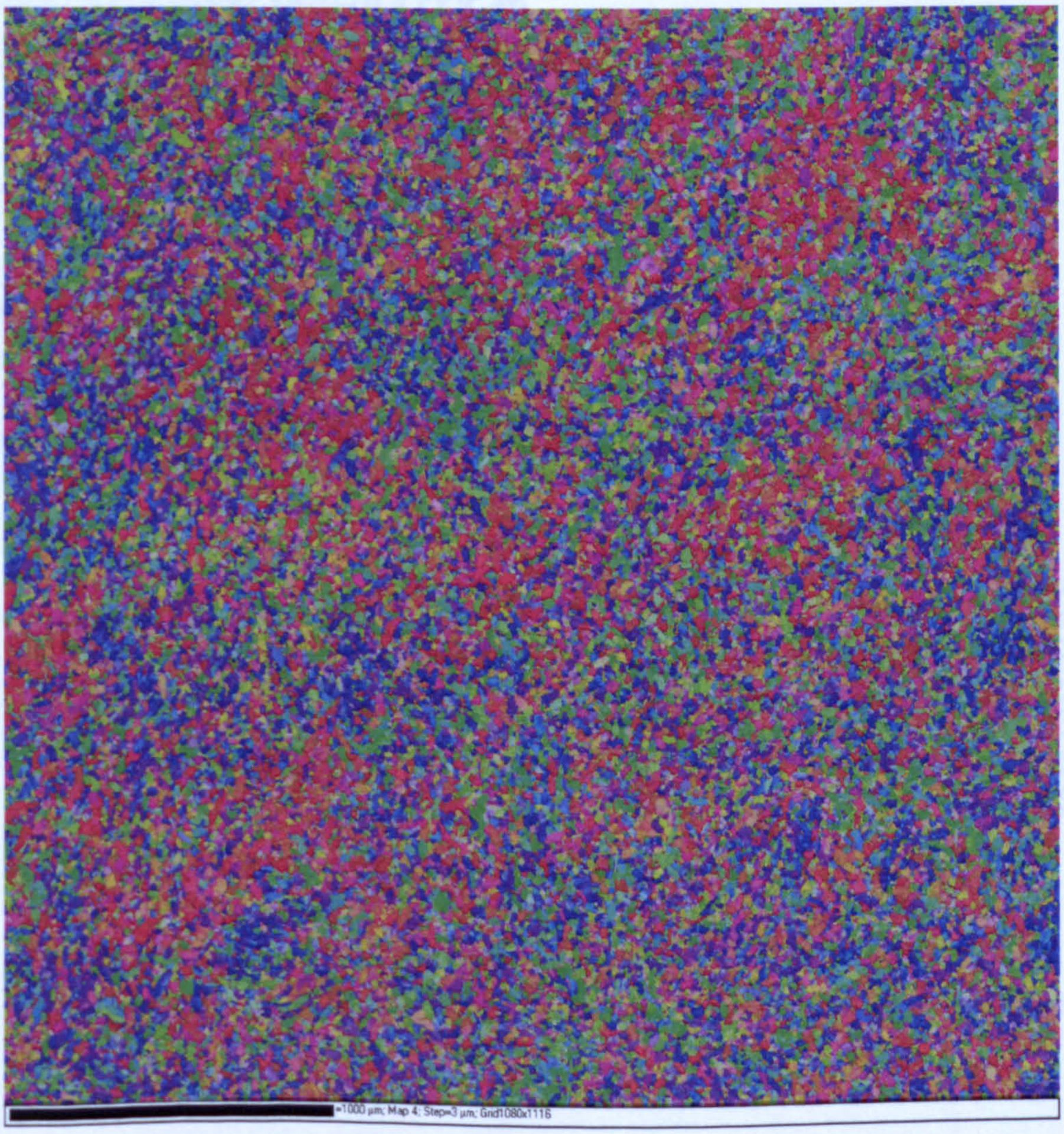

Fig. 5.13 EBSD map of the α phase in a transverse section (perpendicular to billet axis) from the edge of the billet (specimen 1). IPF colouring + band contrast.

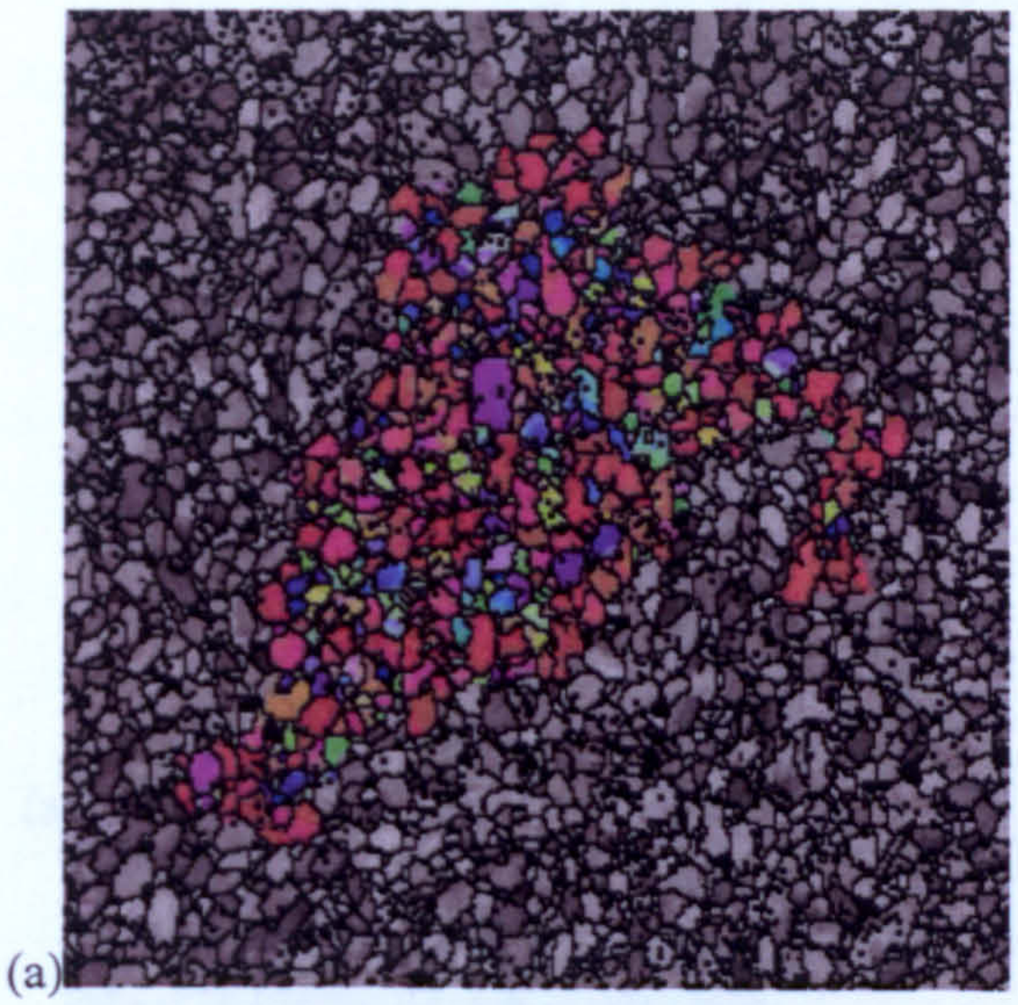

(a)

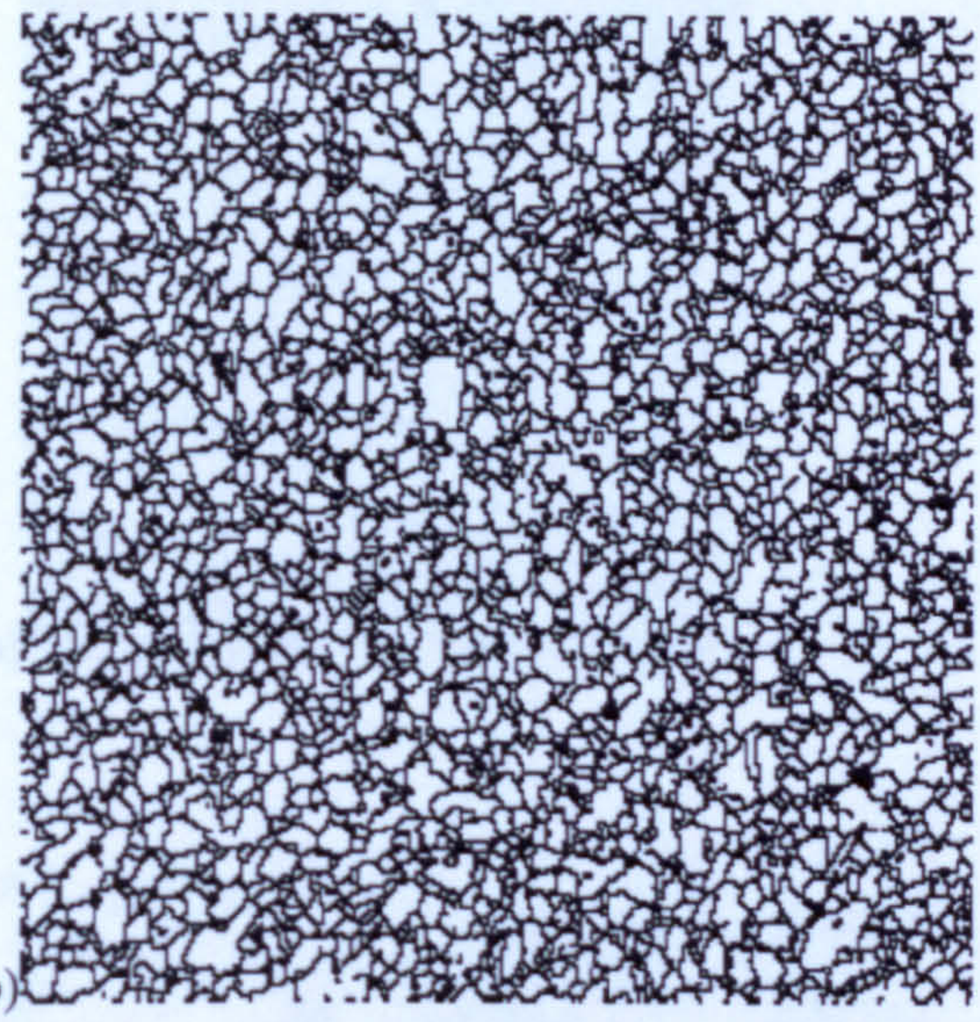

(b)

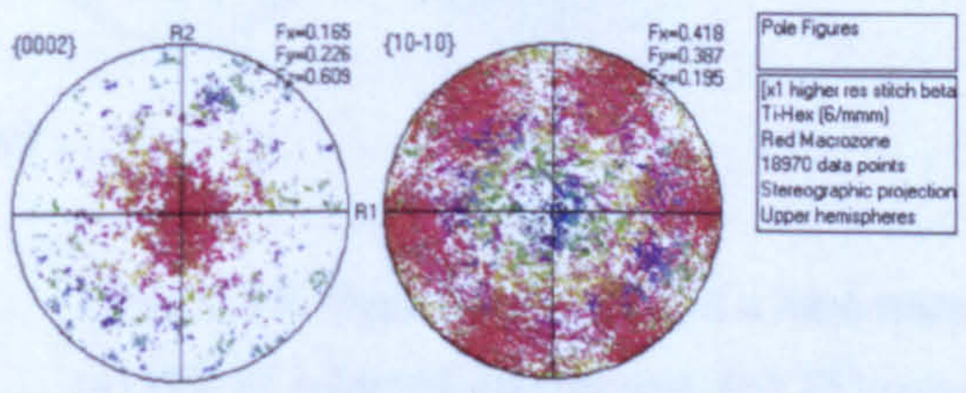

(c)

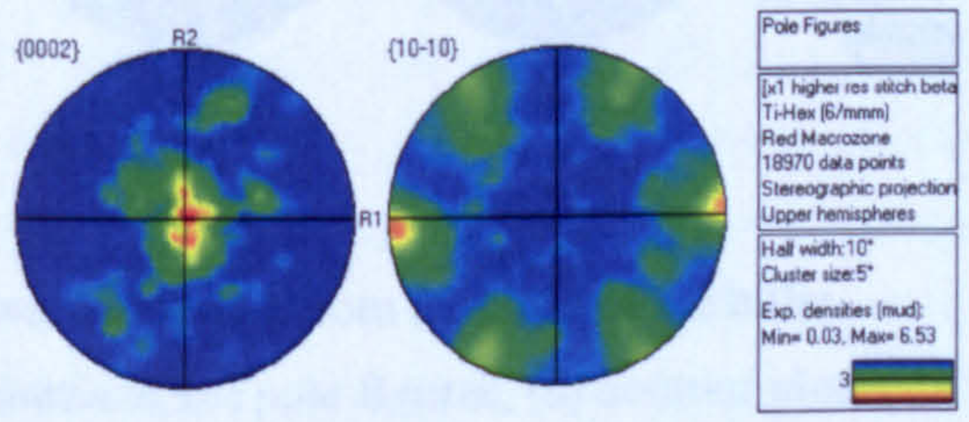

(d)

Fig. 5.14 Typical example of a red axial macrozone from the edge of the billet.
(a) IPF of selected macrozone, (b) 15° misorientations, (c) pole figures, (d) contour plots.

Fig. 5.15 Typical example of a blue transverse macrozone from the edge of the billet.
(a) IPF of selected macrozone, (b) 15° misorientations, (c) pole figures, (d) contour plots.

5.2.3 Characterisation of Global Textures and Macrostructural Alignment

In the previous section, it was demonstrated that the billet contained macrozones with strong local textures. It was shown that the macrozones tend to have two main orientations, with the c-axis either transverse or axial and that there was a difference in the relative amounts of these types between the centre of the billet and a specimen from the edge. For a more detailed study of the preferred macrozone orientations, one needs to examine global textures which encompass many macrozones. Global texture data were acquired using neutron texture analysis and large area, low resolution EBSD maps. The neutron texture analysis was carried out on specimens A to Q, with an illuminated volume of 1800mm^3. The low resolution EBSD maps were acquired from specimens 1 to 7 in the transverse plane of the billet using a step size of 10μm over areas of 4.5 x 7.5mm^2. To measure global textures in a microstructure containing macrozones, the volume or surface analysed must contain a sufficient number of macrozones to ensure that the data is statistically relevant. Randle and Engler (2000) reviewed the findings of various studies which have been carried out on the statistical relevance of single grain orientation measurements. The number of single orientation measurements which is necessary to represent adequately a texture strongly depends on the texture sharpness, with weak textures requiring many more orientation measurements. Drawing from the discussion by Randle and Engler, a reasonable guideline would seem to be that 100 single grain measurements usually yields a good qualitative estimate of the texture, while at least 500 and in some cases up to several thousand measurements are required for a statistically reliable texture to be derived.

Considering the case of the billet, the situation is more complex because the macrozones are not single grains. Despite this, using an estimate of the number of macrozones sampled, the above discussion can be used to gain a general idea on the suitability of the neutron diffraction and EBSD techniques for acquiring global textures. Assuming that the macrozones approximate to cylindrical regions aligned with the billet axis, with diameters of around 500μm and lengths 2000μm, then the specimens analysed by neutron diffraction would contain somewhere in the region of 4500 separate macrozones. This suggests that the neutron texture analysis has the capability of producing statistically representative textures. However, the accuracy of the calculated textures will also depend on the quality of the neutron texture data and the accuracy of the Rietveld fitting and pole figure calculations. For the EBSD analysis, assuming the same macrozone dimensions, each map would contain data from approximately 170 separate macrozones. This suggests that the EBSD analysis should at least produce good qualitative estimates of the global textures. Therefore, in terms of the number of macrozones sampled, both analyses would seem to be suitable for acquiring global texture data.

The results of the neutron and EBSD texture analysis are presented together in Fig. 5.16, in which each texture measurement is superimposed on the billet slice according to its location (see also Fig. 3.2). Each texture measurement is represented by an {0002} and a $\{10\bar{1}0\}$ pole figure contour plot in equal area projection. Orientation image maps for the EBSD analysis on specimens 1 to 7 are displayed in Fig. 5.17. Inverse pole figure (IPF) colouring is used with respect to the billet axis, which means that the colours show which crystallographic planes of the α phase lie in the transverse plane of the billet.

A direct comparison can be made between the EBSD and neutron texture analysis techniques by comparing the textures of specimens taken from adjacent regions in the billet cross-section i.e. 1 with A, 3 with C, 2 with E, and 6 with I. To aid this comparison, the pole figures for these specimens are shown in greater detail in Fig. 5.18. It can be seen that there is reasonably good agreement between the EBSD and neutron texture measurements, apart from relatively small differences in the intensity of some of the poles. The close agreement suggests that the neutron texture analysis has successfully reproduced the global textures, and also indicates that the areas analysed using EBSD were large enough for representative global textures to be acquired.

In general, the global billet textures were found to be quite weak, with maximum multiples of random distribution (m.r.d.) values of between 2 and 3. However, there are clearly global textures present, which indicates that the macrozones tend to have preferred orientations. Furthermore, these textures change depending on the location in the billet.

When the texture results (Fig. 5.16) are viewed in conjunction with the EBSD maps (Fig. 5.17), the most obvious trend is a centre to edge variation in the relative amounts of the transverse and axial macrozones. In the centre of the billet, the radial blue type gives rise to a dominant pole at the centre of the $\{10\bar{1}0\}$ pole figure and blue macrozones occupy the greatest portion of the map. A smaller amount of the axial red type are also present in the centre of the billet but the weaker local textures of the red macrozones means there is only a weak pole at the centre of the {0002} pole figure. As one moves from the centre of the billet to the edge, the relative amounts of the two types of macrozone change, so that at the edge of the billet the dominant macrozones are axial. This means that the pole at the centre of the $\{10\bar{1}0\}$ pole weakens, while the pole at the centre of the {0002} pole figure strengthens and red macrozones occupy the greatest portion of the maps. The centre to edge weakening of the pole at the centre of the $\{10\bar{1}0\}$ pole figures is shown graphically in Fig. 5.19 for both the EBSD and neutron texture measurements. It can be seen that there is an approximately linear decrease in the intensity as one moves from the centre towards the edge of the billet. Further illustration of the centre to edge trend is given in Fig. 5.20, which shows {0002} pole plots for the 7 specimens analysed using EBSD. In all cases, the pole plots are 'u' shaped, with a minimum intensity when the c-axis is rotated between 30° and 50° from the billet axis

and peaks at 0° and 90°, which correspond to the axial and transverse macrozones respectively. It can be seen that the intensity of the transverse peak (90°) is greater in the centre of the billet, the axial (0°) and transverse (90°) peaks have more or less equal intensity at the mid-radial positions and the axial peak (0°) has a higher intensity at the edge.

Another noticeable feature of the global billet textures is that they do not have fibre symmetry about the billet axis. The texture that most closely resembles a fibre is in the centre of the billet (specimens 2 and E). Here, the ring of intensity at the edge of the {0002} pole figures reflects how the c-axes in the transverse macrozones have a range of directions in the transverse plane. However, there is higher intensity in directions which are within approximately ±45° of the arbitrary R2 axis, which shows that there is preferential alignment of the transverse macrozones in these directions. Further away from the centre of the billet, there is a stronger preferential alignment of the c-axes in the transverse plane. In many locations in the cross-section, there is a similar direction for this preferred alignment, with the c-axes lying in a radial direction approximately 30° clockwise from the arbitrary R2 axis. Where the preferential alignment is strongest, a band of intensity connects the {0002} poles at the edge of the pole figure, with the {0002} pole in the centre.

As well as the alignment in the pole figures, there is also a subtle alignment of the macrostructure in some of the low resolution EBSD maps (Fig. 5.17), most notably in specimens 1, 3, 5 and 6. The direction of this macrostructural alignment is similar and corresponds to the direction of the bands of intensity in the {0002} pole figures i.e. a radial direction approximately 30° clockwise from the arbitrary R2 axis. These results indicate that in addition to the very strong primary alignment of the macrostructure along the billet axis, in some locations in the billet, there is also a secondary alignment of the macrostructure in a specific direction in the transverse plane.

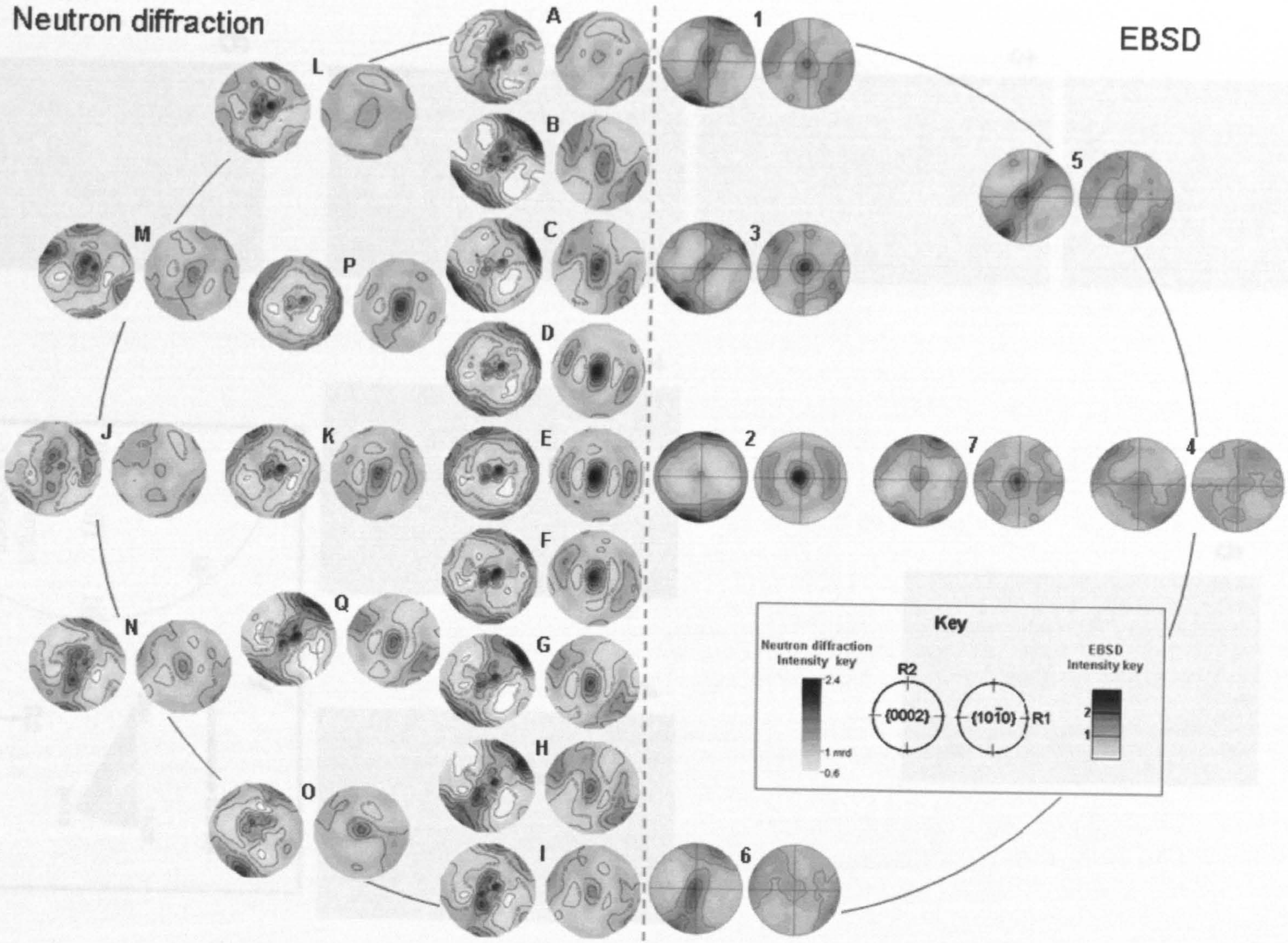

Fig. 5.16 Billet texture results. Specimens A-Q analysed by neutron diffraction, specimens 1-7 analysed by EBSD.

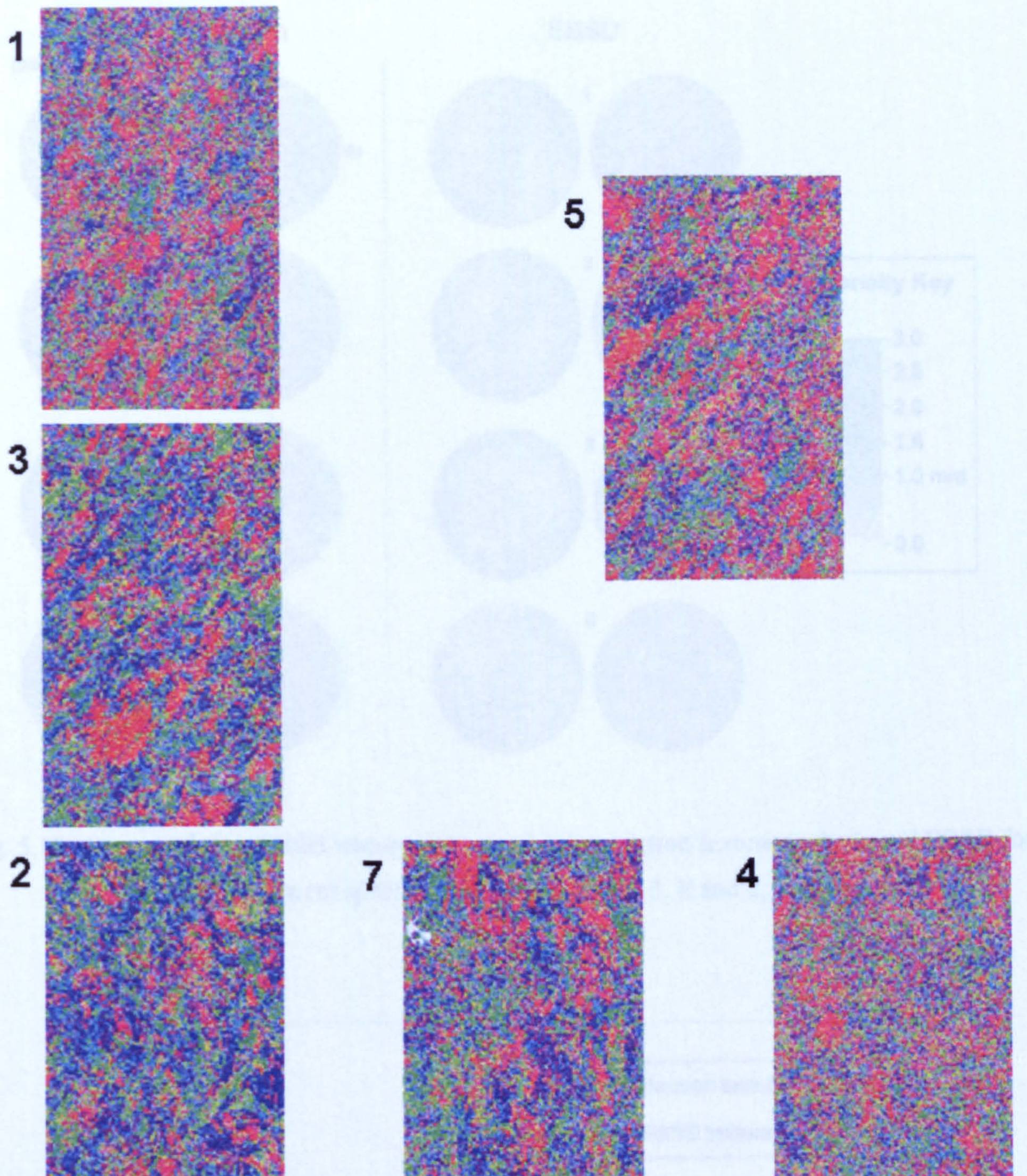

Fig. 5.17 Low resolution orientation image maps from the EBSD analysis.

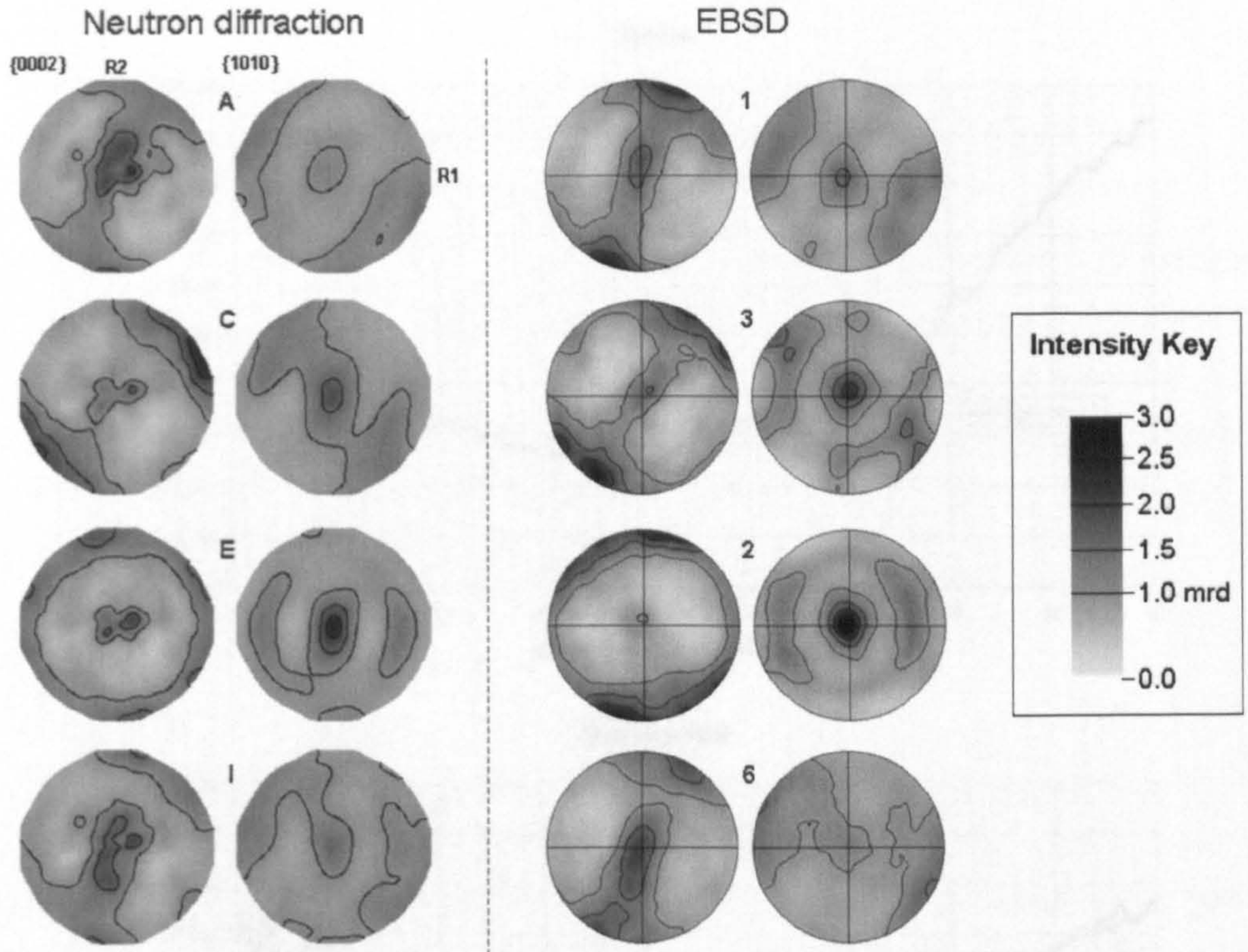

Fig. 5.18 A comparison of billet textures measured using neutron texture analysis and EBSD for 4 pairs of adjacent specimens (A and 1, C and 3, E and 2, I and 6).

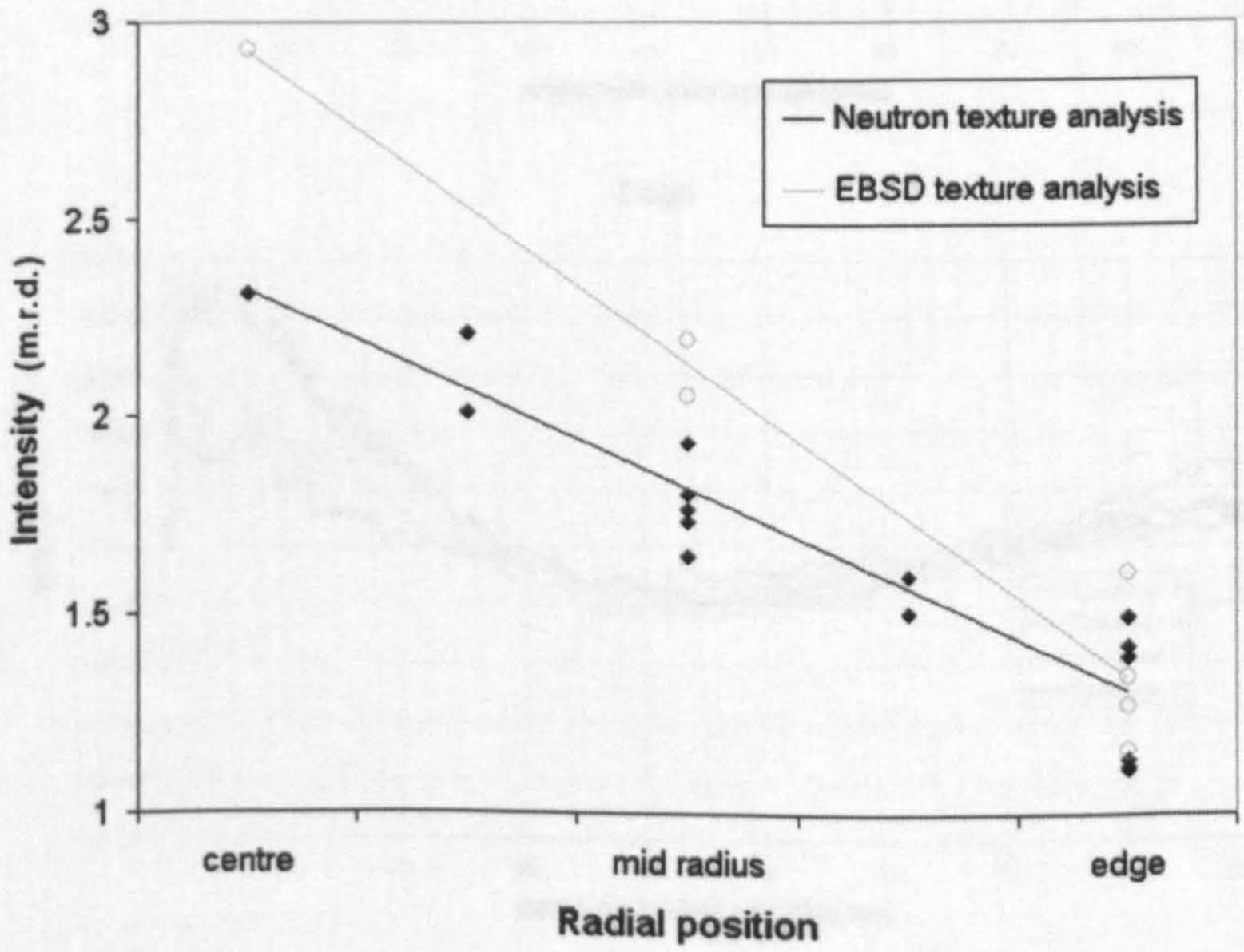

Fig. 5.19 Maximum m.r.d. intensity of the $\{10\,\bar{1}\,0\}$ pole with radial position for neutron and EBSD texture measurements.

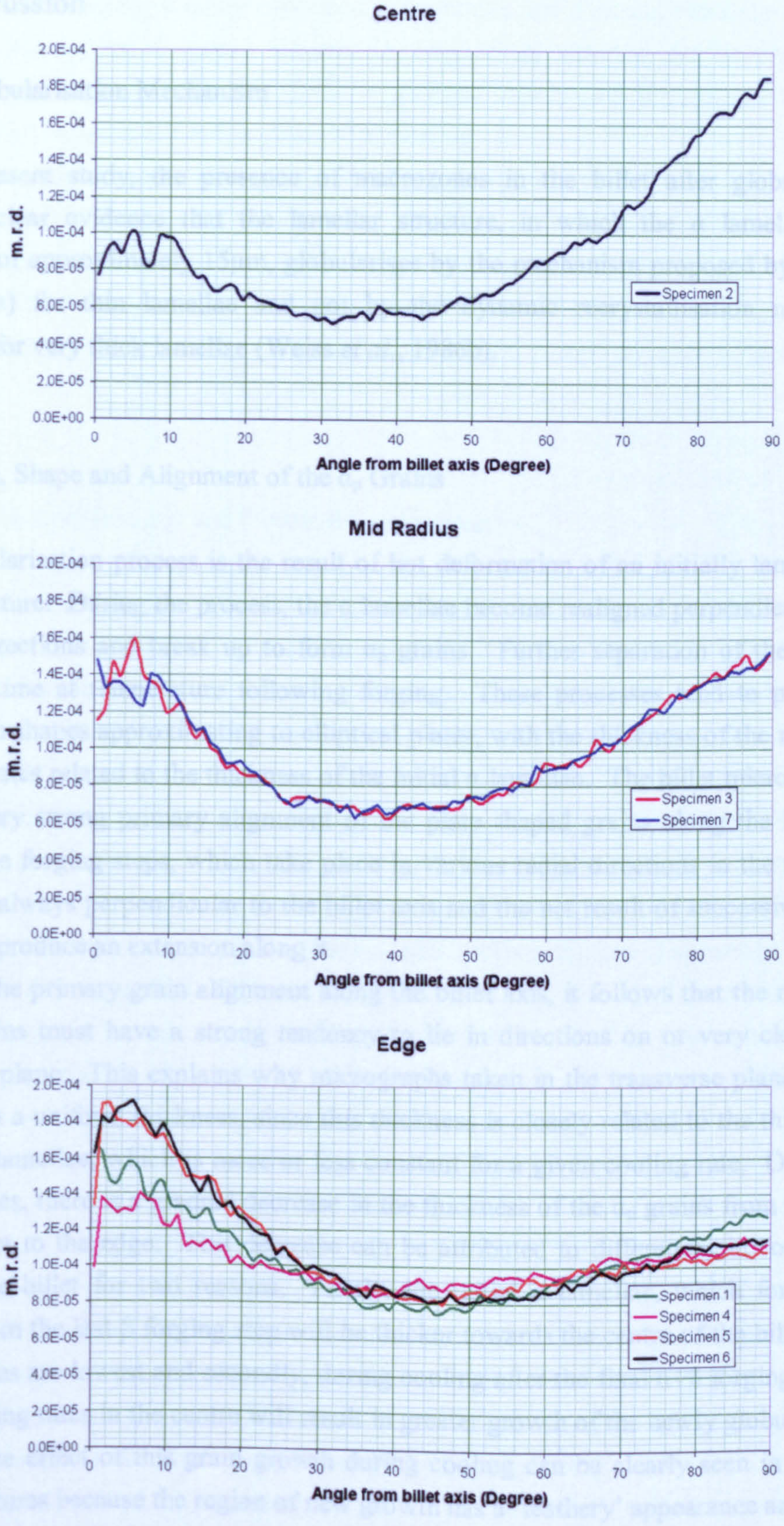

Fig. 5.20 {0002} pole plots for specimens 1 to 7 analysed using EBSD.
(a) Billet centre specimen. (b) Billet mid radius specimens. (c) Billet edge specimens.

5.3 Discussion

5.3.1 Globularisation Mechanism

In the present study, the presence of macrozones in the billet after globularisation provides clear evidence that the lamellar structure, in which the α lamellae had a thickness of approximately 15μm, globularises by the mechanism proposed by Weiss *et al.* (1986a) for thin lamellae and not by the dynamic recrystallisation mechanism proposed for very thick lamellae (Weiss *et al.*, 1986b).

5.3.2 Size, Shape and Alignment of the α_p Grains

The globularisation process is the result of hot deformation of an initially lamellar α+β microstructure. During the process, the α lamellae become realigned perpendicular to the forging directions and break up to form α_p grains. Further separation of the grains is aided by time at temperature following forging. These processes tend to produce α_p grains with shapes approximating to elliptical plates, with the thickness of the minor axis of these plates related to the thickness of the initial α lamellae. The billet microstructures show a very strong primary alignment of the plate shaped grains along the billet axis because the forging steps, which take place in various radial directions in the transverse plane, are always perpendicular to the billet axis and the net result of successive forging steps is to produce an extension along it.

Given the primary grain alignment along the billet axis, it follows that the minor axis of the grains must have a strong tendency to lie in directions on or very close to the transverse plane. This explains why micrographs taken in the transverse plane show α_p grains with a uniform thickness, since this thickness is closely related to the thickness of the initial lamellae, which is more or less constant for a given cooling rate. Over larger length scales, there is a gradual decrease in the thickness of the α_p grains from the centre of the billet to the edge. This decrease can be attributed to differences in cooling rate through the billet for two reasons. Firstly, the initial α lamellae, which form during cooling from the last β forging step will be thicker towards the centre of the billet, where cooling rates are lowest and secondly, during cooling after the final α+β forging step, the lower cooling rates in the centre will result in greater growth of the newly globularised α_p grains. The effect of this grain growth during cooling can be clearly seen in the billet microstructures because the region of new growth has a 'feathery' appearance and there is more of this 'feathery' grain growth in the centre of the billet compared to the edge.

The aspect ratio of α_p grains measured in a 2D section can be used as a measure of the degree of globularisation. This is best measured in a section from the transverse plane

because for the reasons already explained, this section has a strong tendency to contain the minor axis of the α_p grains, whereas in longitudinal sections, similar plate shaped grains may appear very different in terms of size and aspect ratio depending on how they are orientated with respect to the plane of sectioning.

Higher α_p aspect ratios, stronger macrozone textures and more necklace-like α_p grain structures are observed in the billet centre compared to the edge, which shows that the extent of globularisation in the centre is lower compared to the edges. This is in agreement with previous findings and can be attributed to the fact that the forging process generally imparts lower strains on the centre of the billet compared to the edge (Wilson *et al.*, 2003).

5.3.3 Macrozone Textures and Preferred Orientations

The results of the low resolution EBSD analysis (Fig. 5.17) have revealed that the billet contains macrozones throughout the cross section. The macrozones are related to prior colonies of aligned α lamellae, which have the same crystallographic orientation and as a result tend to deform and globularise in a similar manner, thus maintaining similar crystallographic orientations in the globularised α_p grains. The macrozones are large columnar shaped regions elongated along the billet axis. In certain locations of the billet, some macrozones also show a secondary elongation in the transverse plane.

Regardless of the location in the cross section, the α phase texture of a macrozone is always composed of a single hcp component, with varying degrees of spread up to around 30°. This is in agreement with macrozone textures reported by Thomas (2007), but differs from the macrozones analysed by Germain *et al.* (2005), which consisted of a dominant component and in addition, several weaker ones. The absence of the weaker components in this study and Thomas (2007) can be explained by the different proportions of α_p and α_s in the billet that was analysed by Germain *et al.* (2005). The billet in the work of Germain *et al.* (2005) contained 70% α_s, and by analysing the contribution of the α_p and α_s separately, it was shown that the α_s gave rise to the weaker components, while the dominant component was due to overlapping of a single α_p component and the main α_s component. In the present study, the highest volume fraction of α_s was only 30% at the edge of the billet, which is too low to produce significant secondary components in the macrozone textures. Consequently, the high volume fraction of α_p in the billet means that the overall α texture only shows the orientation of the single α_p component and thus a separation of the contribution of the α_p and α_s was not considered to be necessary for the macrozone textures in this work.

Analysis of the orientation image maps in conjunction with measurements of global texture, have shown that there is a tendency for the macrozones to have certain preferred

orientations. The majority of macrozones can be divided into two types: axial and transverse. In axial macrozones, the c-axes are aligned with the billet axis, which means that the basal {0002} planes lie parallel to the transverse plane. In the IPF maps obtained in the transverse plane, the axial macrozones appear as clusters of red grains. The individual α_p grains in the axial macrozones tend to be plate shaped with the plane of the plates parallel to the billet axis. This means that the c-axis direction tends to lie in the plane of the plate shaped grains.

In transverse macrozones, the c-axes lie in the transverse plane i.e. at 90° to the billet axis. The largest and sharpest macrozones in the billet were of this transverse type and also had a $\{10\bar{1}0\}$ plane lying in the transverse plane, thus appearing in the transverse plane IPF maps as clusters of blue grains. The individual α_p grains in the blue transverse macrozones tend to be plate shaped, with the plane of the plates parallel to the billet axis and aligned in the same transverse direction as other α_p grains within the same macrozone. The $<10\bar{1}0>$ direction and the c-axis direction tend to lie in the plane of the plate shaped grains.

The macrozones reported by Germain *et al.* (2005) in Timetal 834 billet and Bantounas *et al.* (2007) in Ti-6Al-4V bar were of the transverse type. Thomas (2007), in Timetal 834 billet reported mainly the transverse type but also one instance of the axial type. In this study, it was found that the relative amount of axial and transverse macrozones varies depending on the location in the cross-section. The most obvious trend is the centre to edge variation in the relative amounts of the two types of macrozone. The centre of the billet consists mainly of the transverse type, which have $(10\bar{1}0)$ planes lying in the transverse plane, and a lesser amount of the axial red type. As one moves from the centre to the edge of the billet, the relative amounts change so that the edge contains more of the axial macrozones and a lesser amount of the blue transverse type. This work suggests that axial macrozones are much more significant than suggested by previous studies, particularly at the edges of a billet.

5.3.4 Secondary Alignment of the Macrostructure in the Transverse Plane

While there is clearly a very strong primary alignment of the microstructure and macrozones along the billet axis, a secondary alignment of the macrozones was also noted in the transverse plane. The low resolution EBSD maps (Fig. 5.17) for specimens 1, 3, 5 and 6 revealed a subtle alignment of the macrostructure in a similar direction in the transverse plane. This direction corresponded to the preferred orientation of transverse macrozones in the global textures (Fig. 5.16). This secondary alignment can be explained by the non equal strains imposed about the billet axis by the forging process due to the fact that the billet was forged from a rectangular cross-section to a circular cross-section.

It is proposed that the long axis of the initial rectangular cross section probably lay perpendicular to the direction of the microstructural alignment in the transverse plane.

It is not surprising that the effect of the non equal strains is evident in the billet macrostructure and textures because work by Bescond *et al.* (2004) has shown that similar effects can also be detected by ultrasonic imaging. The resolution of the ultrasound is such that the noise is highly affected by the microstructure at the scale of the macrozones. Their work on a billet which had been forged from a square section to a circular one revealed two high noise bands separated by 90°, i.e. 2 axes of symmetry in the transverse plane. These were the result of the greater strains imposed between the corners of the billet. The present study differs in that the billet was forged from an initial rectangular cross section, the dimensions of which mean that the effect of the corners seen by Bescond *et al.* would be relatively small compared to the effect of the different lengths of the rectangle. This may explain why only one axis of symmetry in the transverse plane dominates in this work. The effect of the different strains imposed about the billet axis is shown in Fig. 5.20, which shows the percent reductions about the billet axis required for the shape change in the final $\alpha+\beta$ forging step from the initial rectangular cross-section to the round cross-section of the final billet. It should be noted that this figure is a simplified case because it ignores the effects of redundant work due to side spreading and the fact that the final shape produced by forging is actually an octagon and not a perfect circle. However, it serves to show that the required reduction along the long transverse axis is approximately double that of the short transverse axis and that in comparison, the increases in reduction at the corners is relatively small.

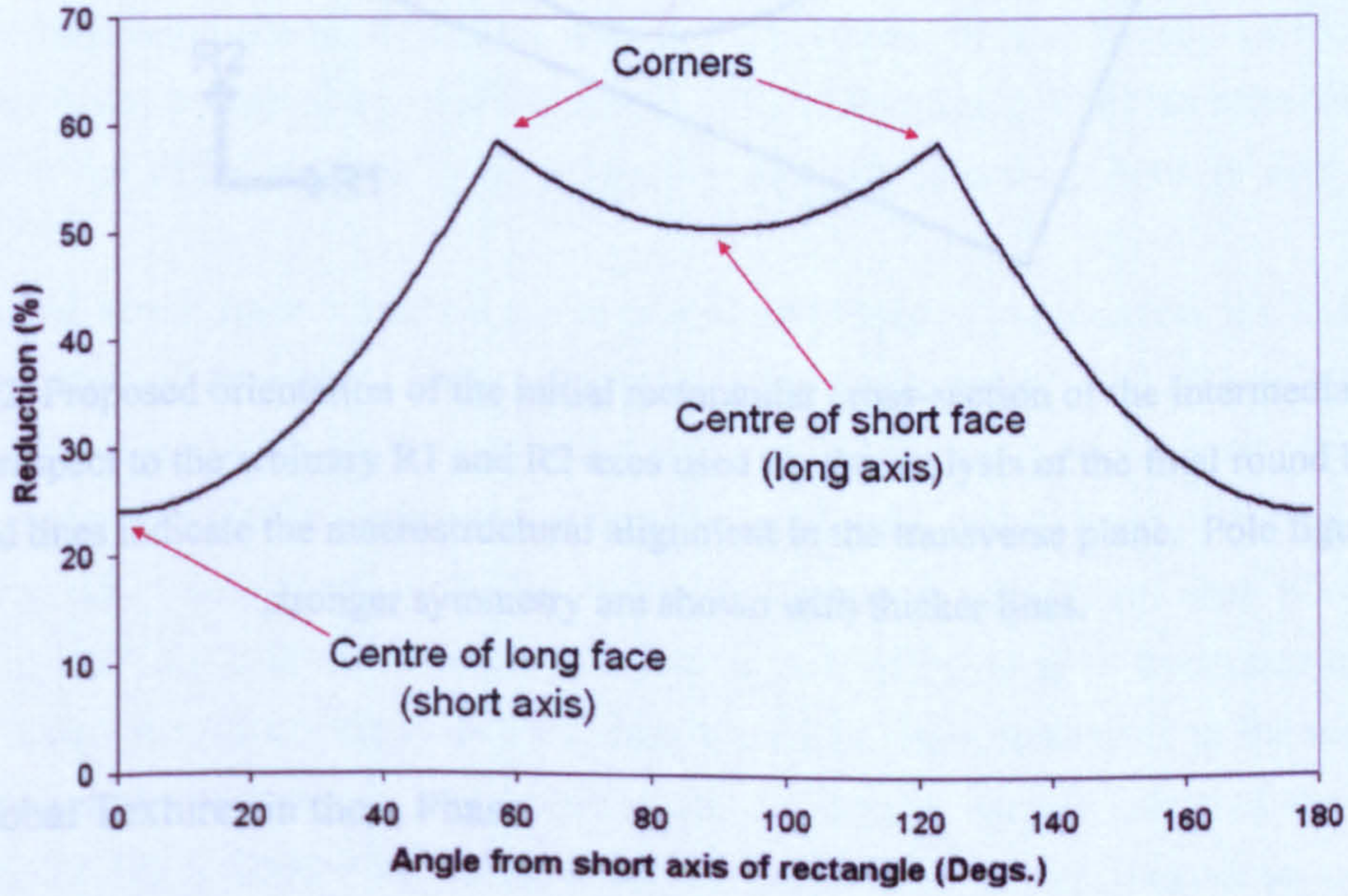

Figure 5.21 The percent reductions about the billet axis for the cross-sectional shape change from a rectangular cross-section to a round cross-section in the final $\alpha+\beta$ forging step.

The low resolution EBSD analysis suggests that there is a correspondence between a macrostructural alignment in the orientation maps and a preferred alignment of the transverse texture in the corresponding pole figures. This means, that although there are no orientation maps for the neutron texture results, a strong preferred alignment of the transverse texture in these pole figures can be used to predict macrostructural alignment in the transverse plane. Then, assuming that the long transverse axis of the initial rectangle is perpendicular to the average direction of macrostructural alignment, the most likely location of the axes of the initial rectangle with respect to the arbitrary R1 and R2 axes as can be established. Fig. 5.22 shows the predicted macrostructural alignment for all locations in the billet where global textures were measured and the proposed orientation of the initial rectangle with respect to R1 and R2. Using this method, the long axis of the rectangle was determined to be approximately 30° clockwise from the R1 axis.

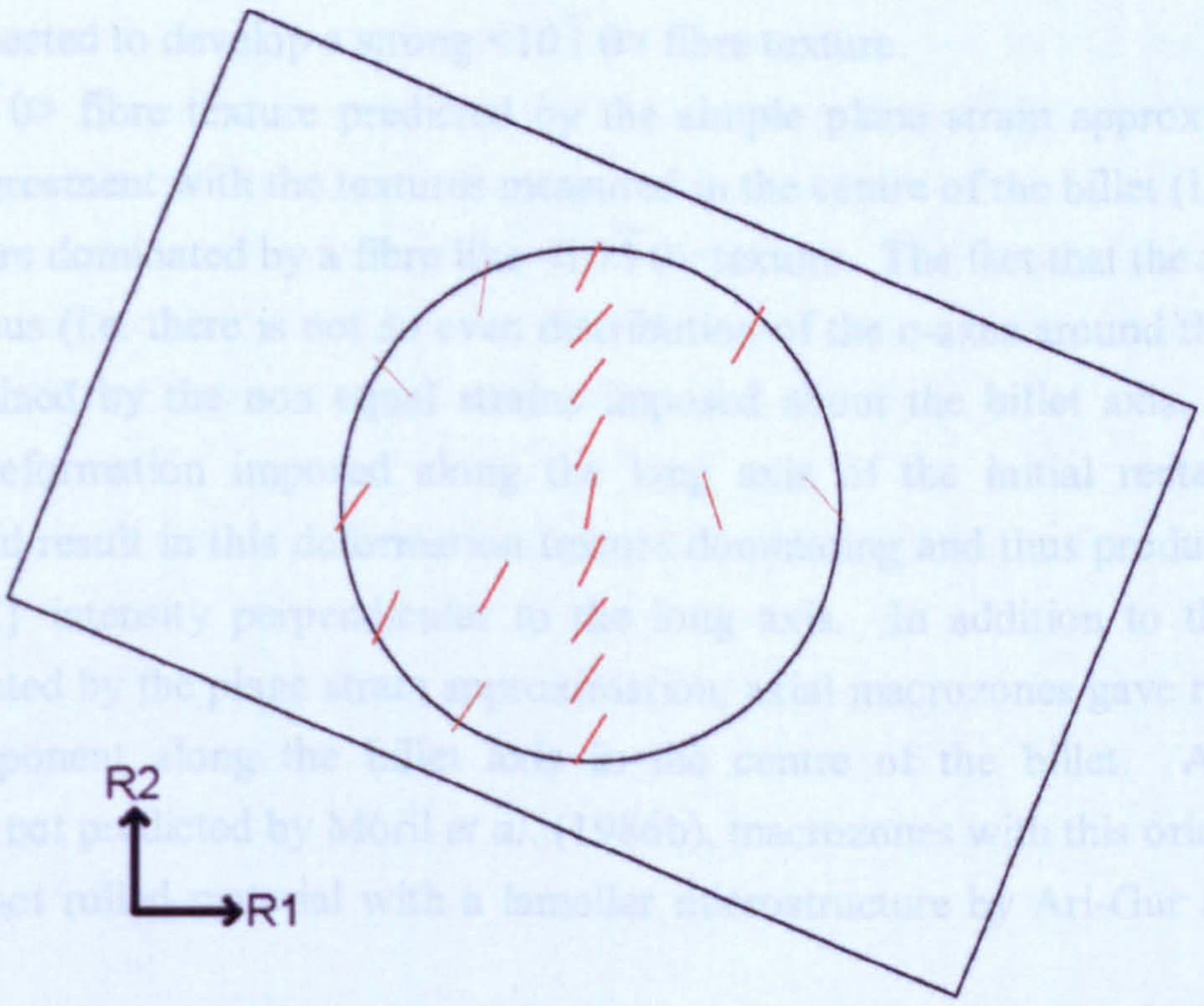

Fig. 5.22 Proposed orientation of the initial rectangular cross-section of the intermediate billet with respect to the arbitrary R1 and R2 axes used for the analysis of the final round billet. Coloured lines indicate the macrostructural alignment in the transverse plane. Pole figures with stronger symmetry are shown with thicker lines.

5.3.5 Global Textures in the α Phase

Forging billets using an open die forge induces 3 dimensional metal flow; however, as most of the deformation involved produces an elongation along the billet axis, previous

workers have shown that in some cases, reasonable approximations can be made by treating each individual forging bite as a plane strain deformation (Fox and Neal, 1995. Dumas *et* al., 1995). Using this plane strain approximation, the expected deformation texture for each forging bite should be the same as the rolling texture for 2 phase titanium alloys reported in the literature. Moril *et al.* (1986b) reported the rolling texture for an initially lamellar microstructure to be $\{1\bar{2}10\}<10\bar{1}0>$, whereas for a globular microstructure, there is still a preference for the $\{1\bar{2}10\}<10\bar{1}0>$ component but there is also a fibre like scatter around RD. Based on this information, deformation of the billet should initially develop $\{1\bar{2}10\}<10\bar{1}0>$ textures with each forging bite, but as the microstructure becomes increasingly globularised and the correlations in morphology and orientation between neighbouring grains become weaker, more of a fibre like scatter around RD would be expected. Regardless of the state of the microstructure (i.e the degree to which it is lamellar or globular), successive deformations around the billet axis would be expected to develop a strong $<10\bar{1}0>$ fibre texture.

The $<10\bar{1}0>$ fibre texture predicted by the simple plane strain approximation is in reasonable agreement with the textures measured in the centre of the billet (i.e. specimens 2/E), which are dominated by a fibre like $<10\bar{1}0>$ texture. The fact that the fibre is rather inhomogeneous (i.e. there is not an even distribution of the c-axes around the billet axis) can be explained by the non equal strains imposed about the billet axis. The greater amount of deformation imposed along the long axis of the initial rectangular cross section, would result in this deformation texture dominating and thus produce regions of higher {0002} intensity perpendicular to the long axis. In addition to the transverse texture predicted by the plane strain approximation, axial macrozones gave rise to a weak <0002> component along the billet axis in the centre of the billet. Although this orientation is not predicted by Moril *et al.* (1986b), macrozones with this orientation were observed in hot rolled material with a lamellar microstructure by Ari-Gur and Semiatin (1998).

The plane strain approximation gives a less satisfactory explanation for the textures seen at the edge of the billet. These textures contain the expected $<10\bar{1}0>$ pole along the billet axis but it is weaker and has a strong preferred alignment of the c-axes. In addition, there is a stronger <0002> component along the billet axis, with a band of higher intensity connecting this component with the basal maximum in the transverse plane. The differences seen towards the edge may be due to flow of material in directions other than the billet axis. A greater degree of spreading would be expected closer to the edge of the billet because the material is less constrained. A greater spread effect at the edges is supported by the evidence of macrostructural alignment in the transverse plane. A significant degree of side spread perpendicular to the rolling direction may be responsible for the increase in axial macrozones at the edge of the billet.

6 DETERMINATION OF THE β APPROACH CURVE

6.1 Introduction

This short chapter shows the results of the work carried out to determine the β approach curve for the billet used in this work. The results are compared with data for two other Timet 834 billets.

6.2 Results

The volume fraction measurements for the eight specimens solution heat treated at different temperatures in the α+β phase field are given in Table 6.1. This data is plotted in Fig. 6.1 to give the β approach curve for the Timet billet used in this study. From the shape of the fitted curve in the upper end of the α+β phase field and the very small amount of α_p present after the solution treatment at 1050°C (i.e. <1%), the β transus temperature (temperature at which α+β → β) is believed to be between 1050 and 1055°C. The gradient of the β approach curve varies in the temperature range investigated, showing a steepening in the temperature range 1000-1020°C.

Table 6.1 Volume fraction measurements for billet solution heat treated at different temperatures in the α+β phase field.

Specimen	Temperature (°C)	% α_p (1)	% α_p (2)	% α_p (3)	Average % α_p	Average β Volume
A	1050	0.8	0.9	0.4	0.7	99.3
B	1040	5.1	5.3	5.0	5.1	94.9
C	1030	16.5	15.1	13.5	15.0	85.0
D	1020	10.2	11.9	12.1	11.4	88.6
E	1010	26.1	28.9	24.5	26.5	73.5
F	1000	47.8	53.7	45.4	49.0	51.0
G	990	55.0	58.3	52.5	55.3	44.7
H	960	75.3	73.2	74.4	74.3	25.7

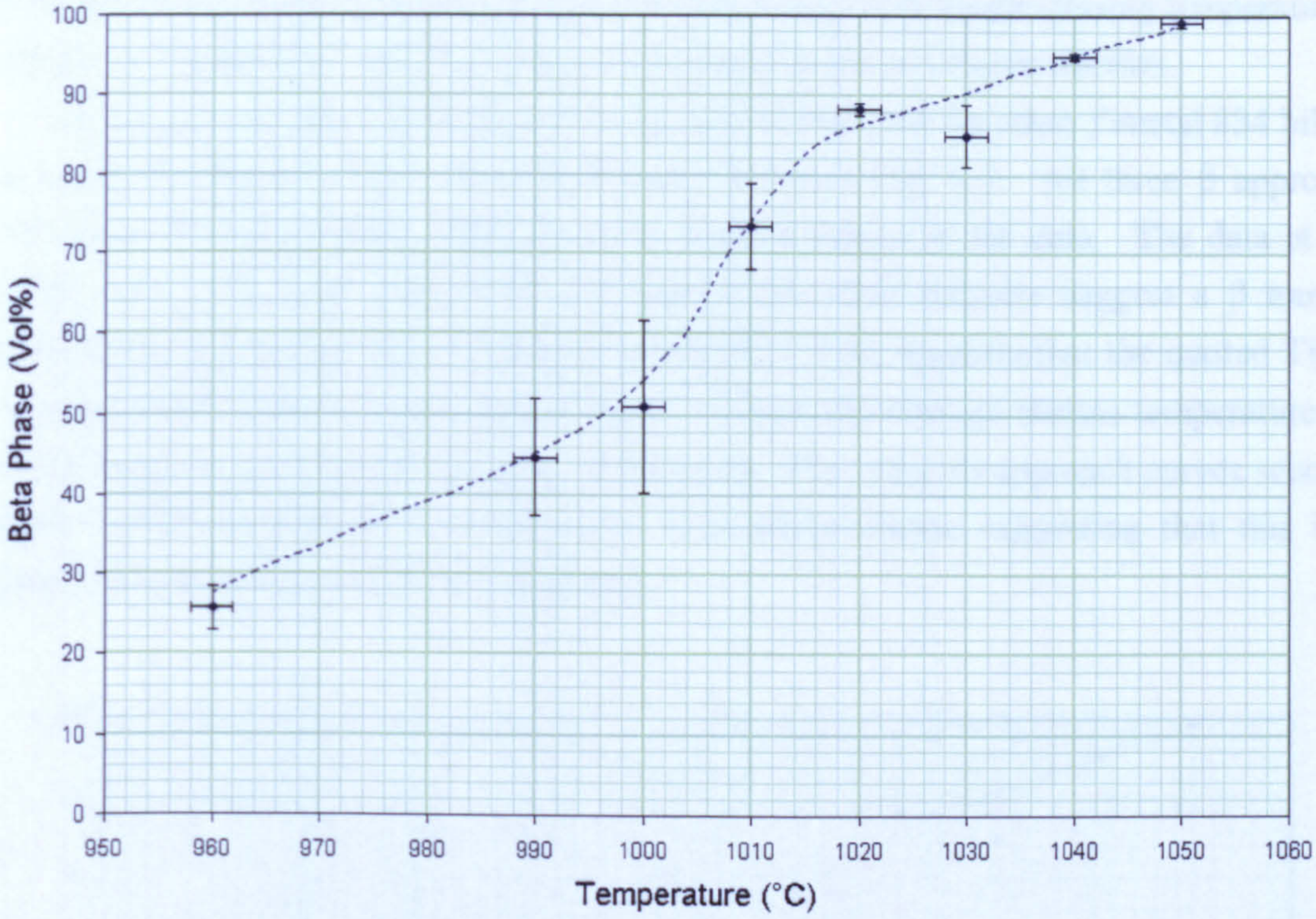

Fig. 6.1 The β approach curve determined for the Timet Billet.

6.3 Discussion

The predicted β transus temperature of between 1050 and 1055°C is higher than the typical value of 1045°C quoted by Timet for the alloy (Timet, 2000). However, values are known to vary from those typically quoted due to the effect that small changes in composition can have on the phase diagram. In particular, small variations in the carbon content, itself a very minor addition can have significant effects on the β approach curve. For this reason, it is industry practise to determine a β approach curve for every ingot produced, rather than relying on a standard. This allows the forging industry to adjust solution treatment temperatures for each forging in order to develop the precise volume fraction of α_p desired in the final microstructure.

The typical solution temperature quoted by Timet to develop a bimodal microstructure containing the recommended 15% α_p is 1015°C (Timet, 2000). The β approach curve for this work is in good agreement, predicting an α_p volume fraction at 1015°C of 17% with an error of approximately ±3%.

The steepening seen in the β approach curve for this work is interesting as the typical solution temperature for secondary forging (1010°C) and final solution heat treatment (1015°C) lie in the steep part of the curve. This means that despite the relatively wide

temperature range of the α+β phase field, at industrially relevant processing temperatures, changes in temperature will lead to greater changes in the α_p volume fraction.

The β approach curve for this work is compared with data for other Timetal 834 billets in work by Thomas (2007) and Blackmore (2008) in Fig. 6.2. All three β approach curves are broadly similar, although there is some scatter in the data. The data at the upper end of the α+β phase field for both of the other datasets suggest a β transus temperature higher than the Timet quoted 1045°C. This suggests that the quoted Timet value of 1045°C may be lower (by at least 5°C) than the average transus temperature for billets produced at Timet's UK plant. Both of the other datasets approach curves seem to show similar steepenings at intermediate α+β temperatures, suggesting that this is a general characteristic of the billet material.

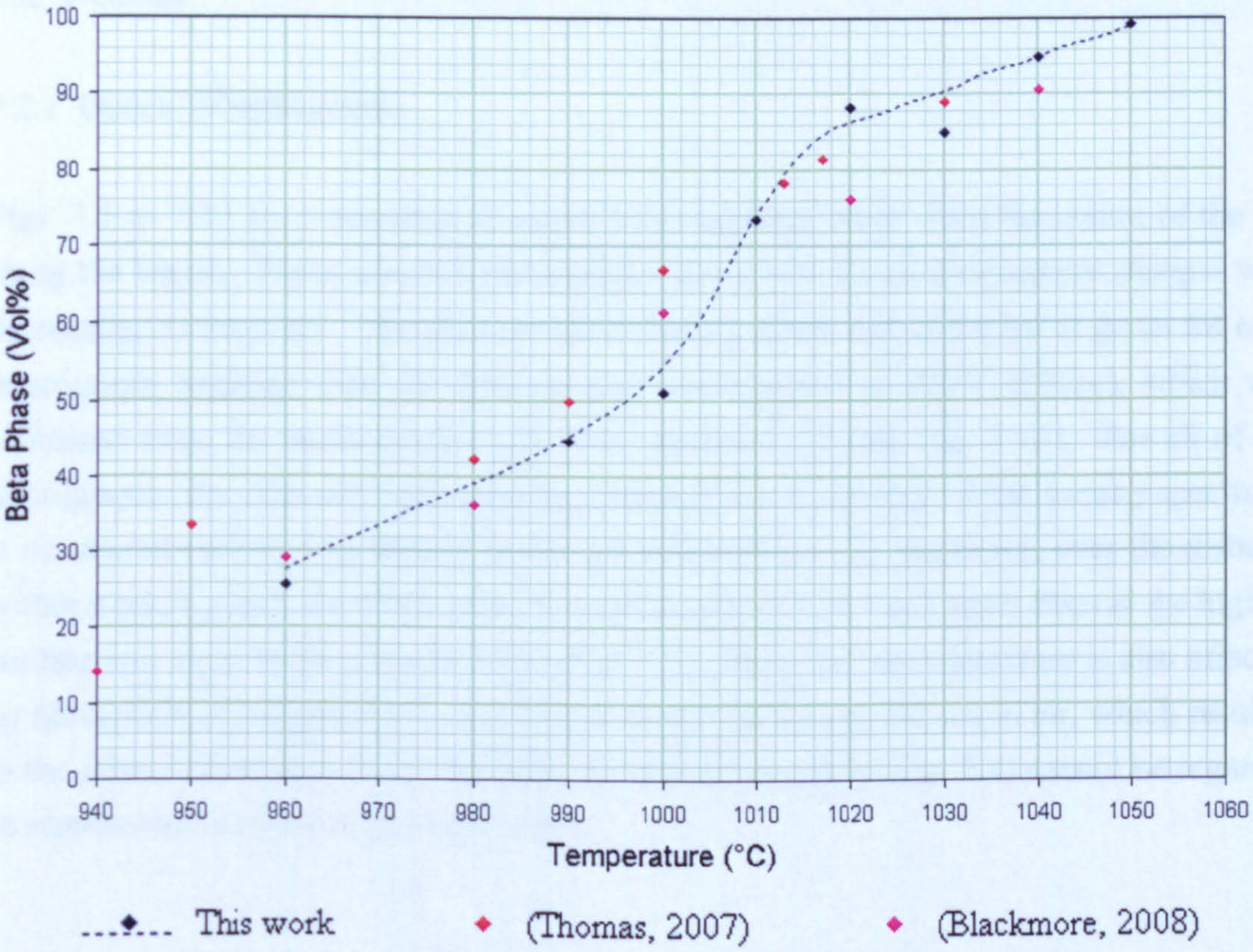

Fig. 6.2 A comparison with β approach curve data for 2 other Timet 834 billets.

7 PHASE TRANSFORMATIONS DURING COOLING

7.1 Introduction

This chapter concerns the work that was carried out to investigate the effect of cooling rate on the β→α phase transformation in Timetal 834 using a modified Jominy end quench test. After initial characterisation of the microstructures along the bar using optical microscopy and SEM, EBSD maps were acquired in selected locations. Use of the β reconstruction program enabled instances of local variant selection to be investigated and the possible effect of these events on the texture to be assessed.

7.2 Results

7.2.1 Optical Metallography

Figs. 7.1 to 7.20 are a selection of optical micrographs, taken from the centre of the bar along the length. These selected micrographs show how the microstructure changes with decreasing cooling rate. The distance from the quenched end of the bar is given for each micrograph, together with the instantaneous cooling rate at 900°C (CR_{900}), which was estimated from the thermocouple data (see section 3.4.2 and Fig. 3.10). For all of the micrographs, the direction of decreasing cooling rate i.e. the axis of the Jominy specimen, is orientated vertically as shown on the left side of Fig. 7.1. However, over the distance within a micrograph, the differences in cooling rate will be small apart from at the highest cooling rate close to the quenched end (Fig. 7.1). Here, the microstructure is also affected by absorption of oxygen due to the heat treatment being carried out in air, which resulted in the formation of an α-case. As such, the first micrograph (Fig. 7.1) cannot be regarded as representative of the bulk composition.

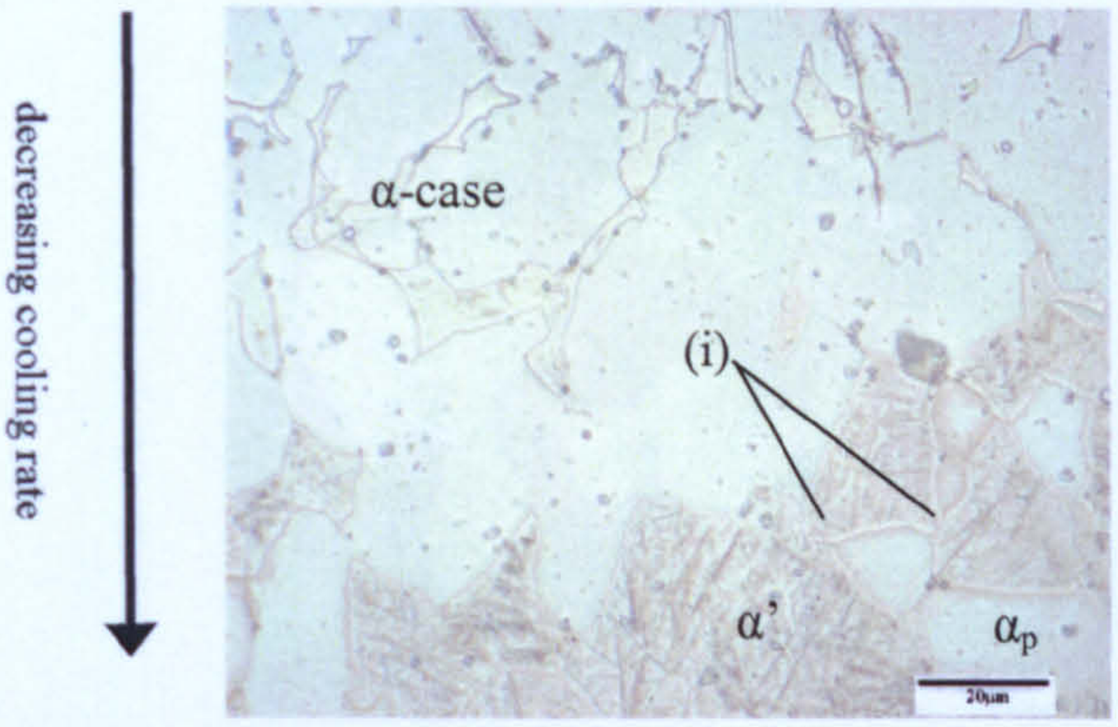

Fig. 7.1 Optical micrograph close to the quenched end (QE). Top edge of micrograph ~50μm from QE. Estimated CR_{900} >>500°C s^{-1}. Due to oxygen enrichment at the surface, the material in this micrograph is not representative of the bulk composition. The top of the micrograph shows part of the α-case, which formed a 100-120 μm thick surface layer. Beneath the α-case, β grains have transformed into fine α' martensite with an acicular appearance. (i) Indicates small pointed protuberances from α_p grains at prior β boundaries.

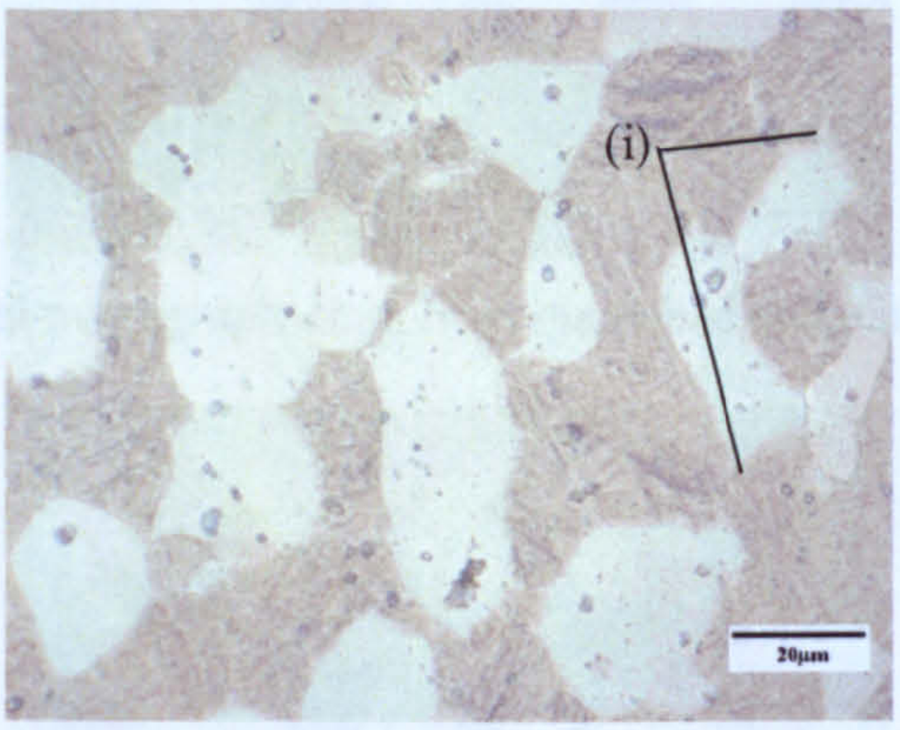

Fig. 7.2 Optical micrograph 1mm from quenched end, estimated CR_{900} ~400°C s^{-1}.
(i) Indicates small pointed protuberances from α_p grains at prior β boundaries.

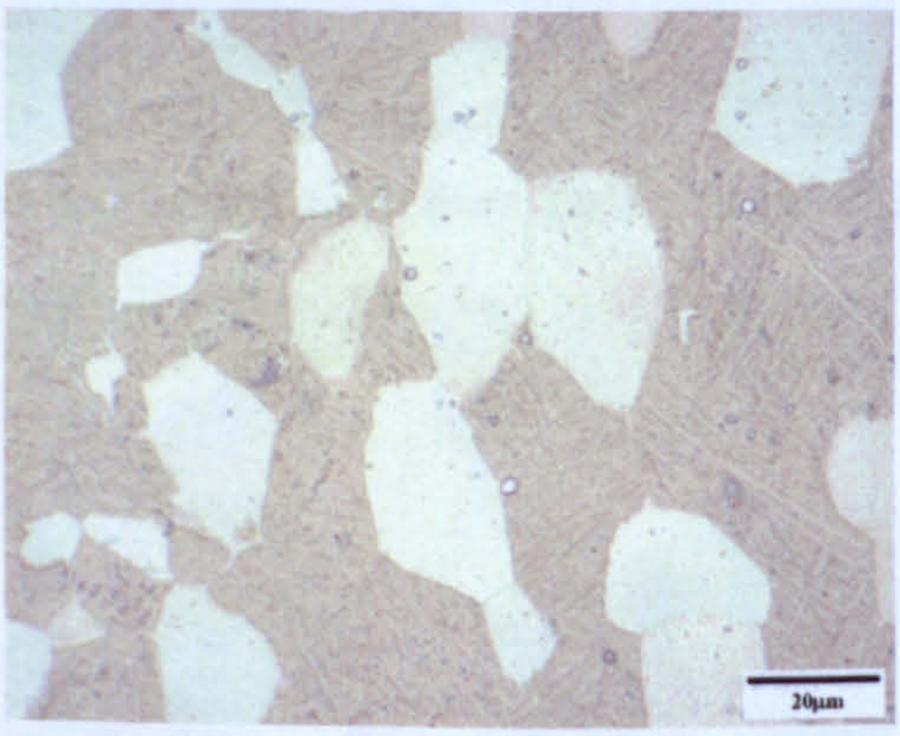

Fig. 7.3 Optical micrograph 2mm from quenched end, estimated CR_{900} ~160°C s^{-1}.

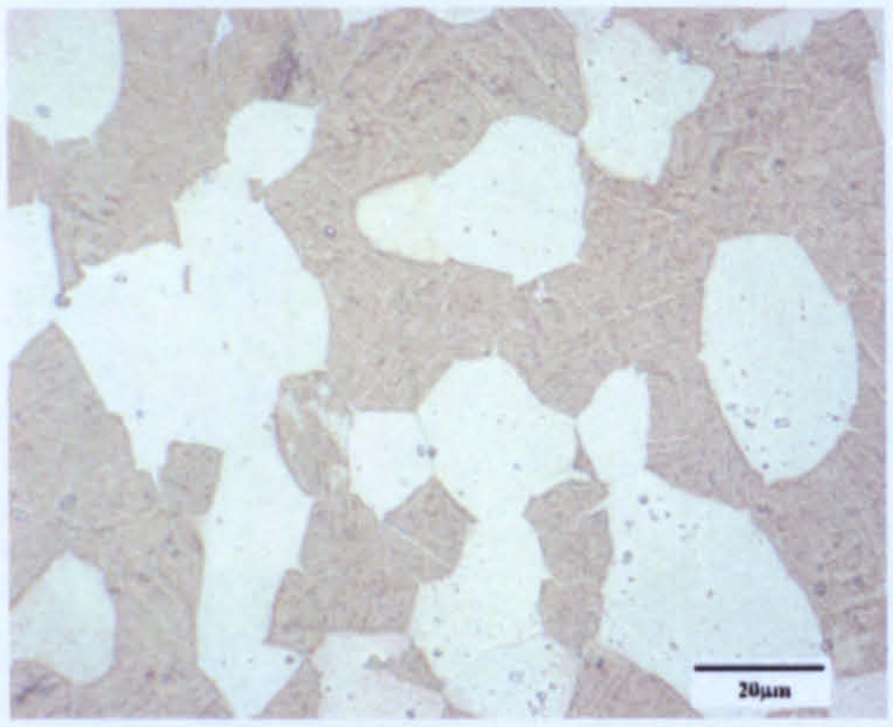

Fig. 7.4 Optical micrograph 3mm from quenched end, measured $CR_{900} = 100°C\ s^{-1}$.

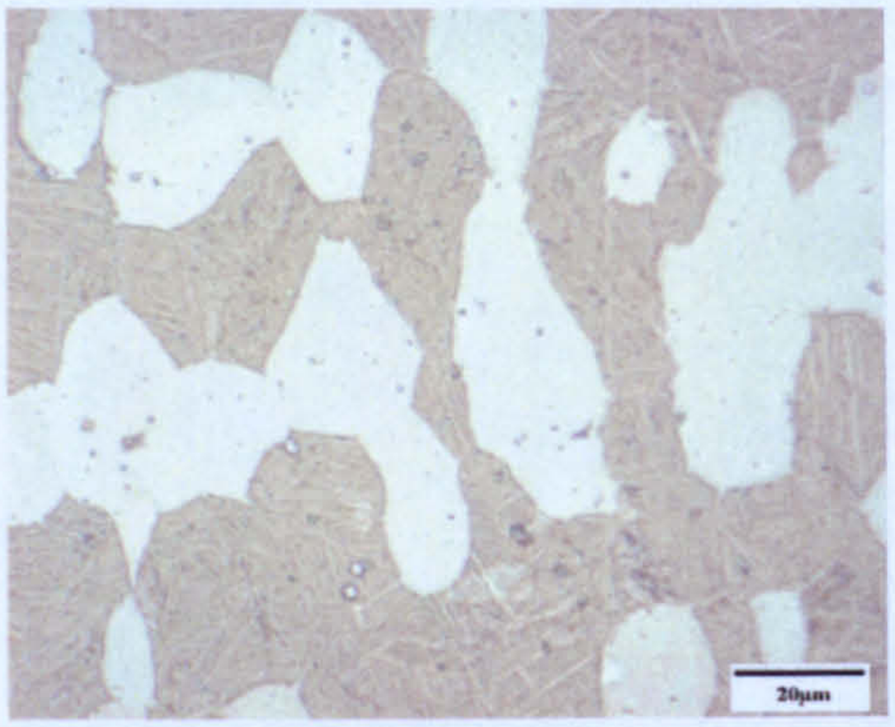

Fig. 7.5 Optical micrograph 4mm from quenched end, $CR_{900} = 63°C\ s^{-1}$.

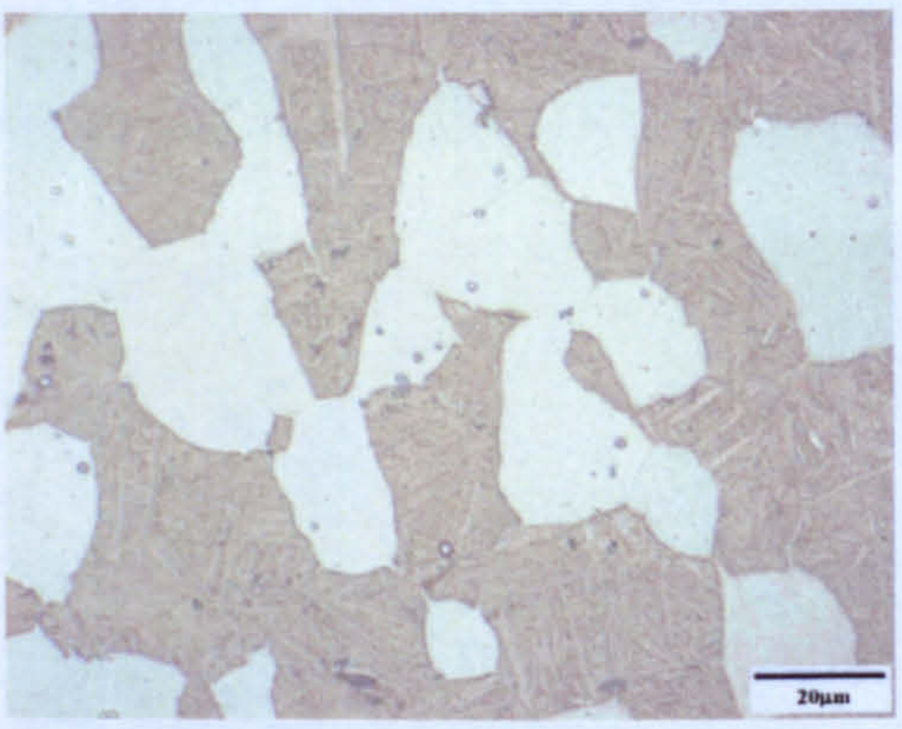

Fig. 7.6 Optical micrograph 5mm from quenched end, $CR_{900} = 47°C\ s^{-1}$.

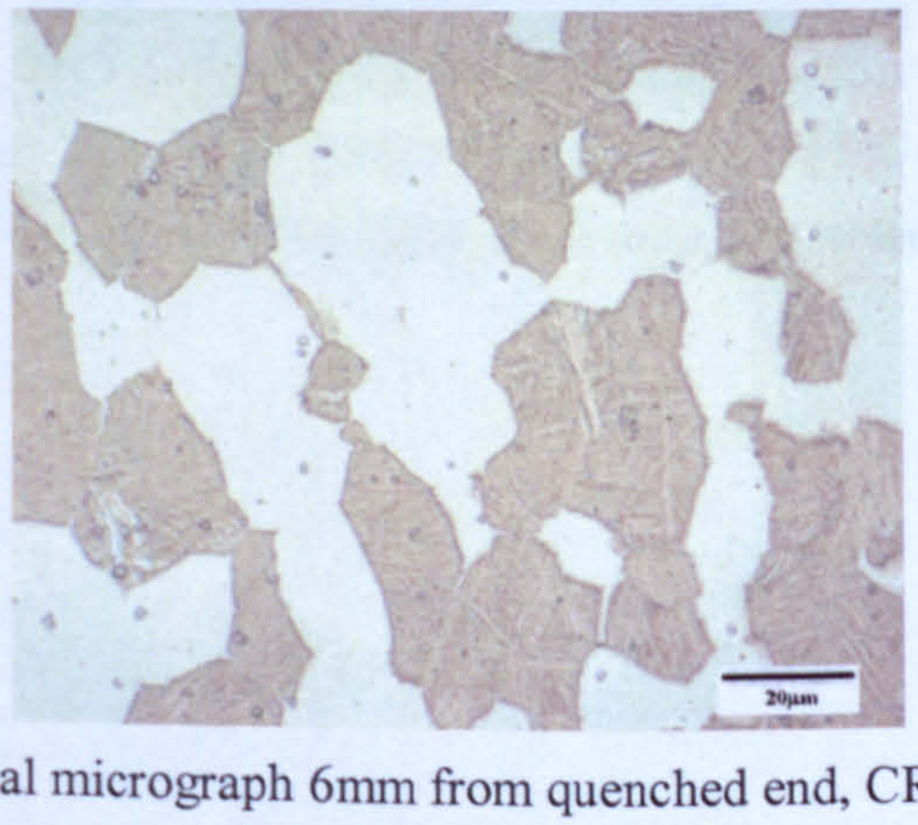

Fig. 7.7 Optical micrograph 6mm from quenched end, $CR_{900} = 37°C\ s^{-1}$.

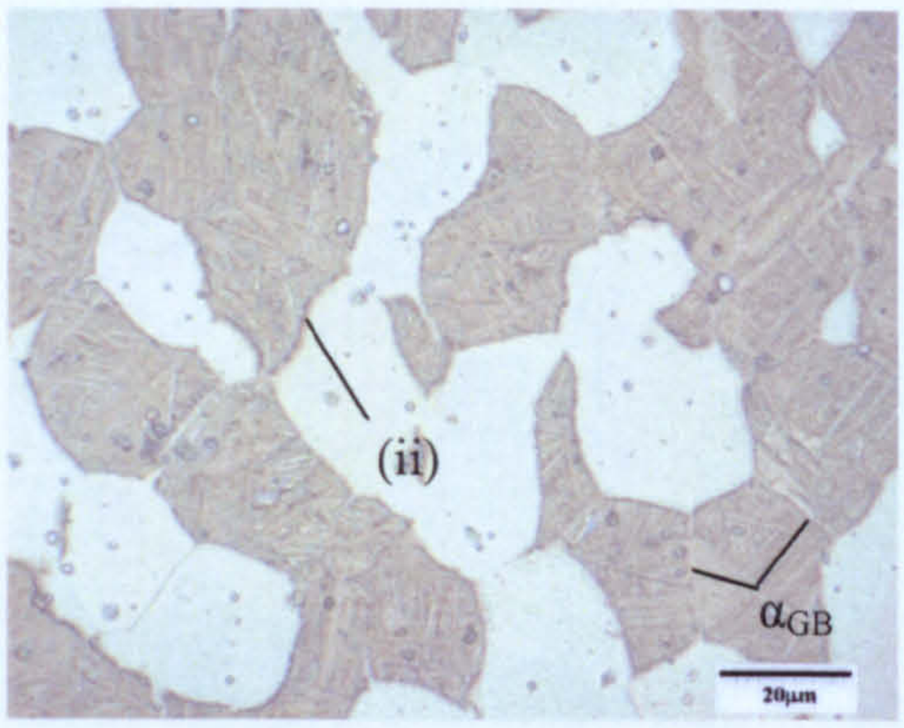

Fig. 7.8 Optical micrograph 7mm from quenched end, $CR_{900} = 30°C\ s^{-1}$. (ii) Indicates an etching effect at the edge of α_p grains due to epitaxial growth, which becomes increasingly prominent and thicker with decreasing cooling rate hereafter.

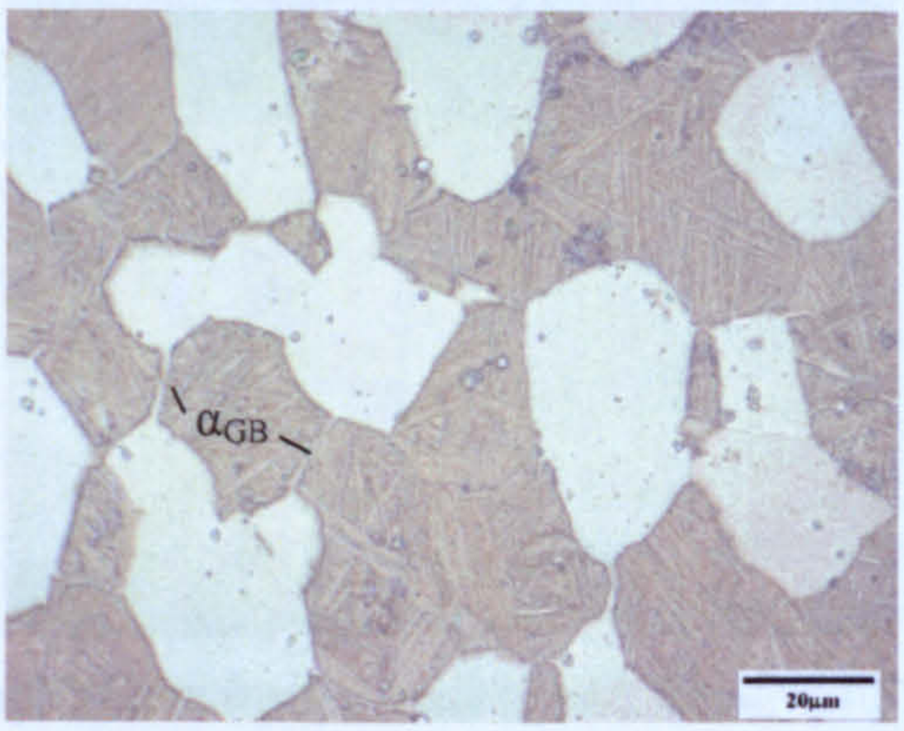

Fig. 7.9 Optical micrograph 8mm from quenched end, $CR_{900} = 25°C\ s^{-1}$.

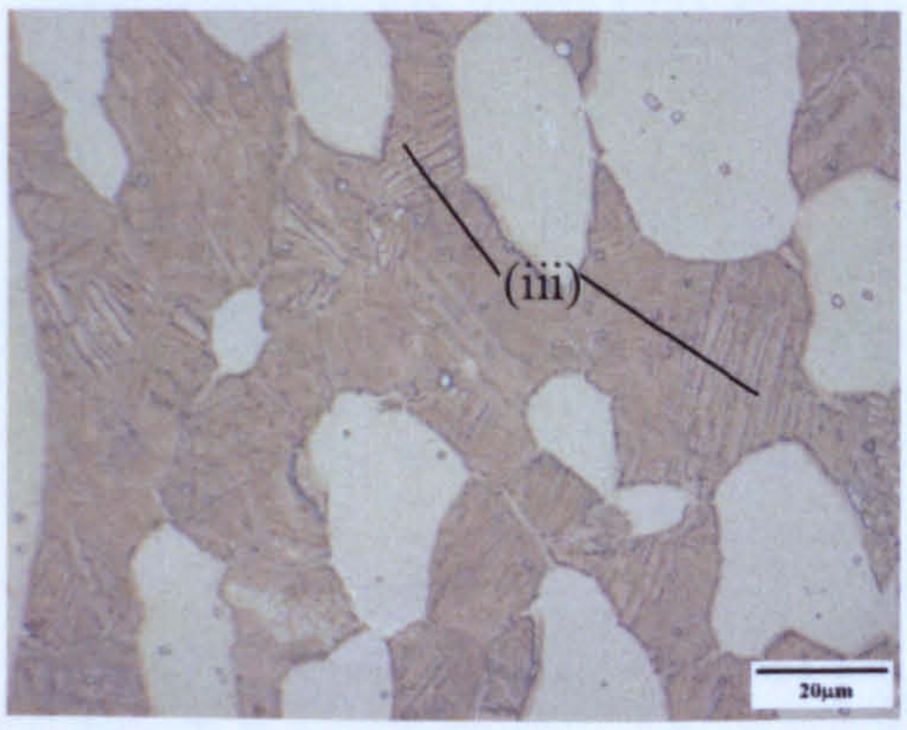

Fig. 7.10 Optical micrograph 9mm from quenched end, $CR_{900} = 21°C\ s^{-1}$. Laths form in colonies. (iii) Indicates colonies of lower aspect ratio laths due to sectioning effects.

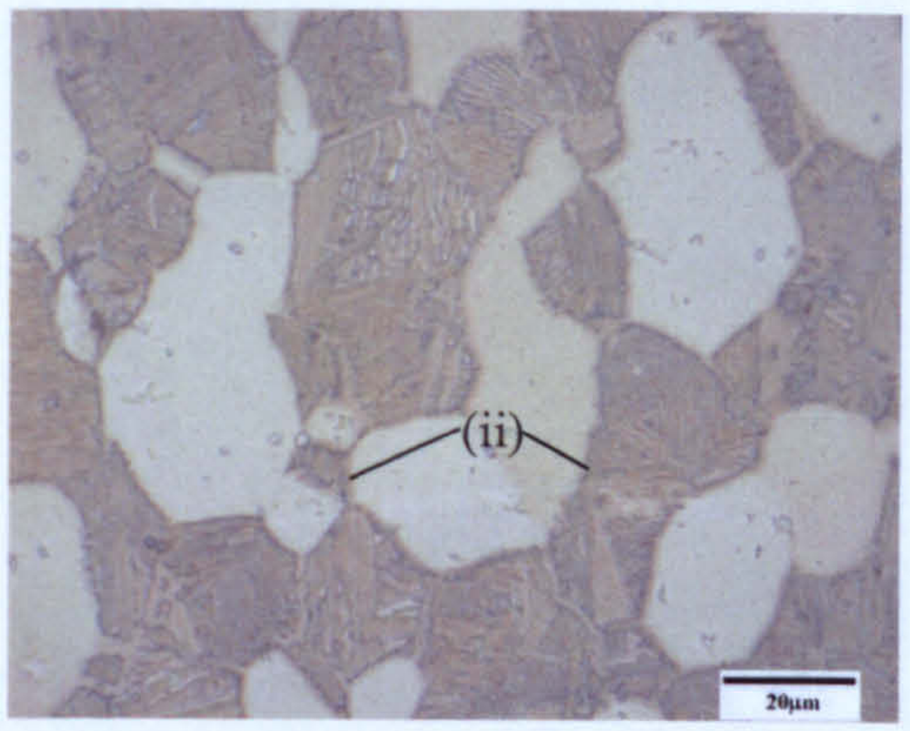

Fig. 7.11 Optical micrograph 12mm from quenched end, $CR_{900} = 15°C\ s^{-1}$. (ii) Growth of the α_p grains begins to be feathery in appearance.

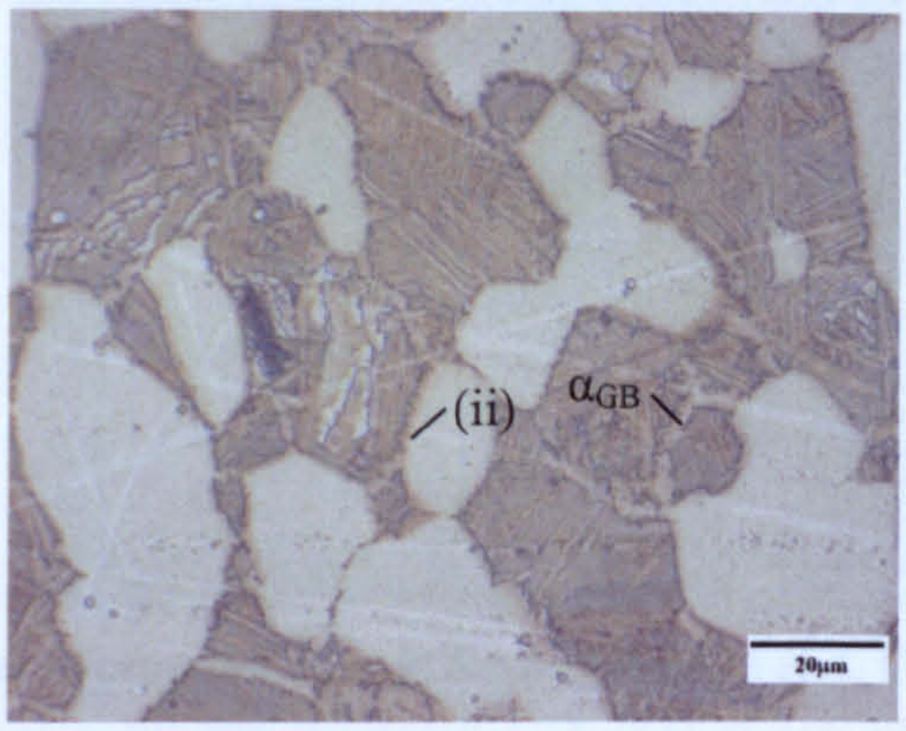

Fig. 7.12 Optical micrograph 16mm from quenched end, $CR_{900} = 10°C\ s^{-1}$. (ii) Feathery growth of α_p. α_{GB} also 'feathery' in appearance.

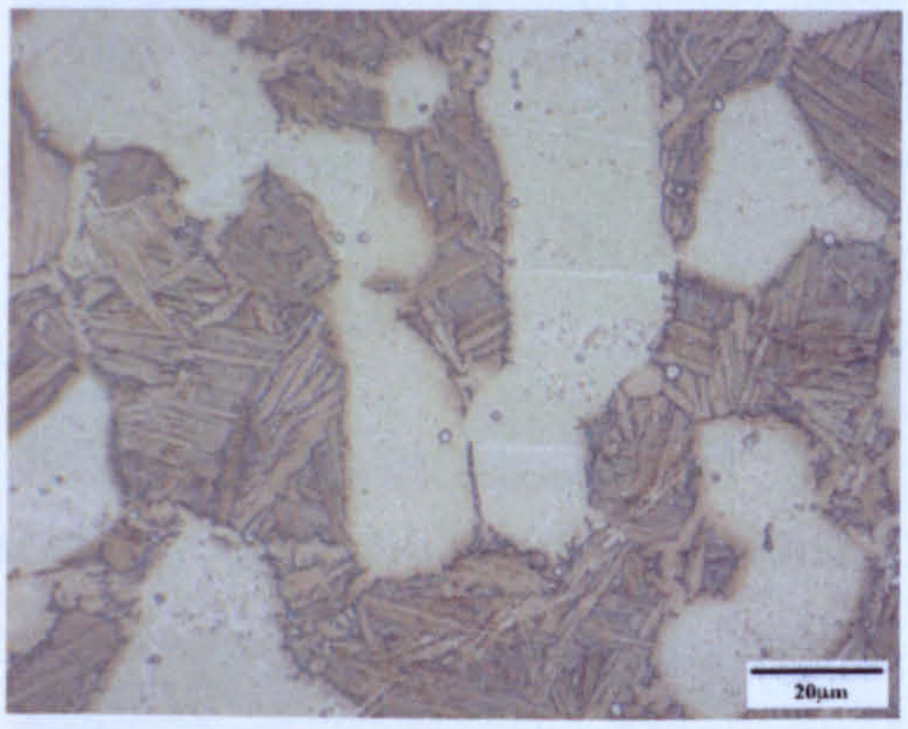

Fig. 7.13 Optical micrograph 20mm from quenched end, $CR_{900} = 7.4°C\ s^{-1}$.

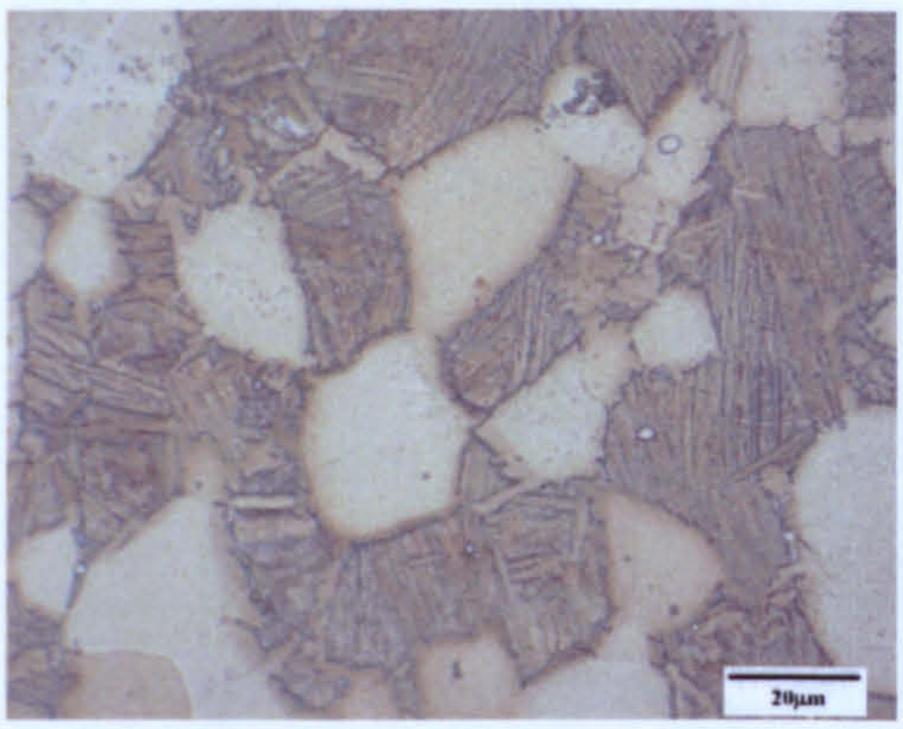

Fig. 7.14 Optical micrograph 24mm from quenched end, $CR_{900} = 5.8°C\ s^{-1}$.

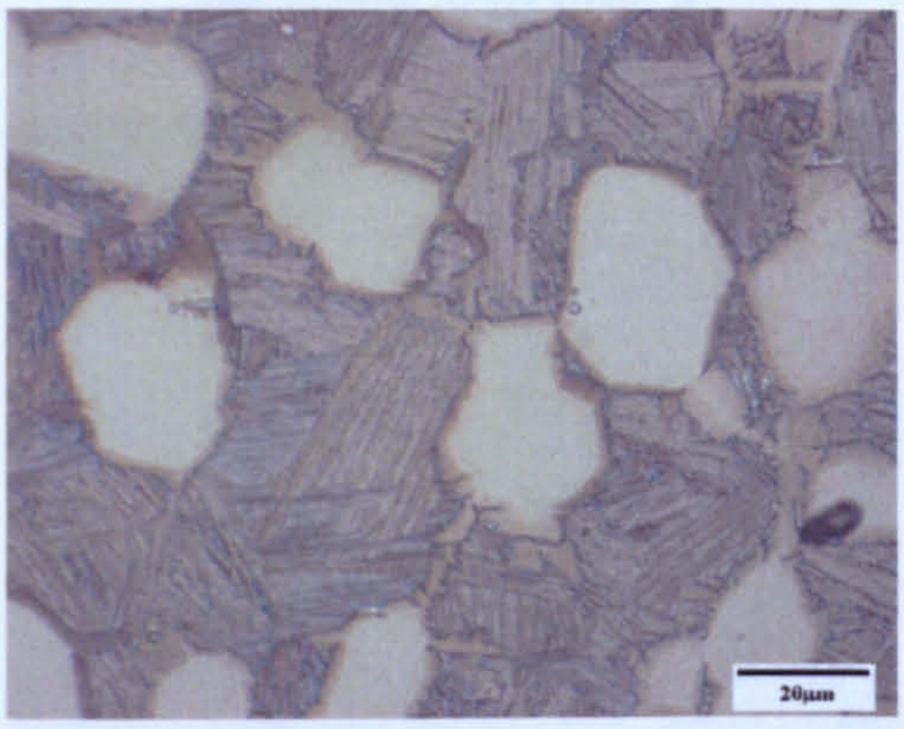

Fig. 7.15 Optical micrograph 28mm from quenched end, $CR_{900} = 4.7°C\ s^{-1}$.

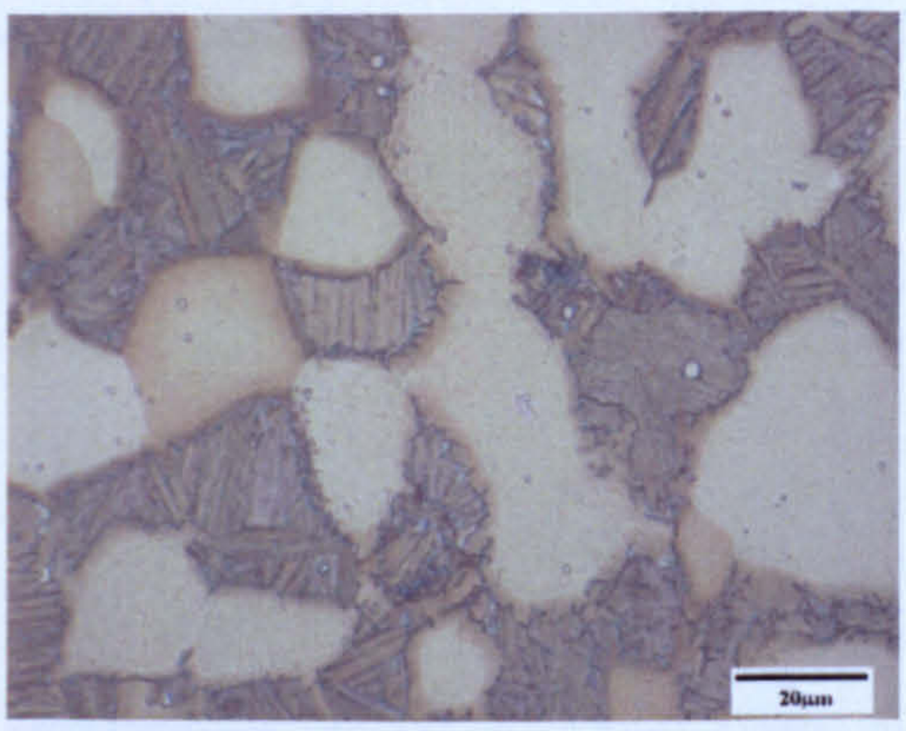

Fig. 7.16 Optical micrograph 34mm from quenched end, $CR_{900} = 3.6°C\ s^{-1}$.

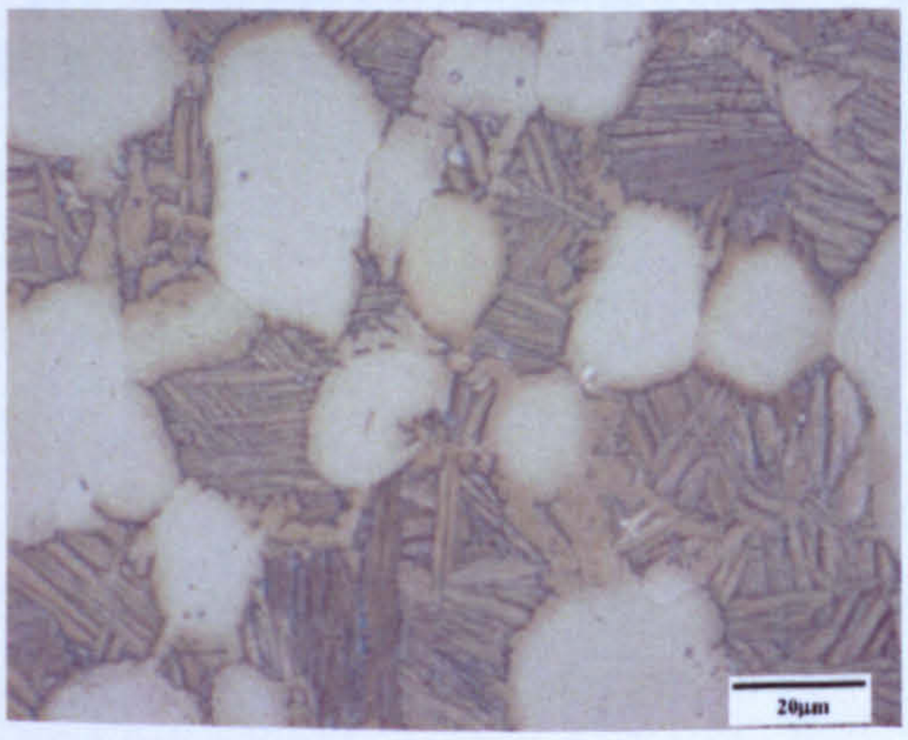

Fig. 7.17 Optical micrograph 40mm from quenched end, $CR_{900} = 2.9°C\ s^{-1}$.

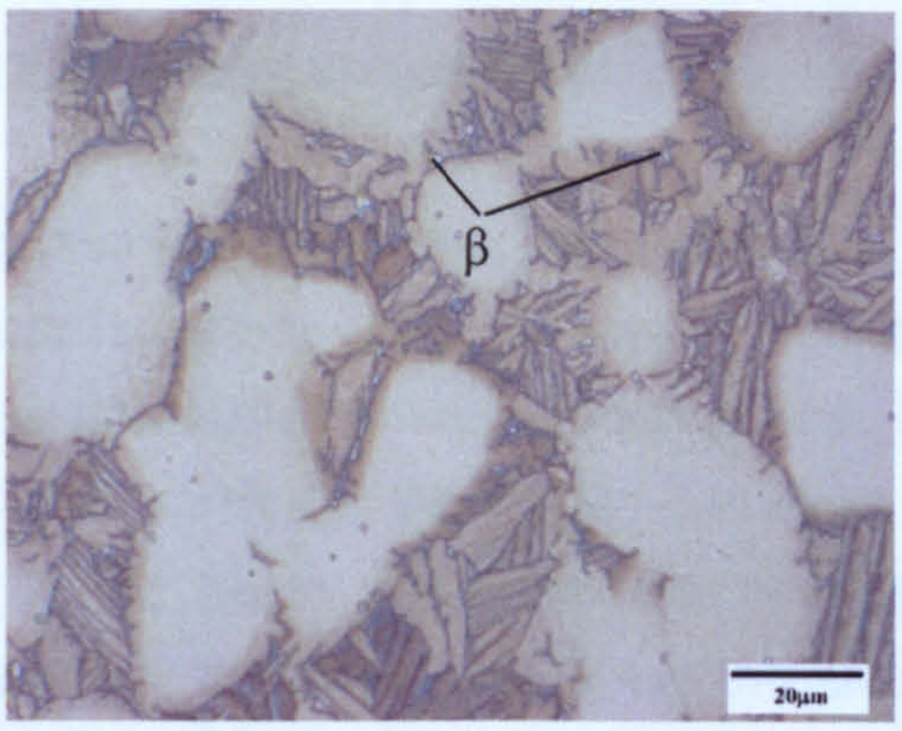

Fig. 7.18 Optical micrograph 48mm from quenched end, $CR_{900} = 2.3°C\ s^{-1}$. Small bright regions are islands of retained β.

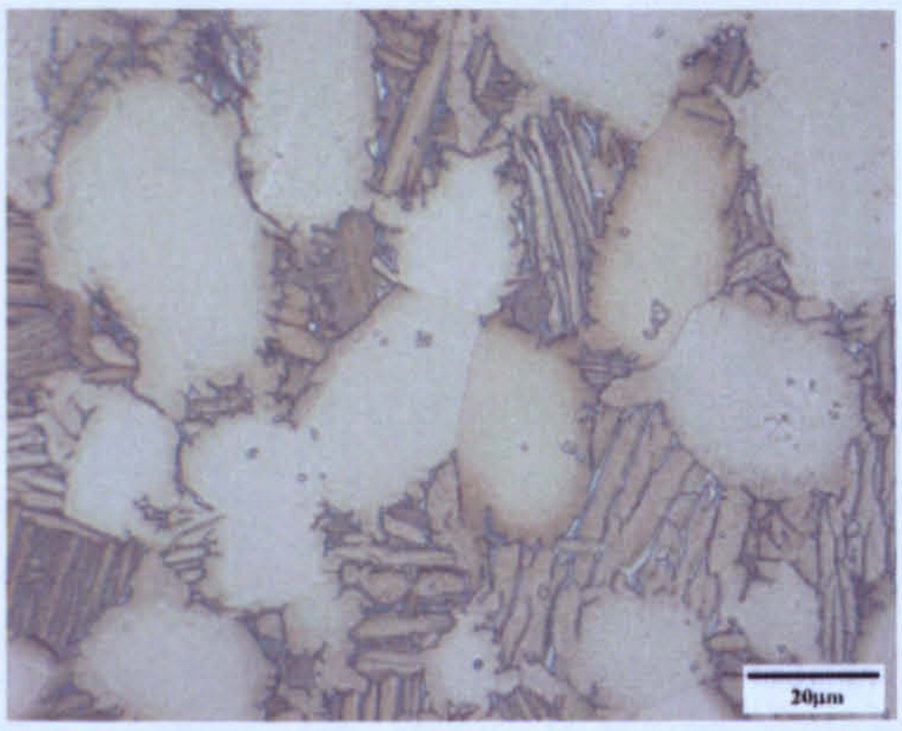

Fig. 7.19 Optical micrograph 54mm from quenched end, $CR_{900} = 2.0°C\ s^{-1}$.

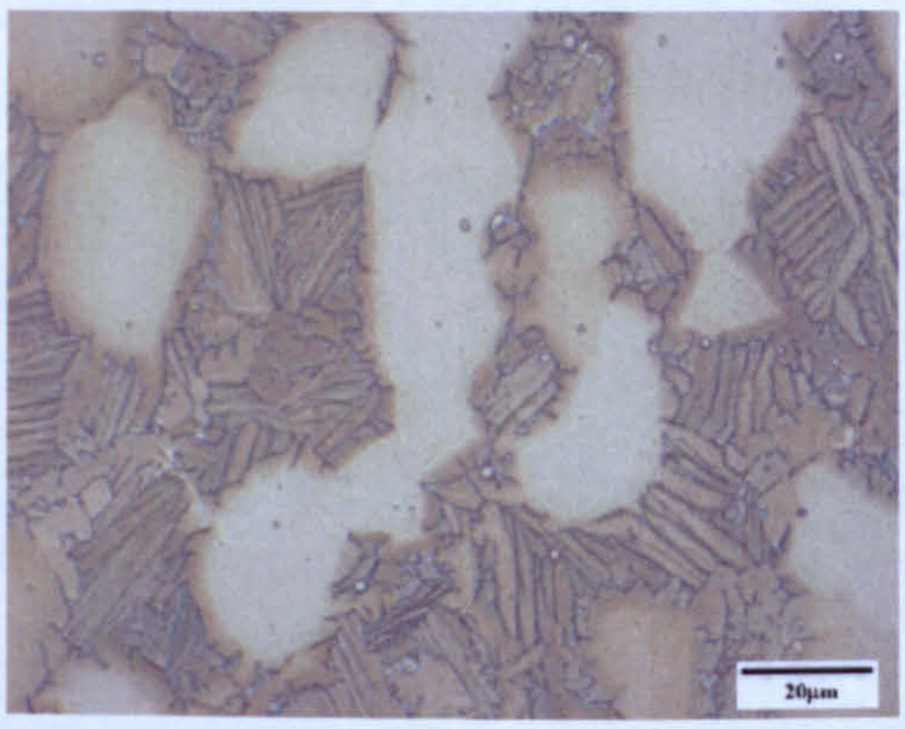

Fig. 7.20 Optical micrograph 65mm from quenched end, measured $CR_{900} = 1.7°C\ s^{-1}$.

7.2.2 Back Scattered and Secondary Electron Imaging

To provide more detailed micrographs of the fine transformed structures formed at the higher cooling rates, back scattered electron imaging on polished specimens and secondary electron imaging after light etching was carried out. Figs. 7.21 to 7.35 show a series of micrographs from the centre of the Jominy bar along its length. The distance from the quenched end of the bar is given for each micrograph, together with the instantaneous cooling rate at 900°C (CR_{900}), which was estimated from the thermocouple data (see section 3.4.2 and Fig. 3.10).

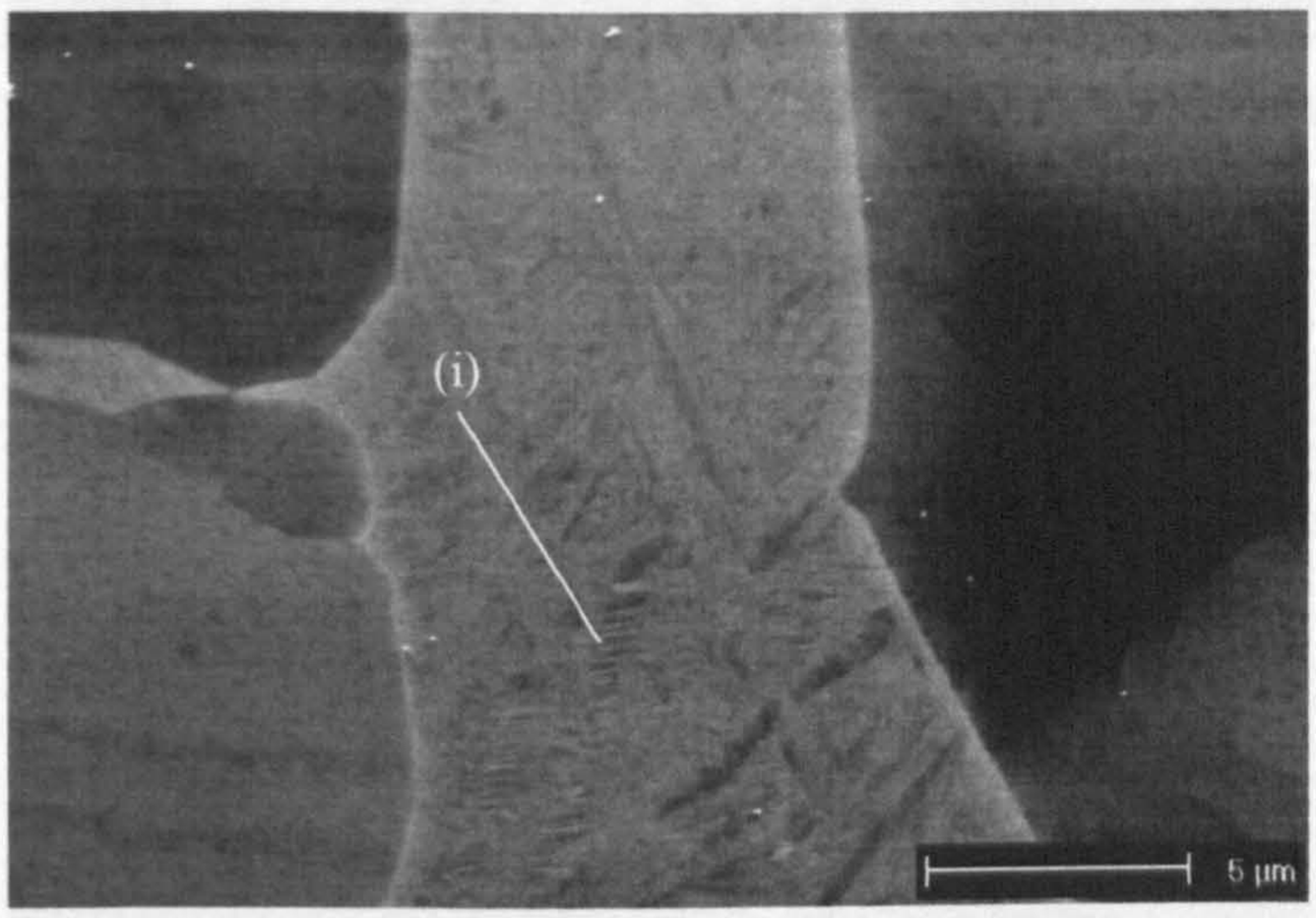

Fig. 7.21 BSE image 0.1mm from quenched end, estimated $CR_{900} >> 500°C\ s^{-1}$. (i) Indicates possible twins in a martensite lath.

Fig. 7.22 SE image from etched specimen 0.2mm from quenched end, estimated $CR_{900} >> 500°C\ s^{-1}$. (ii) Indicates ring of lighter contrast at edges of α_p grains.

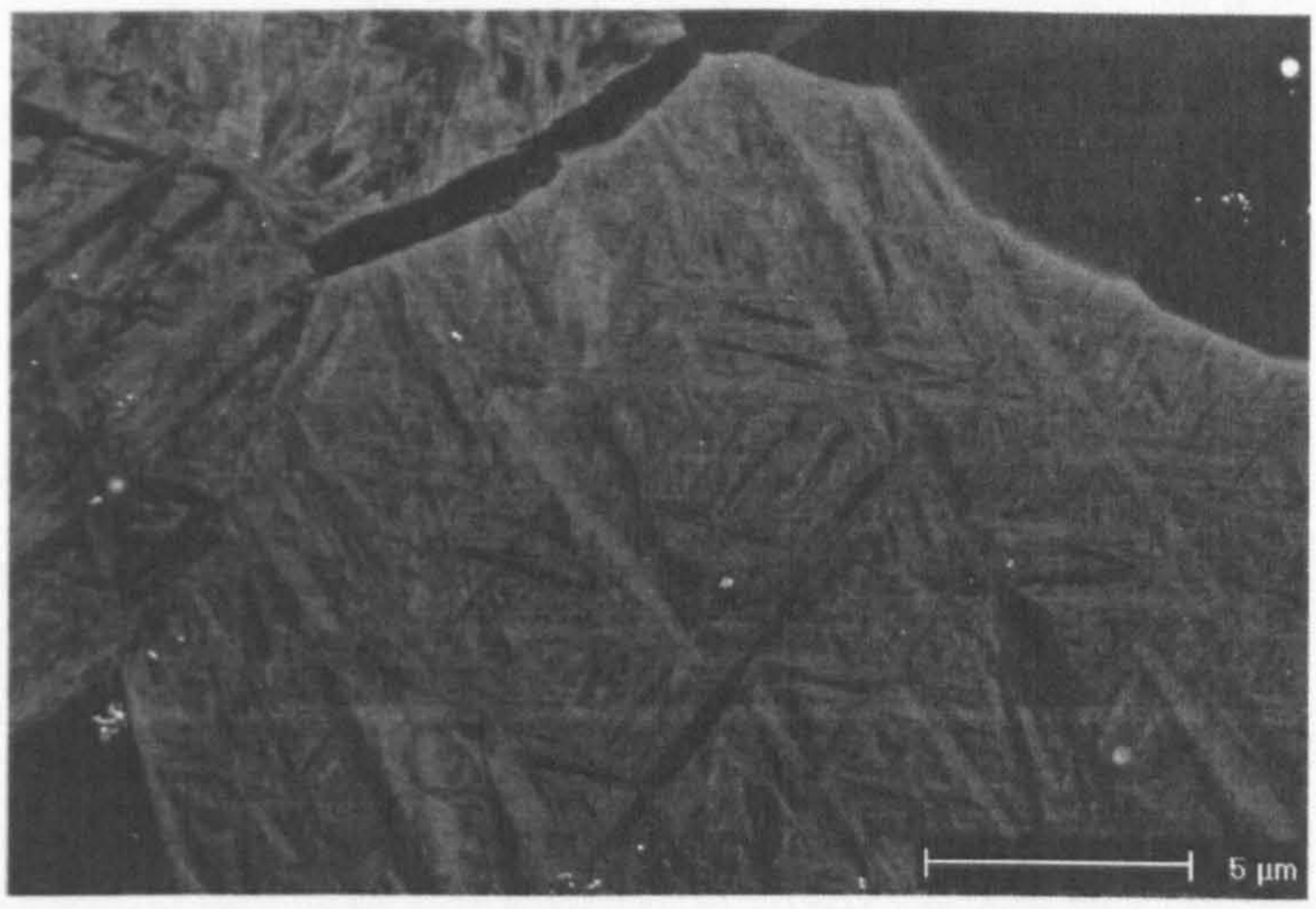

Fig. 7.23 BSE image 0.3mm from quenched end, estimated CR_{900} >>500°C s^{-1}.

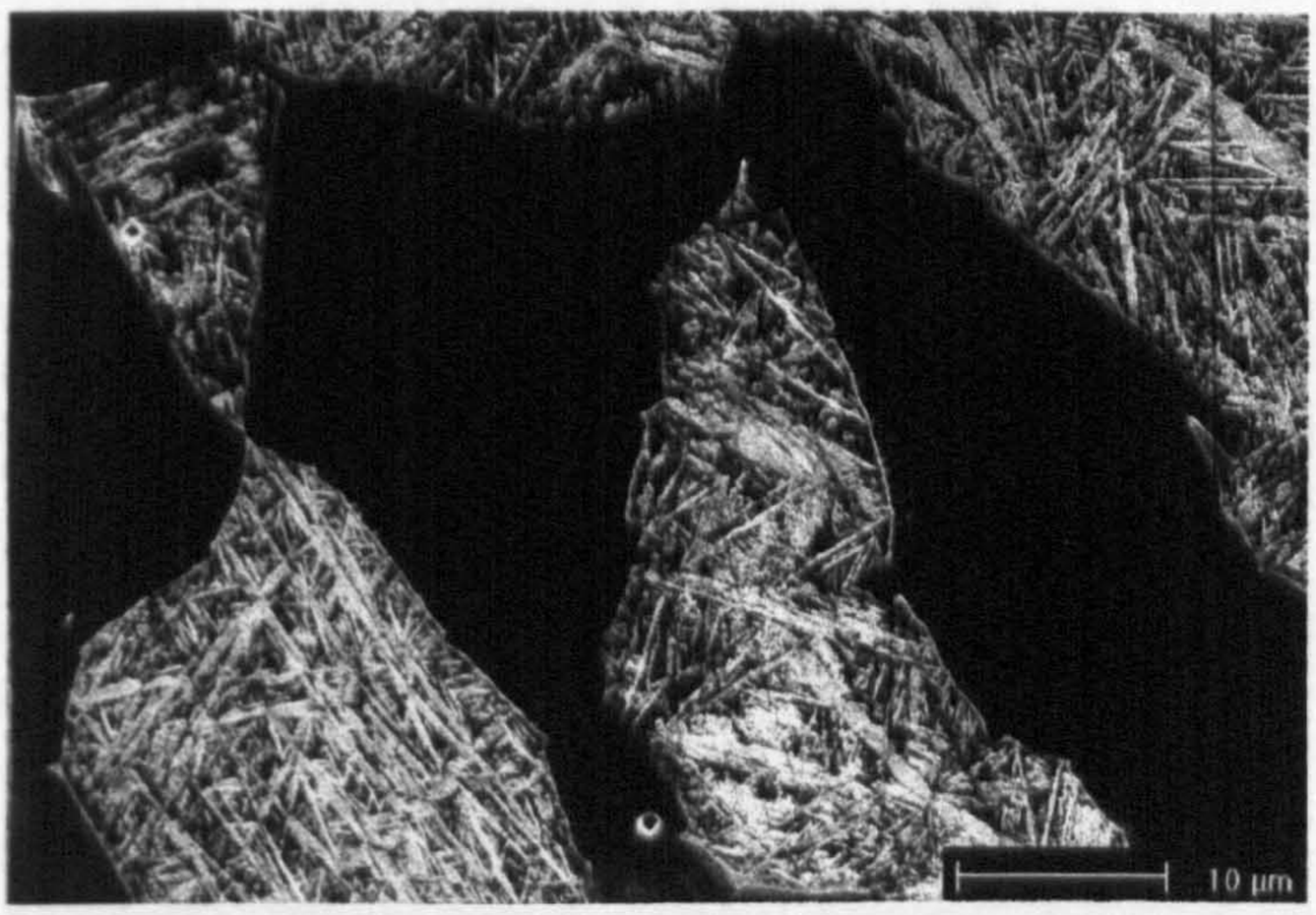

Fig. 7.24 SE image from etched specimen 0.4mm from the quenched end, estimated CR_{900} >> 500°C s^{-1}.

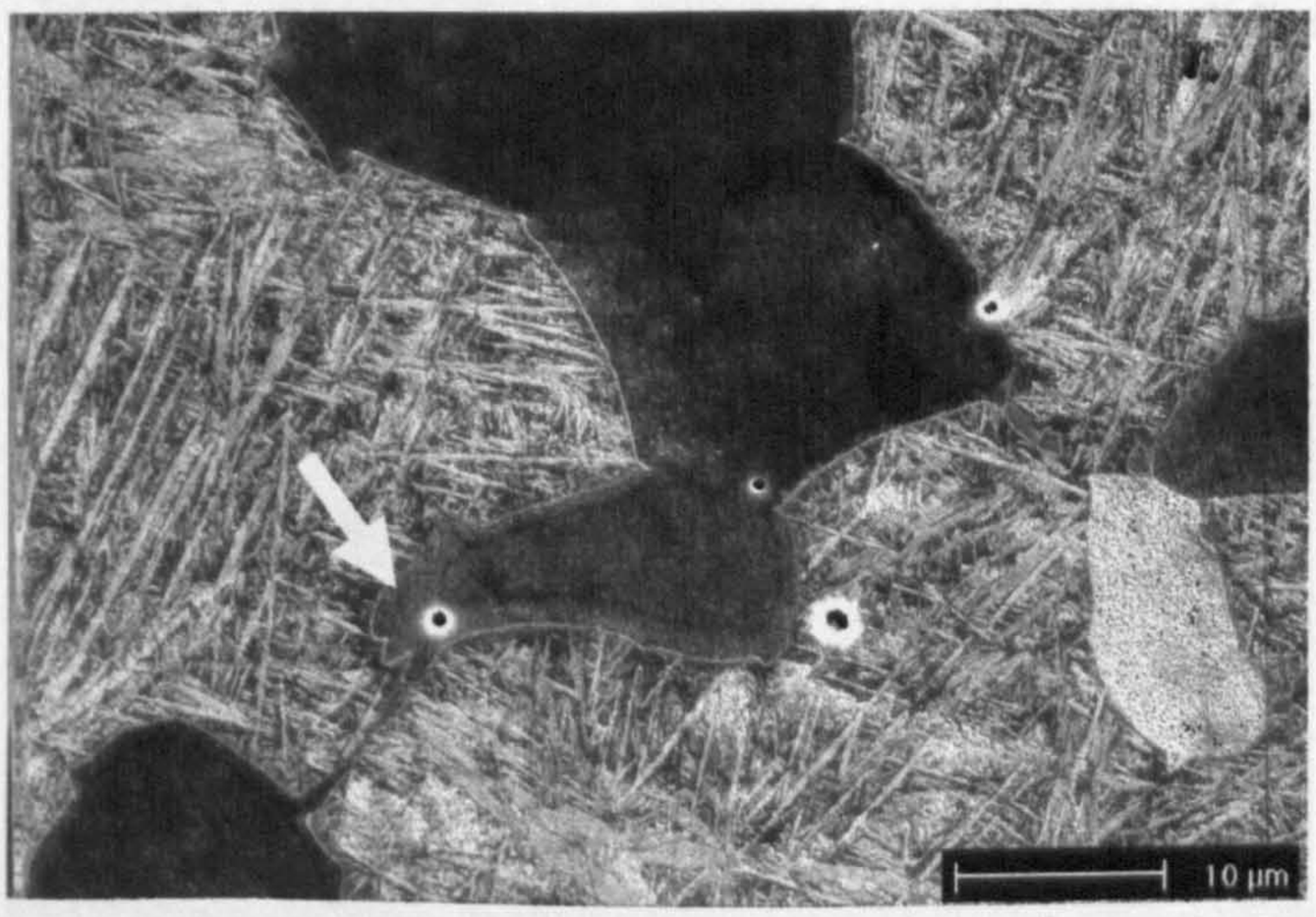

Fig. 7.25 SE image from etched specimen 1.1mm from the quenched end, estimated CR_{900} ~360°C s^{-1}.

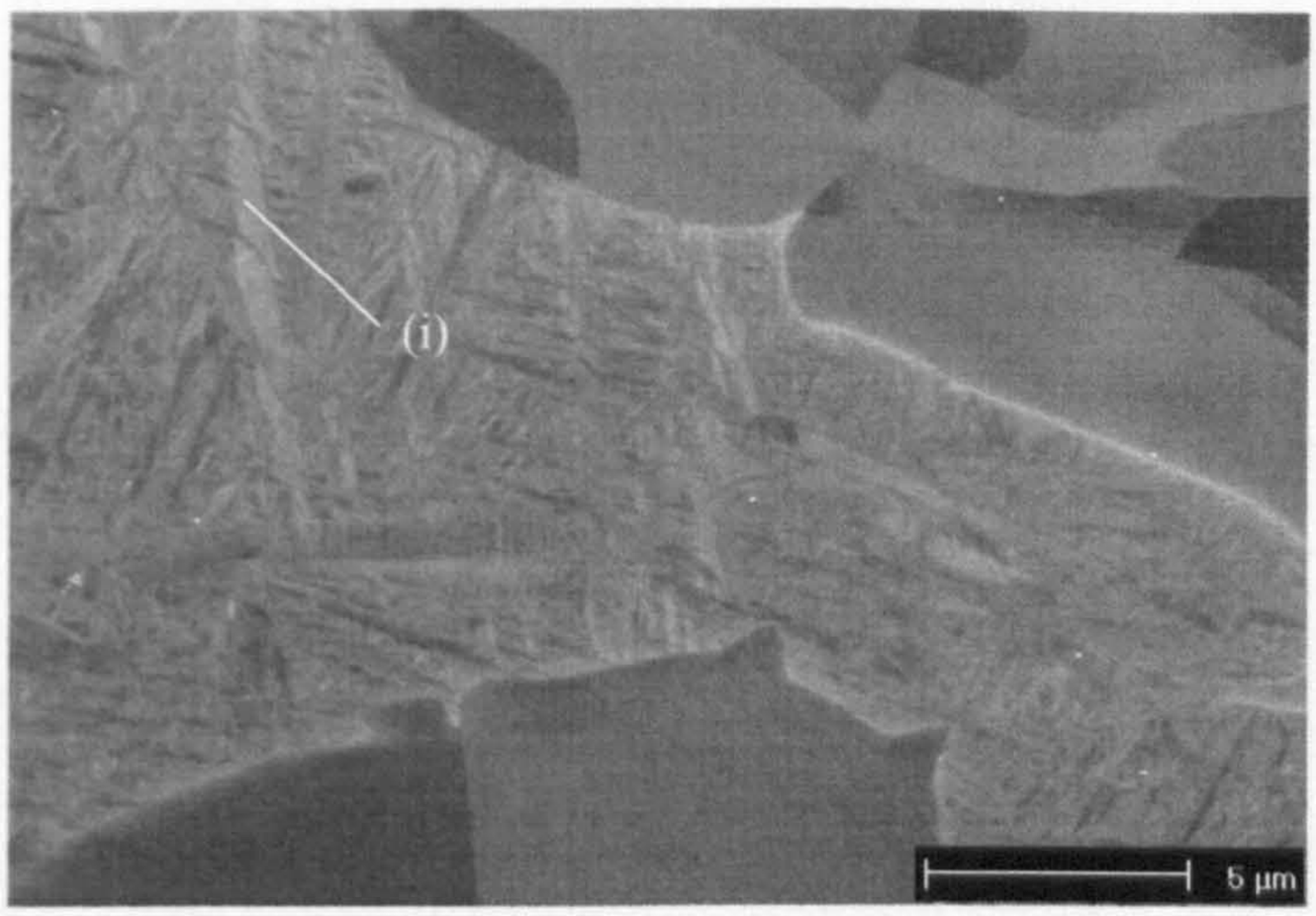

Fig. 7.26 BSE image 1.2mm from quenched end, estimated CR_{900} ~320°C s^{-1}. (i) Indicates possible twins in a martensite lath.

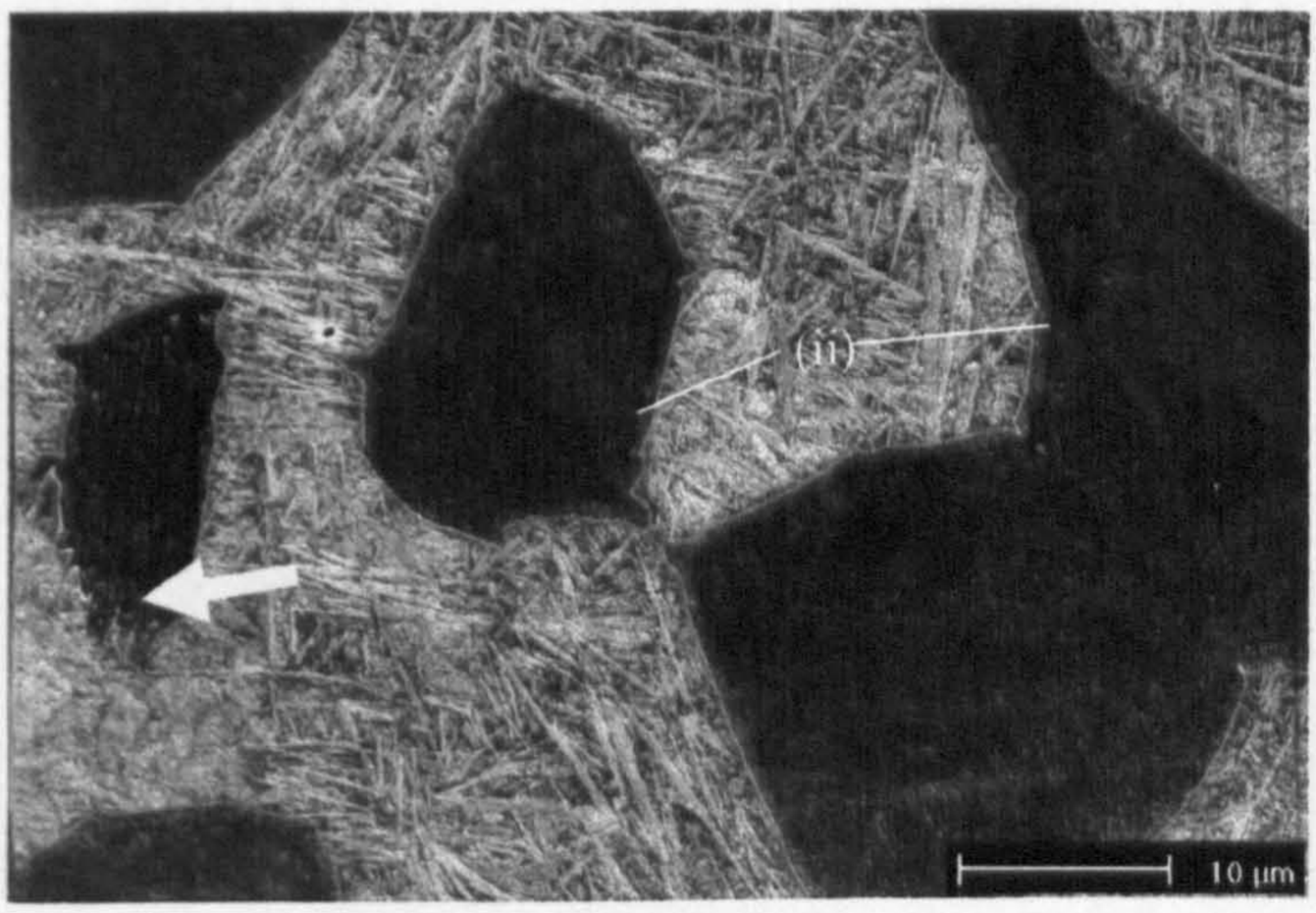

Fig. 7.27 SE image from etched specimen 1.3mm from quenched end, estimated CR_{900} ~280°C s^{-1}. (ii) Indicates ring of lighter contrast at edges of α_p grains.

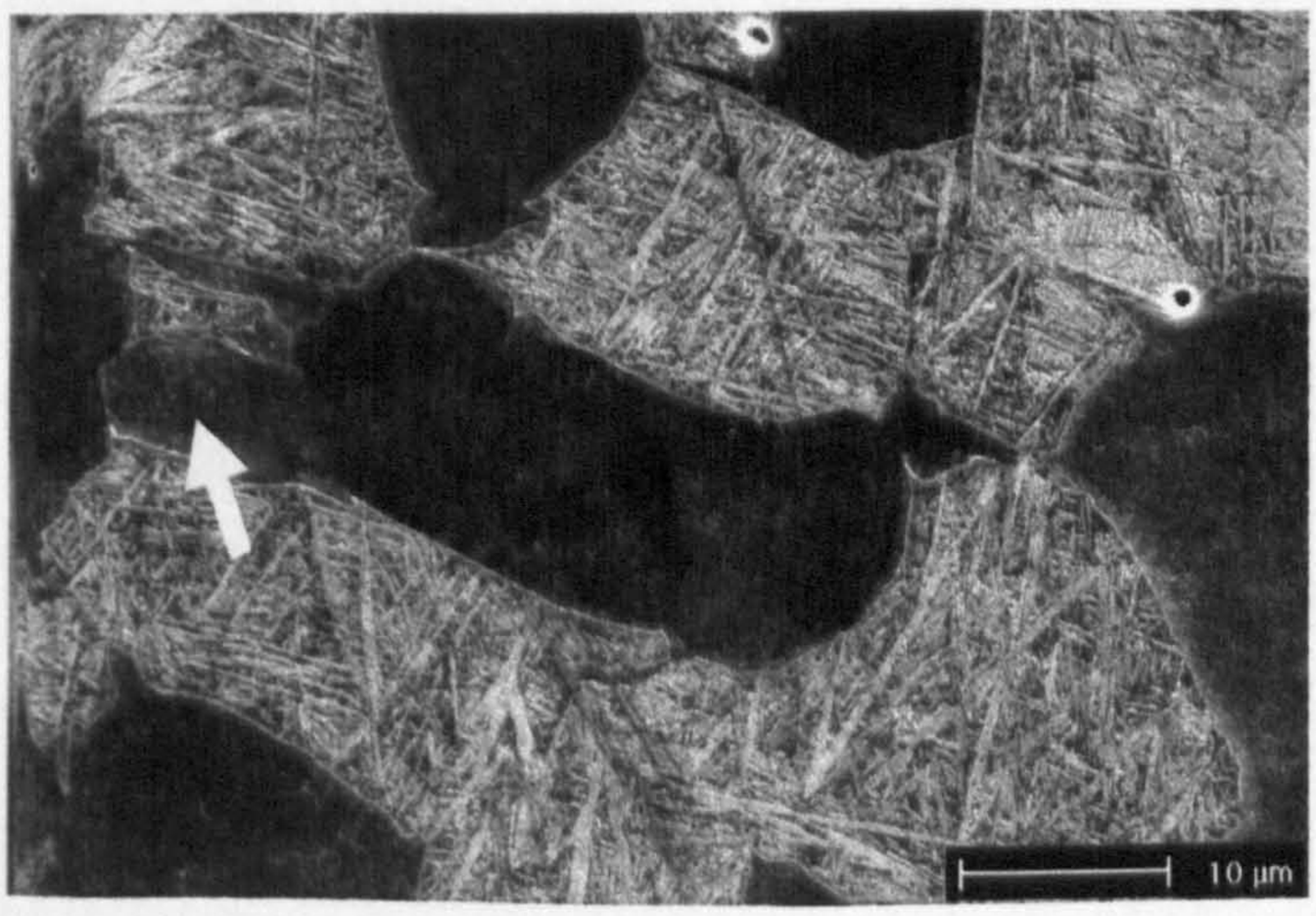

Fig. 7.28 SE image from etched specimen 1.4mm from quenched end, estimated CR_{900} ~260°C s^{-1}.

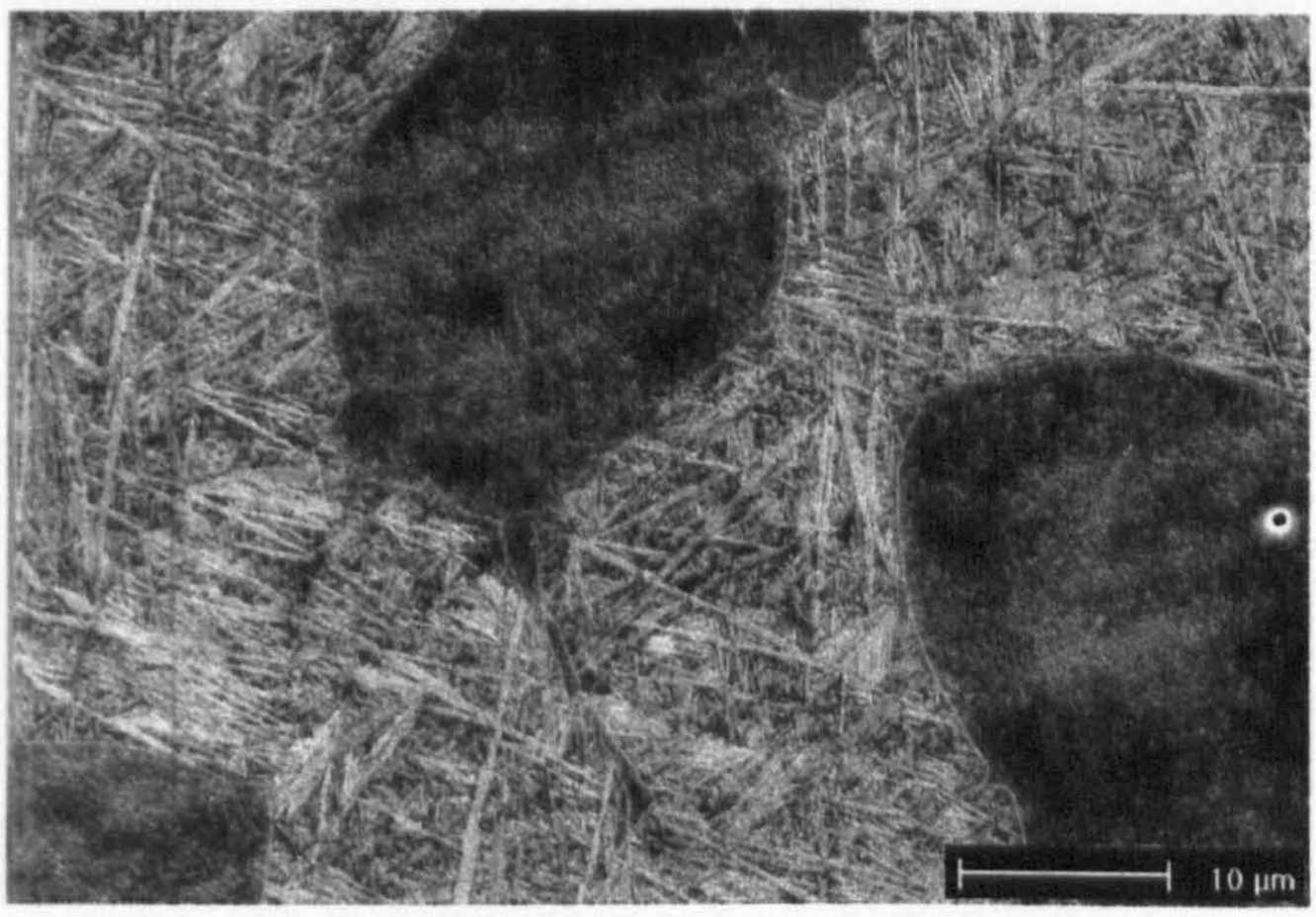

Fig. 7.29 SE image from etched specimen 1.8mm from quenched end, estimated $CR_{900} = \sim 180°C\ s^{-1}$.

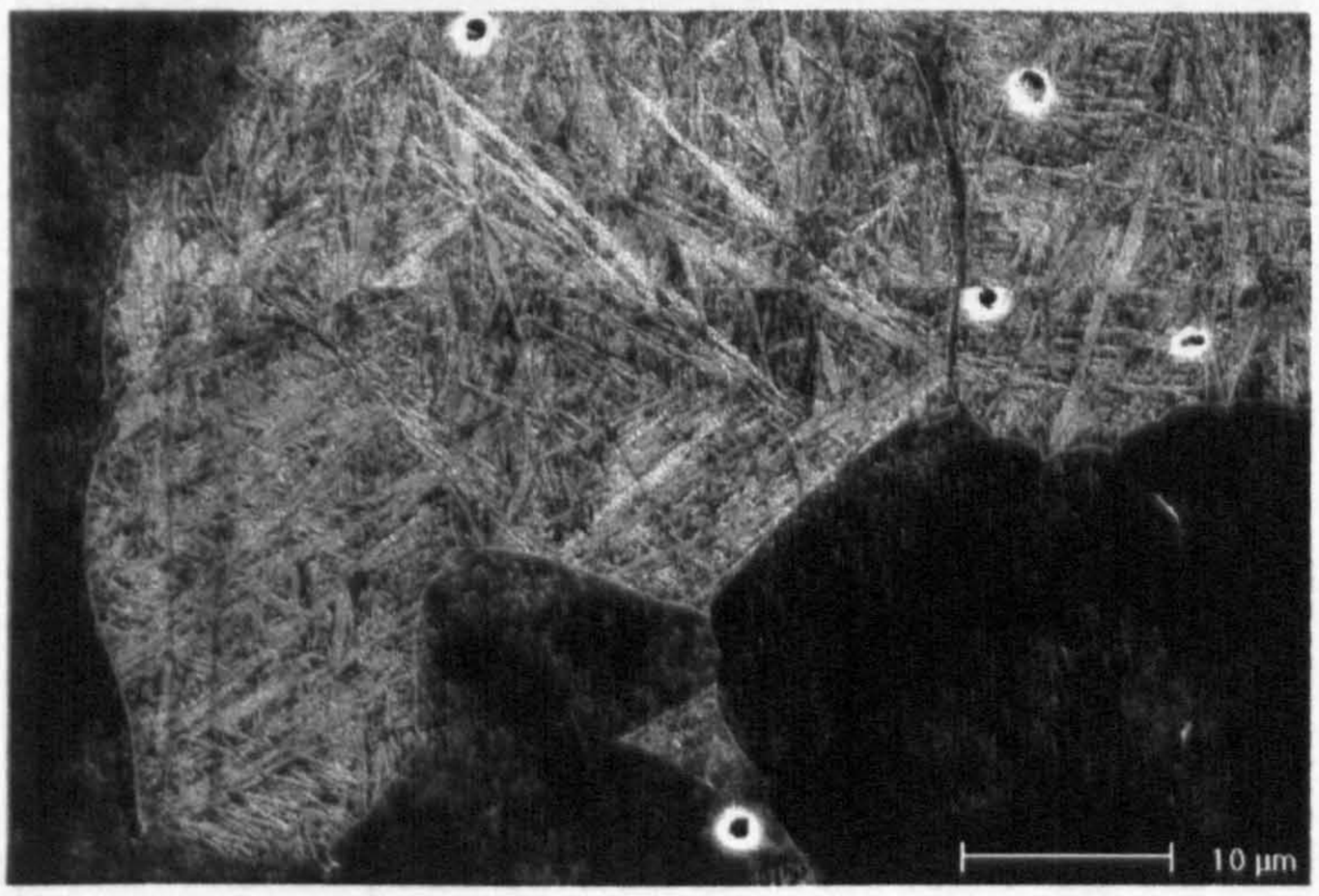

Fig. 7.30 SE image from etched specimen 1.9mm from quenched end, estimated $CR_{900} \sim 170°C\ s^{-1}$.

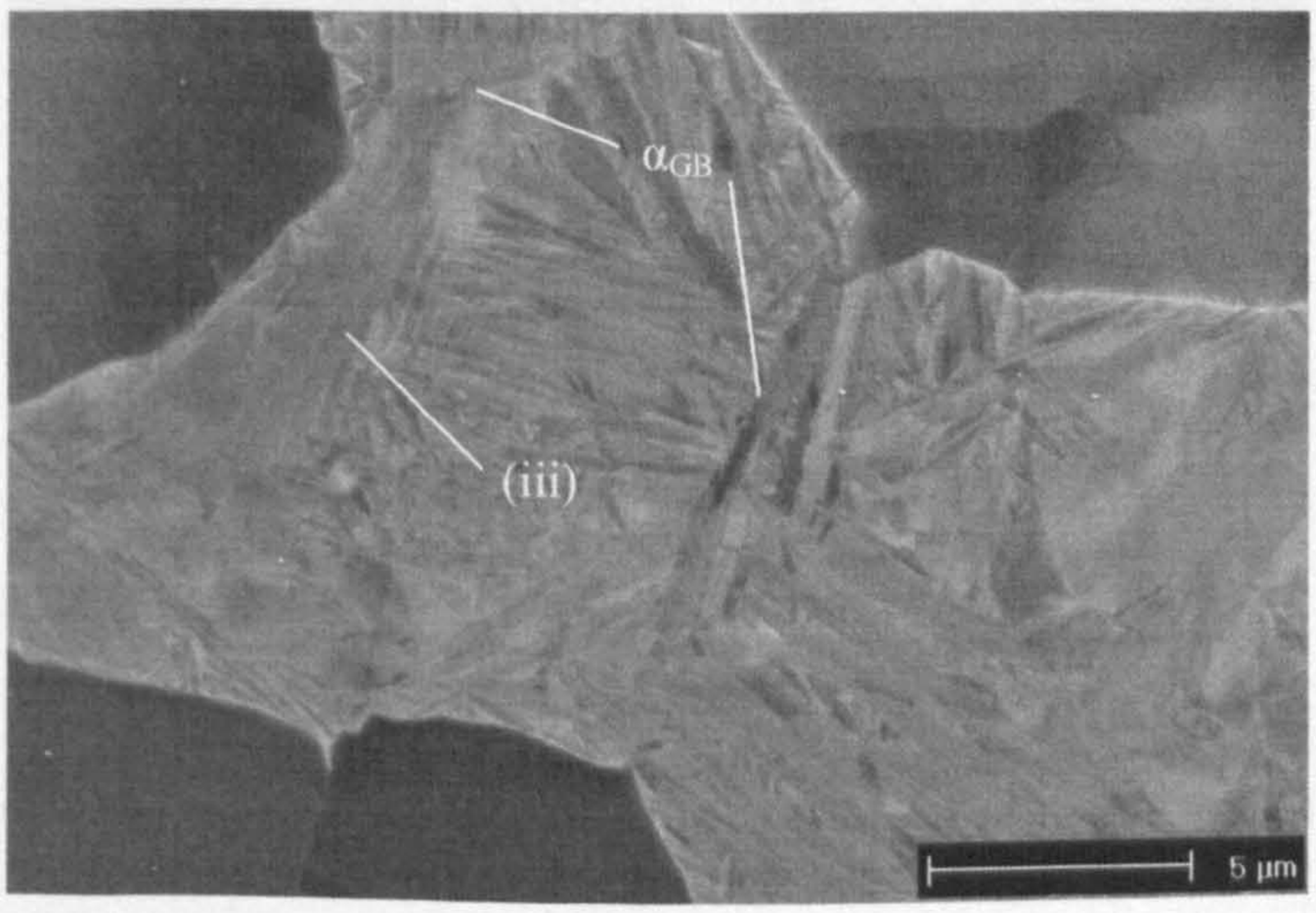

Fig. 7.31 BSE image 3.2mm from quenched end, $CR_{900} = 85°C\ s^{-1}$. (iii) indicates evidence of retained β between α_s laths and the parallel laths forming small colonies.

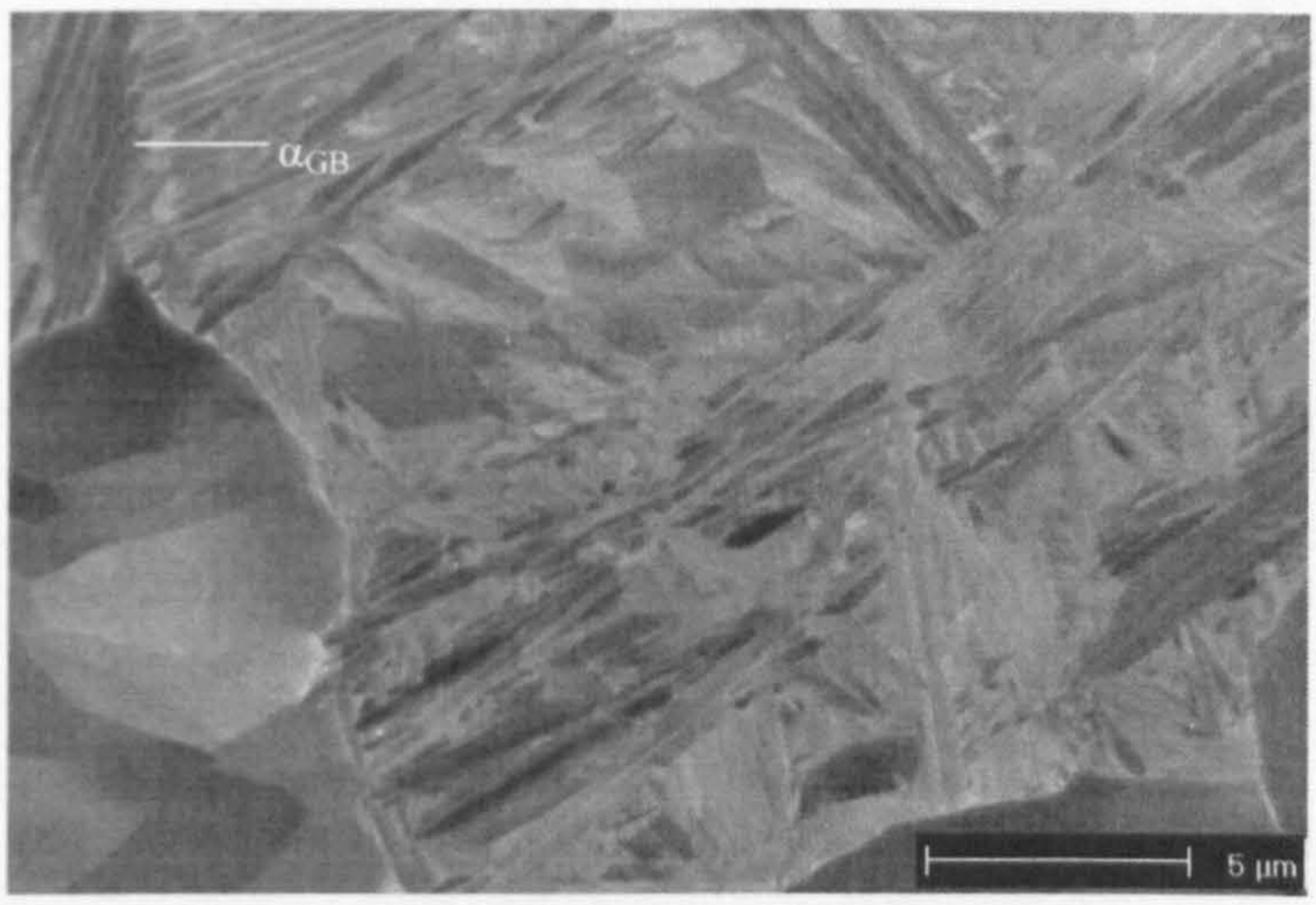

Fig. 7.32 BSE image 4.2mm from quenched end, $CR_{900} = 60°C\ s^{-1}$.

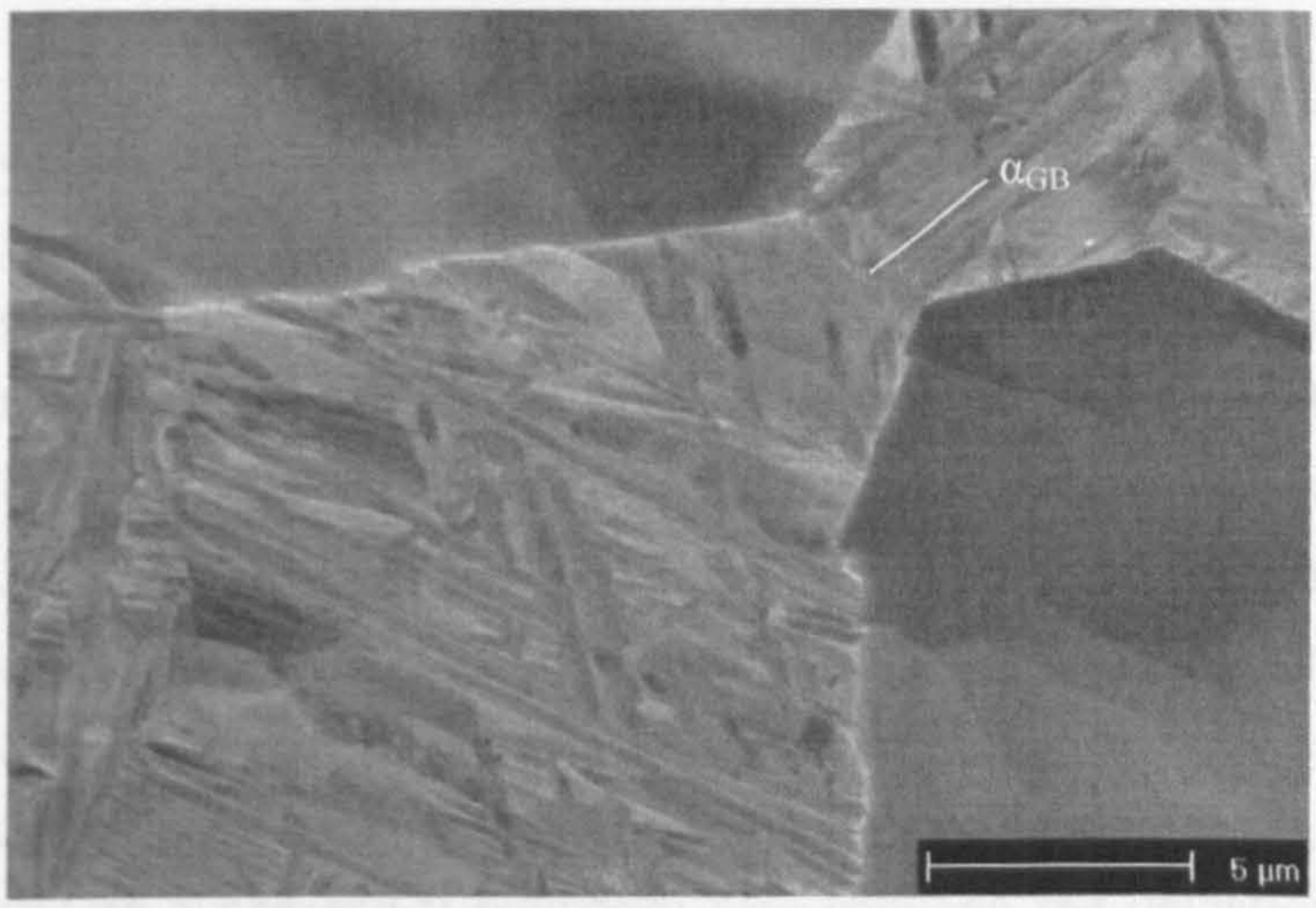

Fig. 7.33 BSE image 5.2mm from quenched end, $CR_{900} = 45°C\ s^{-1}$.

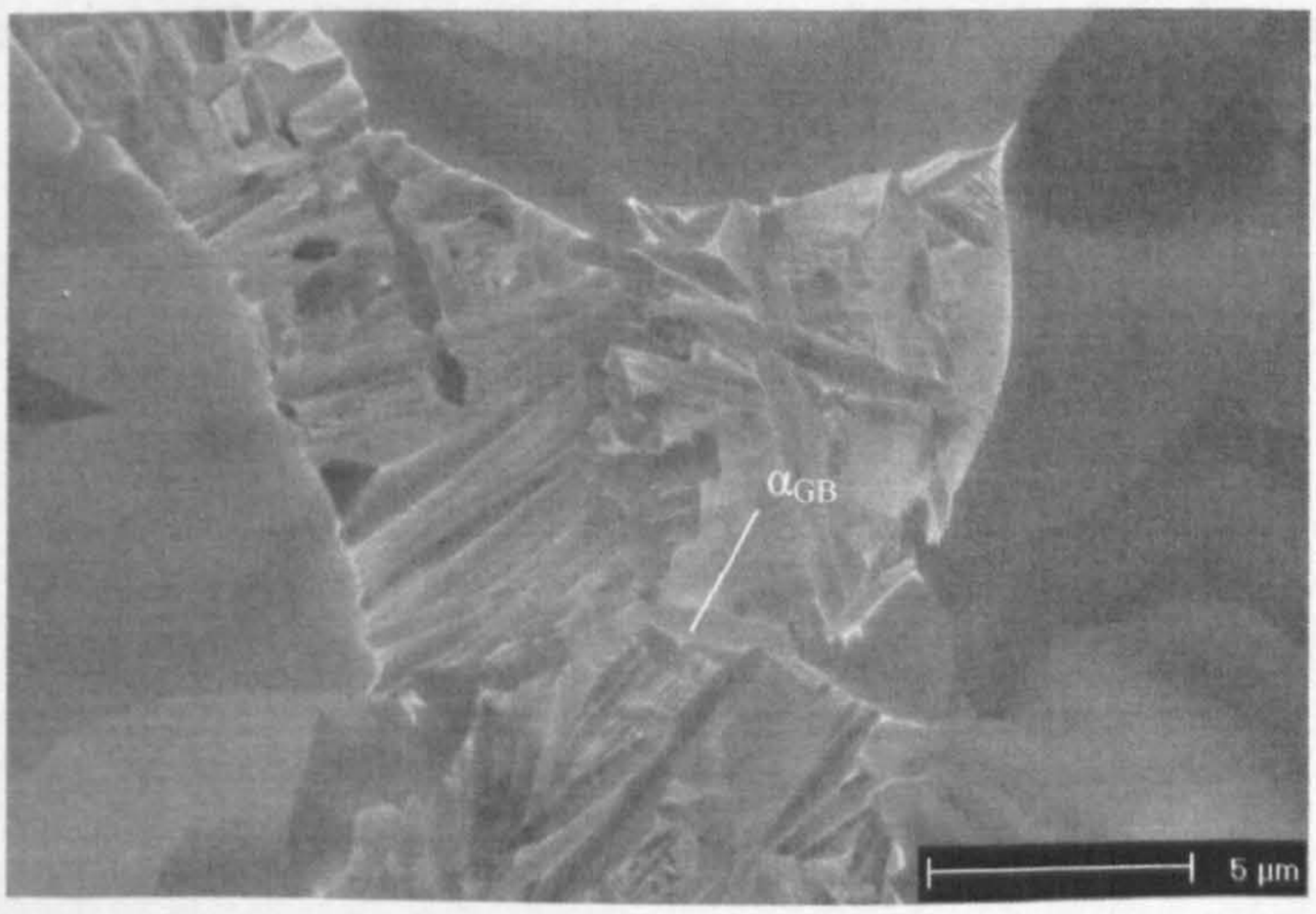

Fig. 7.34 BSE image 7mm from quenched end, $CR_{900} = 30°C\ s^{-1}$.

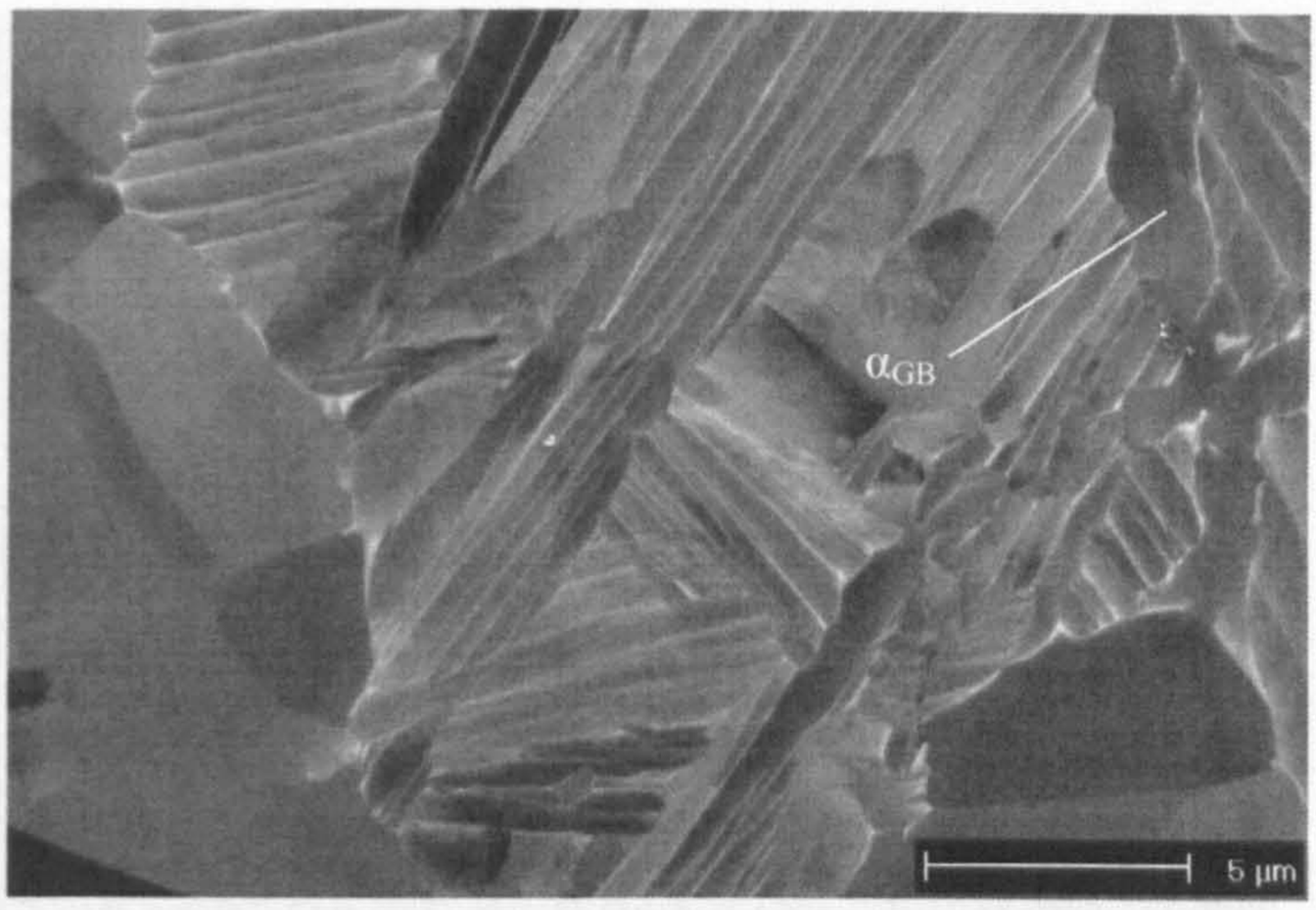

Fig. 7.35 BSE image 10mm from quenched end, $CR_{900} = 19°C\ s^{-1}$.

7.2.3 EBSD analysis

EBSD maps were also obtained at different locations along the Jominy specimen (Note: some of this data was also used in chapter 4 to test the applicability of the β reconstruction technique to transformed microstructures formed at different cooling rates). Figs. 7.36 to 7.45 show a series of EBSD maps obtained from the centre of the Jominy bar at different locations along its length. The direction of decreasing cooling rate i.e. the axis of the Jominy specimen, is orientated vertically with respect to all the maps. Four maps are shown for each figure, these are: (a) band contrast, (b) IPF map of the room temperature α phases (c) boundary map showing the deviation from an ideal Burgers orientation relation and (d) IPF map of the separated and reconstructed high temperature β phase. The distance from the quenched end of the bar is given for each figure, together with the estimated cooling rate at 900°C (CR_{900}).

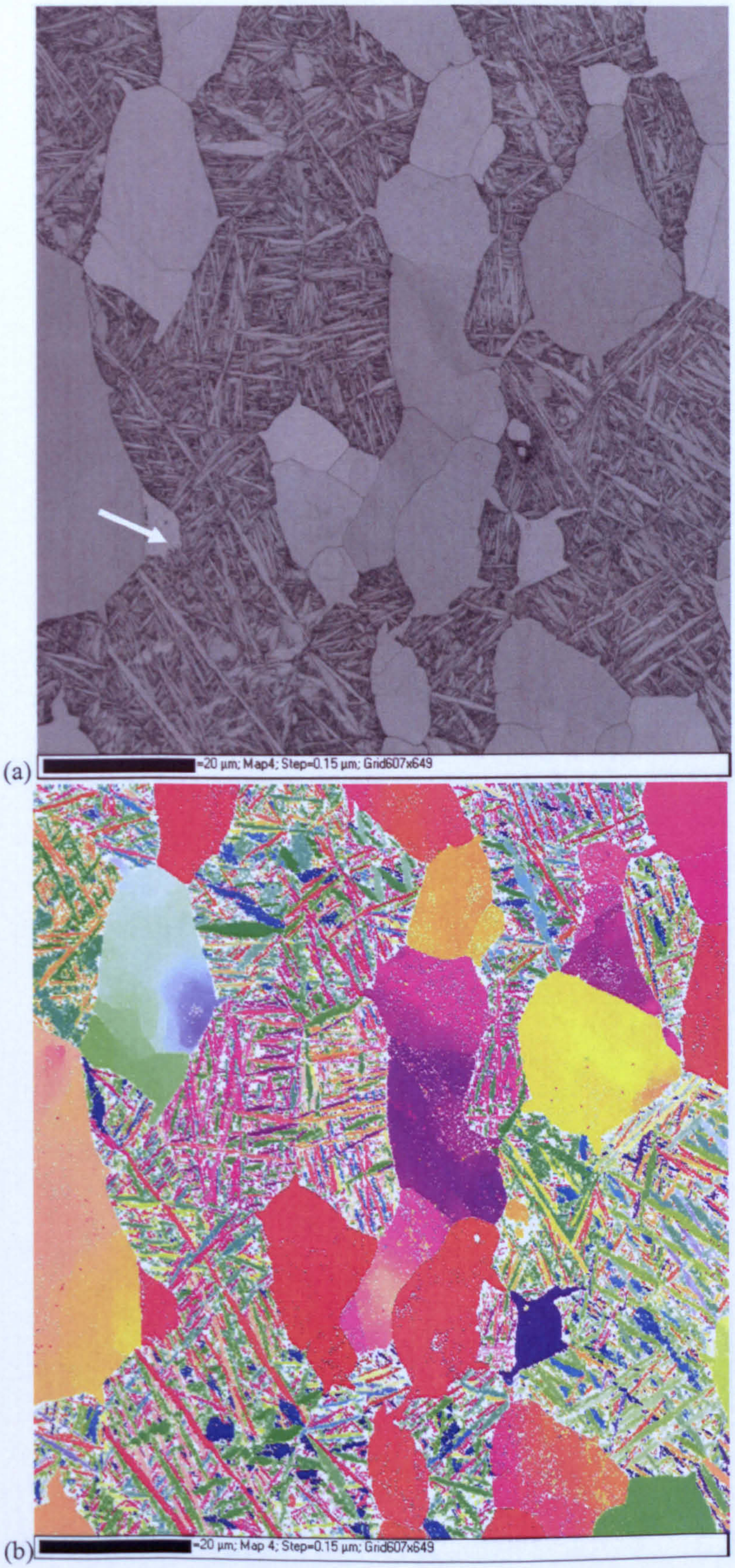
=20 µm; Map4; Step=0.15 µm; Grid607x649
=20 µm; Map 4; Step=0.15 µm; Grid607x649

(a)

(b)

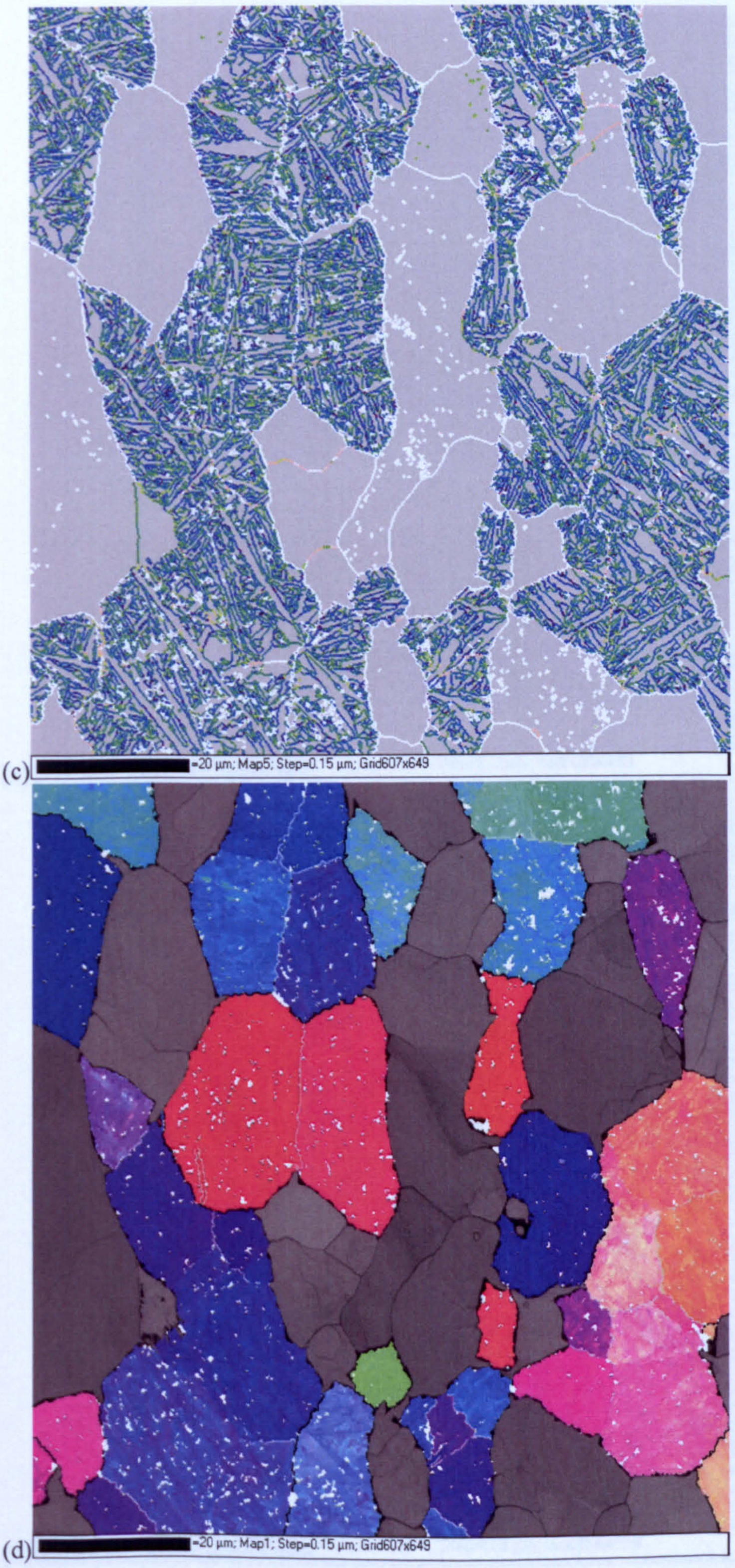

Fig. 7.36 EBSD map acquired 0.2mm from the quenched end using a 0.15µm step size, estimated CR_{900} >>500°C s^{-1}. (a) Band contrast. (b) IPF colouring. (c) Deviation from Burgers relation. (d) Reconstructed β phase.

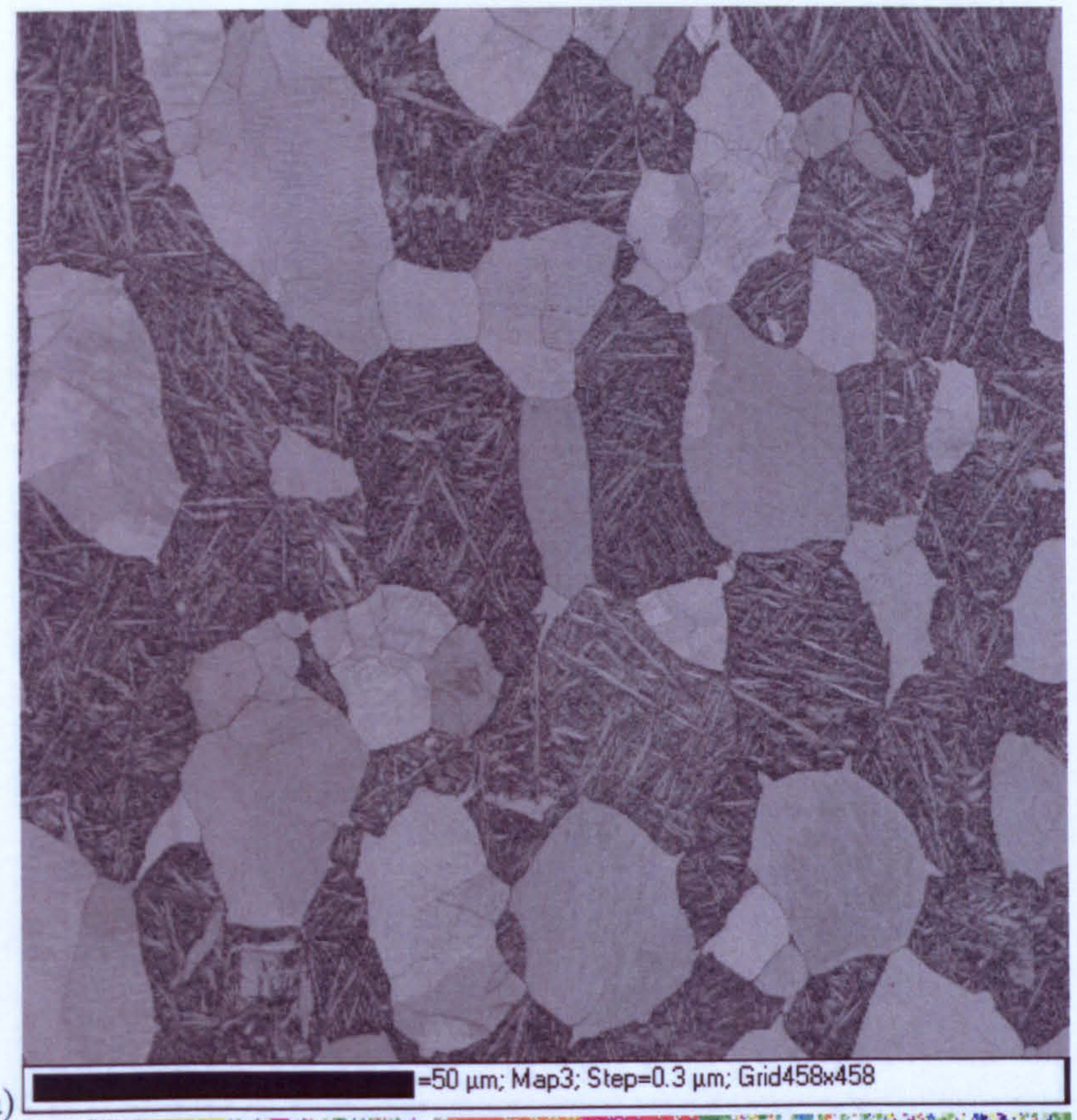
=50 µm; Map3; Step=0.3 µm; Grid458x458

(a)

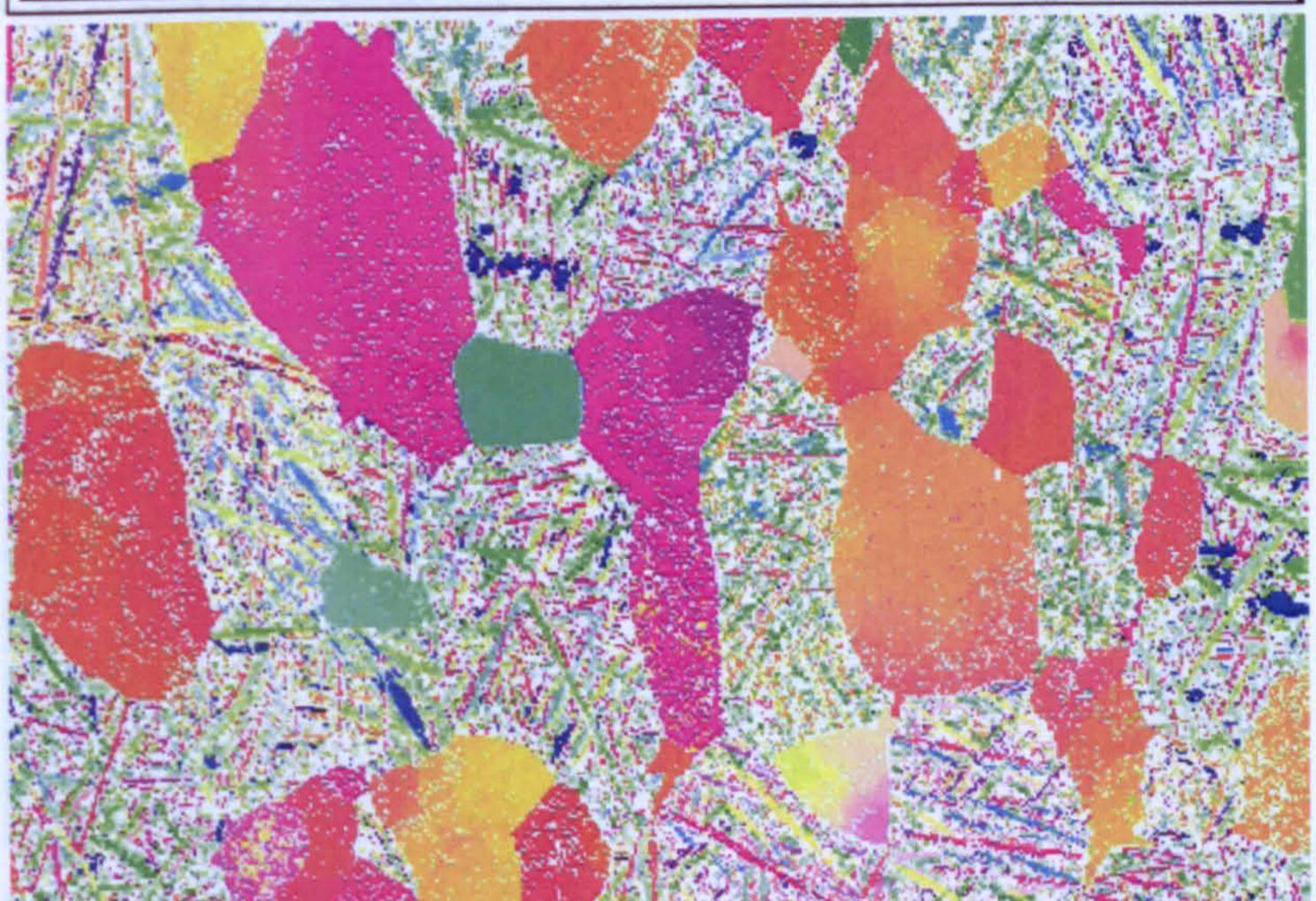

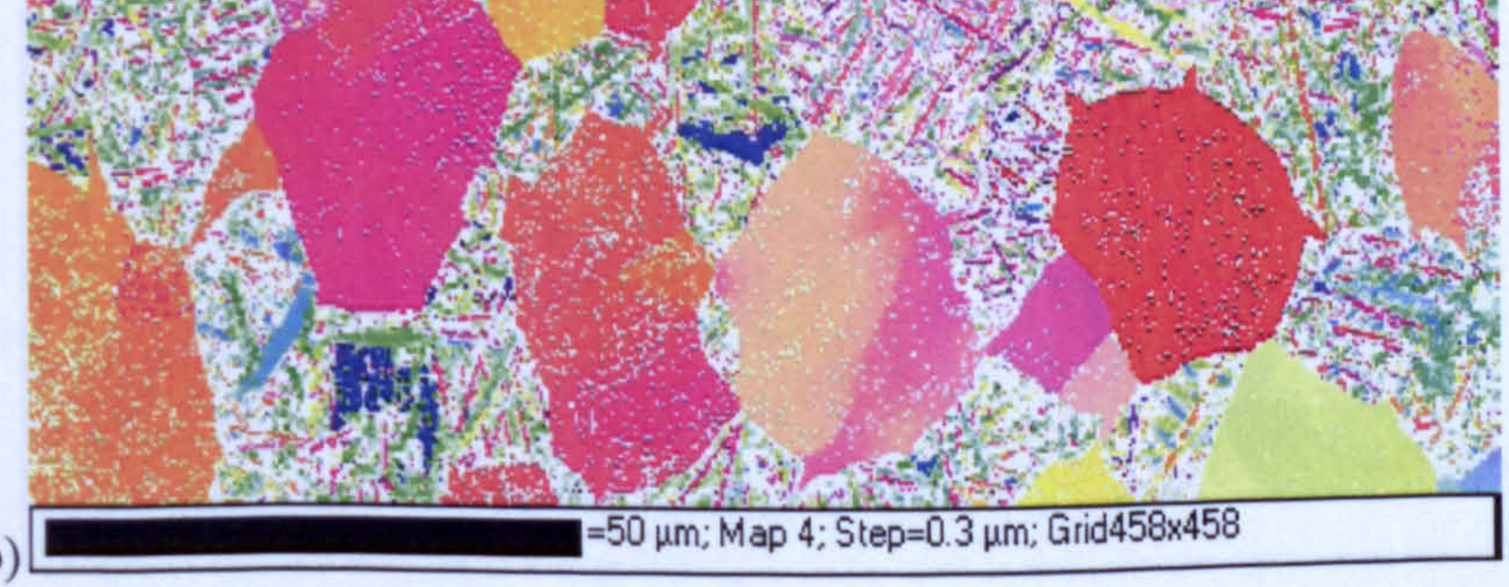
=50 µm; Map 4; Step=0.3 µm; Grid458x458

(b)

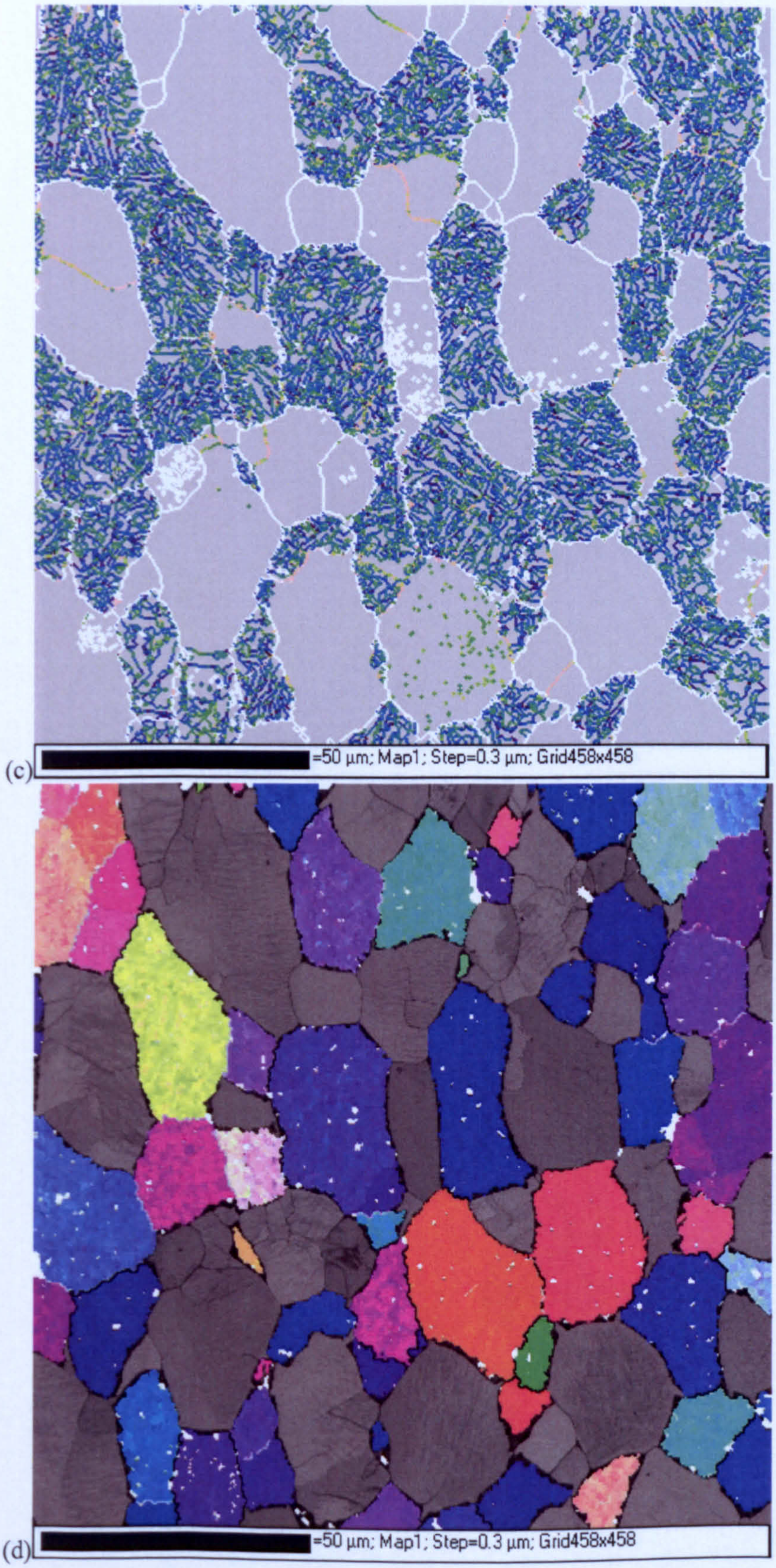

Fig. 7.37 EBSD map acquired 1.0mm from the quenched end using a 0.3µm step size, estimated CR_{900} ~400°C s^{-1}. (a) Band contrast. (b) IPF colouring. (c) Deviation from Burgers relation. (d) Reconstructed β phase.

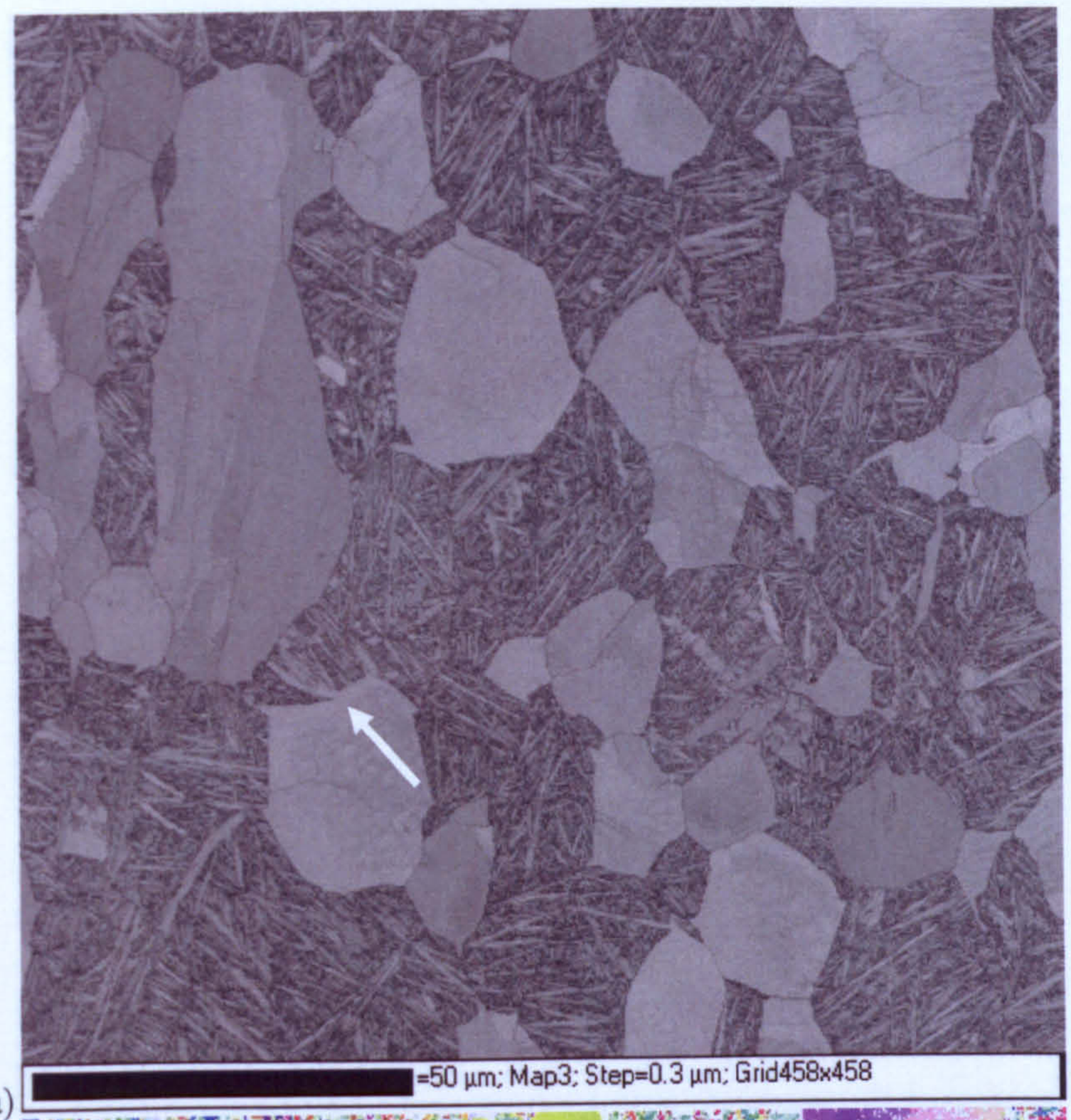
=50 µm; Map3; Step=0.3 µm; Grid458x458

(a)

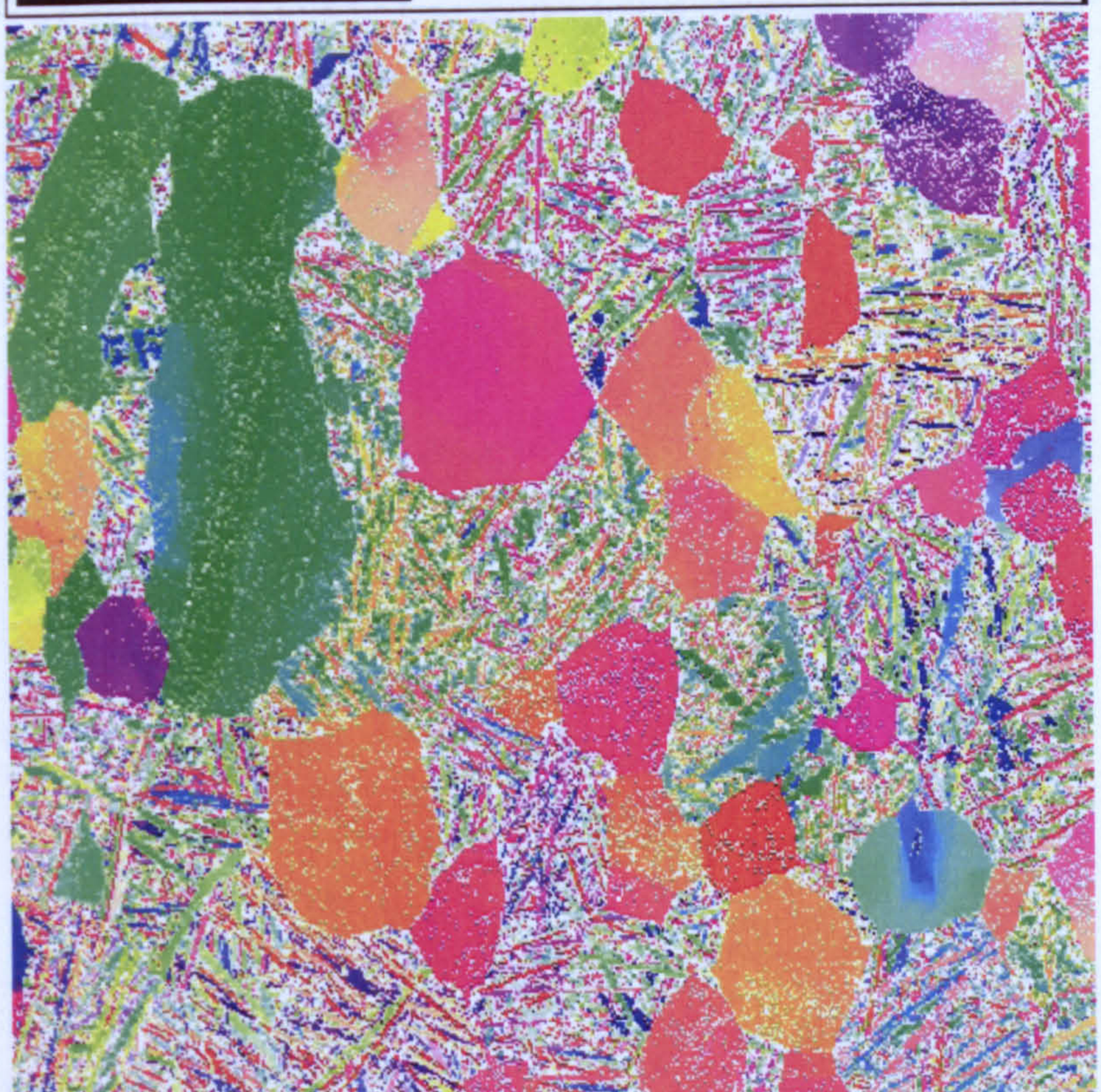

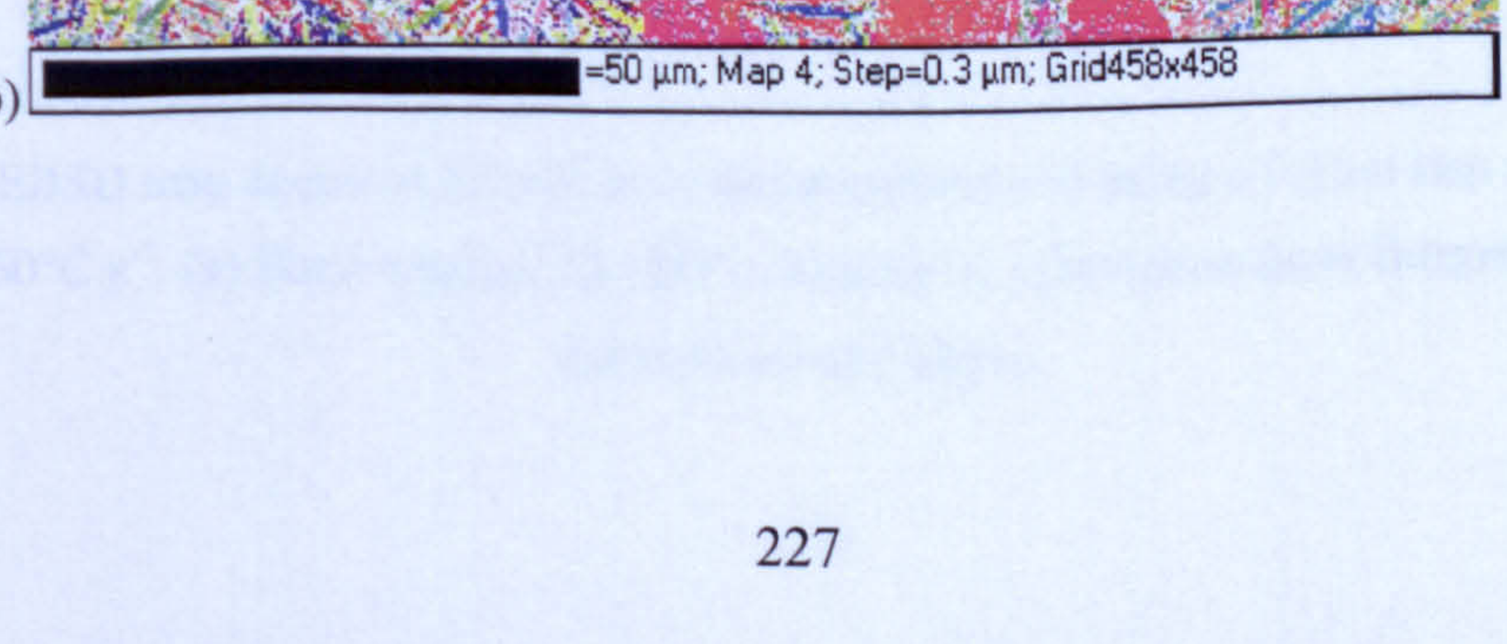
=50 µm; Map 4; Step=0.3 µm; Grid458x458

(b)

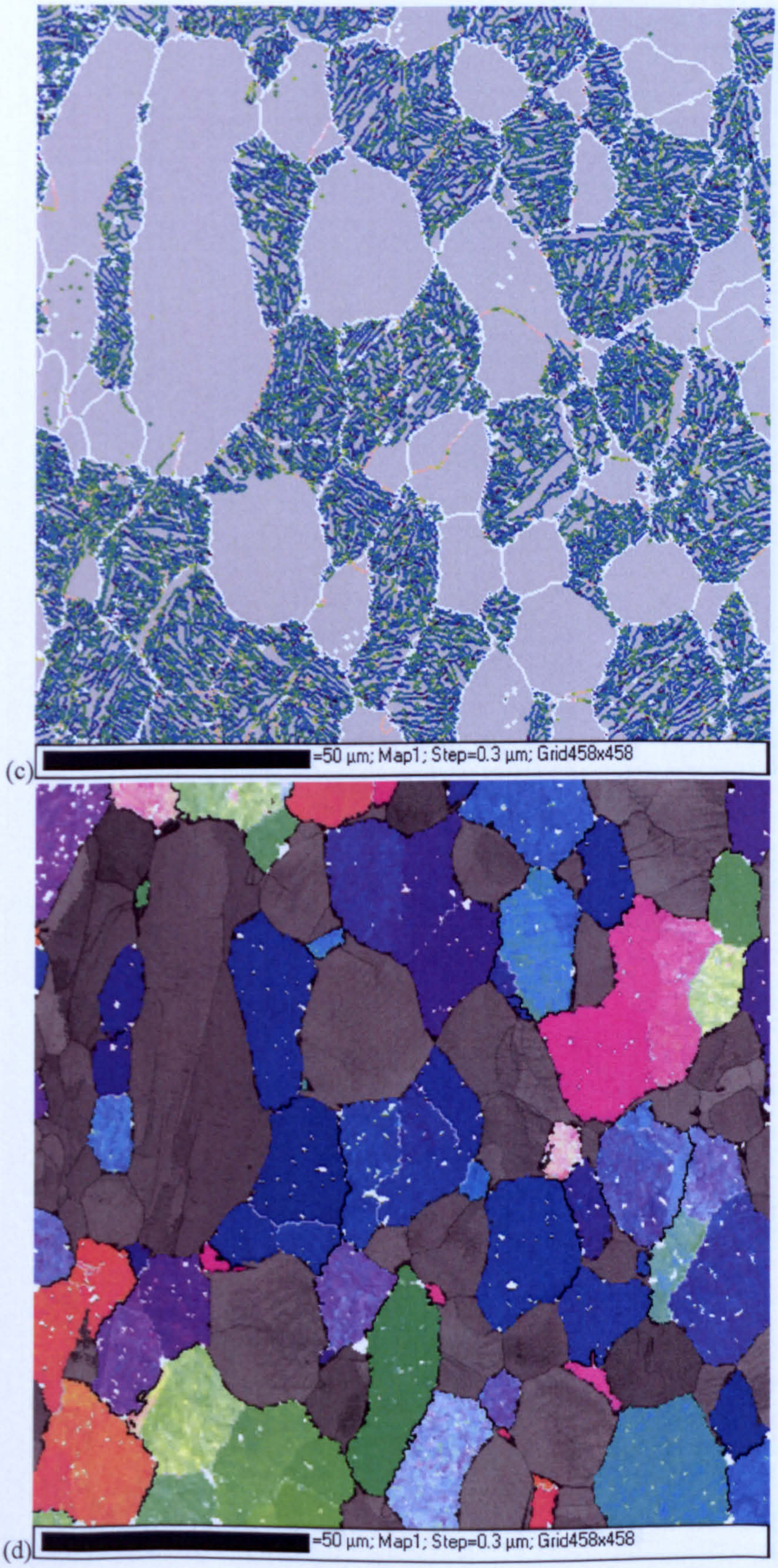

Fig. 7.38 EBSD map acquired 2.0mm from the quenched end using a 0.3µm step size, estimated CR_{900} ~160°C s^{-1}. (a) Band contrast. (b) IPF colouring. (c) Deviation from Burgers relation. (d) Reconstructed β phase.

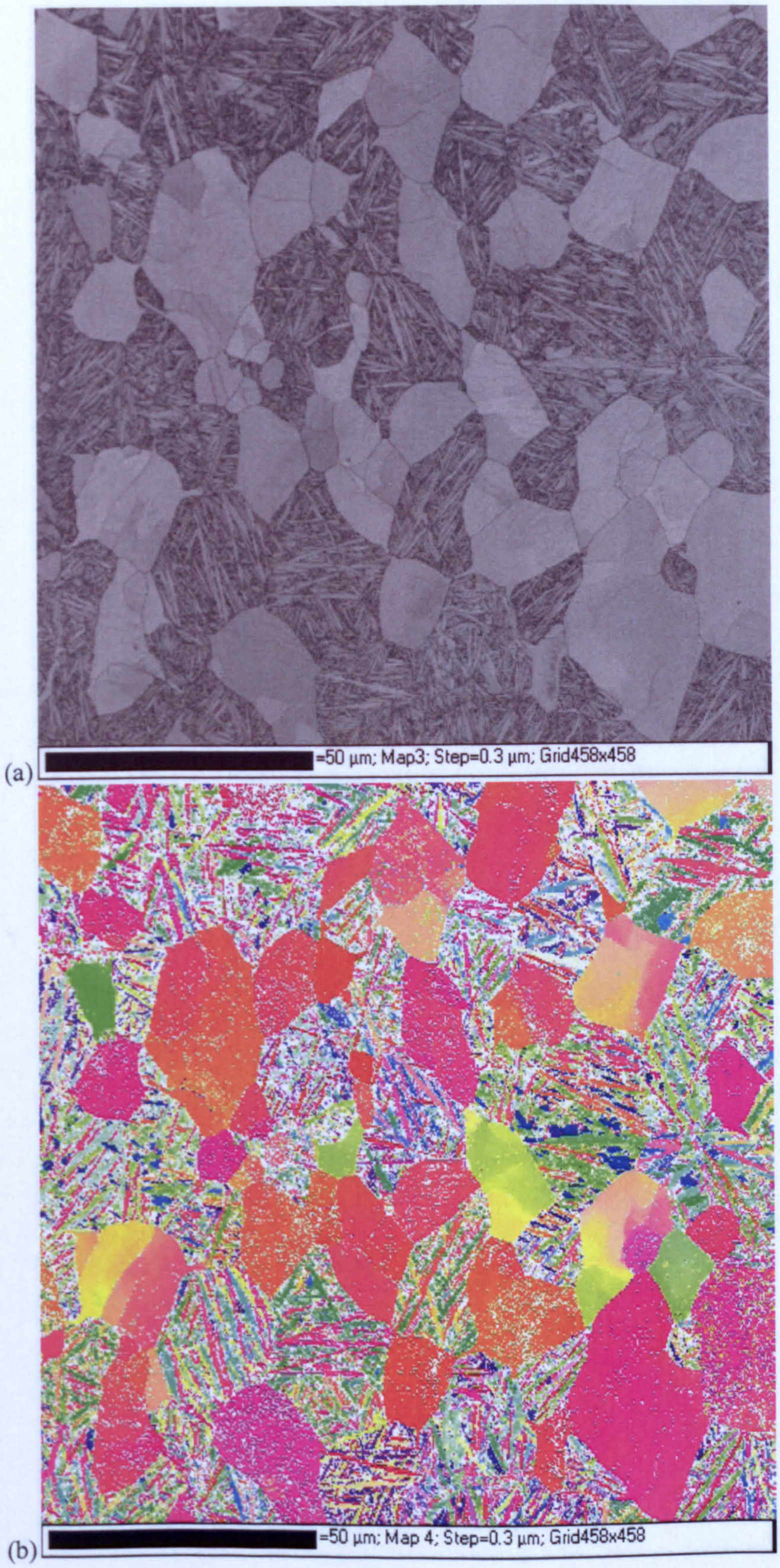
=50 µm; Map3; Step=0.3 µm; Grid458x458
=50 µm; Map 4; Step=0.3 µm; Grid458x458

(a)

(b)

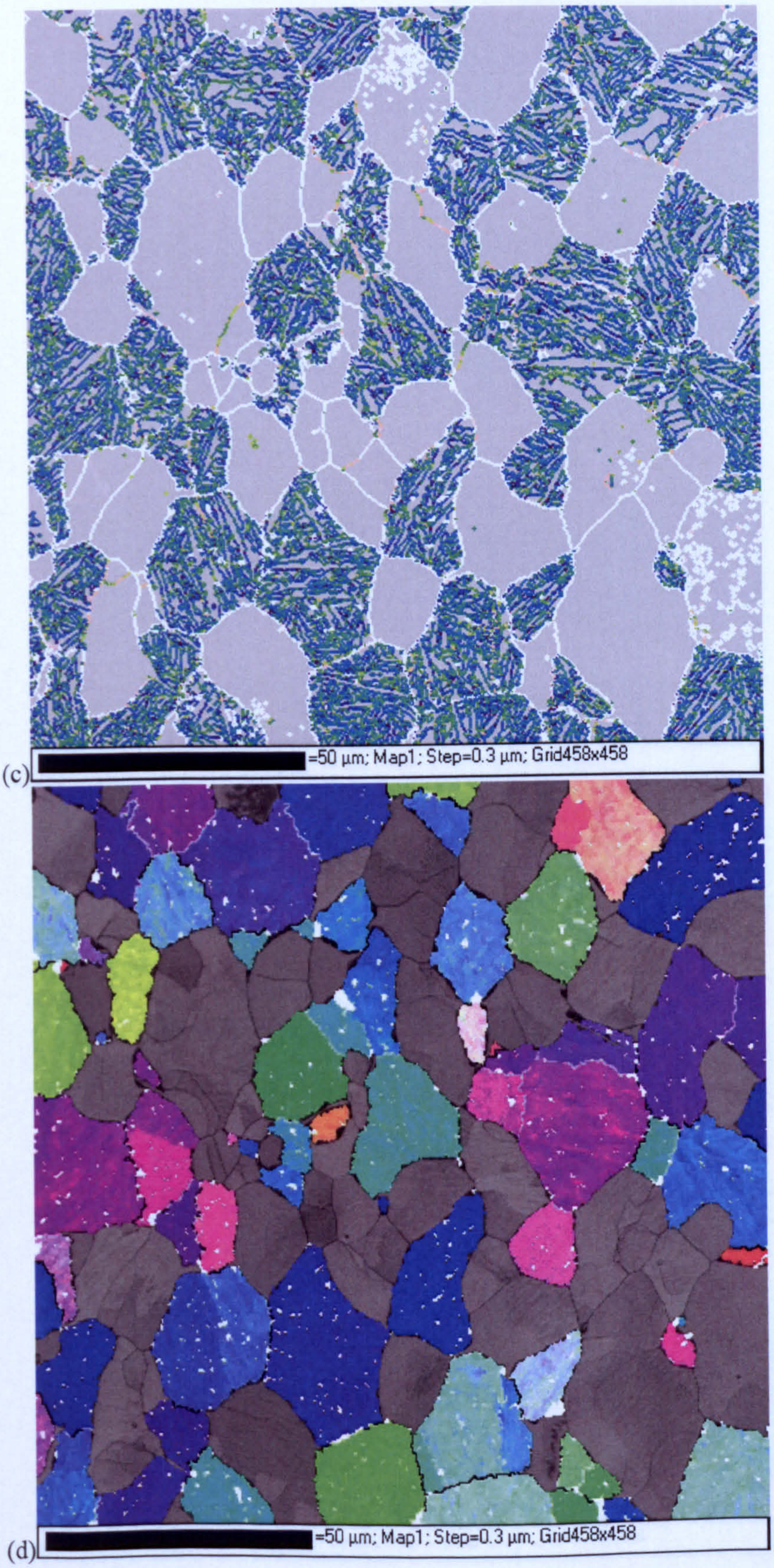

Fig. 7.39 EBSD map acquired 3.0mm from the quenched end using a 0.3µm step size, measured $CR_{900} = 100°C\ s^{-1}$. (a) Band contrast. (b) IPF colouring. (c) Deviation from Burgers relation. (d) Reconstructed β phase.

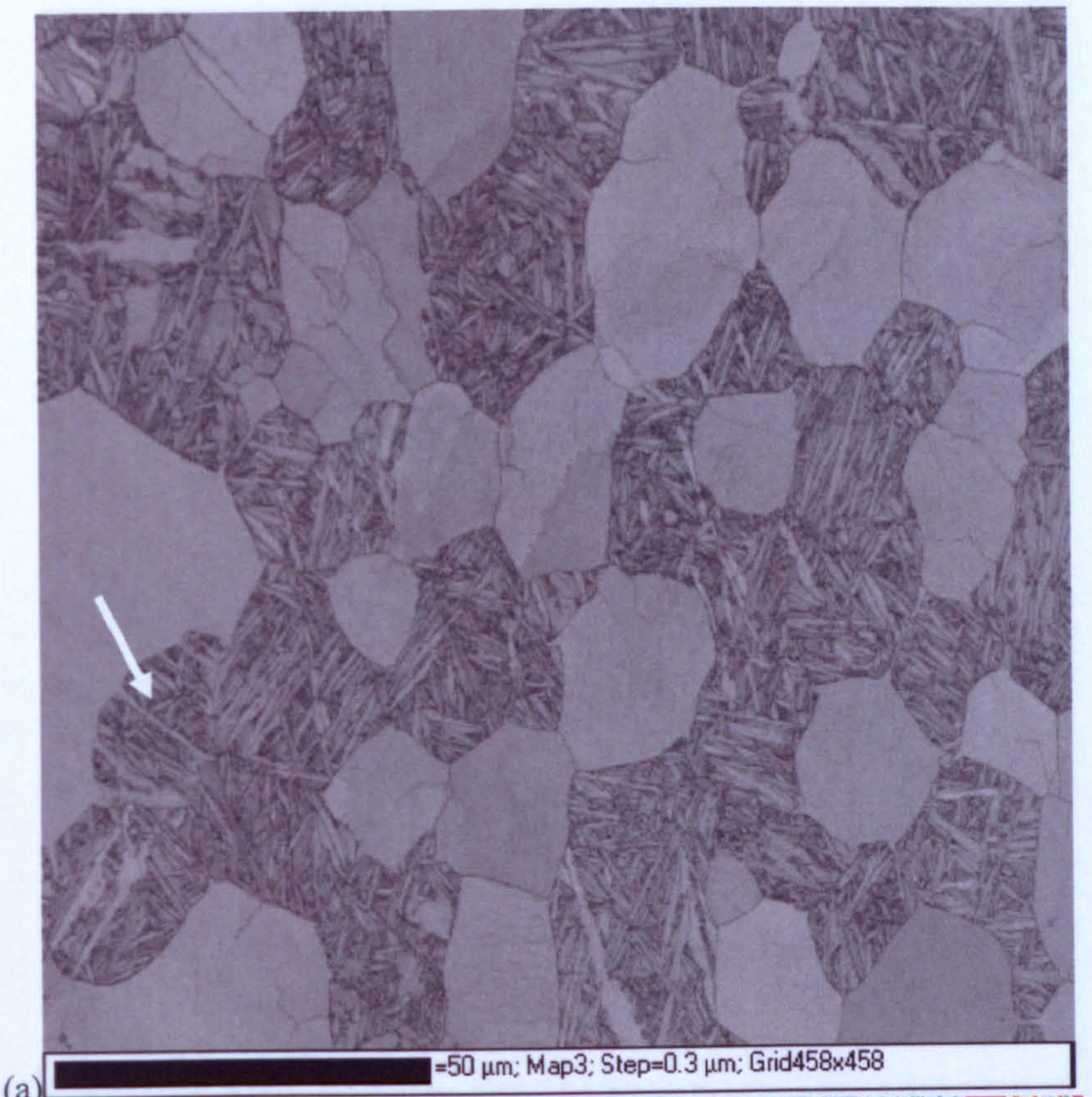
=50 µm; Map3; Step=0.3 µm; Grid458x458

(a)

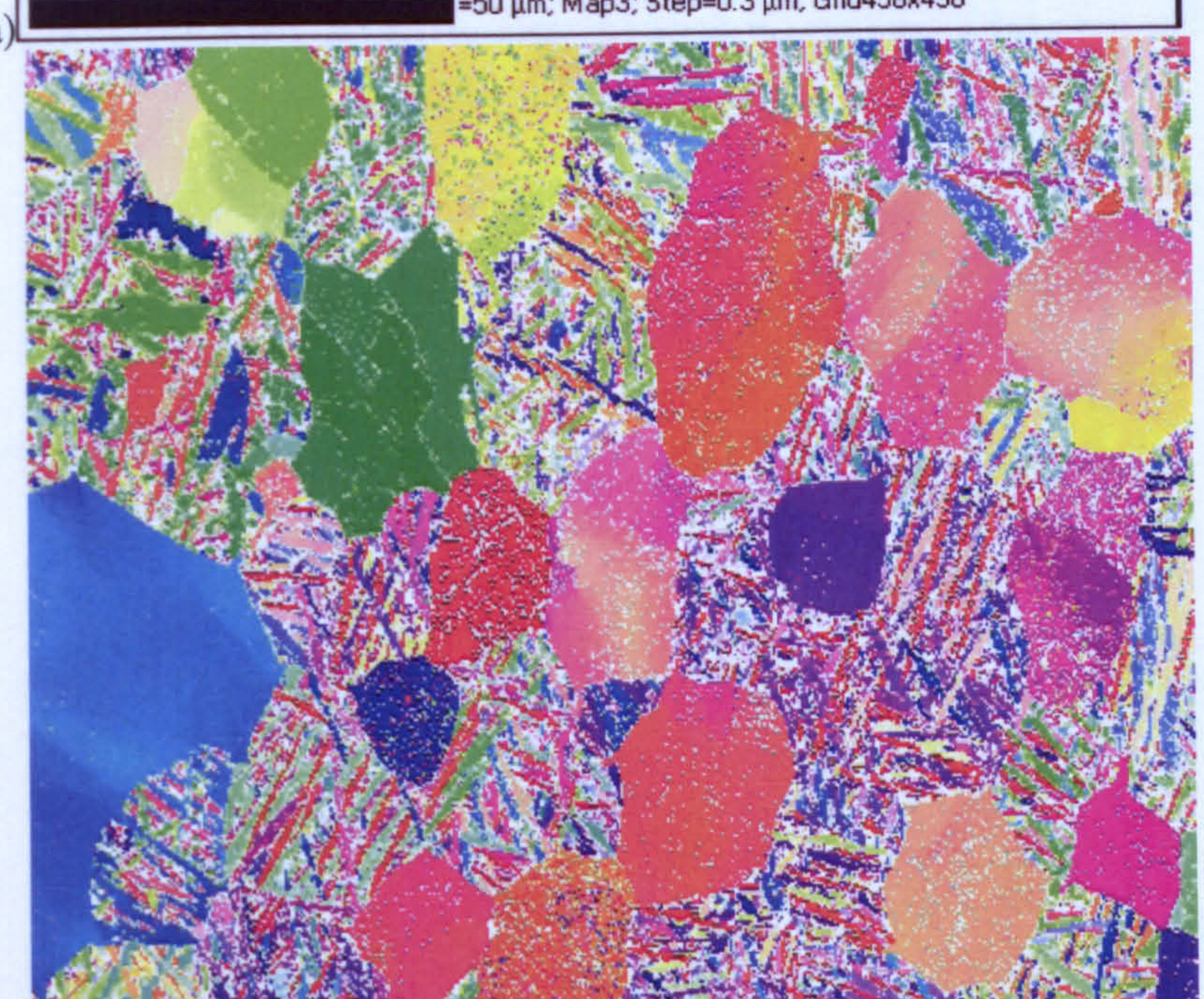


=50 µm; Map 4; Step=0.3 µm; Grid458x458

(b)

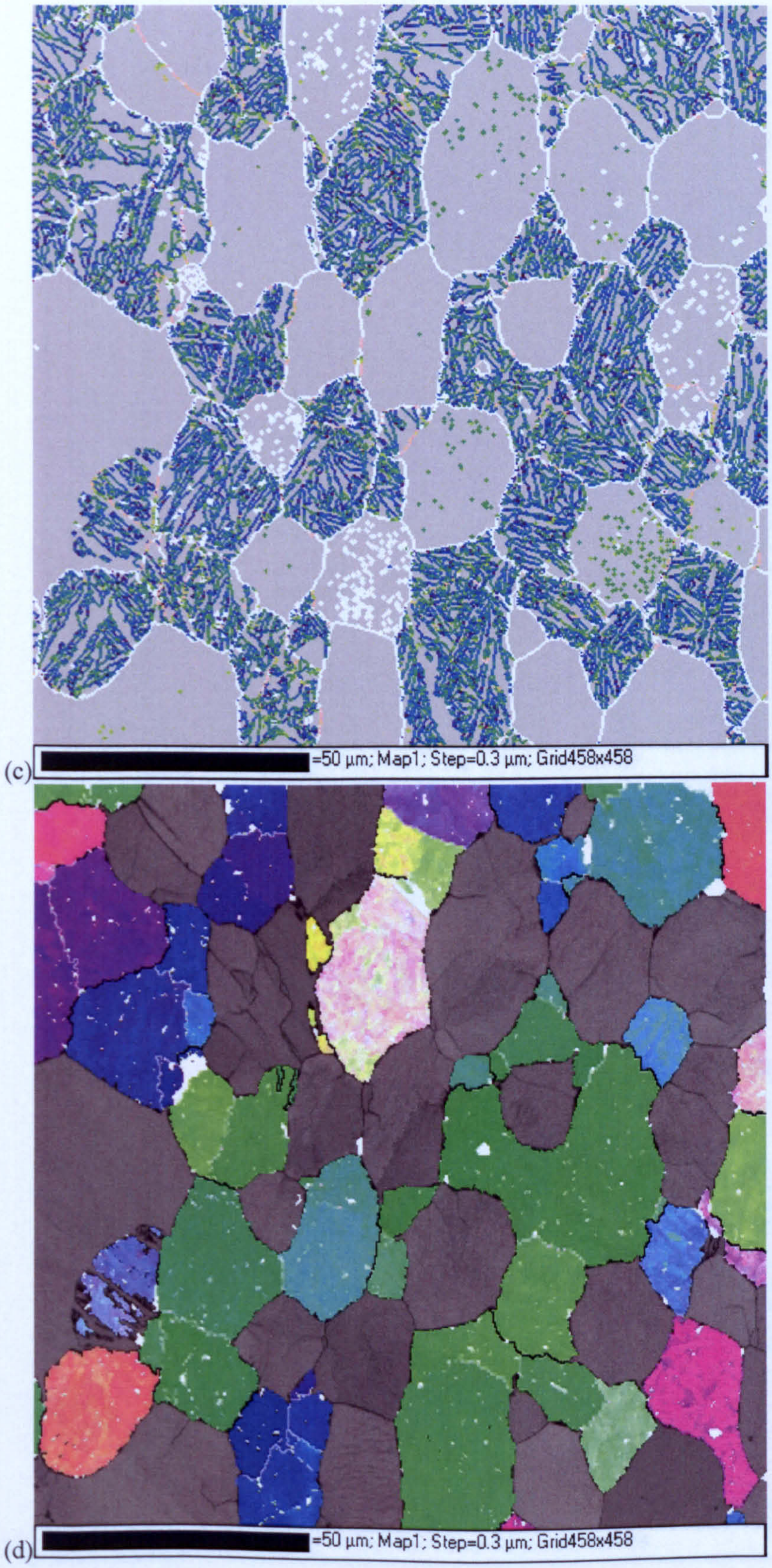

Fig. 7.40 EBSD map acquired 4.0mm from the quenched end using a 0.3µm step size, $CR_{900} = 63°C\ s^{-1}$. (a) Band contrast. (b) IPF colouring. (c) Deviation from Burgers relation. (d) Reconstructed β phase.

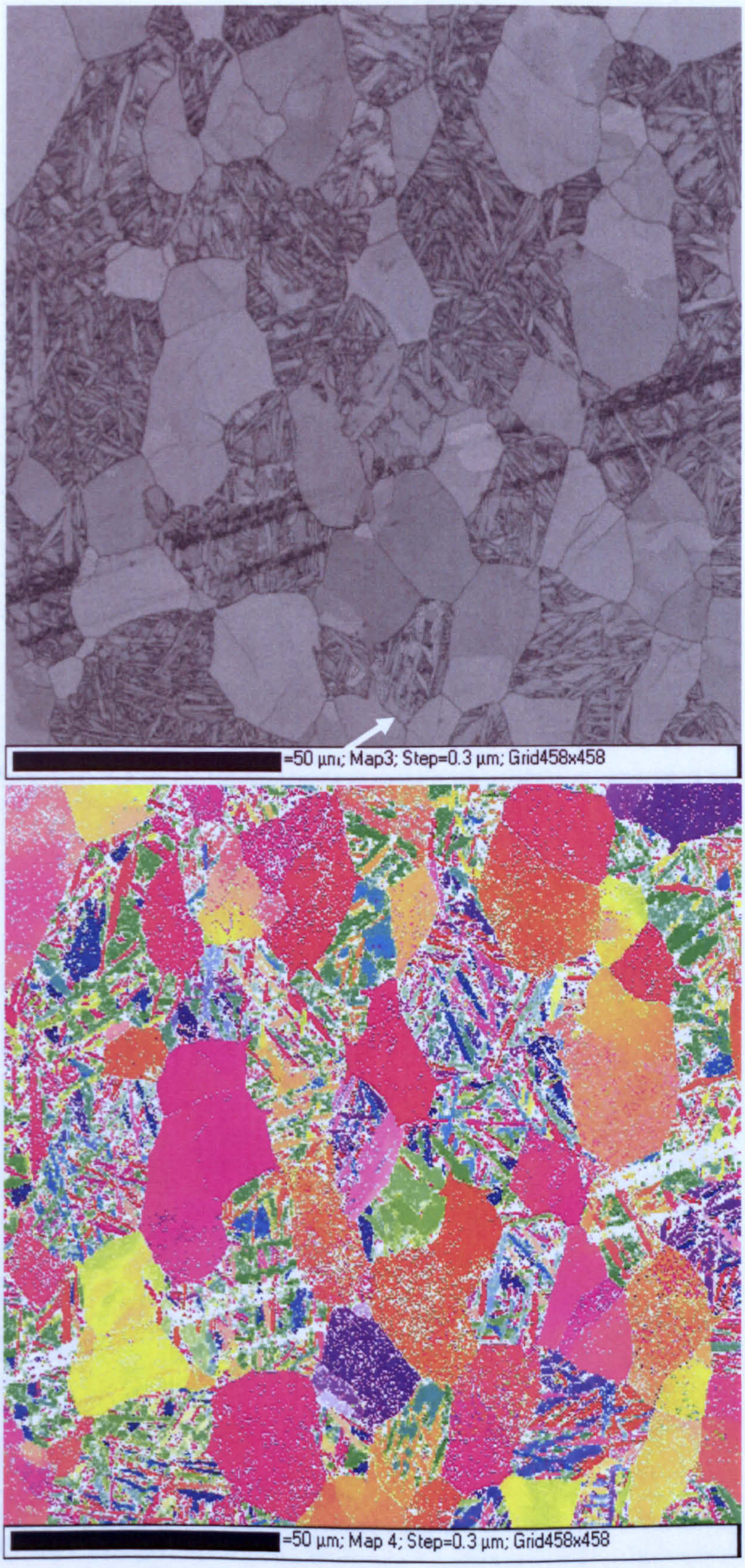
=50 µm; Map3; Step=0.3 µm; Grid458x458
=50 µm; Map 4; Step=0.3 µm; Grid458x458

(a)

(b)

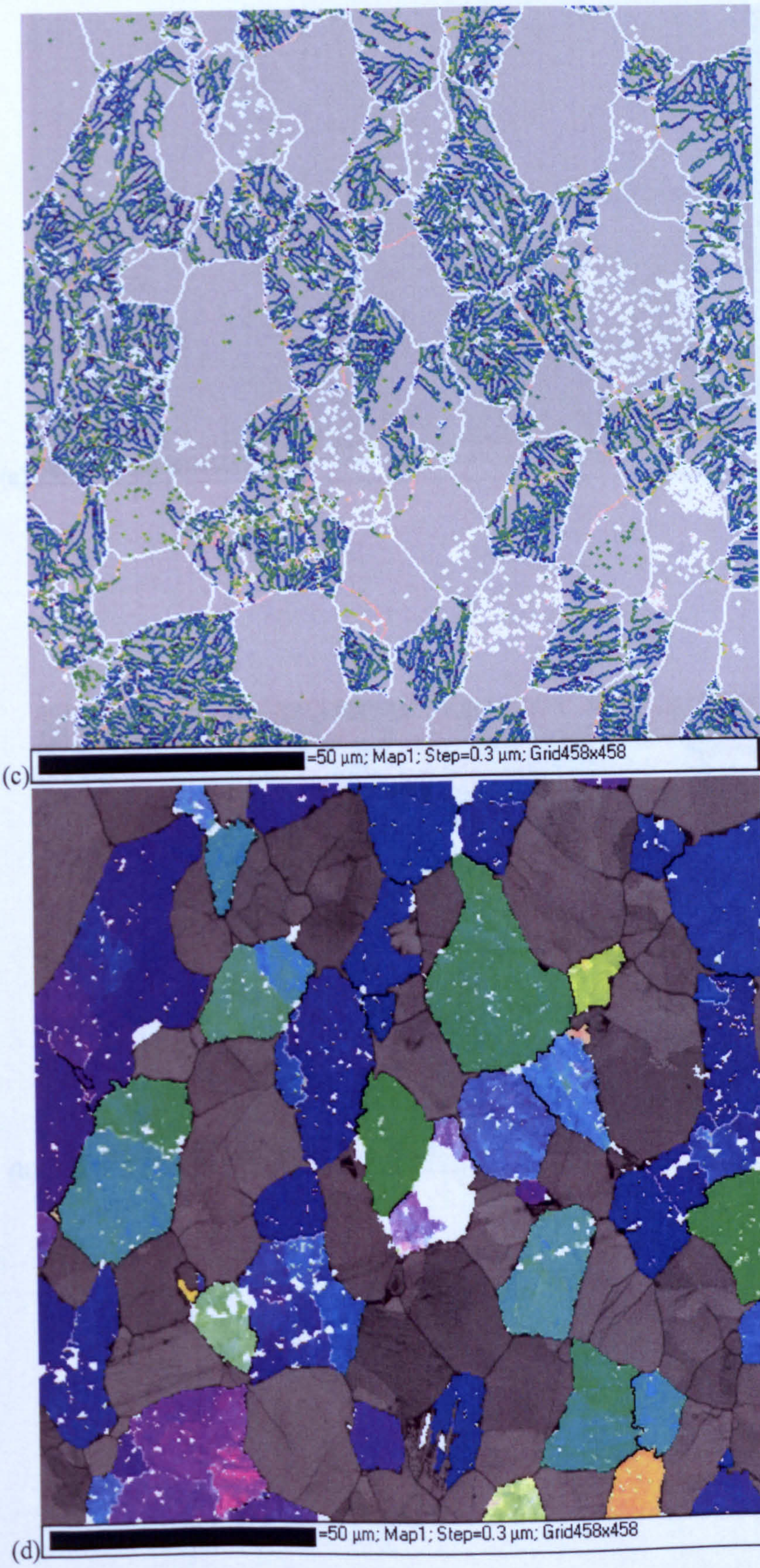

(c)

(d)

Fig. 7.41 EBSD map acquired 5.0mm from the quenched end using a 0.3µm step size, $CR_{900} = 47°C\ s^{-1}$. (a) Band contrast. (b) IPF colouring. (c) Deviation from Burgers relation. (d) Reconstructed β phase

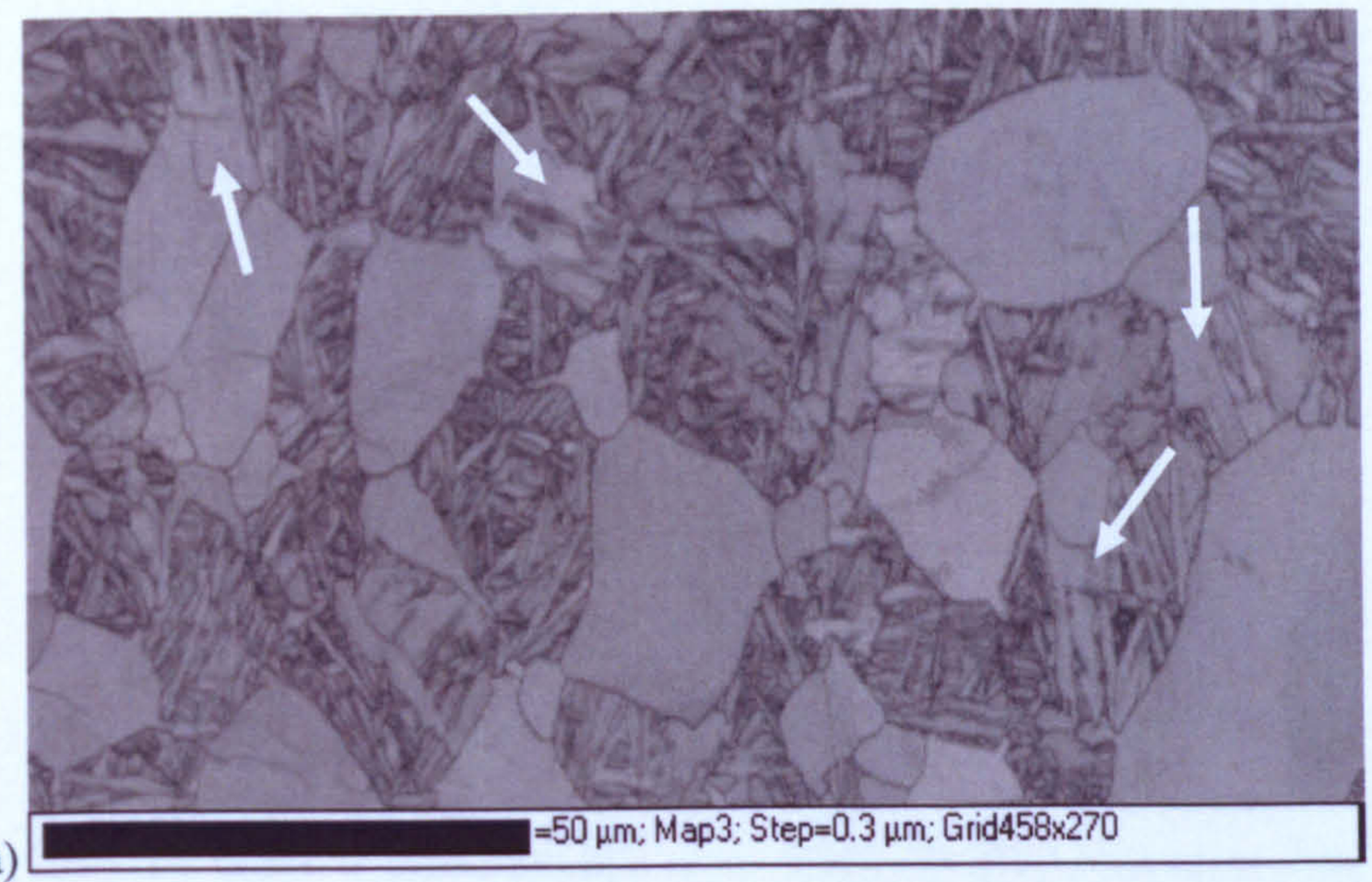
=50 µm; Map3; Step=0.3 µm; Grid458x270

(a)

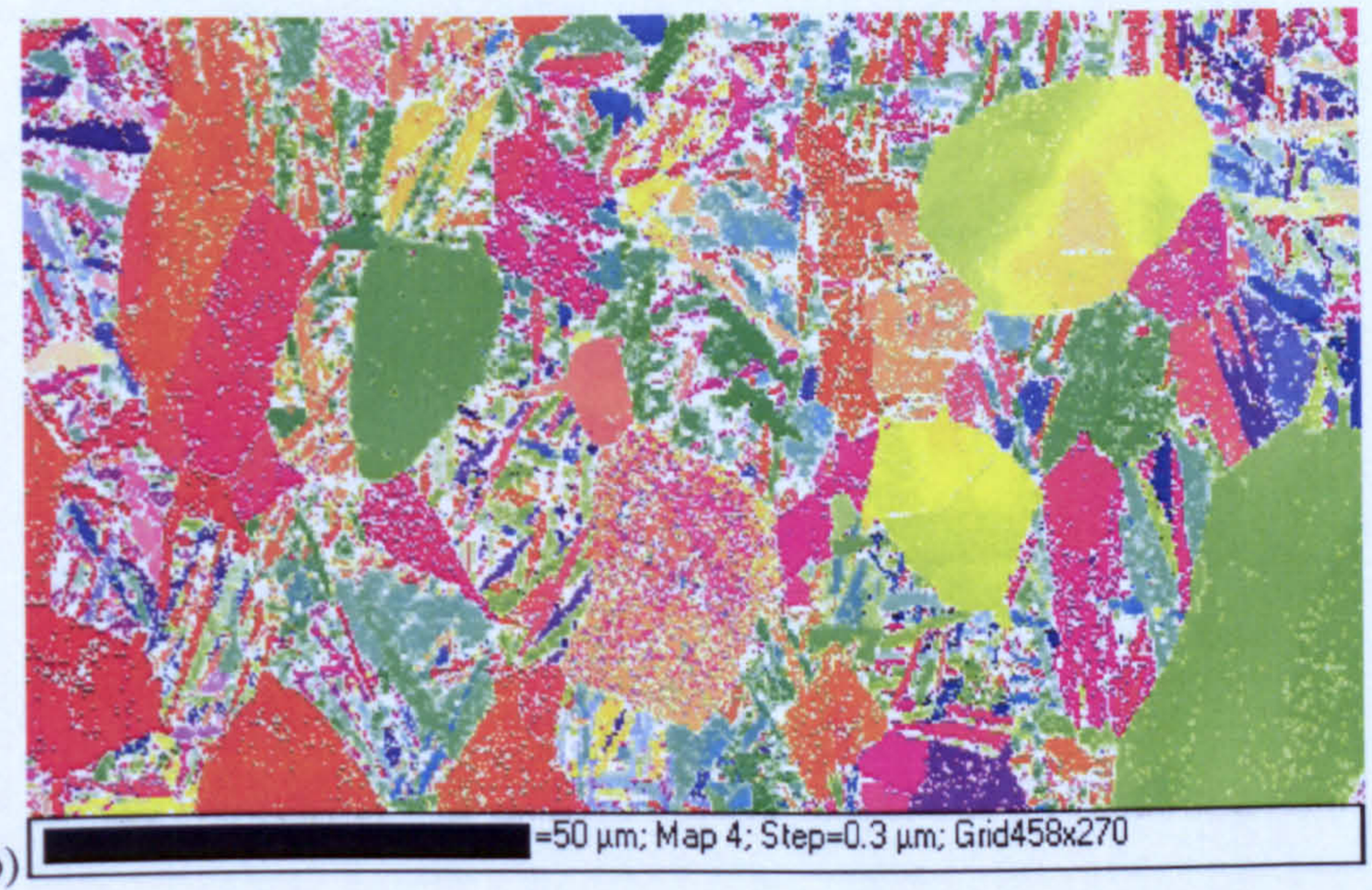
=50 µm; Map 4; Step=0.3 µm; Grid458x270

(b)

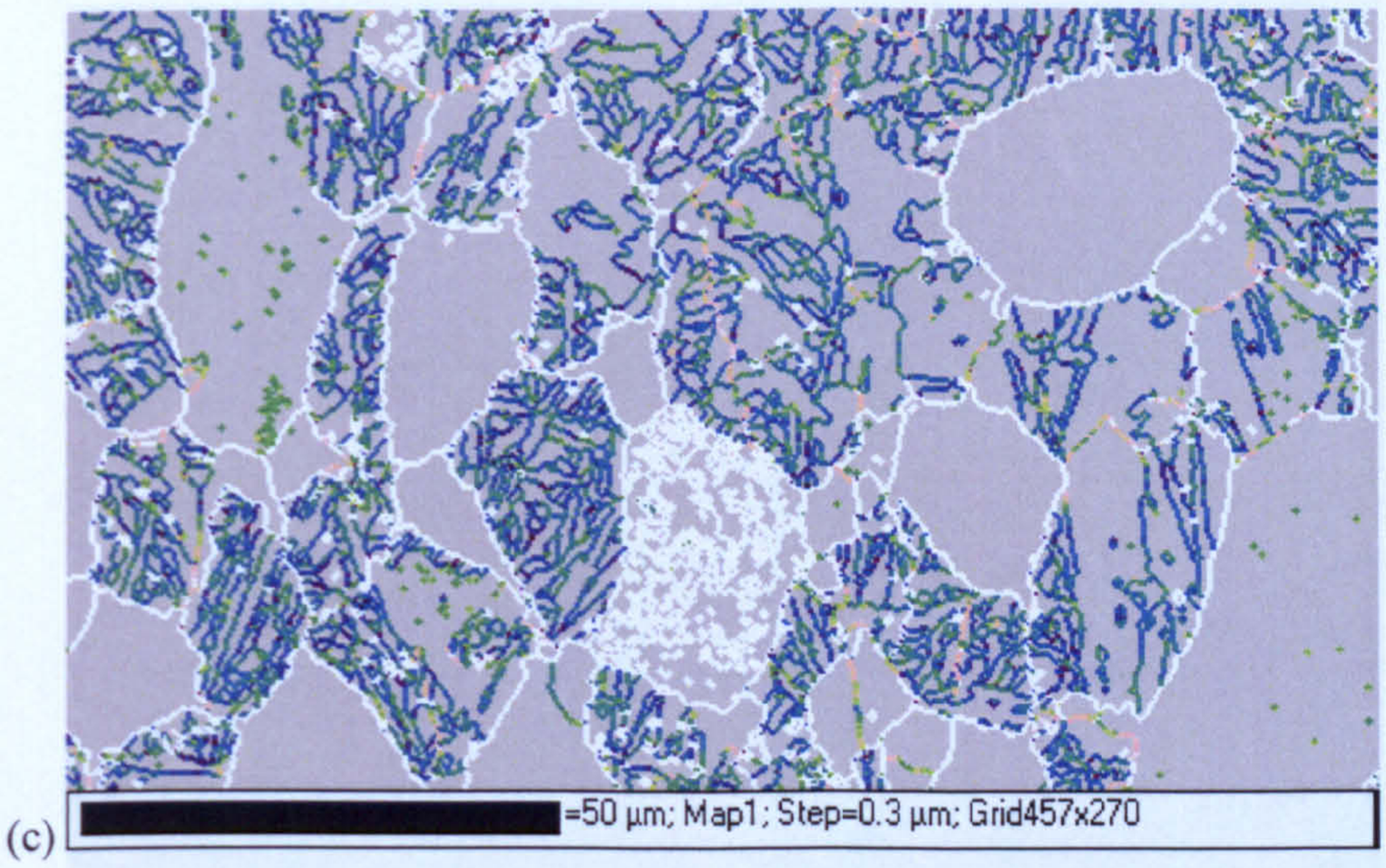

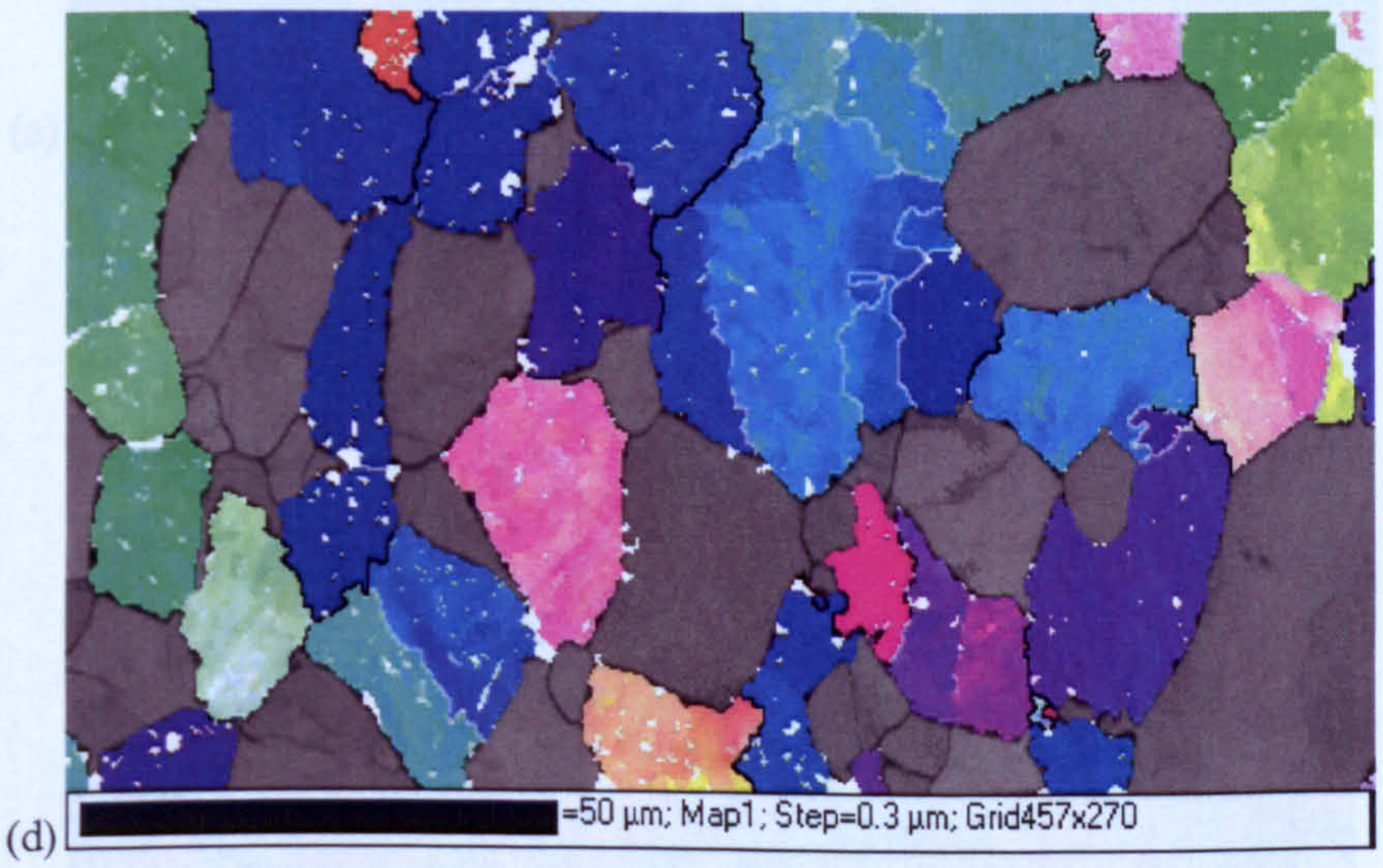

Fig. 7.42 EBSD map acquired 6.0mm from the quenched end using a 0.3µm step size, $CR_{900} = 37°C\ s^{-1}$. (a) Band contrast. (b) IPF colouring. (c) Deviation from Burgers relation. (d) Reconstructed β phase

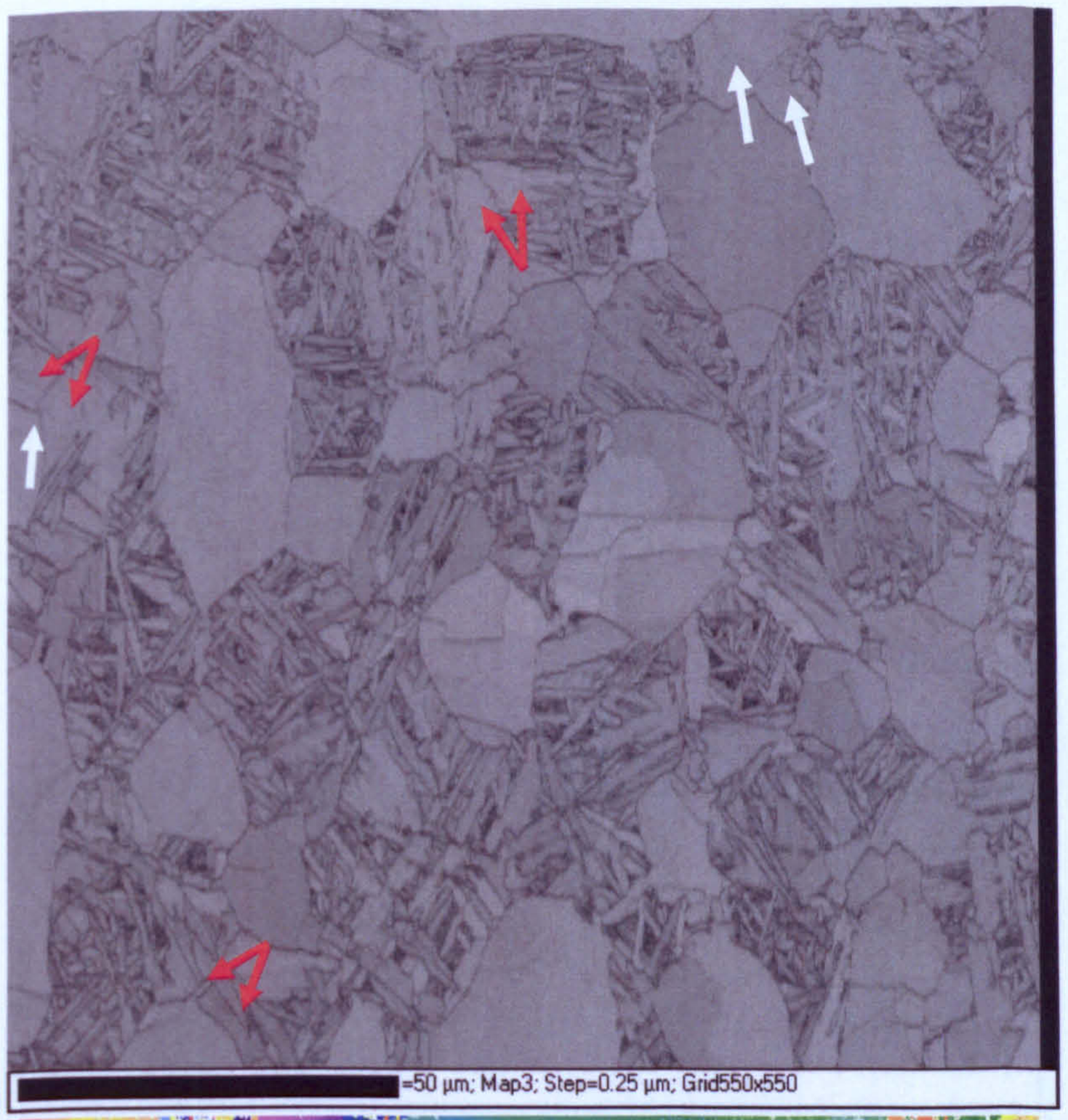
=50 µm; Map3; Step=0.25 µm; Grid550x550

(a)

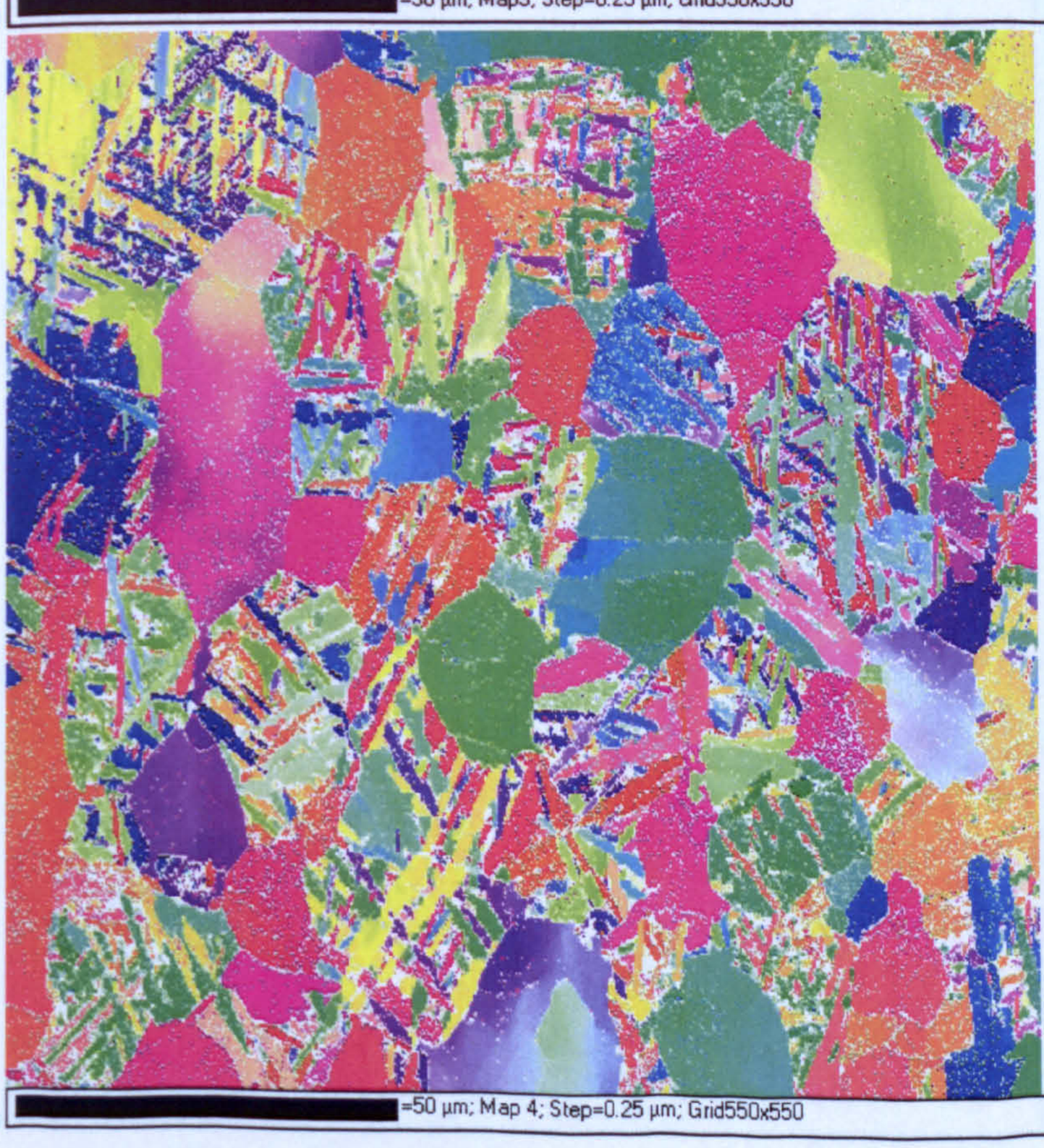

(b)

=50 µm; Map 4; Step=0.25 µm; Grid550x550

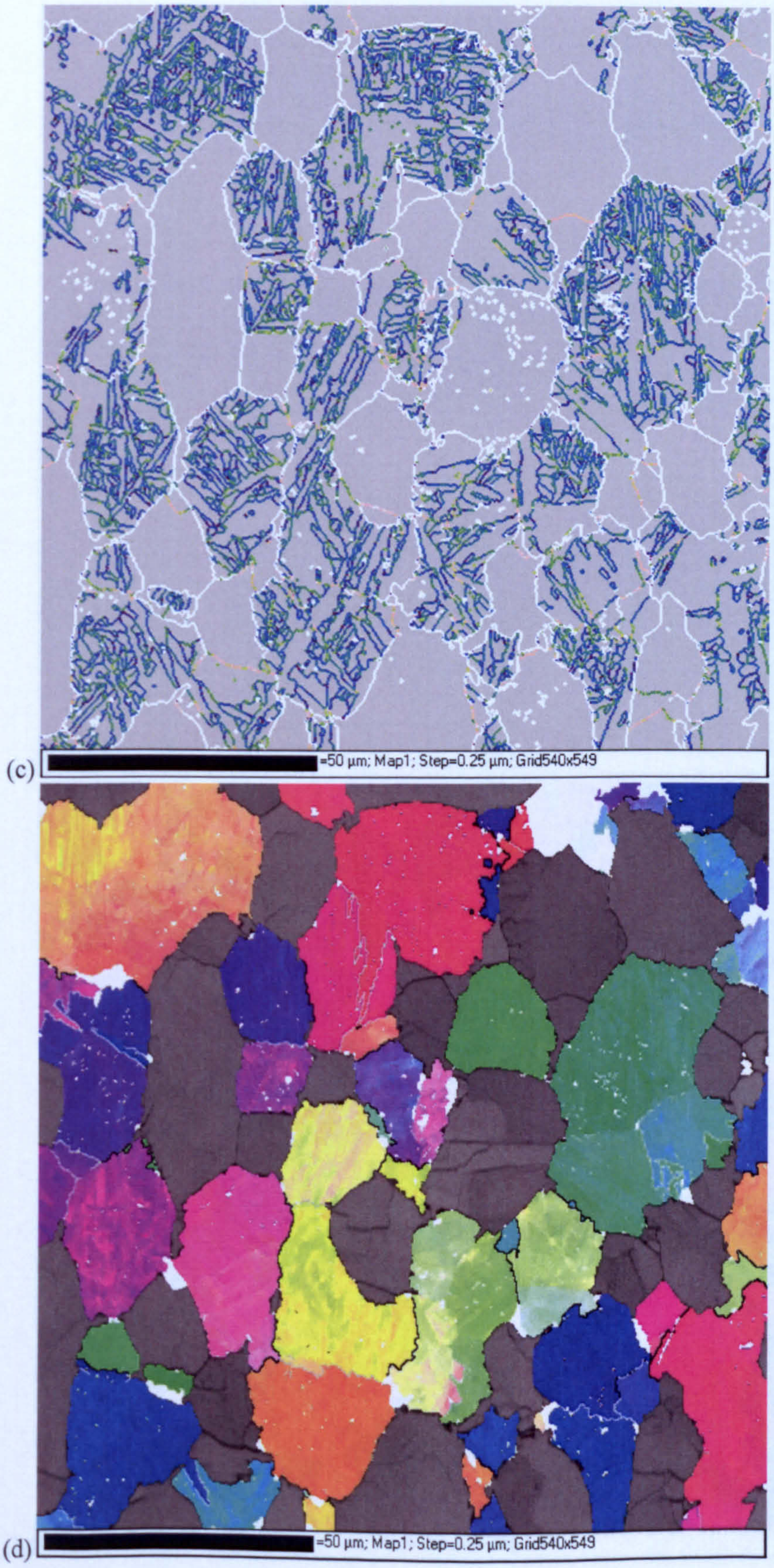

(c)

(d)

Fig. 7.43 EBSD map acquired 8.7mm from the quenched end using a 0.25µm step size, $CR_{900} = 22°C\ s^{-1}$. (a) Band contrast. (b) IPF colouring. (c) Deviation from Burgers relation. (d) Reconstructed β phase.

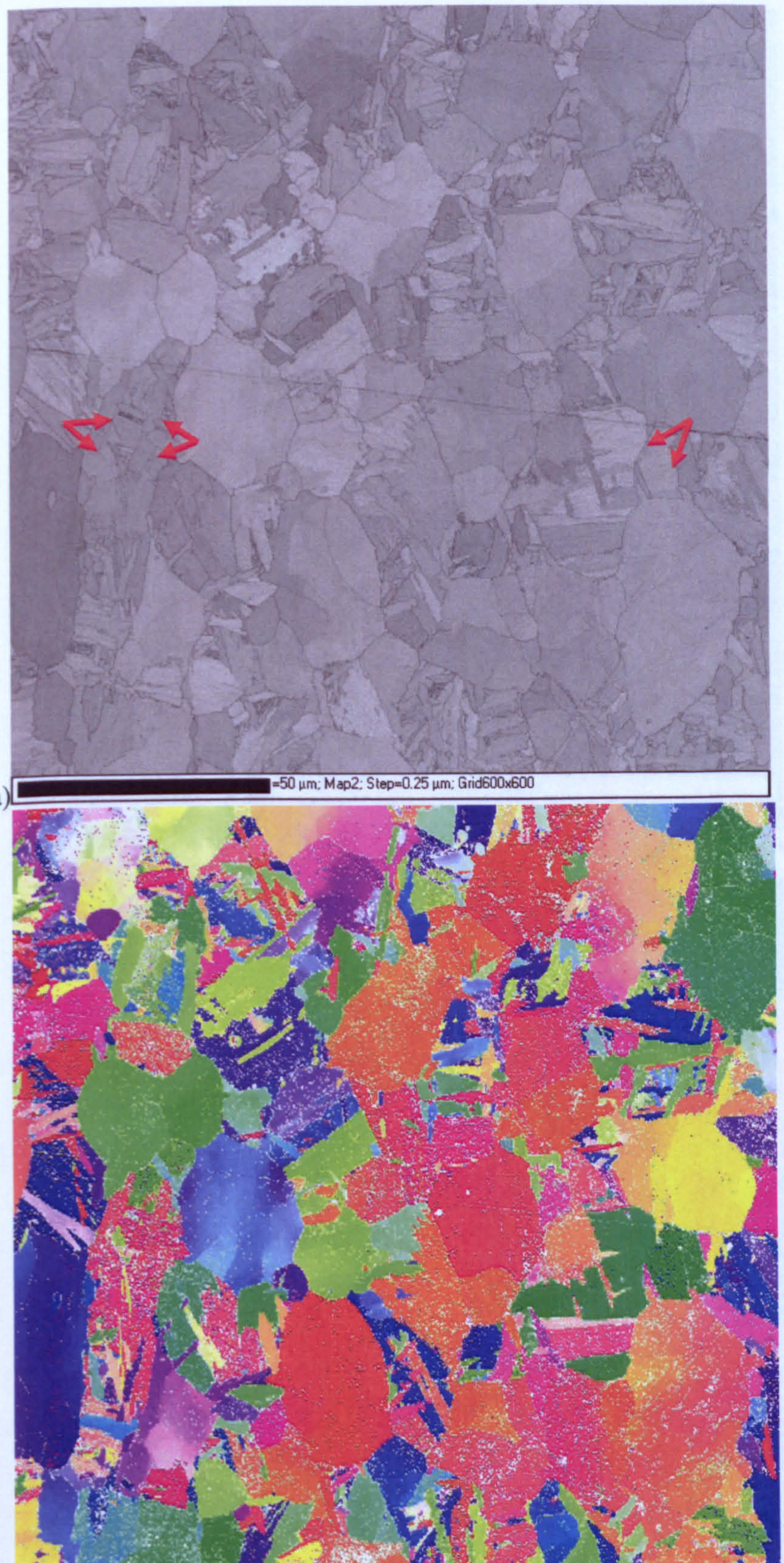
=50 µm; Map2; Step=0.25 µm; Grid600x600
=50 µm; Map1; Step=0.25 µm; Grid600x600

(a)

(b)

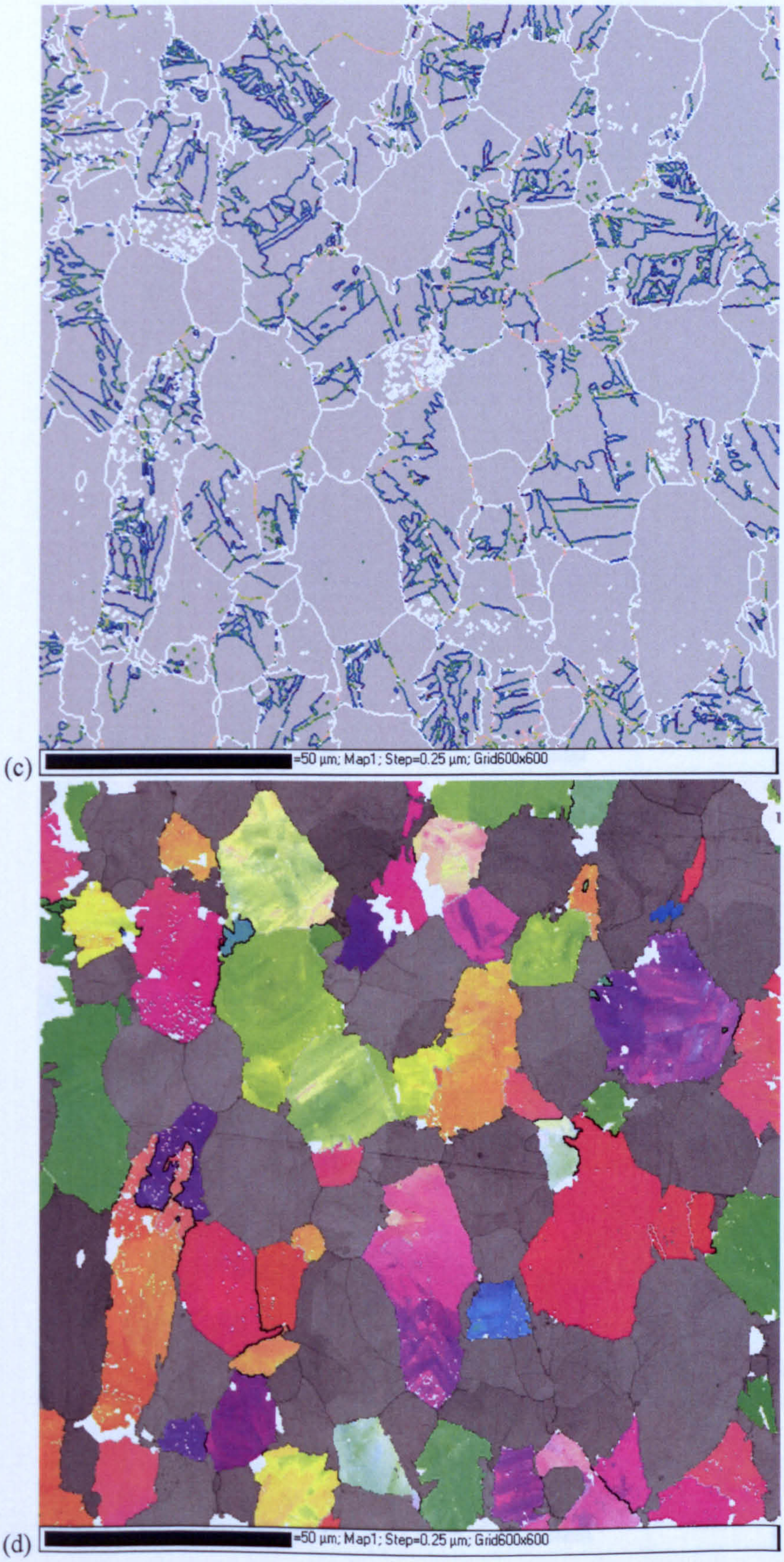

Fig. 7.44 EBSD map acquired 12mm from the quenched end using a 0.25µm step size, $CR_{900} = 15°C\ s^{-1}$. (a) Band contrast. (b) IPF colouring. (c) Deviation from Burgers relation. (d) Reconstructed β phase.

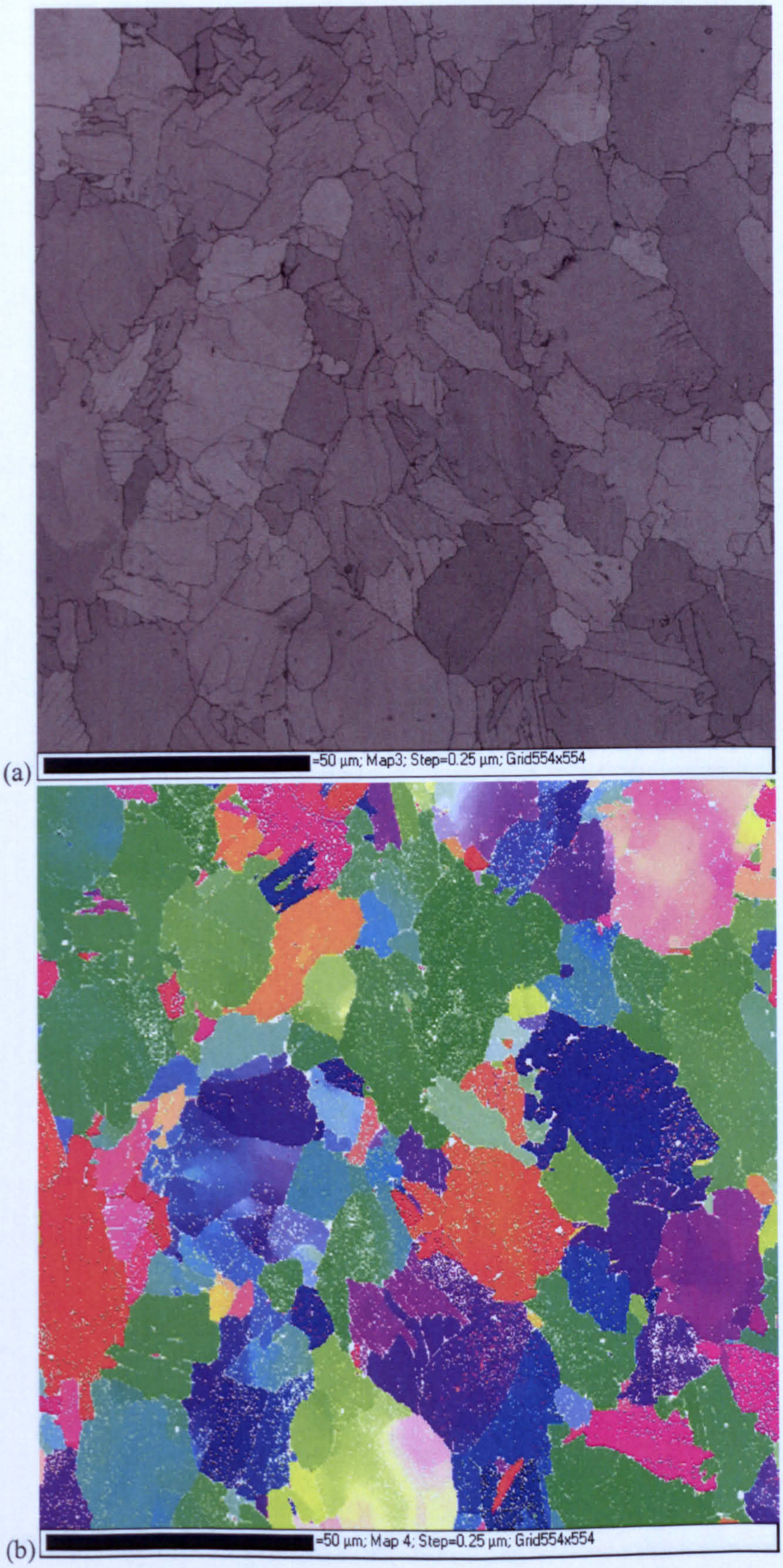

(a)

(b)

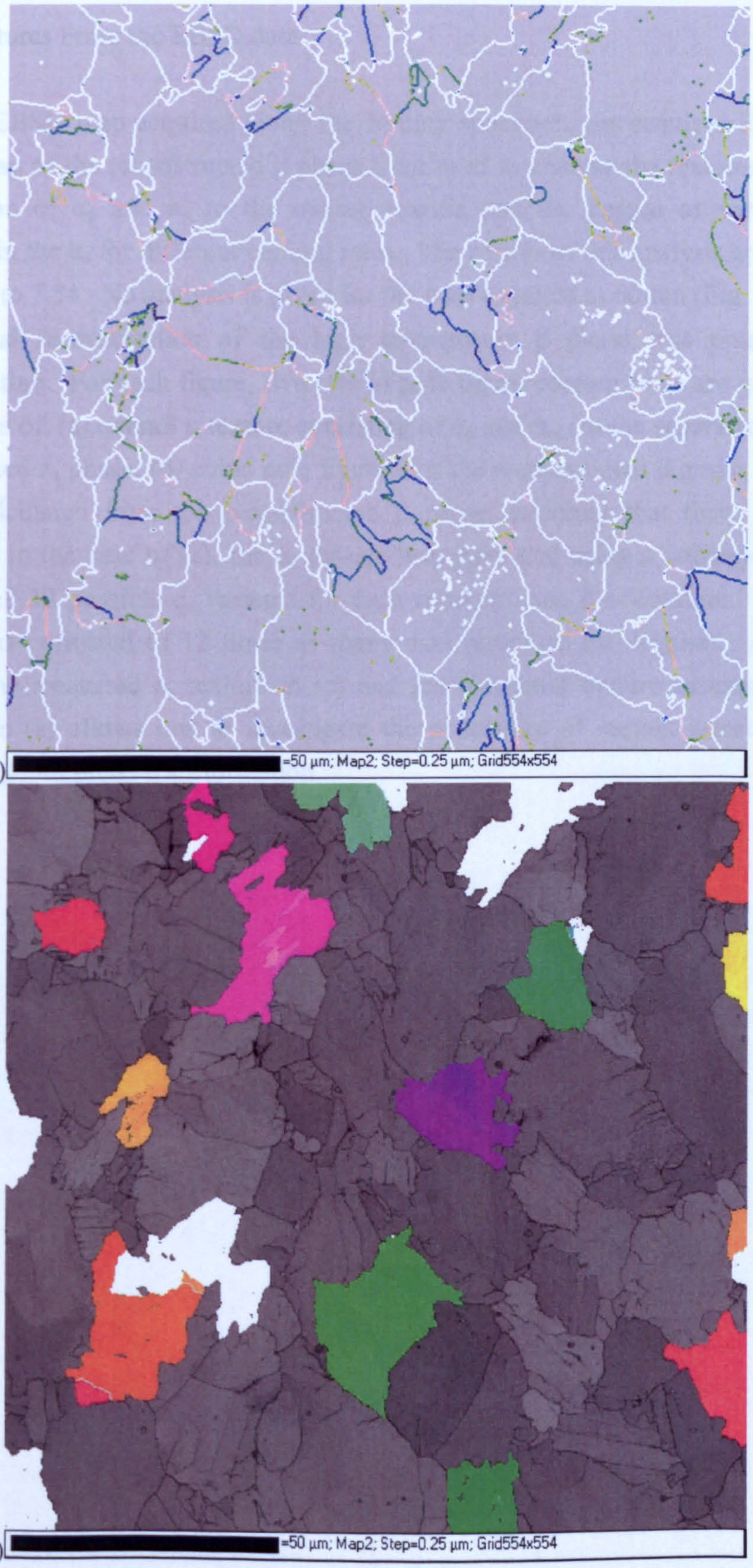

Fig. 7.45 EBSD map acquired 60mm from the quenched end using a 0.25µm step size, $CR_{900} = 1.7°C\ s^{-1}$. (a) Band contrast. (b) IPF colouring. (c) Deviation from Burgers relation. (d) Reconstructed β phase.

7.2.4 Textures From the EBSD data

For each EBSD map acquired along the Jominy specimen, the standard EBSD analysis and the map of the reconstructed β phase were used to analyse the textures to assess the contribution of α_p and α_s to the overall texture and the degree of variant selection occurring in the α_s for different cooling rates. The results of this analysis are presented in Figs. 7.46 to 7.54. No analysis is given for the map acquired at 60mm (Fig. 7.45) because only partial reconstruction of the high temperature β phase was possible for this microstructure. For each figure, five sets of pole figure contour plots are given, showing the textures of: (a) overall α texture consisting of α_p and α_s, (b) the separated α_p phase, (c) the separated α_s phase, (d) cubic pole figures for the reconstructed β grains and (e) the α_s texture calculated from the reconstructed β phase assuming that there is no variant selection. In the case of (e), the α_s dataset was produced using a computer program to calculate all 12 possible α_s variants for each reconstructed β orientation. The resulting dataset thus consisted of 12 times as many data points as the original. A comparison between the measured α_s texture in (c) and the simulated texture assuming no variant selection in (e) allows one to investigate the possibility of variant selection occurring during the $\beta \rightarrow \alpha_s$ phase transformation.

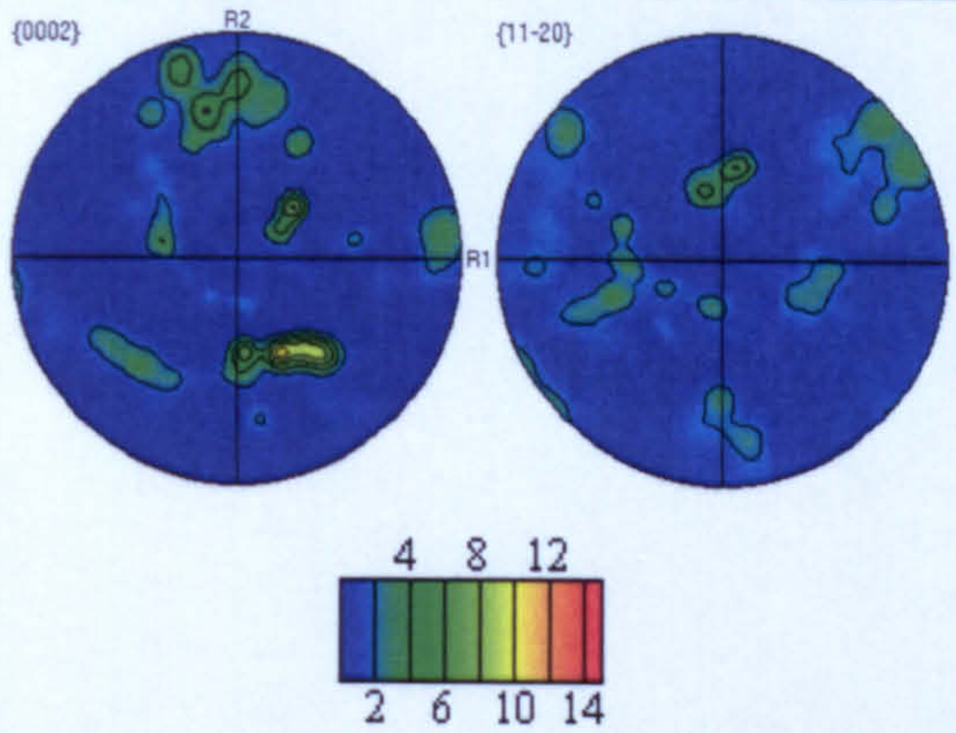

(a) Overall α texture.

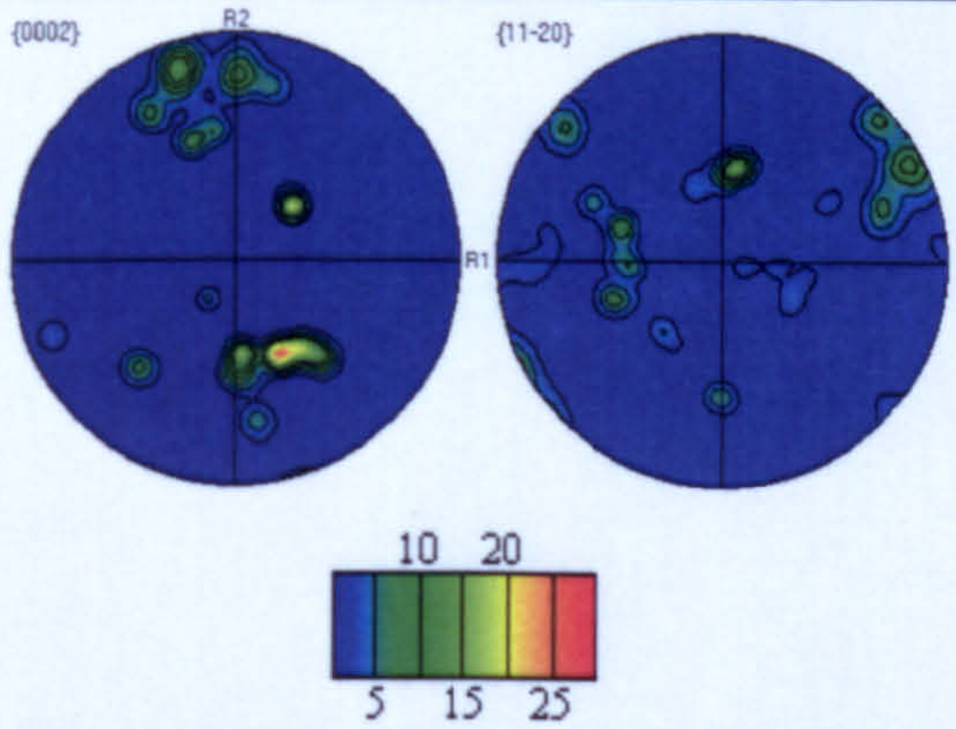

(b) Separated α_p texture.

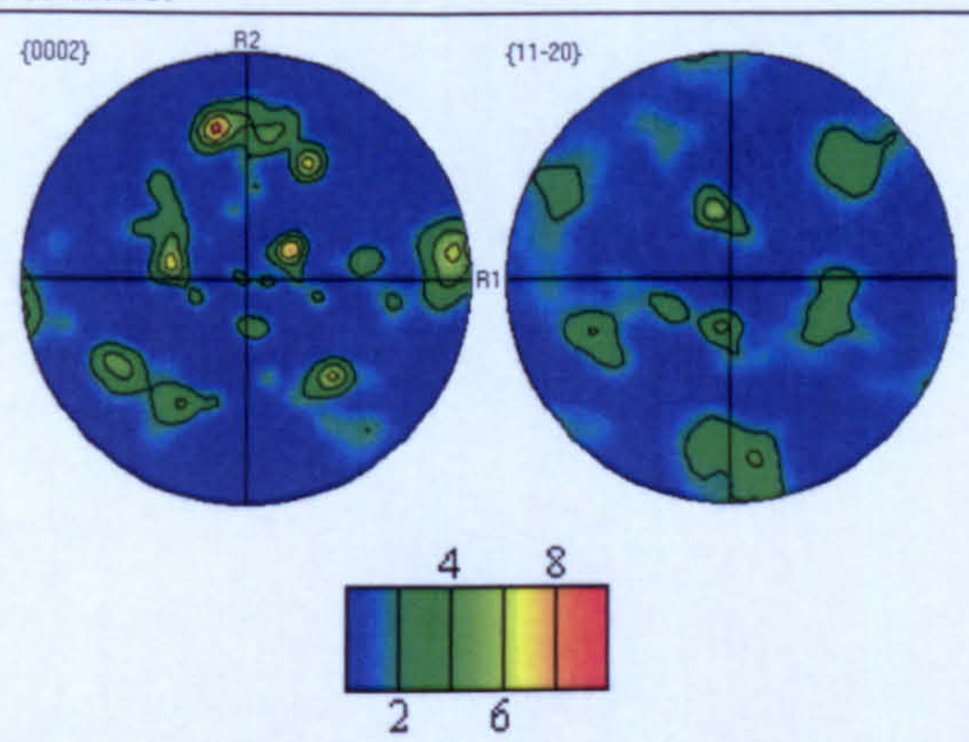

(c) Separated α_s texture

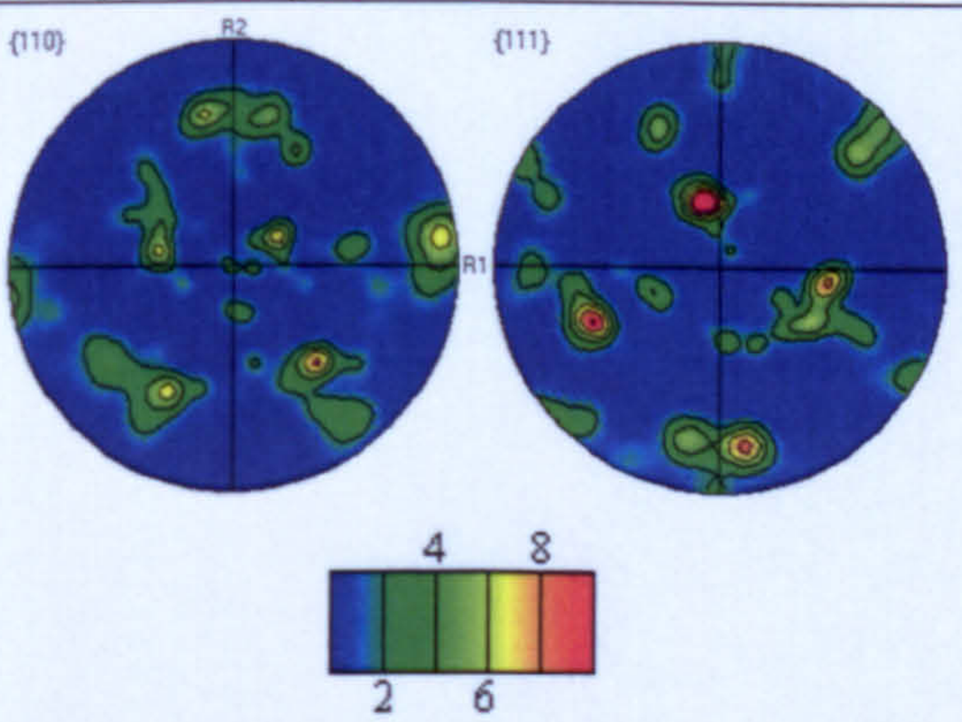

(d) Reconstructed β texture

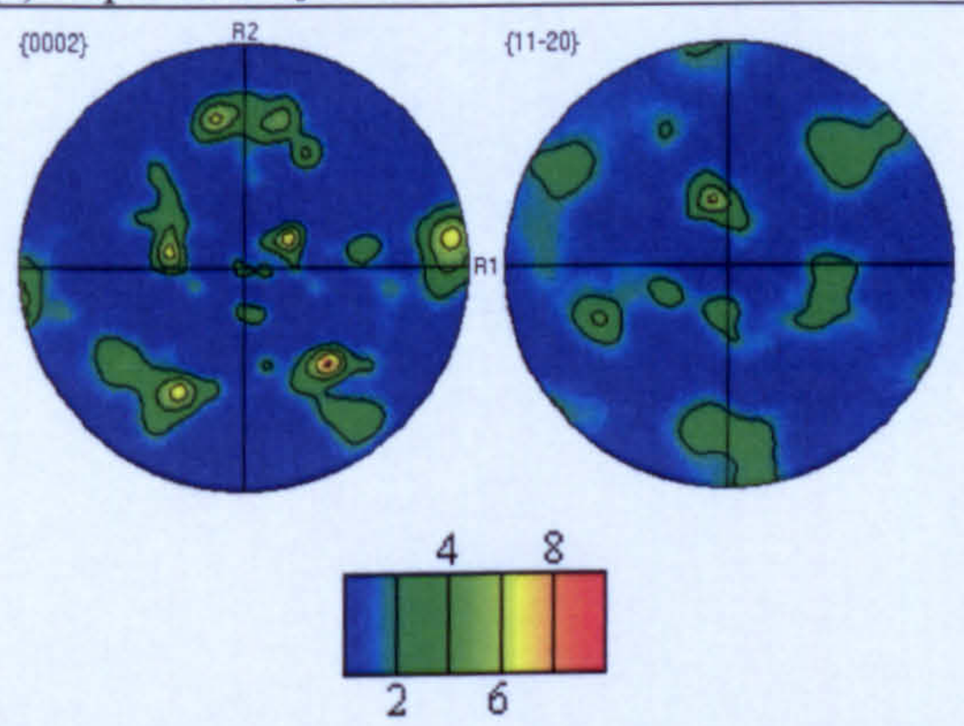

(e) Calculated α_s texture assuming no variant selection.

Fig. 7.46 Texture analysis for the EBSD map acquired 0.2mm from the quenched end, estimated CR_{900} >>500°C s^{-1}.

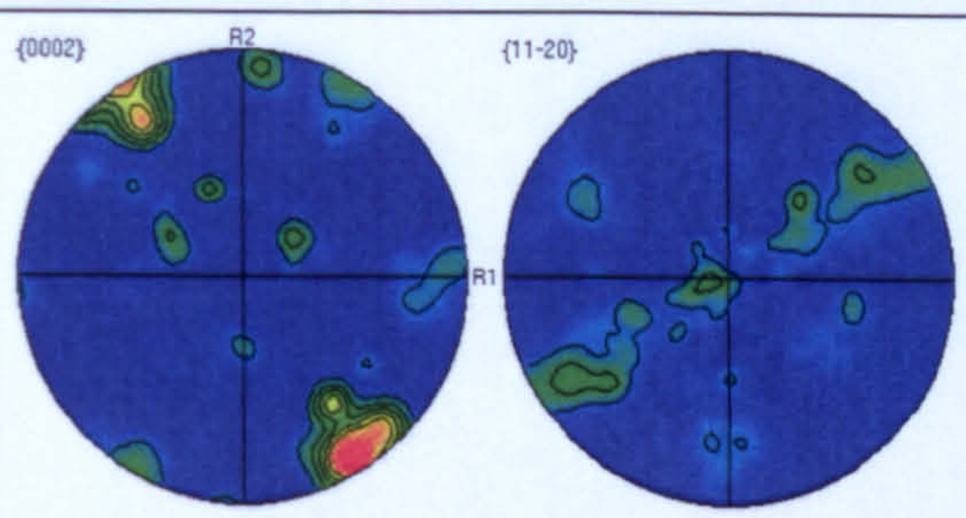

(a) Overall α texture.

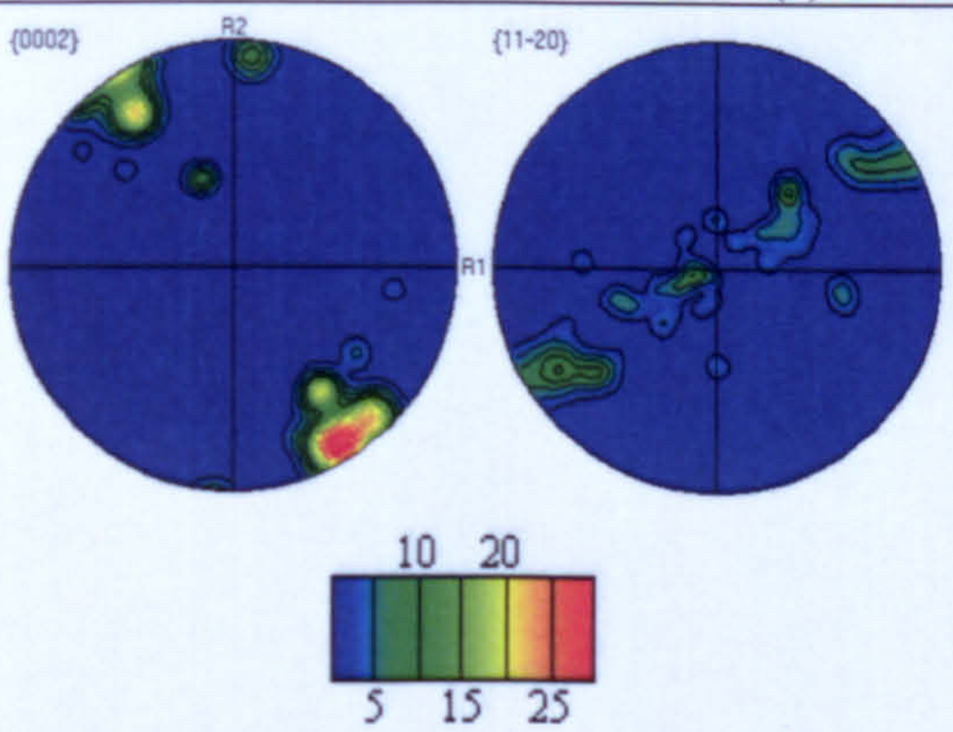

(b) Separated α_p texture.

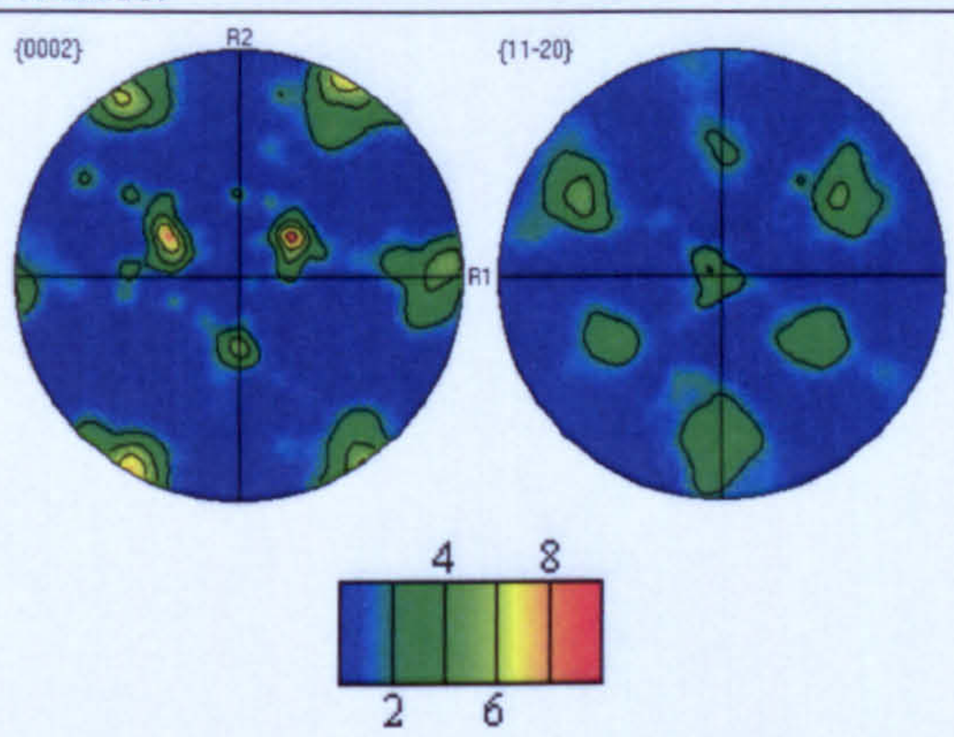

(c) Separated α_s texture

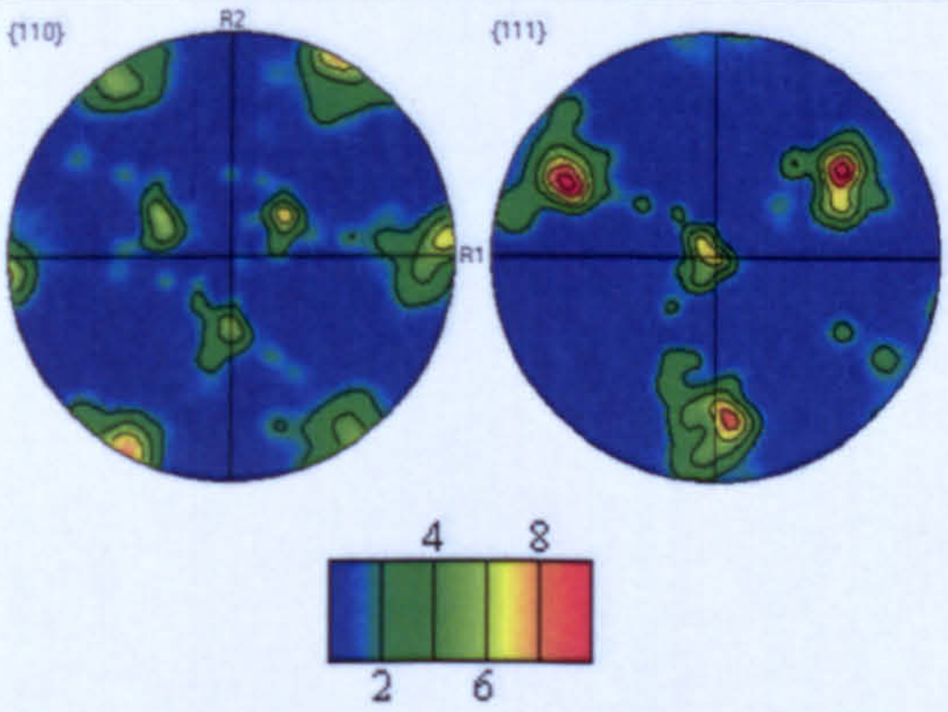

(d) Reconstructed β texture.

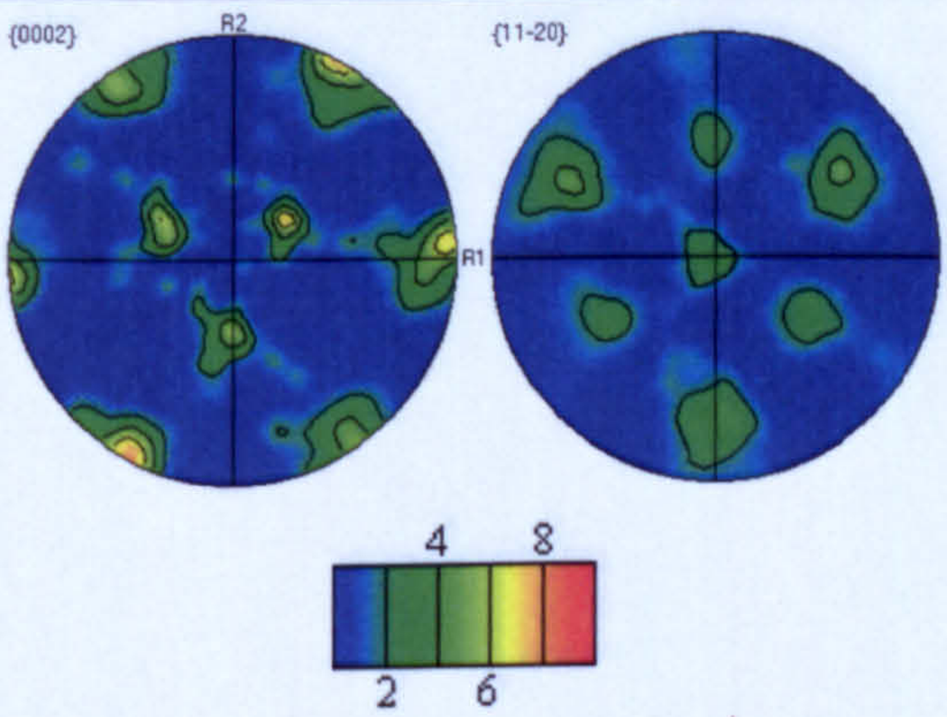

(e) Calculated α_s texture assuming no variant selection.

Fig. 7.47 Texture analysis for the EBSD map acquired 1mm from the quenched end, estimated CR_{900} ~400°C s^{-1}.

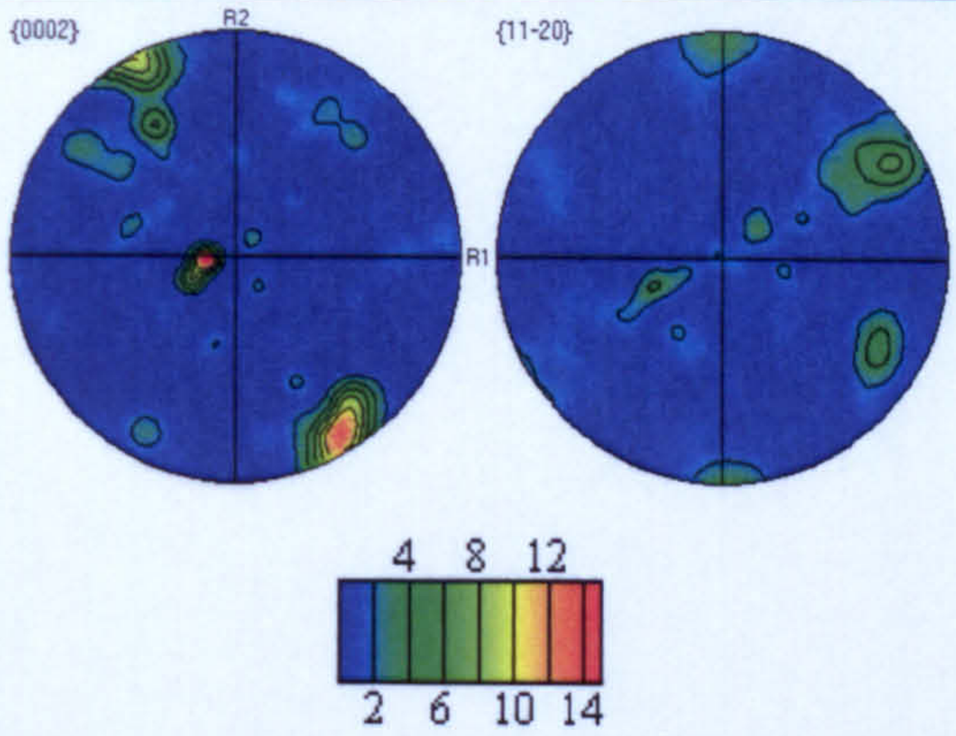

(a) Overall α texture.

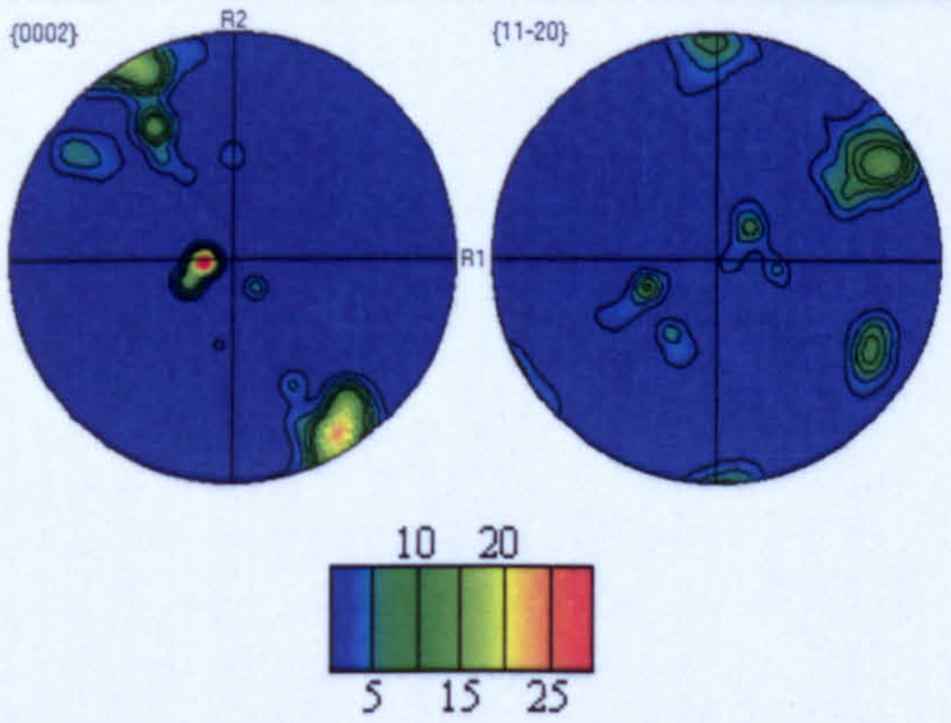

(b) Separated α_p texture.

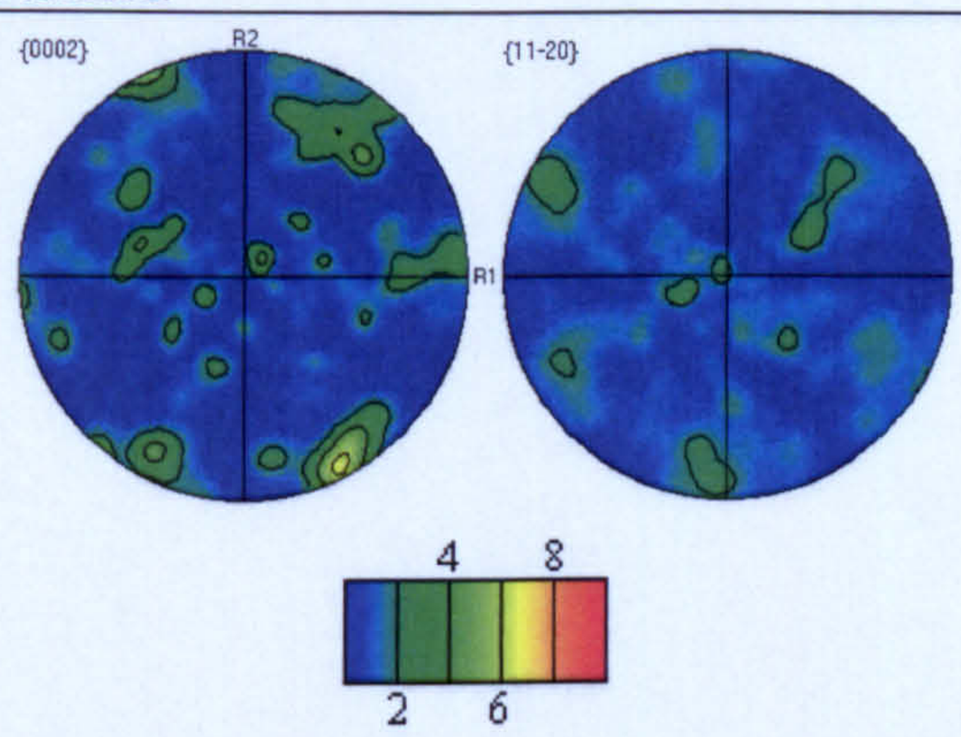

(c) Separated α_s texture

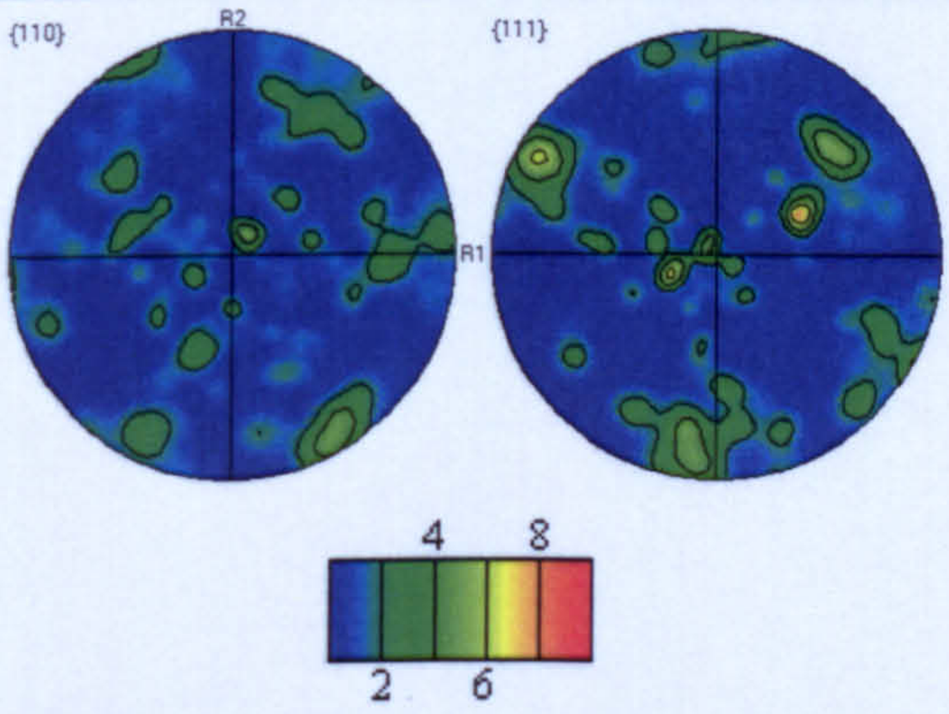

(d) Reconstructed β texture.

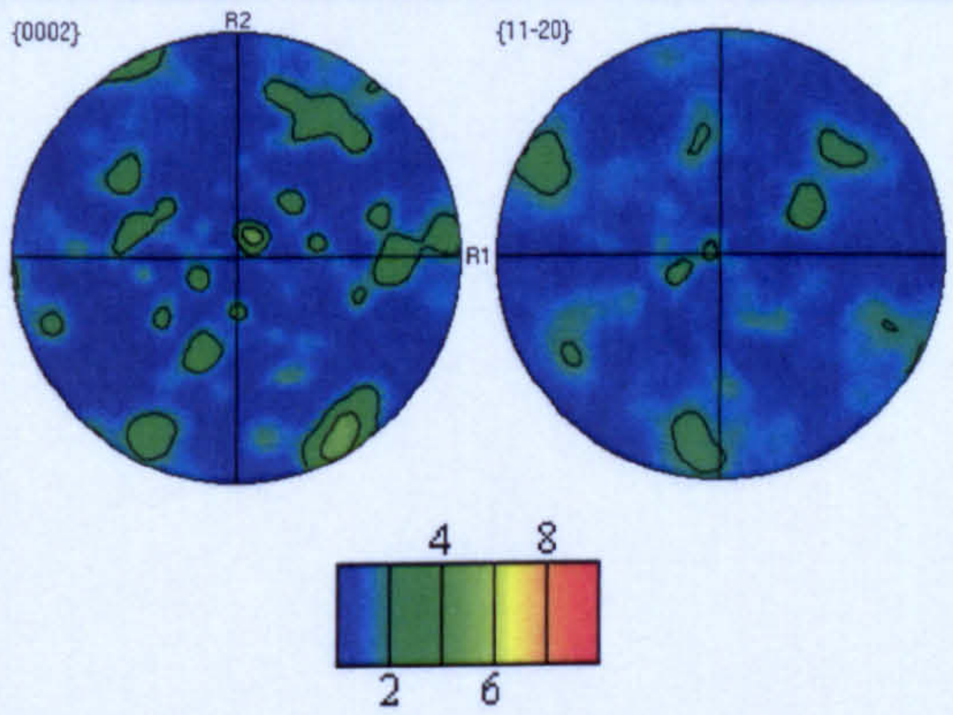

(e) Calculated α_s texture assuming no variant selection.

Fig. 7.48 Texture analysis for the EBSD map acquired 2mm from the quenched end, estimated CR_{900} ~160°C s^{-1}.

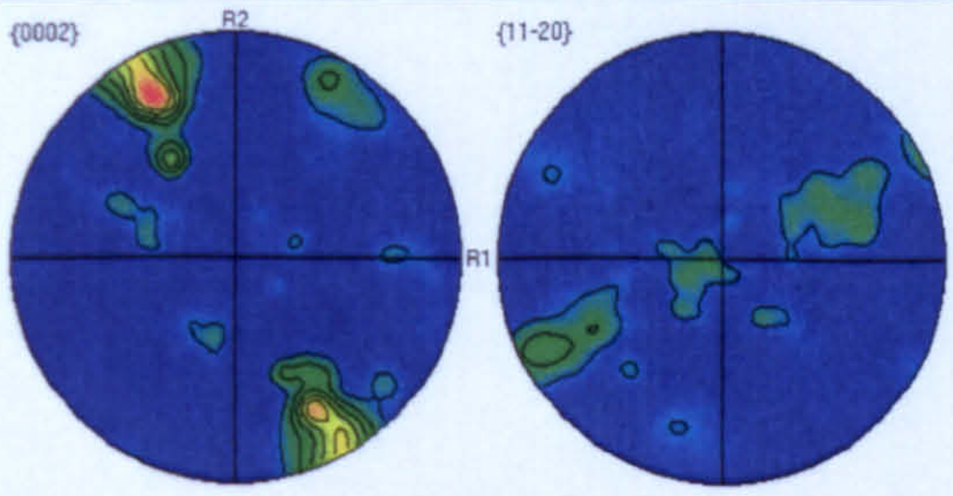

(a) Overall α texture.

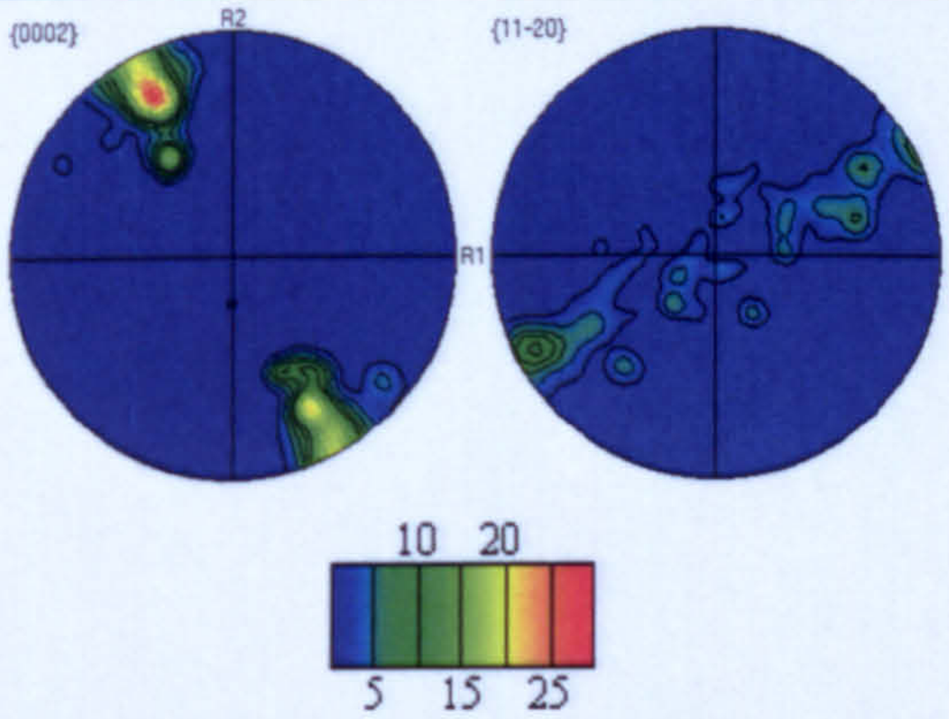

(b) Separated α_p texture.

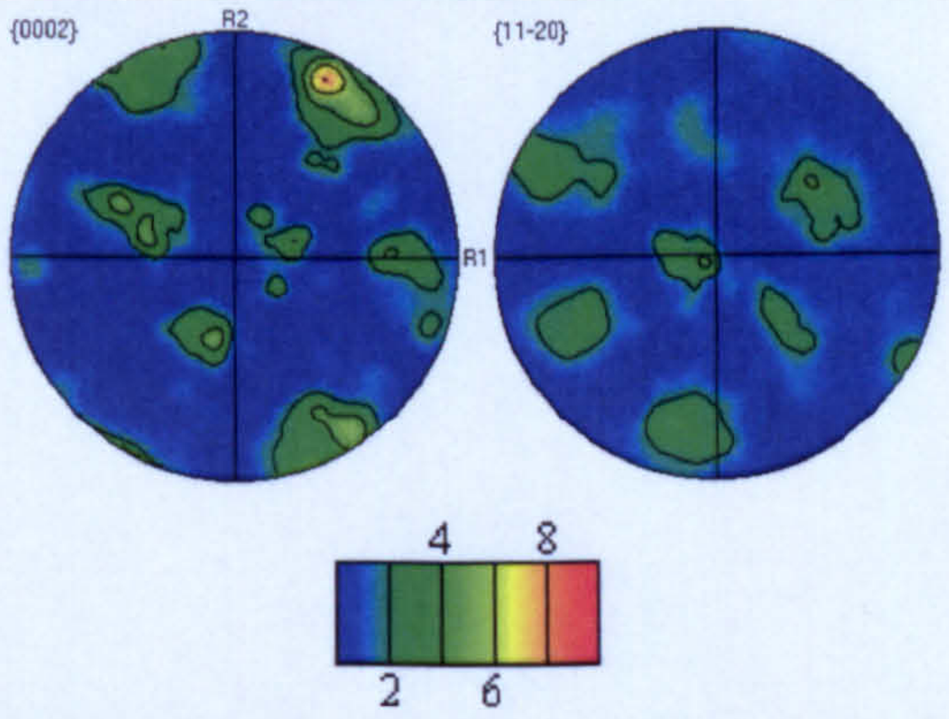

(c) Separated α_s texture

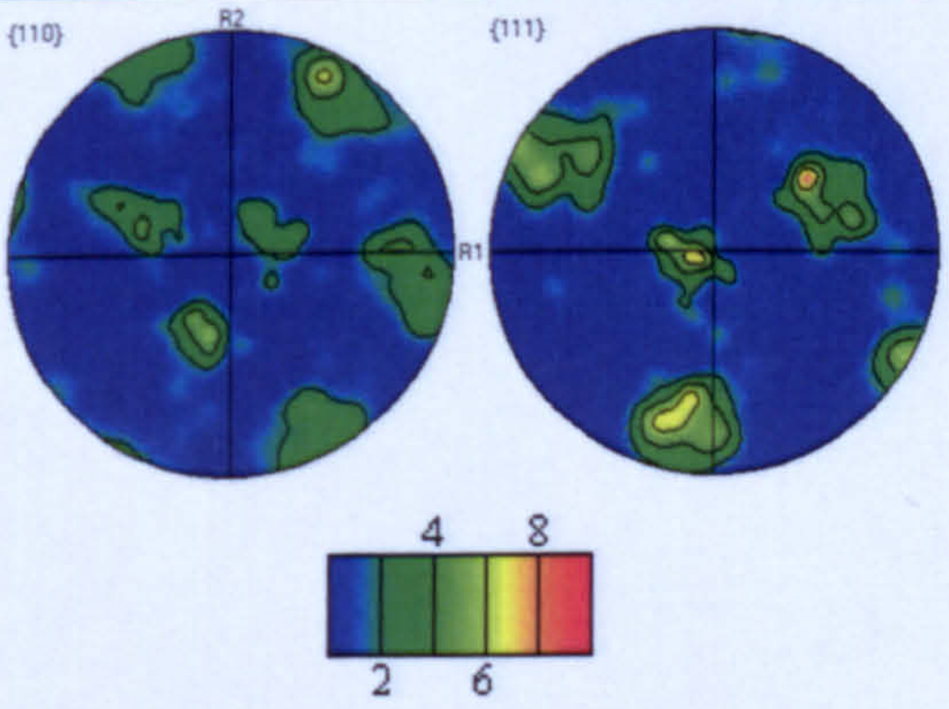

(d) Reconstructed β texture.

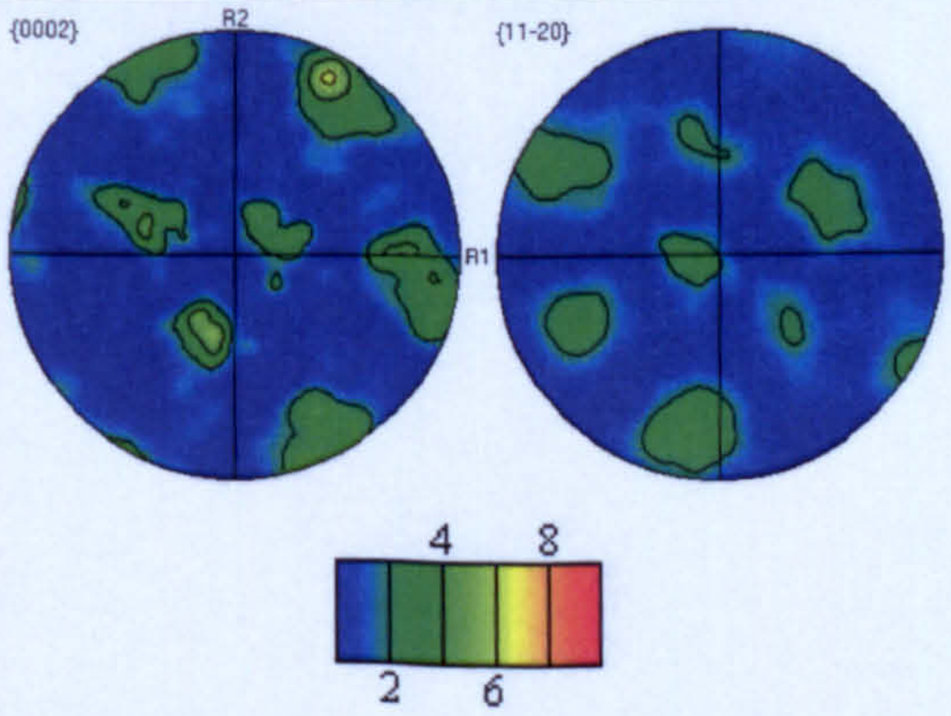

(e) Calculated α_s texture assuming no variant selection

Fig. 7.49 Texture analysis for the EBSD map acquired 3mm from the quenched end, $CR_{900} = 100°C\ s^{-1}$.

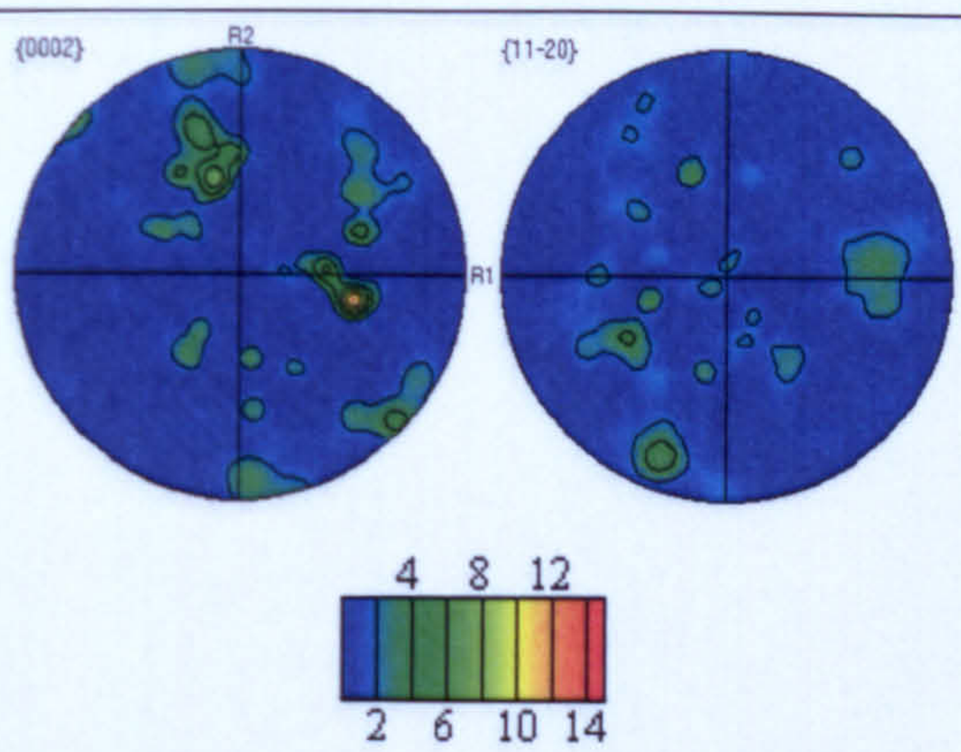

(a) Overall α texture.

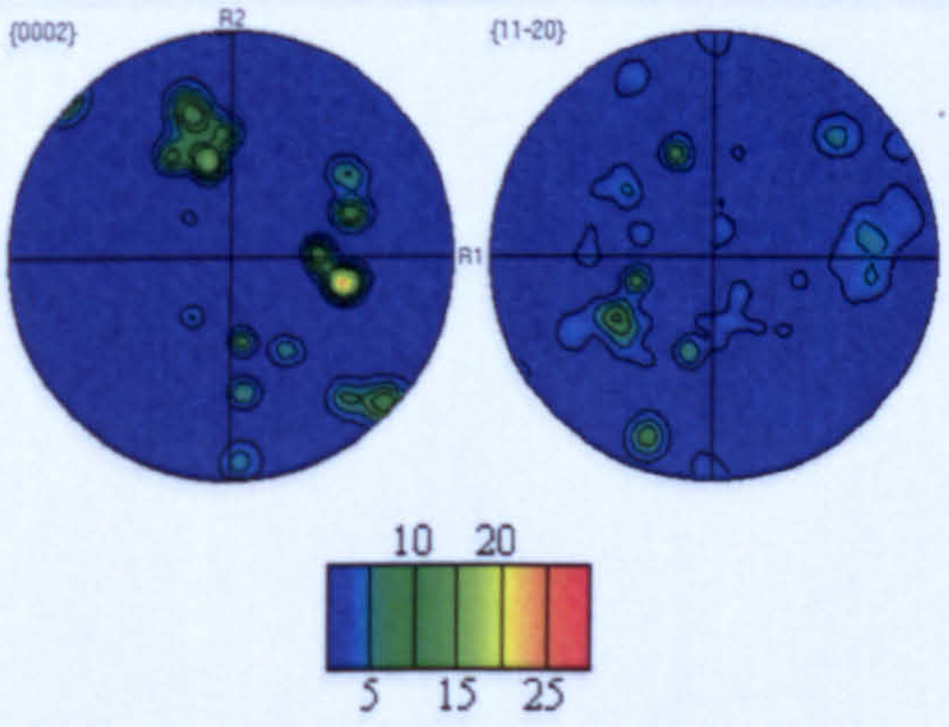

(b) Separated α_p texture.

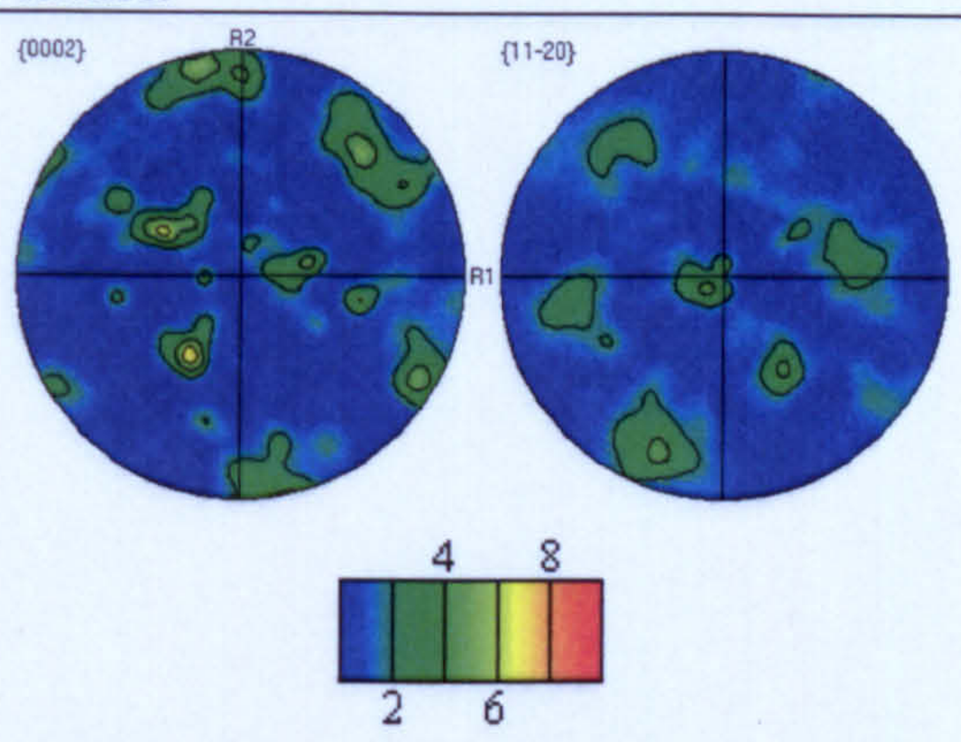

(c) Separated α_s texture.

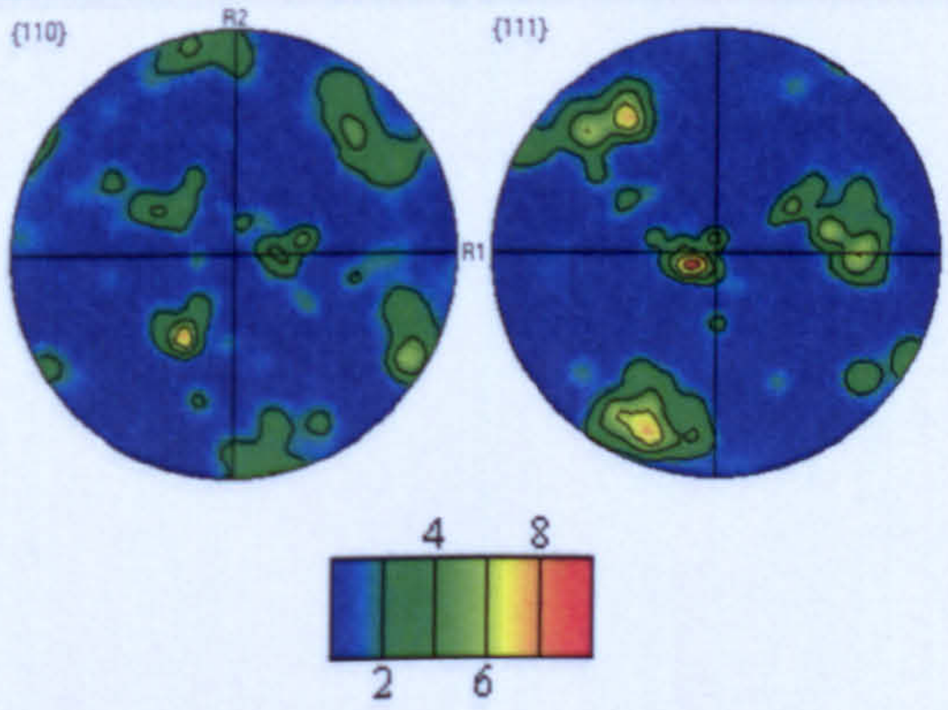

(d) Reconstructed β texture.

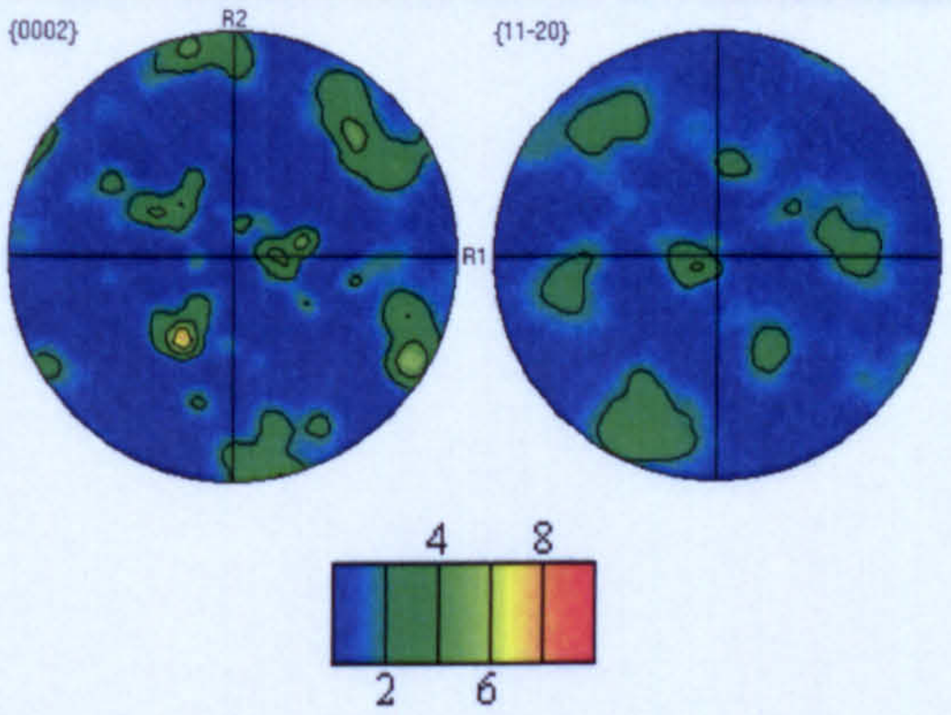

(e) Calculated α_s assuming no variant selection

Fig. 7.50 Texture analysis for the EBSD map acquired 4mm from the quenched end, $CR_{900} = 63°C\ s^{-1}$.

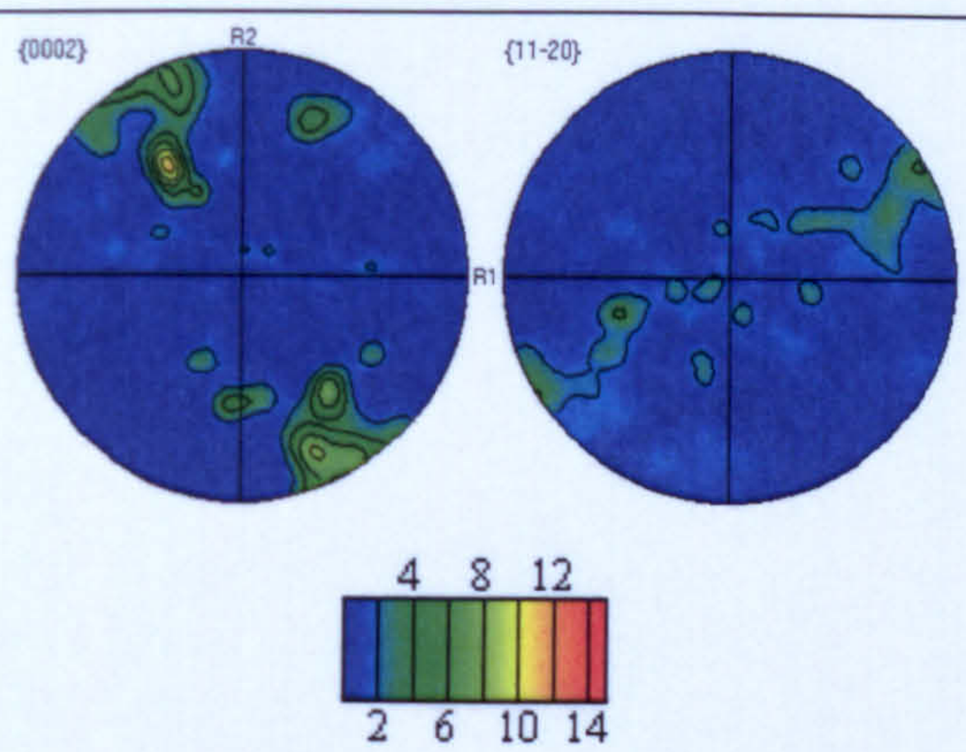

(a) Overall α texture.

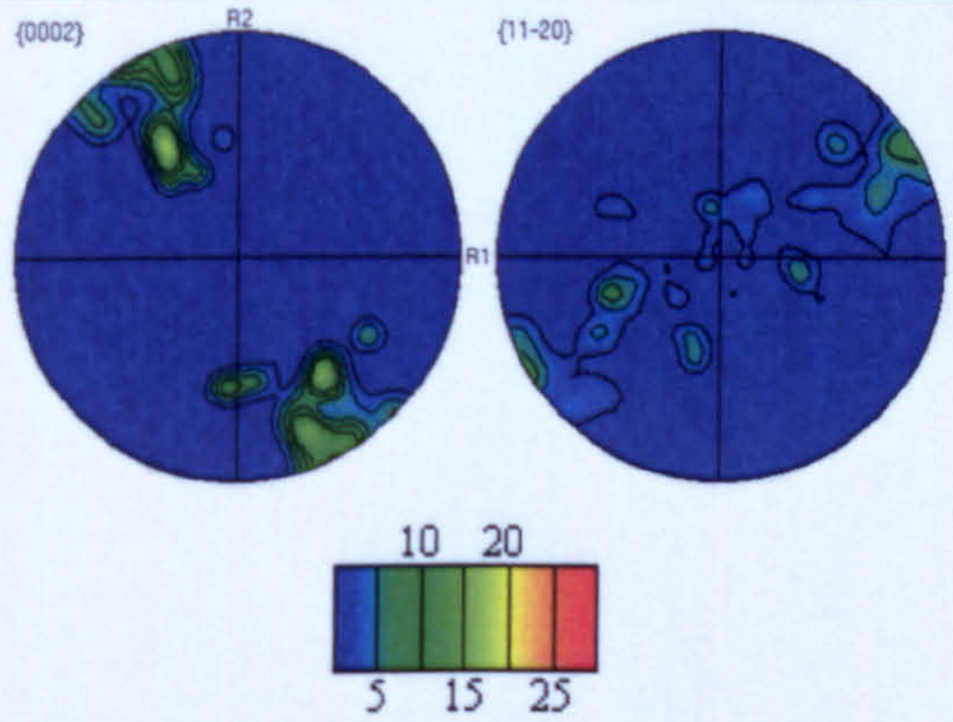

(b) Separated α_p texture.

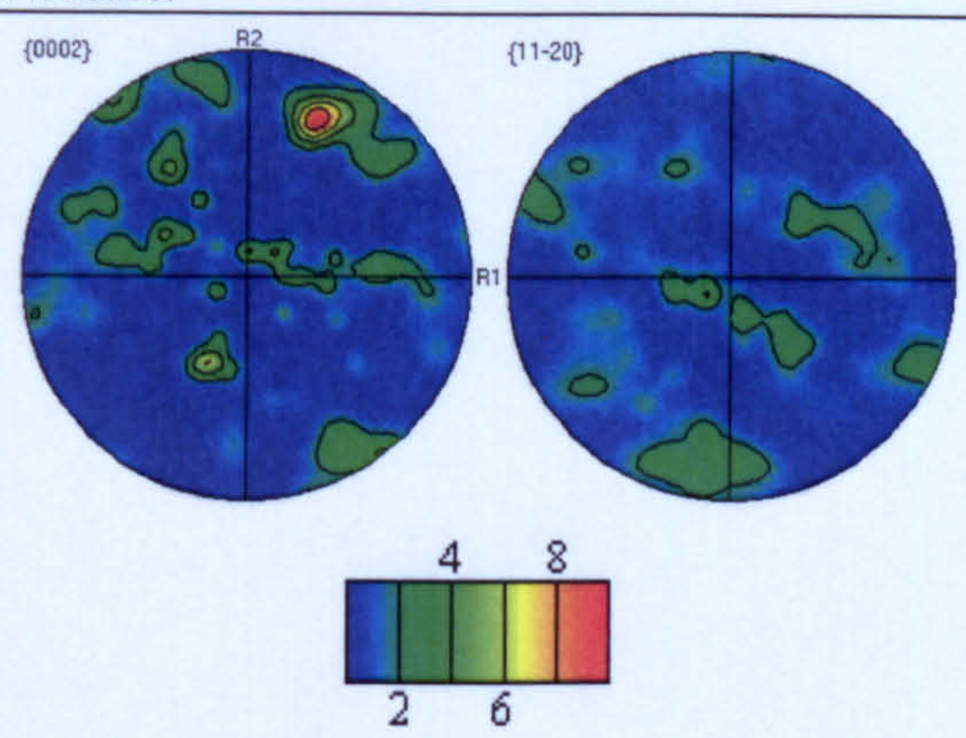

(c) Separated α_s texture.

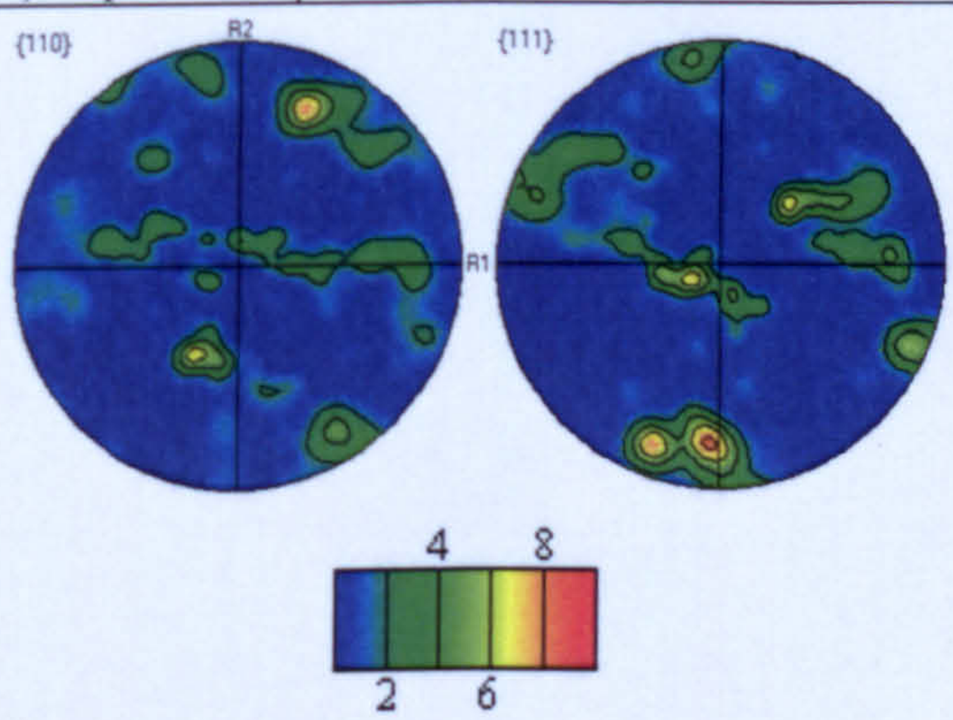

(d) Reconstructed β texture.

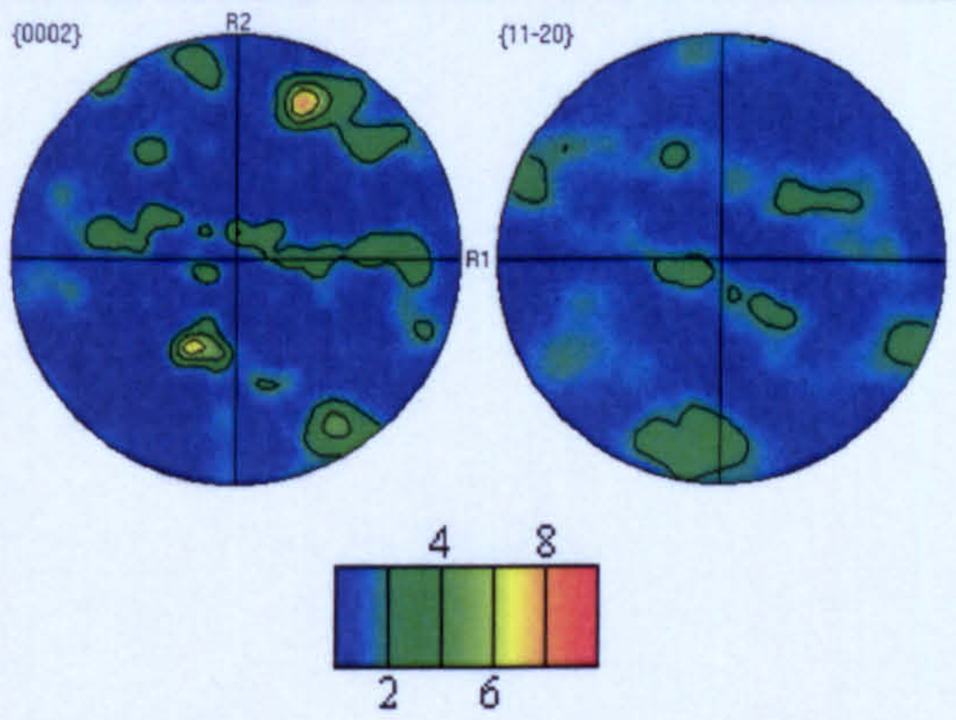

(e) Calculated α_s texture assuming no variant selection.

Fig. 7.51 Texture analysis for the EBSD map acquired 5mm from the quenched end, $CR_{900} = 47°C\ s^{-1}$.

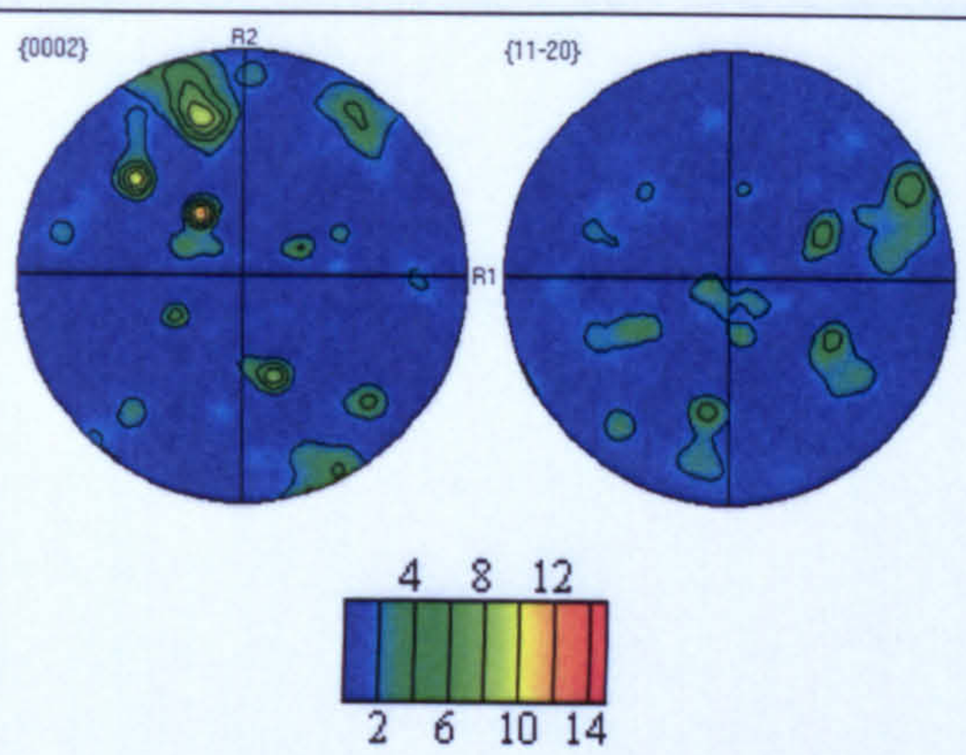

(a) Overall α texture.

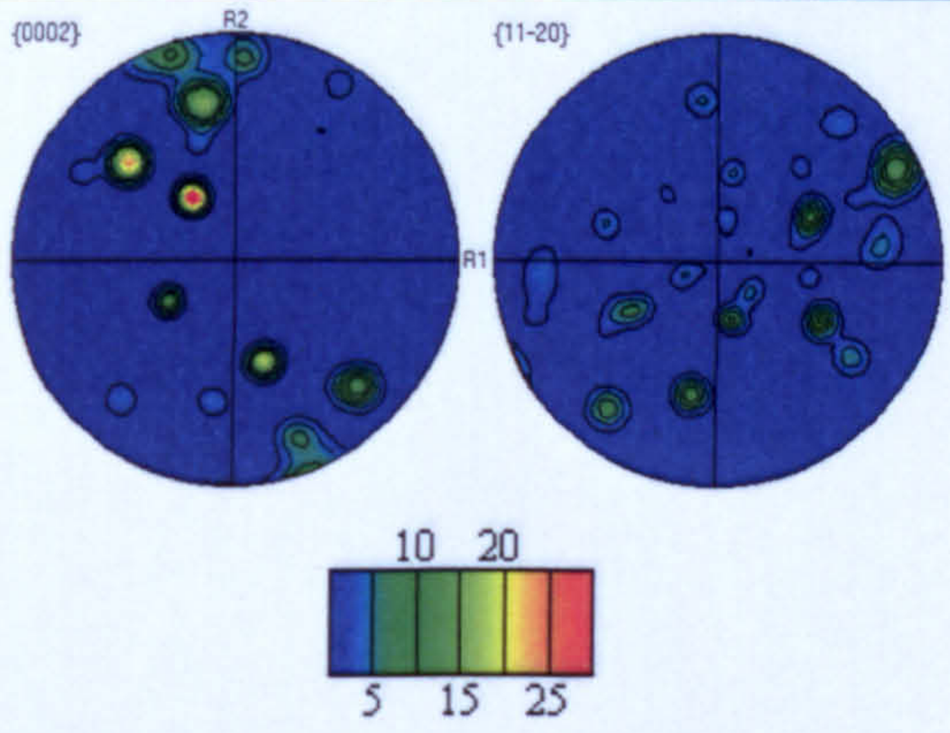

(b) Separated α_p texture.

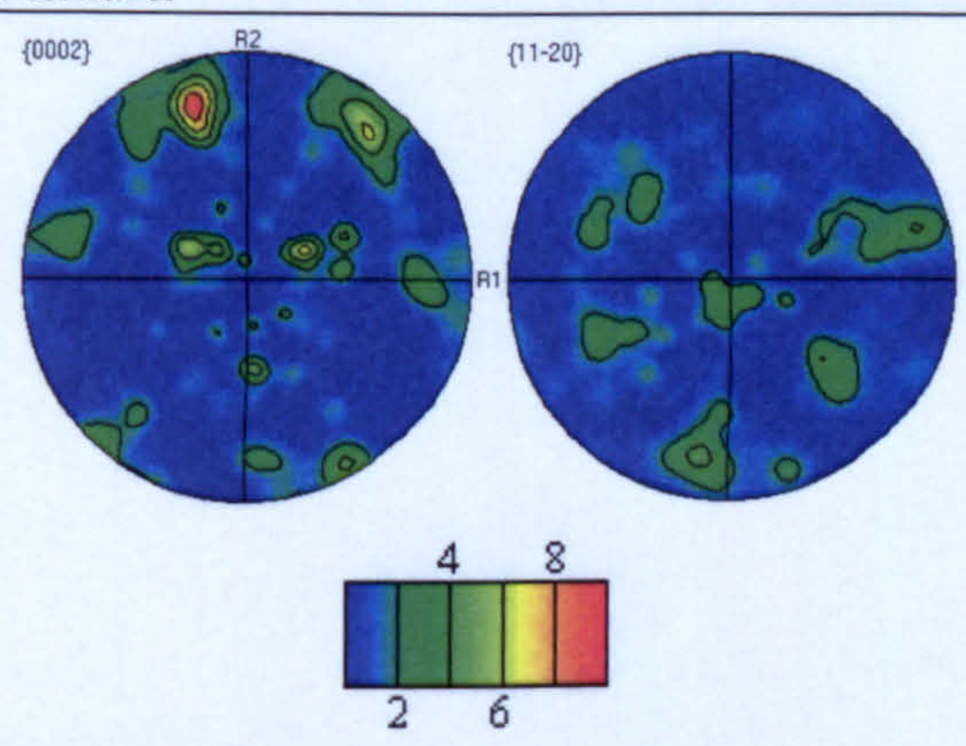

(c) Separated α_s texture.

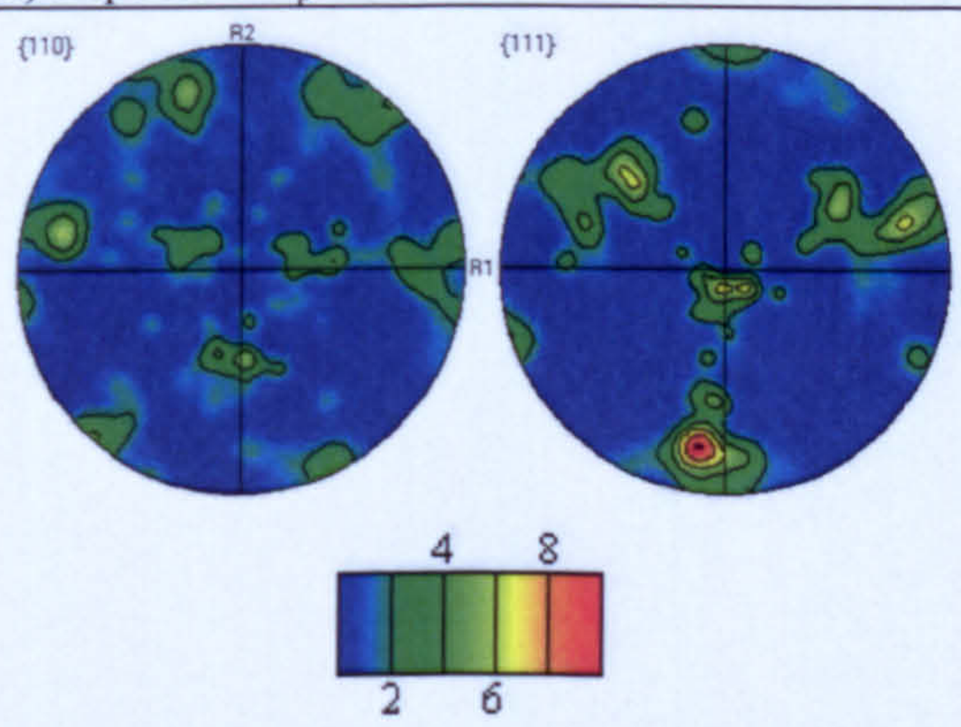

(d) Reconstructed β texture.

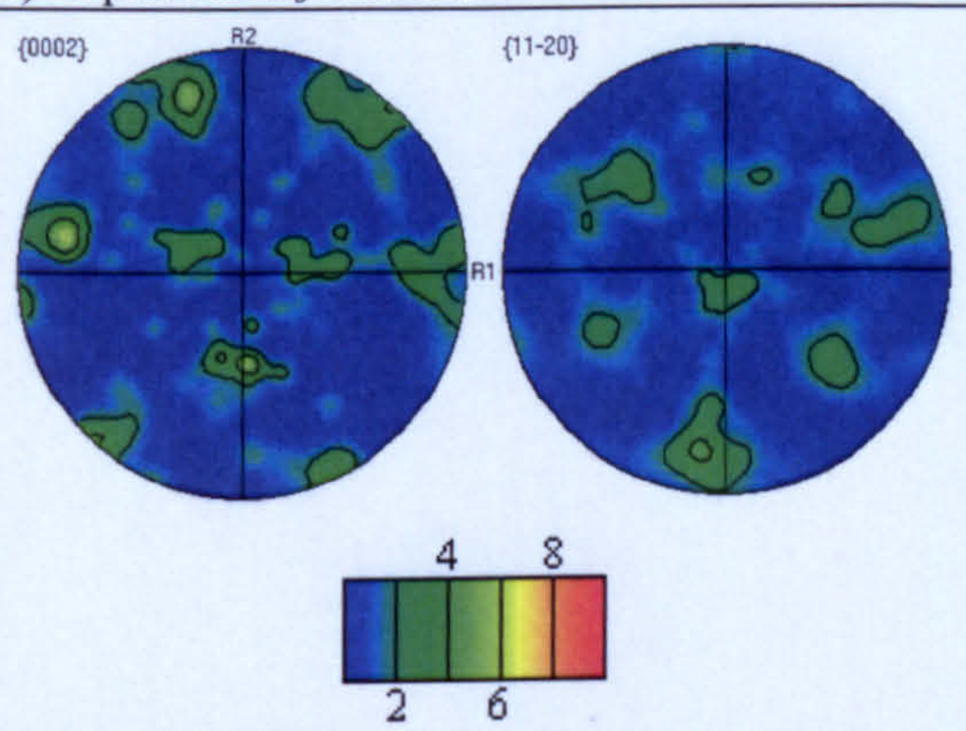

(e) Calculated α_s assuming no variant selection

Fig. 7.52 Texture analysis for the EBSD map acquired 6mm from the quenched end, $CR_{900} = 37°C\ s^{-1}$.

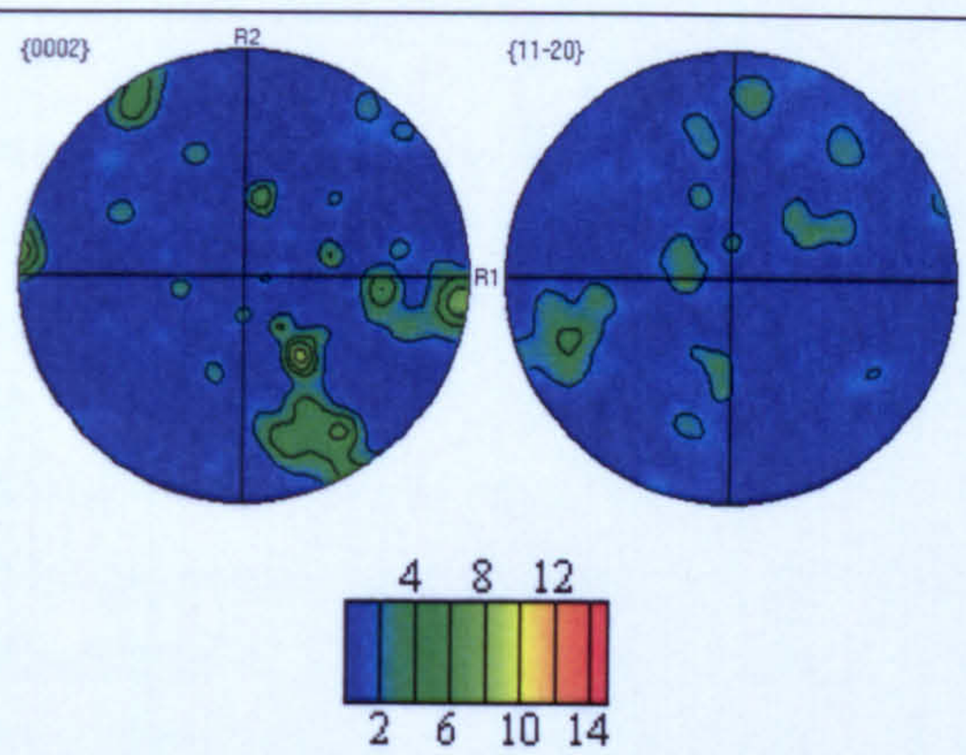

(a) Overall α texture.

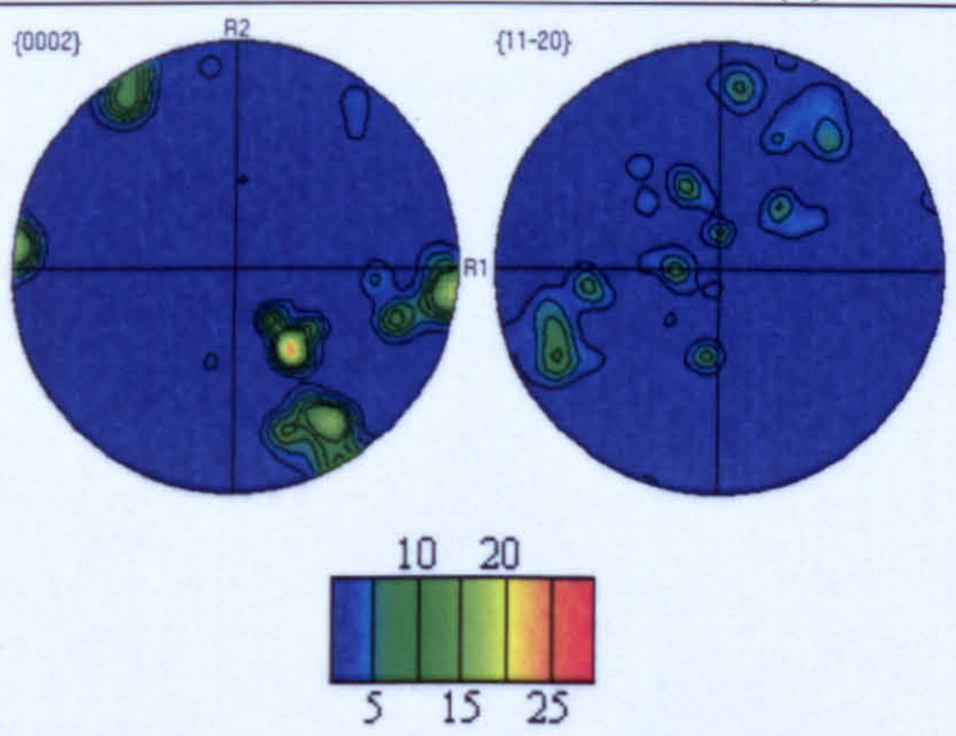

(b) Separated α_p texture.

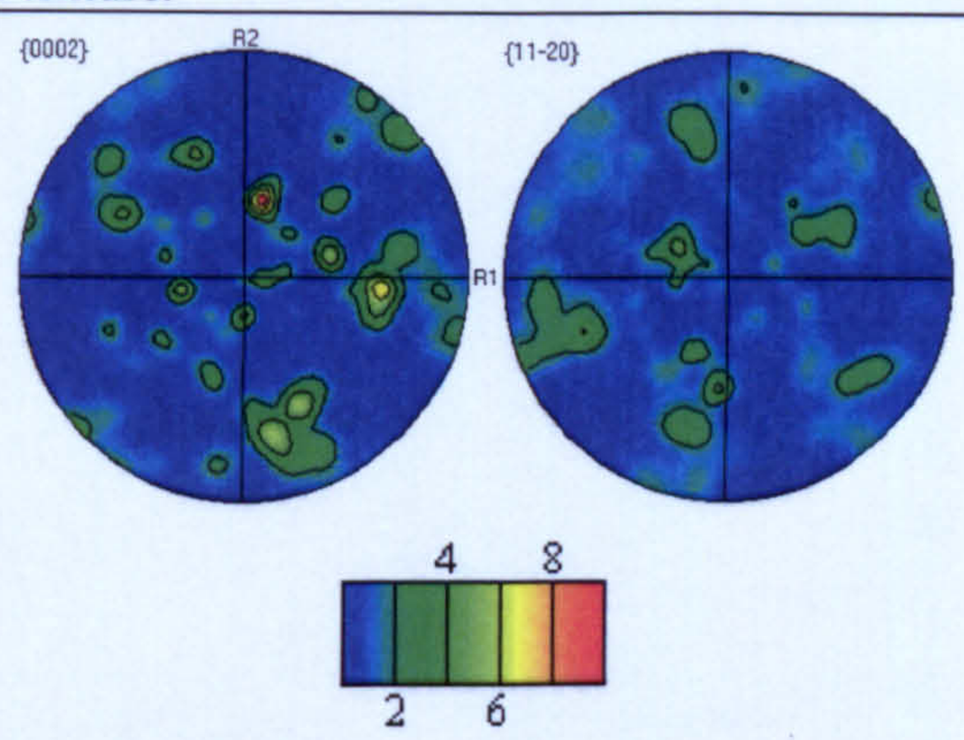

(c) Separated α_s texture.

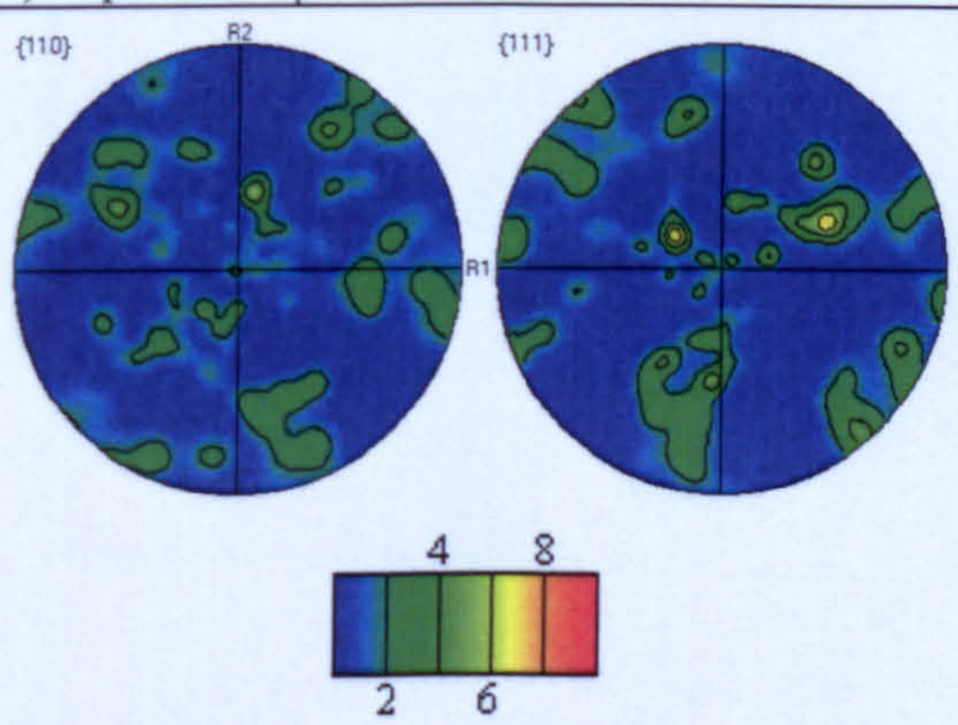

(d) Reconstructed β texture.

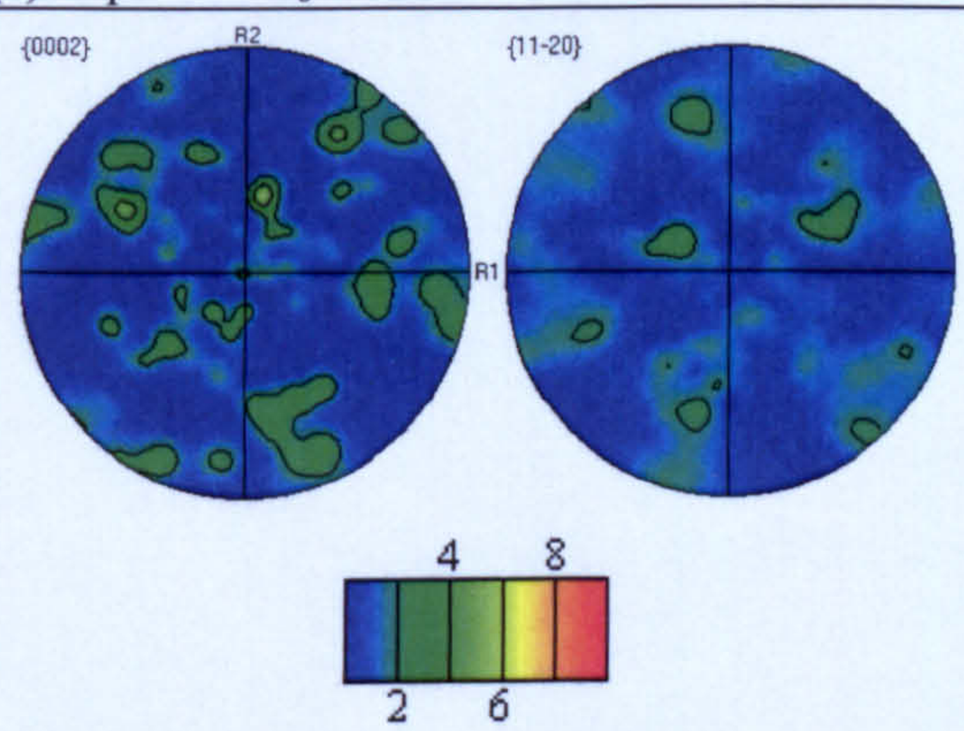

(e) Calculated α_s assuming no variant selection

Fig. 7.53 Texture analysis for the EBSD map acquired 8.7mm from the quenched end, $CR_{900} = 22°C\ s^{-1}$.

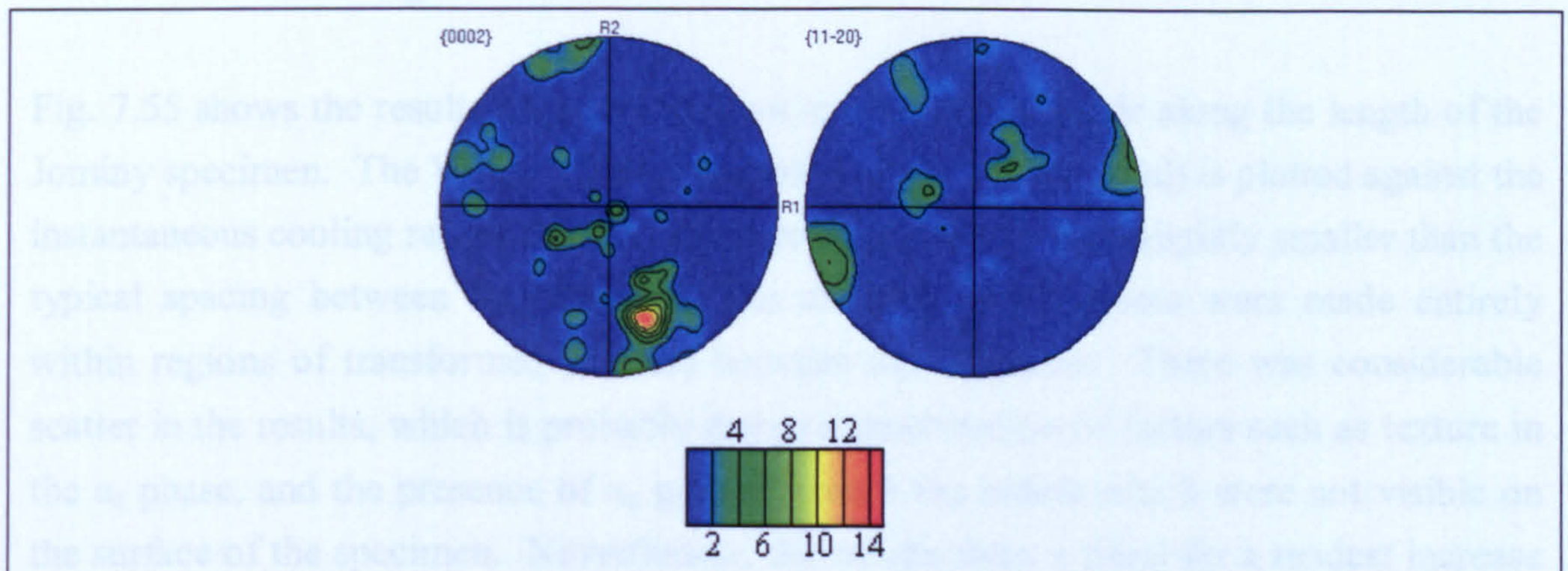

(a) Overall α texture.

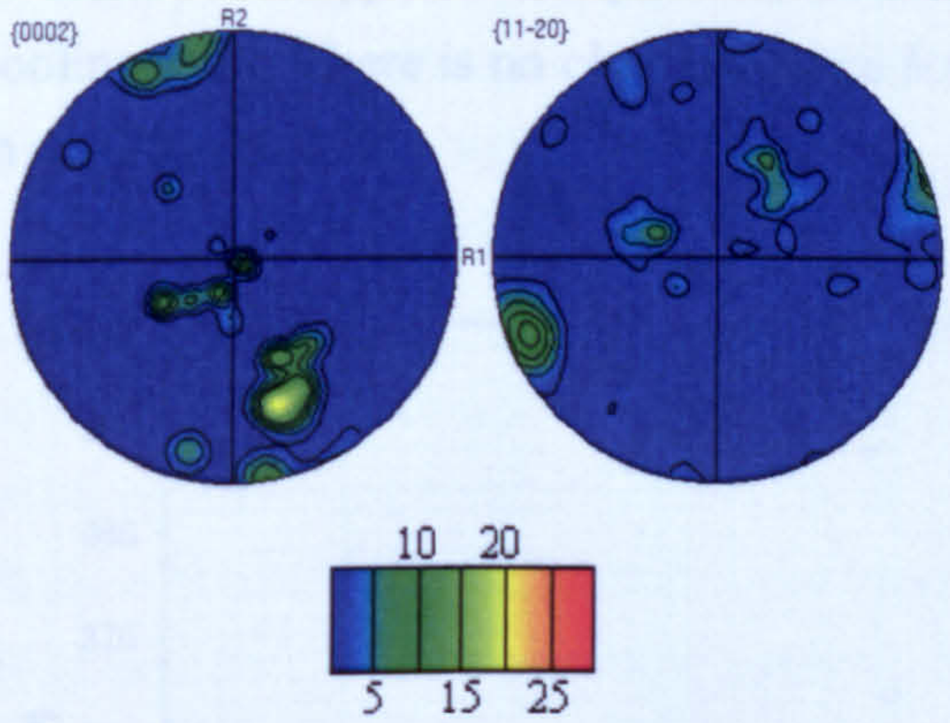

(b) Separated α_p texture.

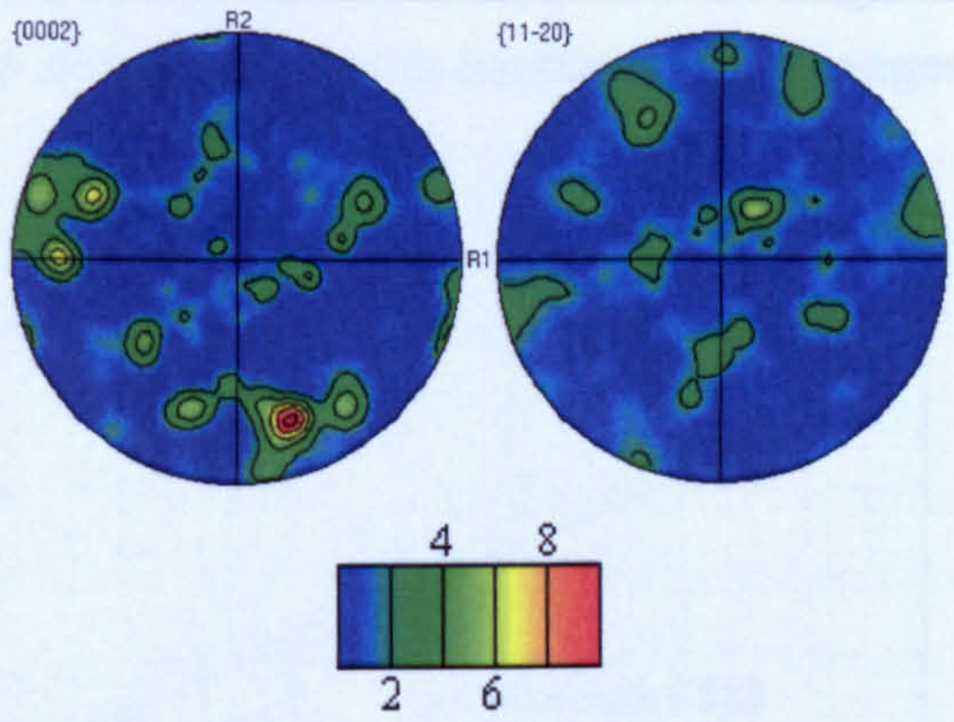

(c) Separated α_s texture.

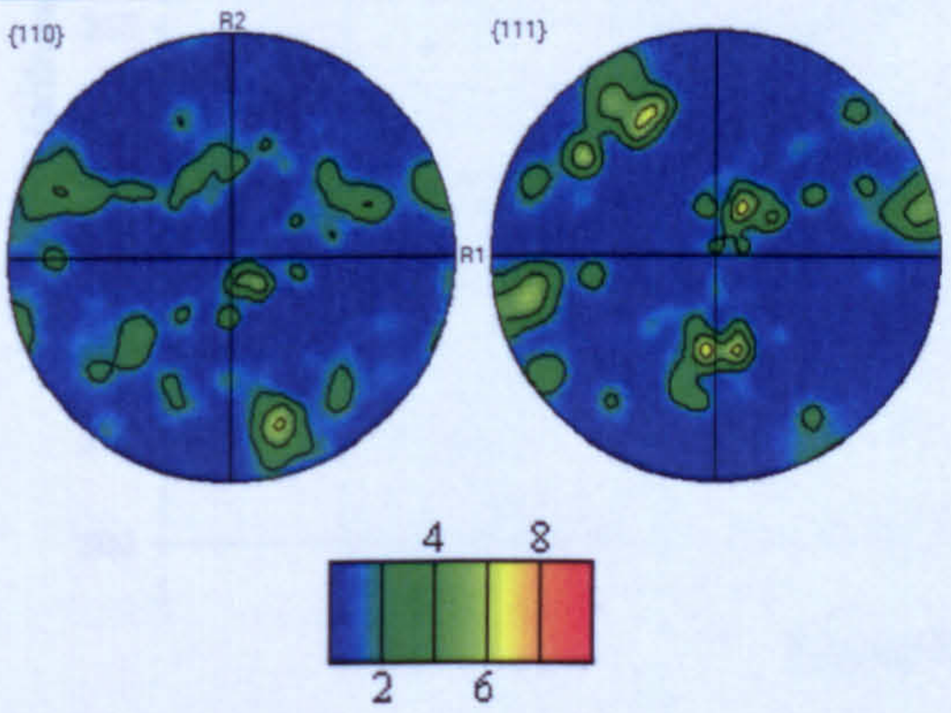

(d) Reconstructed β texture.

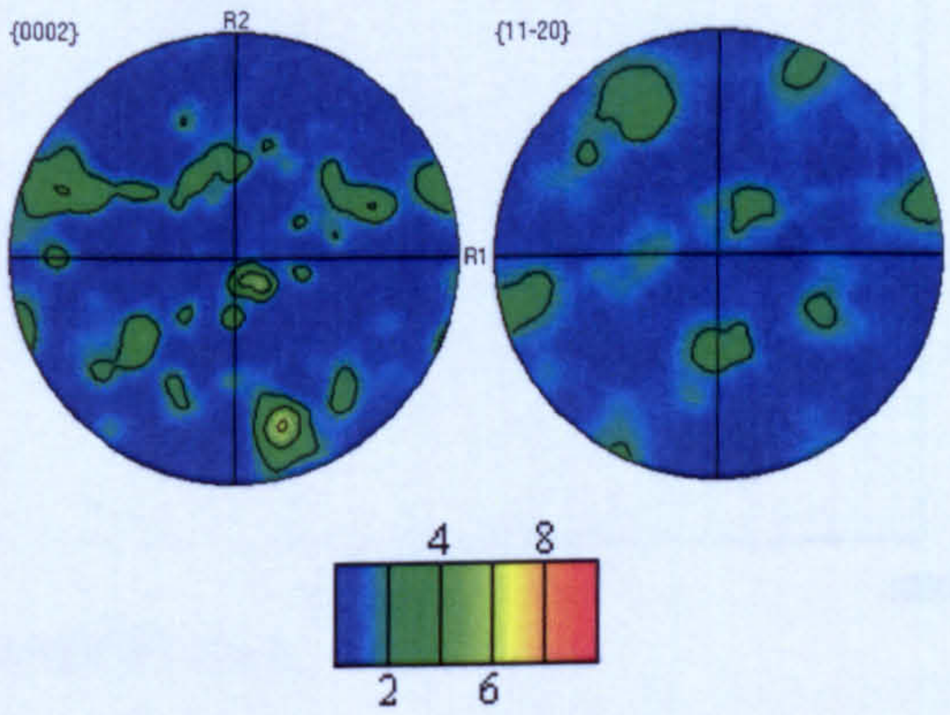

(e) Calculated α_s assuming no variant selection

Fig. 7.54 Texture analysis for the EBSD map acquired 12mm from the quenched end, $CR_{900} = 15°C\ s^{-1}$.

7.2.5 Hardness Testing

Fig. 7.55 shows the results of microhardness measurements made along the length of the Jominy specimen. The Vicker's hardness (micro-indenter, 1kg load) is plotted against the instantaneous cooling rate at 900°C. The size of the indents was slightly smaller than the typical spacing between α_p grains and the microhardness indents were made entirely within regions of transformed β phase between the α_p grains. There was considerable scatter in the results, which is probably due to a combination of factors such as texture in the α_s phase, and the presence of α_p grains beneath the indent which were not visible on the surface of the specimen. Nevertheless, the results show a trend for a modest increase in hardness of approximately 60 H_V in the transformed phase over the observed range of cooling rates. There is no clear evidence for any abrupt changes in hardness with changes in cooling rate.

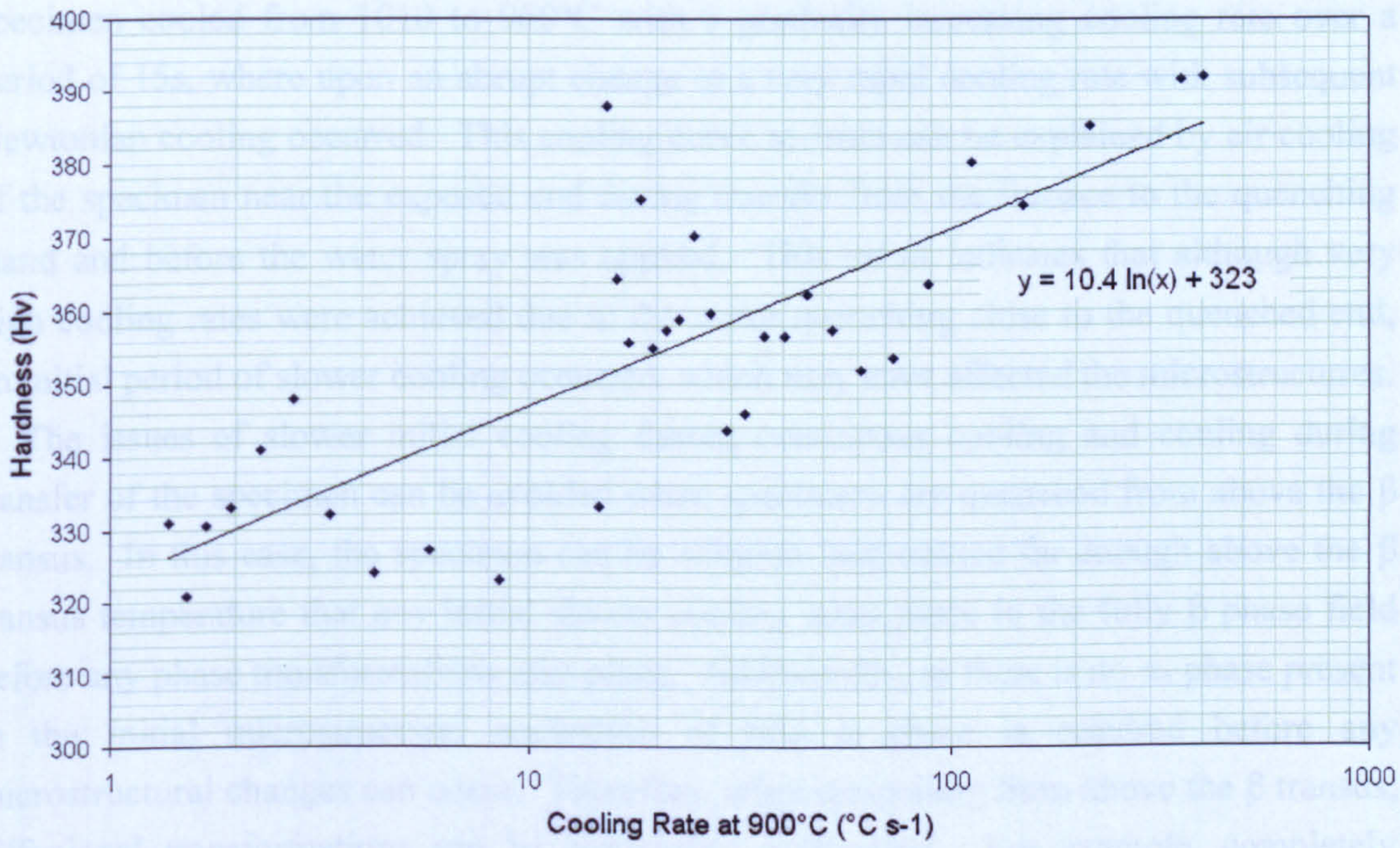

Fig. 7.55 Hardness versus the estimated cooling rate at 900°C for different points along the Jominy specimen.

7.3 Discussion

7.3.1 Variations in Cooling Rate Along the Jominy Specimen

The measured continuous cooling curves at different points along the Jominy specimen were presented in section 3.4.2. The thermocouples located at points 15 mm, 35 mm and 65 mm from the quenched end gave fairly typical continuous cooling curves. These can be described as a gradually increasing cooling rate at the start of the test, which reaches a maximum and thereafter decreases according to Newtonian cooling. For these three positions, the maximum cooling rate occurred at 890, 970 and 990°C for the 65, 35 and 15 mm positions respectively. This pattern suggests that the maximum cooling rate should be achieved at temperatures higher than 990°C for positions less than 15mm from the quenched end. However, the thermocouple located 3mm from the quenched end showed different cooling behaviour to the other thermocouple positions. Here, the specimen cooled from 1010 to 960°C with a gradually increasing cooling rate over a period of 15s, where upon an abrupt change to a very rapid cooling rate with subsequent Newtonian cooling occurred. This cooling curve at 3mm can be explained by air cooling of the specimen near the exposed end during transfer from the furnace to the quenching stand and before the water spray was applied. This result indicates that although very high cooling rates were achieved due to the water quenching close to the quenched end, an initial period of slower cooling occurred, which may have affected the microstructures.

The issues of slower initial cooling during continuous cooling and cooling during transfer of the specimen can be avoided when specimens are quenched from above the β transus. In this case, the specimen can be solution heat treated far enough above the β transus temperature that any initial slower cooling takes place in the fully β phase field before any phase transformations take place. Additionally, as there is no α_p phase present in the initial microstructure, nucleation of new α phase is required before any microstructural changes can occur. Therefore, when quenching from above the β transus, diffusional transformations can be completely suppressed. For example, completely martensitic microstructures were reported for Ti-6Al-4V cooled from the β phase field at cooling rates above 410°C s^{-1} by Ahmed and Rack (1998) and similarly, Stanford and Bate (2005) found no evidence of diffusional transformation in Ti-6Al-4V cooled at ~500°C s^{-1}.

In the present case, the cooling experiment took place from within the α+β phase field. This means that as soon as the temperature drops below the solution treatment temperature, there is a driving force for diffusional transformations to occur and there is already α phase present in the form of the pre-existing α_p grains. As a result, some amount of diffusional transformation may be expected in the microstructures close to the quenched end.

7.3.2 Growth of the Existing α_p Phase During Cooling

Observations from optical microscopy, SEM and EBSD analysis indicated that growth of the α_p phase occurred during continuous cooling. Features attributed to α_p grain growth were seen at all locations along the Jominy specimen, indicating that diffusional transformations were not completely suppressed even at the quenched end. However, between 0 and approximately 9 mm from the quenched end, corresponding to a cooling rate at 900°C of approximately 20°C s^{-1}, the extent of the α_p growth was very small and therefore had no significant effect on the volume fraction of the α_p grains. The small amount of α_p grain growth that occurred at these locations close to the quenched end probably occurred during the initial period of slower cooling during transfer of the Jominy specimen from the furnace to the quenching stand. At distances greater than approximately 9 mm ($CR_{900} < \sim 20°C\ s^{-1}$), growth of the α_p grains began to have a significant effect on the α_p volume fraction. This result is shown in Fig. 7.56, which plots the α_p volume fraction measured by point counting against the log of the cooling rate at 900°C. It can be seen that for cooling rates greater than ~20°C s^{-1}, within the experimental error, the α_p volume fraction does not change significantly. At cooling rates below ~20°Cs^{-1} a logarithmic relationship gives a reasonable fit to the observed increase in volume fraction. At the slowest cooling rate of 1.7°C s^{-1}, α_p grain growth led to a volume fraction of approximately 60%.

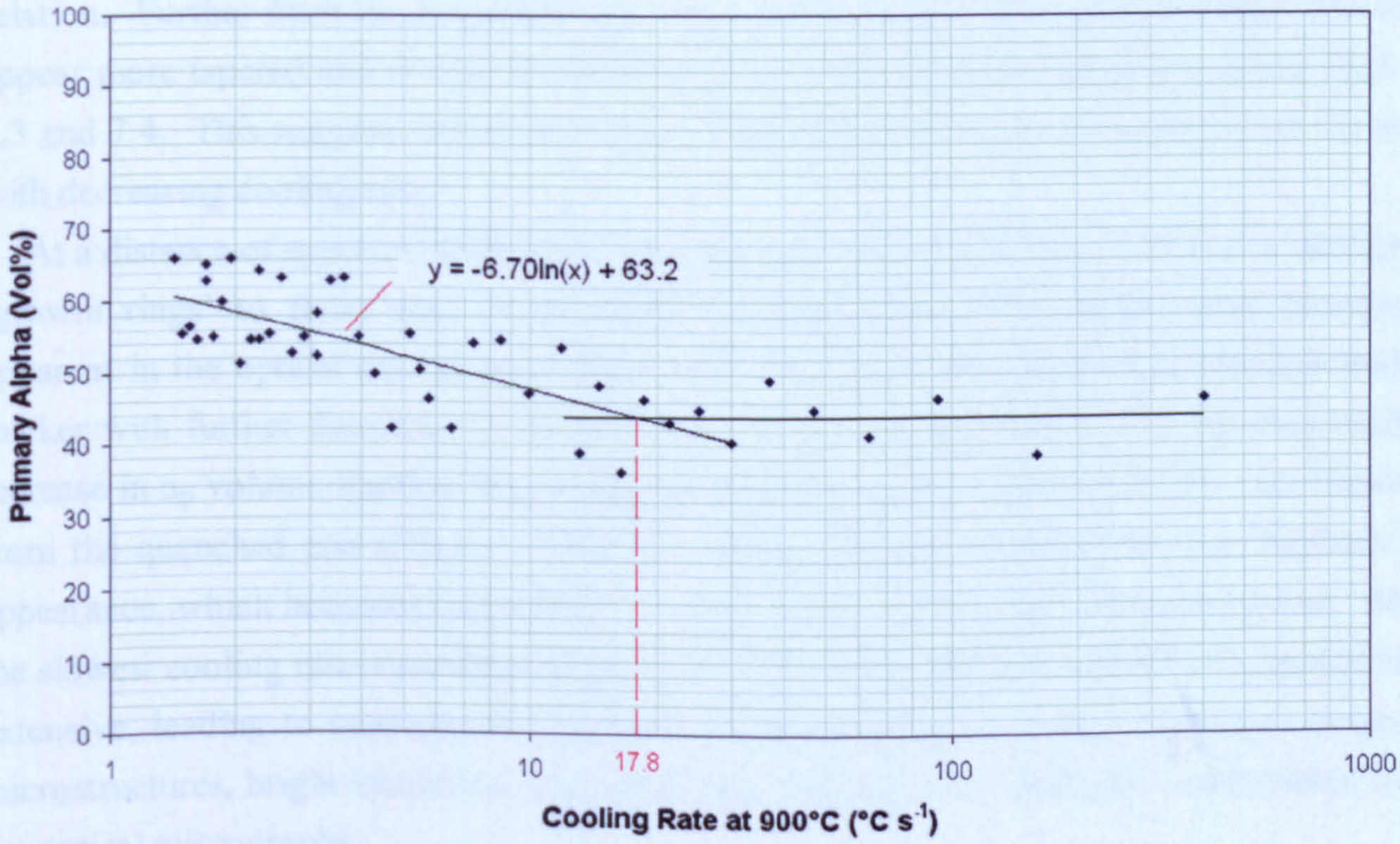

Fig. 7.56 Final α_p content versus the estimated cooling rate at 900°C for different points along the Jominy specimen.

The features attributed to α_p grain growth close to the quenched end were even rings of material at the edges of α_p grains approximately 1 μm thick, which were noticeably lighter compared to the grain interior (observed in lightly etched SEM images) and the presence of small pointed protuberances from all α_p grains extending for a short distance along the β/β boundaries. These ring features and protuberances are believed to be evidence of a small amount of α_p grain growth occurring by epitaxial growth at α_p/β interfaces and preferential growth along β/β grain boundaries resulting in partial penetration of the β/β boundaries. Examples of the light rings of material at the edges of α_p grains in SEM micrographs can be seen in Figs. 7.22 and 7.27. Numerous examples of α_p protuberances can be in the optical and SEM micrographs, see for example Fig. 7.1, Fig 7.2 and Fig. 7.22. The EBSD analysis (see for example Fig. 7.36(a) at 0.2mm) shows that the α_p protuberances tend to have an identical crystallographic orientation to the α_p grains from which they emanate and therefore, in general do not satisfy the Burgers orientation relation with either of the adjacent β grains (Fig. 7.36(c)). This shows that the protuberances must have grown from the α_p grains rather than being newly nucleated grain boundary allotriomorphs. In the general case, where the α_p protuberances do not satisfy the Burgers orientation relation with either of the adjacent β grains, the protuberances from separate α_p grains only connect when the β/β boundary between the α_p grains is relatively short. This limited penetration of the β/β boundaries can be explained by the fact that the interfacial energy of the boundary between a protuberance and the adjacent β grains will be relatively high when they do not adhere to the Burgers relation. Further from the quenched end, there are examples of α_p protuberances which appear more tapered and to extend further into the β/β boundaries, see for example Figs. 7.3 and 7.4. This suggests that more extensive growth of the α_p protuberances can occur with decreasing cooling rate.

At a distance of approximately 7mm from the quenched end (CR_{900} = 30°C s^{-1}), similar 'growth rings' to those seen in the higher magnification SEM images also become apparent in the optical micrographs (Fig. 7.8). These become increasingly obvious and thicker with further decreases in cooling rate, which is in agreement with the measured increase in α_p volume fraction for cooling rates below approximately 20°C s^{-1}. At 12mm from the quenched end (CR_{900} = 15°C s^{-1}), the α_p growth begins to have a 'feathery' appearance, which becomes increasingly so with further decreases in the cooling rate. At the slowest cooling rates examined (Figs. 7.18, 7.20, 7.21), feathery growth of α_p grains is extensive, leading to impingement of many of the growing α_p grains. In these coarser microstructures, bright islands of retained β phase between the 'feathery' α are visible in the optical micrographs.

To summarise, cooling below the solution treatment temperature allowed immediate growth of the existing α_p grains. This initially occurs epitaxially at the α_p/β interfaces and preferentially along the β/β boundaries resulting in protuberances from the α_p grains.

Some limited α_p growth was noted even close to the quenched end due to the slower initial cooling that occurred during transfer to the quenching stand. A significant increase in α_p volume fraction occurred for cooling rates below approximately 20°C s^{-1}. The α_p grain growth became 'feathery' below approximately 15°C s^{-1}.

7.3.3 Development of α_p Protuberances and α_{GB} Precipitates at the β/β Boundaries

As already discussed, cooling below the solution treatment temperature causes α_p grains to grow preferentially at β/β grain boundaries. However, close to the quenched end this did not lead to a complete coverage of the β/β boundaries. SEM and EBSD analyses at 0.2mm from the quenched end (Fig. 7.36), show that apart from the α_p protuberances, the remainder of the β/β boundaries show no evidence of diffusional transformation product, with the boundaries having completely martensitic morphology on either side. This indicates that the cooling rate close to the quenched end was sufficient to suppress nucleation of new grain boundary allotriomorphs (α_{GB}). Between 0 and approximately 3mm from the quenched end, corresponding to CR_{900} = 90°C s^{-1}, in the majority of cases the β/β boundaries also appeared to be free from α_{GB}. However, occasionally isolated instances of α phase extending along β/β grain boundaries were observed, see for example SEM micrographs Figs. 7.29 and 7.30 at 1.8 and 1.9 mm from the quenched end respectively. In these 2D views, the regions of α phase at the grain boundary are not visibly connected to α_p grains. However, it is not clear from a 2D micrograph whether these features are evidence of nucleated α_{GB}, or are simply α_p protuberances connected to α_p grains out of the plane of view. Further work utilising serial sectioning would be required to confirm this. Although these exact same features were not analysed using EBSD, similar features were seen in the EBSD maps acquired at 2mm (Fig. 7.38) and 3mm (Fig. 7.39) from the quenched end. Two examples taken from the map at 2mm are shown in greater detail in Figs. 7.57 and 7.58 and an example taken from the map at 3mm is shown in Fig. 7.59.

In the first example, the feature resembling possible α_{GB}, is indicated with an arrow in Fig. 7.57(a). It can be seen that this feature, which extends along most of a β/β boundary, is larger than the surrounding transformed laths. It is not connected to the α_p grain visible top right and has a different orientation from it, so cannot be a protuberance from this grain. The Burgers map (Fig. 7.57(c)), shows that the feature has close Burgers type misorientations with transformed laths in both adjacent β grains i.e. it appears to 'belong' to both grains. This means that it could conceivably be reconstructed to the orientation of either of the β grains. The reconstructed β map is shown in Fig. 7.57(d). It can be seen that in this case, the program has reconstructed the feature as a part of β grain (b). Examining the cubic pole figure showing the orientations of β grains (a) and (b) in Fig.

7.57(f), it can be seen that the two grains share a near common {110} pole and that the feature of interest has its (0002) pole in this same direction (Fig. 7.57(e)). This feature is possibly nucleated α_{GB} as it is not related to any α_p grains in the 2D section. The (0002) pole of the feature is parallel to the common {110} pole of the two adjacent β grains. This is the expected orientation for the precipitation of diffusional α at the grain boundary due to variant selection when the two adjacent β grains have a close {110} pole (Bhattacharyya *et al.*, 2003. Stanford and Bate, 2004).

In the second example, the feature resembling possible α_{GB}, is indicated with an arrow in Fig. 7.58(a). It can be seen that this feature, morphologically similar to the first example, extends along most of a β/β boundary and also has a different orientation to the nearby α_p grains at either end of the boundary. The Burgers map (Fig.7.58(c)), shows that the feature has close Burgers type misorientations with transformed laths in only one of the adjacent β grains. The reconstructed β map is shown in Fig. 7.58(d). It can be seen that the program reconstructs the feature as a part of β grain (a). Examining the cubic pole figure showing the orientations of β grains (a) and (b) in Fig. 7.58(f), it can be seen that the two grains do not share a common {110} pole and that the feature of interest has its (0002) pole in the direction of one of the {110} poles for β grain (a) (Fig. 7.58(e)). This feature may also be nucleated α_{GB} as it is not related to any α_p grains in the 2D section. In this case, the β grains do not share a common {110} pole. The (0002) pole of the feature is parallel to an {110} pole for one of the adjacent β grains, which is the relationship reported by Stanford and Bate (2004) when no variant selection occurs.

In the third example, the feature resembling possible α_{GB} is indicated with an arrow in Fig. 7.59(a). This feature is morphologically similar to the previous examples and extends along most of a β/β boundary. Although not visibly connected to the α_p grain marked (a), it shares a similar crystallographic orientation (misorientation ~3°). The Burgers map (Fig.7.59(c)), shows that the feature has no Burgers type misorientations with transformed laths in either of the adjacent β grains. The reconstructed β map is shown in Fig. 7.59(d). It can be seen that the program fails to reconstruct the feature as a part of either β grain. Examining the cubic pole figure showing the orientations of β grains (a) and (b) in Fig. 7.59(f) and the hexagonal pole figure for the feature of interest (Fig. 7.59(e)), it can be seen that the two β grains do not share a common {110} pole and that the feature of interest does not have an (0002) pole aligned with {110} poles from either β grain. This feature cannot be nucleated α_{GB} as it has no Burgers relationship with either β grain nor is it a compromise between them. This suggests that in this case the feature is an α_p protuberance. The low misorientation with one of the α_p grains suggests the two may be connected out of the plane of the 2D section.

From the three examples presented, there is evidence that between 0 and approximately 3mm from the quenched end, some of the isolated instances of α along the β/β grain boundaries are in fact α_p protuberances that are connected to α_p grains out of the

plane of view. However, examples of features which belong to one or both adjacent β grains and obey the expected variant selection for nucleated α_{GB}, suggests that some limited nucleation of α_{GB} may have occurred. In an experiment by Stanford and Bate (2004), to study the precipitation of α_{GB}, Ti-6Al-4V was air cooled from above the β transus (1020°C) for a period of 7s before water quenching to arrest the diffusional transformation. This was found to produce a microstructure with nucleated α_{GB} at approximately 1/3 of the β/β boundaries, with the remaining boundaries having complete martensitic morphology on either side. With this in mind, it seems reasonable to presume that some limited nucleated of α_{GB} may have occurred in the Jominy specimen between 0 and 3mm due to the slower initial cooling rates during the test as discussed in section 7.2.1.

(a) Euler Map

(b) Band Contrast

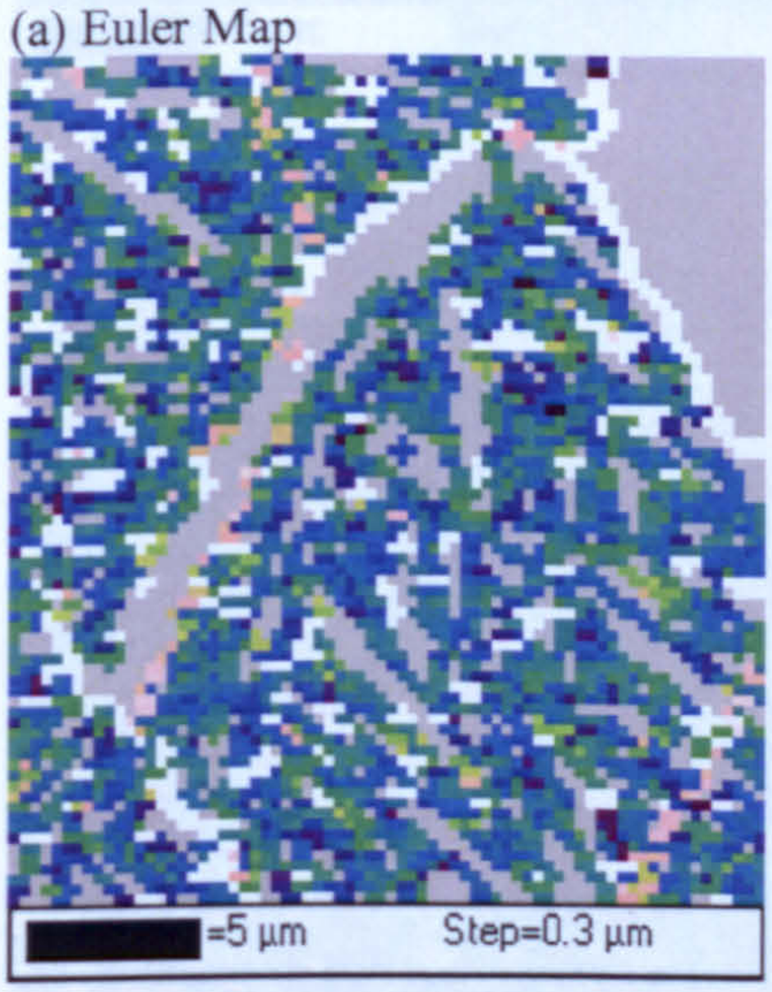

(c) Burgers Map

(d) Reconstructed β phase

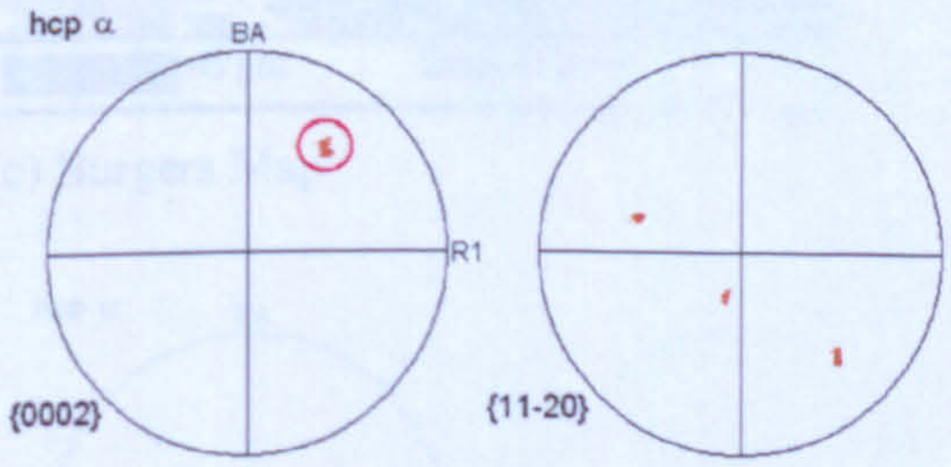

(e) hexagonal pole figures for the feature.

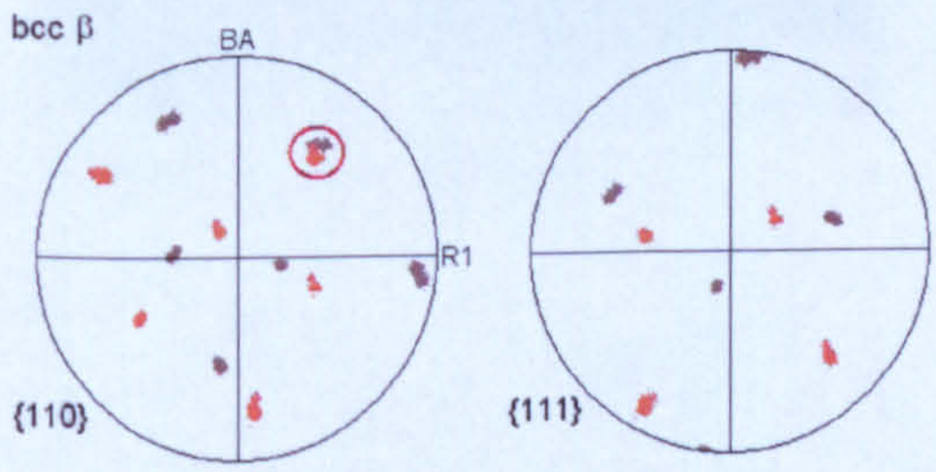

(f) cubic pole figures for adjacent β grains.

Fig. 7.57 Analysis of a feature resembling possible nucleated α_{GB} at a β/β boundary, 2mm from the quenched end.

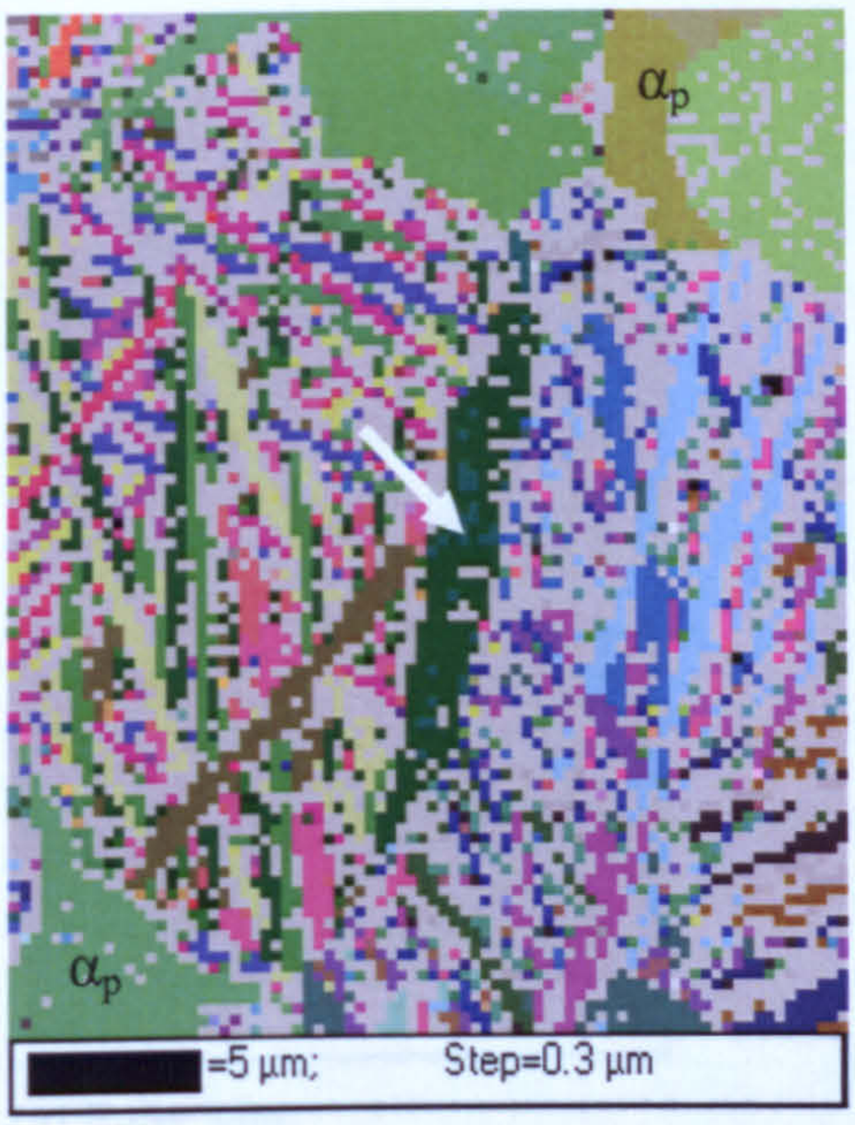

(a) Euler Map

(b) Band Contrast

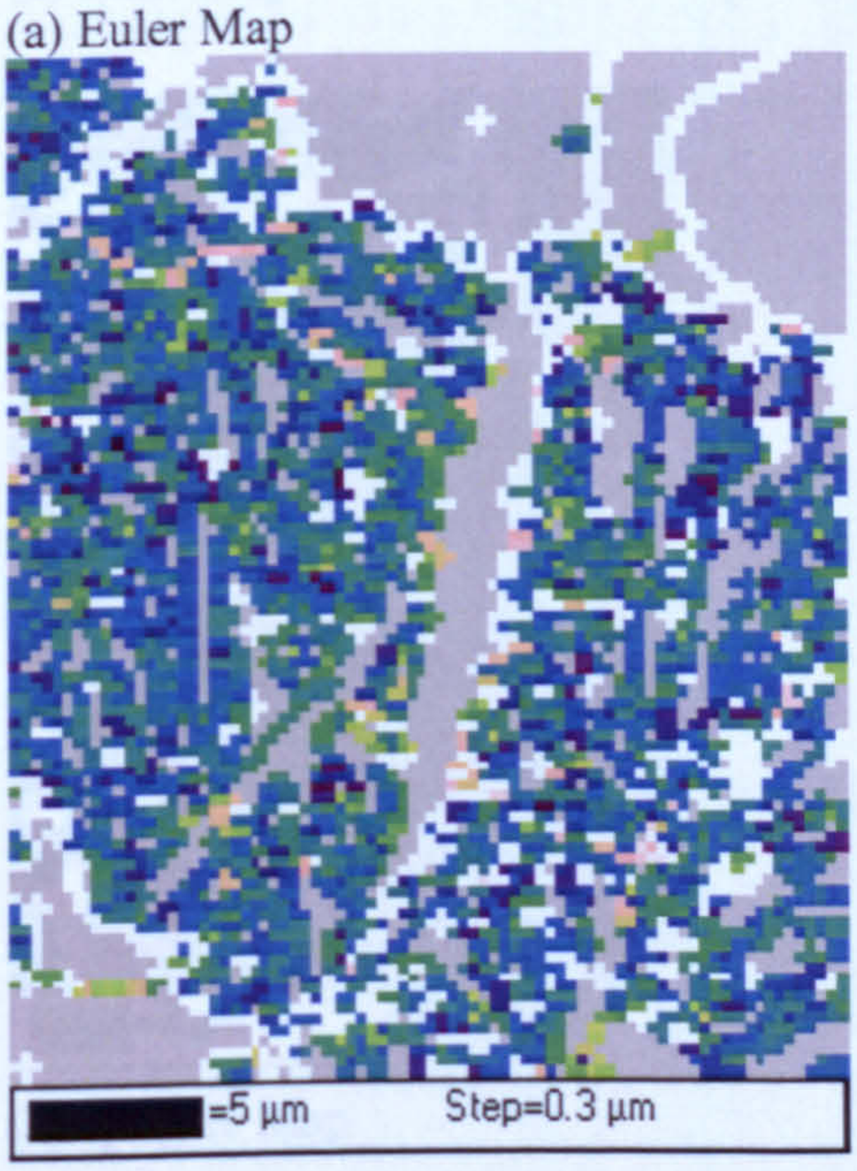

(c) Burgers Map

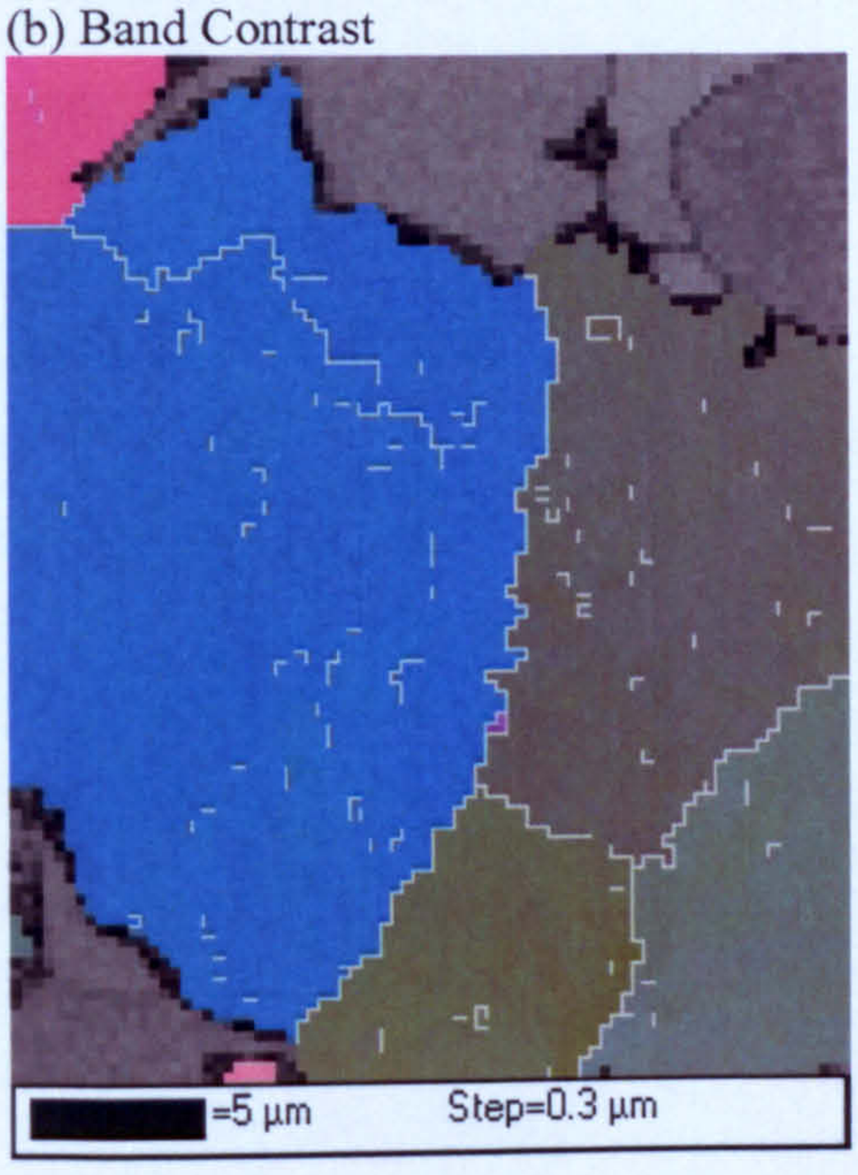

(d) Reconstructed β phase

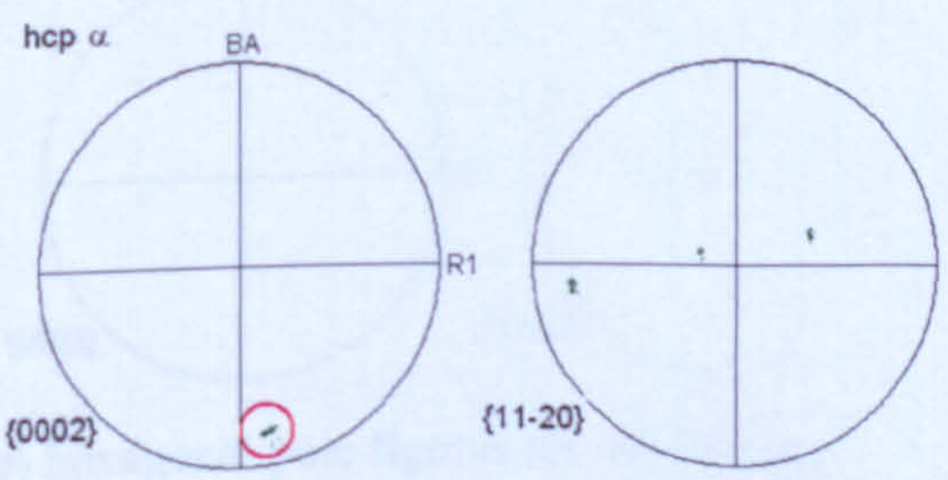

(e) hexagonal pole figures for the feature.

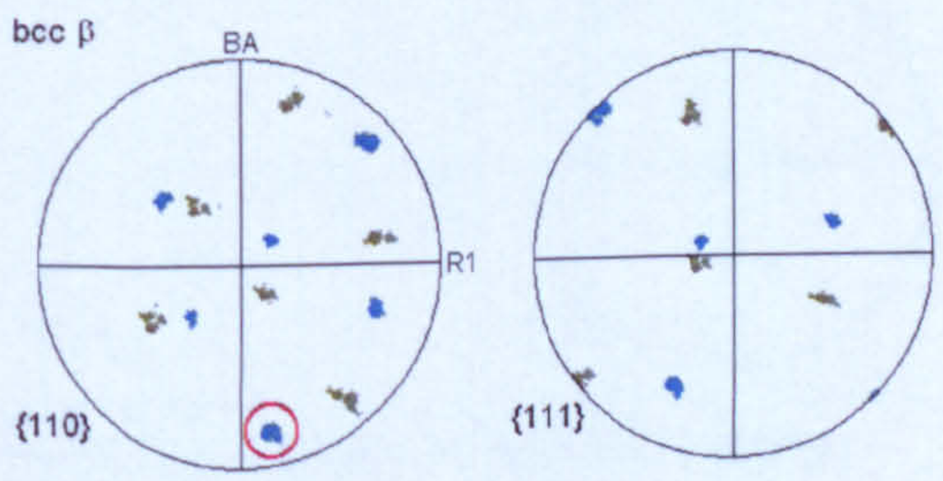

(f) cubic pole figures for adjacent β grains.

Fig. 7.58 Analysis of a feature resembling possible nucleated α_{GB} at a β/β boundary 2mm from the quenched end.

(a) Euler Map

(b) Band Contrast

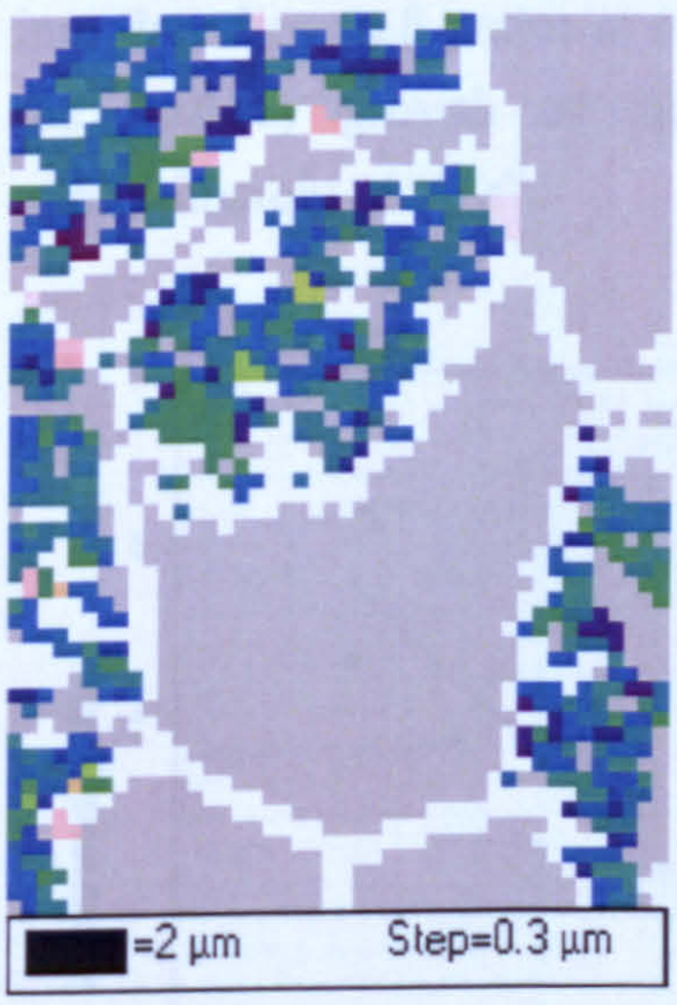

(c) Burgers Map

(d) Reconstructed β phase

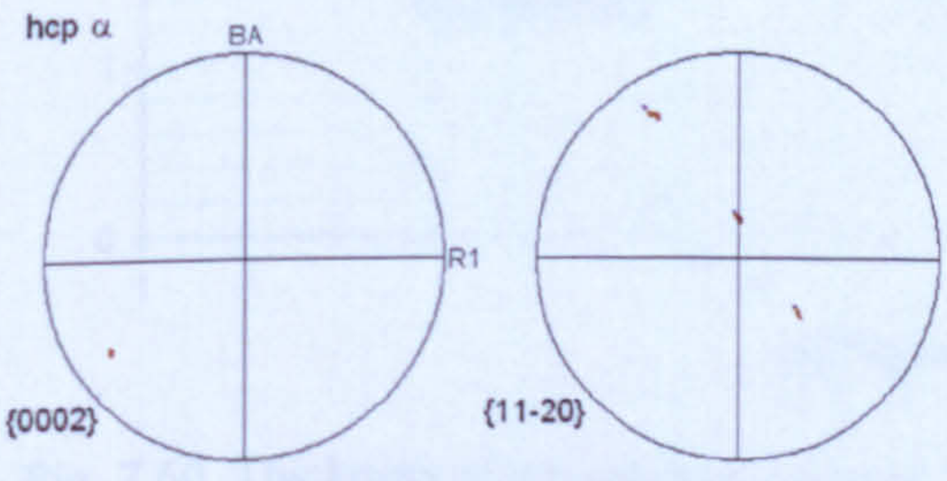

(e) hexagonal pole figures for the feature.

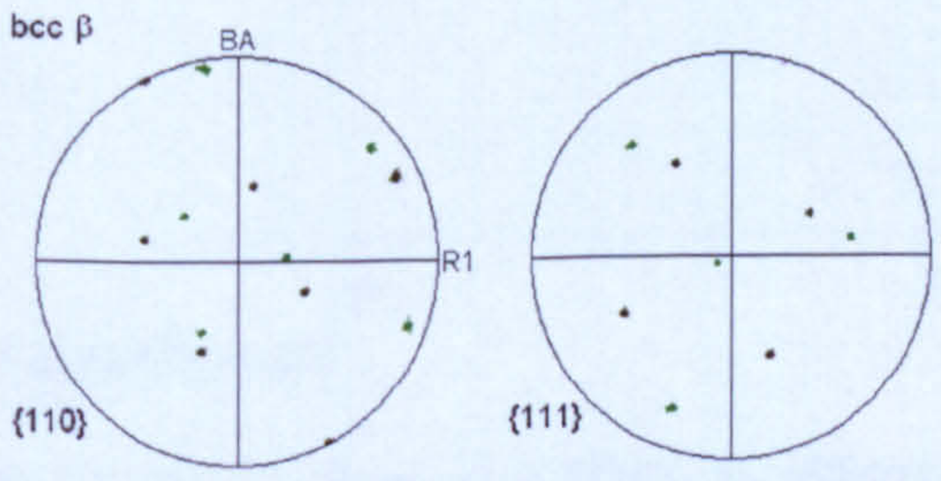

(f) cubic pole figures for adjacent β grains.

Fig. 7.59 Analysis of a feature resembling possible nucleated α_{GB} at a β/β boundary 3mm from the quenched end.

At distances greater than approximately 3mm from the quenched end, corresponding to a cooling rate at 900°C of approximately 90°C s^{-1}, SEM observations showed what appeared to be more continuous thin α_{GB} precipitates along the β/β boundaries, see for example Fig. 7.31. The thickness of the α_{GB} increased with further decreases in cooling rate (Fig. 7.32 – 7.35). At approximately 7mm from the quenched end (CR_{900} = 30°C s^{-1}), all of the β/β boundaries were clearly outlined by a combination of α_{GB} and α_p protuberances. These are thick enough to be easily resolved in etched optical micrographs (Fig. 7.8). From this point, the average thickness of the continuous α at the β/β boundaries was measured from optical micrographs. The results are plotted against the cooling rate in Fig. 7.60. The continual increase in α_{GB} thickness with decreasing cooling rate is best described by a logarithmic relationship. At slow cooling rates below approximately 10°C s^{-1} (see Fig. 7.12), the α_{GB} began to have a 'feathery' appearance, with wider variations in thickness, leading to more scatter in the thickness measurements. However, the same logarithmic trend seems to be obeyed. The feathery growth of α_{GB} into the adjacent β grains at cooling rates below approximately 10°C s^{-1} appears similar to the feathery growth of the α_p grains that was observed at cooling rates below approximately 15°C s^{-1}.

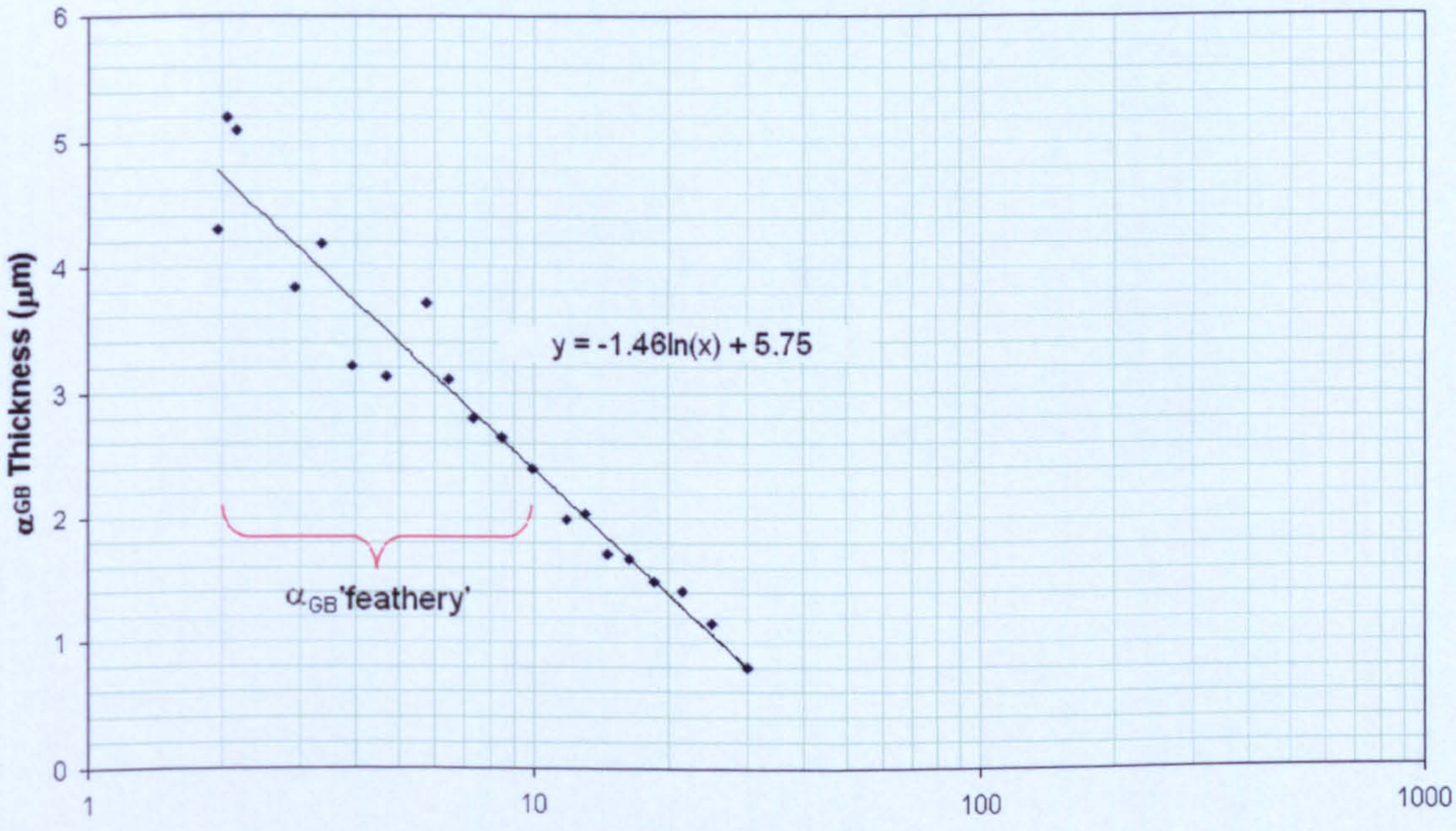

Fig. 7.60 Thickness of continuous α_{GB} versus the estimated cooling rate at 900°C for different points along the Jominy specimen.

There is an apparent discrepancy between the optical metallography results which clearly show α_{GB} on all β/β boundaries for cooling rates below ~30°C $s^{-1}$and the EBSD maps (Figs. 7.43 to 7.45). The band contrast and orientation maps for the EBSD data

reveal the α_p protuberances but in many cases do not show the nucleated α_{GB} as clearly defined grain boundary precipitates. This is due to the growth of Widmanstätten colonies from the α_{GB} with similar crystallographic orientations. Orientation imaging therefore does not reveal the difference between the closely orientated Widmanstätten α_s and the α_{GB} allotriomorphs. Similarly, the band contrast maps do not reveal a boundary between them because the layers of retained β phase at the boundaries are too thin to significantly reduce the pattern quality. To show that the α_{GB} precipitates and thin layers of retained β phase are in fact present in the EBSD maps, a small, high resolution EBSD map was acquired 8mm from the quenched end after light etching and compared with an SEM image from the same area (Fig. 7.61). It can be seen from the SEM image of the etched surface (Fig. 7.61(b)), that what appears in the EBSD map as a relatively large yellow region of similarly orientated α, is in fact composed of two distinct colonies of thin parallel Widmanstätten α plates, separated by very thin layers of retained β, with a different growth direction in each colony. Between the two colonies is a β/β boundary with allotriomorphic α_{GB}, which is separated from the Widmanstätten colonies by a very thin layer of retained β. This map is examined in more detail in section 7.2.4.

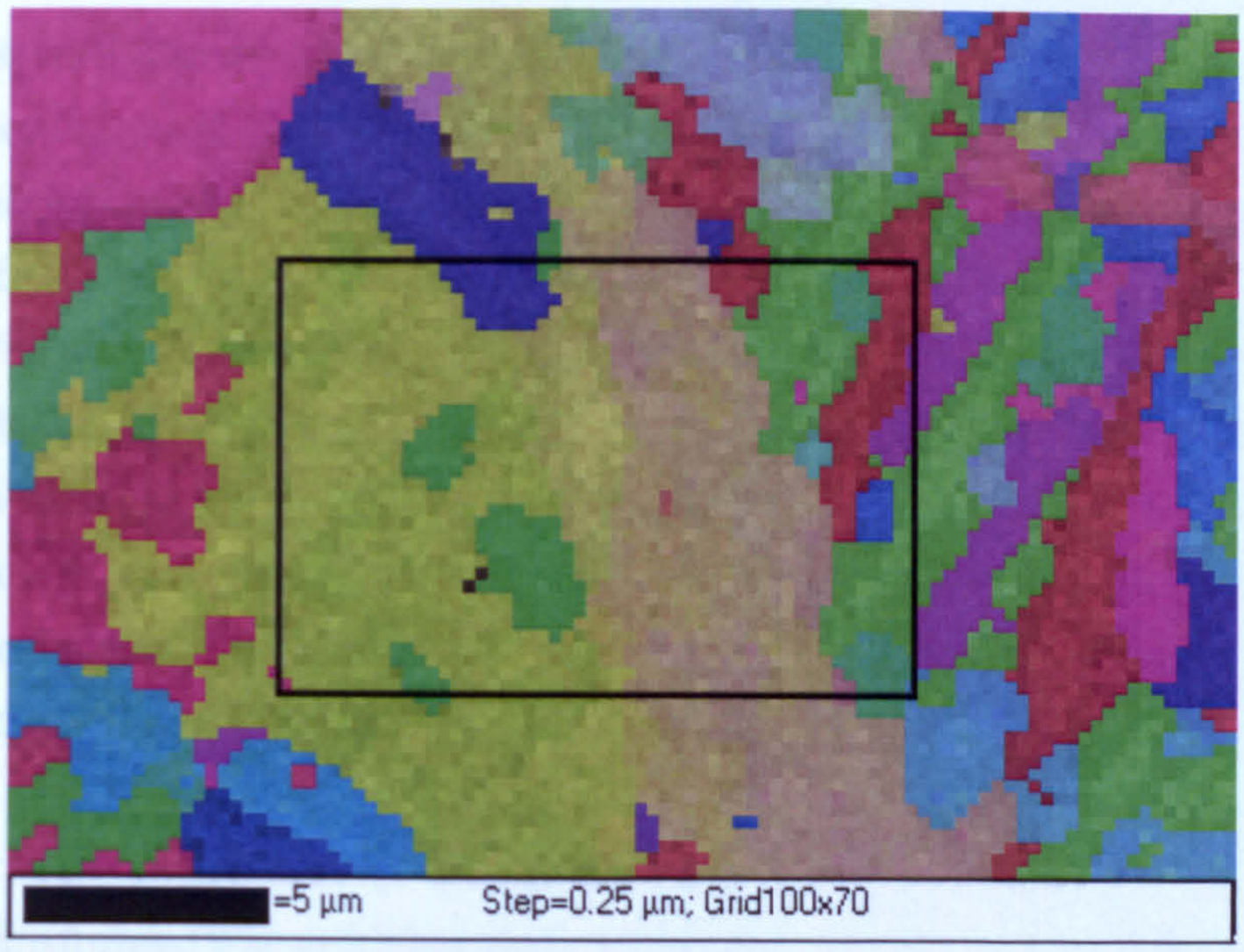

(a) EBSD and band contrast map.

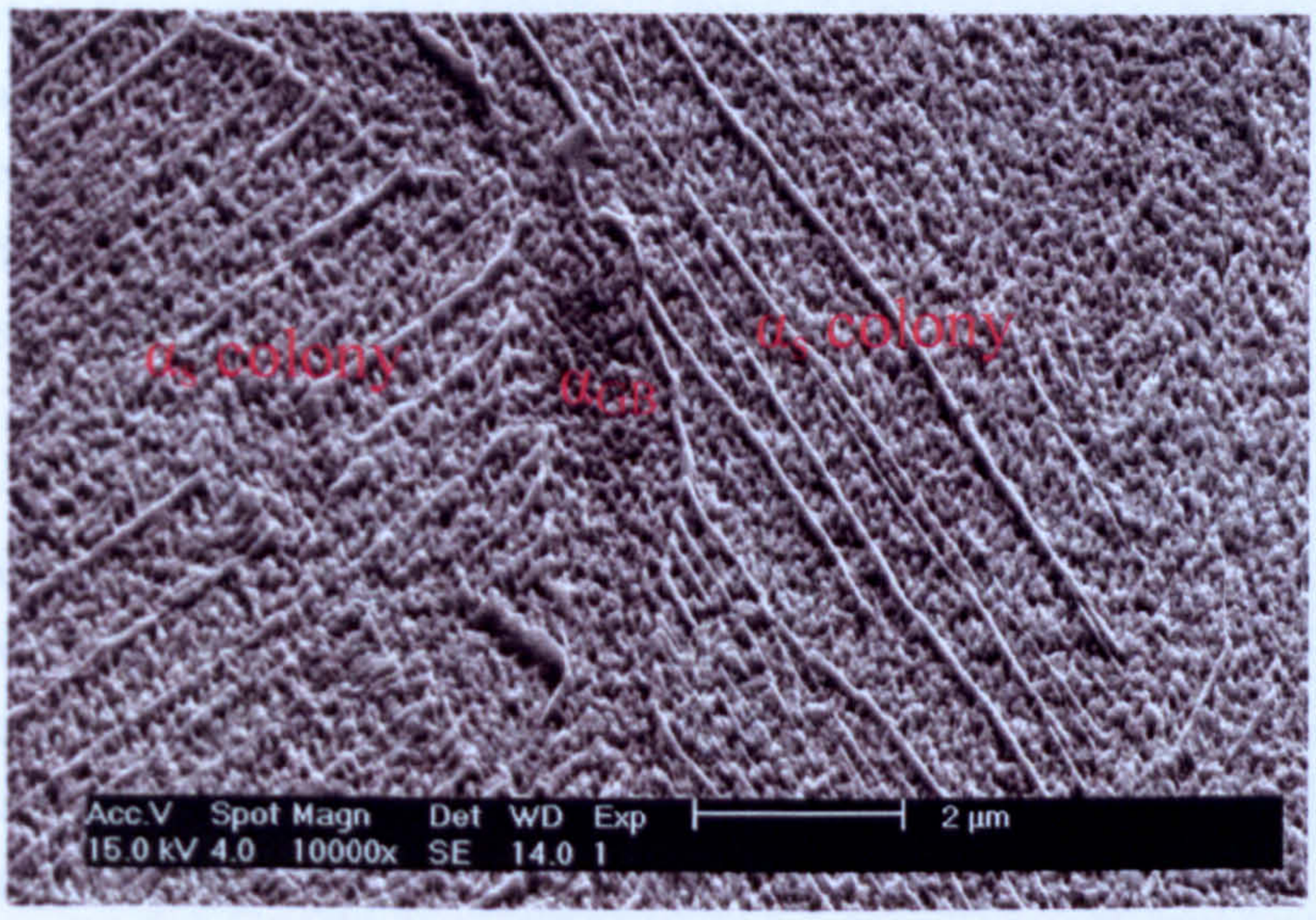

(b) SE image of the area enclosed by the black box in (a).

Fig. 7.61 EBSD map acquired across a β/β boundary 8mm from the quenched end and an SE image from the same area. EBSD does not reveal presence of retained β and boundaries between similarly orientated colonies and α_{GB}.

At cooling rates below approximately 20°C s^{-1}, where the growth of α_p grains and α_p protuberances leads to a significant increase in the α_p volume fraction (Fig. 7.56), there is a decrease in the area of β/β boundaries available for nucleation of α_{GB}, which occurs at lower temperatures. This can be seen in the EBSD map obtained at 60mm (Fig. 7.45) corresponding to a CR_{900} of 1.7°C s^{-1}. The significant α_p grain growth has resulted in the α_p grains becoming the major phase. Impingement of the growing α_p grains and α_p

protuberances with one another results in the isolation of the remaining β grains so that there is less continuous β phase and hence fewer β/β boundaries for nucleation of α_{GB}.

To summarise, nucleation of α_{GB} was suppressed close to the quenched end. Nucleation of α_{GB} was observed at cooling rates below approximately 90°C s^{-1} although there was evidence that some α_{GB} may have formed at higher apparent cooling rates, perhaps due to the slower initial cooling that occurred during transfer to the quenching stand. Below approximately 30°C s^{-1}, all boundaries were outlined by a combination of α_{GB} and the α_p protuberances. Growth of α at the grain boundaries became 'feathery' below approximately 15°C s^{-1}. At slow cooling rates, α_p grain growth reduces the β/β grain boundary area available for nucleation of α_{GB}.

7.3.4 The Transformed Phase Within Prior β Grains

The optical metallography results appear to show an essentially continuous transition from a martensitic transformation at the highest cooling rates to a completely nucleation and growth transformation at slow cooling rates. The increase in the scale of the laths in the transformed phase with decreasing cooling rate is gradual and there is no abrupt change in the microhardness of the transformed phase (Fig. 7.55). This is similar to the observations reported by Baeslack and Mullins (1982) in welds of the near-α alloy Timetal 829. There is no clear evidence for a distinct massive transformation product as reported by Ahmed and Rack (1996) for the continuous cooling of Ti-6Al-4V. However, due to the fine nature of the transformed phase at high cooling rates, a TEM investigation would be required to fully investigate whether or not such a massive transformation occurs. The apparent continuous nature of the transition in the present results can make the interpretation of the microstructures somewhat subjective.

Due to the very high cooling rates at the quenched end, the transformed β phase must be martensitic in nature. From the quenched end to a distance of approximately 1mm from the quenched end (CR_{900} ~400°C s^{-1}), the fine laths in the transformed β grains appear dark under reflected light microscopy after etching (Fig. 7.1 and Fig. 7.2) and thereafter, the laths have a slightly different etching response (Fig. 7.3), appearing light and the regions between the laths dark. This different etching response at the highest cooling rates may be due to a displacive transformation giving rise to laths containing a high density of dislocations, twins and stacking faults. Features resembling twins within laths can be seen in some of the back scattered electron images due to orientation contrast, see for example Fig. 7.21 at 0.2mm and 7.26 at 1.2mm from the quenched end. These observations suggest that the transformed β phase is probably martensite at least as far as 1.2mm from the quenched end (CR_{900} > ~320°C s^{-1}). This seems a reasonable interpretation in light of the work by Ahmed and Rack, in which completely martensitic

microstructures were reported for Ti-6Al-4V above 410°C s^{-1}. All of the laths in these microstructures have a basket-weave structure.

There was evidence from the SEM study of thin layers of retained β within the transformed β grains at distances greater than approximately 1.7mm from the quenched end (CR_{900} < ~200°C s^{-1}). This suggests that there may have been some diffusional element to the transformation at cooling rates below this. Again, the laths in these structures have a basket-weave structure.

Fig. 7.31 shows a back scattered electron SE image taken 3.2mm from the quenched end (CR_{900} = 85°C s^{-1}). Here, there is clear evidence of bright retained β phase between some α_s laths and groups of these laths forming parallel to one another in small colonies. Other parts of the structure appear to have more of the basket-weave structure. The overall transformed structure is therefore mixed in appearance. At lower cooling rates (e.g. Fig. 7.33, CR_{900} = 45°C s^{-1}), the transformed structure appears to have formed entirely through nucleation and growth processes as it consists predominantly of colonies of parallel Widmanstätten α_s laths with thin films of retained β between them. At first, the colonies contain fewer laths and there are many of them within a prior β grain, so that the colonies themselves appear to be in a basket-weave arrangement. The transition to a morphology that would traditionally be described as colony in appearance is therefore gradual. Assessed from the point of view of the optical microscopy, it is felt that a colony morphology best describes the Widmanstätten structure at distances greater than 9mm from the quenched end, corresponding to a cooling rate at 900°C of approximately 20°C s^{-1} and below (see Fig. 7.10). At this point, colonies cross entire β grains and many β grains appear to contain only one or two colonies. With decreasing cooling rate, the thickness of the individual laths within the colonies increases. At the slowest cooling rates examined (Fig. 7.18 to 7.20), the microstructures appear similar to those found in smaller diameter commercial billets.

To summarise, no sharp boundary was observed between diffusionless and diffusional transformations. The microstructures were interpreted as predominantly martensitic at cooling rates higher than approximately 300°C s^{-1} and diffusional below approximately 45°C s^{-1}, with the transformation modes at intermediate cooling rates (45-300°C s^{-1}) unclear and requiring further investigation. The transformed phase was deemed to have a morphology best described as colony in its appearance below approximately 20°C s^{-1}.

7.3.5 Variant Selection in the Transformed Phase

Using the EBSD data in Figs. 7.36 - 7.45, the fractions of variants occurring within individual prior β grains was investigated for the microstructures produced by different rates of continuous cooling. For each cooling rate, the reconstructed β maps were used to

select four β grains with an equivalent circle diameter of at least 18μm. The analysis of the individual grains showed that for high cooling rates, where the microstructure is relatively fine and the variants tend to have a basket-weave arrangement, the transformation consistently produces all 12 possible variants. As an example, the map in Fig. 7.62(a), highlights the transformed variants corresponding to a single prior β grain in the map acquired 0.2mm from the quenched end (estimated CR_{900} >>500°C s^{-1}). The {0002} pole figure for the transformed grain contains 6 poles. In the $\{10\bar{1}0\}$ pole figure, where a single orientation produces three poles, the pole figure shows that there are two distinct orientations about each (0002) pole, separated by a rotation of ~10.5°. Thus, if all 12 possible variants are produced in a transformed β grain, the {0002} pole figure will always contain 6 poles and the $\{10\bar{1}0\}$ and $\{11\bar{2}0\}$ pole figures will each contain 36 poles.

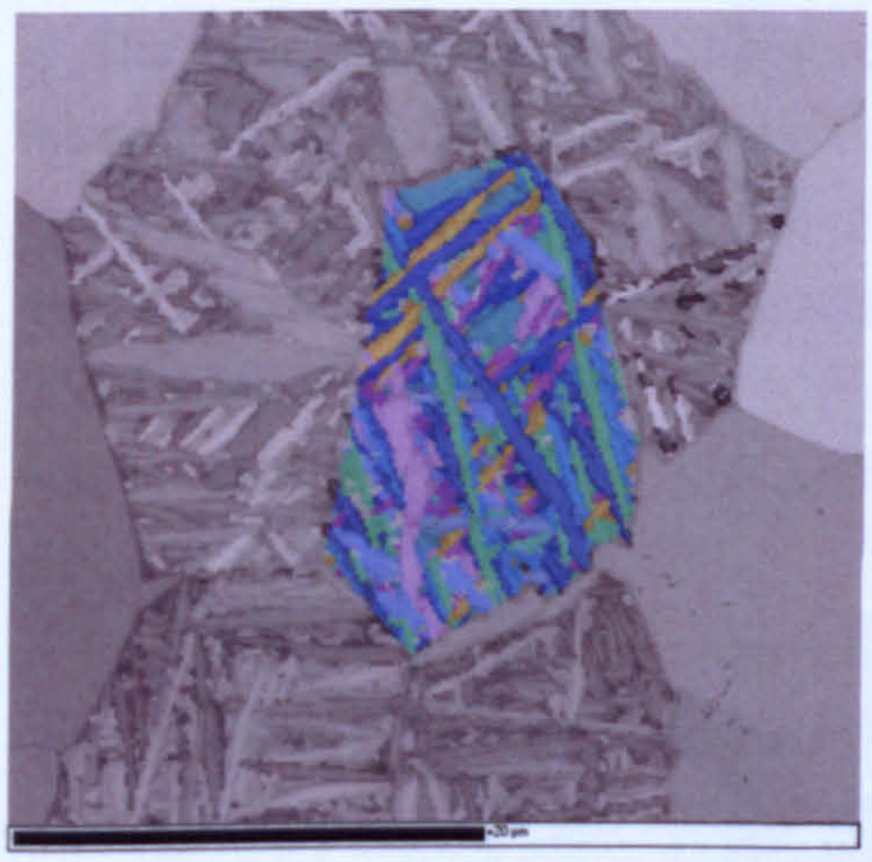

(a) Euler map for the selected prior β grain.

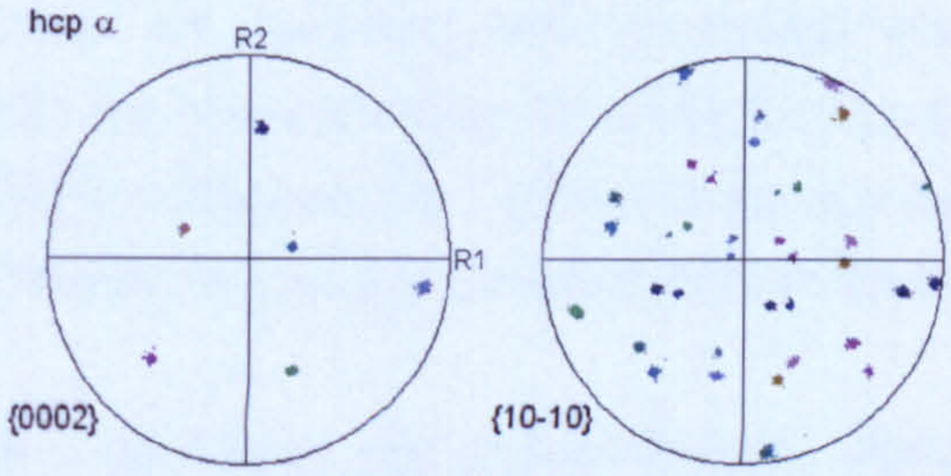

(b) α phase pole figures for the selected grain.

Fig. 7.62 EBSD Euler map for a selected prior β grain and corresponding pole figures showing the occurrence of all 12 variants as evidenced by 36 poles in the $\{10\bar{1}0\}$ pole figure. Map obtained 0.2mm from the quenched end (CR_{900} >>500°C s^{-1}).

At distances greater than 6 mm from the quenched end (CR_{900} = 37°C s^{-1}), instances of transformed β grains containing fewer than 12 variants were observed. This can be attributed to a coarser diffusionally transformed microstructure, in which Widmanstätten colonies of one α_s variant may occupy large percentages of the grain area. With further decreases in cooling rate, grains containing fewer than 12 variants become more numerous. However, at 12 mm from the quenched end (CR_{900} = 15°C s^{-1}), 2 out of the 4 grains examined still contained all 12 possible variants. At the slowest cooling rate, 60 mm from the quenched end, the prior β grains could not be accurately reconstructed and due to α_p grain growth, the area of the grains that transformed to α_s was significantly reduced. However, it is clear from the orientation map (Fig. 7.45(a)), that in most cases,

the areas of prior β grains which have transformed into coarse Widmanstätten colonies consist of far fewer than 12 possible variants, and sometimes contain only 1 or 2 differently orientated colonies.

To examine the relative amounts of each possible variant within the β grains, the number of points belonging to each of the 12 possible variant orientations were counted and divided by the total number of points in the grain to obtain the area fraction. The area fractions were arranged in descending order and then averaged for the four β grains examined at each cooling rate. The results of this analysis are shown in Fig. 7.62. Data is not shown for the slowest cooling rate at 60mm from the quenched end due to the difficulty in reconstructing the β phase in this microstructure. The expected area fraction in the case where all variants occur equally is 8.3% (i.e. 1/12) and is indicated in the figure by a horizontal red line. It can be seen that for all of the cooling rates examined, the variants do not occur equally.

The most equal occurrence happens at the highest cooling rates, where the transformed microstructure is the finest and the variants are arranged in a basket-weave structure. At the highest cooling rates, 0.2 and 1mm from the quenched end, the variant with the maximum area fraction is approximately 15% i.e. approximately twice the level expected if variants occurred equally. With decreasing cooling rate, the variants occur less equally with the area fraction of the most common variant increasing to around 20% at 5mm from the quenched end ($CR_{900} = 47°C\ s^{-1}$).

In the microstructures between 0 and 5 mm from the quenched end, where the microstructures have a predominantly basket-weave arrangement of the variants, it was generally observed that the variant orientation with the maximum grain area tended to be a collection of longer laths, separated from one another, which often traversed an entire β grain. In contrast, the variant orientations with the lowest grain areas tended to be collections of smaller laths in between the larger ones. This suggests that the variant orientations with the largest grain areas are primary laths which form first during the transformation.

At distances greater than 6 mm from the quenched end ($CR_{900} = 37°C\ s^{-1}$), there was a significant increase in the area fraction of the most commonly occurring variant to between 30 and 40%. At these slower cooling rates, the results were also much more variable. For example, in certain grains the variant orientation with the maximum grain area exceeded 70%. In these cases, this was generally due to the occurrence of a large colony, which occupied a large portion of the prior β grain.

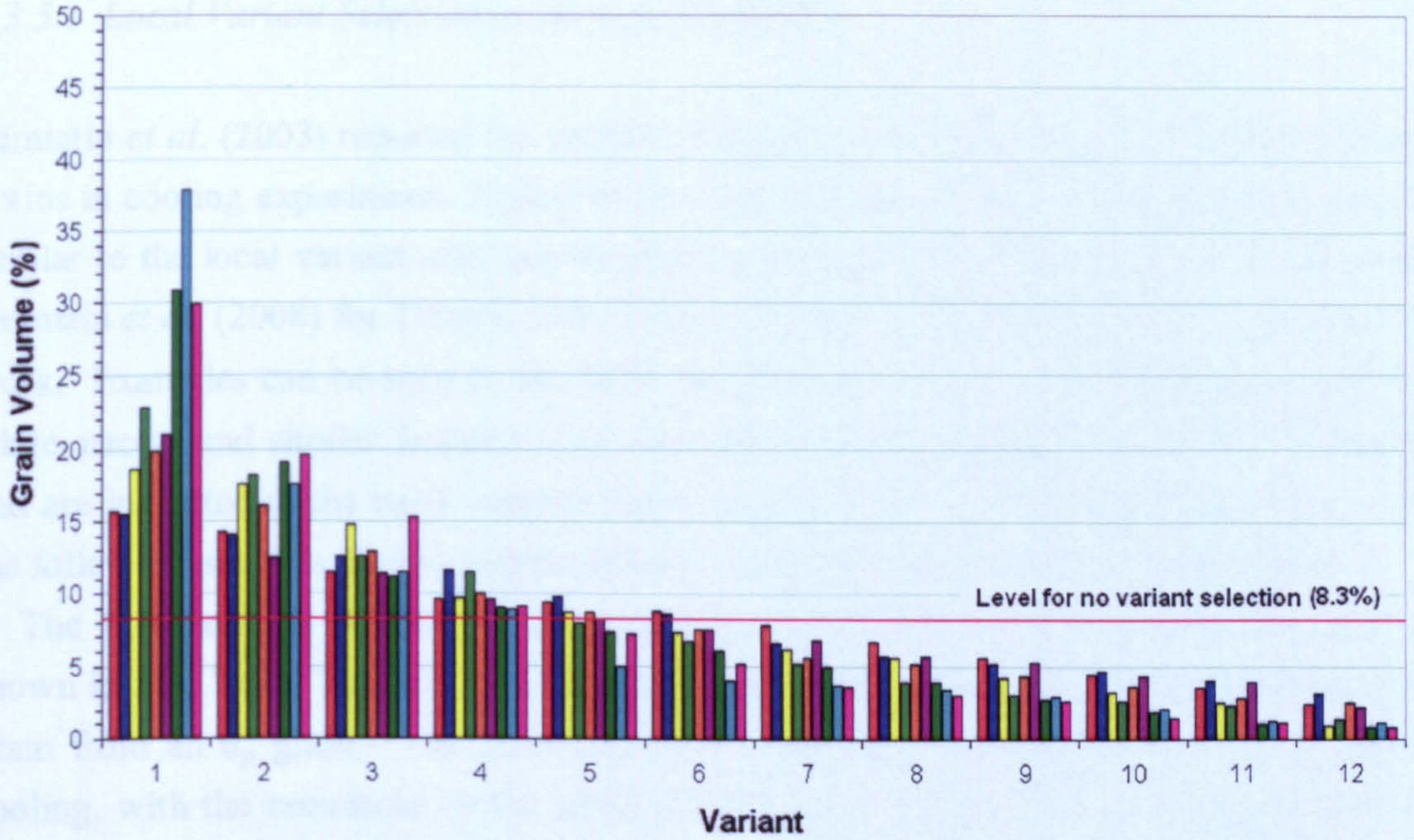

Key

	Distance from quenched end (mm)	Estimated cooling rate at 900°C (°C s^{-1})	Fig. number of EBSD map
■	0.2	>>500	7.36
■	1	400	7.37
■	2	160	7.38
■	3	100	7.39
■	4	63	7.40
■	5	47	7.41
■	6	37	7.42
■	8.7	22	7.43
■	12	15	7.44

Fig. 7.63 Area fraction of the twelve possible variants within prior β grains, arranged in descending order. Data shown for different rates of continuous cooling (see key). For each cooling rate, the data are an average obtained from four separate prior β grains.

The results in Fig. 7.63 for the higher cooling rates are similar to the findings of Stanford and Bate (2004) for martensite in Ti-6Al-4V quenched from above the β transus. In this work, the occurrence of all 12 possible variants was also reported and a comparison of Fig. 2.13 with the highest cooling rate data in Fig. 7.63 (i.e. the red and blue data bars), shows that the area fractions for the 12 variants is also similar. In the work of Stanford and Bate (2004), the observed variant selection in the martensite transformation was modelled on the basis of elastic interaction between martensite events and was found to give a reasonable prediction of the observed variant selection.

7.3.5.1 Local Variant Selection at the α_p/β Boundaries

Semiatin *et al.* (2003) reported the scattered presence of α_s appearing to emanate from α_p grains in cooling experiments carried out on bimodal Ti-6Al-4V. These observations are similar to the local variant selection mechanism discussed by Humbert *et al.* (2006) and Germain *et al.* (2008) for Timetal 834. Similar features were also observed in the present work. Examples can be seen in the SEM images Figs. 7.25, 7.27 and 7.28 indicated by white arrows and similar features were also observed sporadically in the EBSD analysis and are indicated in the band contrast maps of Figs. 7.36 – 7.45 using white arrows. In the following analysis, five examples of these features are examined in greater detail.

The first example is taken from the map at 0.2 mm from the quenched end and is shown in Fig. 7.64. This example appears to show the first signs of α_s growing into a β grain from an α_p grain. The growth has been arrested at an early stage by the rapid cooling, with the remainder of the grain transforming to martensite. This growth of α_s from the α_p grain probably occurred during the slower initial cooling rates at the start of cooling. It can be seen from the Euler map (Fig.7.64(b)) and the hexagonal pole figures (Fig.7.64(d)), that the α_s and the α_p grain from which it emanates, have the same crystallographic orientation. The Burgers map (Fig.7.64(c)) shows that at the point where α_s appears to emanate from the α_p grain, the α_p grain had an orientation relation with the parent β grain that was very close to the Burgers relation.

The second example is taken from the map 4 mm from the quenched end and is shown in Fig. 7.65 below. This example appears to show much more extensive growth of α_s from an α_p grain. In this case, α with a very close crystallographic orientation to the α_p grain has formed around the grain boundary of an adjacent β grain and in several parallel laths crossing it. The Burgers map (Fig.7.65(c)) and pole figures show that the α_p grain had an orientation relation with the adjacent β grain that was very close to the Burgers relation.

The third example from the map 5 mm from the quenched end (Fig. 7.66), again shows that the α_p grain and adjacent β grain were very close to the Burgers relation. In the fourth example, taken from the map 6 mm from the quenched end (Fig. 7.67), the hexagonal pole figures show that the α_p grain contains some orientation spread. In the left part of the α_p grain, where the α_p grain and adjacent β grain are closest to the Burgers relation, α_s is seen to emanate from the α_p grain. The final example is also from the map 6 mm from the quenched end (Fig. 7.68). It can be seen that the α_p grain and the α_s share the same (0002) pole but there is a slight misorientation between them of approximately 4°. The α_s has a strict Burgers relation with the prior β grain, with the α_p grain slightly misorientated from it.

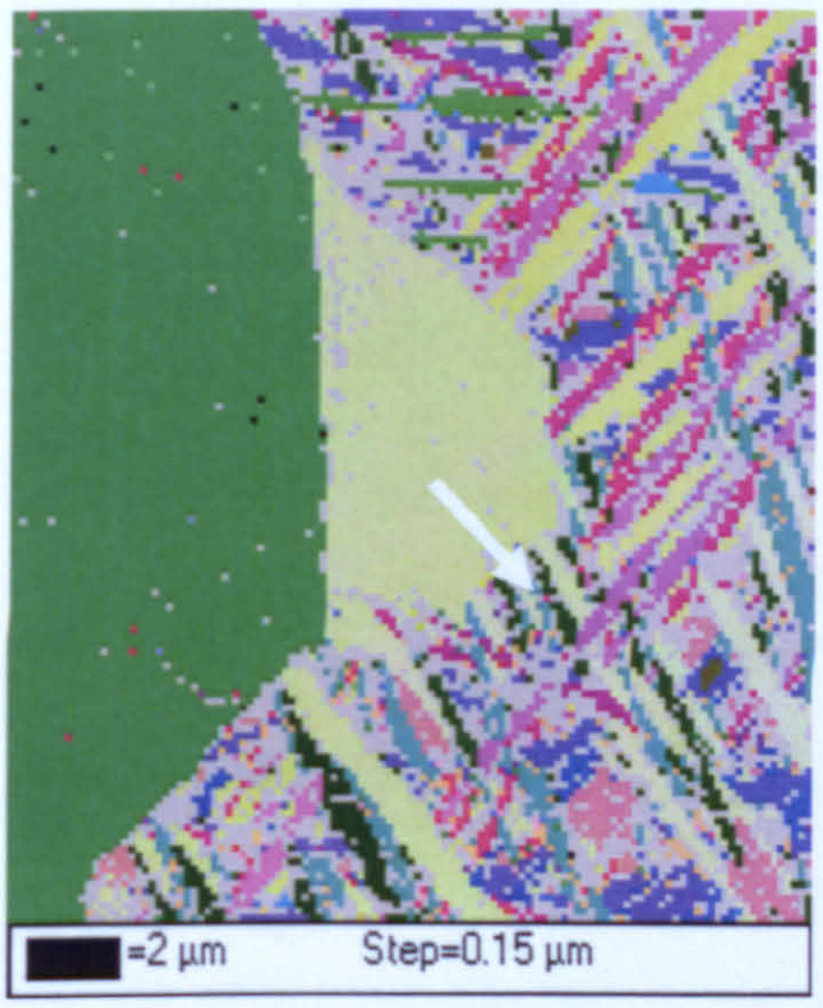

(a) Euler Map

(b) Band Contrast

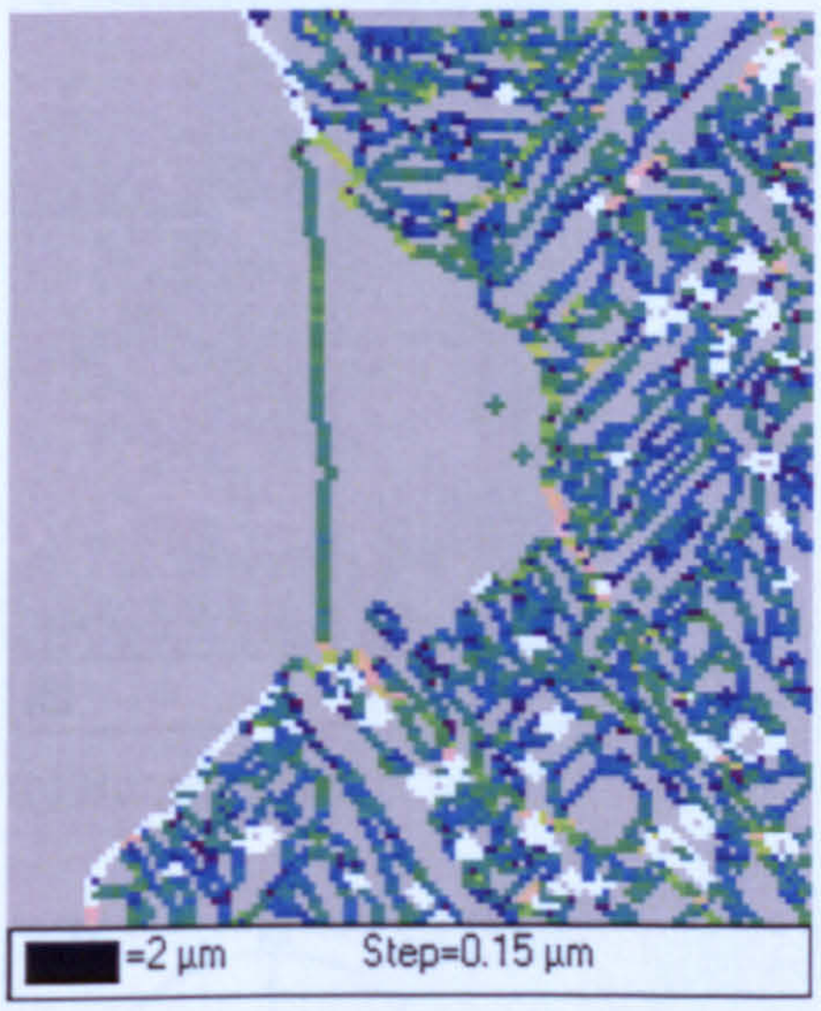

(c) Burgers Map

(d) Reconstructed β phase

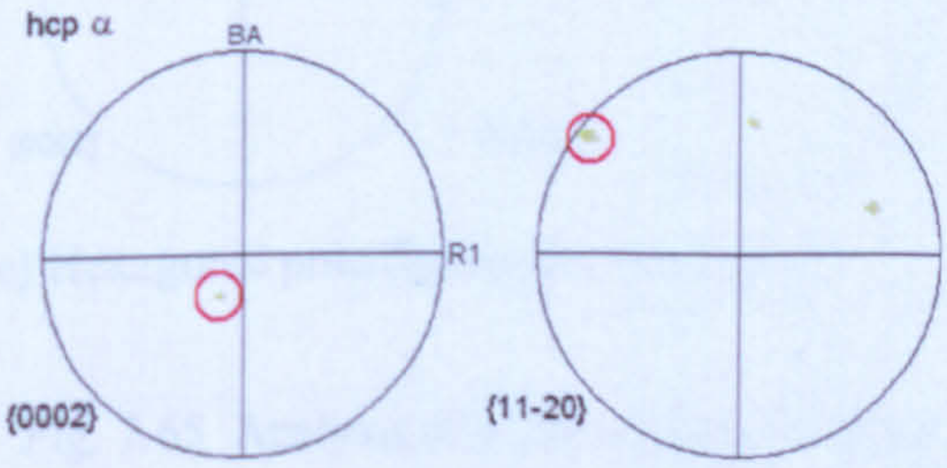

(e) Hexagonal pole figures for the feature.

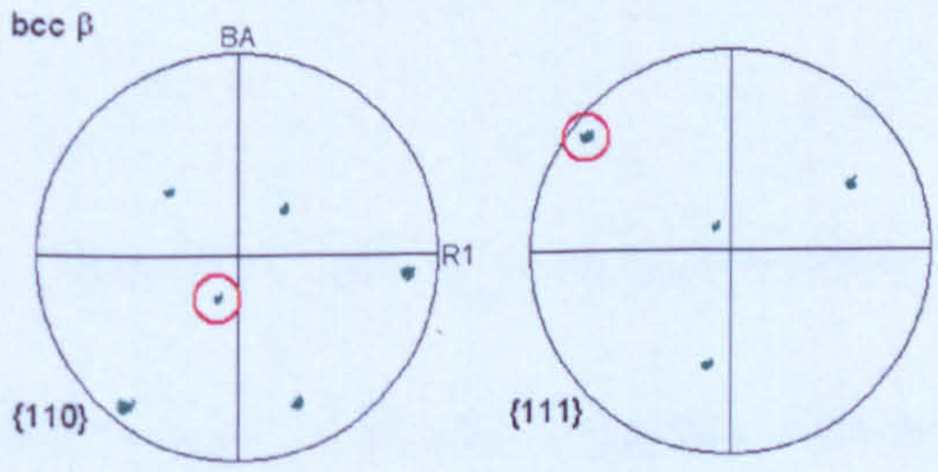

(f) Cubic pole figures for adjacent β grain.

Fig. 7.64 Analysis of a feature resembling possible nucleated α_s from α_p grains 0.2mm from the quenched end.

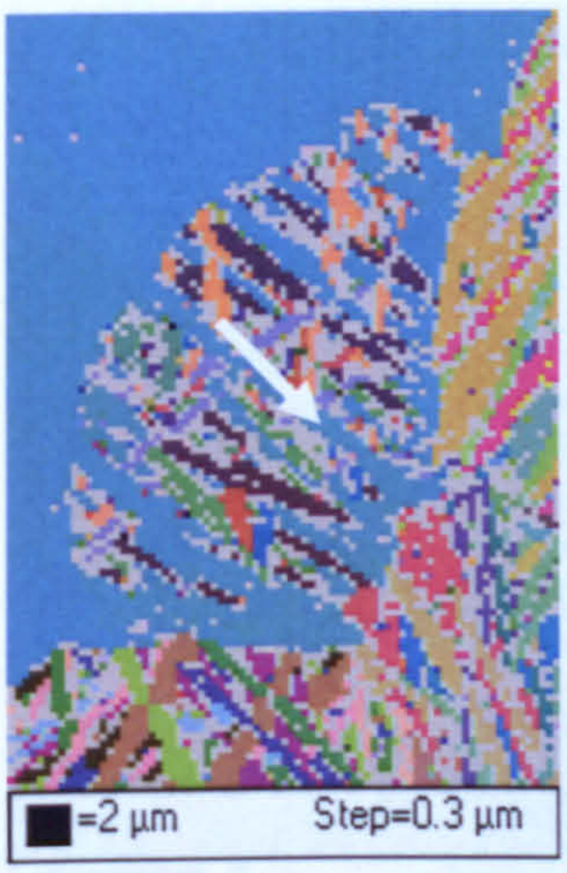

(a) Euler Map

(b) Band Contrast

(c) Burgers Map

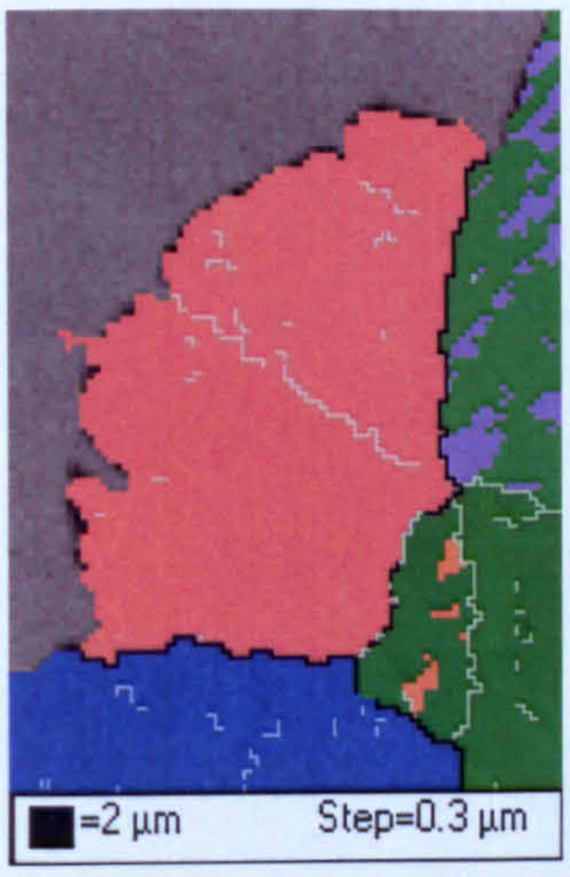

(d) Reconstructed β phase

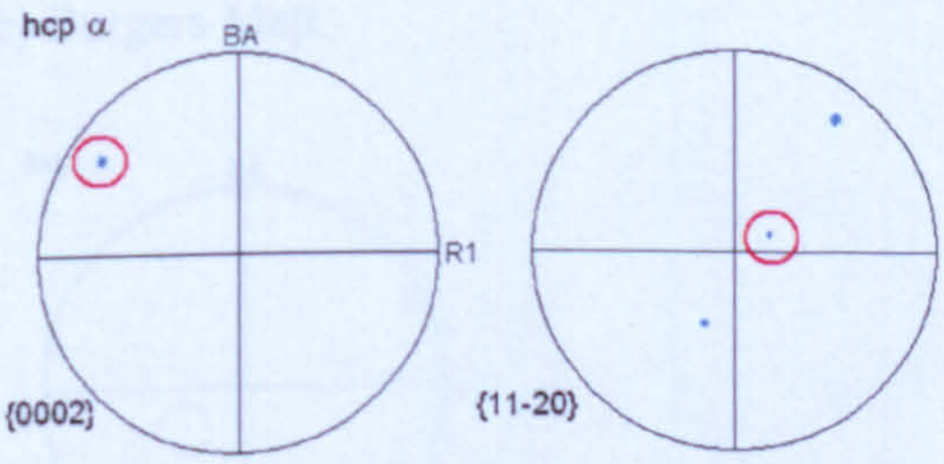

(e) Hexagonal pole figures for the feature.

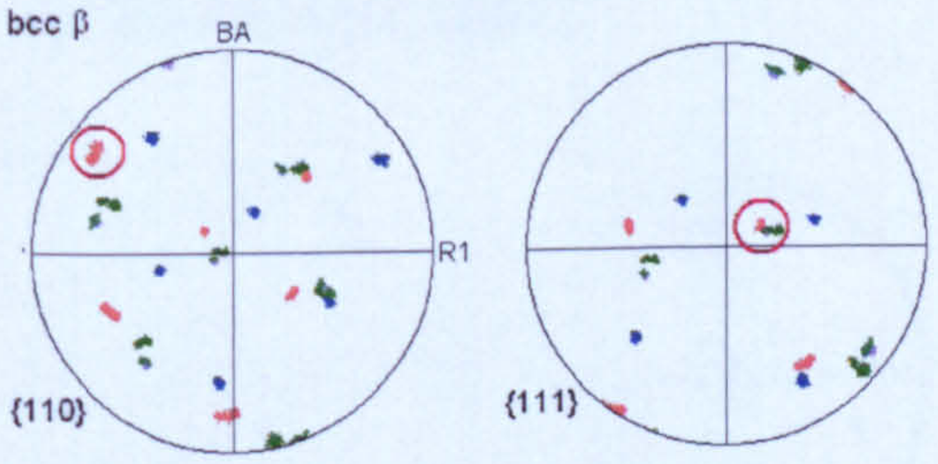

(f) Cubic pole figures for adjacent β grains.

Fig. 7.65 Analysis of a feature resembling possible nucleated α_s from α_p grains 4mm from the quenched end.

(a) Euler Map

(b) Band Contrast

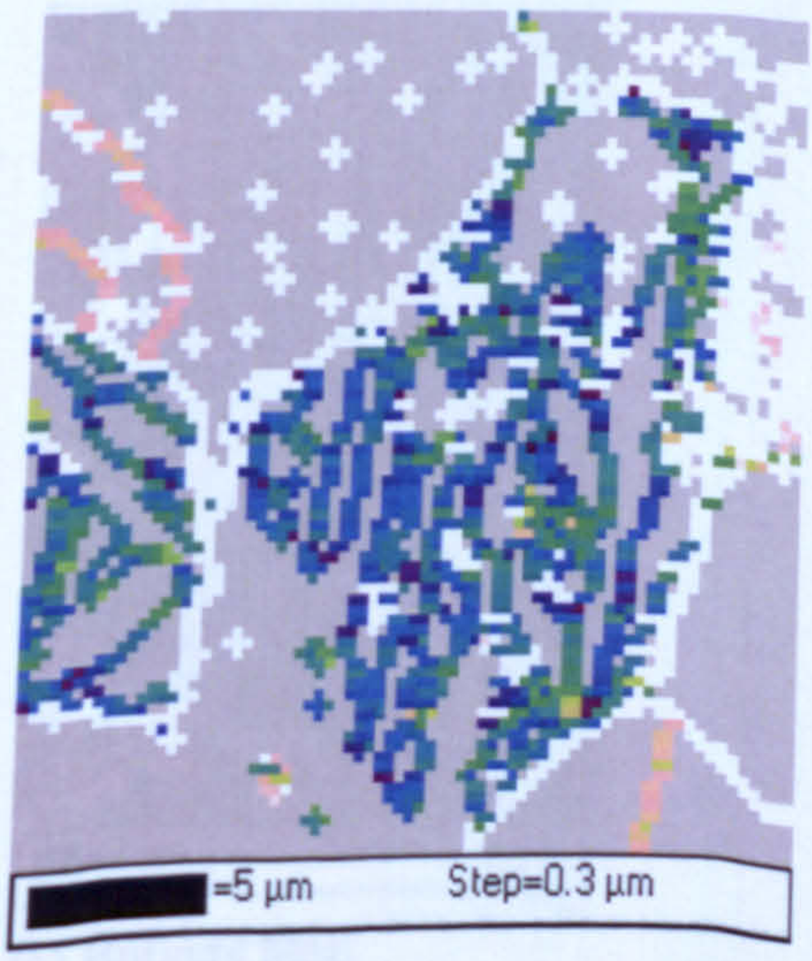

(c) Burgers Map

(d) Reconstructed β phase

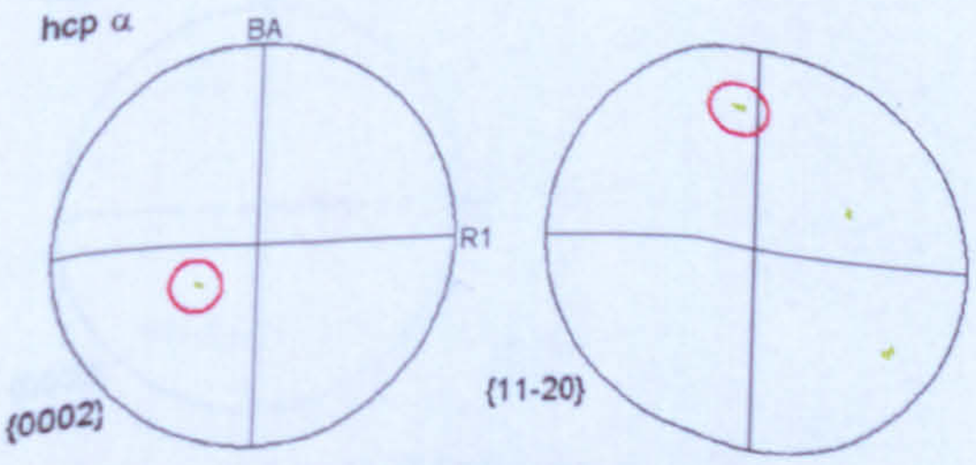

(e) Hexagonal pole figures for the feature.

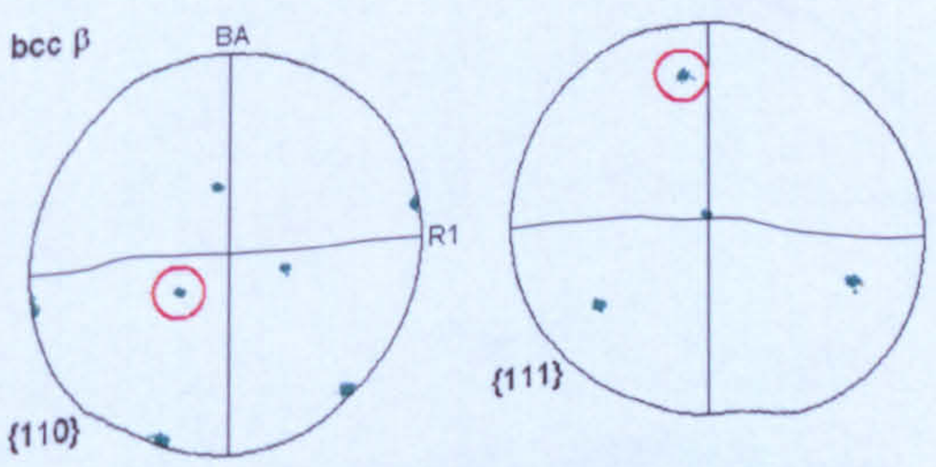

(f) Cubic pole figures for adjacent β grain.

Fig. 7.66 Analysis of a feature resembling possible nucleated α_s from α_p grains 5mm from the quenched end.

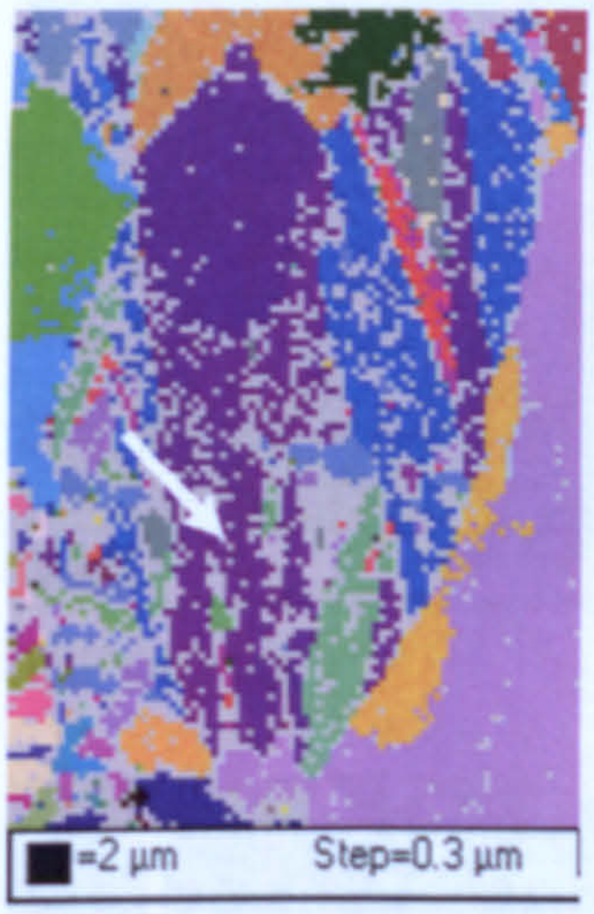

(a) Euler Map

(b) Band Contrast

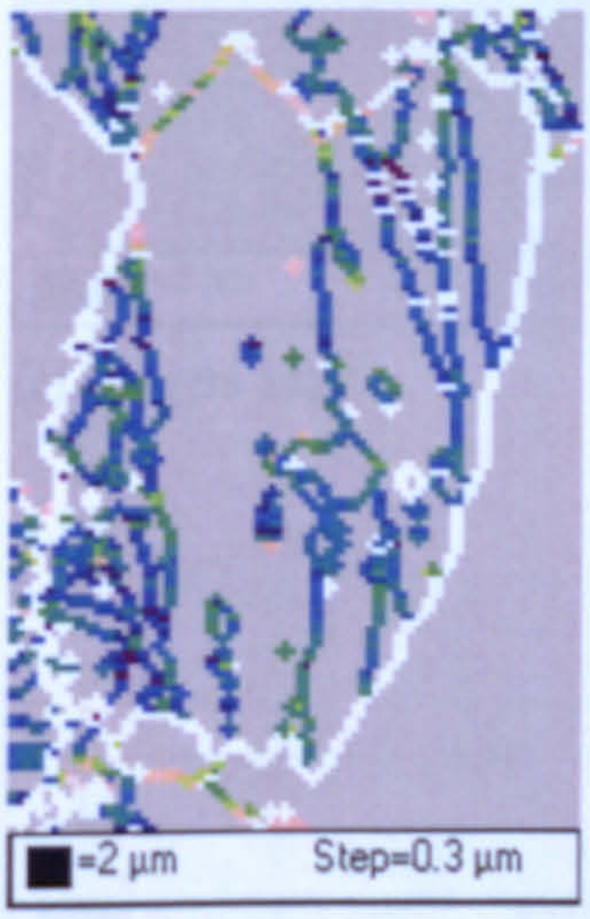

(c) Burgers Map

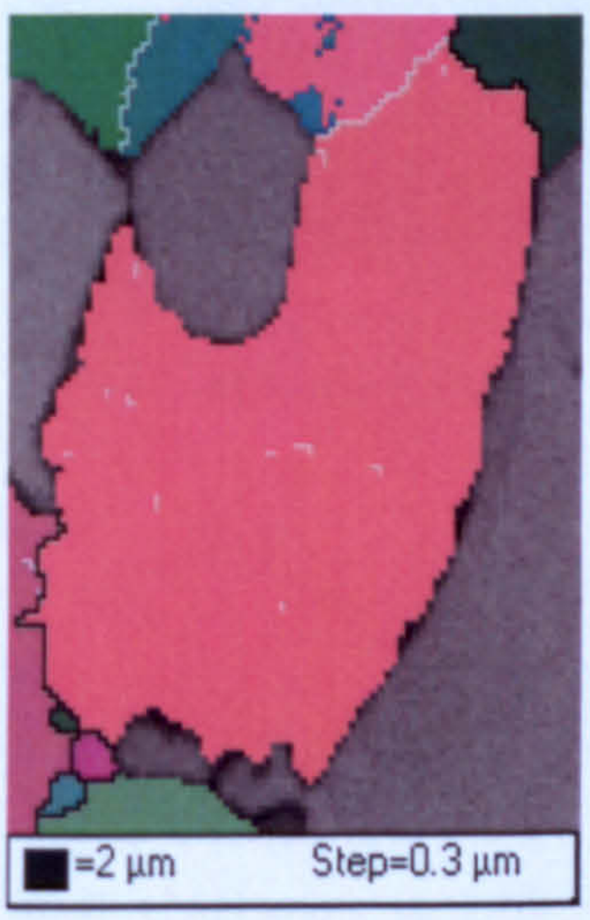

(d) Reconstructed β phase

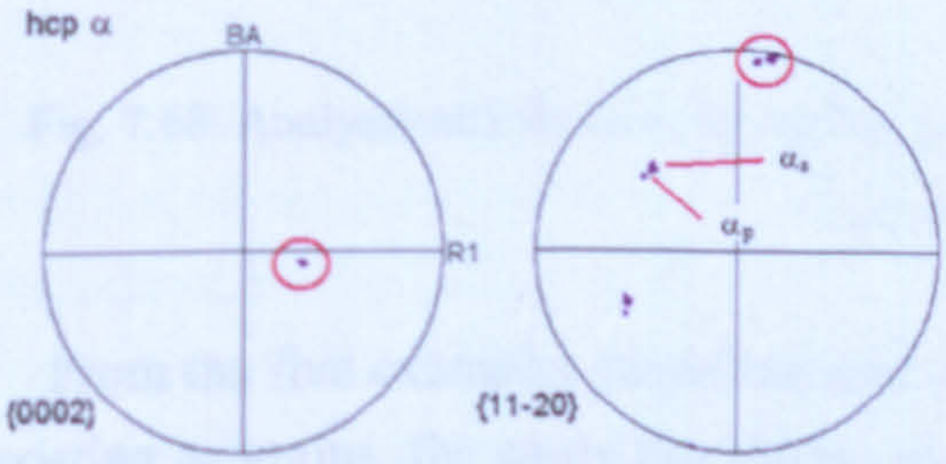

(e) Hexagonal pole figures for the feature.

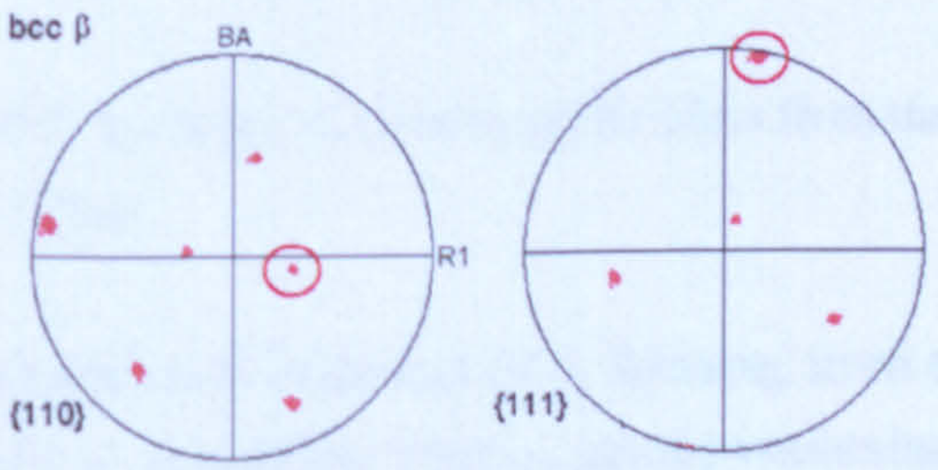

(f) Cubic pole figures for adjacent β grain.

Fig. 7.67 Analysis of a feature resembling possible nucleated α_s from α_p grains 6mm from the quenched end.

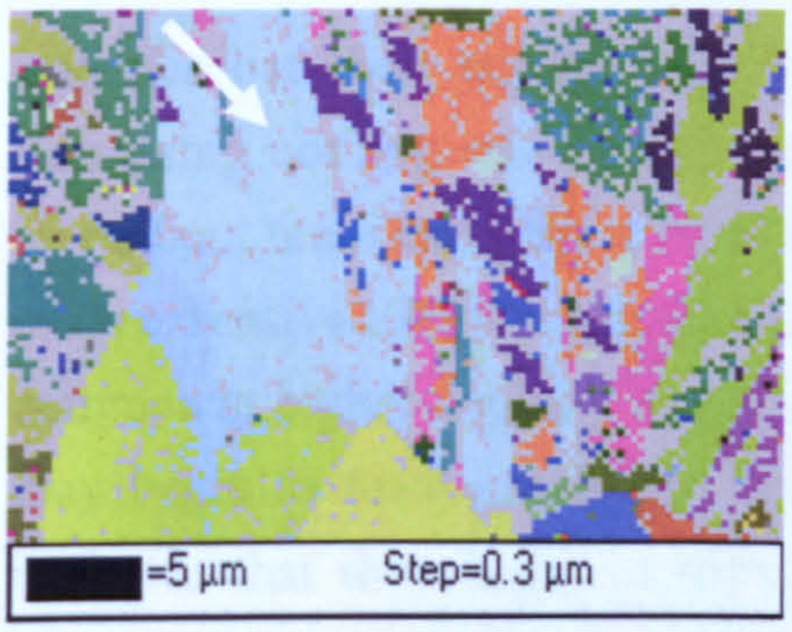

(a) Euler Map

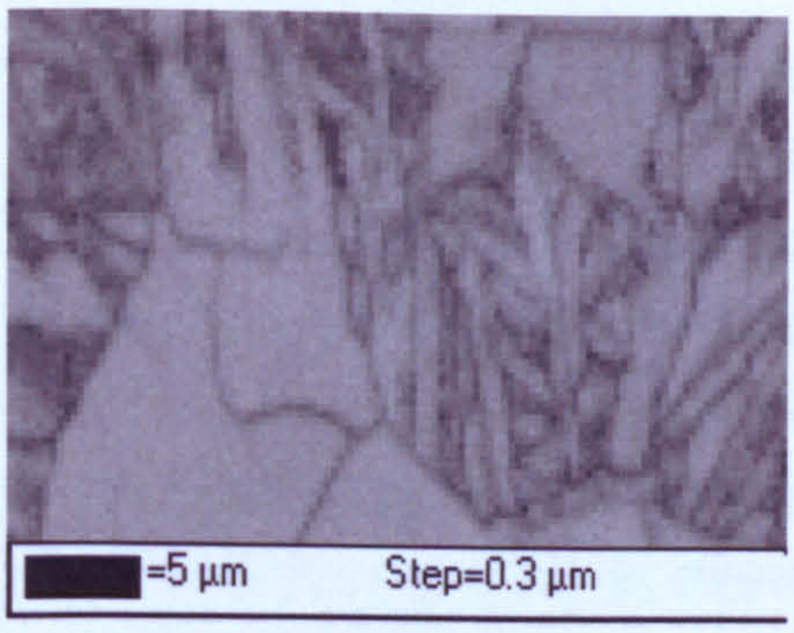

(b) Band Contrast

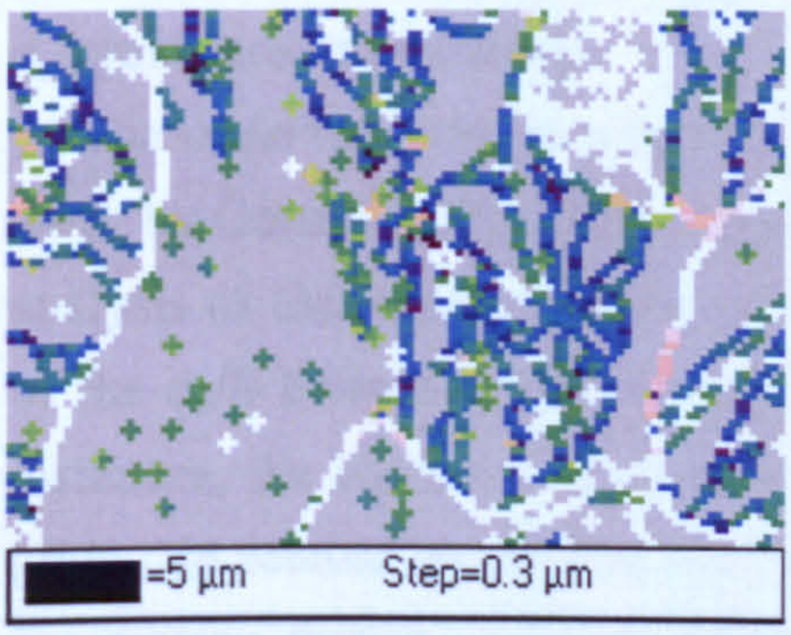

(c) Burgers Map

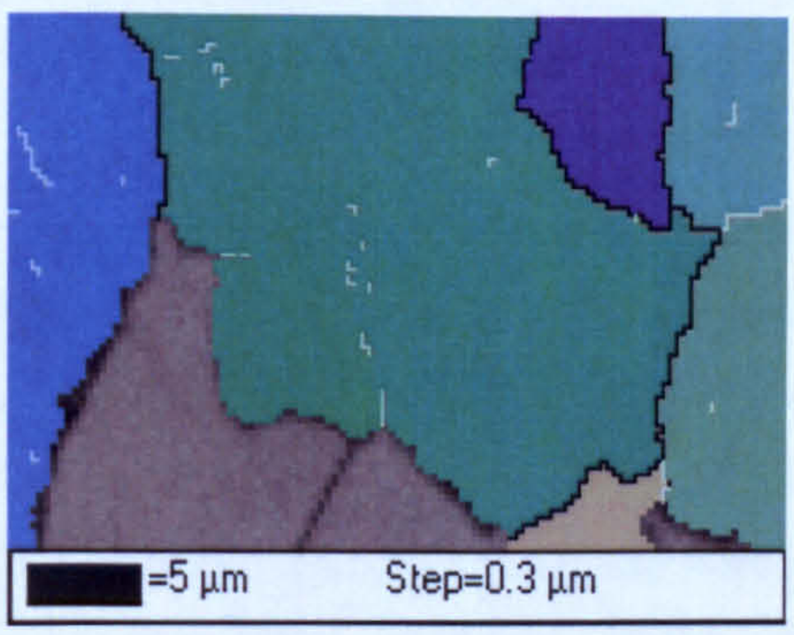

(d) Reconstructed β phase

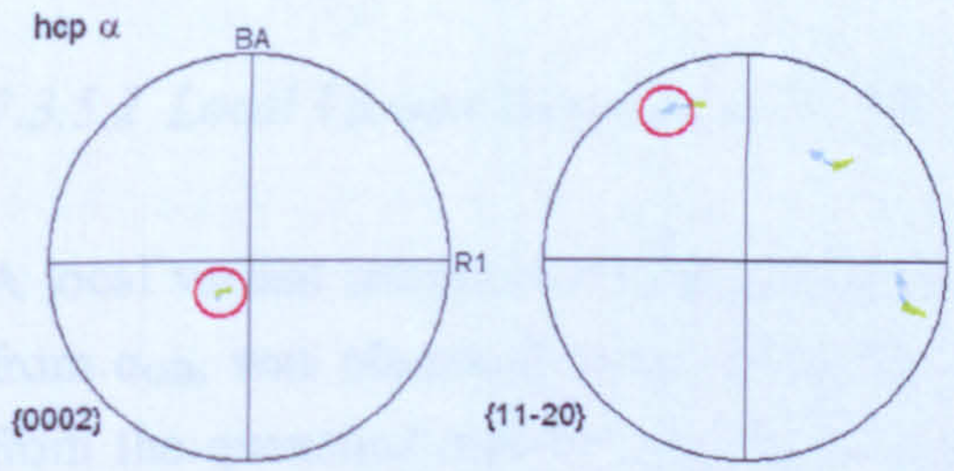

(e) Hexagonal pole figures for the feature.

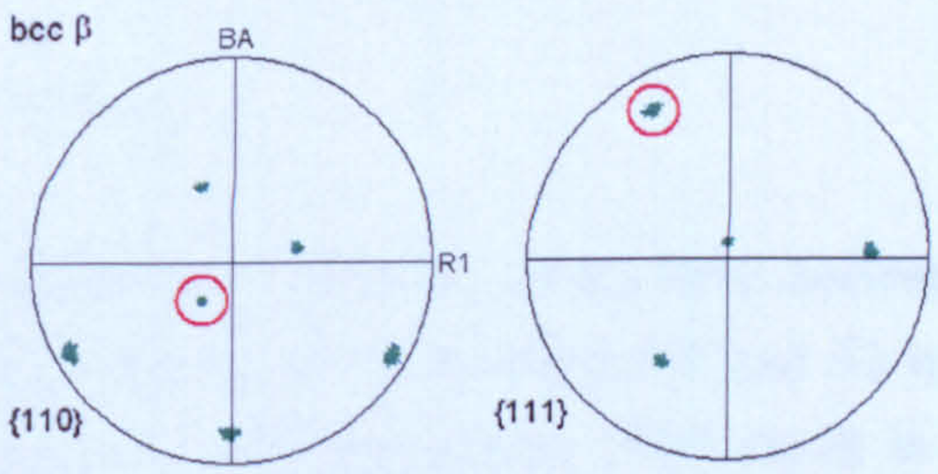

(f) Cubic pole figures for adjacent β grain.

Fig. 7.68 Analysis of a feature resembling possible nucleated α_s from α_p grains 6mm from the quenched end.

From the five examples presented and other analysed instances of α_s forming from the existing α_p grains, the study has shown that the α_s emanating from α_p grains maintains a strict Burgers orientation relation with the parent β phase and has a low misorientation with the α_p grain from which it emanates. In order for it to form therefore, the orientation between an α_p grain and an adjacent β grain must be close to the Burgers orientation relation. In the bimodal microstructures in this work, which were formed from globularised billet, in general, the α_p phase does not have this orientation relationship with the adjacent β grains. This explains why instances of α_s emanating from α_p grains are sporadic. The observed instances of this local variant selection were too few to gather

statistics but their number and the extent of their growth appeared to increase with decreasing cooling rate. They appear to be noticeably more common in the analyses carried out 6mm and greater from the quenched end ($CR_{900} < \sim 37°C\ s^{-1}$). However, much more extensive EBSD mapping would be required to quantify these trends. Although less common at higher cooling rates, the sporadic presence of these features suggests that they may begin to form during the lower initial cooling rates at the start of the test. This indicates that they begin to form at relatively low undercoolings and at shorter times compared to α_s which nucleates from the β/β boundaries or within the β grains. This seems reasonable given that α_{GB} must first nucleate at the grain boundaries, whereas the α_p grains are pre-existing.

The observed variant selection at the α_p/β boundaries is in good agreement with the work by Germain (2008) who investigated microstructures in a Timetal 834 billet. In an analysis of the α_s precipitation at the α_p/β boundaries, it was found that statistically 10% of the α_p/β boundaries were close to the Burgers orientation relation. In 80% of these instances, the observed variants were crystallographically closest to the neighbouring α_p grain. In related work, Humbert *et al.* (2006) simulated the billet textures based on the assumption that the variant selection at the α_p/β boundaries is based on the minimum elastic strain energy and found good agreement with the experimental textures.

7.3.5.2 Local Variant Selection at the β/β boundaries.

A local variant selection of diffusional Widmanstätten α colonies, which have nucleated from α_{GB}, was observed in the EBSD analysis carried out at locations 8.7 and 12 mm from the quenched end but not in the analyses at 6 mm and below. This result is in agreement with the observation from the optical metallography that a continuous layer of α_{GB} formed on all of the β/β boundaries at distances greater than approximately 7 mm from the quenched end ($CR_{900} < \sim 30°C\ s^{-1}$). It proved difficult to analyse the EBSD map acquired at 60mm from the quenched end ($CR_{900} \sim 1.7°C\ s^{-1}$) due to the difficulty in reconstructing the prior β grains in this microstructure, which in any event, were significantly reduced in size due to the α_p grain growth that occurred. However, the local variant selection of the type observed at 8.7 and 12mm was not readily apparent. This can be explained by the absence of α_{GB} precipitates at the slowest cooling rates. At these cooling rates, there are fewer β/β boundaries due to the impingement of growing α_p grains, leaving the β grains isolated from one another. Of the β/β boundaries still remaining, the majority of them are occupied by protuberances grown from the α_p grains and not nucleated α_{GB} precipitates. In the following analysis, four examples of the local variant selection from maps at 8, 8.7 and 12 mm from the quenched end are examined in greater detail.

The first example is taken from the map at 8.7 mm from the quenched end and is shown in Fig. 7.69 below. This example shows two large Widmanstätten α_s colonies, designated α1 and α2, which grow from the same β/β grain boundary into two adjacent β grains, designated β1 and β2. The colonies have similar crystallographic orientations (average misorientation angle ~2.9°) but different growth directions. The presence of α_{GB} at the β/β boundary is not clear from the EBSD analysis in Fig. 7.69 but based on the metallographic results and the work discussed in section 7.2.3 (see Fig. 7.61), α_{GB} with a similar crystallographic orientation to the colonies is presumed to be present at the boundary. In the initial reconstruction of the β phase in the larger EBSD map from which this example was taken (Fig. 7.43), the local variant selection causes one of the colonies to be falsely reconstructed. This occurs because the reconstruction program fails to distinguish between the two colonies due to their low misorientation. In Fig. 7.69(d), the colonies have been manually separated to allow the correct reconstruction of the parent β orientations in both colonies. Examining the cubic pole figures for the adjacent β grains (Fig. 7.69(f)), it can be seen that the two grains share a close {110} pole (circled in red). The average misorientation angle between the β grains, which is mostly due to a rotation about the close {110} pole is approximately 10.4°. It can be seen from the hexagonal pole figures (Fig. 7.69(e)) that the α colonies, α1 and α2, have very similar orientations and that the (0002) pole of the colonies is in the same direction as the common {110} pole.

The second example is taken from the map at 8.7 mm from the quenched end and is shown in Fig. 7.70. This example shows two smaller Widmanstätten α_s colonies extending into two adjacent β grains from a β/β boundary. Again, the colonies share a similar crystallographic orientation (average misorientation angle ~3.0°). In Fig. 7.70(d), the colonies have been manually separated to allow the correct reconstruction of the parent β orientations in both colonies. Examining the cubic pole figures for the adjacent β grains (Fig. 7.70(f)), it can be seen that the grains share a close {110} pole (circled in red) and that the average misorientation angle between the β grains is approximately 10.2°. It can be seen from the hexagonal pole figures (Fig. 7.70(e)) that the α colonies, α1 and α2, have a similar orientation and that their close (0002) poles are in the same direction as the close {110} poles.

The third example is taken from the map at 12 mm from the quenched end and is shown in Fig. 7.71. This example shows two large Widmanstätten colonies extending into two adjacent β grains from a β/β boundary. The colonies share a similar crystallographic orientation (average misorientation angle ~4.5°). In this case, it is possible to identify the α_{GB} at the grain boundary in the band contrast map due to the slight misorientations (~2°) between the α_{GB} and the colonies on either side (Fig. 7.71(b)). The orientation of the α_{GB} can be seen to be a compromise between the orientations of the two colonies. This is shown by the relative misorientation profile extending from α1

across the α_{GB} and into α2, shown in Fig. 7.71(g). In Fig. 7.71(d), the colonies have been manually separated to allow the correct reconstruction of the parent β orientations in both colonies. Examining the cubic pole figures for the adjacent β grains (Fig. 7.71(f)), it can be seen that the grains again share a close {110} pole (circled in red) and that there is an average misorientation angle between the β grains of 15.1°. As in the previous examples, the α colonies have a common (0002) pole, which is in the same direction as the common {110} pole.

The final example is an analysis of the small, high resolution EBSD map that was acquired 8mm from the quenched end and was shown earlier to demonstrate the presence of α_{GB} (see Fig. 7.61). Further maps and pole figures are shown in Fig. 7.72 below. In this example, the two Widmanstätten α_s colonies on either side of the β boundary have an average misorientation angle of 8.1°. The α_{GB} at the grain boundary is a compromise between the orientations of the two colonies α1 and α2. This can be seen in the hexagonal pole figures (Fig. 7.72(d)). The two colonies α1 and α2, and the α_{GB} have the same (0002) pole but $\{11\bar{2}0\}$ poles which are slightly rotated from each other. The $\{11\bar{2}0\}$ pole for the α_{GB} lies mid way between the $\{11\bar{2}0\}$ poles for the two α colonies. The cubic pole figures for the reconstructed β grains show that they share a common {110} pole and are misorientated by approximately 18.6°. The α colonies and the α_{GB} have their (0002) pole in the same direction as the common {110} pole.

The four examples presented are evidence that at slow cooling rates where the $\beta \rightarrow \alpha$ transformation leads to diffusional growth of Widmanstätten α_s, a local variant selection process can occur at β/β boundaries. This local variant selection process was not apparent at the slowest cooling rate examined using EBSD. Previous work has shown that the critical event in this local variant selection process is the precipitation of α_{GB} at the β/β boundaries (Stanford and Bate, 2004). On this basis, it is suggested that the absence of the local variant selection at the slowest cooling rate was due to the extensive growth of the α_p phase in the bimodal microstructure. This isolates many of the β grains, leading to a reduction in the β/β boundaries available for precipitation of α_{GB}.

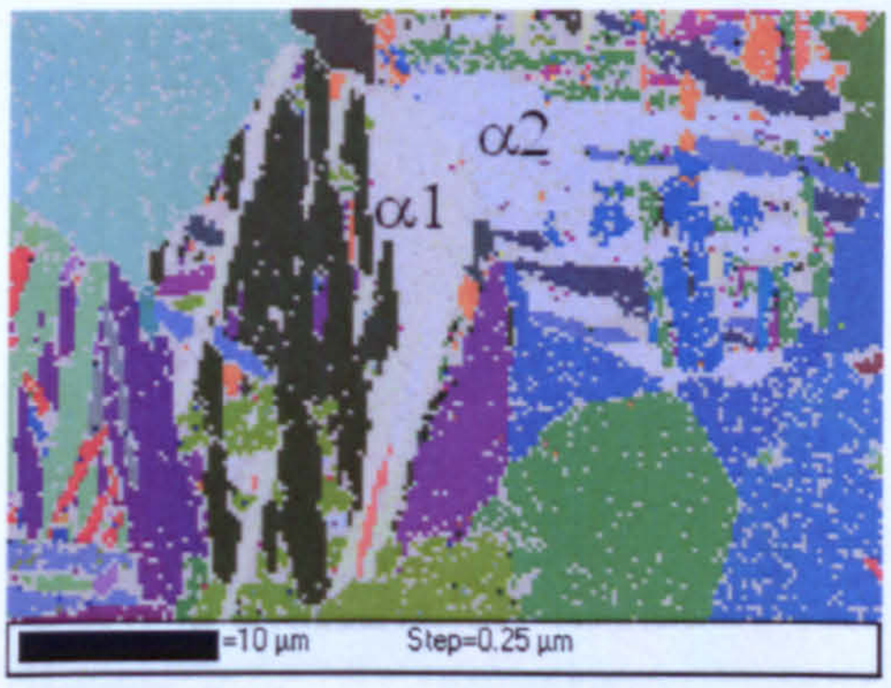

(a) Euler Map

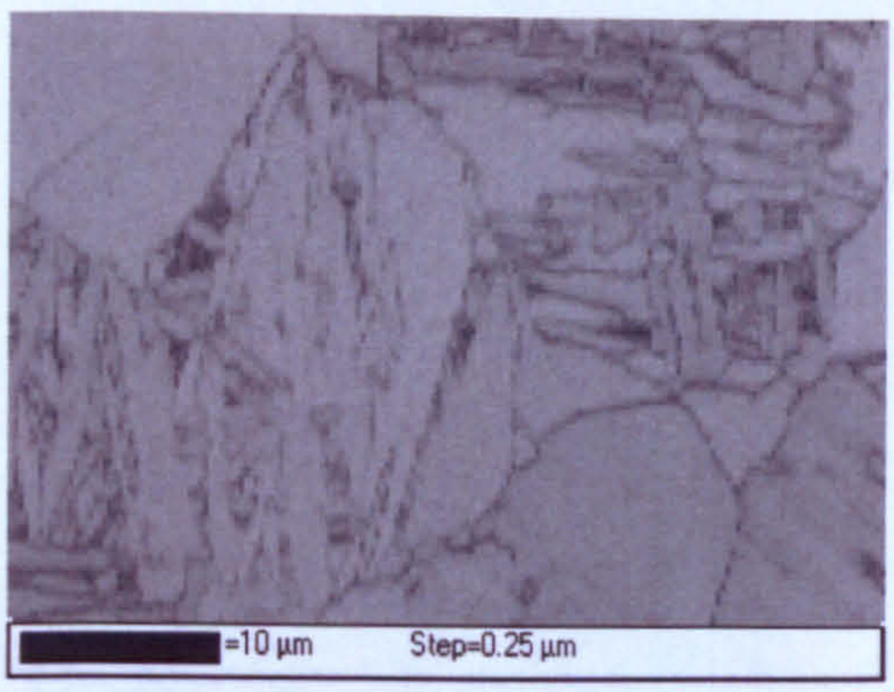

(b) Band Contrast

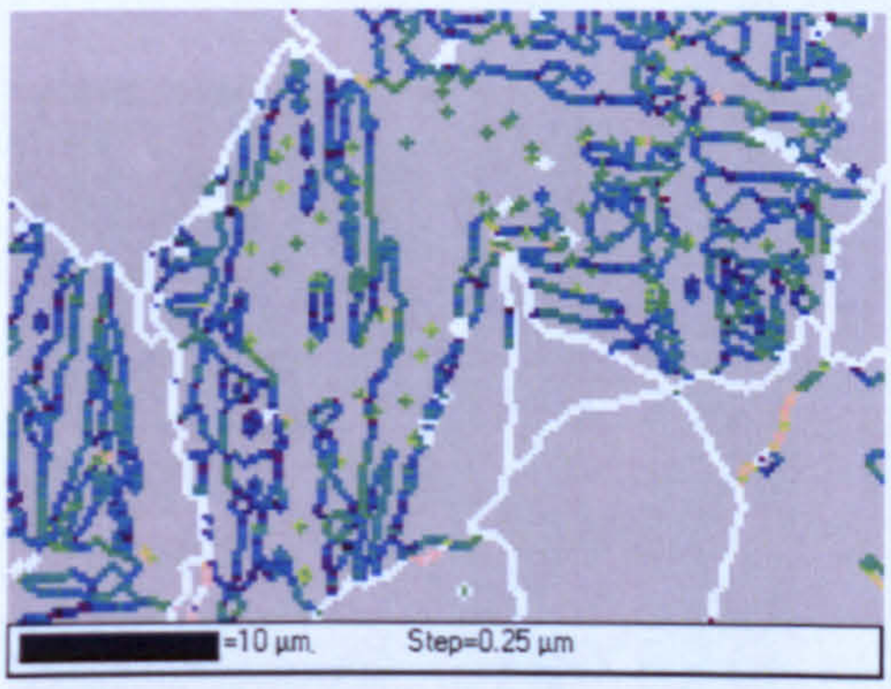

(c) Burgers Map

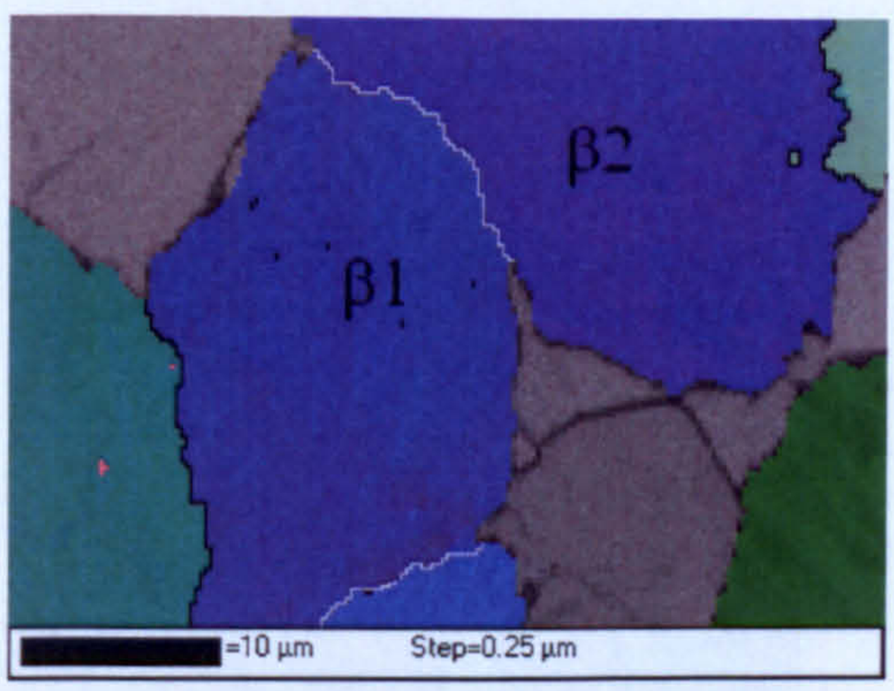

(d) Reconstructed β phase

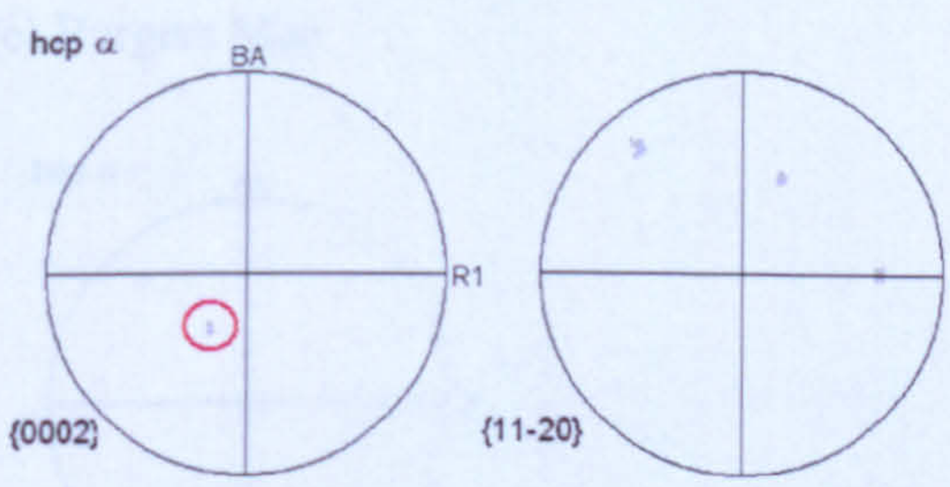

(e) Hexagonal pole figures for the α colonies α1 and α2.

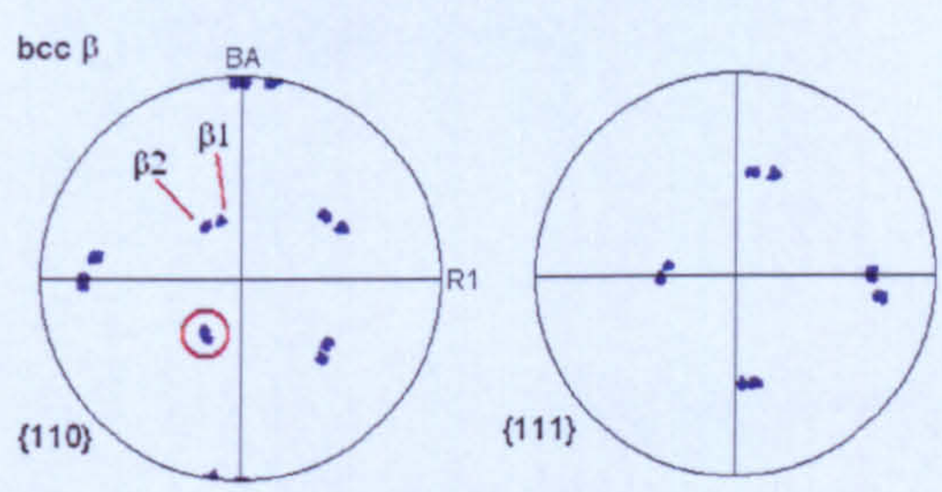

(f) Cubic pole figures for adjacent β grains β1 and β2.

Fig. 7.69 Analysis of local variant selection related to α_{GB} in the map acquired 8.7 mm from the quenched end.

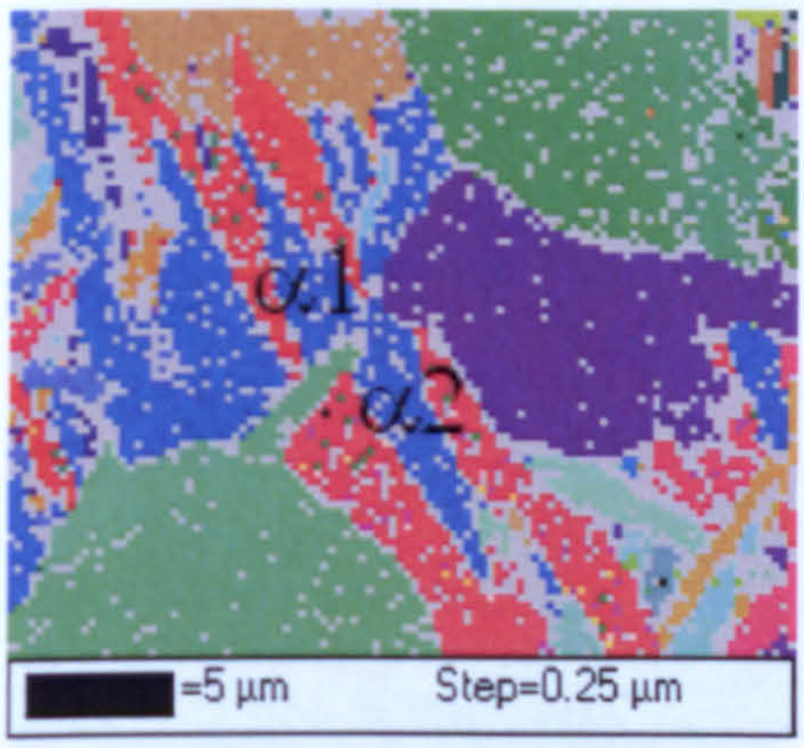

(a) Euler Map

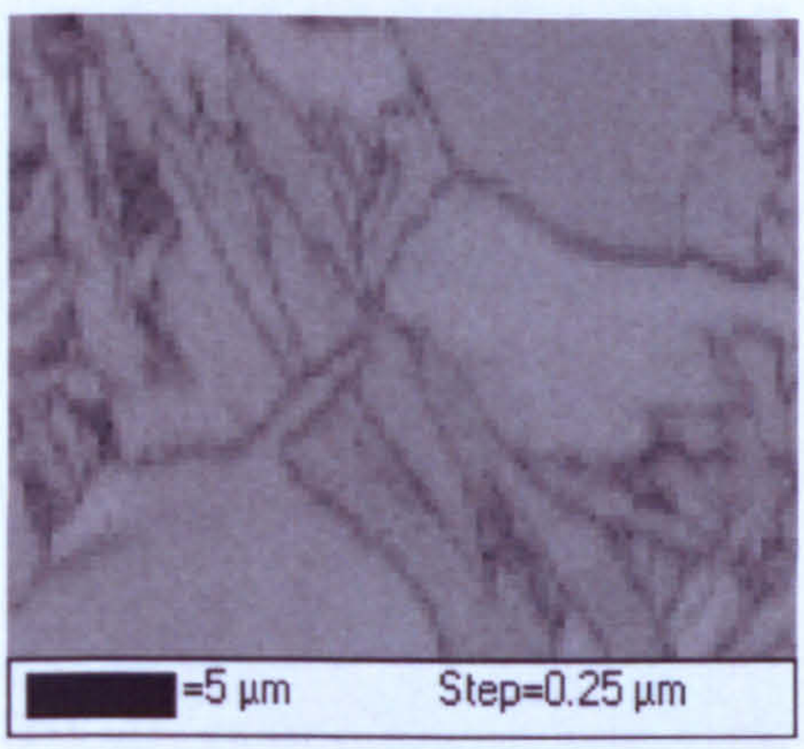

(b) Band Contrast

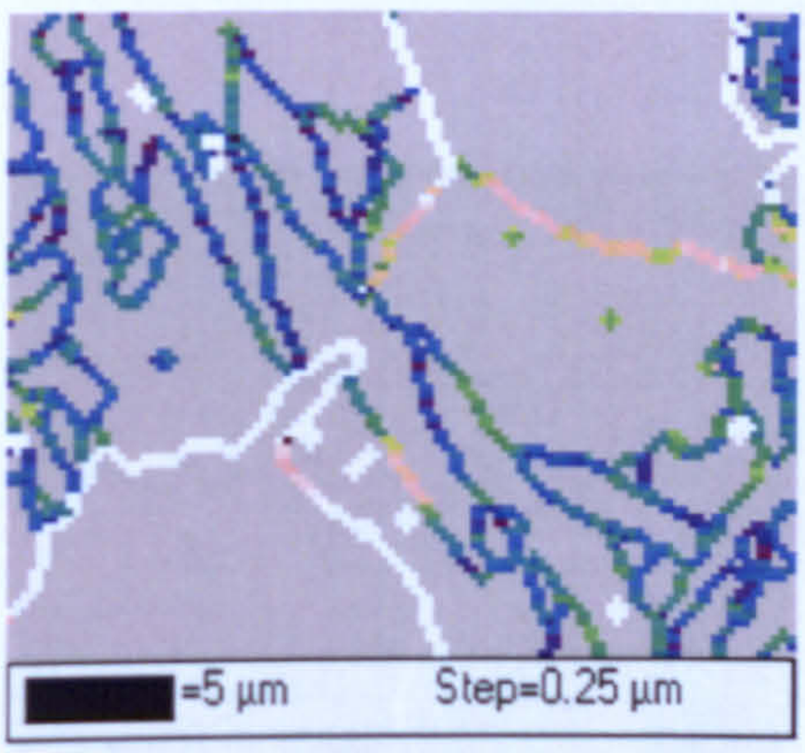

(c) Burgers Map

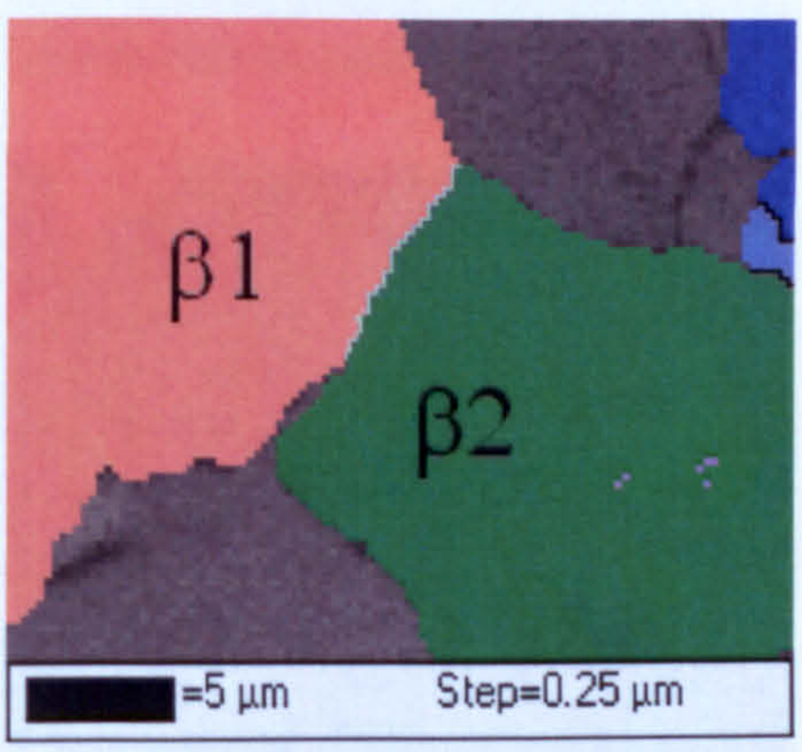

(d) Reconstructed β phase

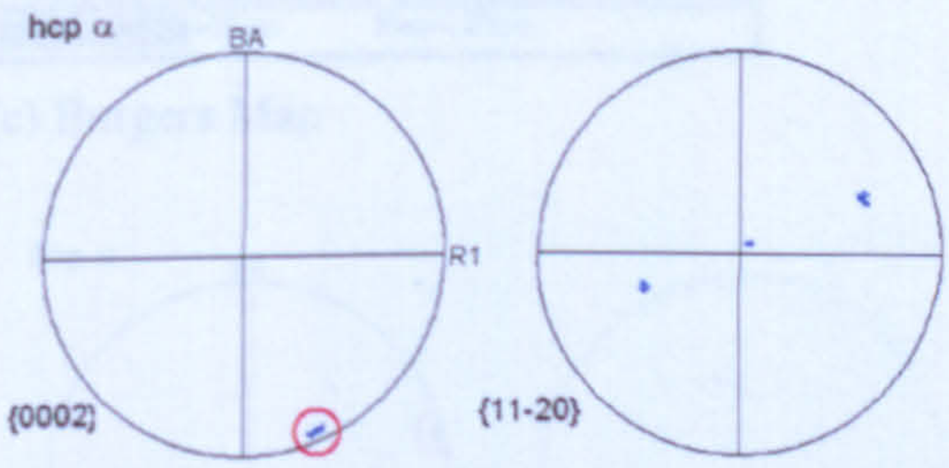

(e) Hexagonal pole figures for the α colonies α1 and α2.

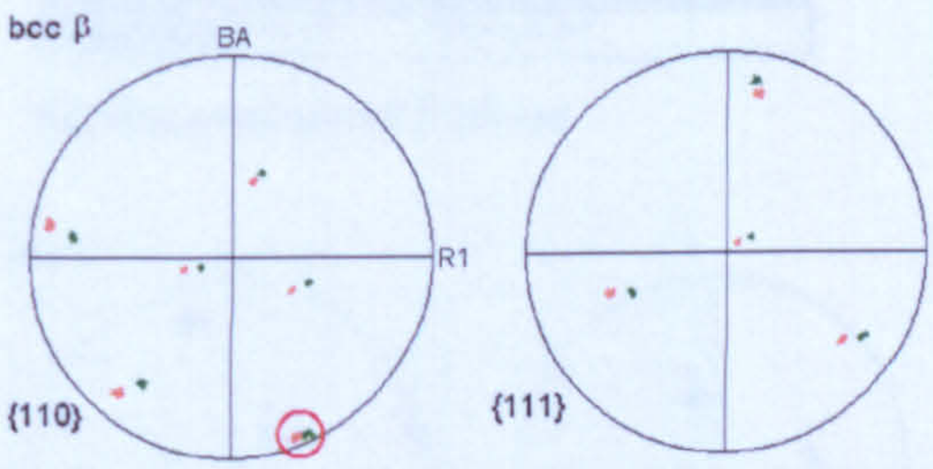

(f) Cubic pole figures for adjacent β grains β1 and β2.

Fig. 7.70 Analysis of local variant selection related to α_{GB} in the map acquired 8.7 mm from the quenched end.

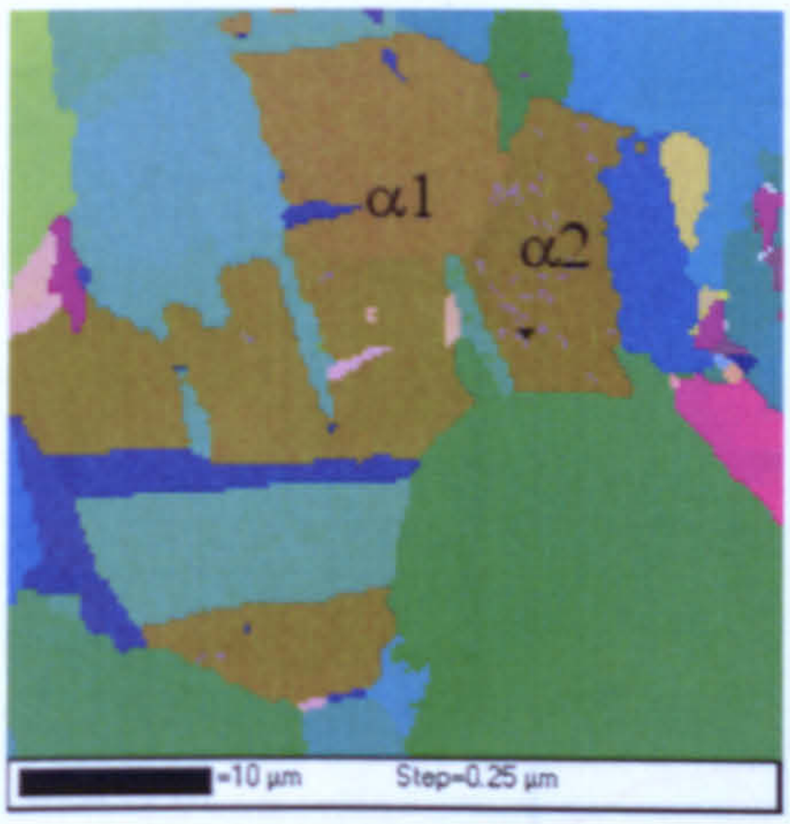

(a) Euler Map

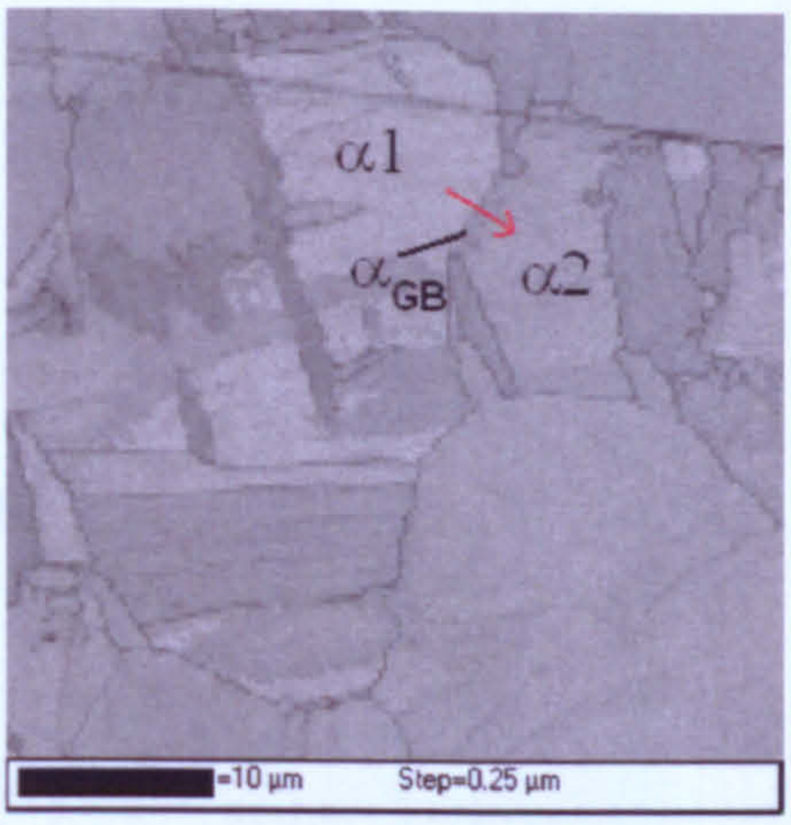

(b) Band Contrast. Red arrows refers to the misorientation profile in (g).

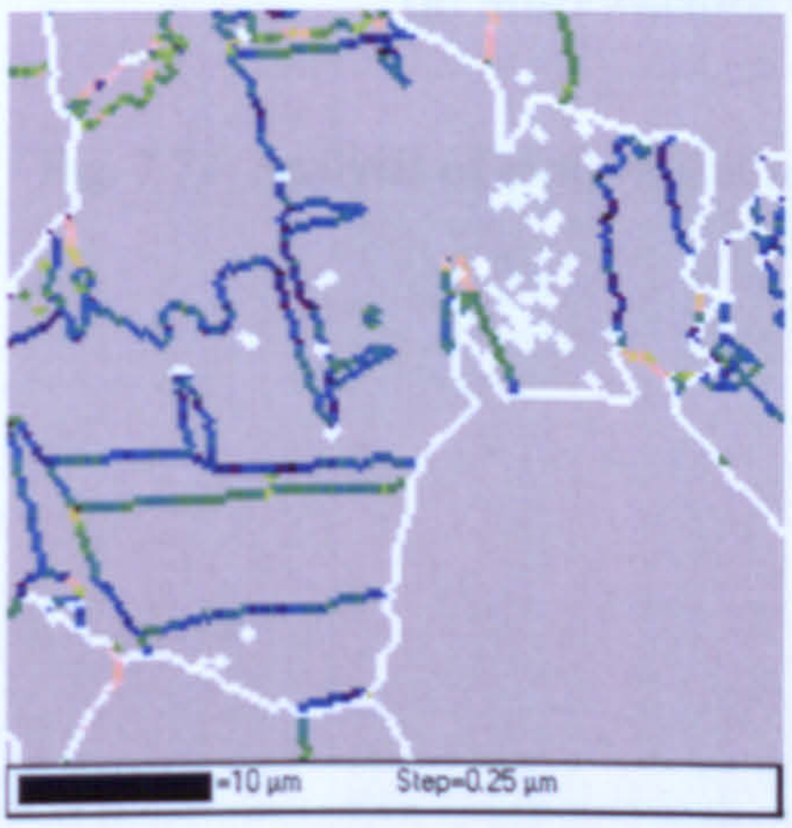

(c) Burgers Map

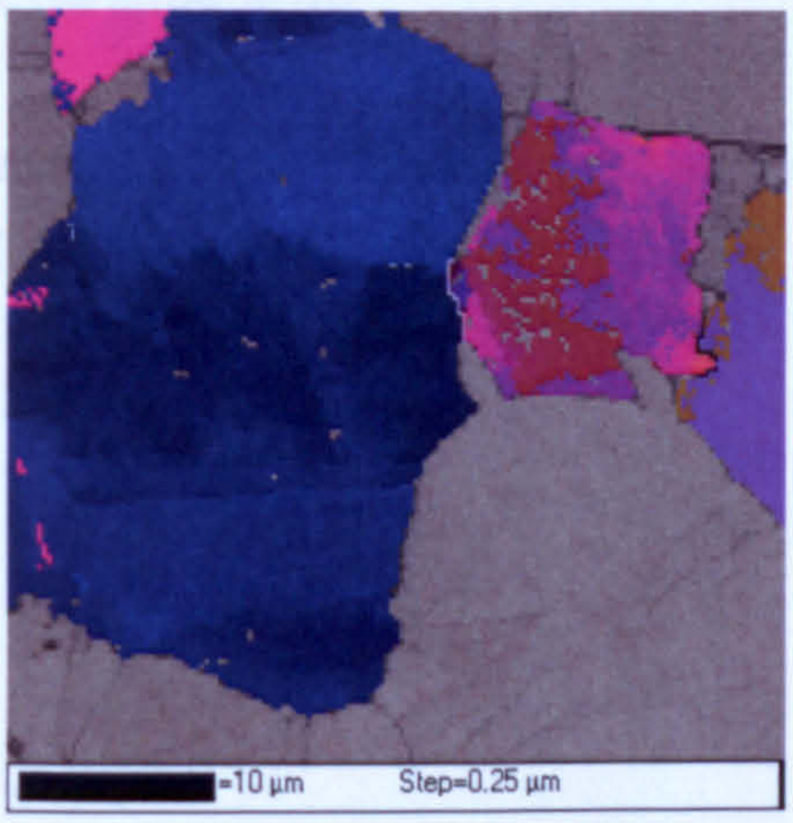

(d) Reconstructed β phase

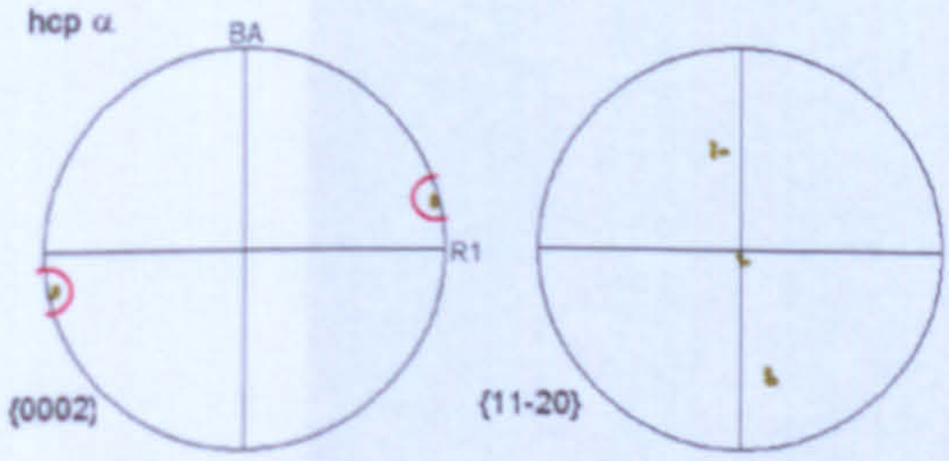

(e) Hexagonal pole figures for the α colonies α1 and α2 and the α_{GB}.

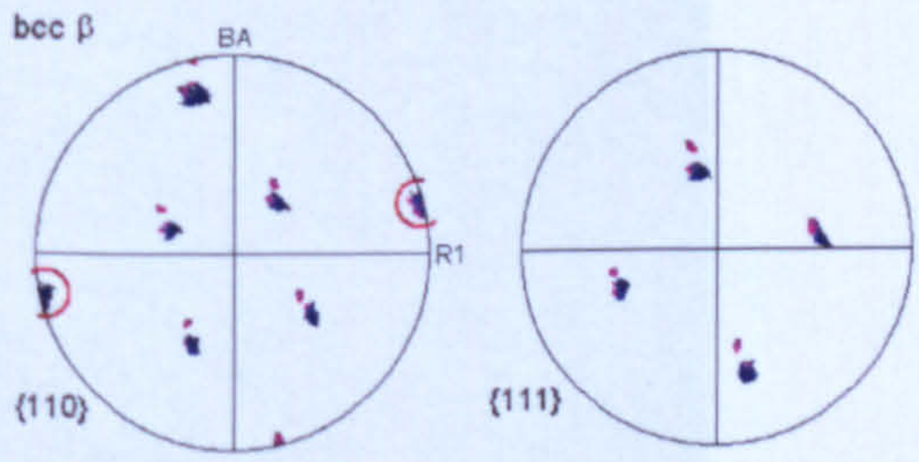

(f) Cubic pole figures for adjacent β grains β1 and β2.

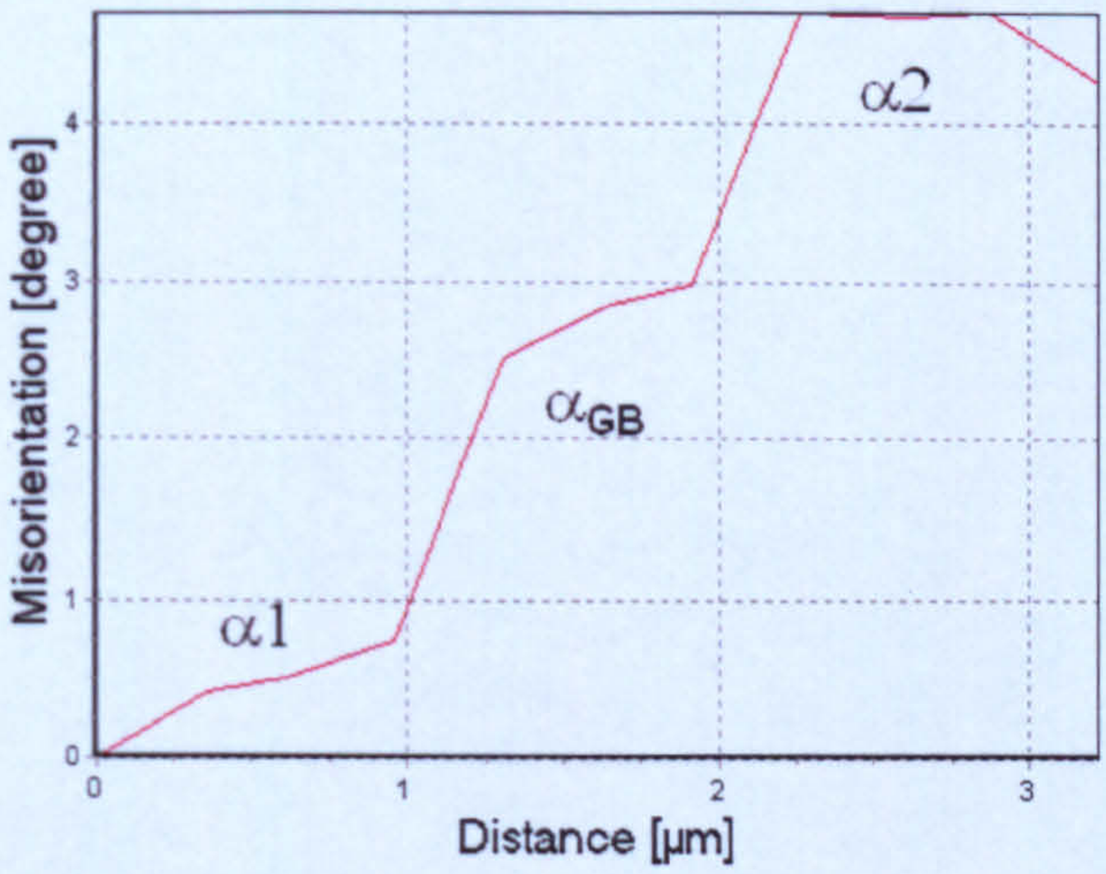

(g) Misorientation profile for the red arrow in (b).

Fig. 7.71 Analysis of local variant selection related to α_{GB} in the map acquired 12 mm from the quenched end.

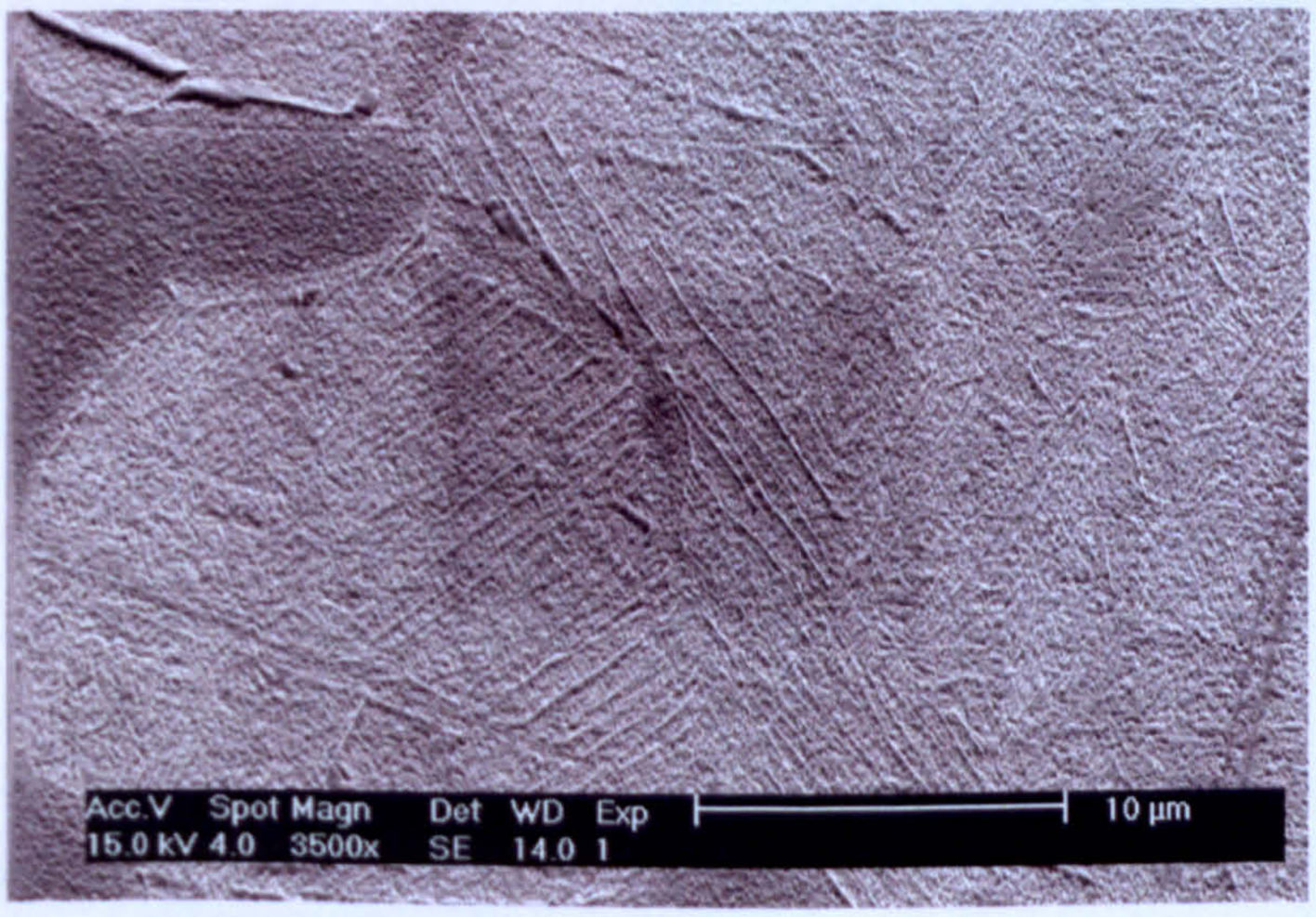

(a) SEM image (see also Fig. 7.61(b)).

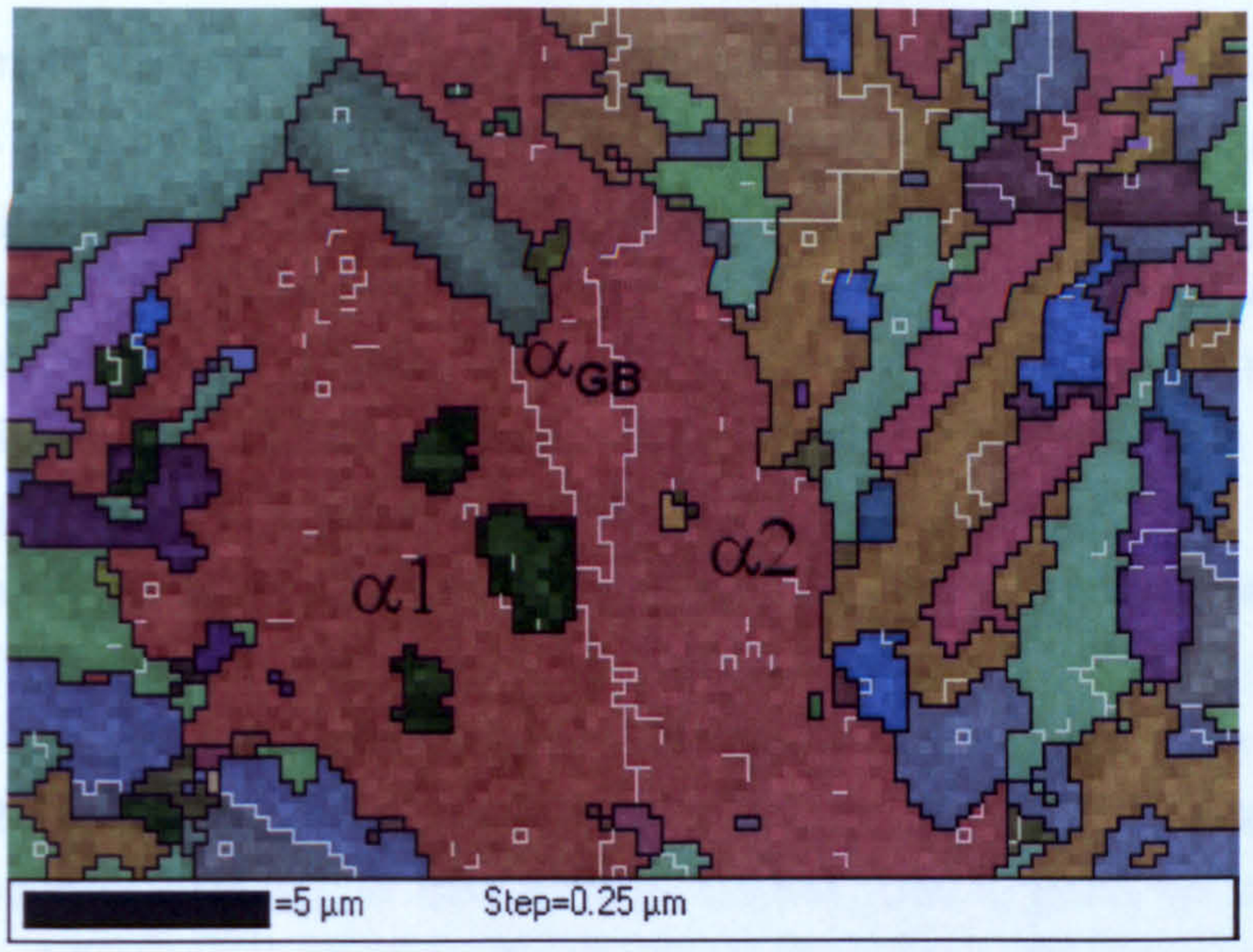

(b) Combined Euler and band contrast map. Silver boundaries > 2°, black boundaries > 15°.

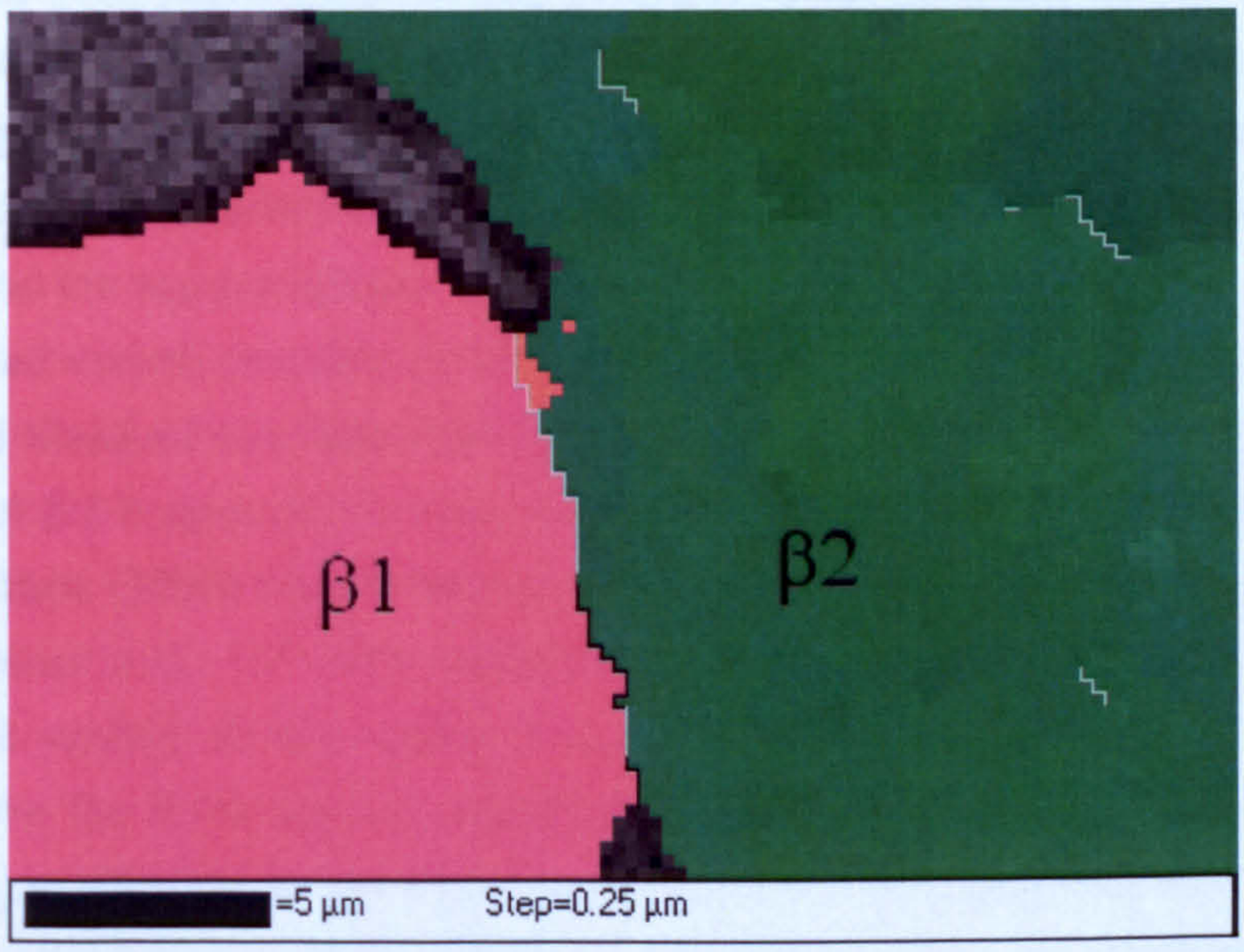

(c) Euler map for the reconstructed β phase. Silver boundaries > 5°, black boundaries > 15°.

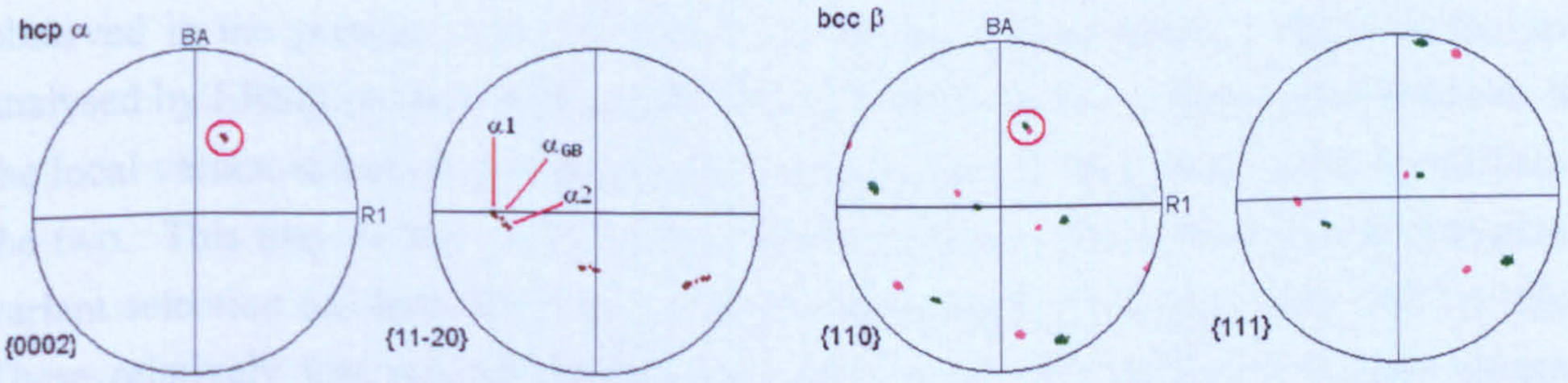

(d) Hexagonal pole figures for α colonies, α1 and α2, and the α_{GB}.

(e) Cubic pole figures for adjacent β grains, β1 and β2.

Fig. 7.72 Analysis of local variant selection related to α_{GB} in a map acquired 8 mm from the quenched end.

In the examples analysed, the variant selection occurred in cases where two adjacent β grains share a common {110} pole. In such cases, the Widmanstätten α_s colonies, which grow into the β grains on either side of the β grain boundary tend to be one of the Burgers variants that have an (0002) pole parallel to the common {110} direction. In each β grain, 2 of the 12 possible Burgers variants have their (0002) pole in the common {110} direction, whilst their $<11\bar{2}0>$ poles are rotated by ~10.5° from each other. The combination of variants selected on each side of the β/β boundary tends to be those that minimise the misorientation between them. This means that if the misorientation about the common {110} pole is close to 10.5°, the Widmanstätten α_s colonies on either side of the boundary will have almost identical crystallographic orientations as in the first two examples. When the misorientation about the common {110} pole is not equal to 10.5°, the selected variants continue to have closely aligned {0002} poles but their $\{11\bar{2}0\}$ poles are rotated from each other. In the observed cases, where this rotation is relatively small, the α_{GB} that precipitates at the boundary may have an orientation that is a compromise between the closest variants and is therefore not in a strict Burgers relation with either β grain. The effect of this is to accommodate the total misorientation between the Widmanstätten α_s colonies in each grain by two lower angle grain boundaries between each colony and the α_{GB} precipitate.

The observed variant selection process is in agreement with work by Bhattacharyya *et al.* (2003) and Stanford and Bate (2004). In both of these works, local variant selection was reported at β/β boundaries in cases where the β grains shared a common {110} pole. Stanford and Bate (2004) found that the critical angle between the {110} poles for this behaviour to occur was ~10°. The material used in these previous works were α+β alloys that had been cooled slowly and/or transformed isothermally after a solution heat treatment above the β transus and therefore had transformed diffusionally and did not contain any α_p grains. Later work by Bhattacharyya *et al.* (2007) showed that a similar local variant selection may occur when two adjacent β grains are misorientated by 60° about a common $<1\bar{1}\bar{1}>$ direction in a twin relationship. Examples of this were not observed in the present work but this is not to say that it does not occur as the areas analysed by EBSD in the present work were relatively small. It does seem however, that the local variant selection process due to a common {110} pole is the more significant of the two. This may be due to the texture in the β phase. The four analysed examples of variant selection occurred for β grains with misorientations ranging from 10.2° to 18.6°. These relatively low misorientations between β grains are likely to be more common when the β phase has a strong single texture component.

The previous work discussed above was for microstructures which did not contain α_p grains. In other work, the occurrence of local variant selection at the β/β boundaries in Timetal 834 billet material, containing 30% α_p was investigated (Germain, 2008). In an analysis of the α_s precipitation at the β/β boundaries, the local variant selection described

in the present work was also observed. It was found that where adjacent β grains had a common {110} pole (with a tolerance of 10°), α_s precipitated at the boundary had their (0002) pole parallel to the common {110} poles in 50% of cases.

7.3.6 Texture Analysis of the Jominy Specimen

The texture analyses for each EBSD map acquired along the Jominy specimen were presented in section 7.1.4, Figs. 7.46-7.54. It is important to note that the resolution of the EBSD maps was chosen to enable the best possible reconstruction of the β grain structure. This relatively small step size means that the maps do not contain sufficient α_p and β grains to allow one to acquire statistically representative textures. Despite this, the pole figures contained in the analyses can still provide much useful information, such as the β textures which develop during the ingot to billet processing and the effects, if any, that the variant selection observed in the β→α transformation has on texture.

7.3.6.1 A Comparison Between the α_p and Reconstructed β textures

It can be seen from the contour plots for the α_p grains (plots (b) in Figs. 7.46-7.54), that the pole figures frequently contain several strong poles due to the high density of orientations originating from each α_p grain and the limited number of α_p grains in the maps. Despite this, there is clear evidence of a clustering and overlapping of these individual α_p grains, that reveals the texture of the α_p grains. This is particularly strong in Figs. 7.47, 7.49 and 7.51, where the vast majority of the α_p grains are clustered around a single orientation, in which the α_p grains have their basal poles in a specific radial direction and a tendency for a $\{10\bar{1}0\}$ pole to be aligned with the billet axis. The other pole figures show this same component to a lesser extent as well as α_p grains with quite different orientations. The main component in the α_p textures is in agreement with the results of the texture analysis for the initial billet in Chapter 5. The maps with the stronger α_p textures probably originate from within single strong macrozones, whereas the weaker ones originate from regions of billet with weaker local textures.

Examining the contour plots for the β grains (plots (d) in Figs. 7.46-7.54), it can be seen that where there is a strong α_p texture (Figs. 7.47, 7.49 and 7.51), the β texture is also strongest. In general, this β texture is based around a single component, in which a {111} pole is aligned with the billet axis and a {110} pole lies in the same specific radial direction as the {0002} pole in the corresponding α_p pole figure. On heating, the β phase in titanium alloys is known to grow epitaxially from the pre-existing β phase, rather than nucleate new β grains (Stanford and Bate, 2004). This means that the main texture component of the β phase in the reconstructed maps is likely to be closely related to the β

texture that resulted from processing of the ingot into billet. The relationship between the α_p and β textures in the globularised billet after deformation in the $\alpha+\beta$ phase field is different to the Burgers relation. There is a tendency for (0002) planes in the α_p phase to remain parallel to {110} planes in the β phase but the $<11\bar{2}0>$ directions do not remain parallel to the <111> directions. Therefore, these results show that although the deformation in the $\alpha+\beta$ phase field that gives rise to globularisation of the α lamellae into α_p grains tends to destroy the Burgers relation, (0002) and {111} planes tend to remain parallel.

7.3.6.2 The Effect of Variant Selection on the α_s Texture at Different Cooling Rates.

The orientations from the reconstructed β grains were used to simulate the texture of the α_s resulting from the $\beta \rightarrow \alpha$ transformation assuming that the 12 possible variants are selected equally. The pole figure contour plots for these simulated α_s textures are shown in plots (e) in Figs. 7.46-7.54. It can be seen that the (0002) pole figures for the simulated α_s textures have the same distribution and density of orientations as the {110} pole figures for the reconstructed β textures. This is the expected case as the simulated texture is calculated using the Burgers relation, which gives two variant orientations for each of the 6 {110} poles.

A comparison between the simulated textures and the measured textures for the separated α_s phase (plots (e) and (c) in Figs. 7.46-7.54), allows one to investigate the effect of variant selection on the α_s textures. Large differences in the pole densities between the simulated and measured pole figures may be evidence of variant selection processes having a significant effect on the overall α_s texture. To aid the comparison between different cooling rates, Fig. 7.73 shows for each EBSD analysis, the difference between the maximum pole density in the (0002) pole figure for the measured and simulated α_s texture. A high bar in the figure shows that the maximum density in the measured texture is significantly higher than that predicted assuming equal selection of variants.

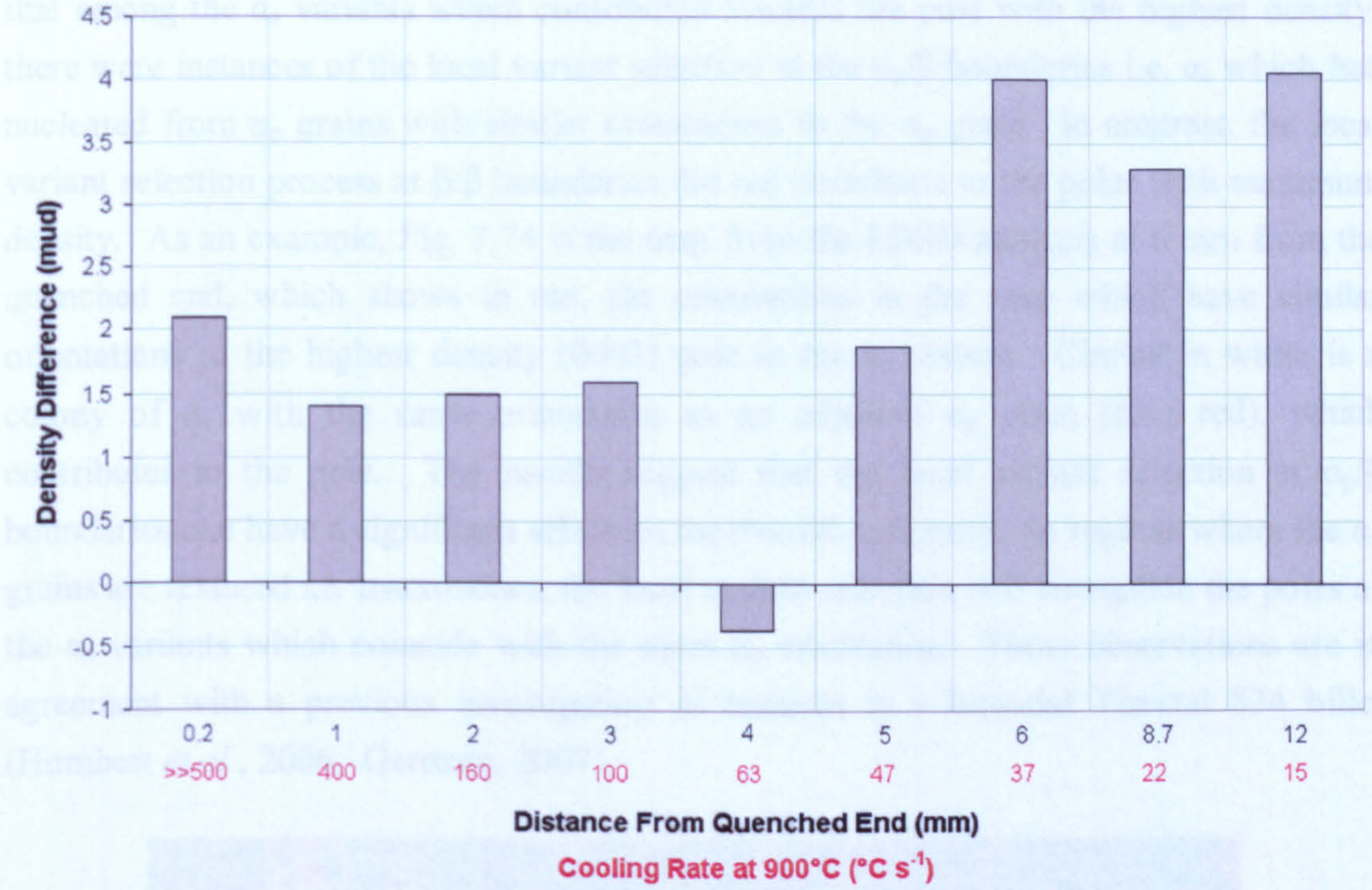

Fig. 7.73 A chart showing the difference between the maximum (0002) pole figure densities for the measured α_s texture and the simulated α_s texture assuming no variant selection. Each bar corresponds to a different distance from the quenched end, for which the estimated cooling rate at 900°C is also shown on the horizontal axis.

In general, the poles in the measured textures are slightly sharper than the equivalent poles in the simulated textures. This is due to greater orientation noise in the simulated textures due to the calculations involved in firstly reconstructing the β orientations and then the α_s orientations. Apart from this greater sharpness, it can be seen from the pole figures that at the higher cooling rates (i.e. 0.2 to 5 mm from the quenched end, Figs. 7.46-7.51), the simulated and measured textures are broadly similar. The strongest poles in the simulated α_s textures are, in most cases also the strongest poles in the measured textures. Where there are differences in the relative strength of the various poles, these do not seem to have a relationship with either the texture of the surrounding α_p grains or the macroscopic axes of the Jominy specimen. This indicates that the variant selection, which was observed within individual β grains at high cooling rates (section 7.2.5) does not have a strong effect on the overall texture of the α_s phase and is not related to the α_p grains or the macroscopic coordinates.

At the slower cooling rates, where the β⟶α transformation was entirely diffusional, (i.e. at locations 6, 8.7 and 12 mm from the quenched end, Figs. 7.52-7.54), there were greater differences between the simulated and measured α_s textures. This can be seen in the pole figures and also in Fig. 7.73, where the difference in the maximum density is significantly higher for these cooling rates. It was found for all three of these locations

that among the α_s variants which contributed towards the pole with the highest density, there were instances of the local variant selection at the α_p/β boundaries i.e. α_s which had nucleated from α_p grains with similar orientations to the α_p grain. In contrast, the local variant selection process at β/β boundaries did not contribute to the poles with maximum density. As an example, Fig. 7.74 is the map from the EBSD analysis at 6 mm from the quenched end, which shows in red, the orientations in the map which have similar orientations to the highest density (0002) pole in the α_s texture. Circled in white is a colony of α_s with the same orientation as an adjacent α_p grain (also red), which contributes to the pole. The results suggest that the local variant selection at α_p/β boundaries can have a significant effect on the overall α_s texture. In regions where the α_p grains are textured i.e. macrozones, the local variant selection will strengthen the poles of the α_s variants which coincide with the main α_p orientation. These observations are in agreement with a previous investigation of textures in a bimodal Timetal 834 billet (Humbert *et al.*, 2006. Germain, 2007).

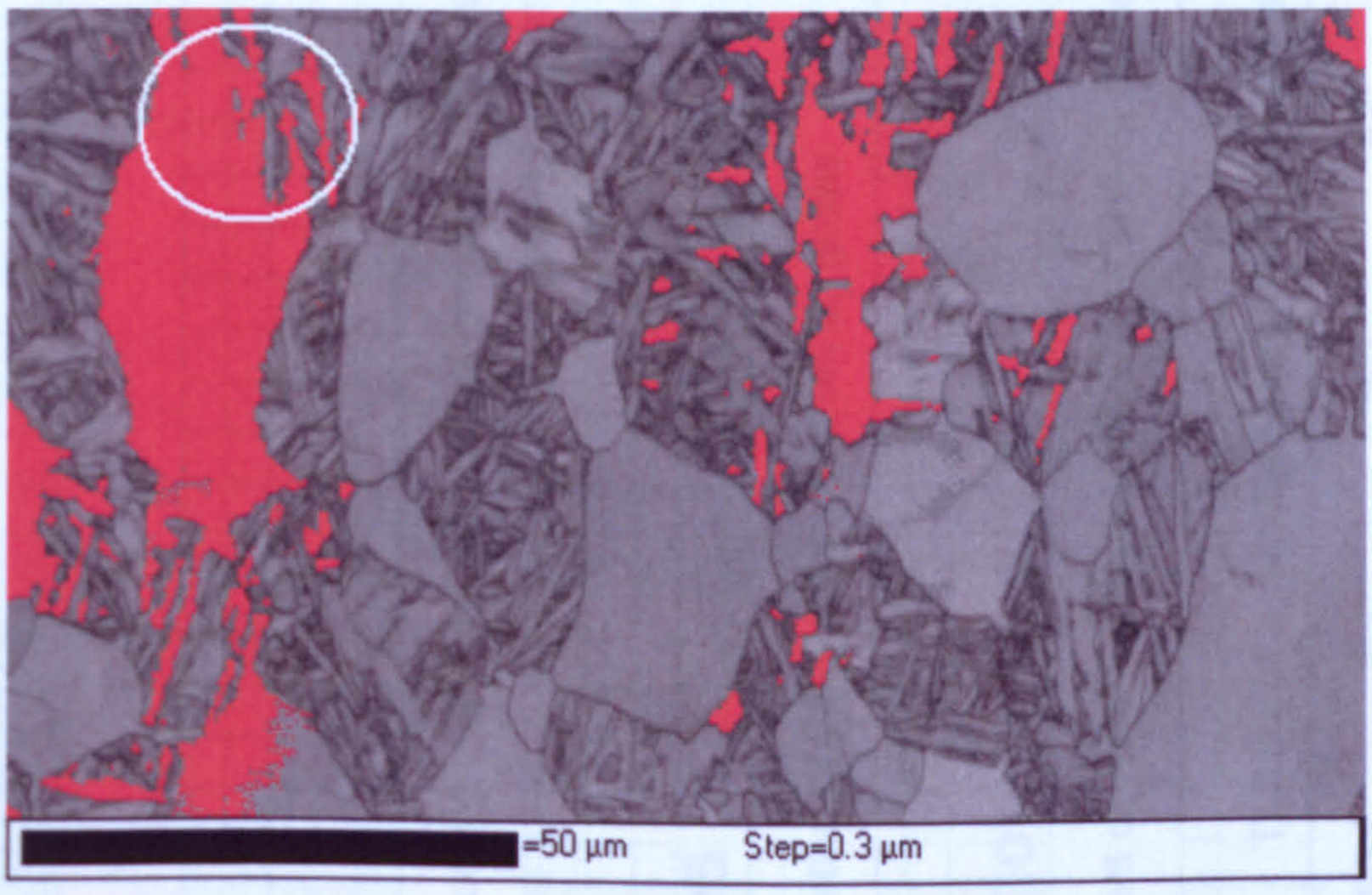

Fig. 7.74 A map from the EBSD analysis 6 mm from the quenched end (CR_{900} = 37°C s^{-1}). Shown in red are α_p grains and α_s variants which have the same orientation as the maximum density (0002) pole in the measured α_s texture. The white circle highlights an instance of local variant selection at an α_p/β boundary, which contributes to this pole.

7.3.7 A Summary of the Main Findings of This Chapter

The main findings from this chapter are summarised in Fig. 7.75.

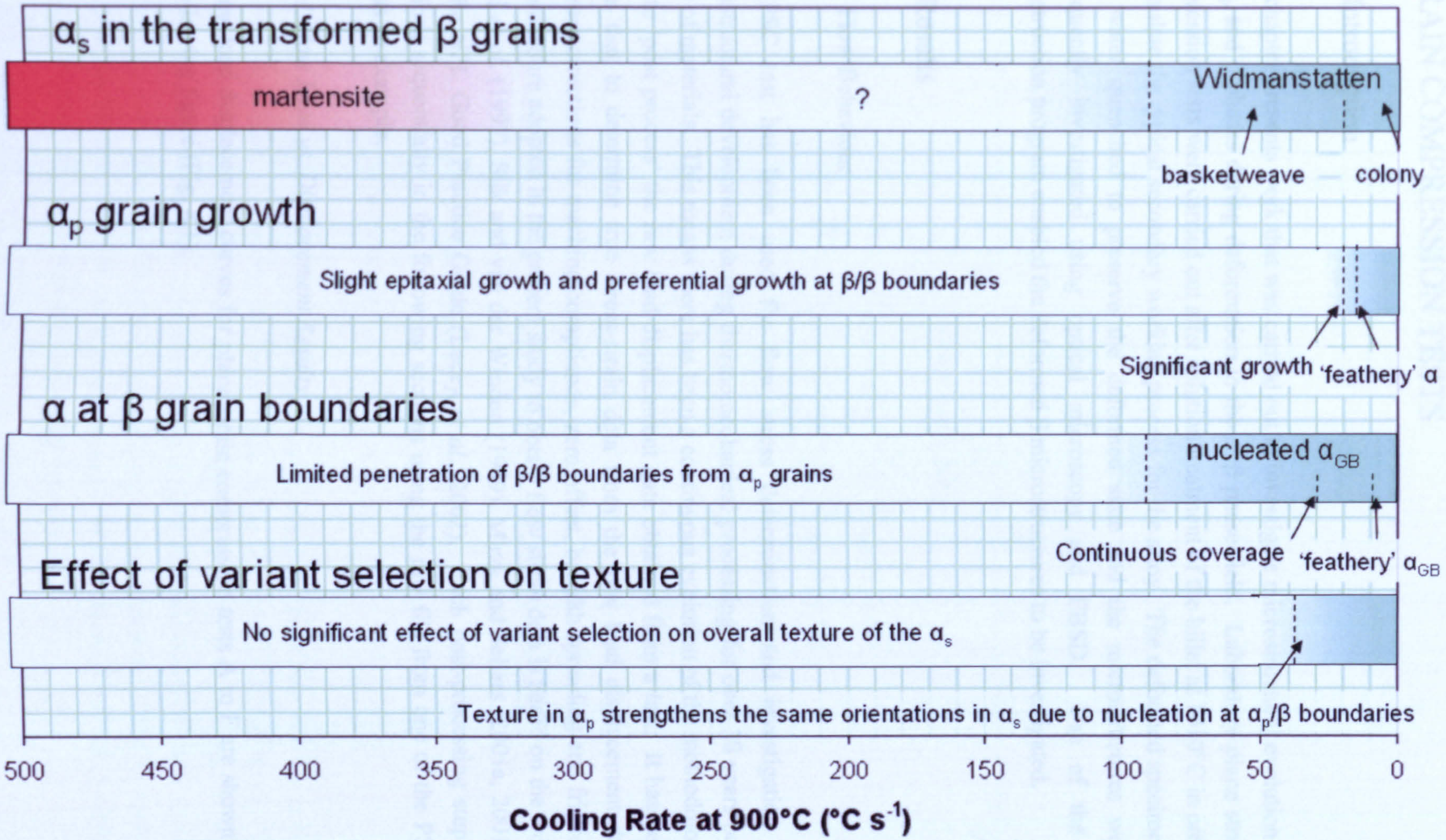

Fig. 7.75 A summary of the main findings from Chapter 7.

8 SIMULATED SECONDARY WORKING USING PLANE STRAIN COMPRESSION TESTS

8.1 Introduction

This chapter presents work that was carried out to investigate microstructural evolution in the α_p and β phases during deformation in the $\alpha+\beta$ phase field. Laboratory plane strain compression tests were carried out after solution treatment of the billet at 1010°C in order to simulate the typical secondary working process for the alloy. The deformed specimens were water quenched to preserve the deformed state and the microstructures were subsequently investigated using optical microscopy and EBSD. Use of the β reconstruction program enabled the deformed β microstructures to be investigated.

8.2 Results

8.2.1 Flow Behaviour

The PSC test has been used for flow stress determination and investigation of microstructural development during thermomechanical processing for over 30 years on a range of materials. This means there has been a continuous evolution of the methodology used to 'post process' the raw load displacement data obtained from a test. It has been shown that to determine true stress-strain data from the raw load displacement data requires corrections for machine compliance, zero offset, breadth spreading and friction. The procedure adopted in the present study to obtain flow stress data is based on the work of Shi *et al.* (1997), Silk and van der Winden (1999), Mirza and Sellars (2001a, 2001b) and the NPL Good Practice Guide (Lacey *et al.*, 2002). Each post-processing step is described sequentially in the following sections using the raw file from one of the PSC tests as an example.

8.2.1.1 Raw Load vs. Displacement Results

The raw load displacement curves for plane strain compression tests A to F are shown in the following figure (Fig. 8.1).

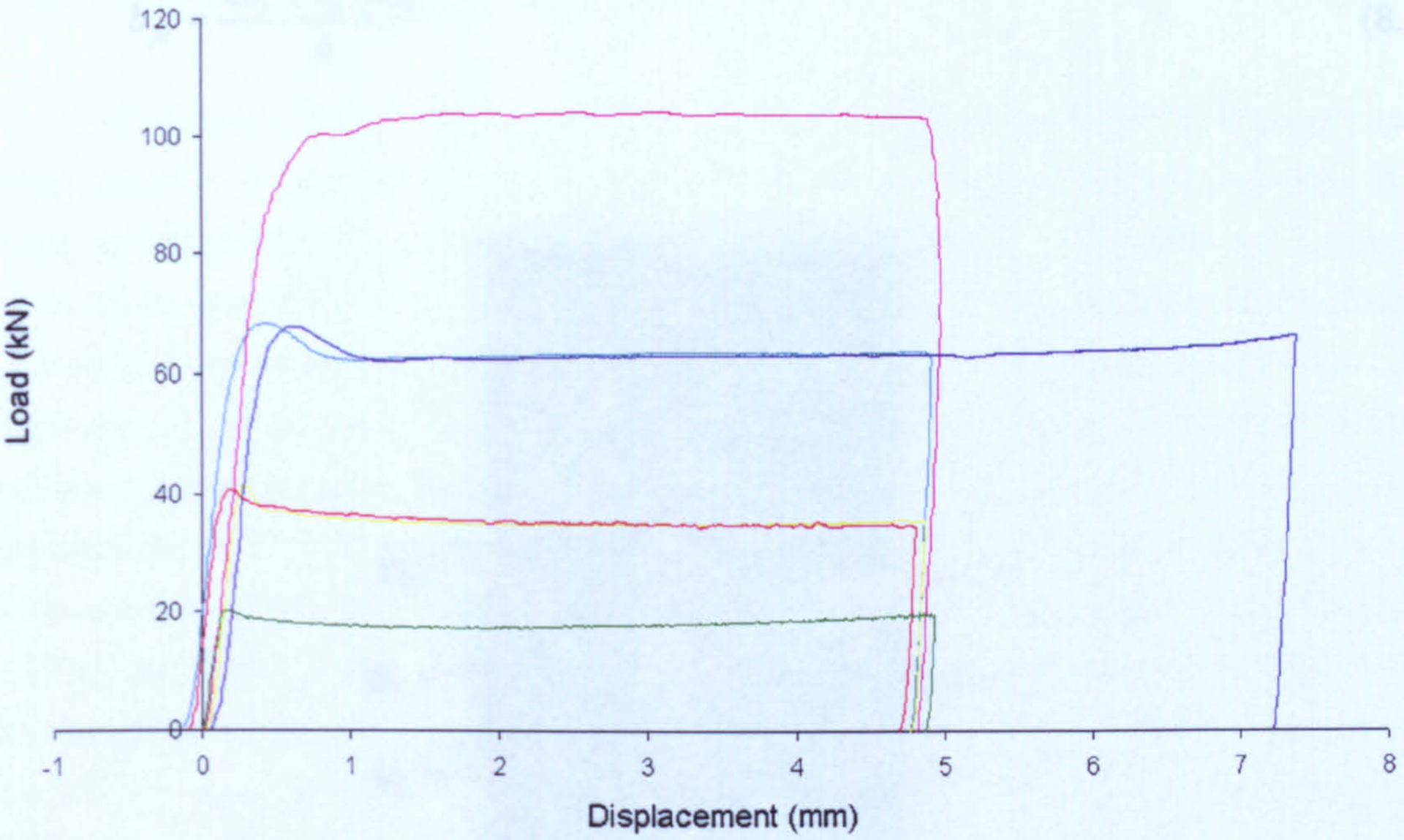

—	A	$\dot{\varepsilon}_{nom} = 20\text{s}^{-1}$	$\varepsilon_{nom} = 0.69$
—	B	$\dot{\varepsilon}_{nom} = 2.0\text{s}^{-1}$	$\varepsilon_{nom} = 0.69$
—	C	$\dot{\varepsilon}_{nom} = 2.0\text{s}^{-1}$	$\varepsilon_{nom} = 1.39$
—	D	$\dot{\varepsilon}_{nom} = 0.2\text{s}^{-1}$	$\varepsilon_{nom} = 0.69$
—	E	$\dot{\varepsilon}_{nom} = 0.2\text{s}^{-1}$	$\varepsilon_{nom} = 0.69$
—	F	$\dot{\varepsilon}_{nom} = 0.02\text{s}^{-1}$	$\varepsilon_{nom} = 0.69$

Fig. 8.1 Load versus displacement curves (uncorrected raw data).

8.2.1.2 Post-processing to Calculate Stress vs. Strain Results

Deformed specimen measurements

The final dimensions of a deformed specimen were measured after a test with the sample at room temperature. Measurements were taken at the positions indicated in Fig. 8.2. The value for the final height of the deformed region was taken as an average of the 5 positions h_1 to h_5, which were measured using a flat-ended micrometer with a spindle diameter of 5 mm. The breadth of the deformed region was measured at the 3 positions b_1 to b_3 using Vernier callipers and a single measure of the degree of spread, weighted towards the centre value (b_1), was obtained using equation 8.1.

$$b_{fc} = \frac{2b_1 + b_2 + b_3}{4} \tag{8.1}$$

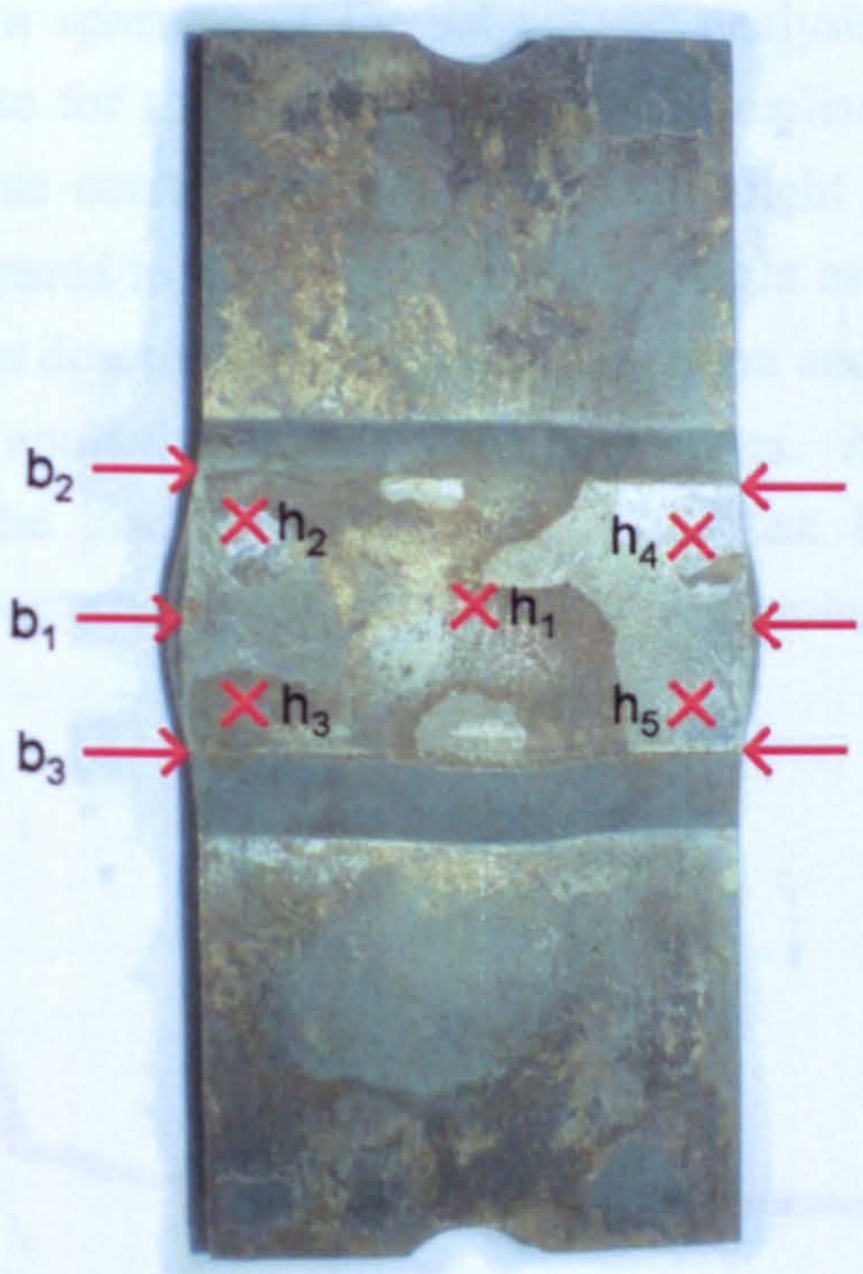

Fig. 8.2 Post deformation measuring locations for height (h_1 to h_5) and breadth (b_1 to b_3) on a PSC specimen.

The room temperature measurement of final height was used to calculate the final 'hot' height of the specimen immediately after deformation (i.e. accounting for thermal expansion) using equation 8.2

$$h_{fh} = h_{fc} + \alpha_t h_{fc}(T - T_0) \tag{8.2}$$

where h_{fh} is the final hot thickness, h_{fc} is the final cold thickness, α_t is the thermal expansion coefficient, T is the measured temperature when the tool reached maximum displacement and T_0 is room temperature. A value of 1.09×10^{-5} °C^{-1} was used for the thermal expansion coefficient. The final 'hot' breadth of the specimen b_{fh} was calculated in a similar manner.

Initial corrections to load displacement data

The TMC machine logged five important variables during the course of a test, these were: time, specimen temperature, load, tool displacement and tool velocity. This data was saved in the form of a spreadsheet for subsequent analysis. This data was initially corrected to compensate for the effects of machine compliance and zero offset (origin correction). After these corrections, the change in height measured by the machine displacement was compared to the actual change in height as indicated by the deformed specimen measurements described in the previous section and a further correction to the displacement data was applied to equate these two values. An example of the effect of these corrections on the load displacement data for test D (nominal temperature = 1010°C, nominal constant true strain rate = 0.2 s^{-1} and nominal true strain = 0.69) are shown in Fig. 8.3.

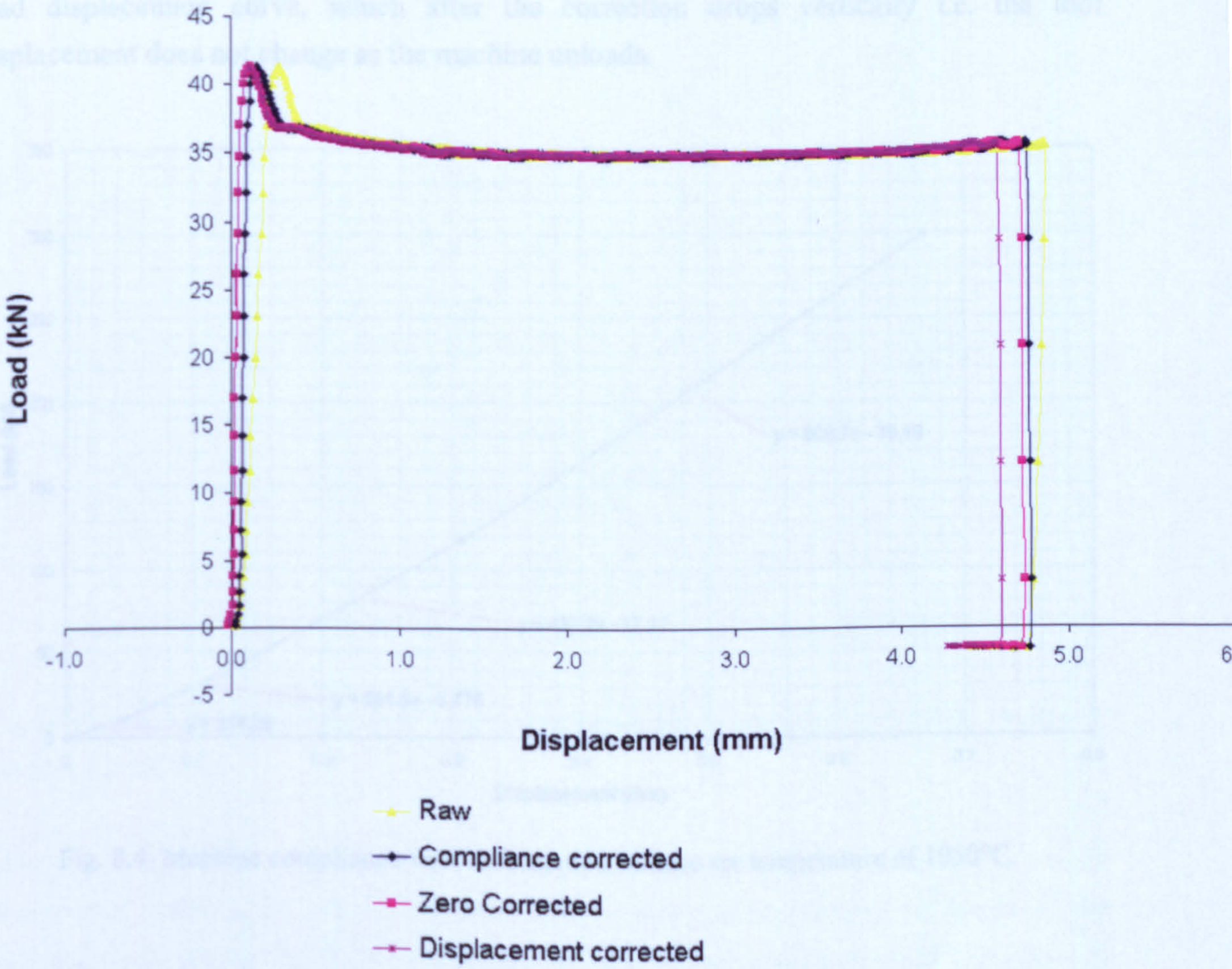

Fig. 8.3 Initial corrections to the load displacement data.
(Example is for test D: T_{nom} = 1010°C, ε_{nom}=0.02s^{-1}, ε_{nom} = 0.69).

Correction for test machine compliance

The compliance of the TMC machine / tooling set-up at the temperature of the tests was measured in a separate experiment by positioning the top and bottom tools in direct contact and loading to a value in excess of the maximum load recorded in the plane strain compression tests. This test was repeated several times to confirm the validity of the data. The displacement readings gave a direct measure of compliance as a function of load. In mechanical testing, the relationship between machine compliance and load is often assumed to be linear. However, the results from the test showed that in the case of the TMC machine, this was not the case. The machine compliance was approximated by fitting four straight lines to the data from the compliance test as shown in Fig. 8.4. This was used to correct displacement readings from plane strain compression tests as a function of load. Correction of the raw data for machine compliance produces a steeper gradient in the initial part of the load displacement curve, and reduces the total displacement of the tool. It also changes the shape of the final 'unloading' part of the load displacement curve, which after the correction drops vertically i.e. the tool displacement does not change as the machine unloads.

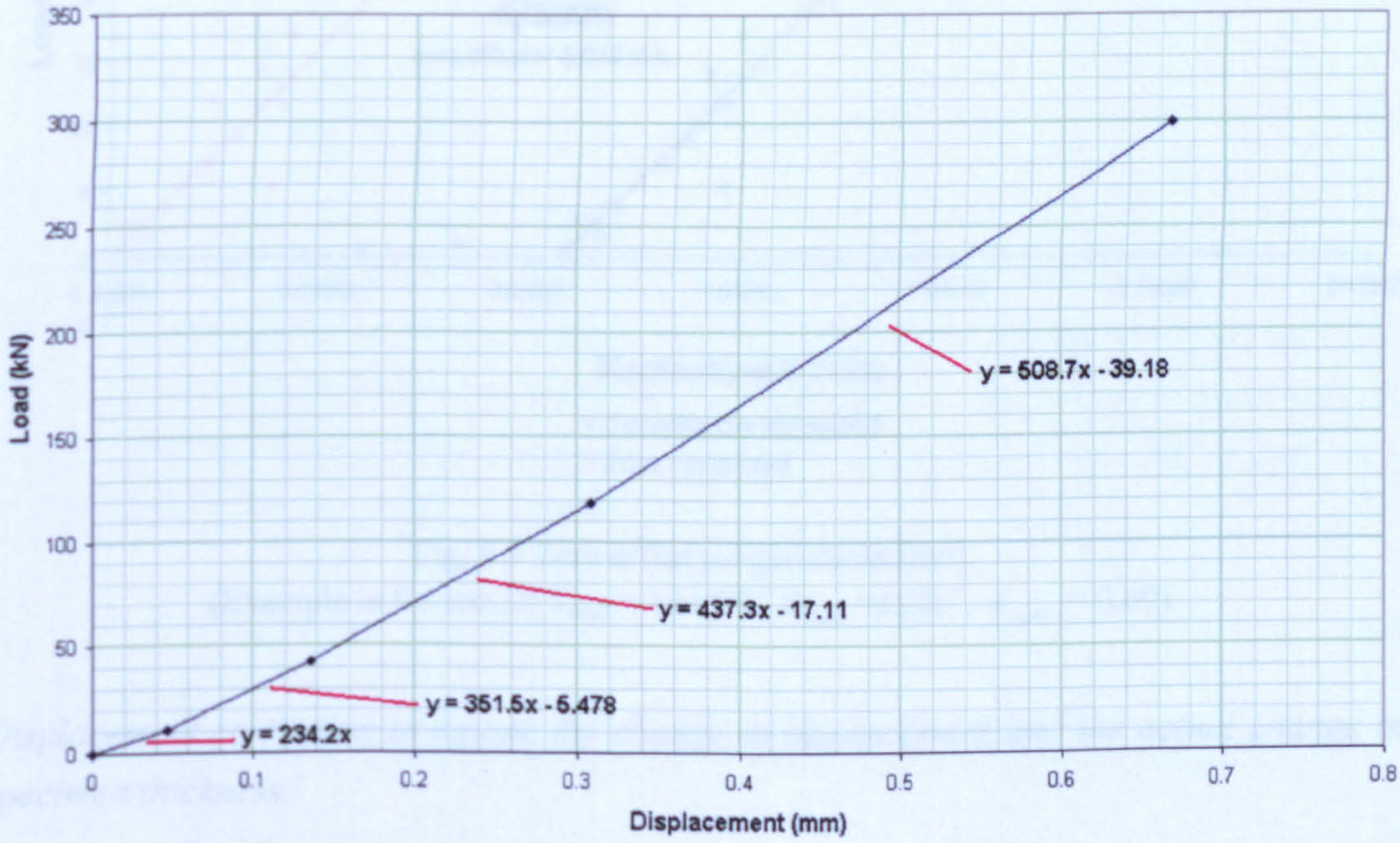

Fig. 8.4 Machine compliance with deformation furnace set temperature of 1050°C.

Correction for zero offset (origin correction)

The next correction applied was for errors in the zero position, i.e. the displacement at which deformation starts. This displacement should correspond to the initial 'hot' height of the specimen but errors arise from the increased thickness due to the layer of glass lubricant on the specimen surface and from slight misalignments between the tools. The zero offset was corrected by fitting a straight line to the elastic part of the load displacement data and finding the displacement of this line at zero load (0kN). This value was then added or subtracted to the displacement data, so that after correcting for zero offset, the line of best fit passed through the origin. The zero offset correction for test D is shown in Fig. 8.5.

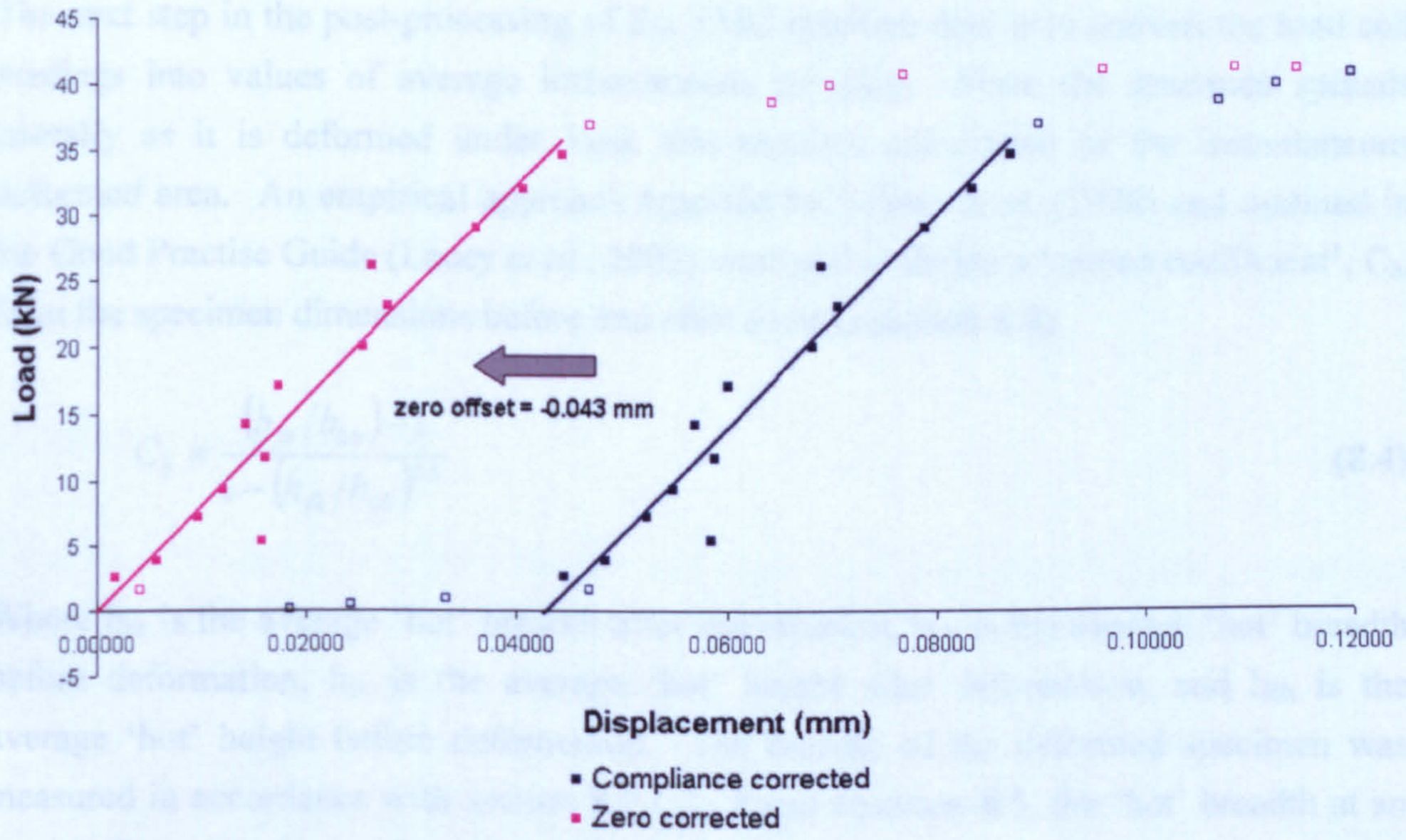

Fig. 8.5 Zero offset (origin correction).
(Example is for test D: T_{nom} = 1010°C, $\dot{\varepsilon}_{nom}$=0.02s^{-1}, ε_{nom} = 0.69).

Displacement correction to equate the change in displacement and the actual change in specimen thickness.

After applying the aforementioned corrections, there usually remained a small discrepancy between the maximum tool displacement and the change in height of the 'hot' specimen calculated from the final room temperature specimen measurements. In the case of the example shown in Fig. 8.3 (test D), the maximum tool displacement was 4.74 mm, whereas the calculated change in specimen height was 4.61 mm. This relatively small error of 0.13 mm i.e. less than 3% error is believed to be due to

temperature effects on the displacement calibration. To equate the maximum tool displacement with the true change in specimen height, the displacement data was corrected using equation 8.3

$$x_{corr} = \frac{h_{0h} - h_{fh}}{x_{\max}} \times x \tag{8.3}$$

where x_{corr} is the corrected displacement, h_{0h} is the initial 'hot' height, h_{fh} is the final 'hot' height, x_{max} is the maximum recorded tool displacement.

Calculating the average instantaneous pressure (breadth spreading correction)

The next step in the post-processing of the TMC machine data is to convert the load cell readings into values of average instantaneous pressure. Since the specimen spreads laterally as it is deformed under load, this requires calculation of the instantaneous deformed area. An empirical approach reported by Sellars *et al.* (1976) and outlined in the Good Practise Guide (Lacey *et al.*, 2002) was used to define a 'spread coefficient', C_b, from the specimen dimensions before and after a test (equation 8.4).

$$C_b = \frac{(b_{fh}/b_{0h}) - 1}{1 - (h_{fh}/h_{0h})^{0.5}} \tag{8.4}$$

Where b_{fh} is the average 'hot' breadth after deformation, b_{0h} is the average 'hot' breadth before deformation, h_{fh} is the average 'hot' height after deformation, and h_{0h} is the average 'hot' height before deformation. The breadth of the deformed specimen was measured in accordance with section 8.2.1.2. From equation 8.5, the 'hot' breadth at an intermediate time, b_h, can be estimated using

$$b_h = b_{0h}\left[1 + C_b - C_b(h_h/h_{0h})^{0.5}\right] \tag{8.5}$$

Using b_h, the average instantaneous pressure could then calculated with equation 8.6

$$\bar{p} = \frac{L}{w \times b_h} \tag{8.6}$$

where L is the load and w is the tool width. The corrected load displacement curve and the corresponding pressure displacement curve are shown in Fig. 8.6 for test D.

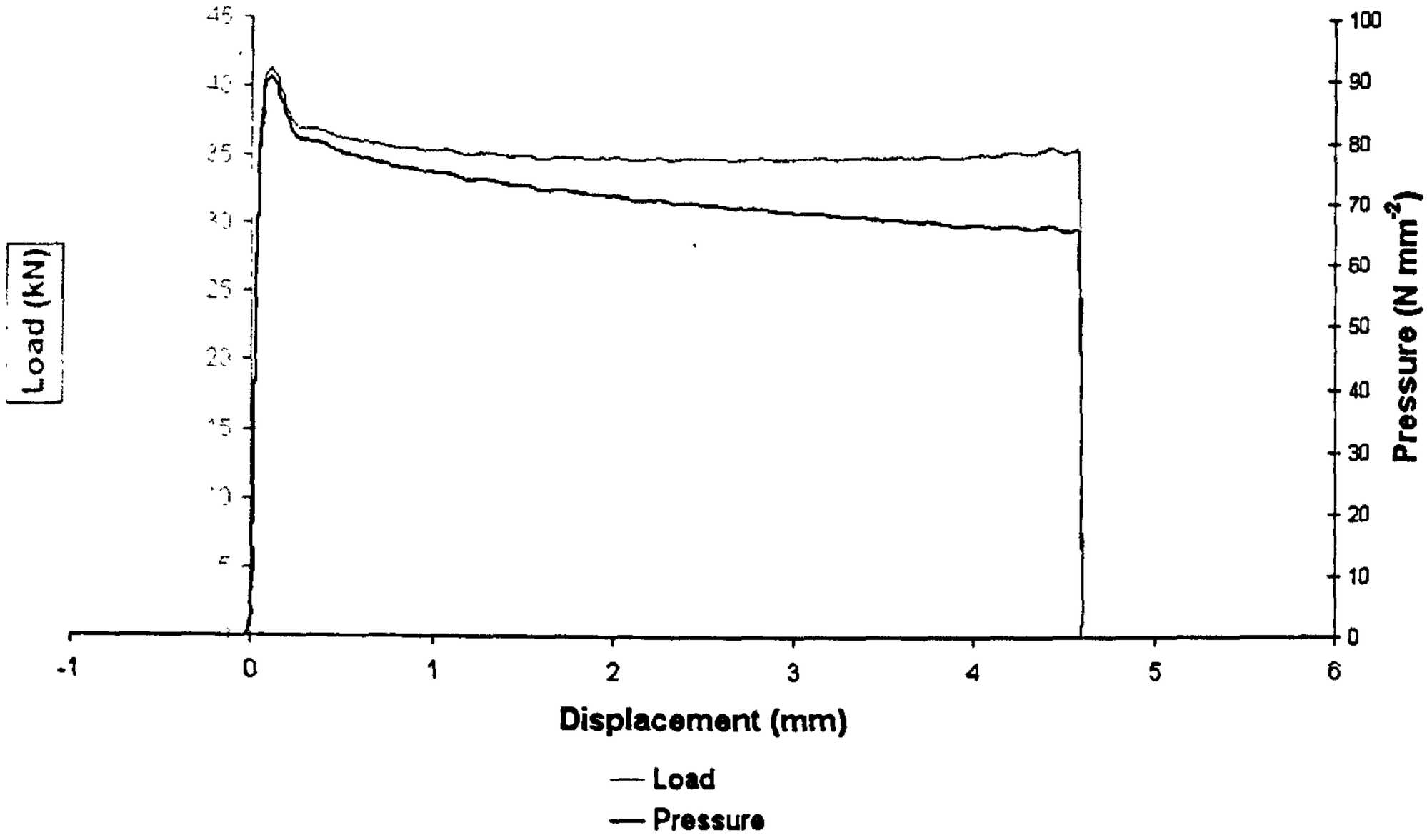

Fig. 8.6 The corrected load displacement data and the corresponding pressure displacement data after correcting for breadth spreading.
(Example is for test D: T_{nom} = 1010°C, $\dot{\varepsilon}_{nom}$=0.02s^{-1}, ε_{nom} = 0.69).

Calculating equivalent strain

From the corrected displacement measurements, the next step in the analysis is to convert this to an equivalent true tensile strain $\bar{\varepsilon}$, which must include a correction for breadth spreading. Equivalent strain, $\bar{\varepsilon}$, is given by:

$$\bar{\varepsilon} = \frac{\sqrt{2}}{3}\left[(\varepsilon_1 - \varepsilon_2)^2 + (\varepsilon_2 - \varepsilon_3)^2 + (\varepsilon_3 - \varepsilon_1)^2\right]^{1/2} \tag{8.7}$$

If the equivalent strain is calculated assuming ideal plane strain conditions, i.e. no breadth spreading, then $\varepsilon_1 = -\varepsilon_3$ and $\varepsilon_2 = 0$, which means equation 8.7 becomes

$$\bar{\varepsilon} = \frac{\sqrt{2}}{3}\left[\varepsilon_3^{\,2} + \varepsilon_3^{\,2} + 4\varepsilon_3^{\,2}\right]^{1/2} \tag{8.8}$$

$$\therefore \quad \bar{\varepsilon} = \frac{\sqrt{2}}{3}\varepsilon_3 \tag{8.9}$$

$$\therefore \quad \bar{\varepsilon} = \frac{\sqrt{2}}{3}\ln\frac{h}{h_0} \tag{8.10}$$

However, accounting for lateral spread, $\varepsilon_3 = \ln (h/h_0)$, $\varepsilon_2 = \ln (b/b_0)$, and $\varepsilon_1 = -\varepsilon_3 - \varepsilon_2$. Then, by substitution, the expression for equivalent strain is given by:

$$\bar{\varepsilon} = \frac{\sqrt{2}}{3}\left[(2\varepsilon_2 + \varepsilon_3)^2 + (\varepsilon_2 - \varepsilon_3)^2 + (\varepsilon_2 + 2\varepsilon_3)^2\right]^{1/2} \tag{8.11}$$

$$\therefore \quad \bar{\varepsilon} = \frac{\sqrt{2}}{3}\left[\varepsilon_2{}^2 + \varepsilon_2\varepsilon_3 + \varepsilon_3{}^2\right]^{1/2} \tag{8.12}$$

Because $\varepsilon_2 = \ln (b_h/b_{0h})$ is related to $\varepsilon_3 = \ln (h_h/h_{0h})$ by equation 8.5, a factor, f, can be defined as:

$$\bar{\varepsilon} = -f\varepsilon_3 \tag{8.13}$$

This correction factor for breadth spreading varies in the limits of $f = 2/\sqrt{3} = 1.155$ for zero spread to $f = 1$ for axisymmetric conditions i.e. when the spread = extension ($\varepsilon_{11}=\varepsilon_{22}$). Curves for pressure versus equivalent strain assuming ideal plane strain conditions and after correcting for the breadth spreading are shown in Fig. 8.7 for test D.

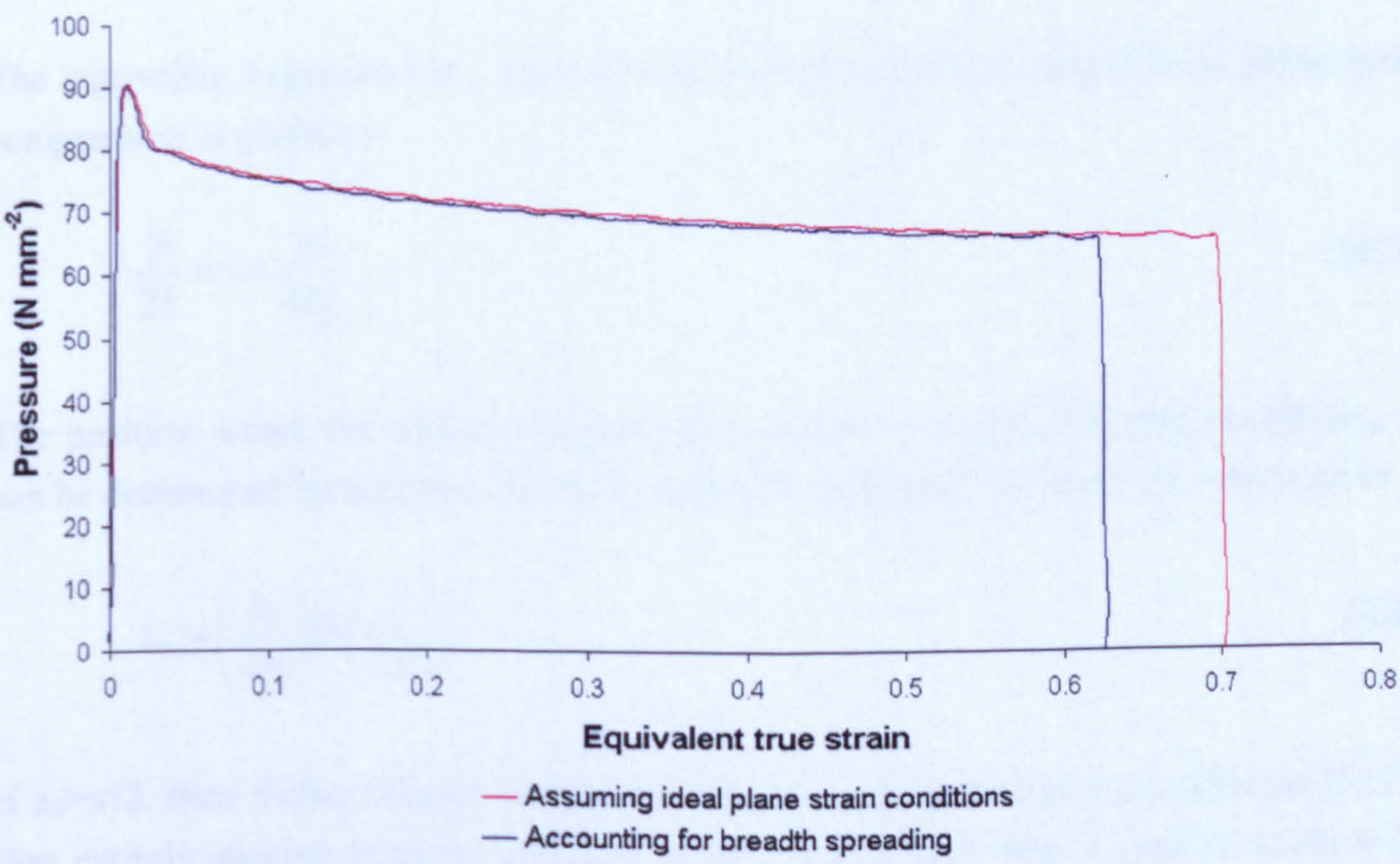

Fig. 8.7 Pressure versus equivalent strain with and without the correction for breadth spreading. (Example is for test D: $T_{nom} = 1010°C$, $\dot{\varepsilon}_{nom}=0.02s^{-1}$, $\varepsilon_{nom} = 0.69$).

Calculating equivalent flow stress

To determine the equivalent flow stress, σ_0, of the material, the shear flow stress, k, must first be calculated from the instantaneous pressure. This calculation has to consider the friction forces developed between the specimen and the tools during the test because friction increases the pressure required to produce yielding. It is assumed that the friction conditions are predominantly sliding friction, sticking friction, or a combination of the two. Sliding friction assumes a constant Coulomb friction coefficient, μ, whereas sticking friction assumes that the contact stress at the specimen/tool interface is equal to the material flow stress in pure shear. When both conditions occur in different regions of the contact area at the same time, it is assumed that the two types of behaviour occur in distinct bands across the width of the specimen. In this intermediate situation, sticking friction occurs in a central band, with sliding friction at the outer edges.

In the case of pure sliding friction, for ideal plane strain compression, the average pressure exerted by the tools $\bar{p}$, in terms of the shear flow stress, k is given by (Colas-Ortiz, 1983), (Foster, 1981), (Silk and van der Winden, 1999):

$$\frac{\bar{p}}{2k} = \frac{h_h}{\mu w}\left[\exp\left(\frac{\mu w}{h_h}\right) - 1\right] \tag{8.14}$$

The equivalent expression for pure sticking friction conditions under ideal plane strain compression is given by

$$\frac{\bar{p}}{2k} = 1 + \frac{w}{4h_h} \tag{8.15}$$

The position where the friction changes from sliding to sticking friction conditions, z_0, can be determined by equating the dp/dx terms of equations 8.14 and 8.15, which gives

$$z_0 = \left(\frac{h_h}{2\mu}\right)\ln\left(\frac{1}{2\mu}\right) \tag{8.16}$$

If $z_0 > w/2$, then sliding friction conditions exist over the entire tool face, whereas If $z_0 < 0$, then entirely sticking friction conditions occur. If $0 < z_0 < w/2$, then a band of width $w-2z_0$ exists down the centre of the tool, in which there will be sticking friction, with sliding friction on either side of the band. In this intermediate situation, the average pressure in terms of the shear flow stress is given by

$$\frac{\bar{p}}{2k} = \frac{h_h}{\mu w}\left(\frac{1}{2\mu} - 1\right) + \frac{(w/2) - z_0}{\mu w} + \frac{[(w/2) - z_0]^2}{h_h w} \tag{8.17}$$

Equations 8.14 to 8.17 are for ideal plane strain conditions. In practice, there will always be some breadth spreading which relaxes the frictional effects at the edges of the specimen. Silk and van der Winden (1999) derived expressions to account for this effect for all three friction conditions. They suggested that at large specimen breadths, the correction is relatively insignificant, but if the breadth is less than 6 to 8 times the testpiece thickness, then such a correction becomes essential. In this investigation, the correction for spread of the specimen can not be ignored because b = 3h. The modified expressions for each friction condition are summarised as follows (Silk and van der Winden, 1999).

If $z_0 > w/2$ (sliding friction)

$$\frac{\bar{p}}{2k} = \frac{1}{b_h w}\left[\frac{2h_h^2}{\mu^2} + \frac{(b_h - w)h_h}{\mu}\right]\left[\exp\left(\frac{\mu w}{h_h}\right) - 1\right] - \frac{2h_h}{\mu b_h} \tag{8.18}$$

If $0 < z_0 < w/2$ (partial sticking friction)

$$\begin{aligned}\frac{\bar{p}}{2k} &= \frac{h_h}{\mu w}\left(\frac{1}{2\mu} - 1\right) + \frac{(w/2) - z_0}{\mu w} + \frac{[(w/2) - z_0]^2}{h_h w} \\ &+ \frac{1}{\mu b_h}\left(\frac{2z_0^2}{w} - z_0 - \frac{2h_h z_0}{\mu w} + \frac{h_h}{2\mu} - h + \frac{h_h^2}{w\mu^2} - \frac{2h_h^2}{\mu w}\right) \\ &+ \frac{1}{h_h b_h}\left(z_0^2 - \frac{4z_0^3}{3w} - \frac{w^2}{12}\right)\end{aligned} \tag{8.19}$$

If $0 > 2z_0$ (sticking friction)

$$\frac{\bar{p}}{2k} = 1 + \frac{w}{4h_h} - \frac{w^2}{12h_h b_h} \tag{8.20}$$

It can be seen that z_0 is dependent on the height, h_h. This means that the friction conditions will change during the course of a test as the instantaneous height decreases. To apply these corrections to the test data, z_0 is calculated for each data point using the instantaneous height to determine which friction conditions prevail. The instantaneous values of breadth and height are then substituted into equations 8.18, 8.19 or 8.20 to determine the instantaneous shear flow stress, k. The equivalent flow stress is then given by

$$\sigma = \frac{2k}{f} \tag{8.21}$$

where f is the empirical correction factor defined in equation 8.13, which is calculated for each data point using the instantaneous values of breadth (b_h) and height (h_h).

Before the calculations for equivalent flow stress can be made, a value must be selected for μ, the coefficient of friction that represents the conditions during testing. Mirza and Sellars (2001b) reported a value of 0.1 for glass lubricated tests on stainless steel type 316L and 0.3 for unlubricated tests. It is therefore reasonable to assume that the friction coefficient for titanium specimens lubricated with the AMLUBE 1000 glass lubricant will lie within or fairly close to this range of values. The effect of different values for the coefficient of friction on the calculated equivalent flow stress versus equivalent strain is shown in Fig. 8.8 for test D.

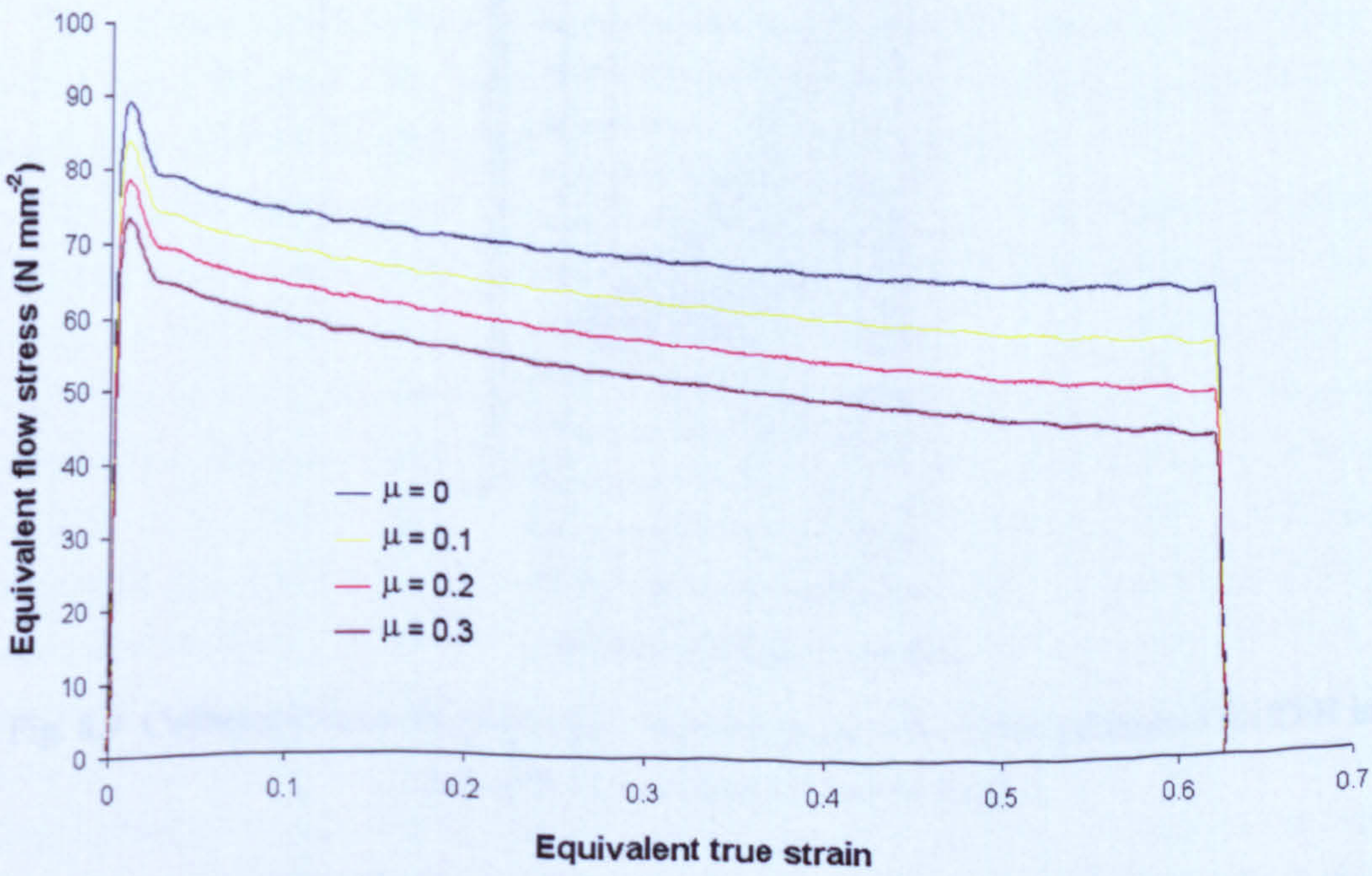

Fig. 8.8 The effect of friction correction on the calculated stress strain curve. (Example is for test D: T_{nom} = 1010°C, $\dot{\varepsilon}_{nom}$ =0.02s^{-1}, ε_{nom} = 0.69).

Determining the coefficient of friction

There are two established approaches for measuring μ under metal working conditions when the flow stress is unknown (Dieter, 1989). The most established technique is the ring compression test. An alternative technique is to perform plane strain compression tests on specimens of varying initial height.

The ring compression test was initially developed by Kunogi (1956) and was further developed by Male and Cockcroft (1965). The test uses a thin ring with the dimensions outer diameter (OD_0) : inner diameter (ID_0) : height (H_0) usually in the ratio 6:3:2. When the flat ring is plastically compressed between two flat platens, a unique value for the friction coefficient can be determined from the change in the inner diameter (ID) of the ring. For low values of μ, the ID increases, while for higher values of μ the ID of the ring decreases. The friction coefficient is determined from the percentage change in the ID of the ring for a given percentage reduction using a calibration chart determined analytically for the initial ring geometry. A calibration chart for an initial geometry of 6:3:2 is shown in Fig. 8.9. One of the advantages of the ring compression test is that it is not necessary to know the flow stress or to measure the deformation force in order to determine μ.

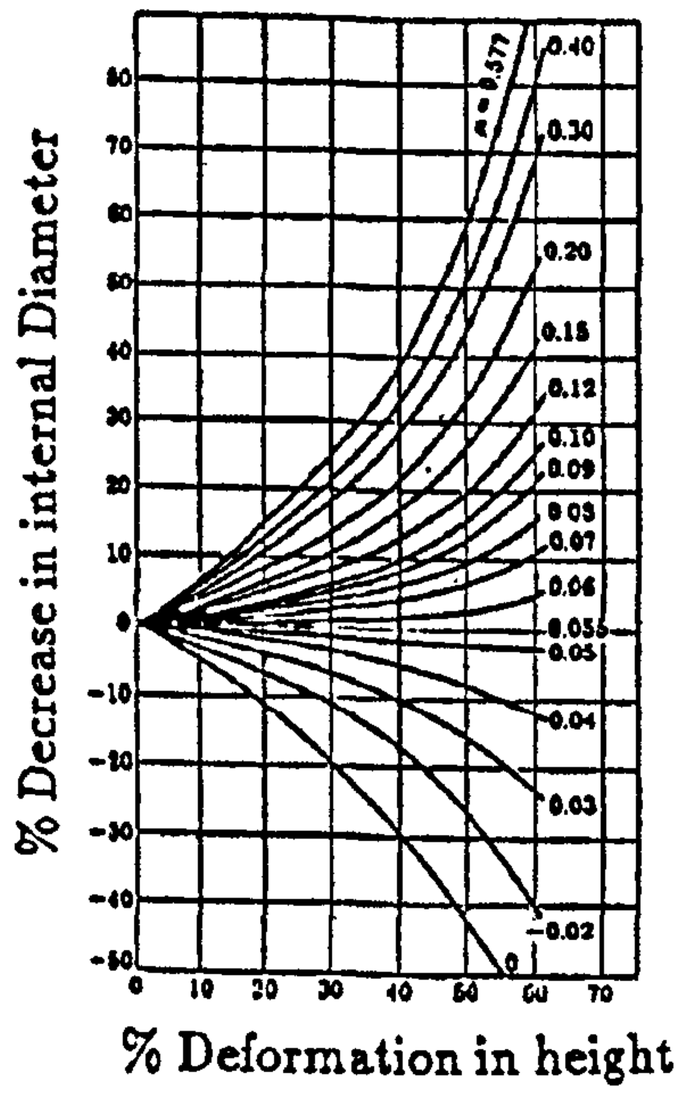

Fig. 8.9 Calibration chart for upset ring compression test with initial geometry OD:ID:H in the ratio 6:3:2 (from Sufogulu *et al*, 2002).

Ring compression tests have been performed previously for Timetal 834 using the AMLUBE 1000 glass lubricant (Thomas, 2007). In this work, 3 different sized rings were used, whilst maintaining an initial outer diameter (OD_0) : inner diameter (ID_0) : height (H_0) ratio of 6:3:2. The sizes of these rings are shown in Table 8.1. The rings were deformed at 1010°C, to a nominal strain of 0.7 at a nominal strain rate of $2s^{-1}$. The deformed rings exhibited a small degree of shearing i.e. lateral offset of the top and bottom surfaces of the rings, which it is believed led to an underestimate of the post deformation inner diameters and hence an overestimation of the average friction coefficient, μ. For this study, the post deformation dimensions were reappraised and the estimated friction coefficients revised. These results are shown in Table 8.2.

Table 8.1. Nominal initial dimensions of ring tests by Thomas (2007).

Specimen	OD_0 (mm)	ID_0 (mm)	H_0 (mm)	OD_0:ID_0:H_0
1	24	12	8	6:3:2
2	30	15	10	6:3:2
3	36	18	12	6:3:2

Table 8.2. Change in ring test dimensions and corresponding values of μ.

Specimen	% Decrease in H	% Decrease in ID	μ
1	48.2	-0.25	0.055
2	48.4	16.6	0.10
3	46.5	21.8	0.15

The values of μ determined from the ring compression tests varied from 0.055 to 0.15, with a mean value of 0.10, which is in agreement with the value of μ reported by Mirza and Sellars (2001b) for glass lubricated stainless steel specimens.

The second technique that can be used to determine μ, is to make identical reductions on plane strain compression specimens with varying values of initial height. The flow curves for these tests can then be plotted for different values of μ. The best value for μ will be found when the curves are most closely matched. In this study, two plane strain compression specimens with reduced initial heights of 7mm and 5.4mm were deformed at 1010°C, to a nominal strain of 1.34, at a nominal strain rate of $2s^{-1}$. The plots of calculated pressure versus equivalent strain for these tests and for a test under the same nominal conditions for a full height specimen (i.e. 10mm) are shown in Fig. 8.10. The specimen with an initial height of 7 mm was not a valid test because the specimen became skewed with respect to the tools during the test. The effect of this skewing can be seen by abrupt changes in the gradient of the pressure versus strain plot. Although the test was not accepted as valid, the data at low strains has been kept as it is still considered useful for this analysis. Both the 5.4 mm and 10 mm high specimens were both valid tests. It can be seen from Fig. 8.10, that reducing the initial specimen height, increases the pressure required to deform a specimen due to the increased frictional forces at high values of b/h. This results in higher average pressures for the thinner samples and a characteristic 'upturn' in the curve for the 5.4 mm specimen at high strains.

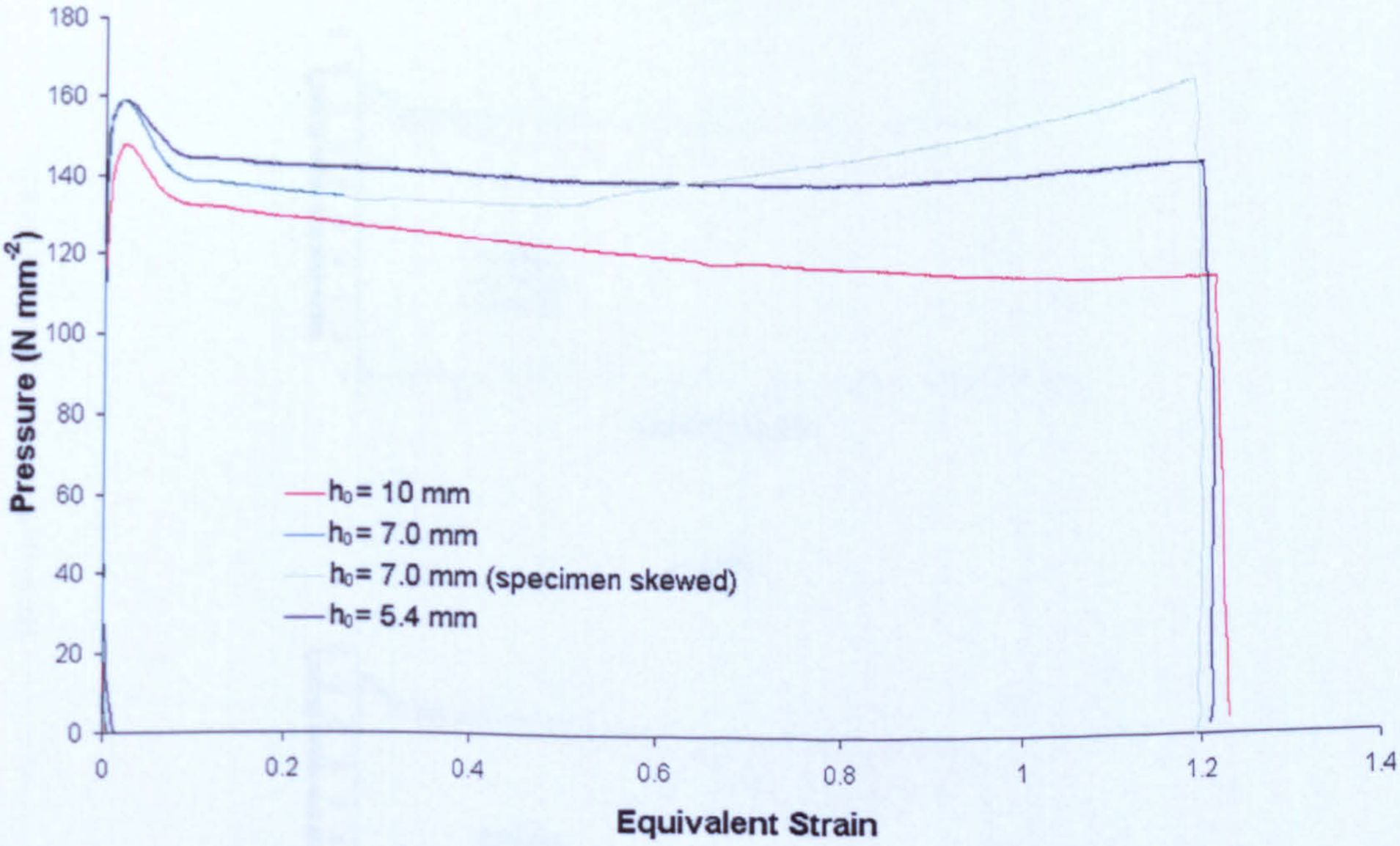

Fig. 8.10 Pressure versus equivalent strain for plane strain compression specimens deformed under the same nominal conditions but different initial specimen heights.

Plots of equivalent flow stress versus equivalent strain calculated using μ values of 0, 0.055, 0.1 and 0.15 are shown in Fig. 8.11. A μ value of 0 corresponds to zero friction, whereas 0.055, 0.1 and 0.15 are the values determined from each of the three ring compression tests discussed previously. The results suggest that 0.055 and 0.1 are lower than the ideal value of μ, whereas 0.15 is too high. The best match in the curves is obtained with a μ value of 0.125, shown in Fig. 8.12. This value (0.125) determined from the tests with specimens of varying initial height was used to correct for friction effects in the remainder of this work. This value falls within the range of values determined by the ring compression tests and is similar to the value of 0.1 determined by Mirza and Sellars (2001b) for glass lubricated stainless steel specimens.

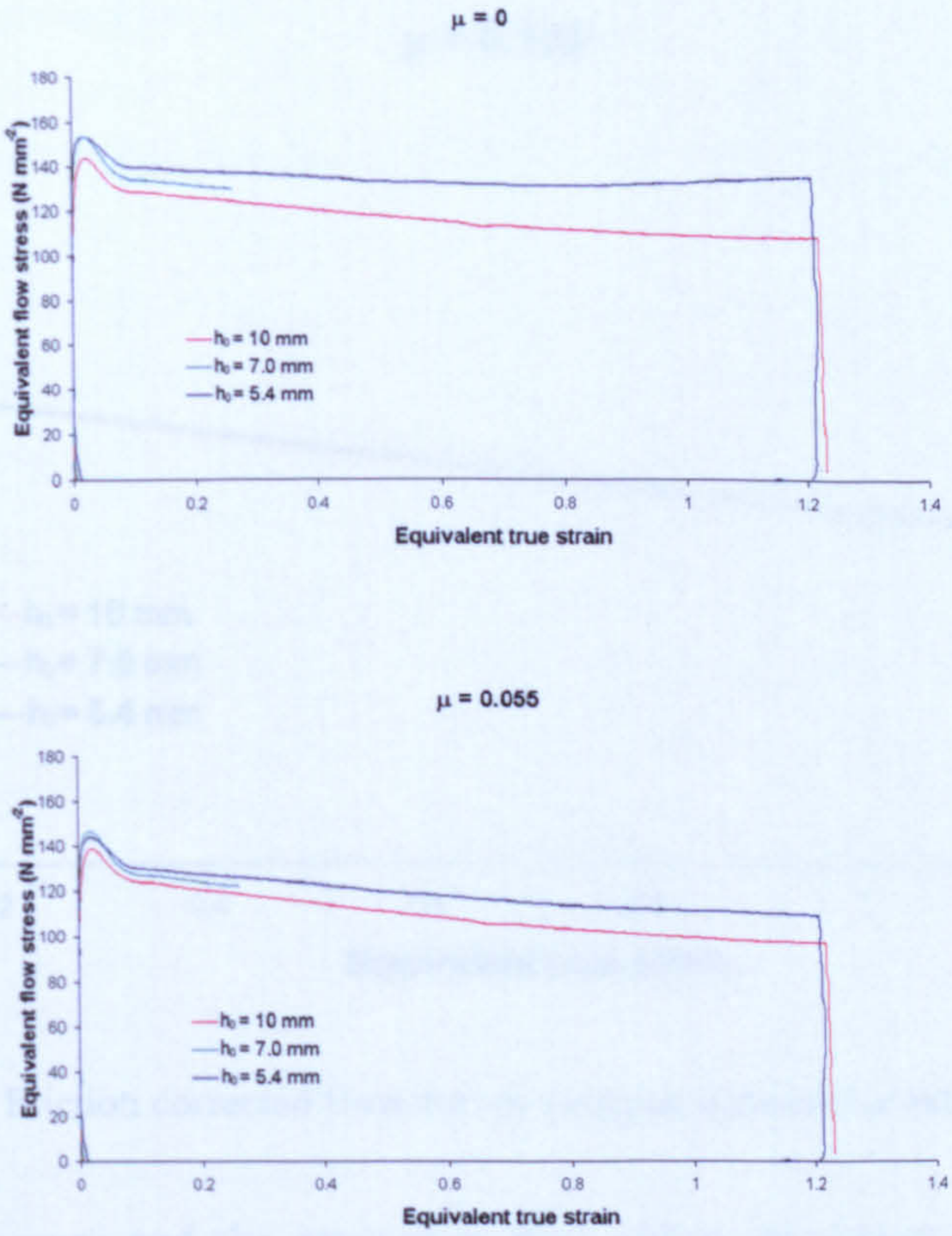

Fig. 8.11 Friction corrected flow curves using different values of μ for plane strain compression specimens with different initial specimen heights.

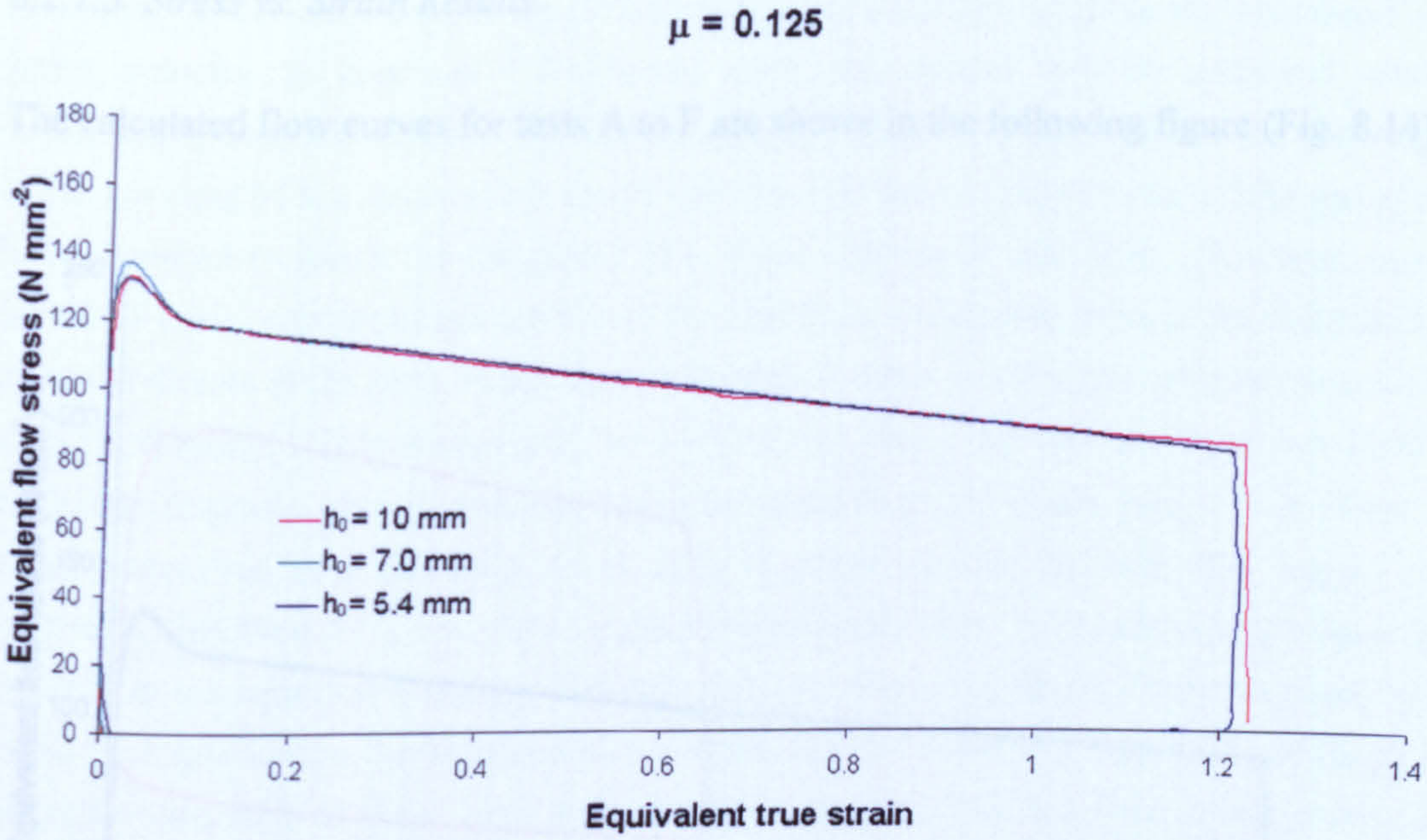

Fig. 8.12 Friction corrected flow curves using an optimum μ value of 0.125.

The curves for pressure and the equivalent flow stress calculated using $\mu = 0.125$ are shown in Fig. 8.13 for test D.

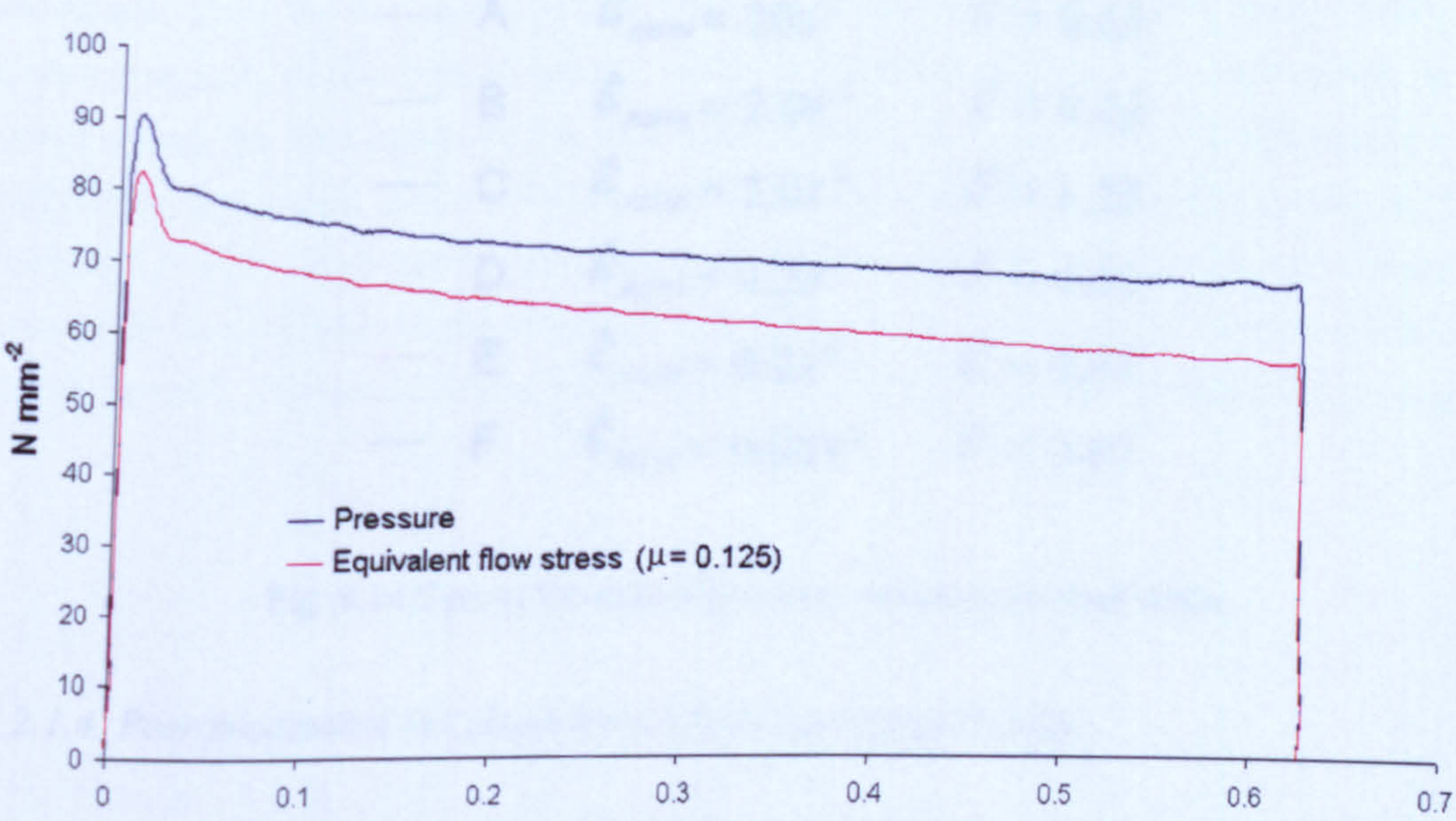

Fig. 8.13 Pressure and equivalent flow stress (calculated with $\mu = 0.125$) versus equivalent strain. (Example is for test D: $T_{nom} = 1010°C$, $\dot{\varepsilon}_{nom} = 0.02s^{-1}$, $\varepsilon_{nom} = 0.69$).

8.2.1.3 Stress vs. Strain Results

The calculated flow curves for tests A to F are shown in the following figure (Fig. 8.14).

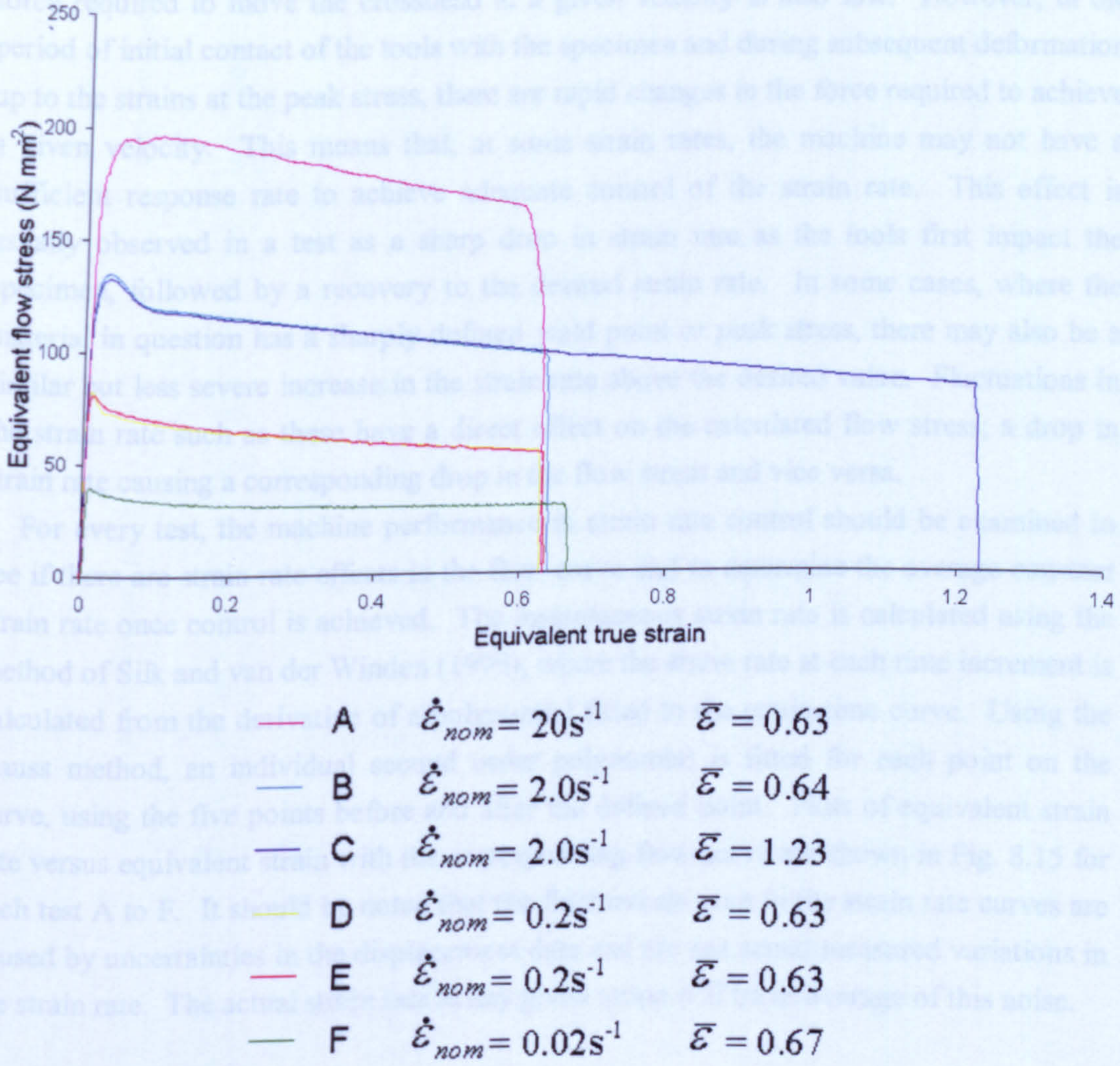

Fig. 8.14 Curves for equivalent stress versus equivalent strain.

8.2.1.4 Post-processing to Obtain Strain Rate Corrected Results

The plane strain compression tests in this study were performed in true strain rate control. This means that in an ideal test, the specimen should be deformed at a constant nominal strain rate for the entire duration of the test. Such a test requires the deformation velocity to decrease in proportion to the decrease in specimen height. The TMC machine controls the crosshead speed and hence the deformation velocity via a closed loop control system. When there is no deformation taking place i.e. zero load, near perfect control of the

crosshead speed can be achieved because the force required to move the crosshead at a given velocity is constant. Similarly, excellent control can be achieved during deformation once the material has passed the peak stress and there are no sharp changes in the gradient of the stress-strain curve because this means that the rate of change of the force required to move the crosshead at a given velocity is also low. However, in the period of initial contact of the tools with the specimen and during subsequent deformation up to the strains at the peak stress, there are rapid changes in the force required to achieve a given velocity. This means that, at some strain rates, the machine may not have a sufficient response rate to achieve adequate control of the strain rate. This effect is usually observed in a test as a sharp drop in strain rate as the tools first impact the specimen, followed by a recovery to the desired strain rate. In some cases, where the material in question has a sharply defined yield point or peak stress, there may also be a similar but less severe increase in the strain rate above the desired value. Fluctuations in the strain rate such as these have a direct effect on the calculated flow stress; a drop in strain rate causing a corresponding drop in the flow stress and vice versa.

For every test, the machine performance in strain rate control should be examined to see if there are strain rate effects in the flow curve and to determine the average constant strain rate once control is achieved. The instantaneous strain rate is calculated using the method of Silk and van der Winden (1999), where the strain rate at each time increment is calculated from the derivative of a polynomial fitted to the strain-time curve. Using the Gauss method, an individual second order polynomial is fitted for each point on the curve, using the five points before and after the defined point. Plots of equivalent strain rate versus equivalent strain with the corresponding flow curve are shown in Fig. 8.15 for each test A to F. It should be noted that the fluctuations seen in the strain rate curves are caused by uncertainties in the displacement data and are not actual measured variations in the strain rate. The actual strain rate at any given strain will be an average of this noise.

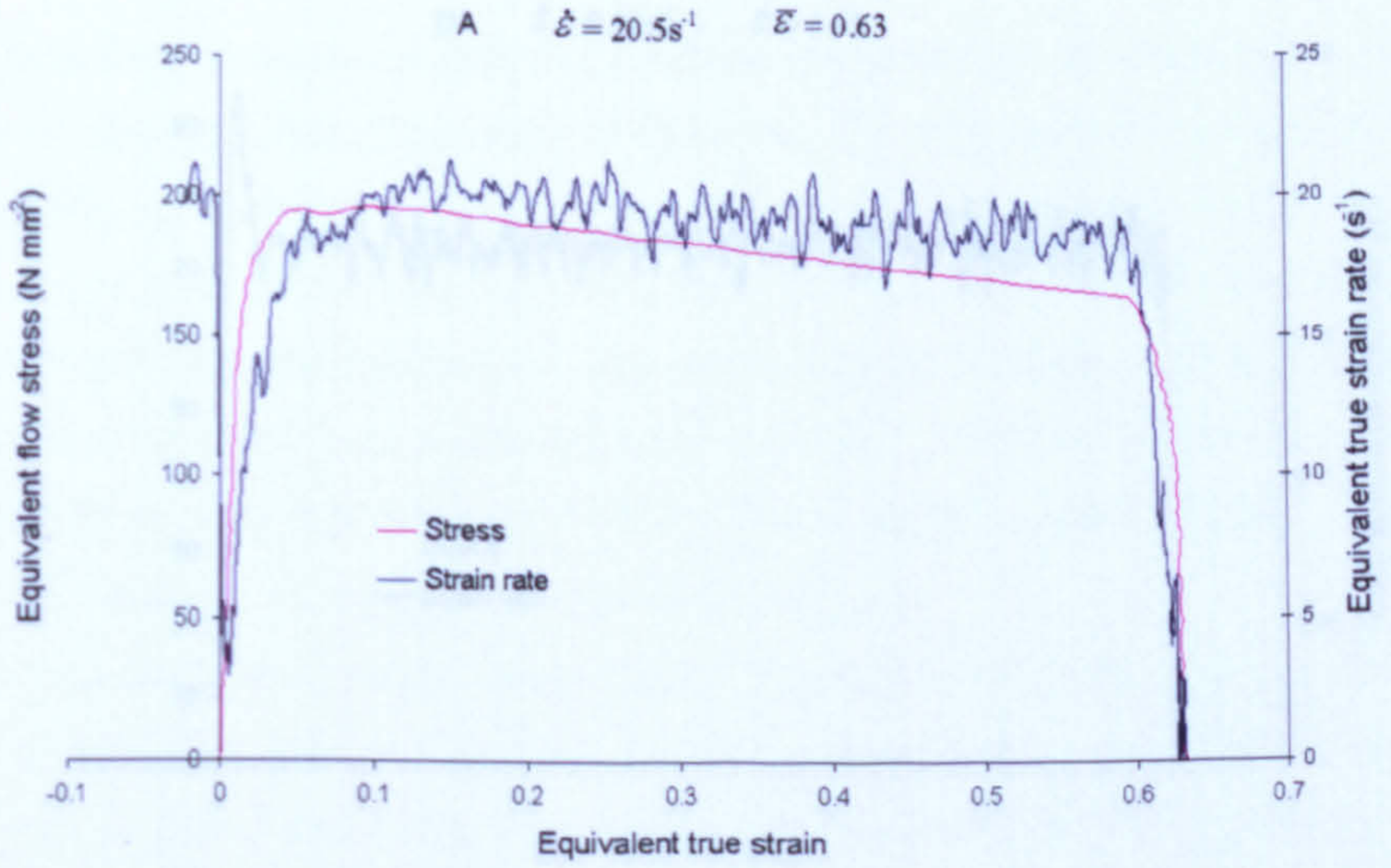
A $\dot{\varepsilon} = 20.5s^{-1}$ $\bar{\varepsilon} = 0.63$
Equivalent flow stress (N mm^{-2})
Equivalent true strain rate (s^{-1})
Stress
Strain rate
Equivalent true strain

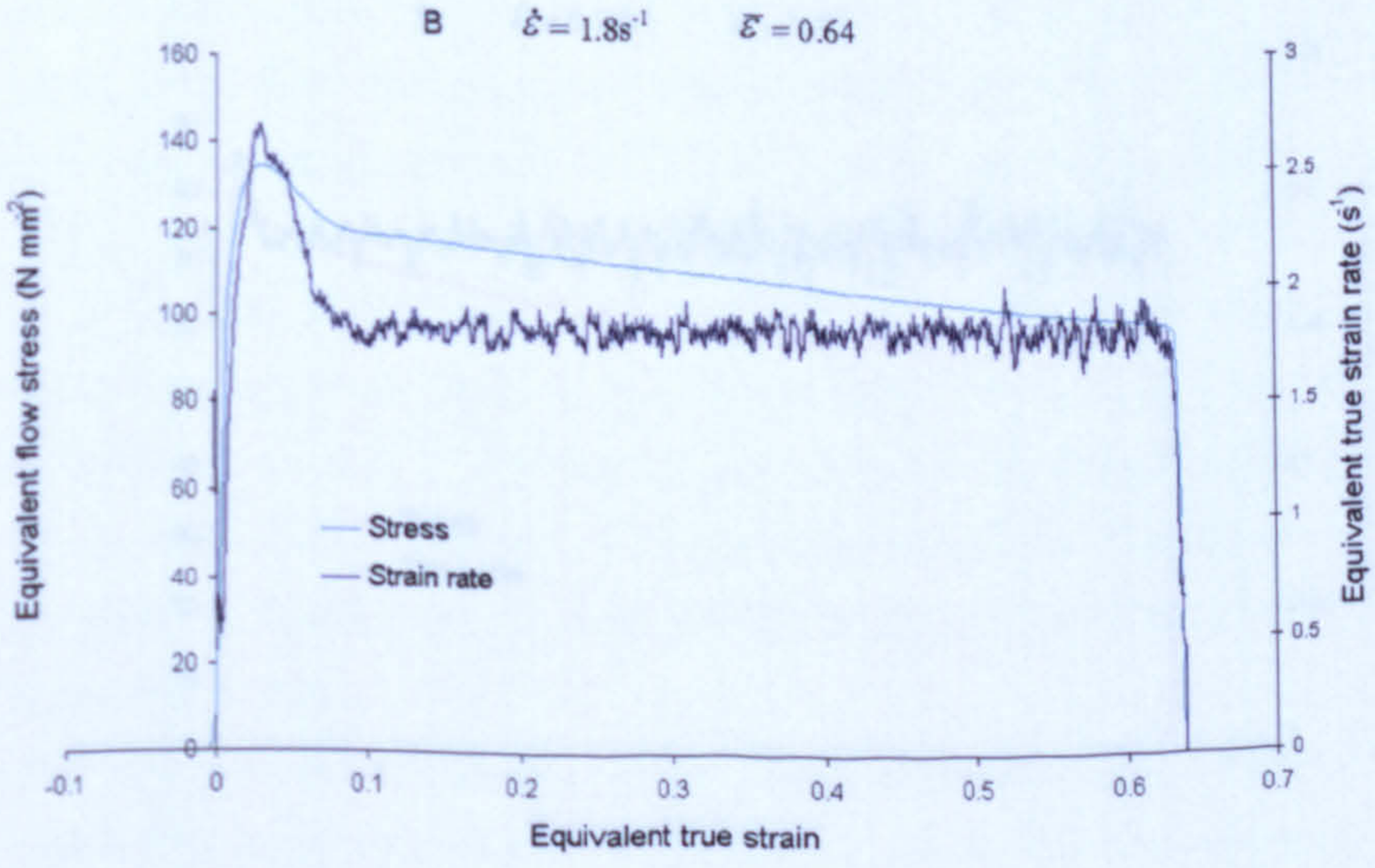
B $\dot{\varepsilon} = 1.8s^{-1}$ $\bar{\varepsilon} = 0.64$
Equivalent flow stress (N mm^{-2})
Equivalent true strain rate (s^{-1})
Stress
Strain rate
Equivalent true strain

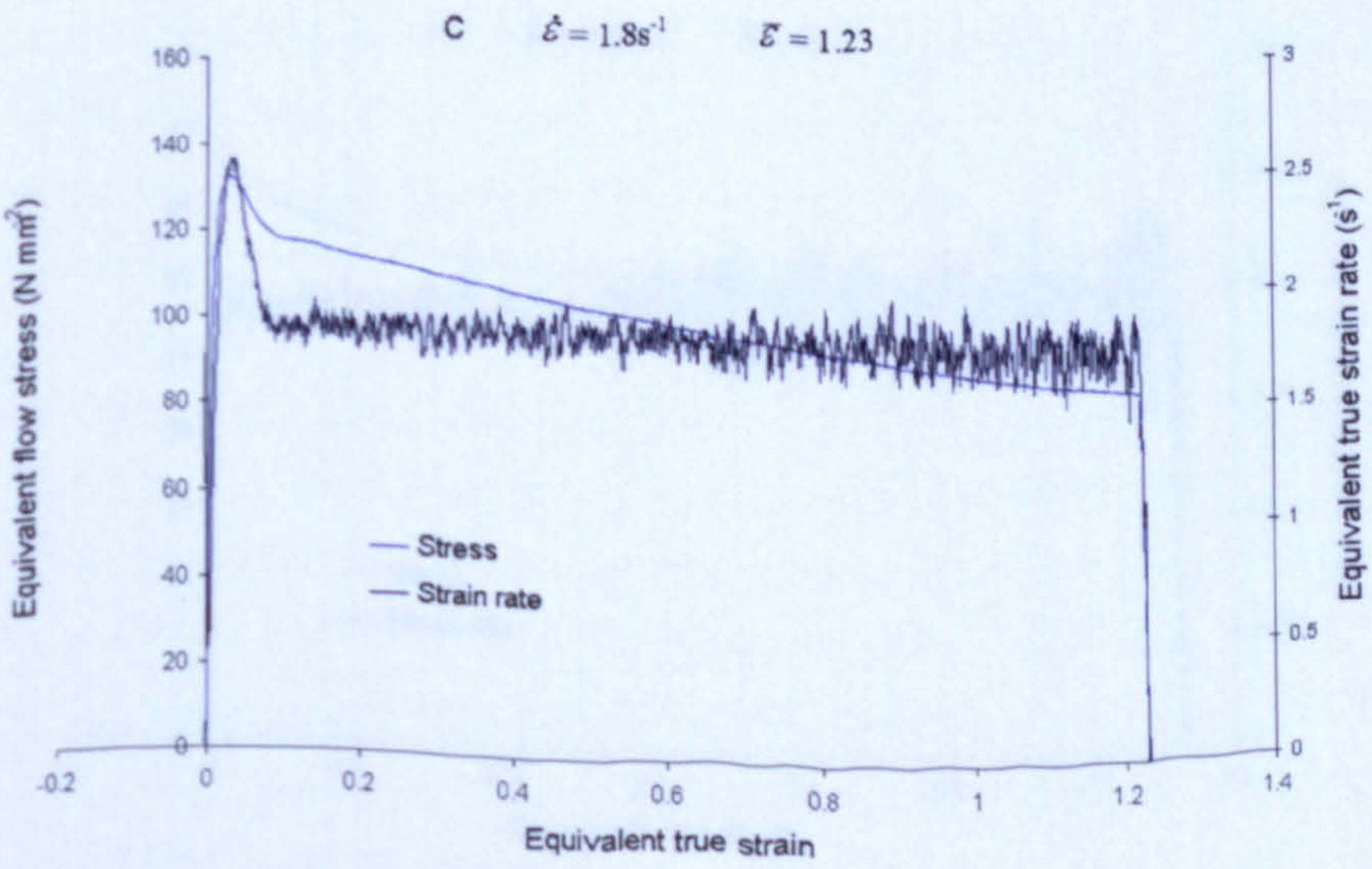
C $\dot{\varepsilon} = 1.8s^{-1}$ $\varepsilon = 1.23$
Equivalent flow stress (N mm^{-2})
Equivalent true strain rate (s^{-1})
Stress
Strain rate
Equivalent true strain

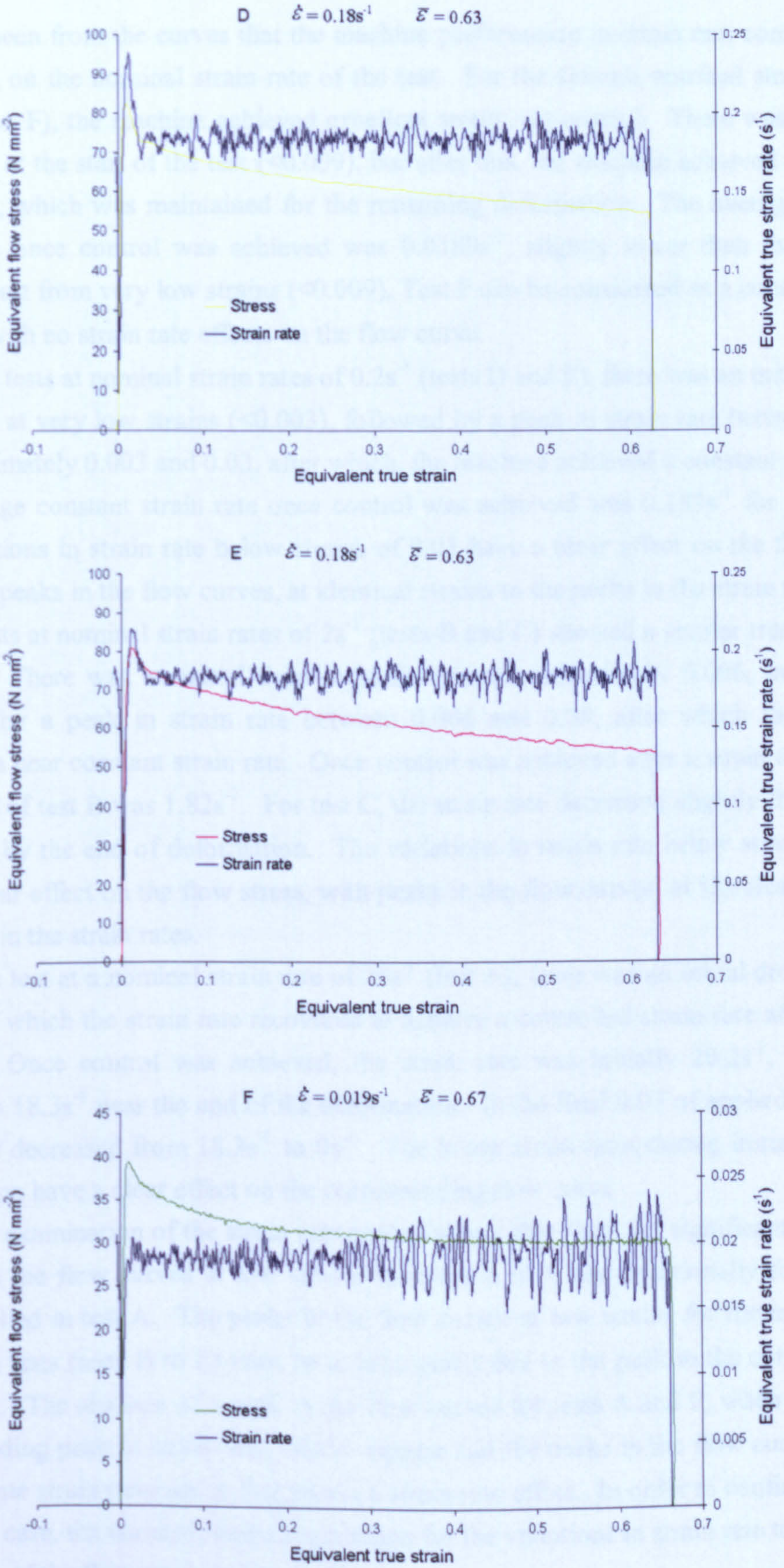

Fig. 8.15 Plots of equivalent strain rate versus equivalent strain and the corresponding flow curve for each test A to F.

It can be seen from the curves that the machine performance in strain rate control varied depending on the nominal strain rate of the test. For the slowest nominal strain rate of $0.02s^{-1}$ (test F), the machine achieved excellent strain rate control. There was a drop in strain rate at the start of the test (<0.009), but after this, the machine achieved a constant strain rate, which was maintained for the remaining deformation. The average constant strain rate once control was achieved was $0.0189s^{-1}$, slightly lower than the nominal value. Apart from very low strains (<0.009), Test F can be considered as a constant strain rate test, with no strain rate effects on the flow curve.

For the tests at nominal strain rates of $0.2s^{-1}$ (tests D and E), there was an initial drop in strain rate at very low strains (<0.003), followed by a peak in strain rate between strains of approximately 0.003 and 0.03, after which, the machine achieved a constant strain rate. The average constant strain rate once control was achieved was $0.183s^{-1}$ for both tests. The variations in strain rate below strains of 0.03 have a clear effect on the flow stress. There are peaks in the flow curves, at identical strains to the peaks in the strain rates.

The tests at nominal strain rates of $2s^{-1}$ (tests B and C) showed a similar trend to those at $0.2s^{-1}$. There was an initial drop in strain rate at strains below 0.006, immediately followed by a peak in strain rate between 0.006 and 0.08, after which the machine achieved a near constant strain rate. Once control was achieved after a strain of 0.08, the strain rate of test B was $1.82s^{-1}$. For test C, the strain rate decreased slightly from $1.84s^{-1}$ to $1.76s^{-1}$ by the end of deformation. The variations in strain rate below strains of 0.08 have a clear effect on the flow stress, with peaks in the flow curves, at identical strains to the peaks in the strain rates.

For the test at a nominal strain rate of $20s^{-1}$ (test A), there was an initial drop in strain rate, after which the strain rate recovered to achieve a controlled strain rate after a strain of 0.09. Once control was achieved, the strain rate was initially $20.2s^{-1}$, decreasing steadily to $18.3s^{-1}$ near the end of the deformation. In the final 0.07 of applied strain, the strain rate decreased from $18.3s^{-1}$ to $0s^{-1}$. The lower strain rates during initial and final deformation have a clear effect on the corresponding flow curve.

The examination of the strain rate control shows that there are significant strain rate effects on the flow curves at low strains for tests A to E and additionally for the final strain applied in test A. The peaks in the flow curves at low strains for the intermediate strain rate tests (tests B to E) must be at least partly due to the peak in the corresponding strain rate. The absence of a peak in the flow curves for tests A and F, when there is no corresponding peak in strain rate, would suggest that the peaks in the flow curves for the intermediate strain rates are in fact purely a strain rate effect. In order to confirm whether this is the case, the curves require a correction for the variations in strain rate to reveal the true shape of the flow curve at low strains.

The curves were corrected for variations in flow stress by calculating the strain rate sensitivity of the material. A general relationship between flow stress and strain rate, at constant strain and temperature is given by (Dieter, 1989):

$$\sigma = C(\dot{\varepsilon})^m\Big|_{\varepsilon,T} \tag{8.22}$$

where m is the strain rate sensitivity and C is a constant. The values of C and m can be obtained from the slope and intercept respectively of a plot of $\log\sigma$ vs. $\log\dot{\varepsilon}$, which should yield a straight line. The values used for this plot were obtained by taking the instantaneous flow stress and strain rate from each curve at a strain of 0.12. A strain of 0.12 was chosen because this was the lowest strain at which a controlled strain rate was achieved for all tests. At increasing strains, the specimen temperatures became increasingly different for different strain rates due to a combination of deformation heating and heat losses to or from the surroundings. The flow stress, strain rate and temperature data at a strain of 0.12 are shown for each test in Table 8.3 and the data plotted using logarithmic axes in Fig. 8.16.

Table 8.3 Flow stress, strain rate and temperature data at a strain of 0.12.

* Uncertainty exists over the accuracy of this temperature reading

	$\sigma_{0.12}$ (N mm^{-2})	$\dot{\varepsilon}_{0.12}$	$T_{0.12}$ (°C)
A	195.1	20.2	1010
B	118.4	1.82	998
C	117.4	1.84	1003
D	66.9	0.183	1002
E	68.5	0.183	1002
F	33.3	0.0188	988*

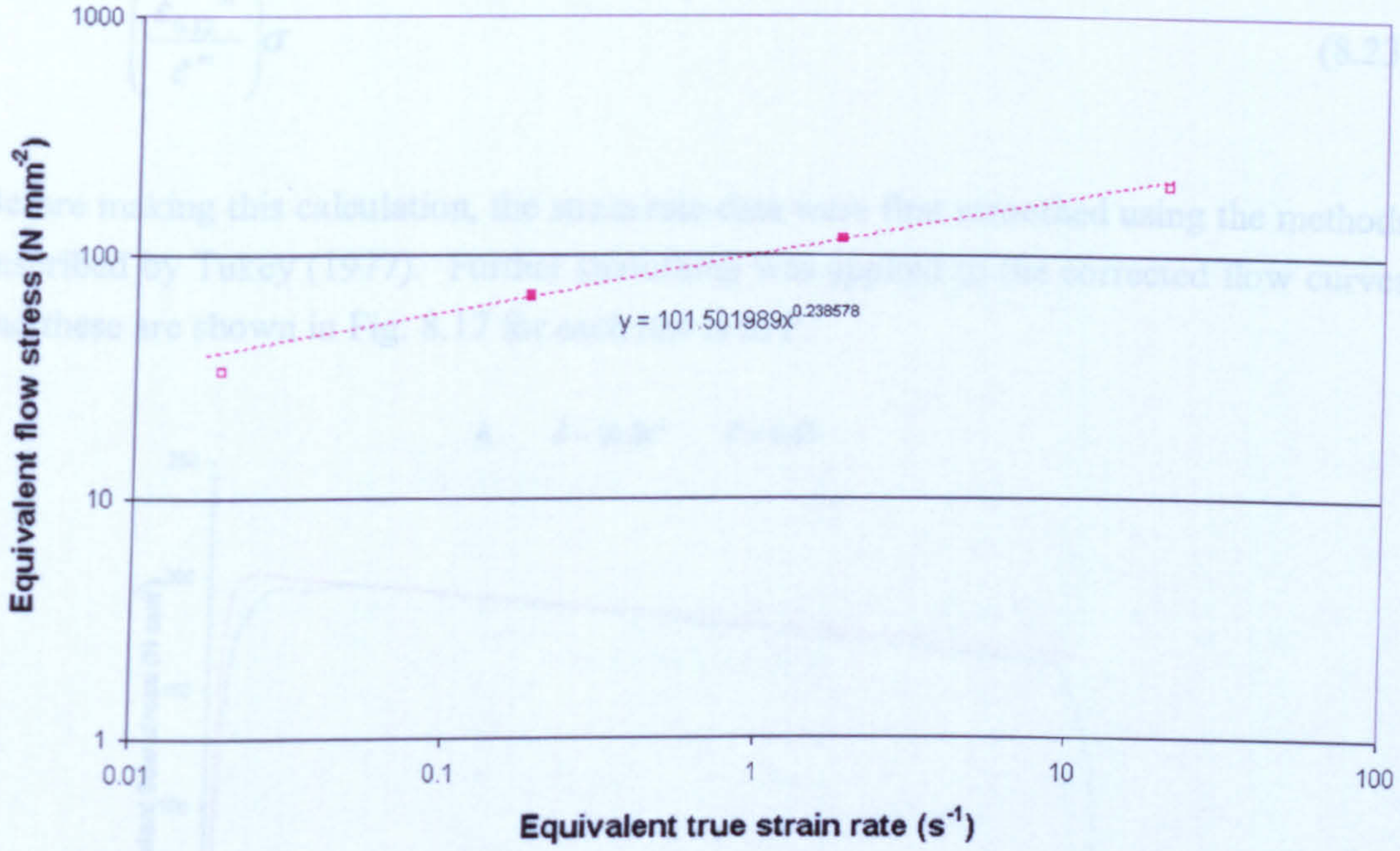

Fig. 8.16 Flow stress vs. strain rate for $\bar{\varepsilon} = 0.12$.

It can be seen from Fig. 8.16 that there is a good linear fit to the plot of $\log\sigma$ vs. $\log\dot{\varepsilon}$. The straight line used to determine C and m was a line fitted to the data points for Tests C, D and E because the temperatures of these specimens were within 1°C at a strain of 0.12. The straight line fitted to the data gave a value of 101.5 for C and a value of 0.239 for the strain rate sensitivity m at 1002°C (1275K).

The high strain rate point (Test A) falls slightly below the trend line, which can be explained by the higher temperature of this specimen (1010°C) compared to the other points. The slowest strain rate point (Test F) did not require any corrections for strain rate; however it is interesting to note that the data point for this test also falls below the trend line in Fig. 8.16. The lower specimen temperature of 988°C for test F suggests that it should in fact lie above the line i.e. have a higher flow stress. This may indicate that the logarithmic relationship does not describe the relationship between flow stress and strain rate as well at low strain rates (<~$0.1s^{-1}$). However, there was uncertainty in the accuracy of the temperature measurements for test F and the strain rate was such that there was time for significant microstructural changes to occur both between the end of the solution treatment and the start of deformation and during the deformation itself, which may explain this point.

The flow stress data for each test were strain rate corrected to the instantaneous strain rate at a strain of 0.12 in the following equation using the previously determined strain rate sensitivity m.

$$\left(\frac{\dot{\varepsilon}_{0.12}{}^{m}}{\dot{\varepsilon}^{m}}\right)\sigma \tag{8.23}$$

Before making this calculation, the strain rate data were first smoothed using the methods described by Tukey (1977). Further smoothing was applied to the corrected flow curves and these are shown in Fig. 8.17 for each test A to F.

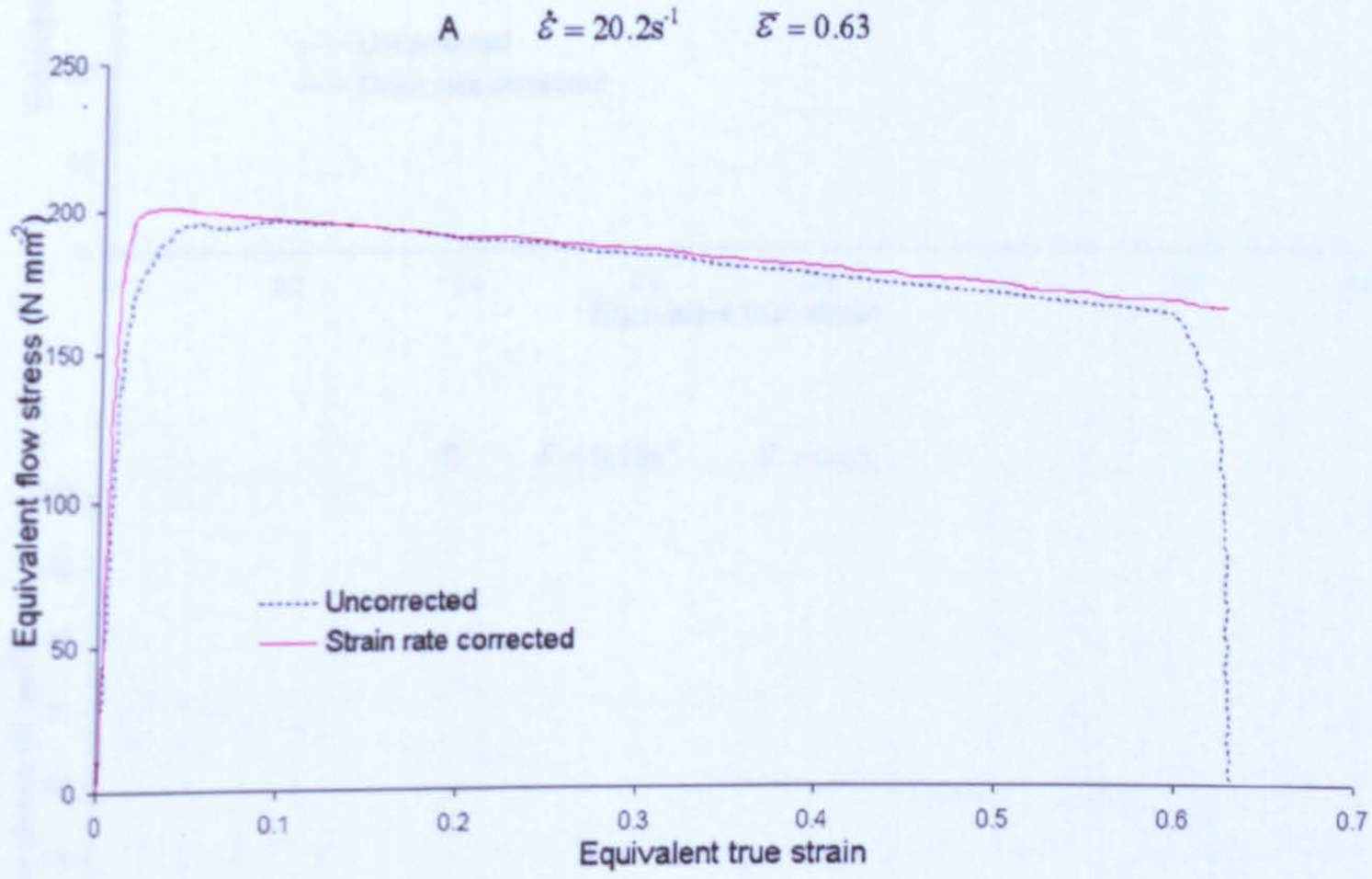

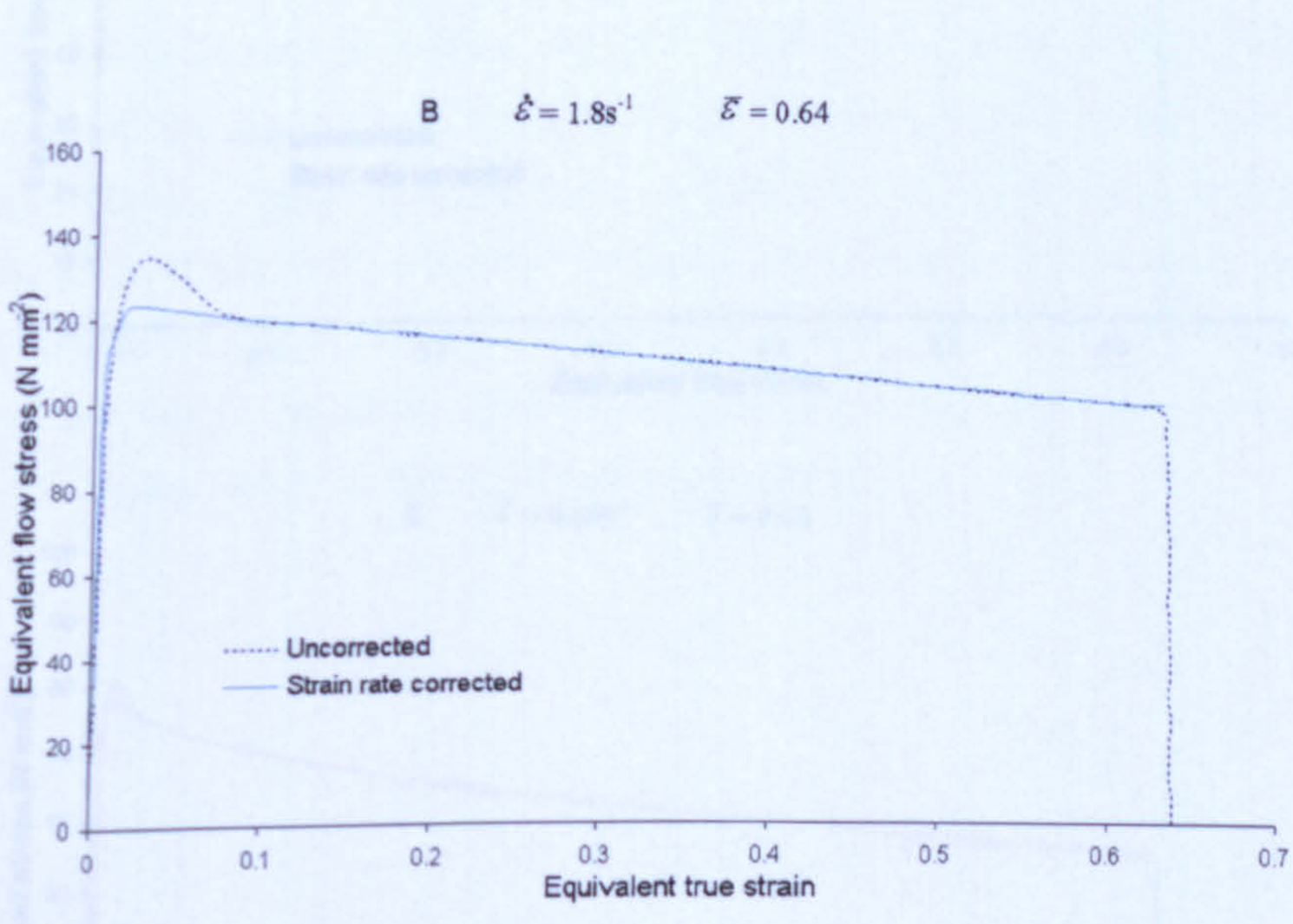

C $\dot{\bar{\varepsilon}} = 1.8s^{-1}$ $\bar{\varepsilon} = 1.23$

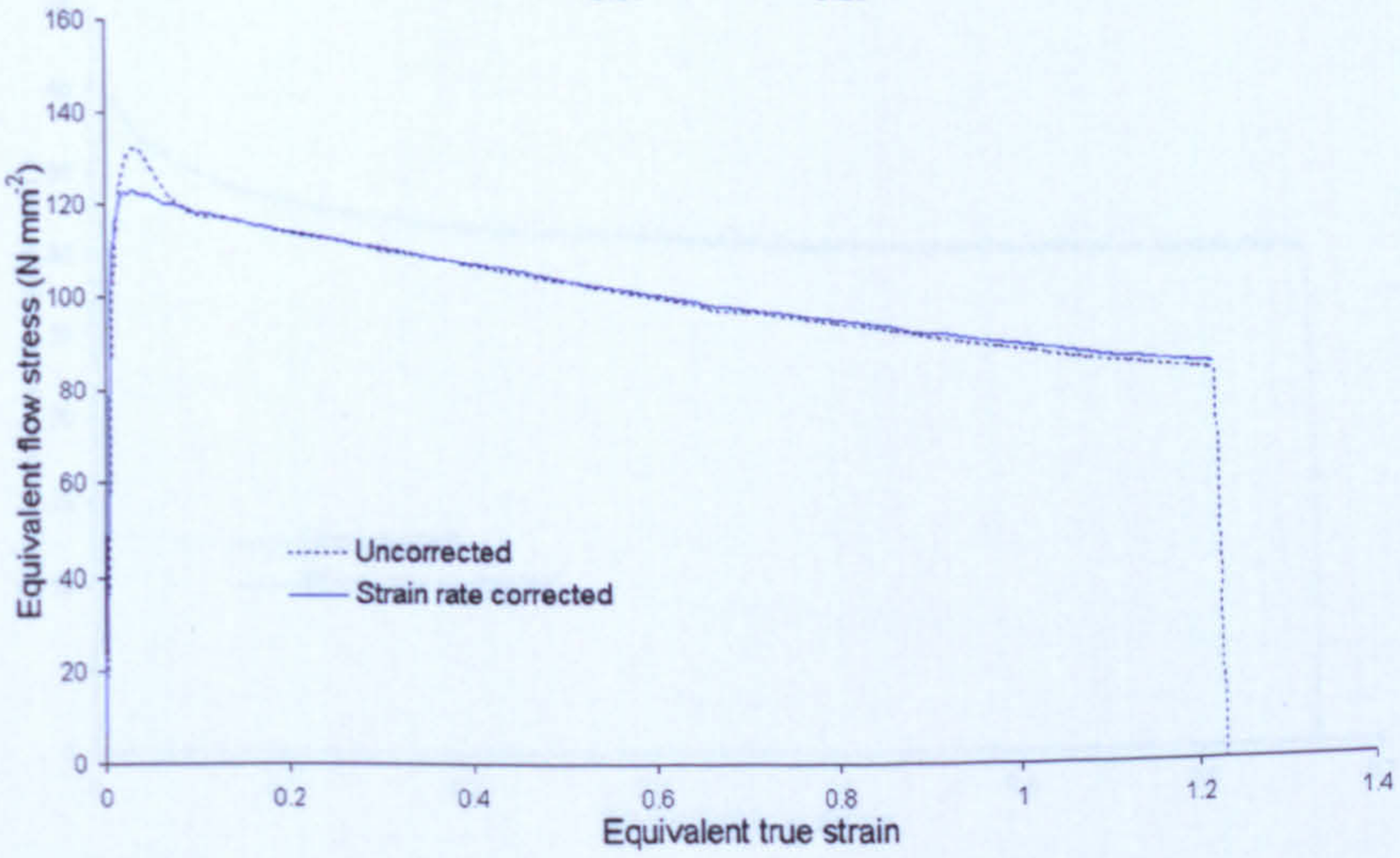

D $\dot{\bar{\varepsilon}} = 0.18s^{-1}$ $\bar{\varepsilon} = 0.63$

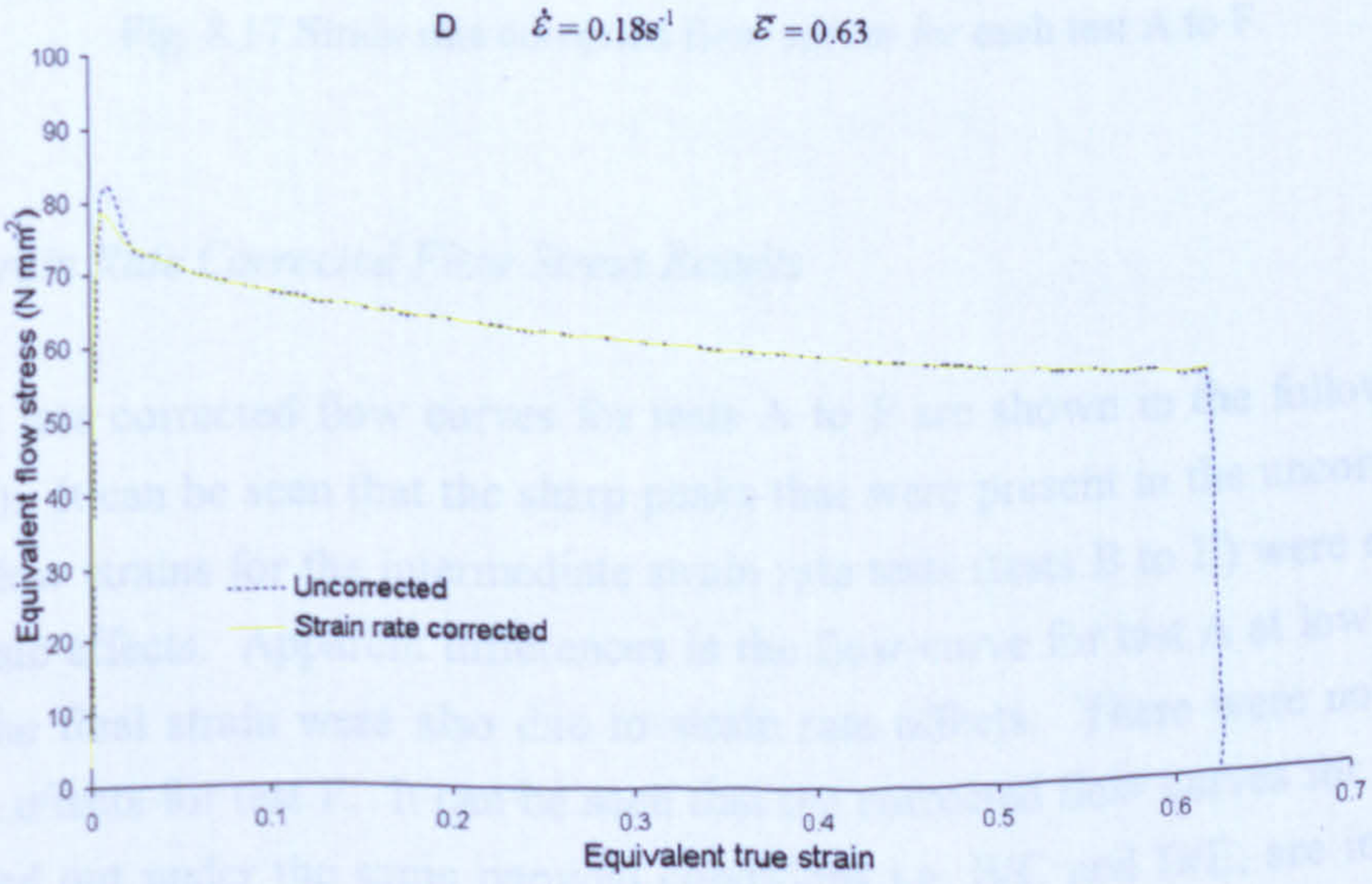

E $\dot{\bar{\varepsilon}} = 0.18s^{-1}$ $\bar{\varepsilon} = 0.63$

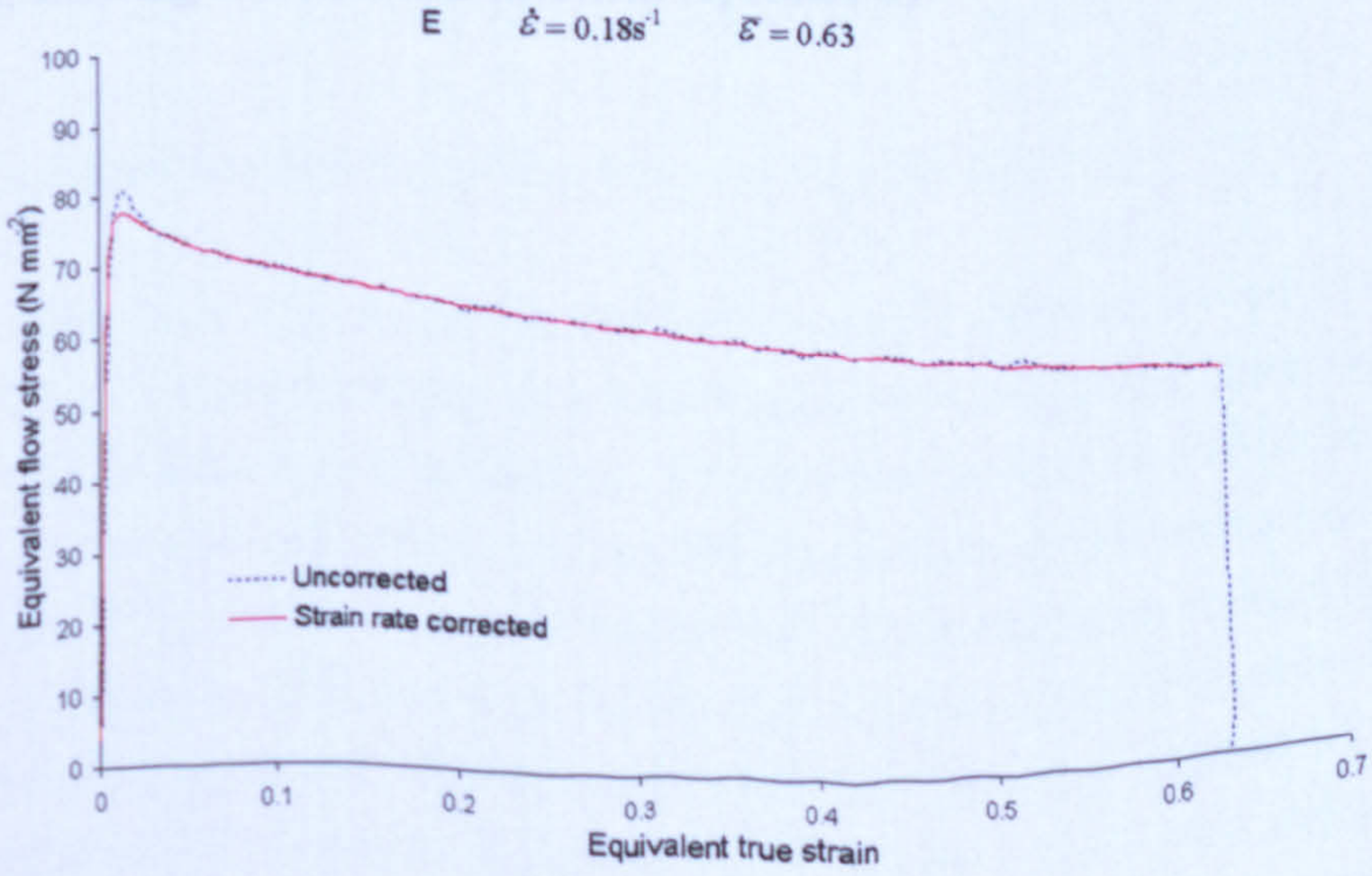

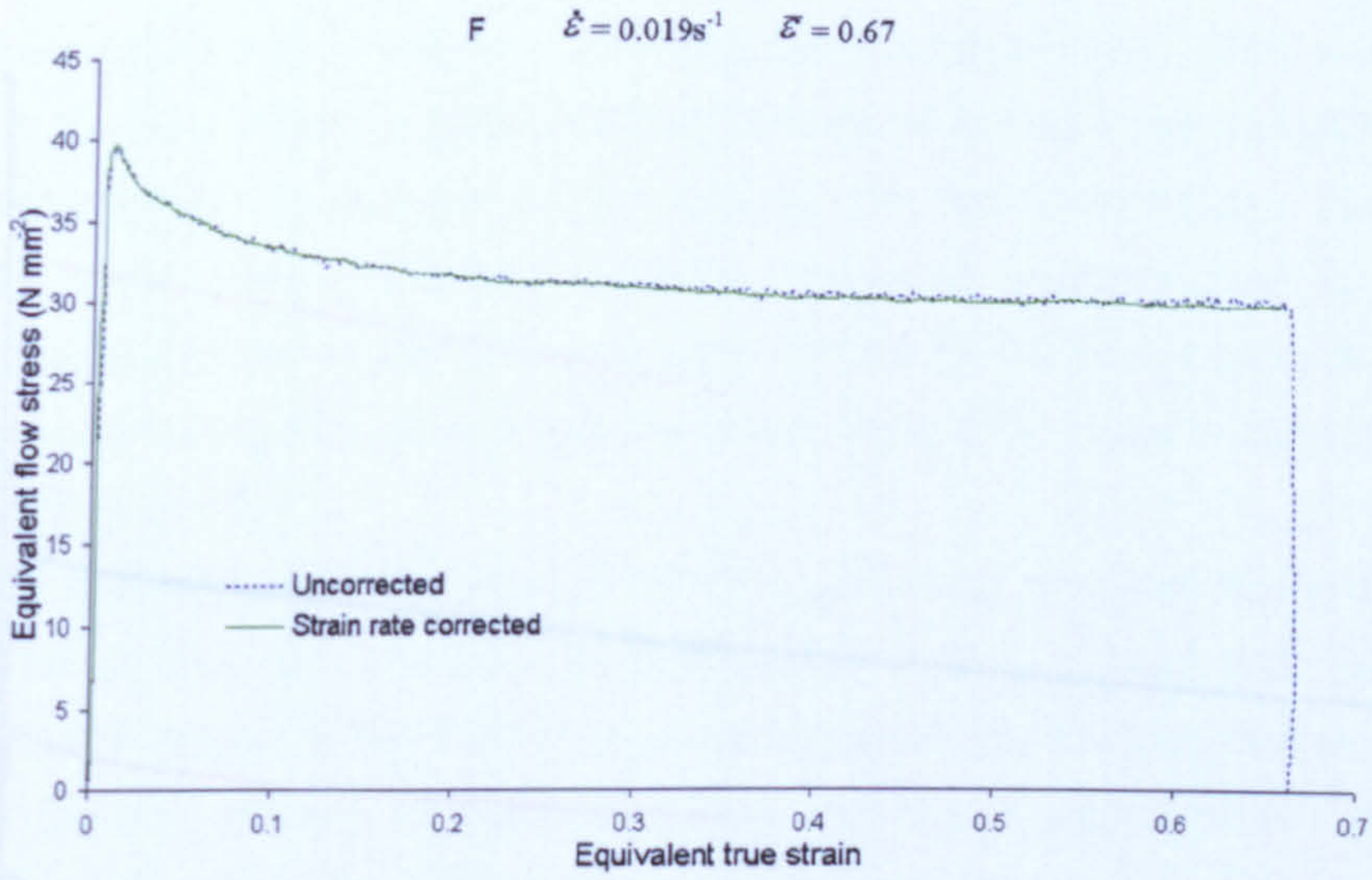

Fig. 8.17 Strain rate corrected flow curves for each test A to F.

8.2.1.5 Strain Rate Corrected Flow Stress Results

The strain rate corrected flow curves for tests A to F are shown in the following figure (Fig. 8.18). It can be seen that the sharp peaks that were present in the uncorrected flow curves at low strains for the intermediate strain rate tests (tests B to E) were entirely due to strain rate effects. Apparent differences in the flow curve for test A at low strains and close to the final strain were also due to strain rate effects. There were no significant strain rate effects for test F. It can be seen that the corrected flow curves for the pairs of tests carried out under the same nominal conditions i.e. B/C and D/E, are in very close agreement, showing that tests had excellent repeatability.

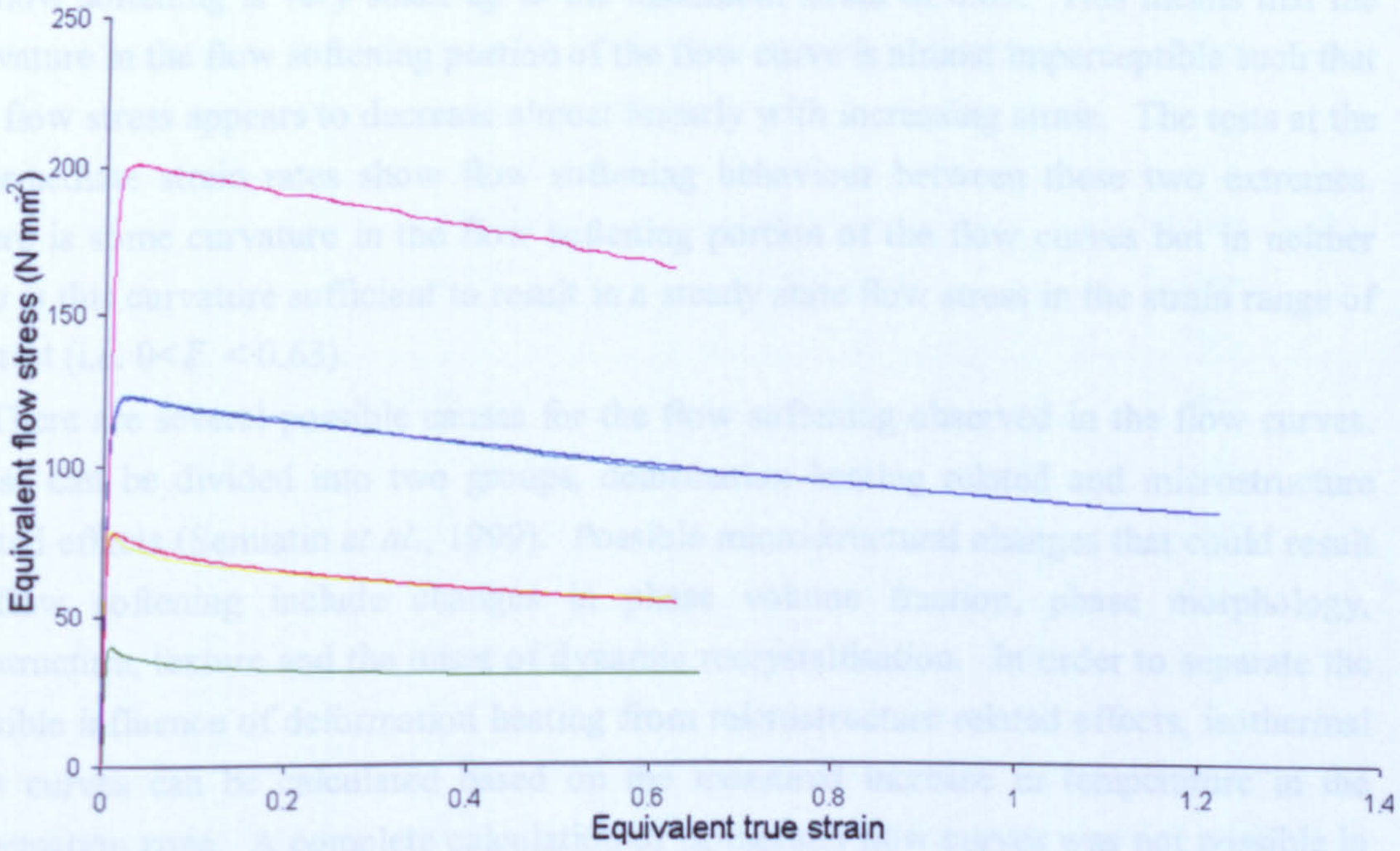

—	A	$\dot{\varepsilon} = 20.2\text{s}^{-1}$	$\bar{\varepsilon} = 0.63$
—	B	$\dot{\varepsilon} = 1.8\text{s}^{-1}$	$\bar{\varepsilon} = 0.64$
—	C	$\dot{\varepsilon} = 1.8\text{s}^{-1}$	$\bar{\varepsilon} = 1.23$
—	D	$\dot{\varepsilon} = 0.18\text{s}^{-1}$	$\bar{\varepsilon} = 0.63$
—	E	$\dot{\varepsilon} = 0.18\text{s}^{-1}$	$\bar{\varepsilon} = 0.63$
—	F	$\dot{\varepsilon} = 0.019\text{s}^{-1}$	$\bar{\varepsilon} = 0.67$

Fig. 8.18 Strain rate corrected flow curves.

8.2.1.6 Flow Softening Behaviour: Deformation Heating Effects

It can be seen from Fig. 8.18, that the deformation behaviour for all strain rates is characterised by a rapid hardening to a peak stress at a relatively low strain and thereafter all of the curves exhibit flow softening. The greatest amount of flow softening occurs immediately after the peak stress and then decreases steadily with increasing strain. The extent to which the flow softening decreases with increasing strain depends on the strain rate. For the slowest strain rate (test F), the flow softening decreases more rapidly for a given increase in strain, so that a steady state flow stress is reached by a strain of approximately 0.4. This results in a pronounced curvature in the flow softening portion of the flow curve. In contrast, for the highest strain rate (test A), the decrease in the rate

of flow softening is very small up to the maximum strain of 0.63. This means that the curvature in the flow softening portion of the flow curve is almost imperceptible such that the flow stress appears to decrease almost linearly with increasing strain. The tests at the intermediate strain rates show flow softening behaviour between these two extremes. There is some curvature in the flow softening portion of the flow curves but in neither case is this curvature sufficient to result in a steady state flow stress in the strain range of the test (i.e. $0<\bar{\varepsilon}<0.63$).

There are several possible causes for the flow softening observed in the flow curves. These can be divided into two groups, deformation heating related and microstructure related effects (Semiatin *et al.*, 1999). Possible microstructural changes that could result in flow softening include changes in phase volume fraction, phase morphology, substructure, texture and the onset of dynamic recrystallisation. In order to separate the possible influence of deformation heating from microstructure related effects, isothermal flow curves can be calculated based on the measured increase in temperature in the deformation zone. A complete calculation of isothermal flow curves was not possible in the present work as this correction requires more extensive testing at a range of temperatures in order to determine the effect of temperature on flow stress. The isothermal correction also has an added complication in the case of a duplex microstructure because the volume fractions of the phases changes with temperature but in the case of deformation heating, these changes will not be the same as the equilibrium volume fraction predicted by the β approach curve, particularly for high strain rates because there is insufficient time for the equilibrium volume fractions to develop. Although this work cannot include a thorough correction for the effects of deformation heating, the following discussion considers the likely contribution of deformation heating to the observed flow softening.

During the course of each test, temperature measurements from the thermocouple located in the deformation zone of each specimen were recorded to show the effects of deformation heating. No data was recorded for test F ($\dot{\varepsilon}=0.019s^{-1}$) due to failure of the thermocouple. For the other tests (A to E), there was an initial drop in temperature when the specimen was transferred from the FTTU to the deformation furnace, followed by significant deformation heating. The overall changes in specimen temperature due to deformation heating are summarised in Table 8.4. For the purpose of this simple estimation of the magnitude of the deformation heating related softening, it was assumed that the temperature within the deformation zone was homogenous and increased linearly with increasing strain from the temperature at the start of deformation through the maximum measured temperature at the final strain.

Table 8.4 Measured temperature changes in the deformation zone resulting from deformation heating.

Test	Test conditions $\dot{\varepsilon}$ & final $\bar{\varepsilon}$	Temperature at start of deformation (°C)	Max. temperature after final strain (°C)
A	$20.2s^{-1}$ & 0.63	1004	1033
B	$1.8s^{-1}$ & 0.64	1004	1024
C	$1.8s^{-1}$ & 1.23	1005	1032
D	$0.18s^{-1}$ & 0.63	1004	1017
F	$0.019s^{-1}$ & 0.67	No data	

To understand the effect of the temperatures changes on flow stress, data from the literature were examined to enable estimates to be made for the approximate temperature dependency of flow stress. Data for Timetal 834 for various strain rates in the temperature range of interest i.e. from 1000 to 1030°C are shown in Fig. 8.19. It can be seen that the temperature dependency of flow stress decreases with decreasing strain rate. As the temperature range of interest for the deformation heating is relatively small, a reasonable approximation for the temperature dependency of flow stress can be made using the gradient of a straight line fitted to the data in this temperature range at each strain rate. The data from Thomas (2007) was acquired on the same thermomechanical apparatus as the present work using the same nominal strain rates and the initial microstructures were also similar. Therefore, it was decided to base the estimates on the gradients of the lines fitted to this data (Table 8.5).

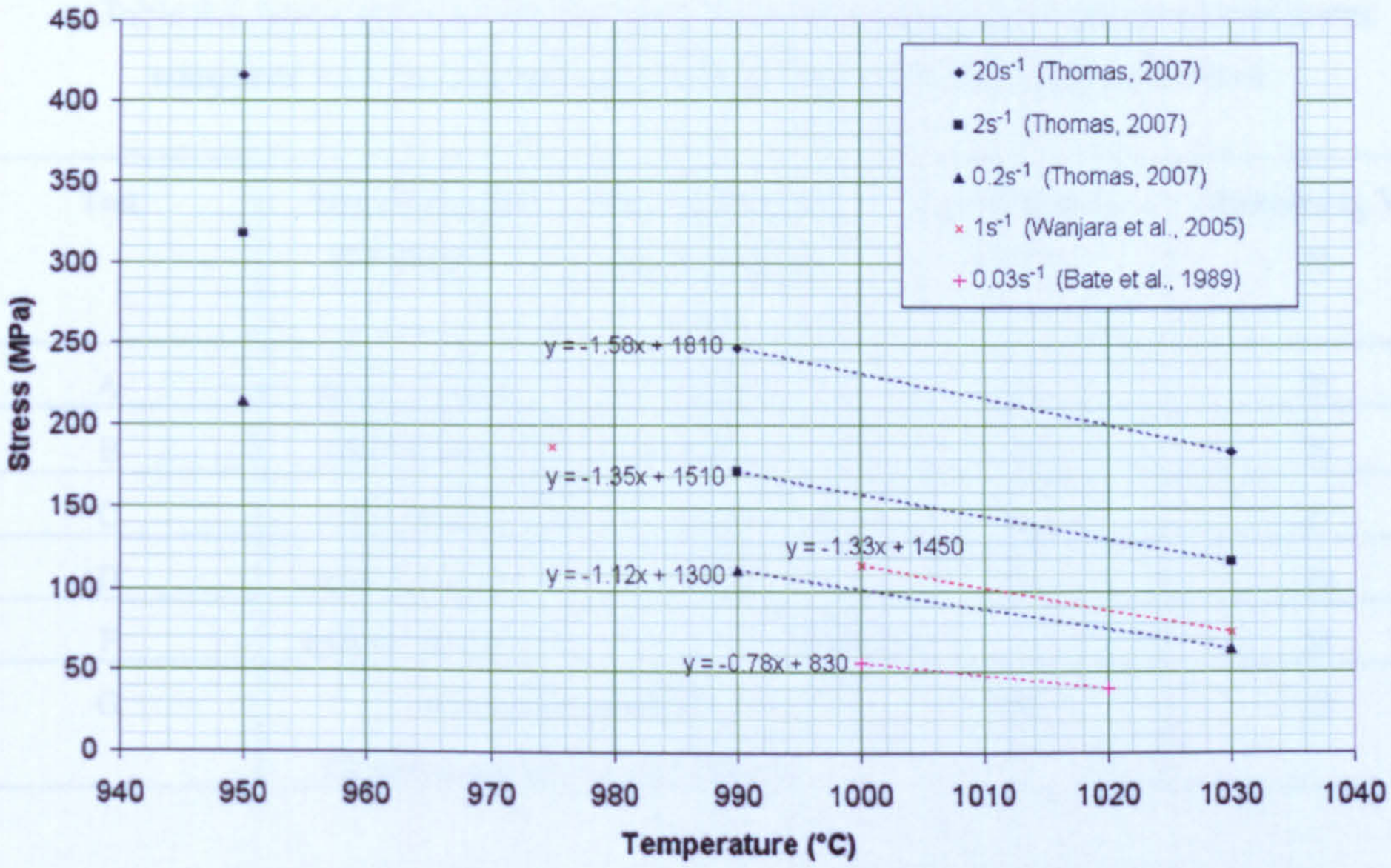

Fig. 8.19. Temperature dependency of the peak flow stress for Timetal 834 at various strain rates.

Table 8.5 Values used for the approximate temperature dependency of flow stress in the temperature range 1000-1030°C at three strain rates.

$\dot{\varepsilon}$ (s^{-1})	$\Delta\sigma / \Delta T$ (MPa $°C^{-1}$)
20.2	1.58
1.8	1.35
0.18	1.12

It should be noted that the values in Table 8.5 are based on flow stress data from hot compression tests at different temperatures i.e. 990°C and 1030°C. At the start of the compression tests at these test temperatures, the material was solution treated to allow the microstructure to develop the equilibrium volume fractions of α and β for these temperatures. In the case of the deformation heating in the present work, the volume fractions of α_p and β changed as the specimen temperature increased during the test but these changes were not in line with those predicted for phase equilibrium according to the β approach curve. The equilibrium values based on the maximum specimen temperature and the actual values based on point counting measurements are shown in Table 8.6 (optical microscopy results are shown in 8.2.2).

Table 8.6 Measured volume fractions of α_p in the deformed and quenched specimens compared with the expected equilibrium values from the β approach curve.

Test	Test conditions $\dot{\varepsilon}$ & final $\bar{\varepsilon}$	Max. temperature after final strain (°C)	Equilibrium α_p Vol. %	Measured α_p Vol. %
A	$20.2s^{-1}$ & 0.63	1033	8	27
B	$1.8s^{-1}$ & 0.64	1024	12	29
C	$1.8s^{-1}$ & 1.23	1032	8	27
D	$0.18s^{-1}$ & 0.63	1017	15	29
F	$0.019s^{-1}$ & 0.67	No data		24
G	Initial microstructure No deformation, WQ from 1010°C		26	33

It can be seen that the decreases in volume fraction of the α_p phase are relatively modest compared to the predicted equilibrium values. This means that the estimate of the deformation heating related flow softening, which is based on phase equilibrium is an upper estimate. The true deformation heating related softening will be lower because for a given specimen temperature, there will be more than the equilibrium value of the harder α_p phase in the microstructures.

Using the simplified linear temperature versus strain relationship for the temperature during the test and the values in Table 8.5 for the approximate temperature dependency, the flow stress data were corrected to the solution treatment temperature of 1010°C. The results of this approximate temperature correction are shown in Fig. 8.20 for tests A to D. It can be seen that the estimated contribution of deformation heating is comparable to the observed flow softening at all three strain rates, resulting in curves which show near steady state flow behaviour. For all three strain rates, after the approximate correction for deformation heating, the difference between the peak flow stress and the flow stress at the final strain is less than 10MPa. This suggests that deformation heating may account for the observed flow softening with no requirement for significant microstructure related flow softening to explain the flow behaviour.

A $\dot{\varepsilon} = 20.2s^{-1}$ $\bar{\varepsilon} = 0.63$

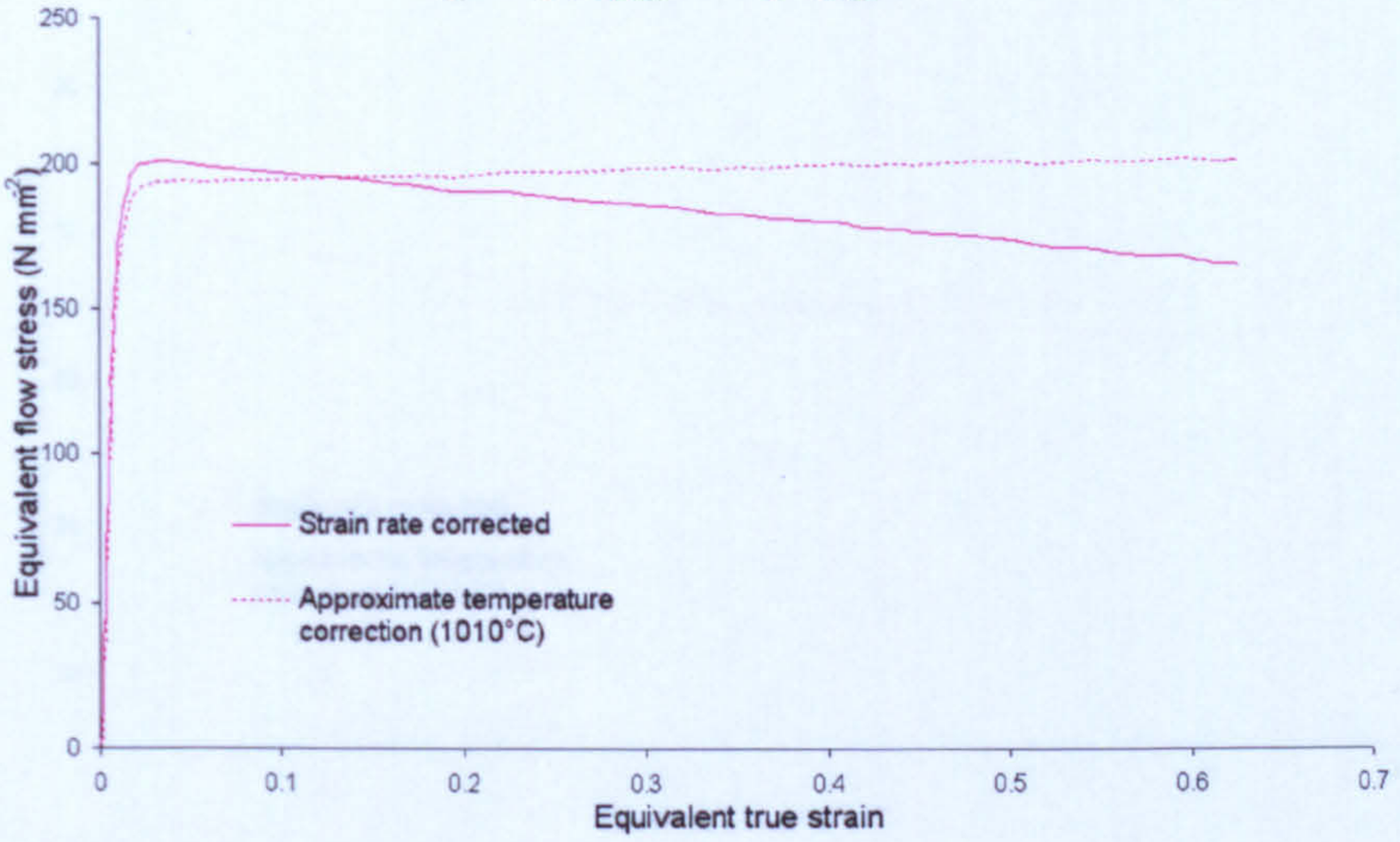

B $\dot{\varepsilon} = 1.8s^{-1}$ $\bar{\varepsilon} = 0.64$

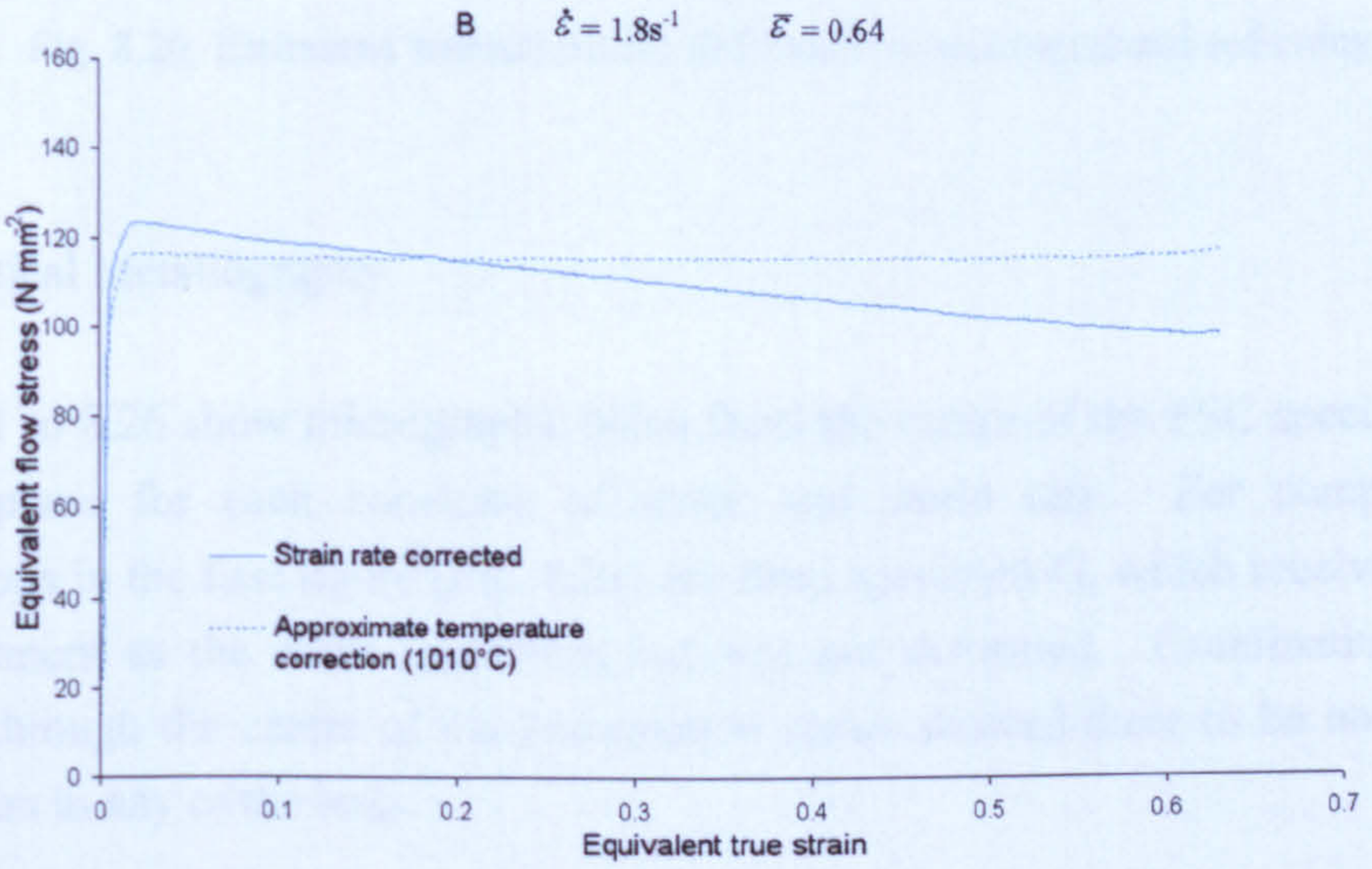

C $\dot{\varepsilon} = 1.8s^{-1}$ $\bar{\varepsilon} = 1.23$

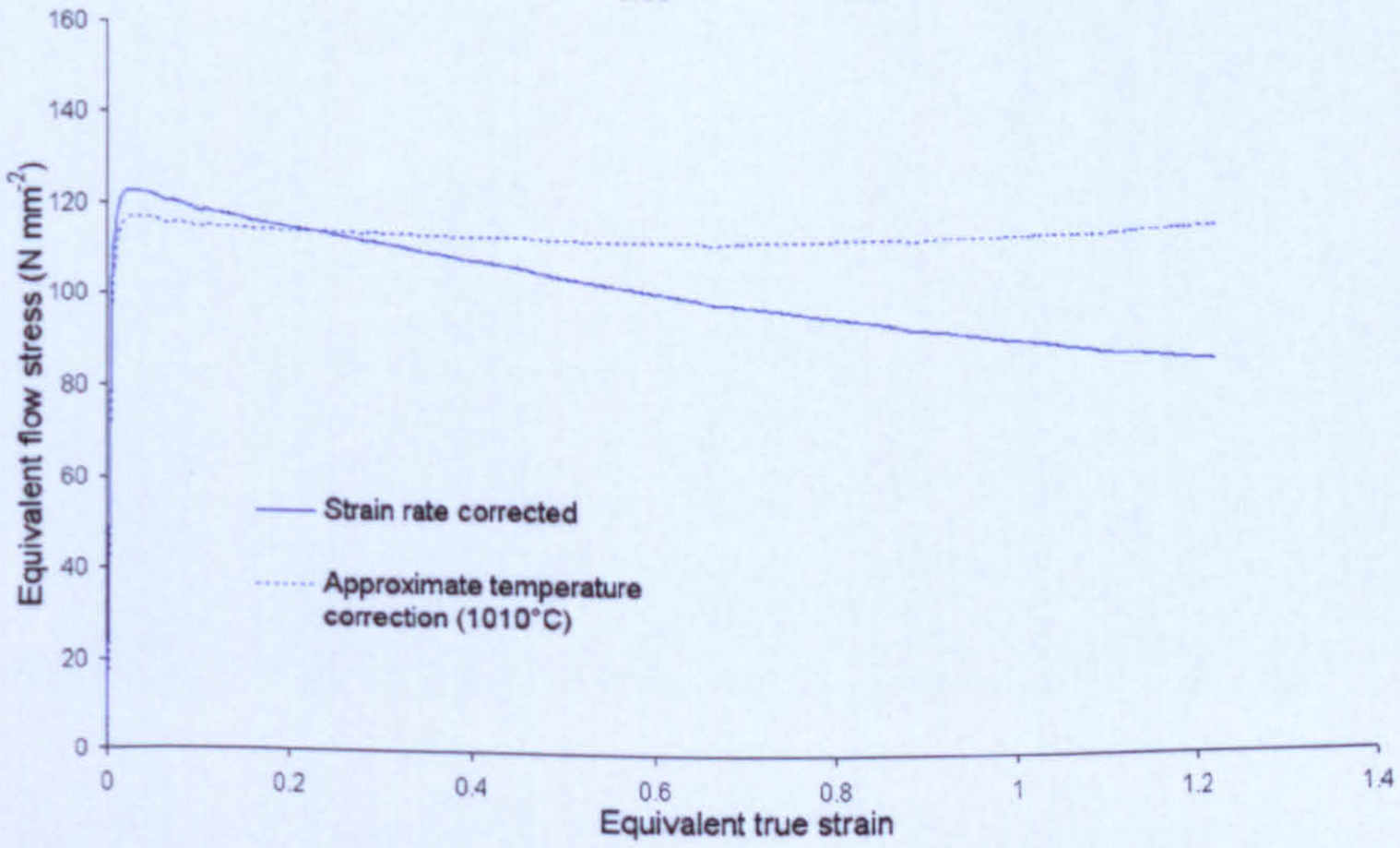

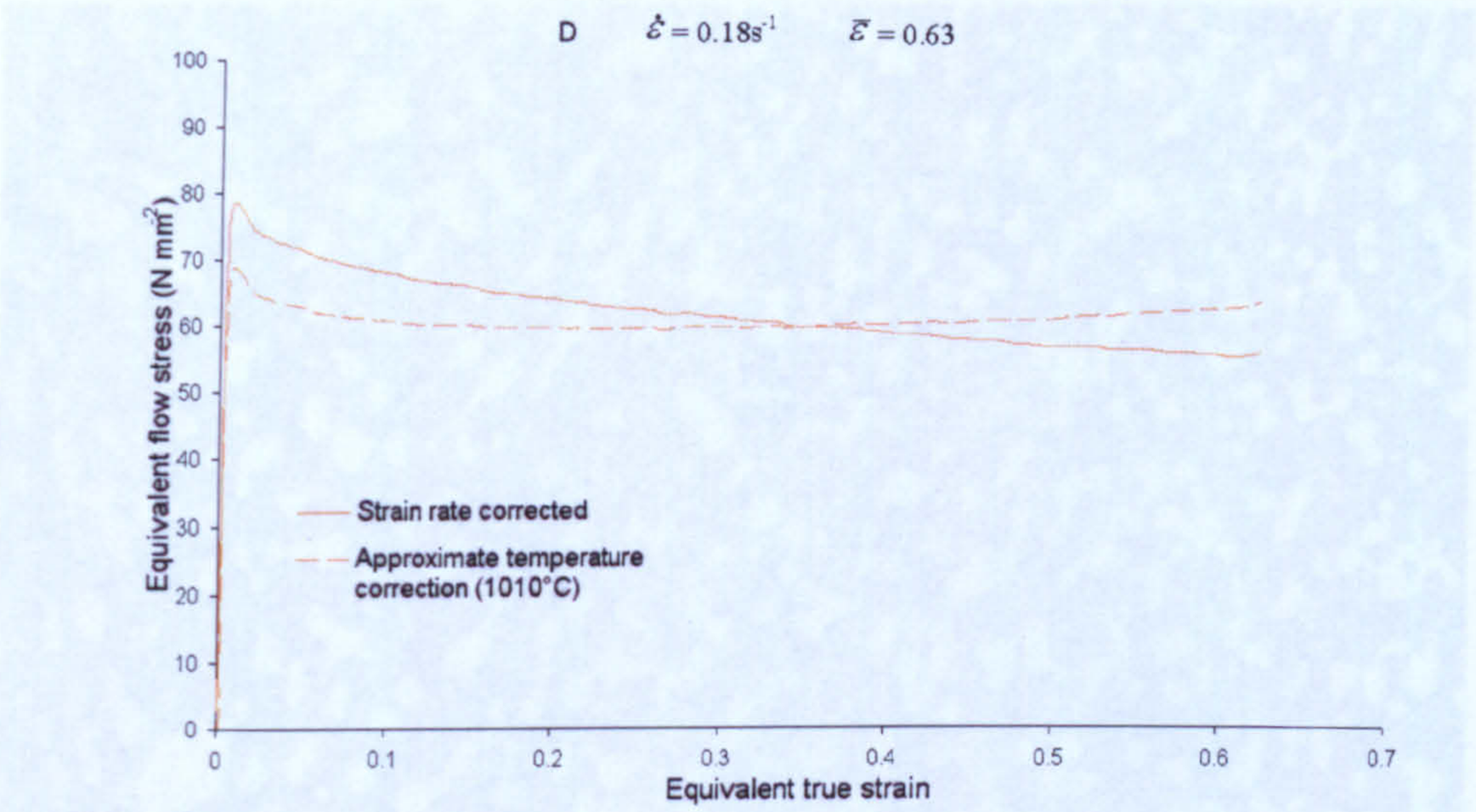

Fig. 8.20 Estimated corrections for deformation heating related softening.

8.2.2 Optical Metallography

Figs. 8.21 to 8.26 show micrographs, taken from the centre of the PSC specimens in the ND/RD plane for each condition of strain and strain rate. For comparison, the micrographs in the first figure (Fig. 8.21) are from specimen G, which received the same heat treatment as the other specimens but was not deformed. Examination of cross-sections through the centre of the deformation zones showed there to be no shear band localisation in any of the tests.

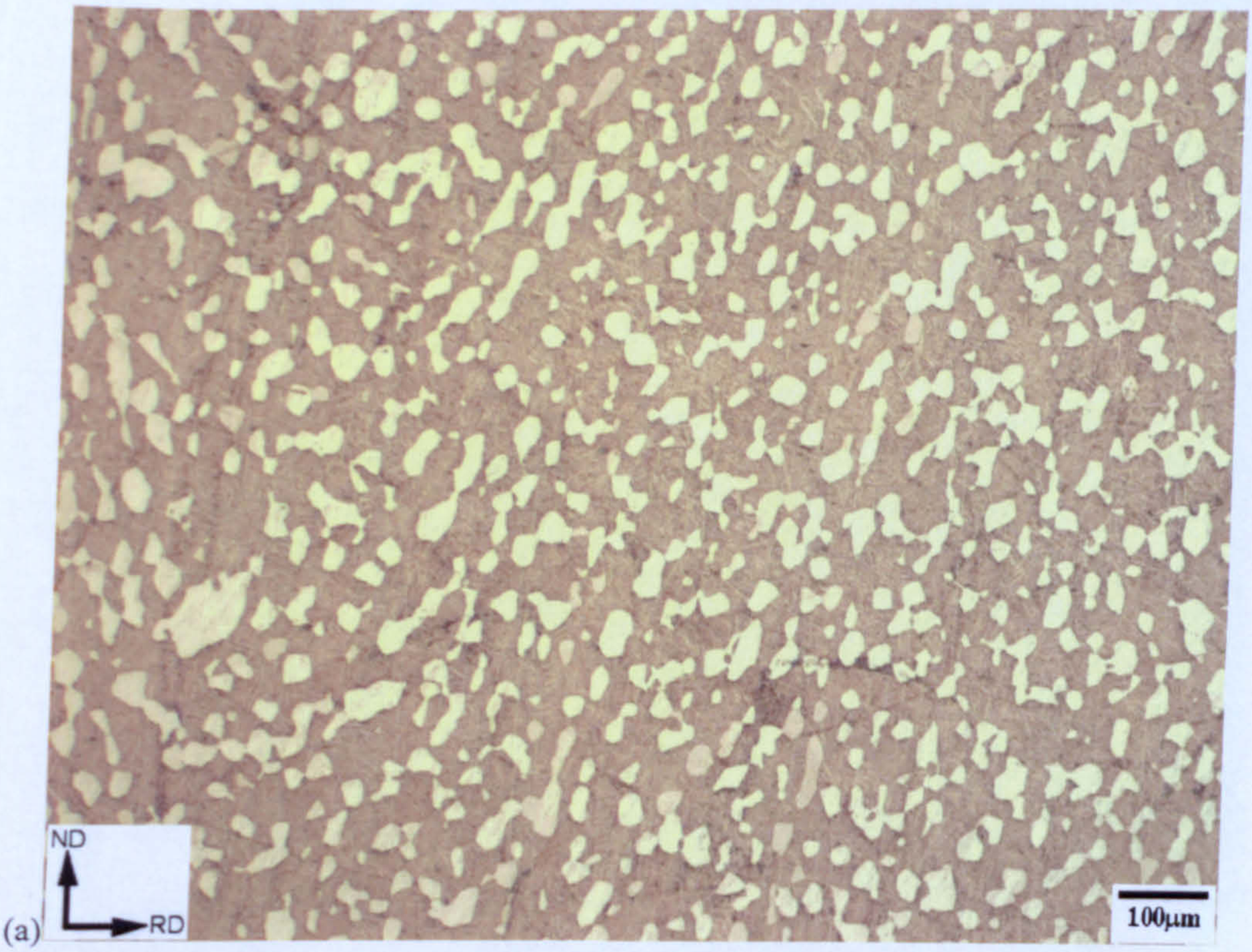

(a)

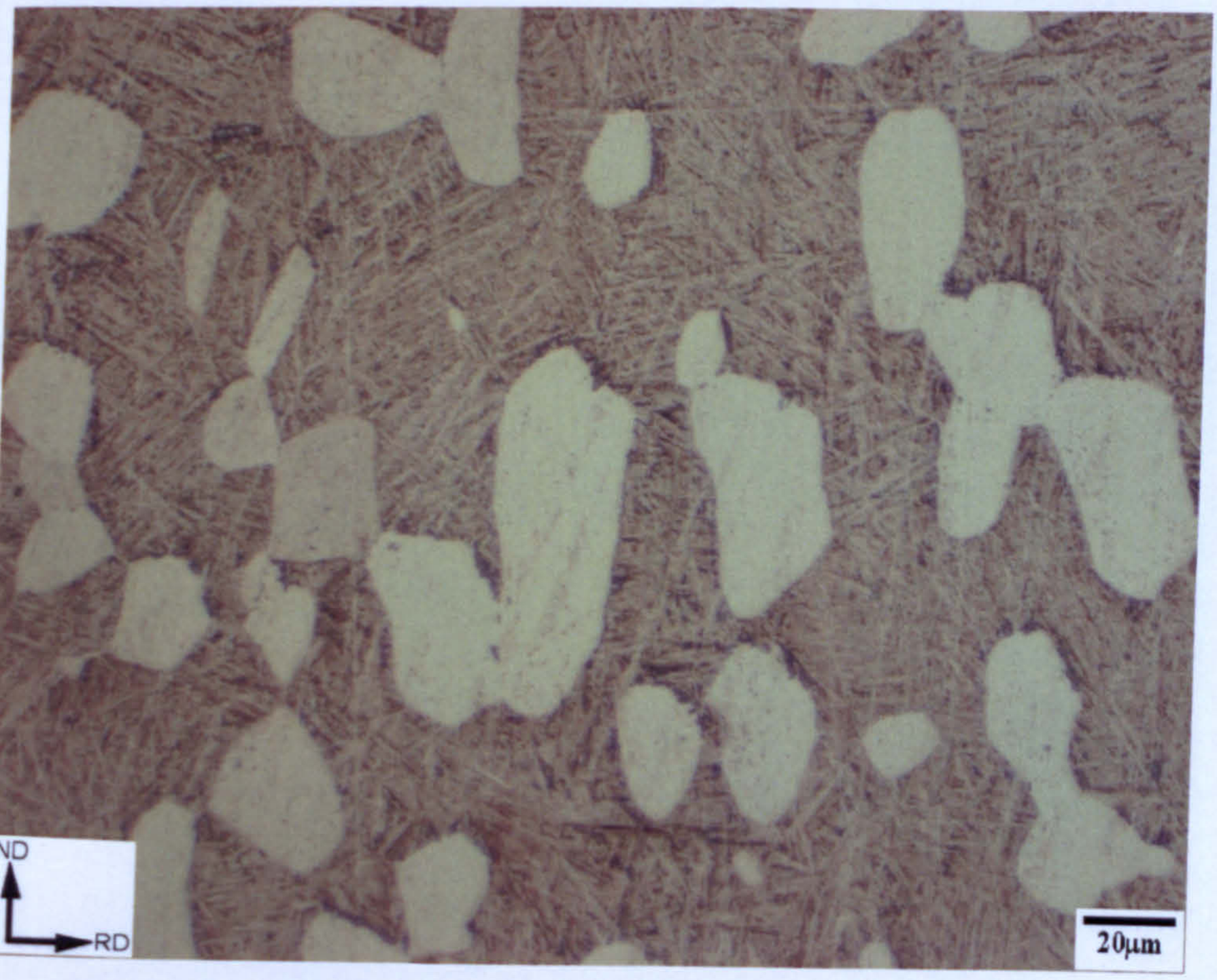

(b)

Fig. 8.21 Optical micrographs from the undeformed specimen G.

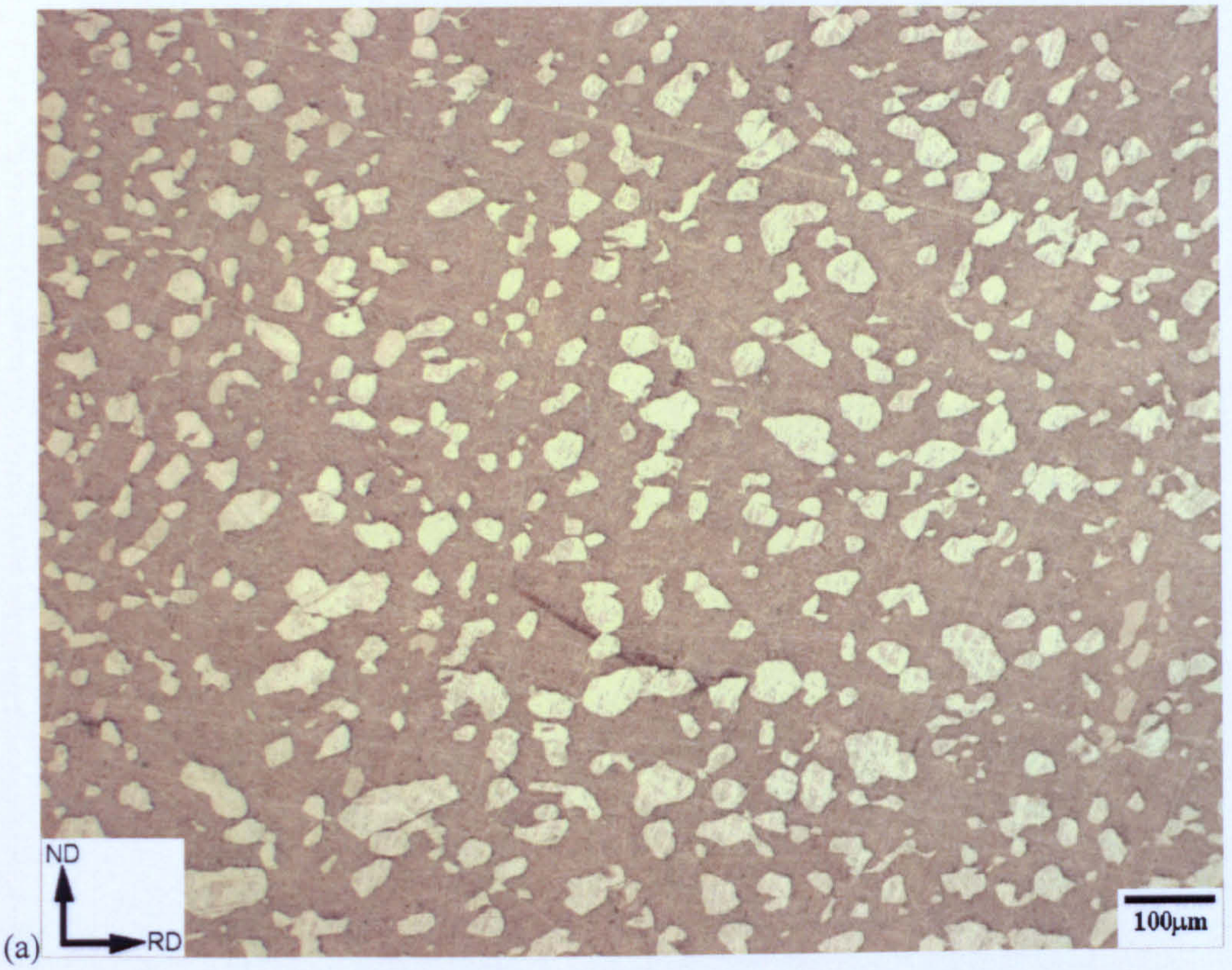

(a)

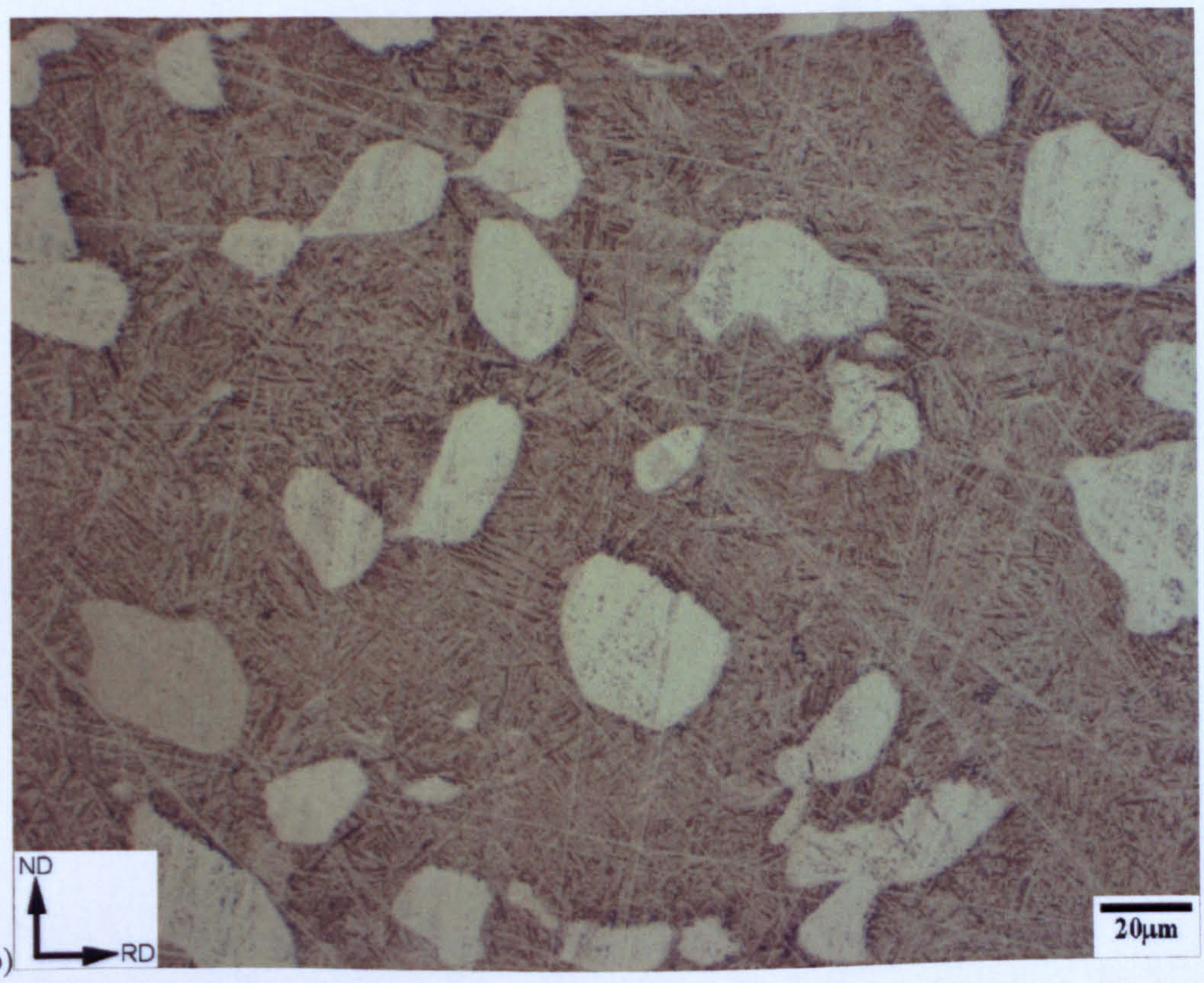

(b)

Fig. 8.22 Optical micrographs from specimen A, which was deformed at a true strain rate of $20.2s^{-1}$, to an equivalent true strain of 0.63.

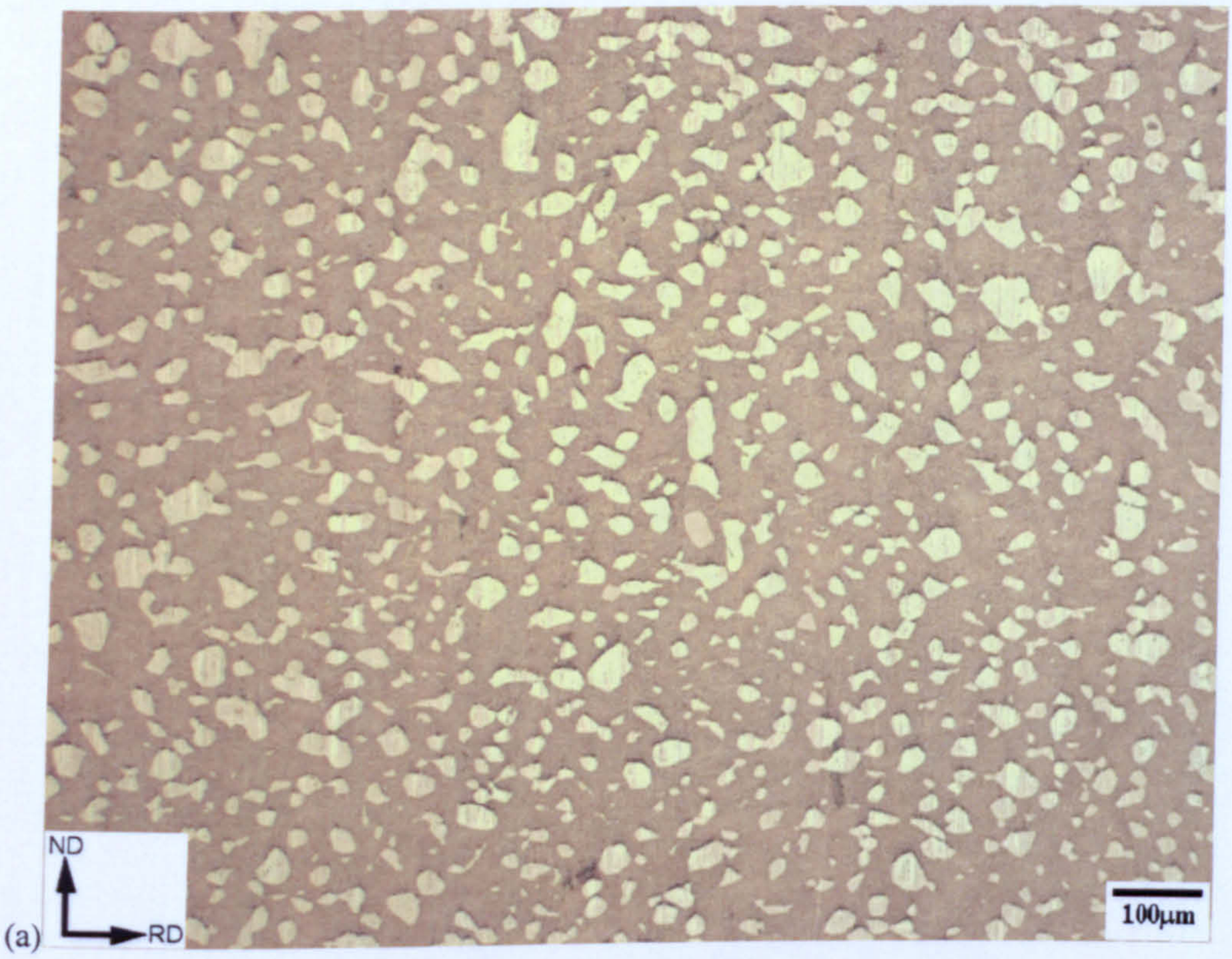

(a)

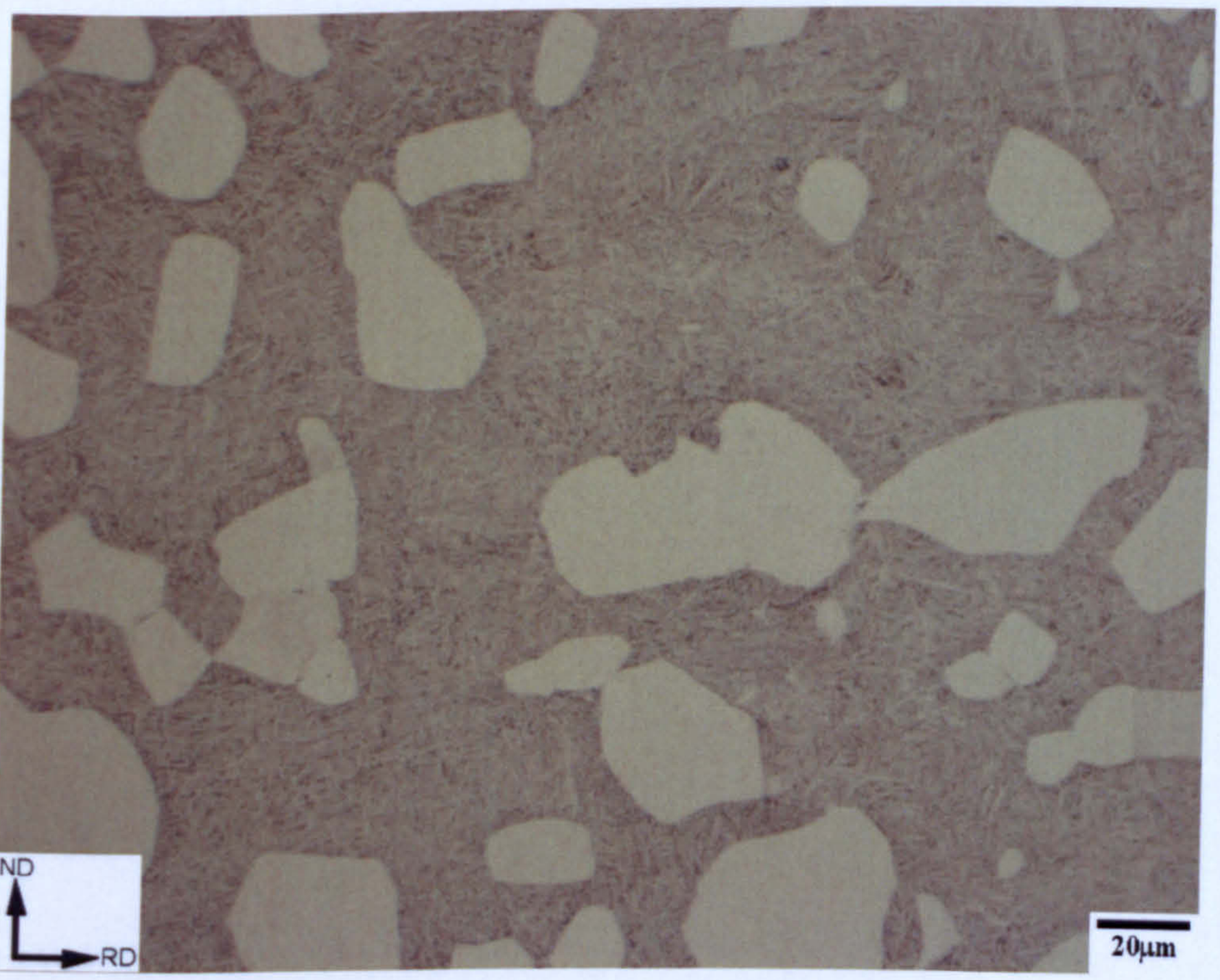

(b)

Fig. 8.23 Optical micrographs from specimen B, which was deformed at a true strain rate of $1.8s^{-1}$, to an equivalent true strain of 0.64.

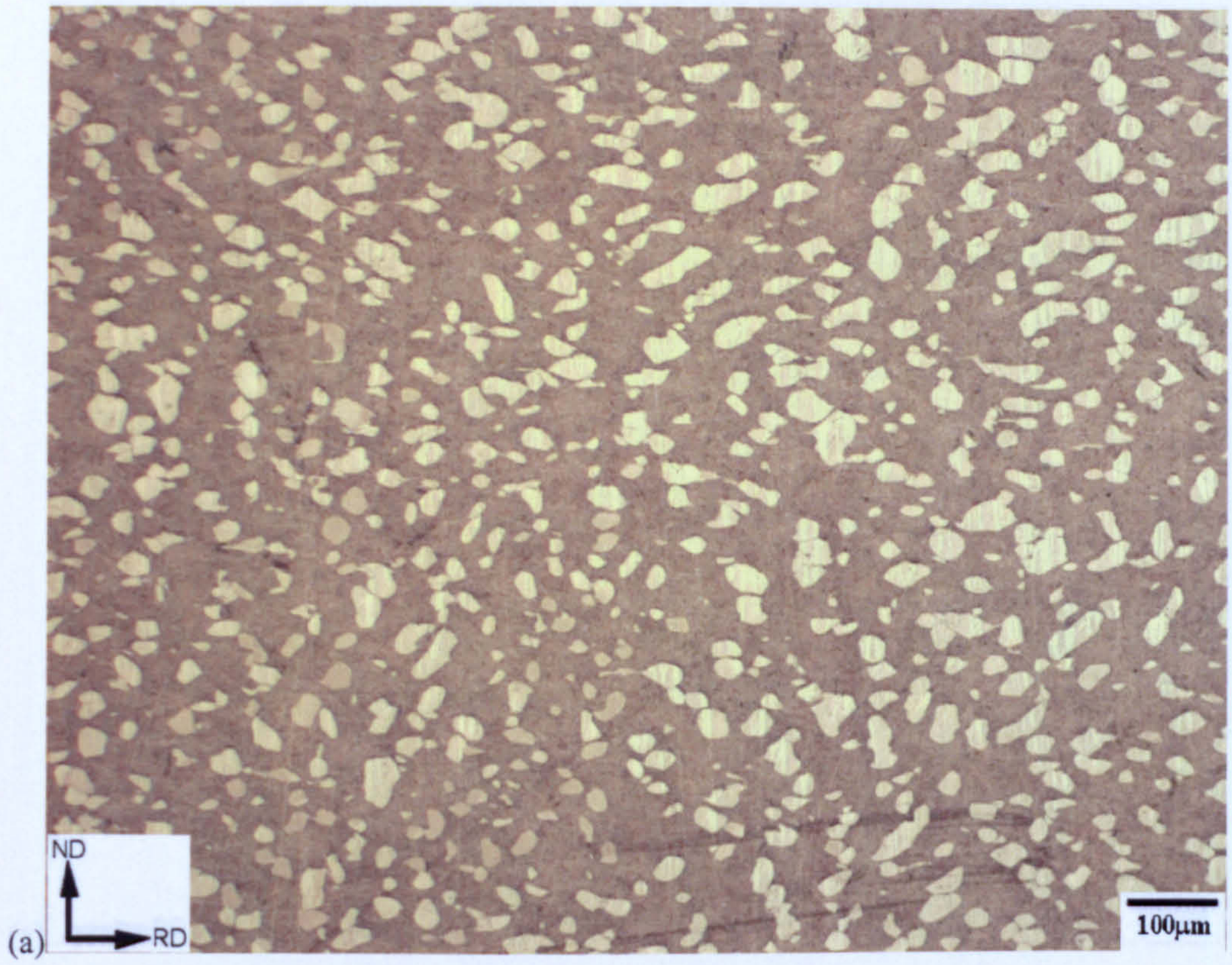

(a)

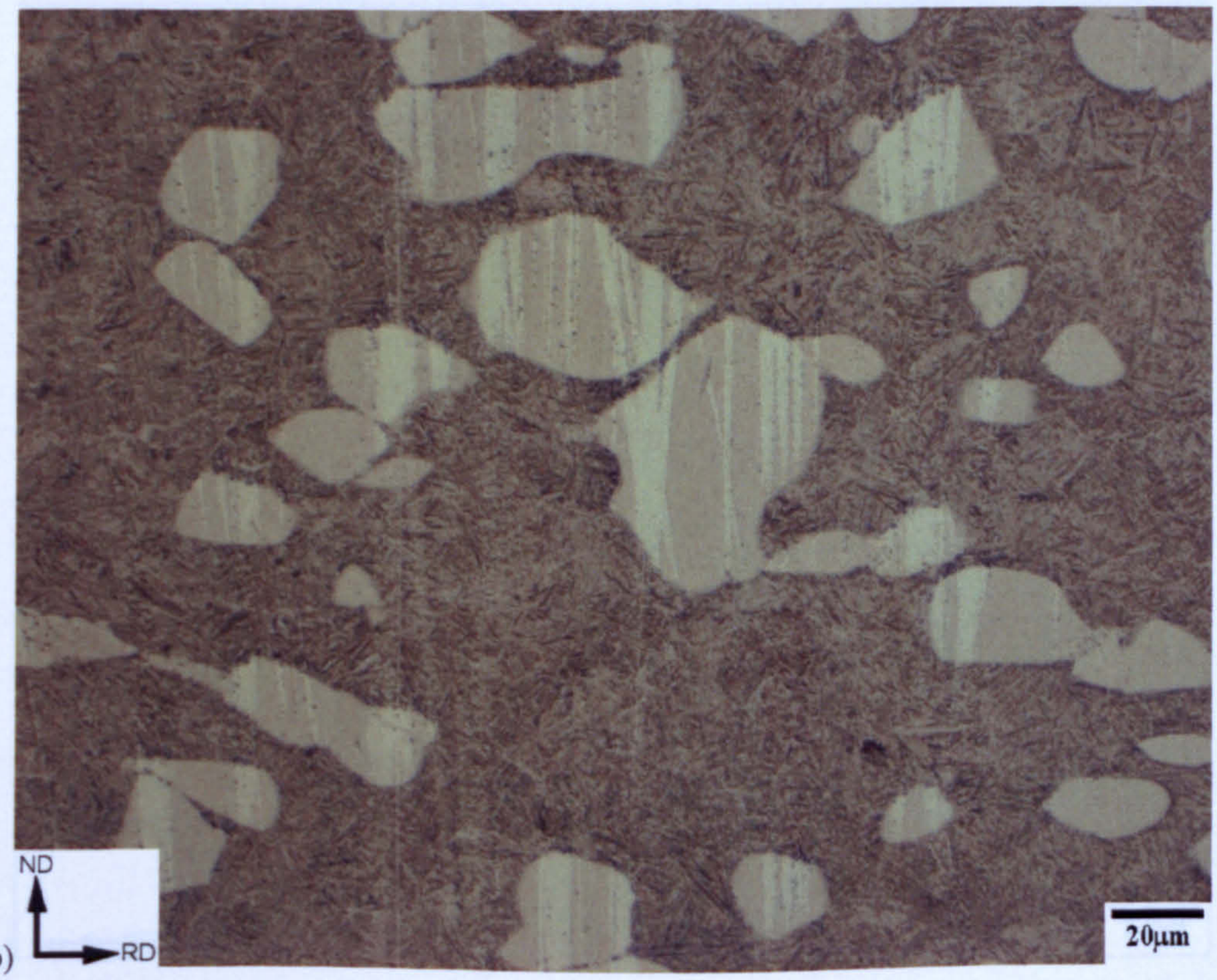

(b)

Fig. 8.24 Optical micrographs from specimen C, which was deformed at a true strain rate of $1.8s^{-1}$, to an equivalent true strain of 1.23.

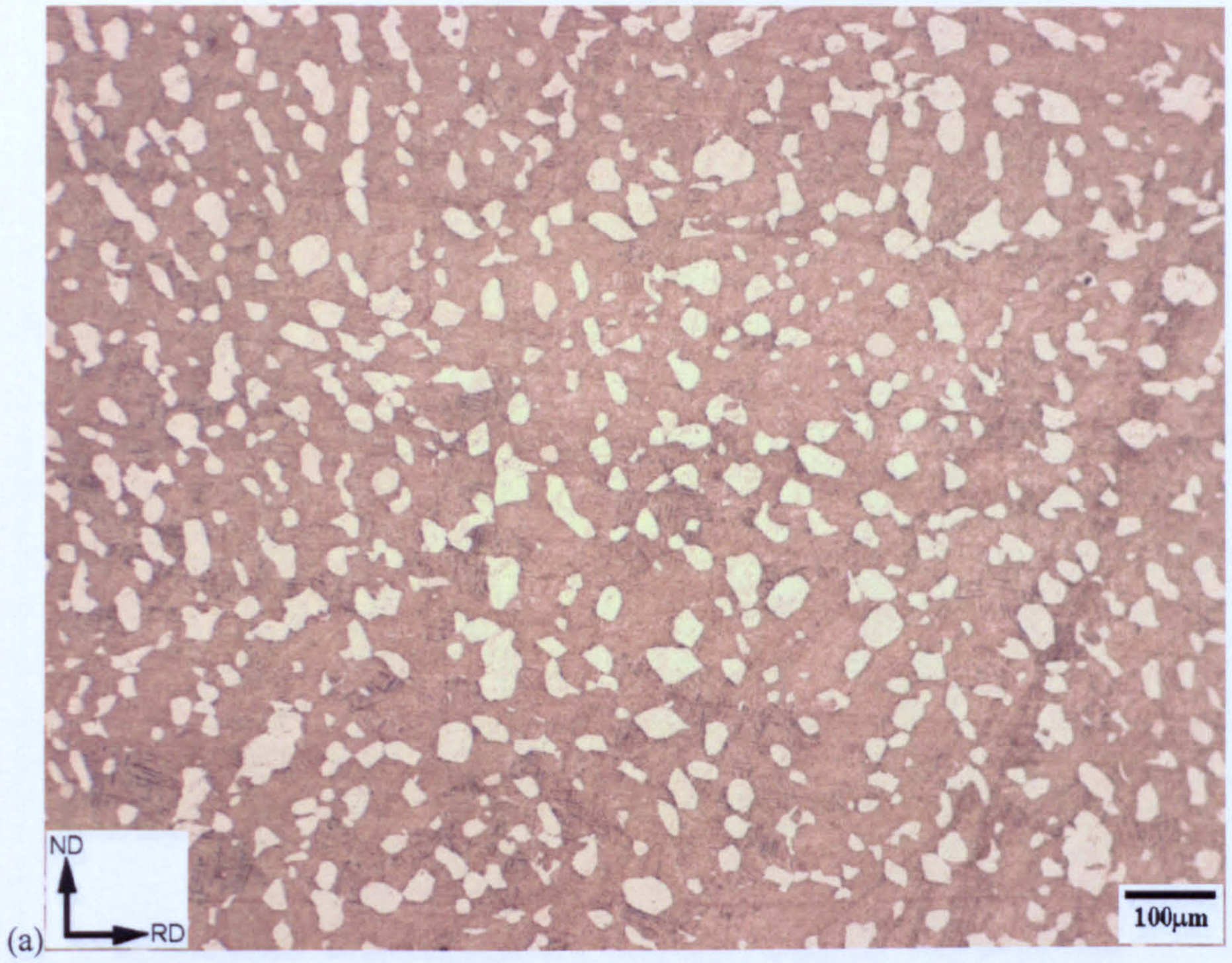

(a)

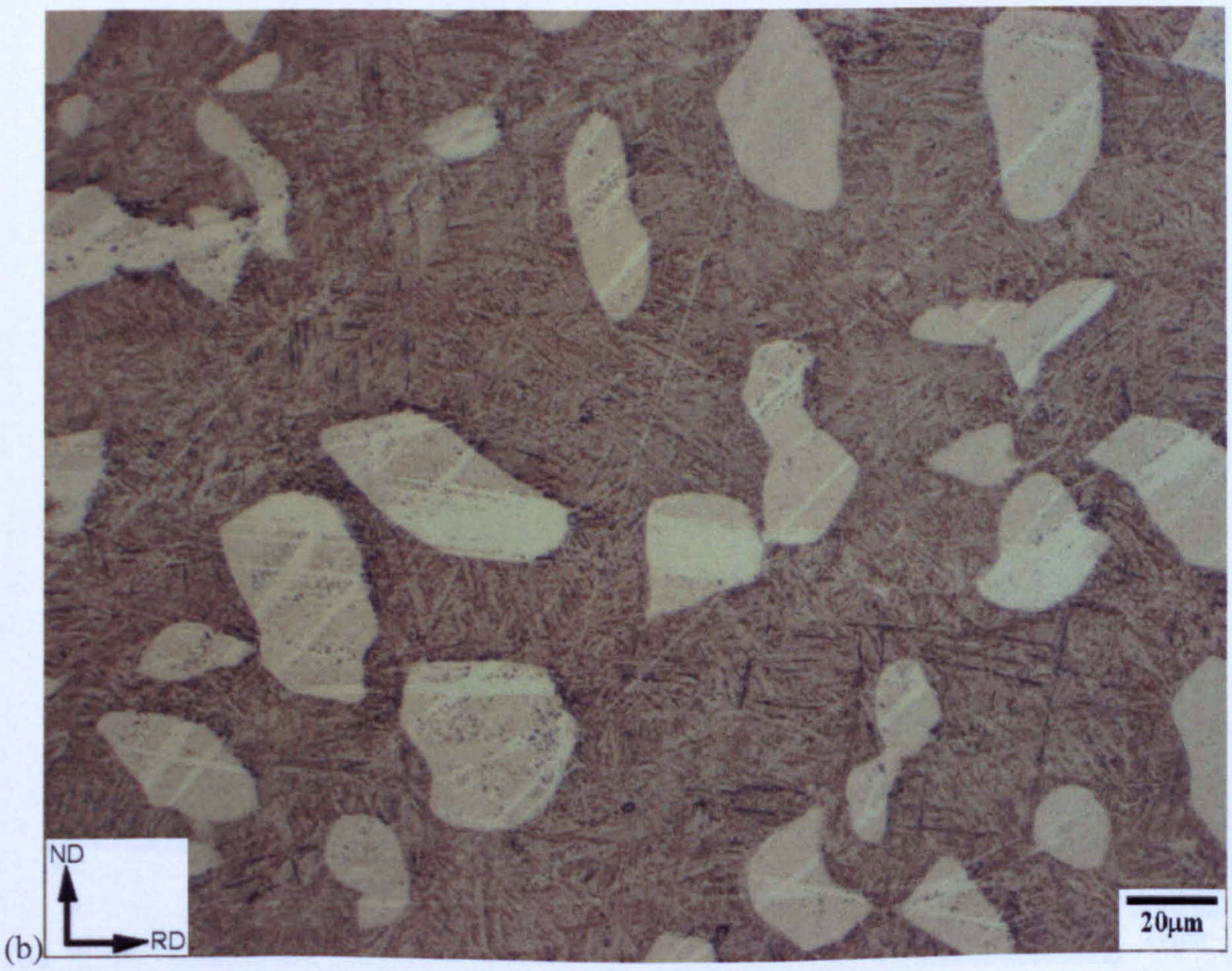

(b)

Fig. 8.25 Optical micrographs from specimen D, which was deformed at a true strain rate of $0.18s^{-1}$, to an equivalent true strain of 0.63.

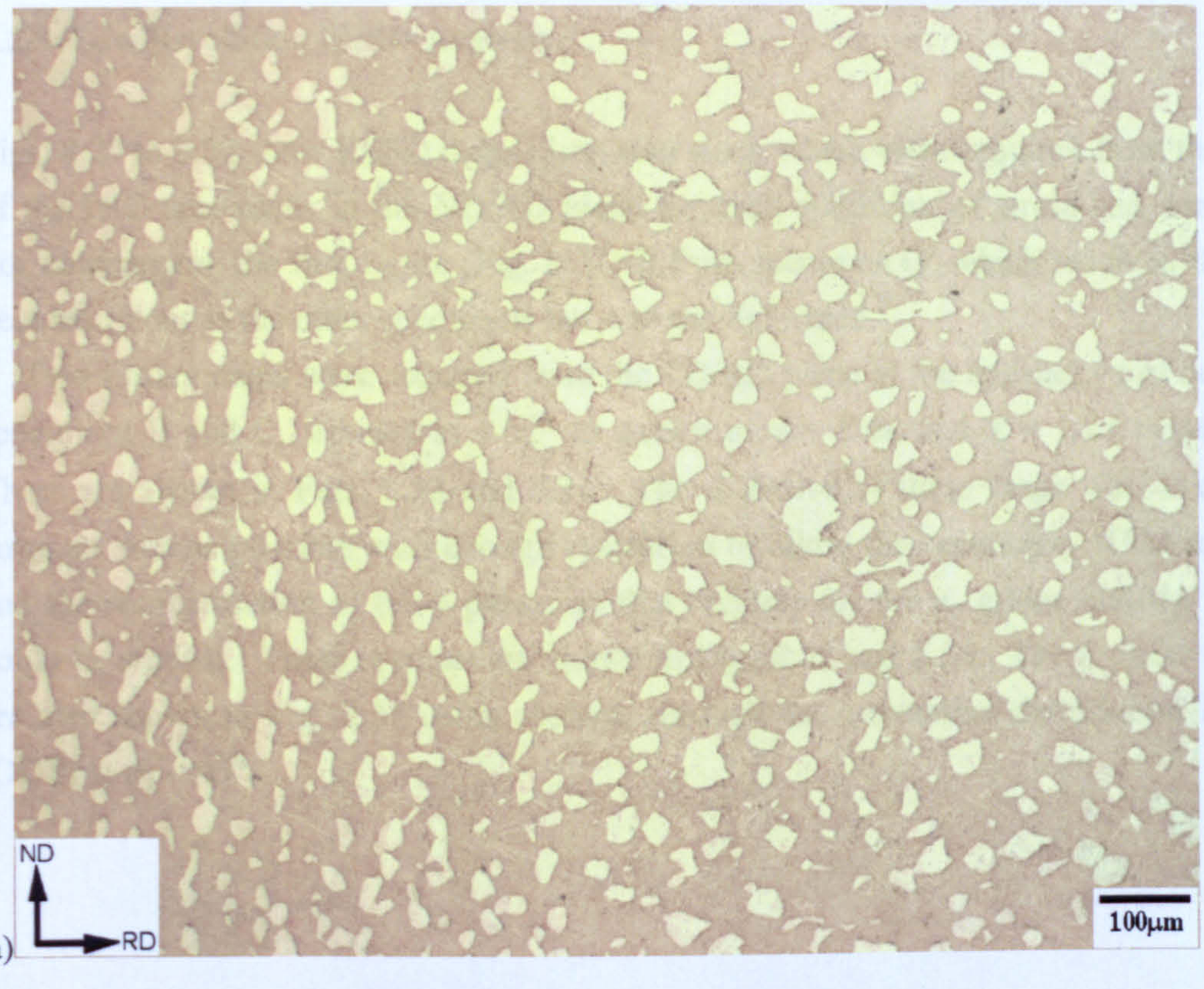

(a)

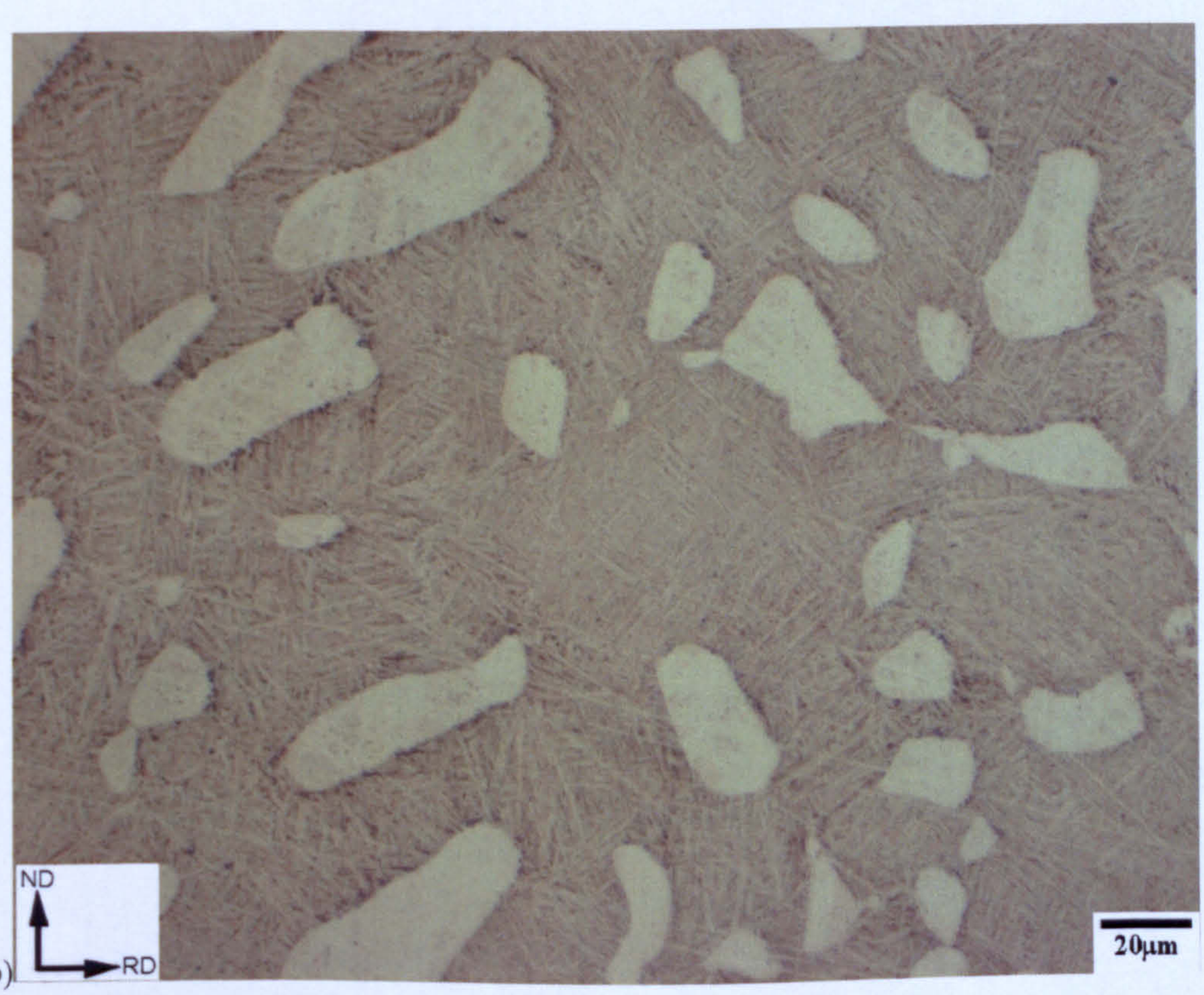

(b)

Fig. 8.26 Optical micrographs from specimen F, which was deformed at a true strain rate of $0.019s^{-1}$, to an equivalent true strain of 0.67.

8.2.3 Low Resolution EBSD Analysis

Figs. 8.27 to 8.32 show EBSD maps (3μm step size), which were acquired from the centre of the PSC specimens in the ND/RD plane for each condition of strain and strain rate. For comparison, the first figure (Fig. 8.27) is from specimen G, which received the same heat treatment as the other specimens but was not deformed.

Two further maps were acquired from the TD/RD plane at the mid-height of deformed specimens B and C, strained at $1.8s^{-1}$ to strains of $\bar{\varepsilon} = 0.64$ and $\bar{\varepsilon} = 1.23$ respectively. These are shown in Figs. 8.33 and 8.34. The objective of these maps was to cover as large an area as possible with enough resolution to allow the separation of the α_p grains and the reconstruction of the β phase, so that textures for the α_p grains and the β phase could be studied. These textures are shown in Figs 8.35 and 8.36. The β phase textures are also shown in Fig. 8.37 using sections through the orientation distribution function (ODF) at $\phi_2 = 45°$.

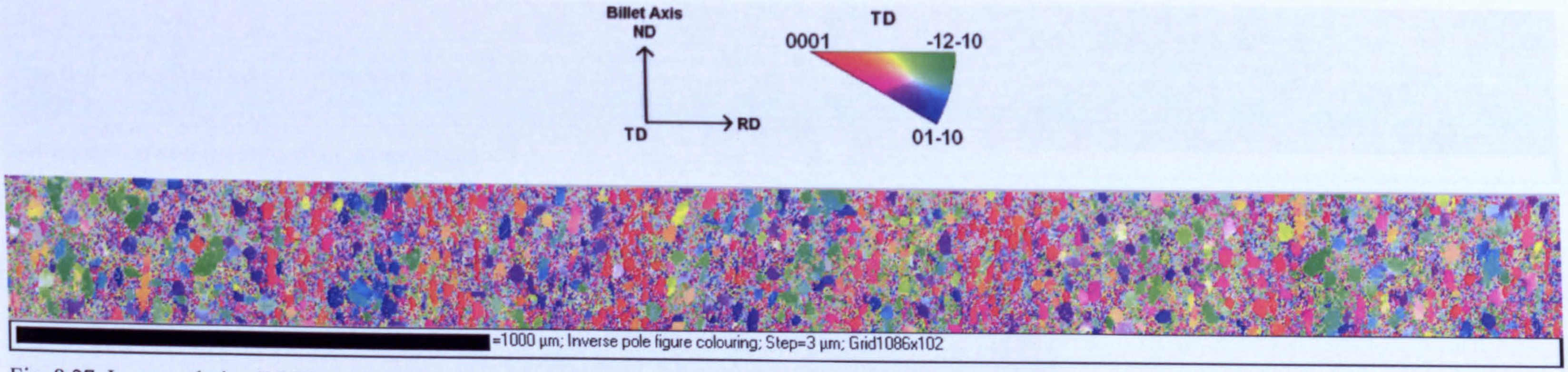

Fig. 8.27 Low resolution EBSD analysis from the undeformed specimen G (73% indexed).

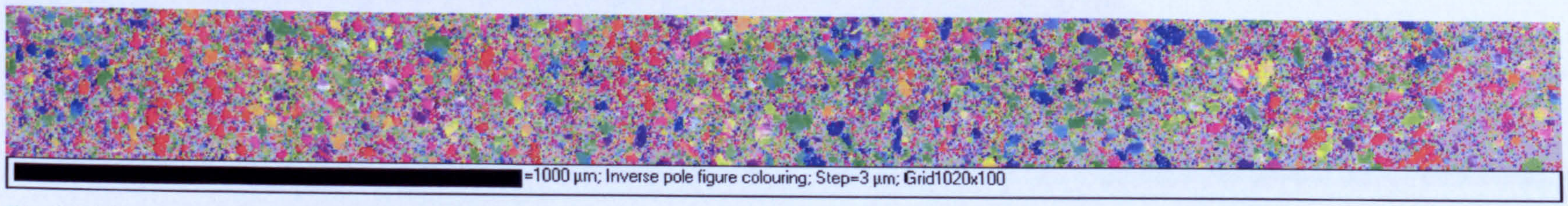

Fig. 8.28 Low resolution EBSD analysis from specimen A, deformed at a true strain rate of $20.2s^{-1}$ to an equivalent true strain of 0.63 (65% indexed).

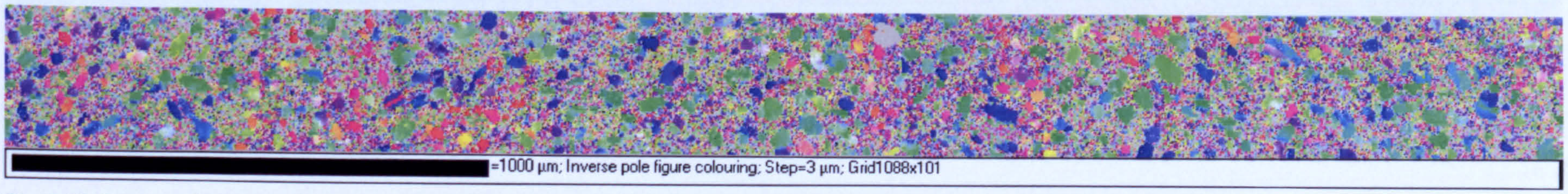

Fig. 8.29 Low resolution EBSD analysis from specimen B, deformed at a true strain rate of $1.8s^{-1}$ to an equivalent true strain of 0.64 (75% indexed).

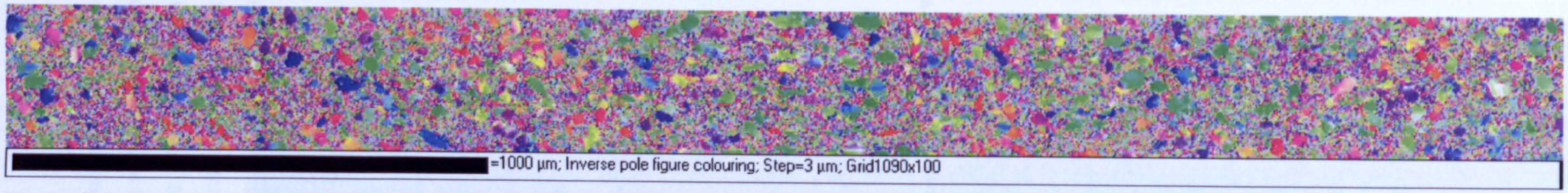

Fig. 8.30 Low resolution EBSD analysis from specimen C, deformed at a true strain rate of $1.8s^{-1}$ to an equivalent true strain of 1.23 (71% indexed).

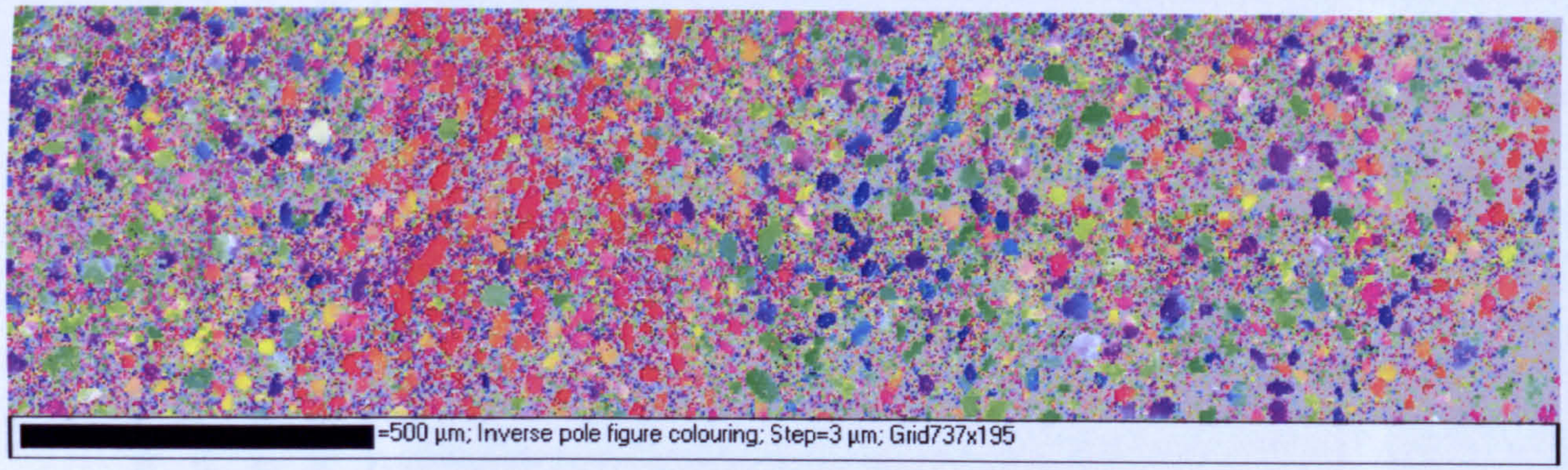

Fig. 8.31 Low resolution EBSD analysis from specimen D, deformed at a true strain rate of $0.18s^{-1}$ to an equivalent true strain of 0.63 (59% indexed).

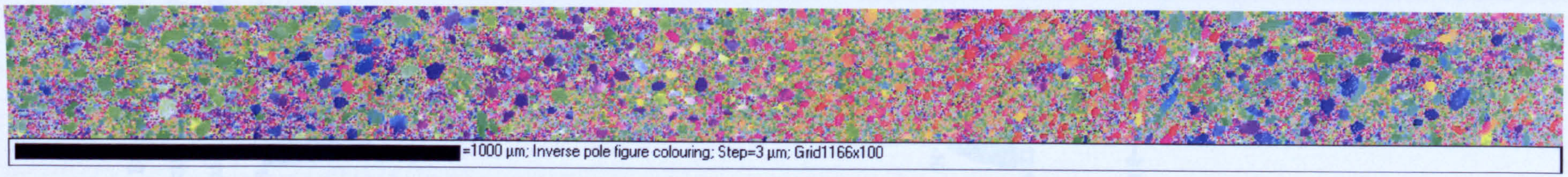

Fig. 8.32 Low resolution EBSD analysis from specimen F, deformed at a true strain rate of $0.019s^{-1}$ to an equivalent true strain of 0.67 (72% indexed).

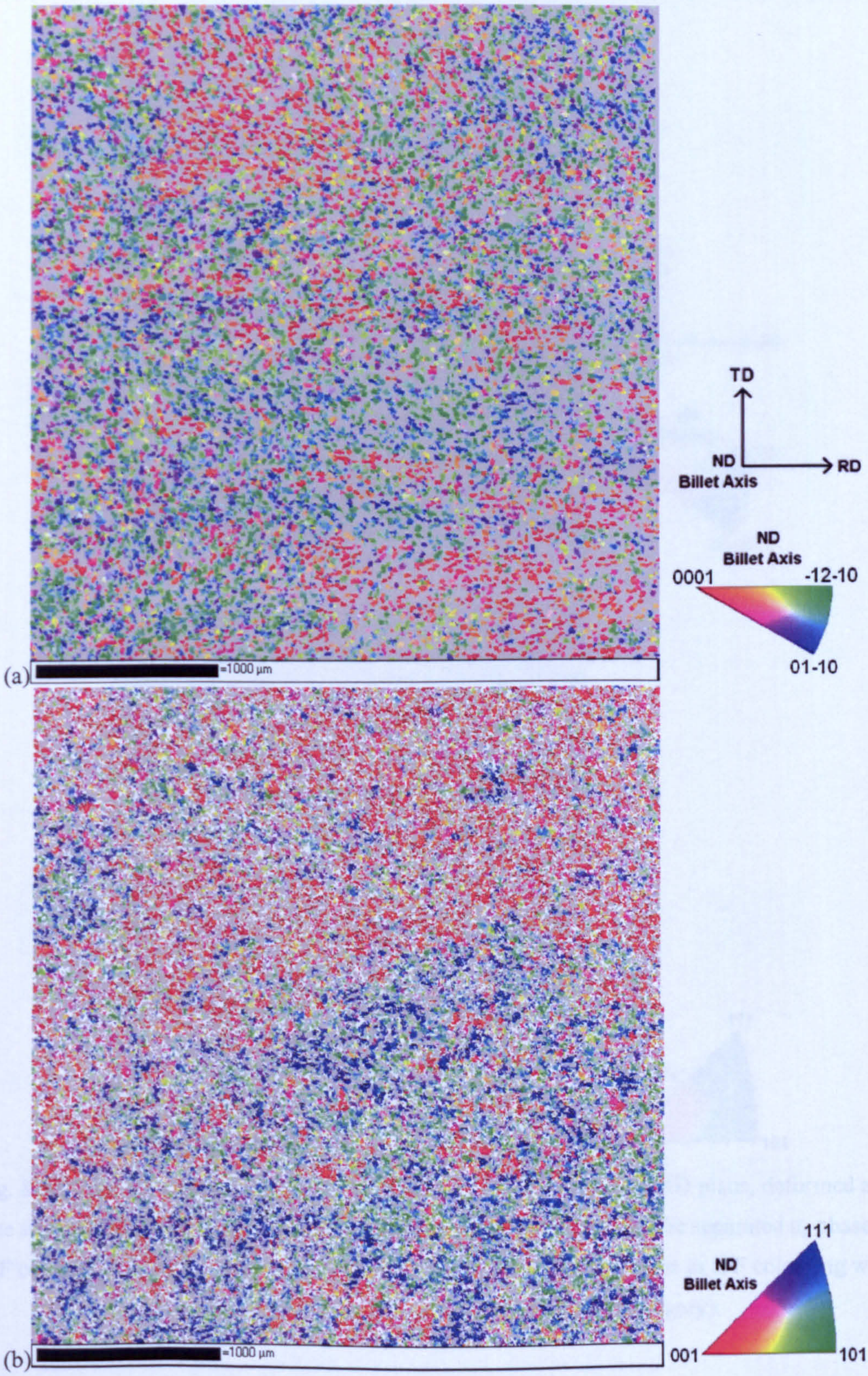

Fig. 8.33 Low resolution EBSD analysis from specimen B in the TD/RD plane, deformed at a true strain rate of $1.8s^{-1}$ to an equivalent true strain of 0.64. (a) shows the separated α_p phase in IPF colouring (α_s phase in grey). (b) shows reconstructed β orientations in IPF colouring with unreconstructed points remaining white (α_p phase in grey).

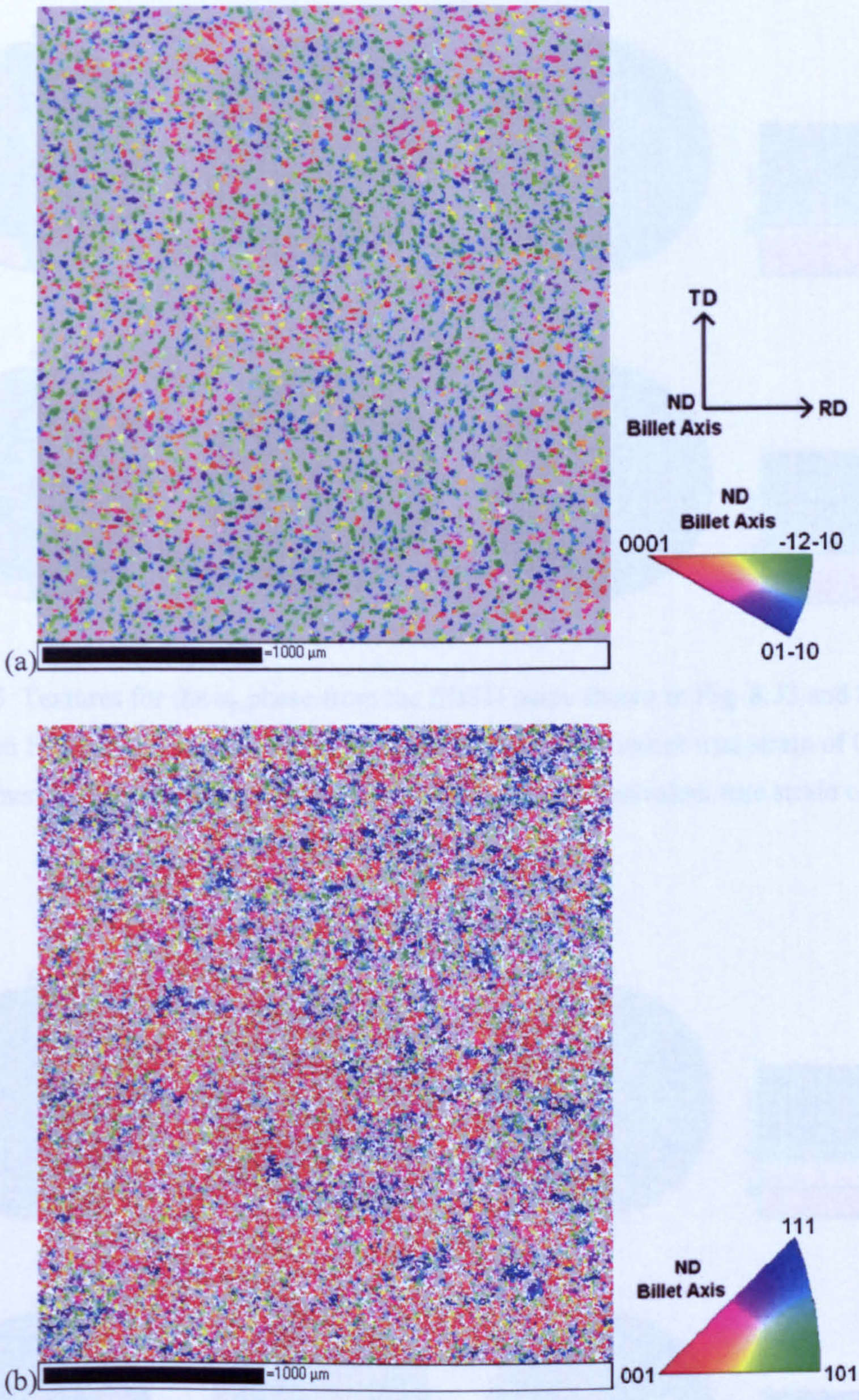

Fig. 8.34 Low resolution EBSD analysis from specimen C in the TD/RD plane, deformed at a true strain rate of $1.8s^{-1}$ to an equivalent true strain of 1.23. (a) shows the separated α_p phase in IPF colouring (α_s phase in grey). (b) shows reconstructed β orientations in IPF colouring with unreconstructed points remaining white (α_p phase in grey).

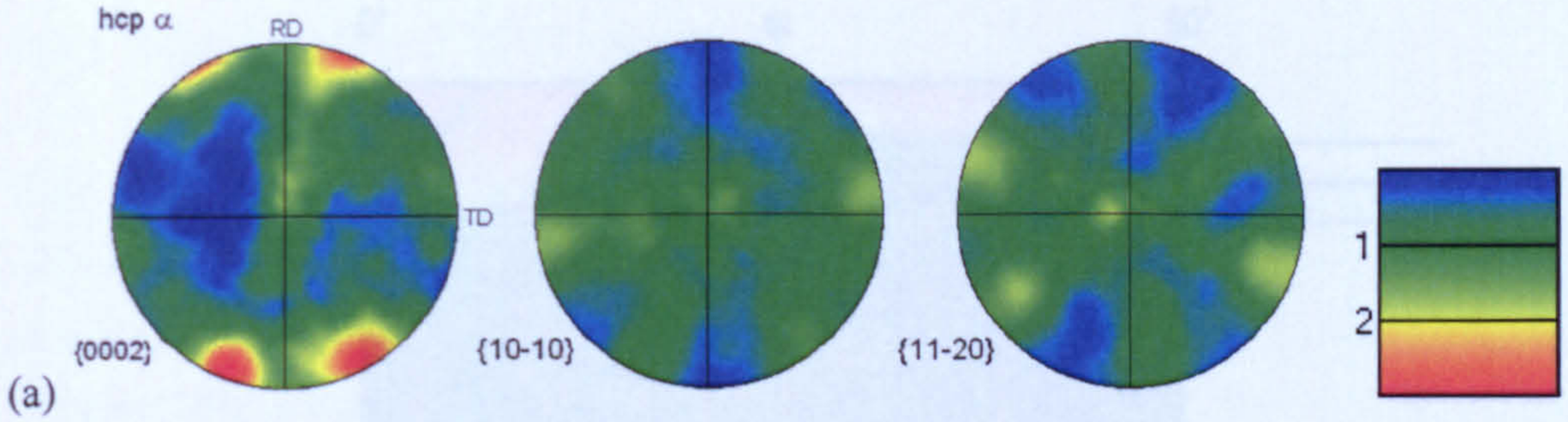

Fig. 8.35 Textures for the α_p phase from the EBSD maps shown in Fig. 8.33 and 8.34. (a) Specimen B deformed at a true strain rate of $1.8s^{-1}$ to an equivalent true strain of 0.64. (b) Specimen C deformed at a true strain rate of $1.8s^{-1}$ to an equivalent true strain of 1.23.

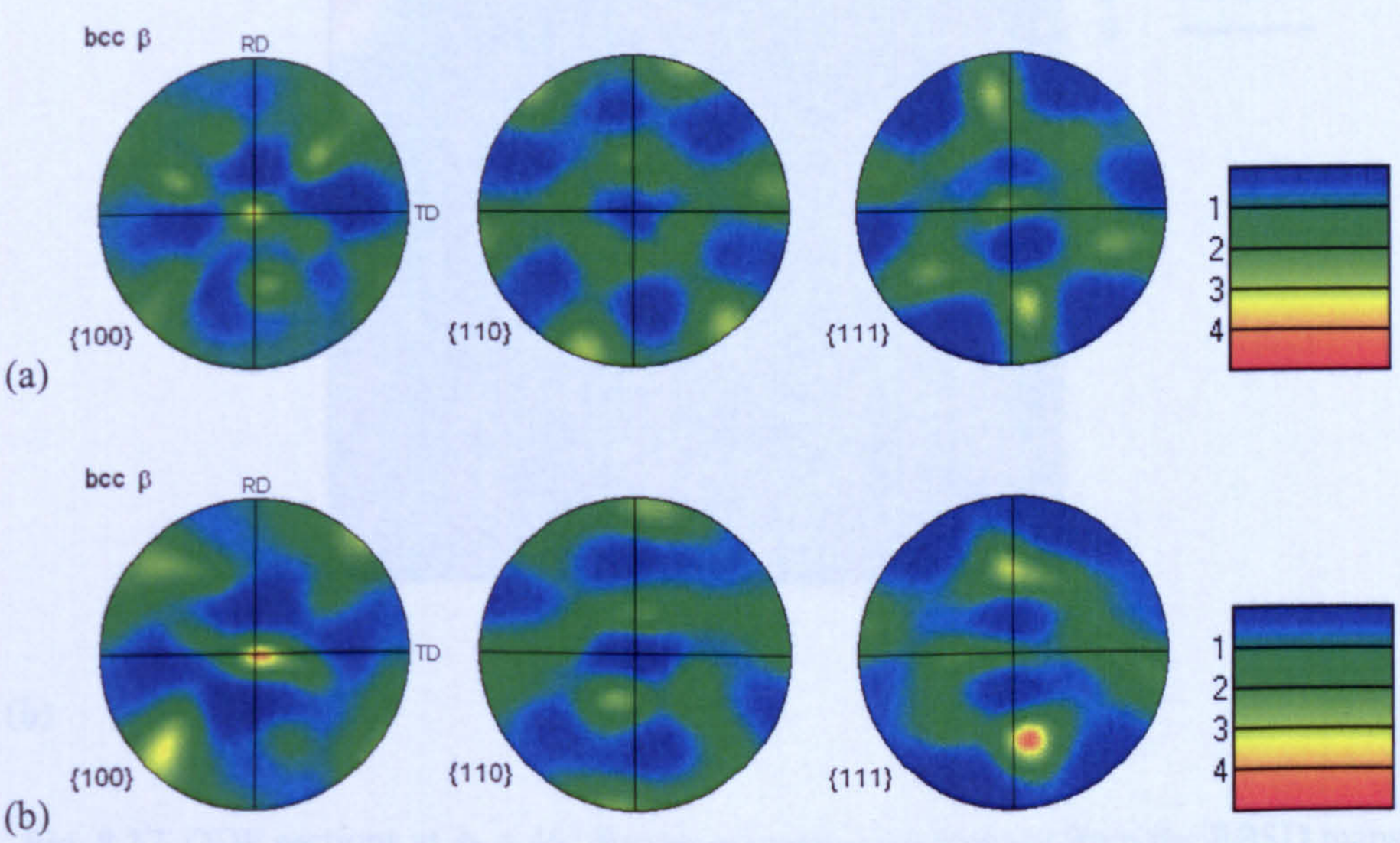

Fig. 8.36 Textures for the reconstructed β phase from the EBSD maps shown in Fig. 8.33 and 8.34. (a) Specimen B deformed at a true strain rate of $1.8s^{-1}$ to an equivalent true strain of 0.64. (b) Specimen C deformed at a true strain rate of $1.8s^{-1}$ to an equivalent true strain of 1.23.

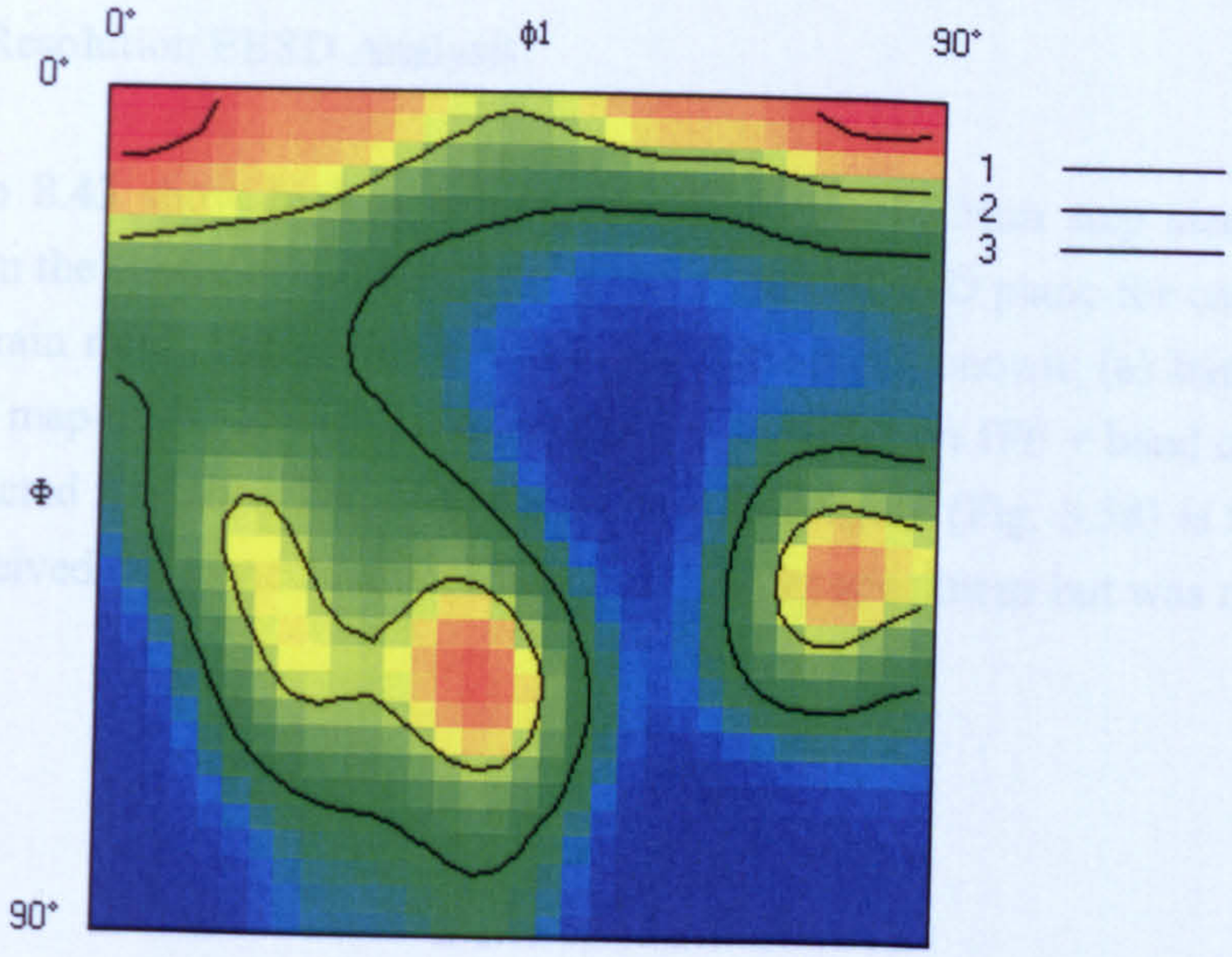

$\phi_2 = 45°$

(a)

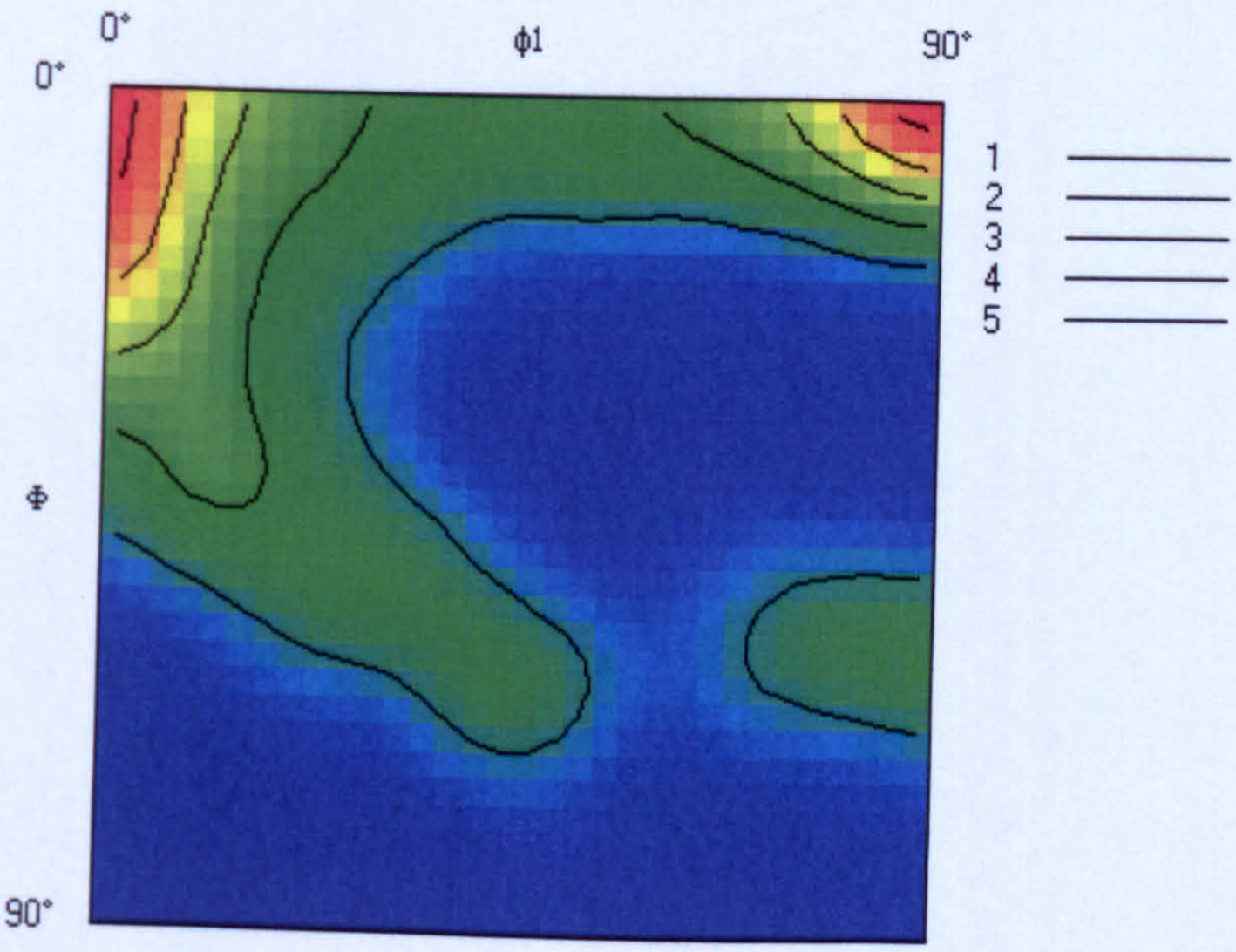

$\phi_2 = 45°$

(b)

Fig. 8.37 ODF sections at $\phi_2 = 45°$ for the reconstructed β phase from the EBSD maps shown in Fig. 8.33 and 8.34. (a) Specimen B deformed at a true strain rate of $1.8s^{-1}$ to an equivalent true strain of 0.64. (b) Specimen C deformed at a true strain rate of $1.8s^{-1}$ to an equivalent true strain of 1.23.

8.2.4 High Resolution EBSD Analysis

Figs. 8.38 to 8.43 show high resolution EBSD maps (0.25μm step size), which were acquired from the centre of the PSC specimens in the ND/RD plane for each condition of strain and strain rate. For each condition, three maps are shown: (a) band contrast, (b) standard IPF map of the hexagonal phases (α_p+α_s) and (c) an IPF + band contrast map of the reconstructed β phase. For comparison, the first figure (Fig. 8.38) is from specimen G, which received the same heat treatment as the other specimens but was not deformed.

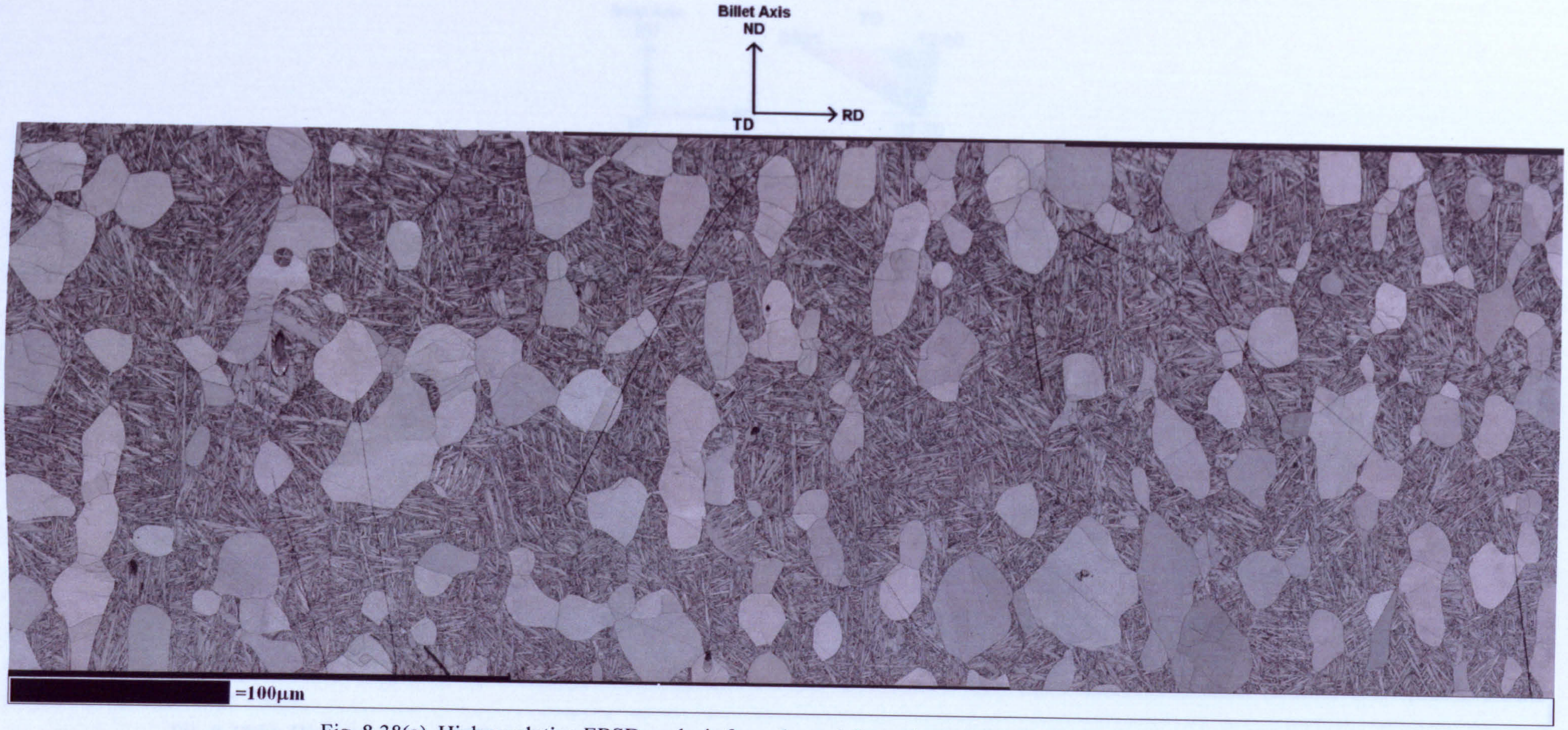

Fig. 8.38(a) High resolution EBSD analysis from the undeformed specimen G showing band contrast.

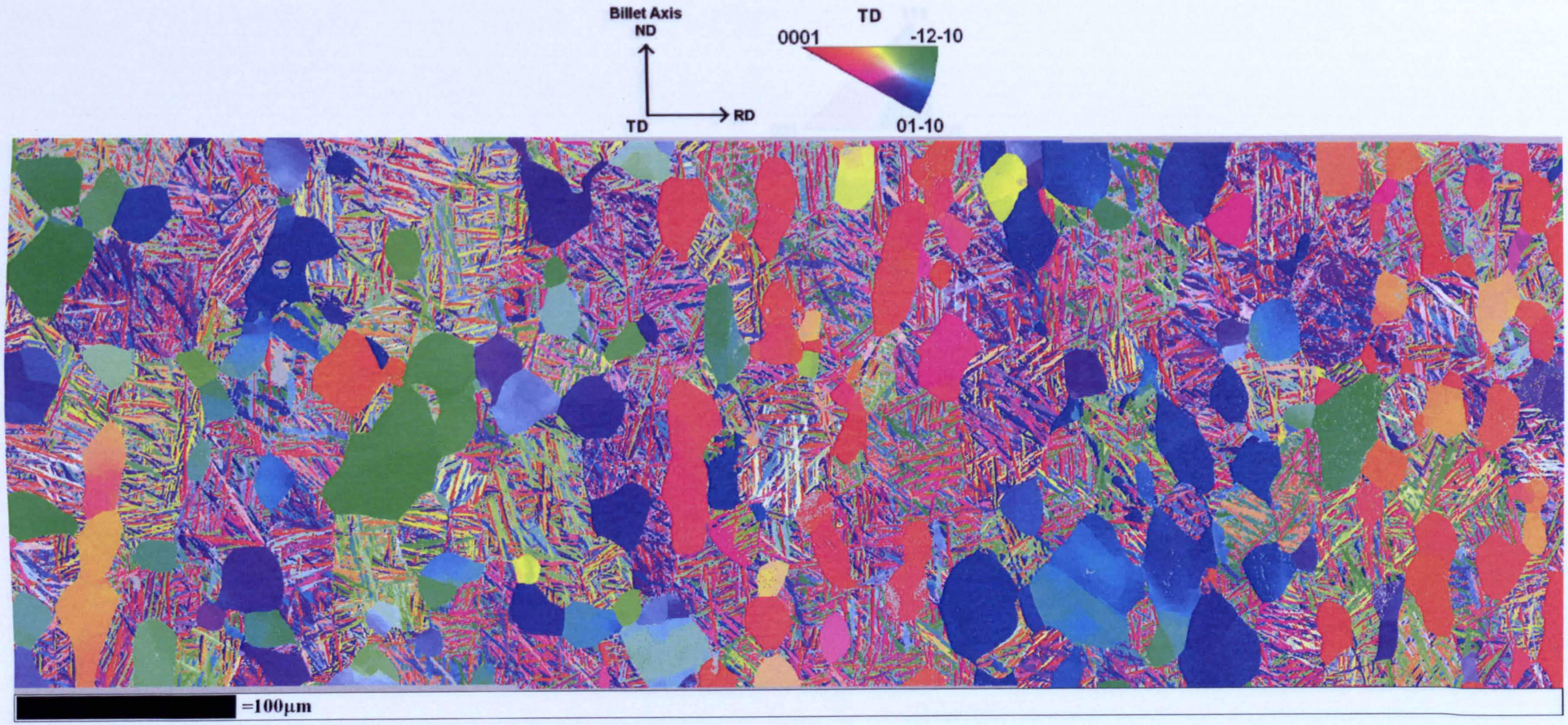

Fig. 8.38(b) High resolution EBSD analysis from the undeformed specimen G showing IPF colouring and non indexed points in grey.

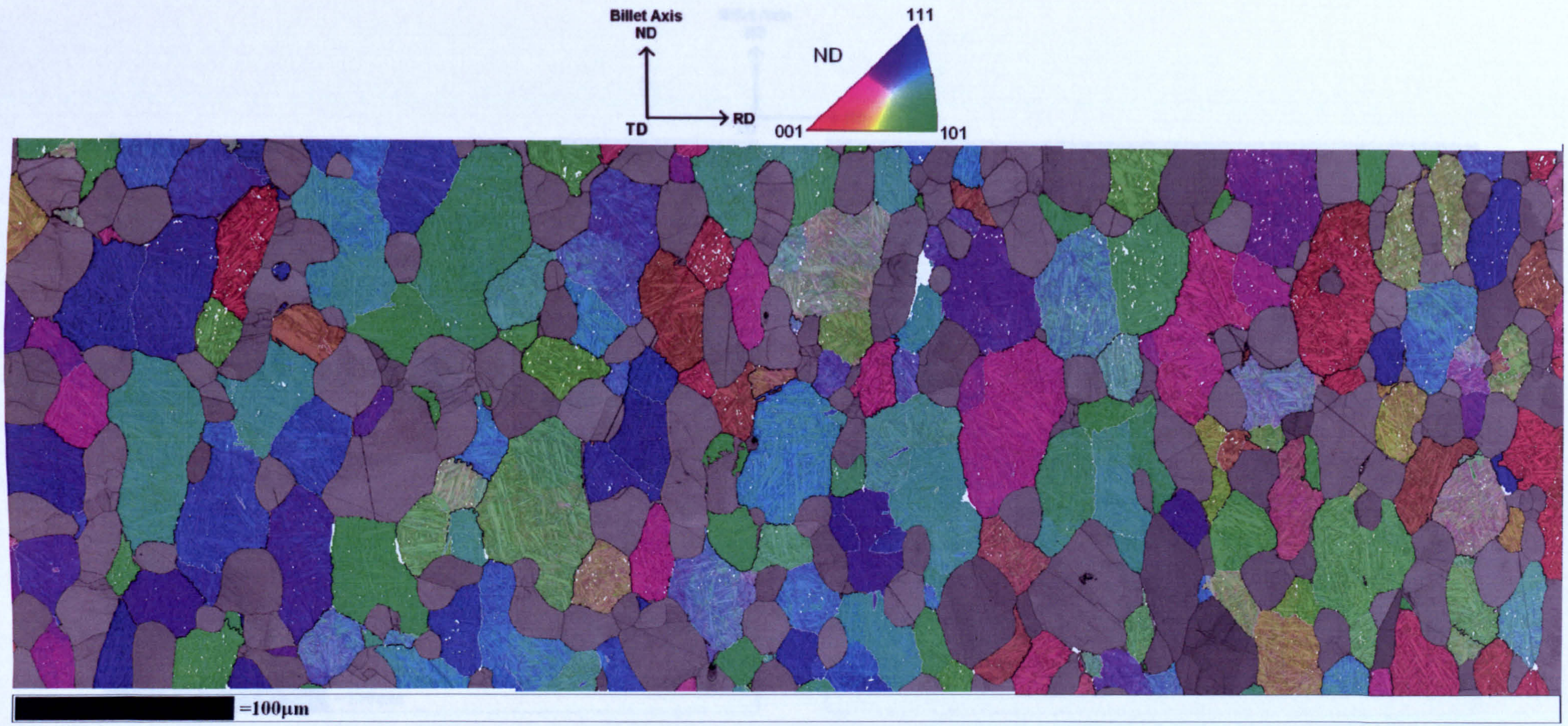

Fig. 8.38(c) High resolution EBSD analysis from the undeformed specimen G after separation of the α_p and α_s and subsequent β reconstruction of the α_s. The α_p is shown with band contrast and the reconstructed β grains with a combination of band contrast and IPF colouring (with respect to ND). Unreconstructed points are coloured white. Within the reconstructed β phase, misorientations greater then 5° are coloured silver and misorientations greater than 15° black.

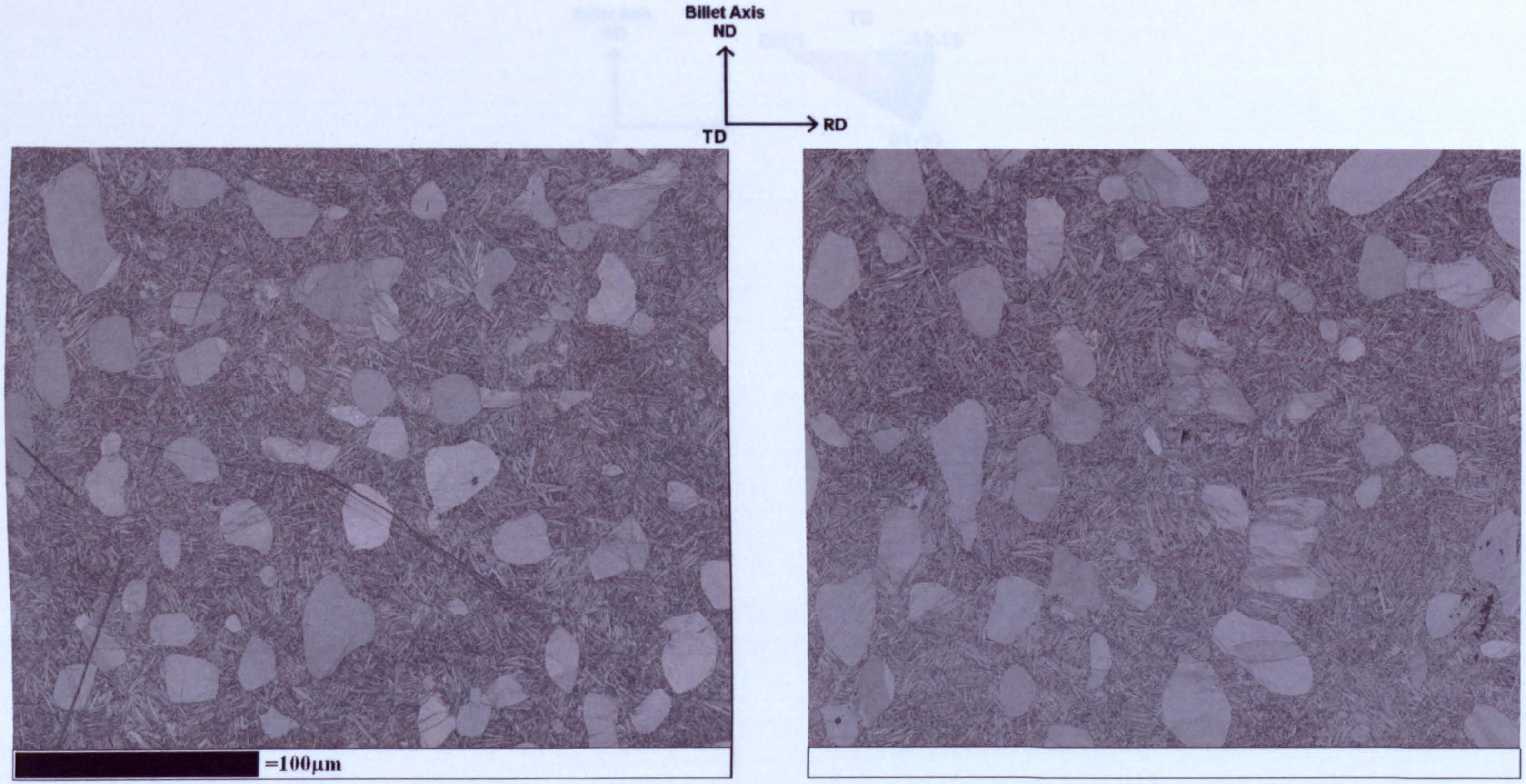

Fig. 8.39(a) High resolution EBSD analyses from specimen A, deformed at a true strain rate of $20.2s^{-1}$ to an equivalent true strain of 0.63. These maps show band contrast.

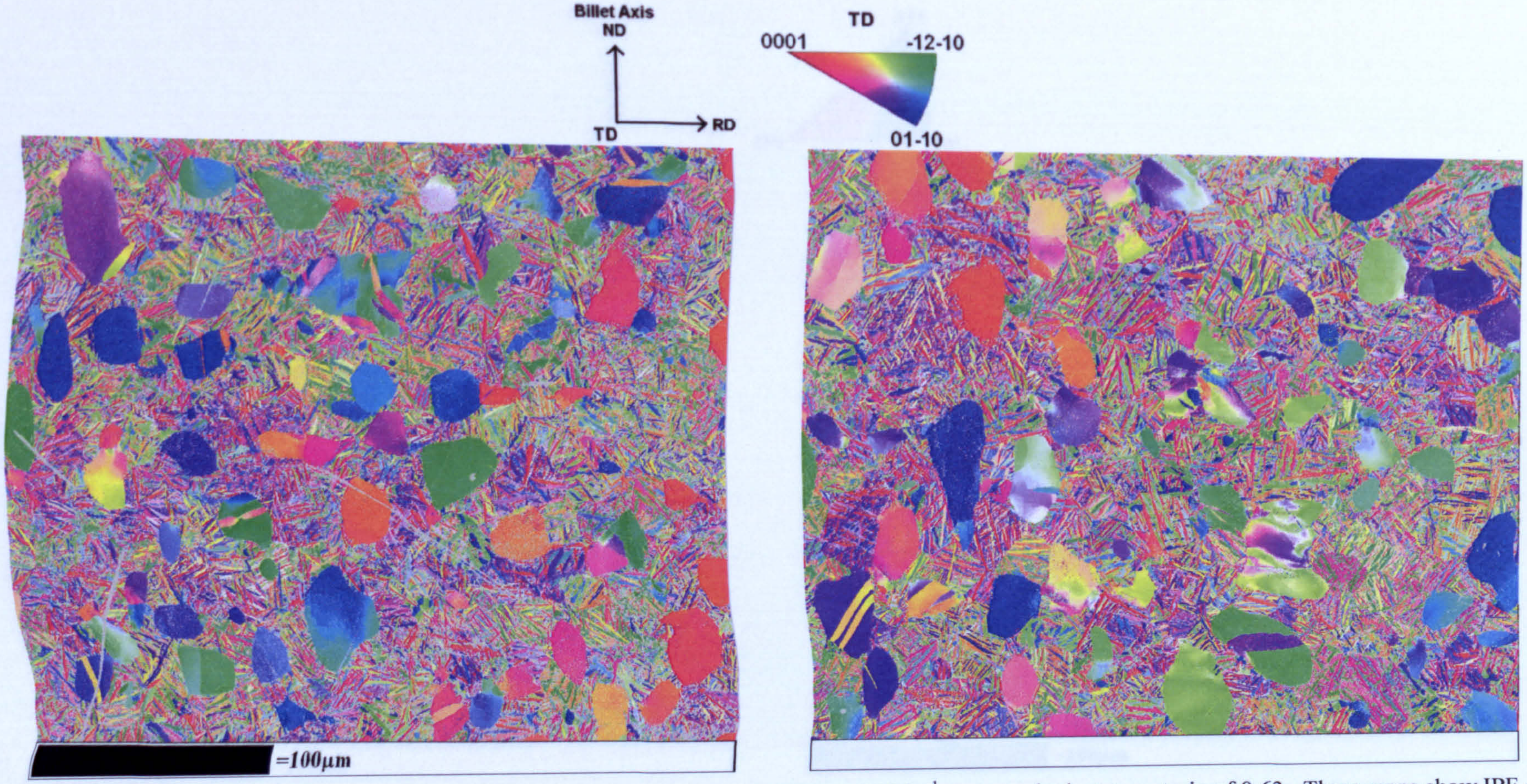

Fig. 8.39(b) High resolution EBSD analyses from specimen A, deformed at a true strain rate of 20.2s^{-1} to an equivalent true strain of 0.63. These maps show IPF colouring with non indexed points in grey.

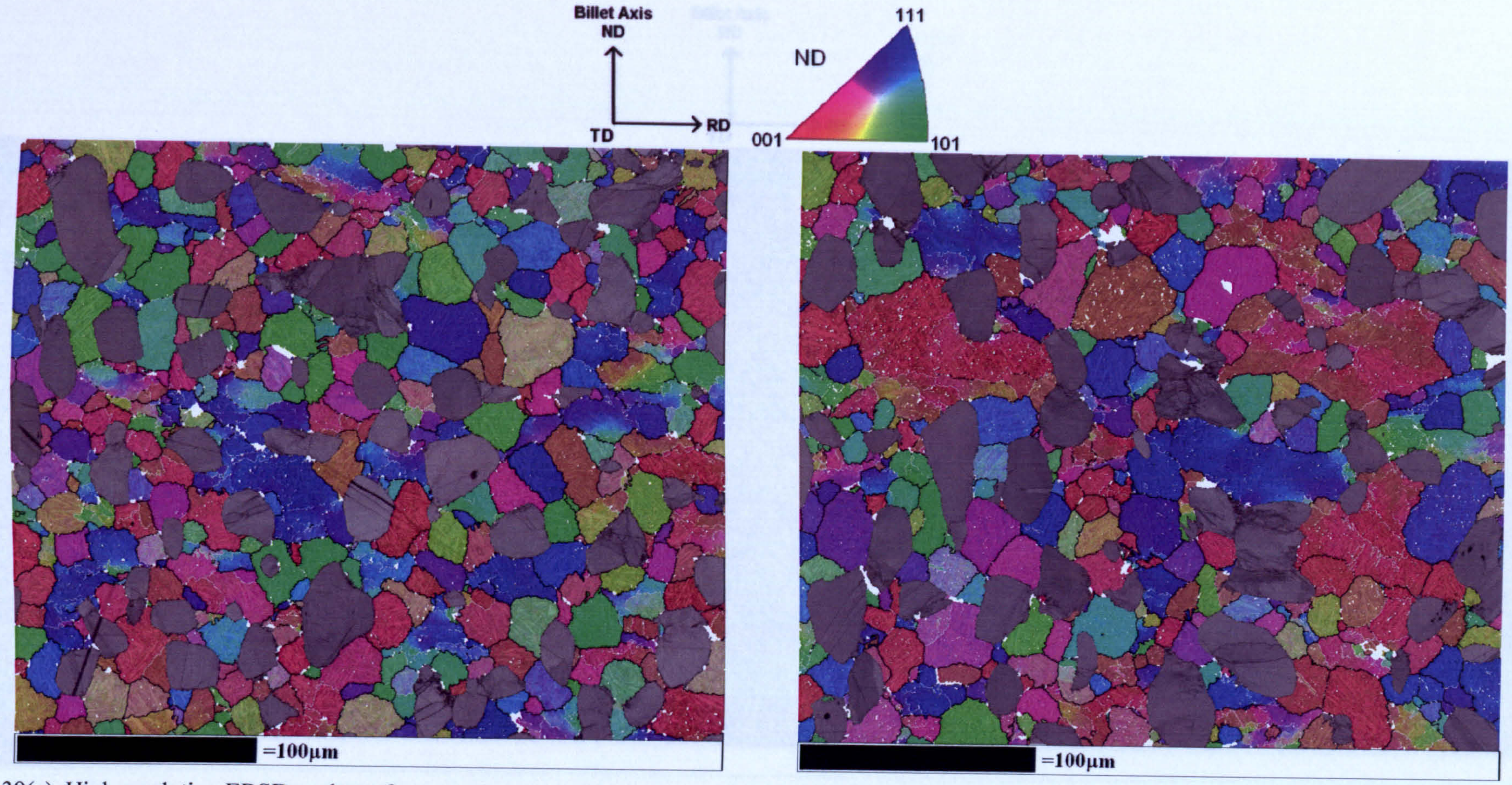

Fig. 8.39(c) High resolution EBSD analyses from specimen A, deformed at a true strain rate of $20.2s^{-1}$ to an equivalent true strain of 0.63. In these maps, the α_p and α_s phases have been separated and β reconstruction carried out on the α_s. The α_p is shown with band contrast and the reconstructed β grains with a combination of band contrast and IPF colouring (with respect to ND). Unreconstructed points are coloured white. Within the reconstructed β phase, misorientations greater then 5° are coloured silver and misorientations greater than 15° black.

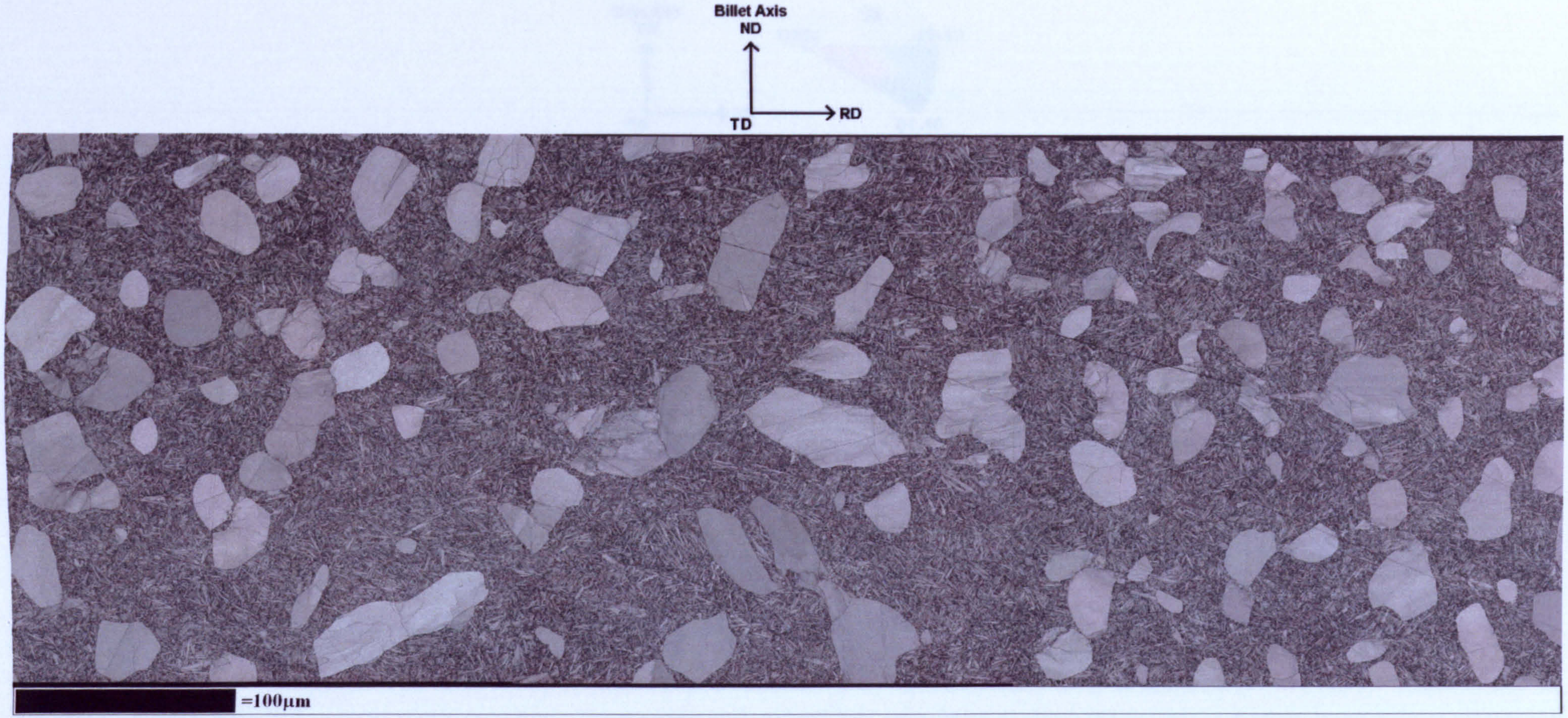

Fig. 8.40(a) High resolution EBSD analysis from specimen B, deformed at a true strain rate of $1.8s^{-1}$ to an equivalent true strain of 0.64. This map shows band contrast.

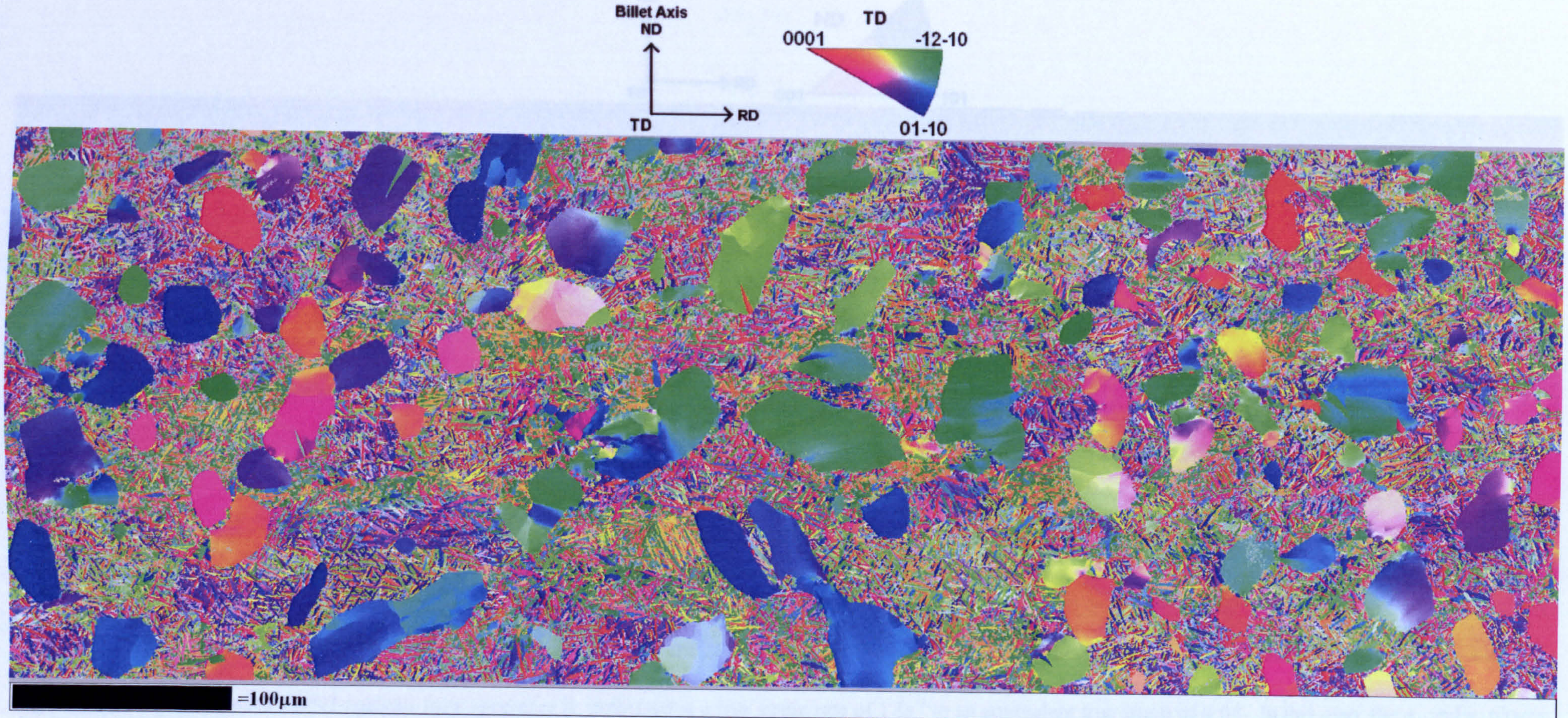

Fig. 8.40(b) High resolution EBSD analysis from specimen B, deformed at a true strain rate of $1.8s^{-1}$ to an equivalent true strain of 0.64. This map shows IPF colouring with non indexed points in grey.

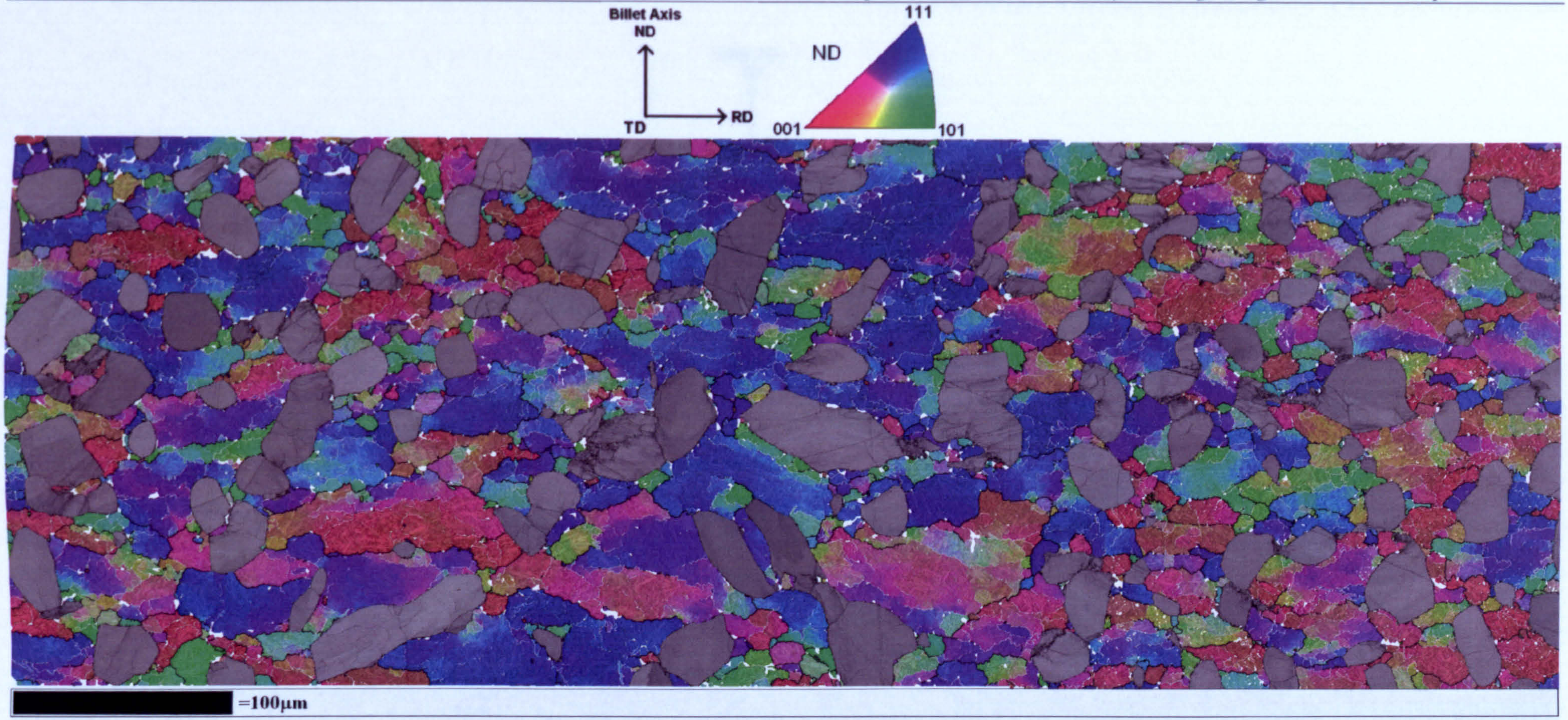

Fig. 8.40(c) High resolution EBSD analysis from specimen B, deformed at a true strain rate of $1.8s^{-1}$ to an equivalent true strain of 0.64. In this map, the α_p and α_s phases have been separated and β reconstruction carried out on the α_s. The α_p is shown with band contrast and the reconstructed β grains with a combination of band contrast and IPF colouring (with respect to ND). Unreconstructed points are coloured white. Within the reconstructed β phase, misorientations greater then 5° are coloured silver and misorientations greater than 15° black.

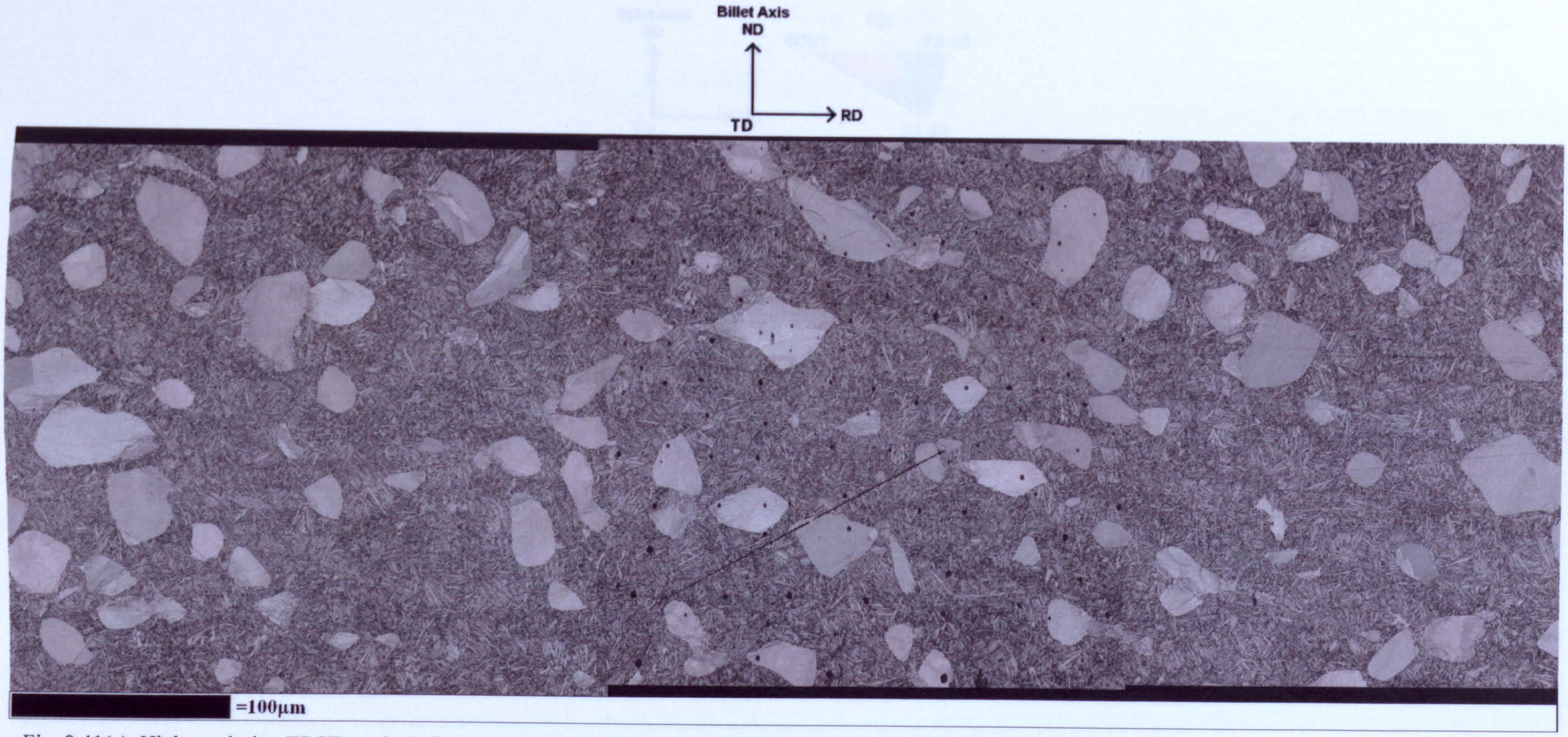

Fig. 8.41(a) High resolution EBSD analysis from specimen C, deformed at a true strain rate of $1.8s^{-1}$ to an equivalent true strain of 1.23. This map shows band contrast.

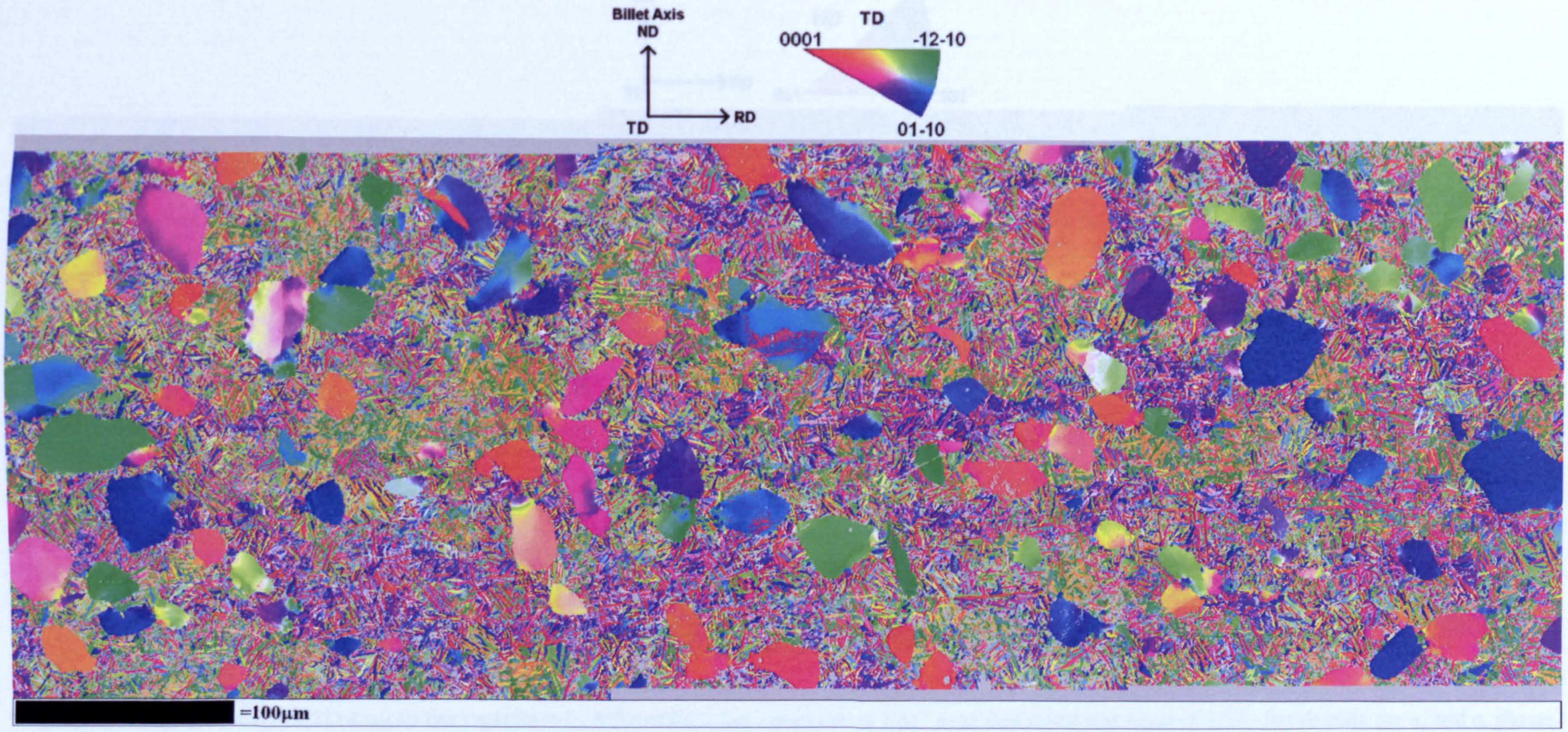

Fig. 8.41(b) High resolution EBSD analysis from specimen C, deformed at a true strain rate of $1.8s^{-1}$ to an equivalent true strain of 1.23. This map shows IPF colouring with non indexed points in grey.

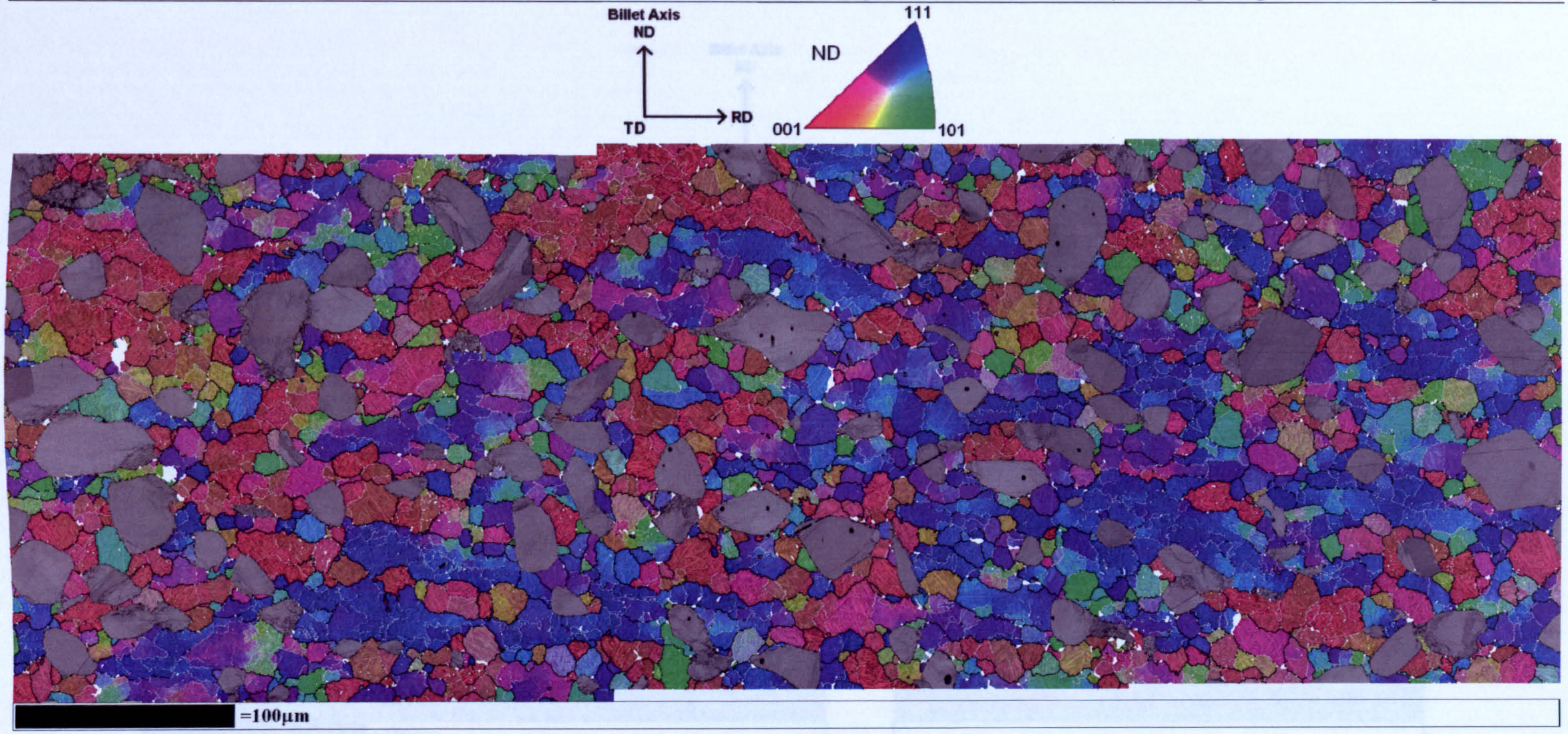

Fig. 8.41(c) High resolution EBSD analysis from specimen C, deformed at a true strain rate of $1.8s^{-1}$ to an equivalent true strain of 1.23. In this map, the α_p and α_s phases have been separated and β reconstruction carried out on the α_s. The α_p is shown with band contrast and the reconstructed β grains with a combination of band contrast and IPF colouring (with respect to ND). Unreconstructed points are coloured white. Within the reconstructed β phase, misorientations greater then 5° are coloured silver and misorientations greater than 15° black.

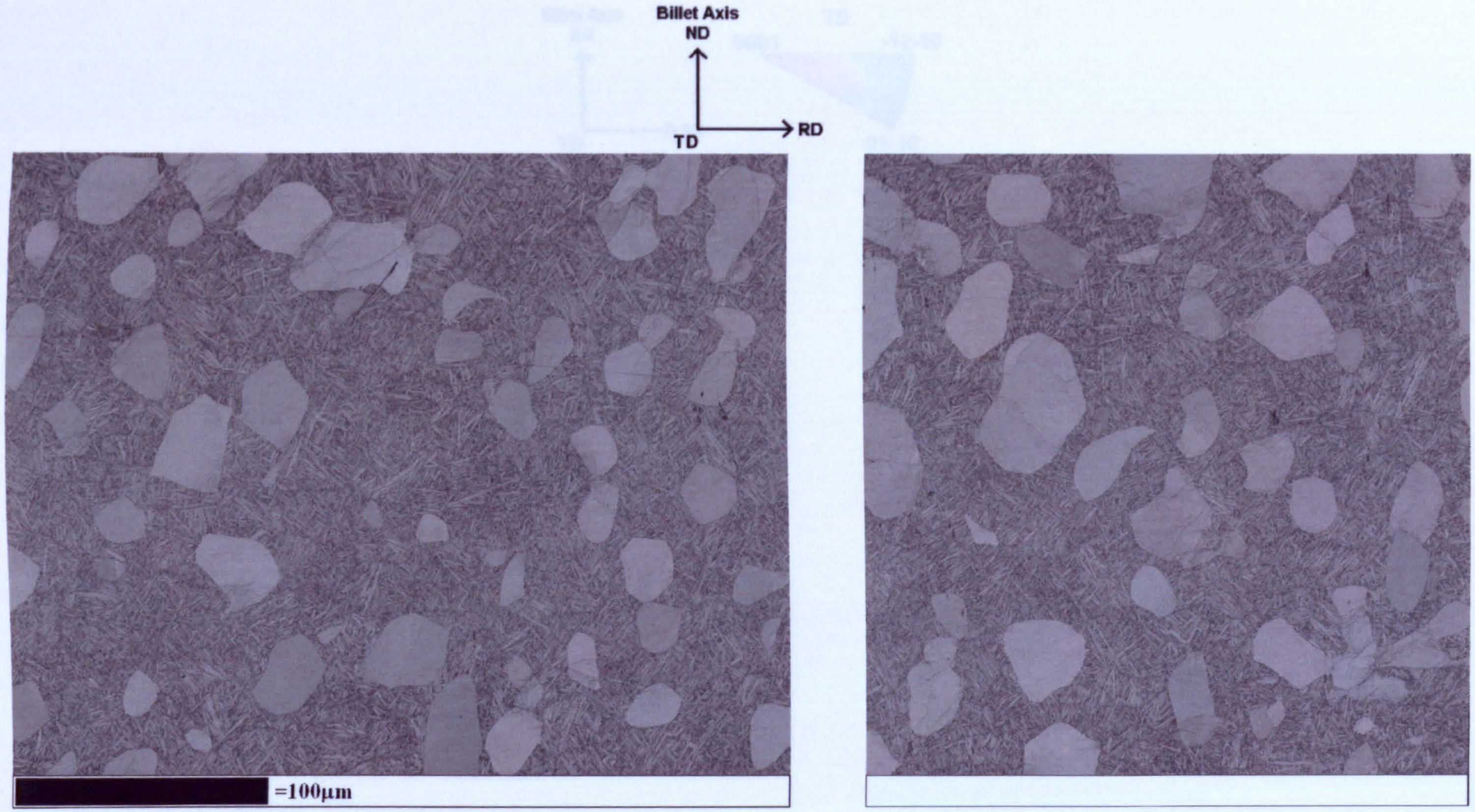

Fig. 8.42(a) High resolution EBSD analyses from specimen D, deformed at a true strain rate of $0.18s^{-1}$ to an equivalent true strain of 0.63. These maps show band contrast.

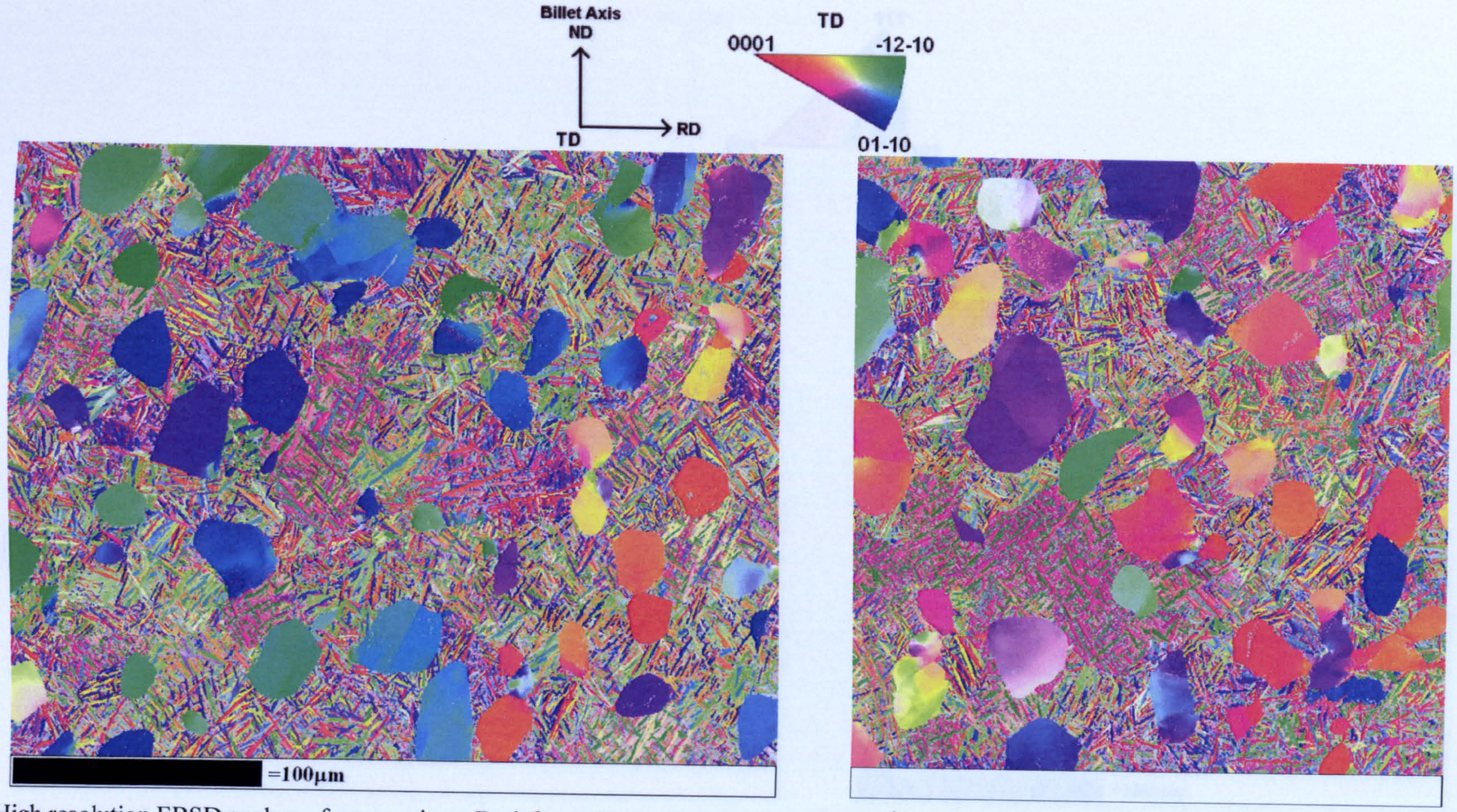

Fig. 8.42(b) High resolution EBSD analyses from specimen D, deformed at a true strain rate of $0.18s^{-1}$ to an equivalent true strain of 0.63. These maps show IPF colouring with non indexed points in grey.

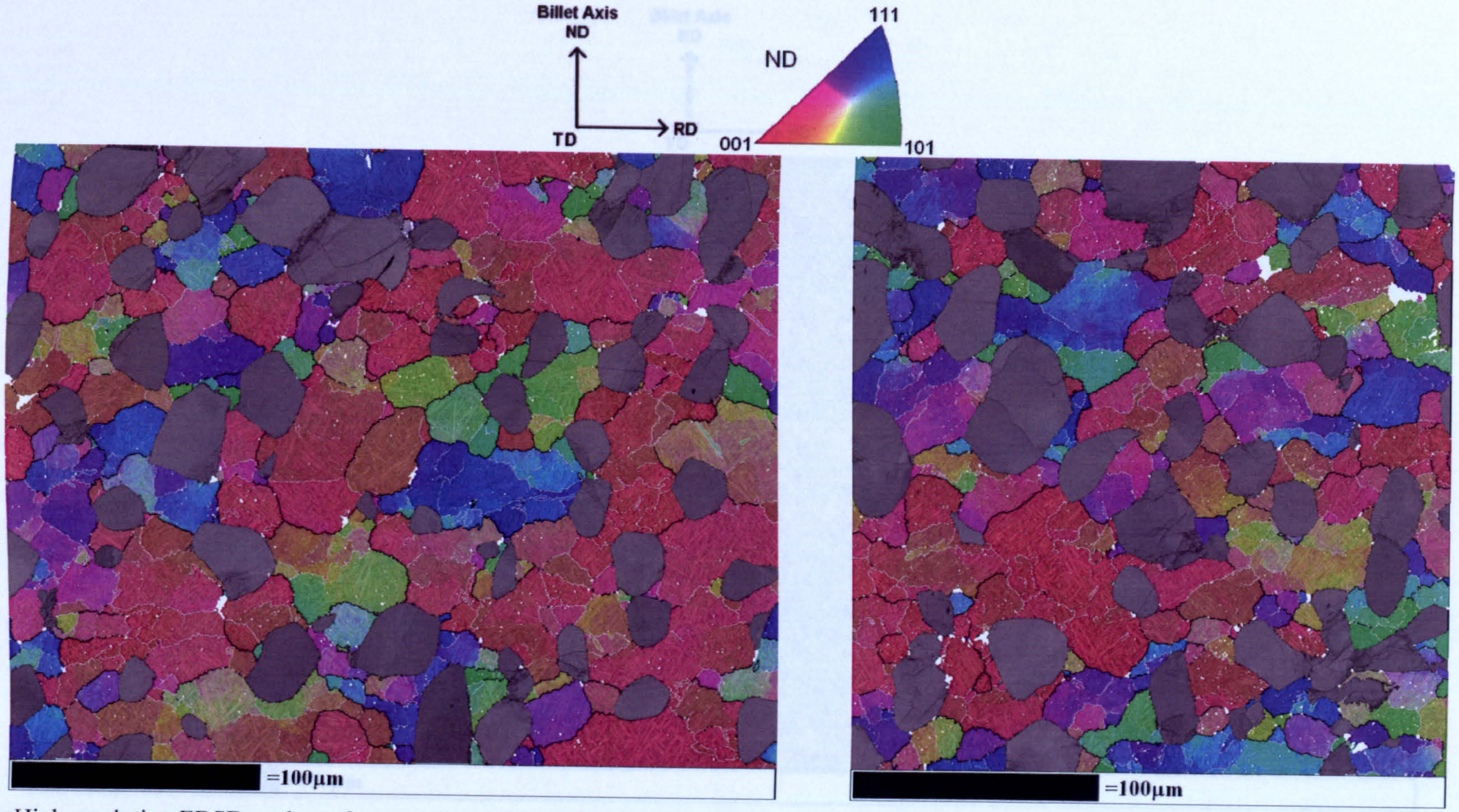

Fig. 8.42(c) High resolution EBSD analyses from specimen D, deformed at a true strain rate of $0.18s^{-1}$ to an equivalent true strain of 0.63. In these maps, the α_p and α_s phases have been separated and β reconstruction carried out on the α_s. The α_p is shown with band contrast and the reconstructed β grains with a combination of band contrast and IPF colouring (with respect to ND). Unreconstructed points are coloured white. Within the reconstructed β phase, misorientations greater then 5° are coloured silver and misorientations greater than 15° black.

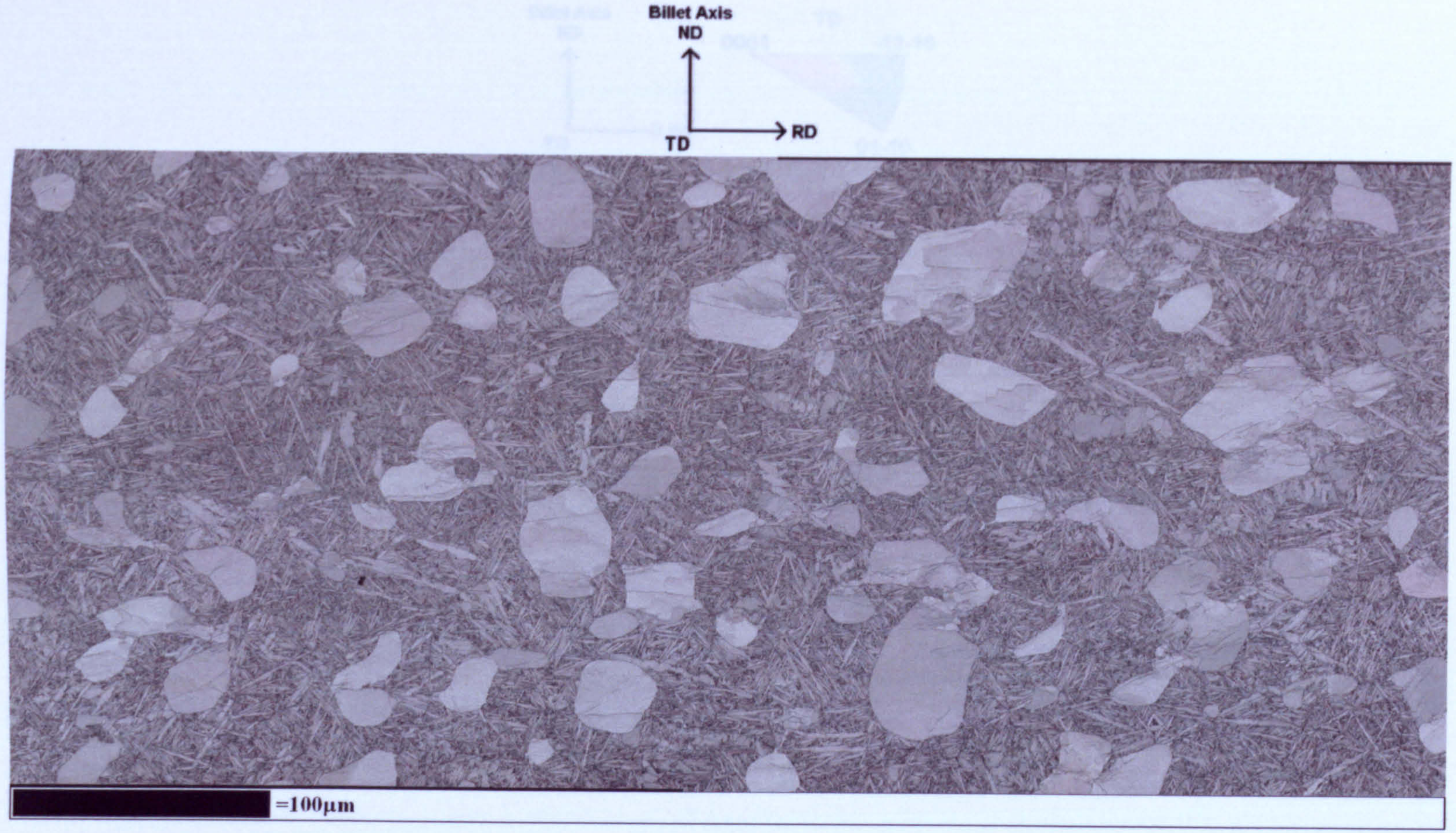

Fig. 8.43(a) High resolution EBSD analysis from specimen F, deformed at a true strain rate of $0.019s^{-1}$ to an equivalent true strain of 0.67. This map shows band contrast.

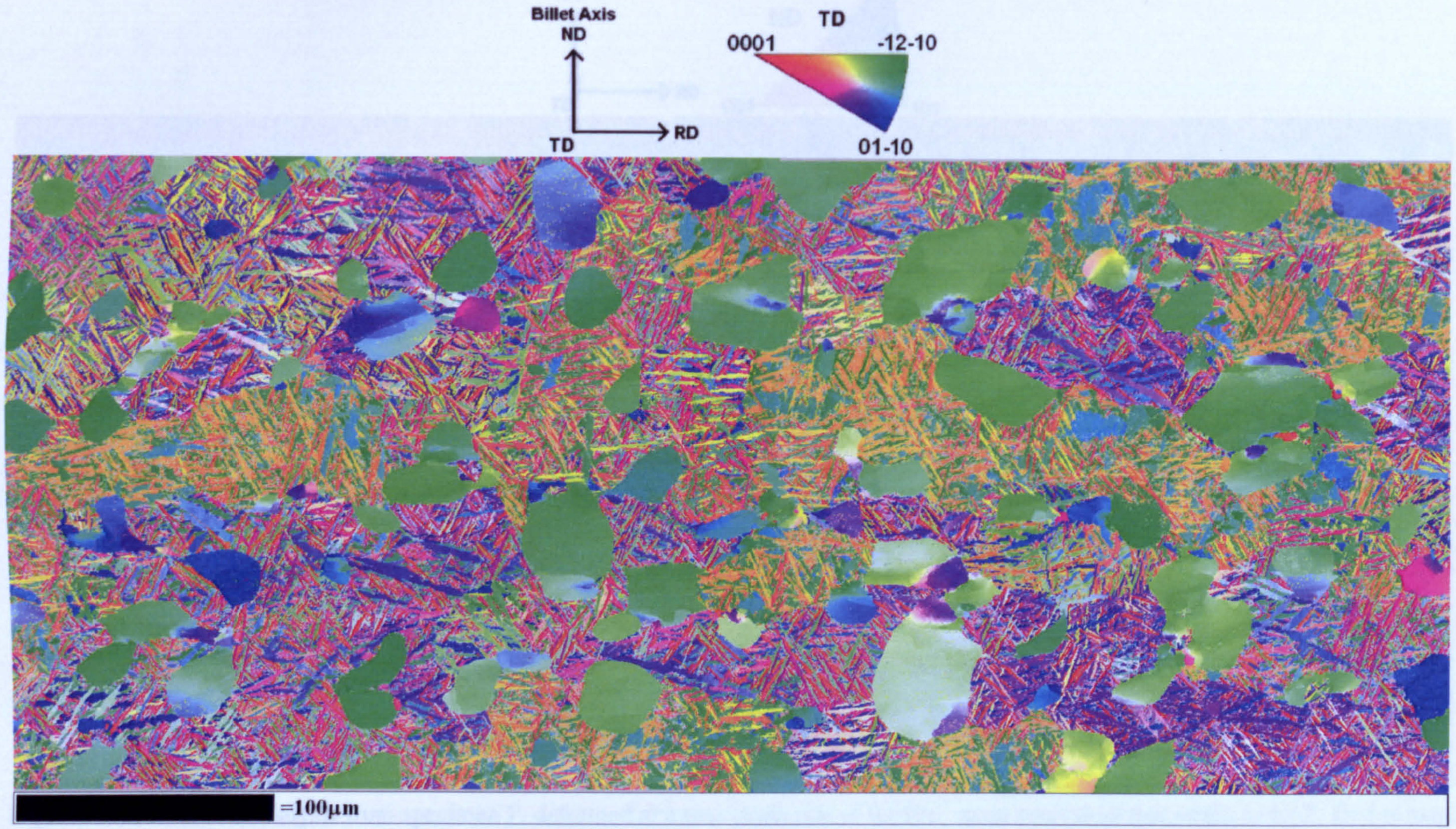

Fig. 8.43(b) High resolution EBSD analysis from specimen F, deformed at a true strain rate of $0.019s^{-1}$ to an equivalent true strain of 0.67. This map shows IPF colouring with non indexed points in grey.

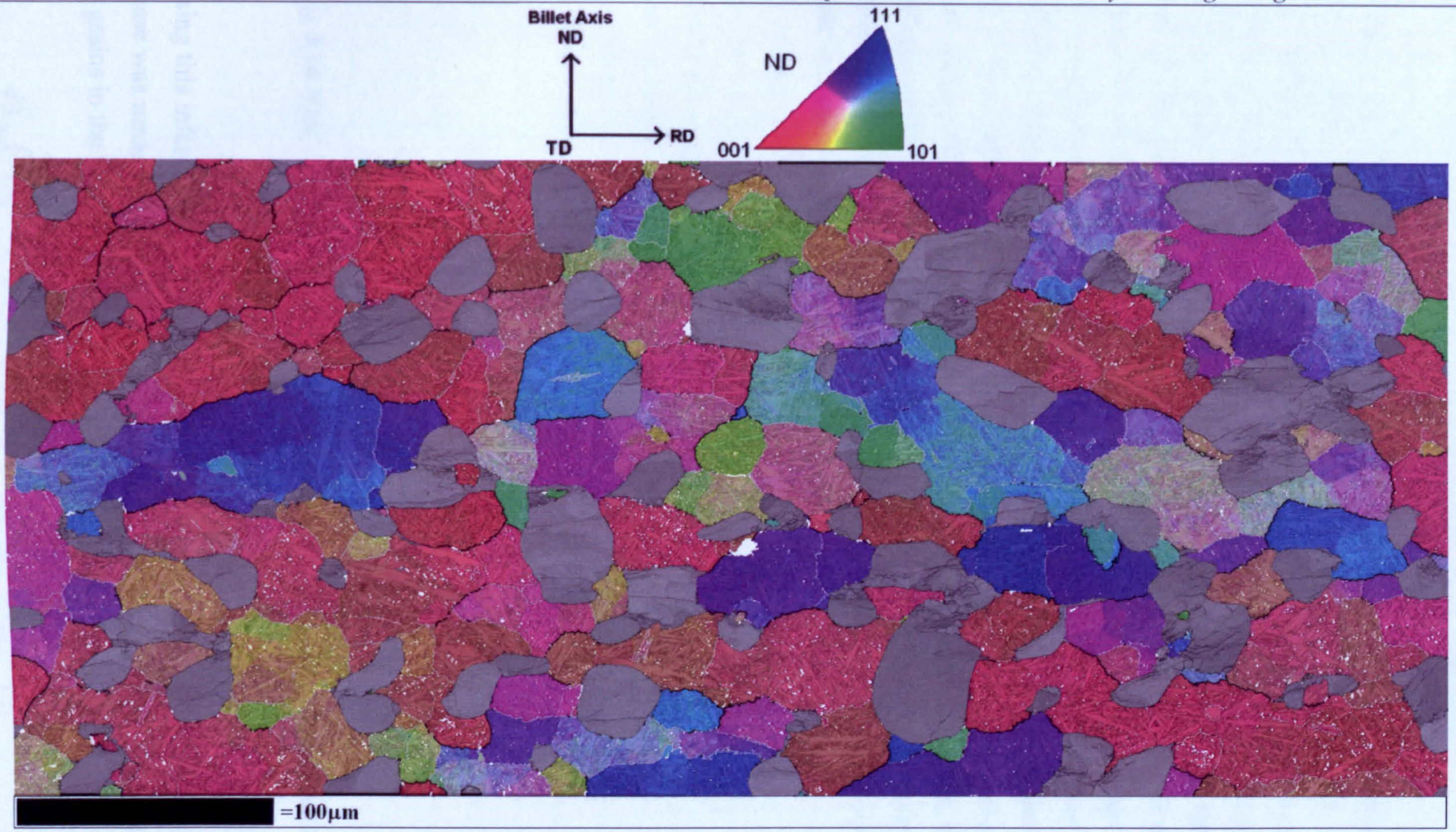

Fig. 8.43(c) High resolution EBSD analysis from specimen F, deformed at a true strain rate of $0.019s^{-1}$ to an equivalent true strain of 0.67. In this map, the α_p and α_s phases have been separated and β reconstruction carried out on the α_s. The α_p is shown with band contrast and the reconstructed β grains with a combination of band contrast and IPF colouring (with respect to ND). Unreconstructed points are coloured white. Within the reconstructed β phase, misorientations greater then 5° are coloured silver and misorientations greater than 15° black.

8.3 Discussion

8.3.1 The Degree of Strain Accommodated in the α_p and β Phases

As discussed in chapter 5, the as received billet contained a strong primary alignment of the α_p grains along the billet axis, which can be seen in Fig. 5.1. In the initial microstructure test (i.e. heat treated but undeformed), the microstructure after quenching was bimodal but there was the same tendency for non equiaxed and contiguous α_p grains to be aligned with the billet axis (ND), which can be seen in both the optical (Fig. 8.21) and EBSD maps (Figs. 8.27 and 8.38). In the specimens that were deformed to equivalent strains of between 0.63 and 0.67 (~50% reduction) at a range of strain rates, the α_p grains were more equiaxed and less contiguous. For specimen C, which was deformed to the higher equivalent strain of 1.23, there was a tendency for the α_p grains to be slightly pancaked along RD. These relatively modest changes in the α_p phase with increasing strain are shown in Fig. 8.44, which plots the ratio between the mean linear intercept grain size measured in the RD and ND directions for the starting billet, the initial microstructure test (specimen G) and specimens B and C, which were deformed at $1.8s^{-1}$ to strains of 0.64 and 1.23 respectively.

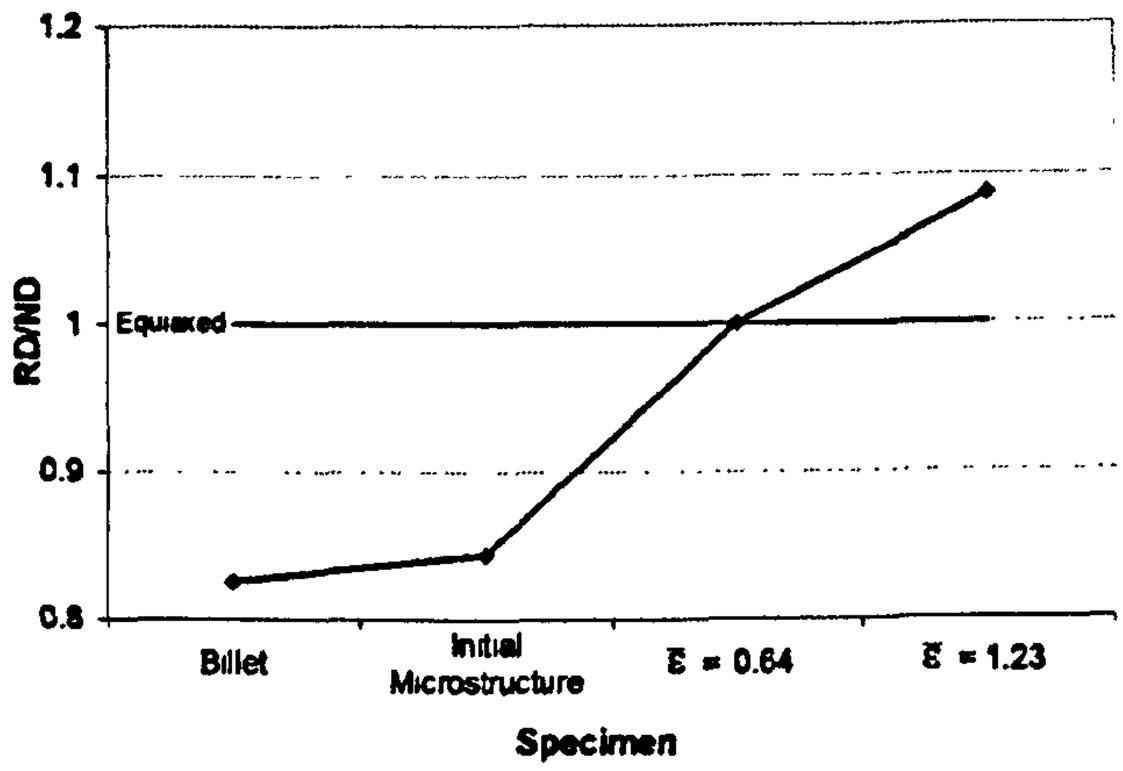

Fig. 8.44 Ratio of α_p RD/ND mean linear intercept grain size for the as-received billet, the initial microstructure test and deformed specimens, B and C.

Using this information, an estimate for the equivalent true strain accommodated by the α_p phase was made using equation 8.24, where A_1 and A_2 are the RD/ND aspect ratios of the α_p grains in the initial and deformed microstructures respectively.

$$\frac{\sqrt{3}}{4}\ln\left(\frac{A_2}{A_1}\right) \tag{8.24}$$

Such an approach although approximate, shows that for the PSC specimen deformed to an equivalent strain of 1.23, the α_p phase undergoes an average strain of approximately 0.2. This behavior is typical of titanium alloys deformed in the $\alpha+\beta$ phase field at temperatures at which β becomes the continuous phase, where the isolated α_p particles behave like hard inclusions in the soft β matrix (Flower, 1990). Similar low levels of strain in the α_p phase has been shown previously for several alloys by Chaze and Monthelliet (1994).

8.3.2 Flow Behaviour

Due to the low level of strain accommodated by the isolated and well globularised α_p grains, the flow behaviour of the material at temperatures in the upper $\alpha+\beta$ phase field will mostly reflect the deformation occurring in the much softer continuous β phase (Flower, 1990). After considering the likely effect of deformation heating, the analysis of the flow behaviour suggests that there is little microstructure related flow softening in the flow behaviour and that the flow behaviour is characterised by a near steady state flow stress. Such flow behaviour is similar to that reported by Thomas (2007) for deformation in the upper $\alpha+\beta$ phase field in Timetal 834 with a globular (equiaxed) microstructure and by other workers for a number of titanium alloys (Weiss and Semiatin, 1998, 1999). Steady state flow of this type suggests that in the deformation of the β phase, there is a balance between working hardening and the softening process of dynamic recovery and an absence of typical discontinuous dynamic recrystallisation in which nucleation and growth of new recrystallised grains is taking place during hot deformation. Discontinuous dynamic recrystallisation of this type is common in low stacking fault energy materials and results in a characteristic drop in the flow stress after a critical strain (Sellars, 1990). In titanium alloys, the medium to high stacking fault energy prevents this type of dynamic recrystallisation due to the ease with which the deformed β grains undergo dynamic recovery.

8.3.3 Microstructural Evolution in the α_p Phase

Despite the relatively low strains in the α_p phase, the high resolution EBSD maps clearly show that the α_p grains develop substructure as a result of the deformation.

8.3.3.1 Initial Microstructure Specimen

In the billet and the initial microstructure specimen, G, smaller α_p grains generally contained no substructure, while larger α_p grains were generally divided into a few large subgrains separated by low angle grain boundaries. Both low and high angle boundaries were observed between contiguous α_p grains. Accumulated misorientations across the interior of the subgrains were low, which is indicative of a low dislocation density. In addition, the subgrain boundaries are clearly visible in the band contrast maps as sharp boundaries even for misorientations as low as 1°. These features suggest a well recovered microstructure. Fig. 8.45 shows part of the high resolution EBSD map from specimen G in greater detail, showing the typical substructure within the α_p grains in the initial microstructure.

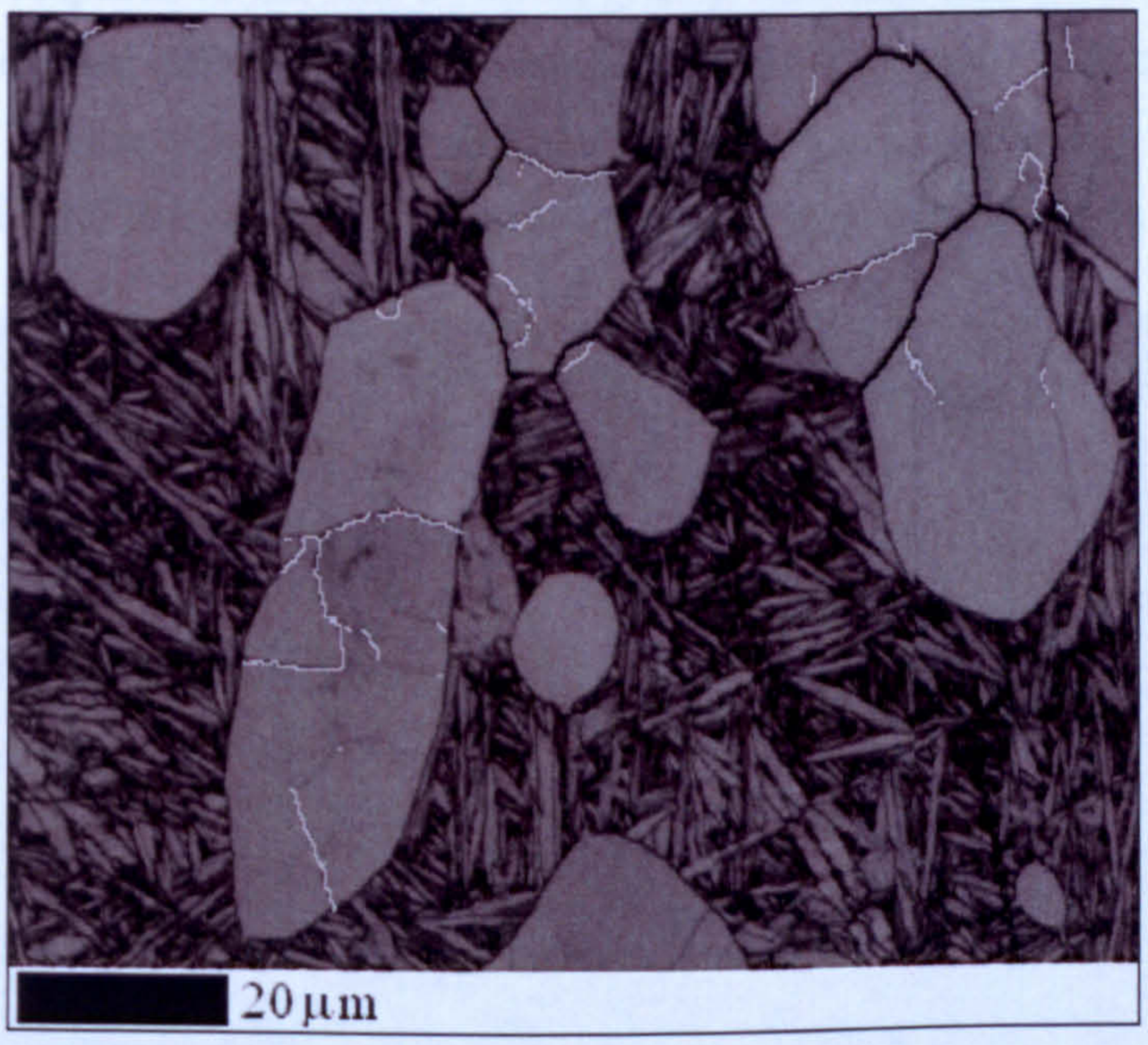

Fig. 8.45 Band contrast map from the initial microstructure test (specimen G), showing low and high angle grain boundaries in the α_p phase. Light grey boundaries > 2° and black boundaries > 15°.

8.3.3.2 Analysis of the Tests at a Strain Rate of $1.8s^{-1}$

In the $\bar{\varepsilon} = 0.64$ test at a strain rate of $1.8s^{-1}$ (specimen B), accumulated misorientations across the subgrains and grains were higher and there was an increase in low angle grain boundaries compared to the initial microstructure. Fig. 8.46 shows part of the high resolution EBSD map from specimen B in greater detail, showing the typical substructure within the α_p grains. Strain in the α_p phase was heterogeneous between α_p grains and within the grains themselves. Some grains showed only modest increases in accumulated

misorientations and substructure, whereas in other grains it was much higher. This heterogeneity can be explained by the limited number of available slip systems in the hcp structure. This means that certain grain orientations, which are not favorable for the activation of slip are thus harder and deform less. Within the grains, the substructure and accumulated misorientations were often concentrated within smaller areas of the grains, with the remainder of the grain containing little or no substructure. In areas where the level of substructure was particularly high, it often had the appearance of a fine equiaxed cell structure. The areas of concentrated substructure were almost always at the edges of the grains and were often located around the boundaries between adjoining α_p grains. A small amount of deformation twinning was also observed within the α_p grains. In the high resolution map of Fig. 8.40, 5% of the α_p grains contained one or more twins. Most of the twins observed in this map terminated within the interior of the α_p grains and are relatively small compared to the size of the α_p grains, meaning that the twinned volume in this specimen was only 0.4% of the total volume of the α_p grains. This suggests that at a strain rate of $2s^{-1}$, although a small amount of deformation twinning is observed, the overall contribution of this mechanism to the strain in the α_p phase is low.

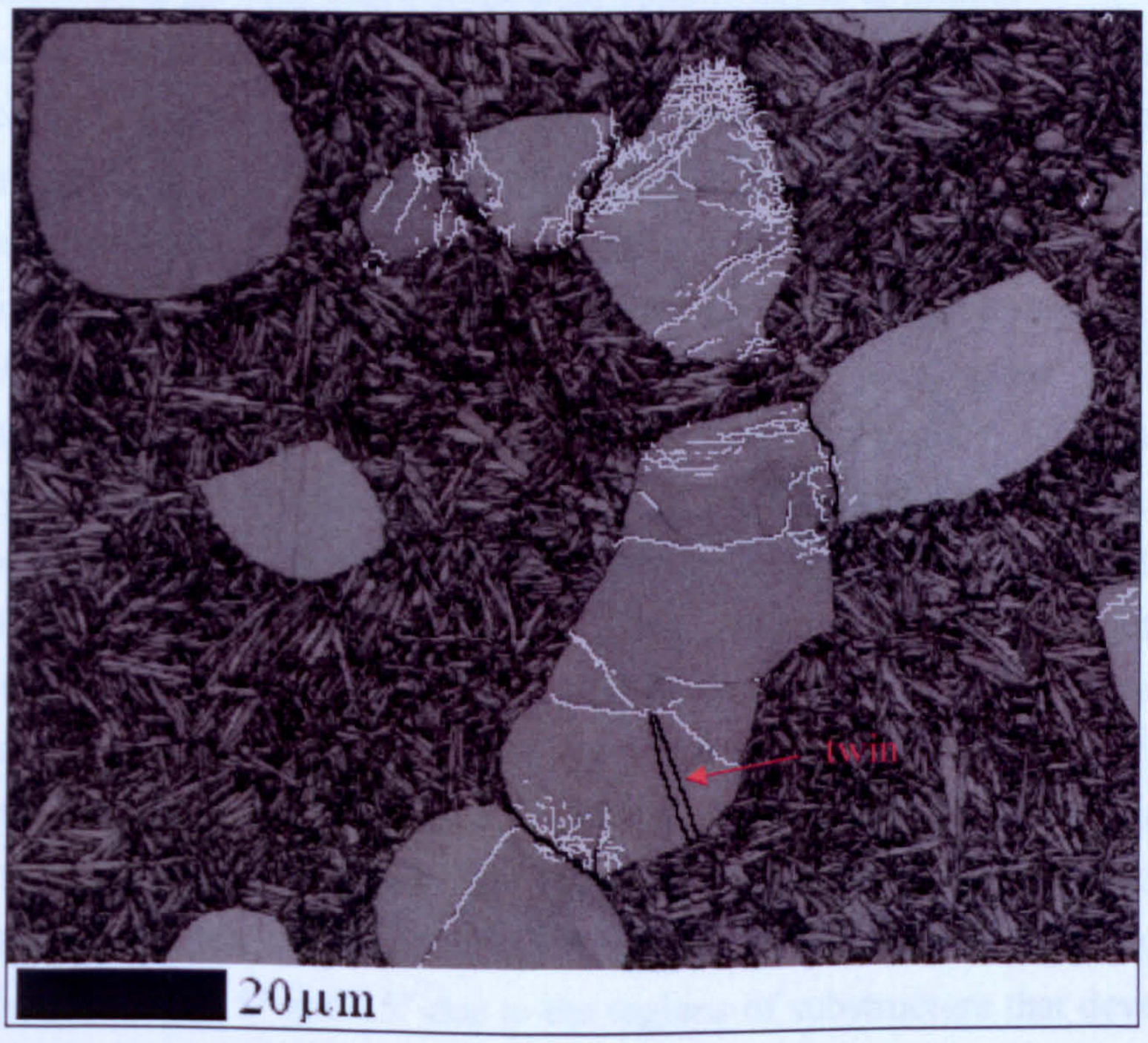

Fig. 8.46 Band contrast map from specimen B ($\dot{\varepsilon}$ =1.8s^{-1}, $\bar{\varepsilon}$ = 0.64), showing low and high angle grain boundaries in the α_p phase. Light grey boundaries > 2° and black boundaries > 15°.

For the higher strain of $\bar{\varepsilon}$ = 1.23 (specimen C), there was a further increase in accumulated misorientations and substructure within the α_p grains. Fig. 8.47 shows four regions of the high resolution EBSD map from specimen C in greater detail, which shows

the typical substructure within the α_p grains. It can be seen that although there is increased substructure compared to the lower strain specimen, the strain within the α_p grains remains very heterogeneous with large parts of many α_p grains containing little or no substructure. In some grains, localised areas of very fine equiaxed grains, separated by high angle grain boundaries, developed from the cell like substructures seen at the lower strain. These were mainly found at the boundaries of adjacent α_p grains (Fig. 8.47(a)), in small thin grains (Fig. 8.47(b)) and at the edges of larger grains (Fig. 8.47(d)). Examining the example shown in Fig. 8.47(a), the pole figures in Fig. 8.48 show the orientations of the small high angle grains in the region at the boundary indicated, ReX, with respect to the orientations of the two α_p grains marked α_p1 and α_p2, which lie on either side of the boundary. It can be seen that the two α_p grains, α_p1 and α_p2, contain a large spread of orientations due to the deformation. The small high angle grains are widely misorientated from the α_p grains and from each other. The significantly higher misorientations between the small grains suggests that they are not simply substructure that has become more highly misorientated but are in fact evidence of localised dynamic recrystallisation. The volume fraction of these areas of recrystallised grains was small however, accounting for only 1.8% of the total volume of the α_p grains.

There was no significant increase in the level of deformation twinning in the $\bar{\varepsilon} = 1.23$ specimen compared to the $\bar{\varepsilon} = 0.64$ specimen. Furthermore, the twins in the higher strain specimen appeared to be more heavily deformed than those in the lower strain specimen. This suggests that the small amount of deformation twinning which occurs at a strain rate of $1.8s^{-1}$ tends to take place during the early stages of deformation at low strains.

Fig. 8.49 shows misorientation angle distributions in the α_p phase for the initial microstructure and the specimens deformed at $1.8s^{-1}$ to strains of $\bar{\varepsilon} = 0.64$ and $\bar{\varepsilon} = 1.23$ respectively. The data are for an equal volume of α_p phase allowing a comparison between the level of substructure in each specimen as well as the angular distribution. Misorientations of less than 5° have been excluded. As expected, the distribution for the initial microstructure contains far fewer misorientations above 5° compared to the deformed specimens due to the recovered condition of this microstructure. Due to the subgrains present within the α_p grains, and clusters of similarly orientated α_p grains, there are more misorientations between 5° and 15° compared to higher misorientation angles. The distributions for the deformed specimens are similar, consisting of mostly small misorientations between 5° and 15° due to the regions of substructure that develop within the α_p grains. Small broad peaks around misorientation angles of approximately 65° and 86° are due to two different types of deformation twin. As expected, the higher strain specimen contains more misorientations for the same volume of α_p phase. The increase between 5° and 15° reflects an increase in substructure and the increase at higher misorientations is caused by the localised recrystallisation, which although small in terms of volume contains a significant grain boundary area due to the large number of small

grains within these regions.

Fig. 8.50 shows the misorientation axes for the misorientations in the α_p phase for the $\bar{\varepsilon} = 0.64$ test (specimen B). It can be seen in Fig. 8.50(a) that the misorientation axes for low misorientations (5-15°), cover the entire pole figure but that there is a higher than random density around <0001> (Fig. 8.50(b)). This may indicate that the most active slip system is prismatic $\{10\bar{1}0\}\langle 1\bar{2}10\rangle$ slip. The two poles at higher angles correspond to the axes for the two types of deformation twin.

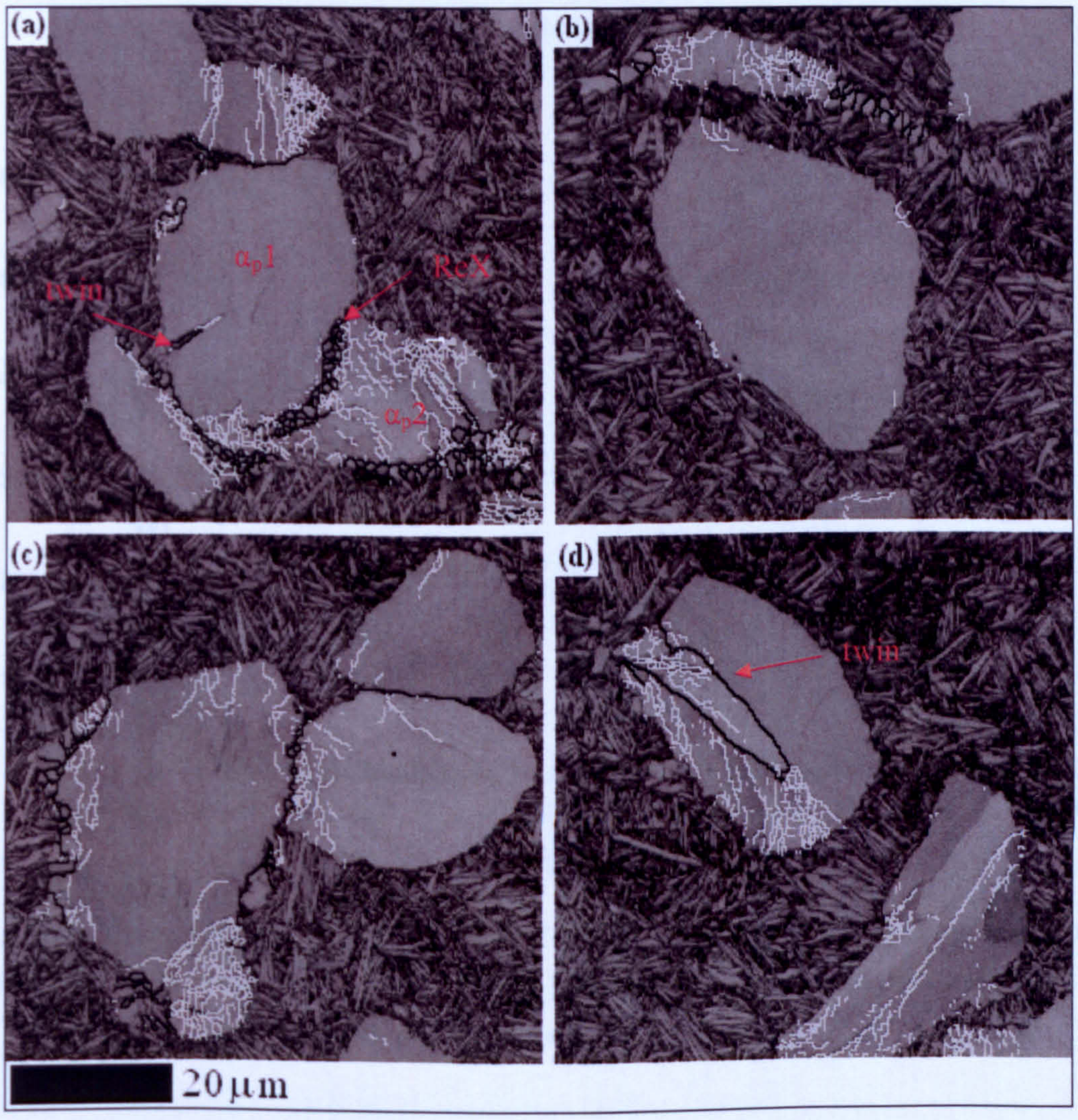

Fig. 8.47 Band contrast maps from specimen C ($\dot{\varepsilon}$ =1.8s^{-1}, $\bar{\varepsilon}$ = 1.23), showing low and high angle grain boundaries in the α_p phase. Light grey boundaries > 2° and black boundaries > 15°.

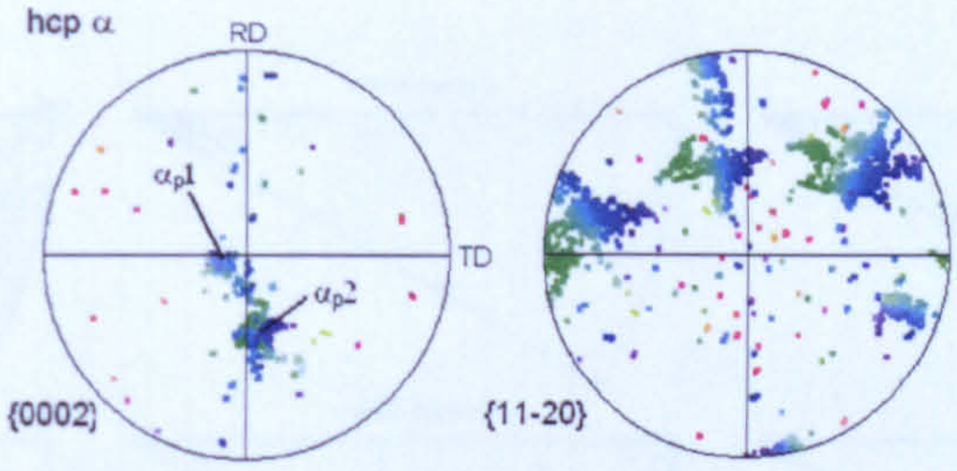

Fig. 8.48 Pole figures for the grains labeled as α_p1, α_p2 and Rex in Fig. 8.47(a). The two orientations with a large degree of spread correspond to α_p1 and α_p2. The remaining sharp poles correspond to the small grains at the boundary between α_p1 and α_p2.

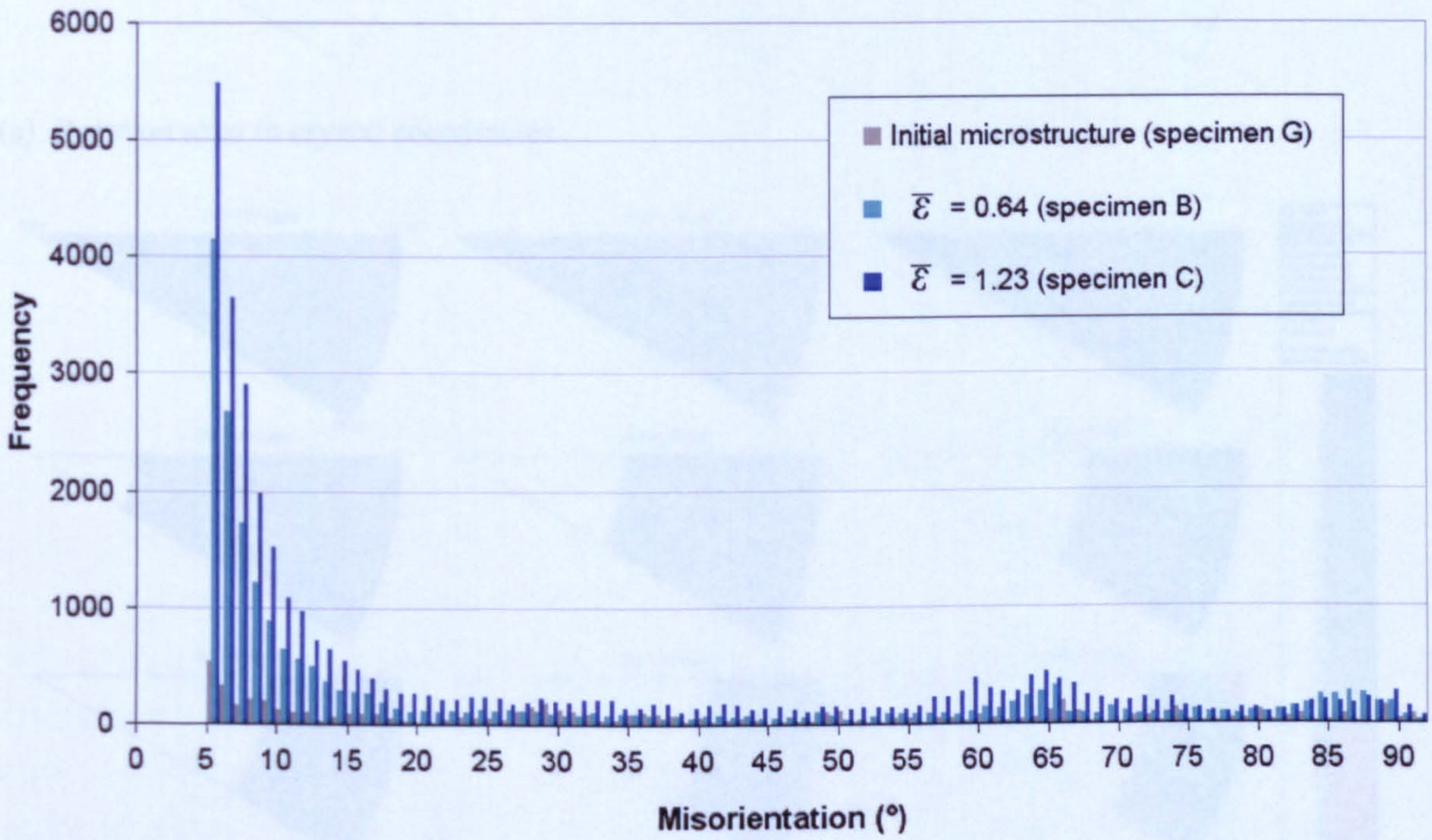

Fig. 8.49 Misorientation angle distributions (>5°) in the α_p grains for the initial microstructure test (G) and the two tests at a strain rate of $1.8s^{-1}$ (B and C). The frequencies were calculated for an equal volumes of α_p phase.

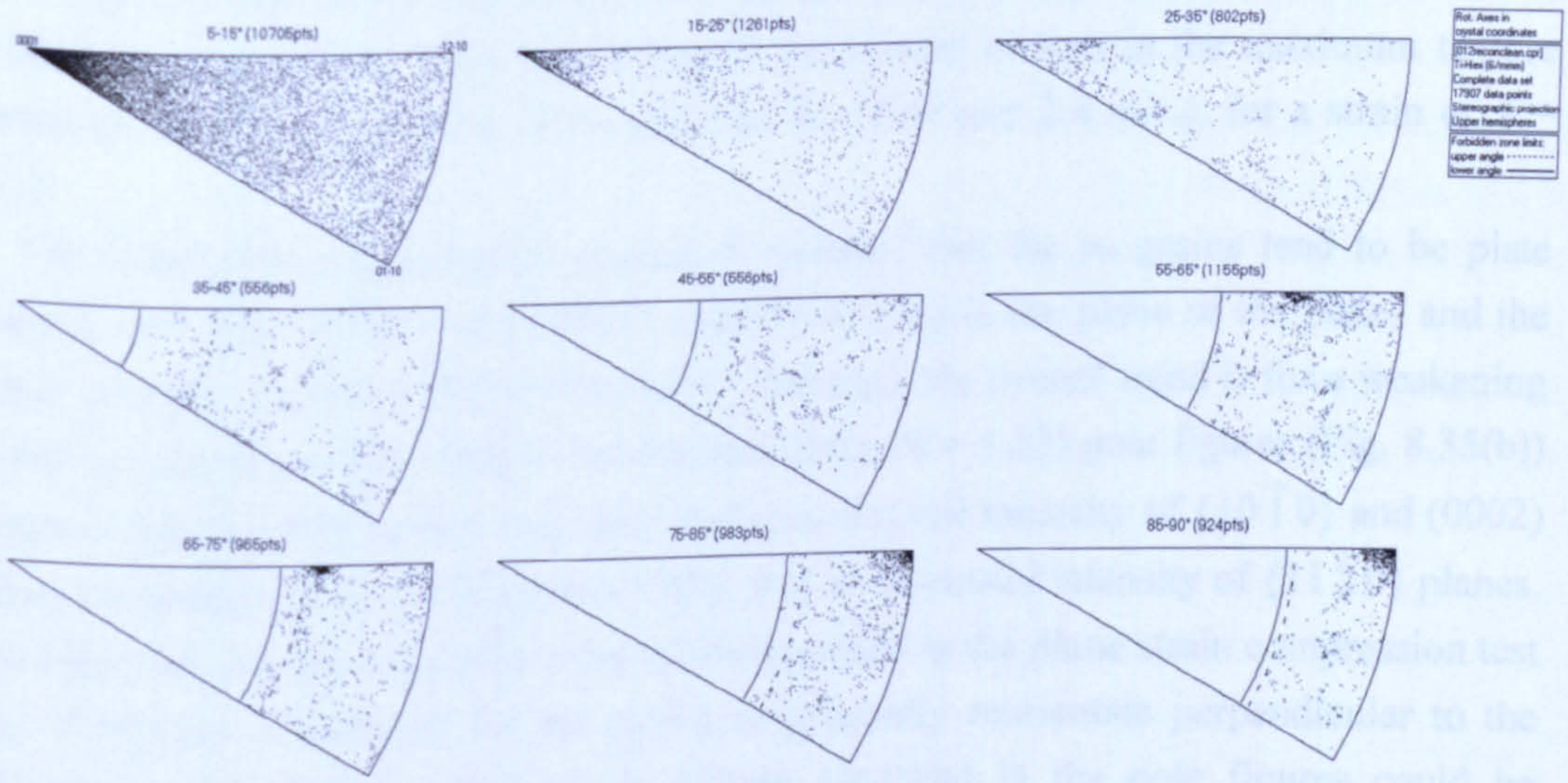

(a) Rotation axes in crystal coordinates.

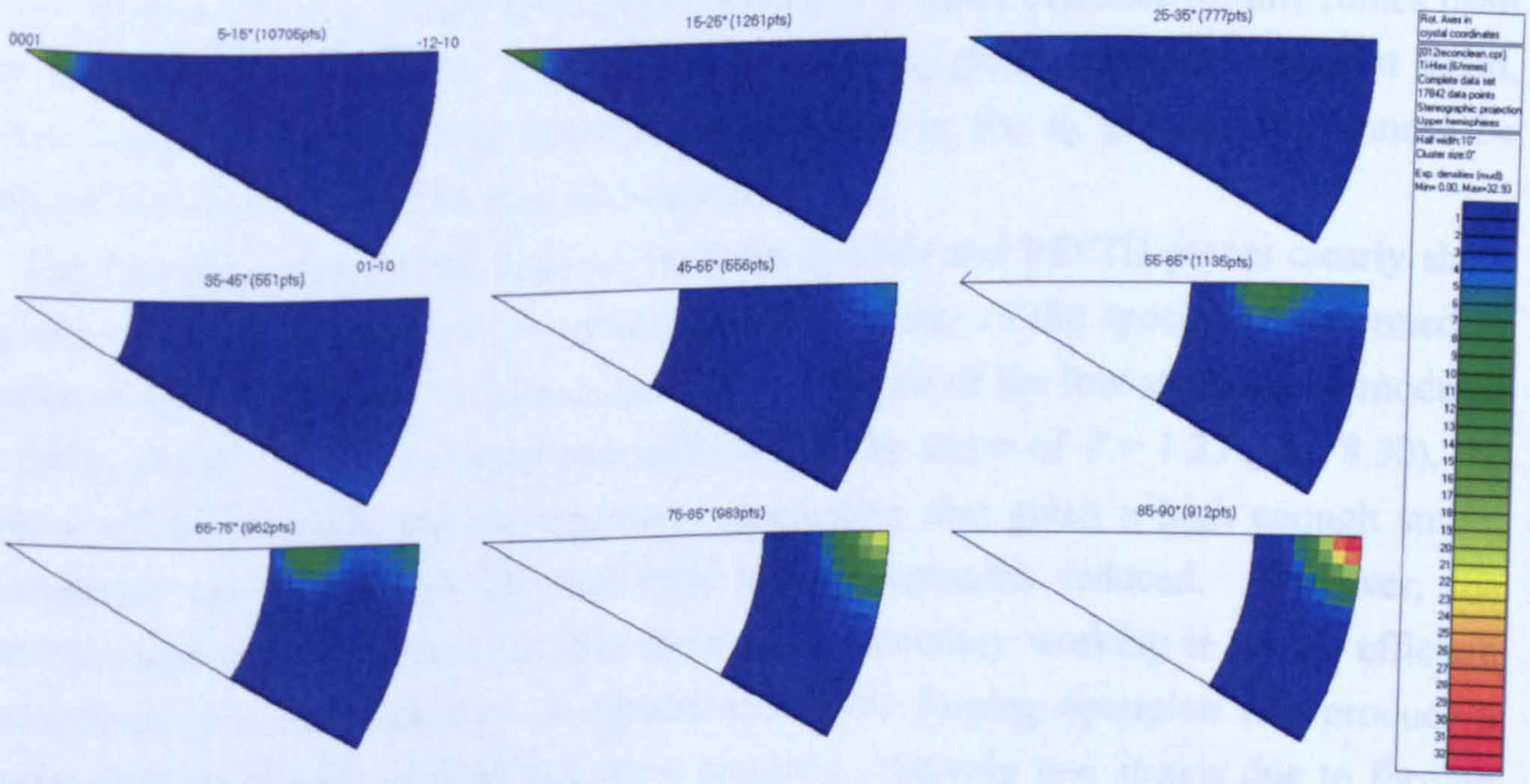

(b) Contour plot from the data above.

Fig. 8.50 Misorientation axes in crystal coordinates for misorientations greater than 5° in the α_p phase for specimen B ($\dot{\varepsilon}$ =1.8s^{-1}, $\bar{\varepsilon}$ = 0.64).

8.3.3.3 Texture Development in the α_p Phase.

Textures in the α_p phase in specimens B and C deformed at a strain rate of 1.8s^{-1} were given in Fig. 8.35(a) and Fig. 8.35(b) respectively. These show that the α_p phase does not develop a strong deformation texture even at the highest level of strain. This is to be expected given the low levels of strain accommodated by the α_p phase compared to the softer β matrix. Instead, the results show that the deformed α_p textures mostly resemble

the textures in the as-received billet (see Fig. 6.17) but become weaker and more random with increasing strain. This weakening of the texture is seen in the maximum texture intensity, which was 3 m.r.d. for a strain of $\bar{\varepsilon} = 0.64$ and 2.4 m.r.d. for a strain of $\bar{\varepsilon} = 1.23$.

The billet characterisation in chapter 5 revealed that the α_p grains tend to be plate shaped, with the <10 $\bar{1}$ 0> and <0002> directions lying in the plane of the plates and the plates strongly aligned with the billet axis. Although the overall trend is for a weakening of the α_p texture, careful study of the highest strain ($\bar{\varepsilon} = 1.23$) pole figures (Fig. 8.35(b)) suggests that the deformation may also lead to a reduced intensity of {10 1 0} and (0002) planes perpendicular to the billet axis (ND), and an increased intensity of {11 $\bar{2}$ 0} planes. The observed change in the alignment of the α_p grains in the plane strain compression test (Fig. 8.44) was a tendency for the grains to gradually reorientate perpendicular to the billet axis. The possible changes in texture observed in the pole figures could be explained if a significant amount of the reorientation of the α_p grains occurred by a rigid body rotation of the α_p grains in the softer β matrix. Further evidence for this comes from the low level of substructure in large parts of many α_p grains even at the highest strain, which suggests that slip and deformation twinning in the α_p grains alone cannot be responsible for the change in α_p grain alignment.

The low resolution EBSD maps in both the RD/ND and RD/TD planes clearly show regions of similarly orientated α_p grains persist in many of the specimens deformed to strains of approximately $\bar{\varepsilon} = 0.64$, a direct consequence of the low strain accommodated by the α_p phase. In the one specimen deformed to the strain of $\bar{\varepsilon} = 1.23$ (Fig. 8.30), the regions of microtexture are less apparent, suggesting that given a high enough strain, macrozones can be broken up and their texture strengths reduced. However, the relatively high strain required for this shows that secondary working is not an efficient means to remove microtexture. A typical closed die forging operation will produce a forging with significant regions that have received relatively low strains due to forging dead zones and thus can be expected to contain clusters of similarly orientated α_p grains, where they are present in the initial billet.

8.3.3.4 Analysis of the Tests at the Lower Strain Rates of $0.18s^{-1}$ and $0.019s^{-1}$

In the orientation maps for the slower strain rates of $0.18s^{-1}$ and $0.019s^{-1}$ (Figs. 8.42 and 8.43), no deformation twins were observed. Apart from the absence of twins, the level and distribution of substructure appeared similar to the specimen deformed at $1.8s^{-1}$. Once again, the substructure indicated that the strain in the α_p phase was heterogeneous between α_p grains and within the grains themselves, with some grains showing only modest increases in accumulated misorientations and substructure, whereas in other grains it was much higher. These observations are supported by the misorientation angle

distributions, shown in Fig. 8.51. The data are for the same volume of α_p phase as the earlier analysis allowing a direct comparison between the levels of substructure in all tests. It can be seen that the distribution and level of low angle grain boundaries (5-15°) is similar for all three strain rates. This suggests that the level of strain in the α_p phase due to slip does not change significantly with decreasing strain rate. It can be seen that the broad low peaks present at approximately 65 and 86° for the strain rate of $2s^{-1}$, which were due to a small amount of deformation twinning are absent in the distributions for the slower strain rates, confirming that deformation twinning in the α_p phase is not active at slow strain rates.

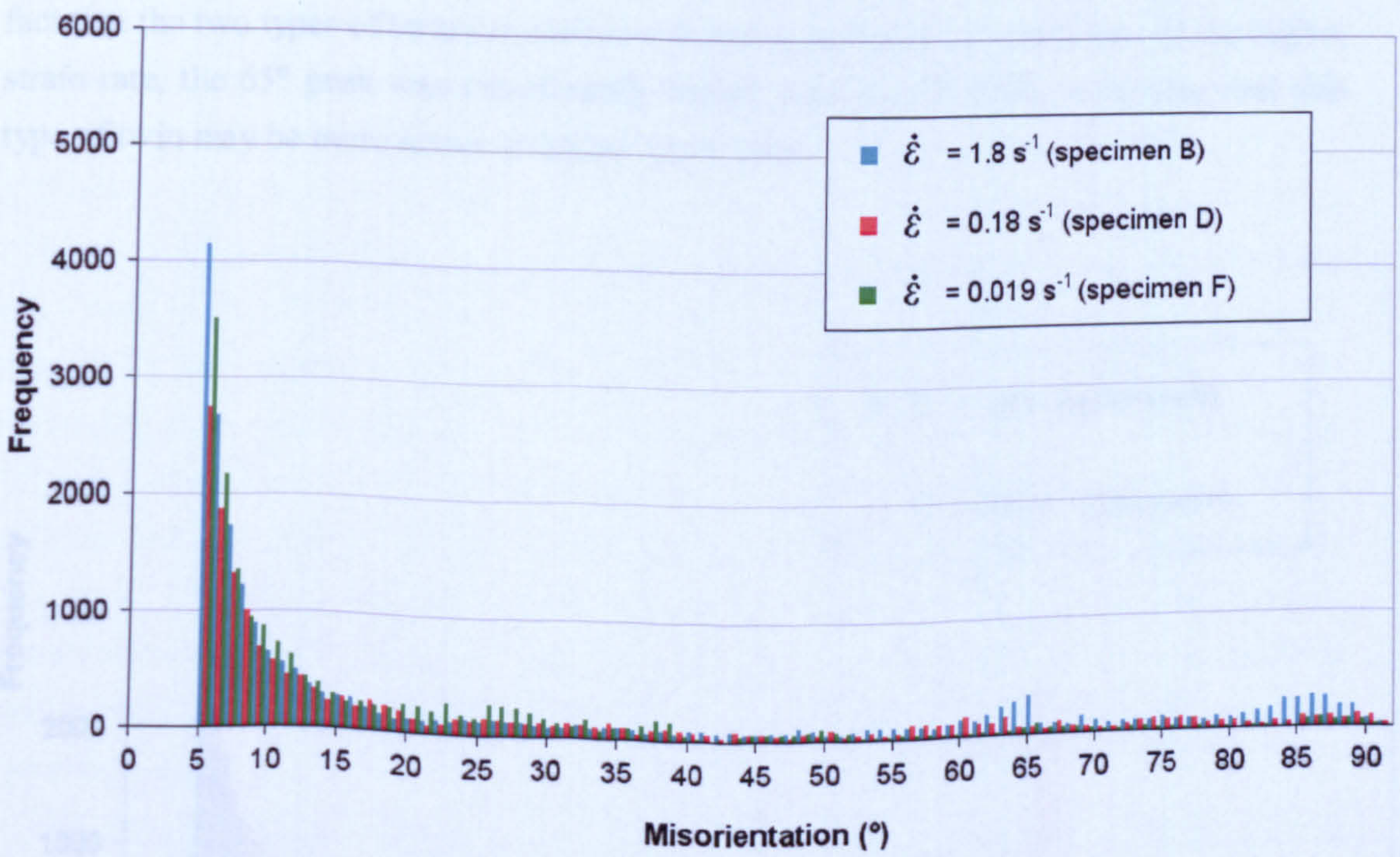

Fig. 8.51 Misorientation angle distributions (>5°) in the α_p grains for the specimens deformed to a strain of approximately $\bar{\varepsilon} = 0.64$ at strains rates of 1.8, 0.18 and $0.019s^{-1}$. The frequencies are for equal volumes of α_p phase.

8.3.3.5 Analysis of the Tests at the Higher Strain Rate of $20.2s^{-1}$

In the orientation maps for the highest strain rate of $20.2s^{-1}$ (Fig. 8.39), the number of deformation twins in the α_p phase increased significantly compared to the strain rate of $1.8s^{-1}$. In the high resolution map of Fig. 8.39, approximately 25% of the α_p grains contained one or more twins. Compared to the lower strain rate, the twinned regions were larger and in some cases crossed entire α_p grains. The twinned volume in this specimen was 3.8% of the total volume of the α_p grains, indicating a more significant contribution to strain in the α_p phase. The level and distribution of lower angle grain

boundaries (5-15°) appeared to be similar to the lower strain rate tests. The substructure indicated that strain in the α_p phase was again heterogeneous between α_p grains and within the grains themselves, with some grains showing only modest increases in accumulated misorientations and substructure, whereas in other grains it was much higher. These observations are supported by the misorientation angle distributions, shown in Fig. 8.52 for the 1.8 and 20.2s^{-1} tests. It can be seen that the distribution and level of low angle grain boundaries (5-15°) does not change significantly for the higher strain rate. At higher angles, the peaks present at approximately 66° and 86°, due to deformation twinning are much higher for the specimen deformed at 20.2s^{-1}. At the lower strain rate, the peaks due to deformation twinning were similar in height, reflecting the fact that the two types of twin were observed in roughly equal proportions. At the higher strain rate, the 65° peak was significantly higher than the 86° peak, indicating that this type of twin may be more active at higher strain rates.

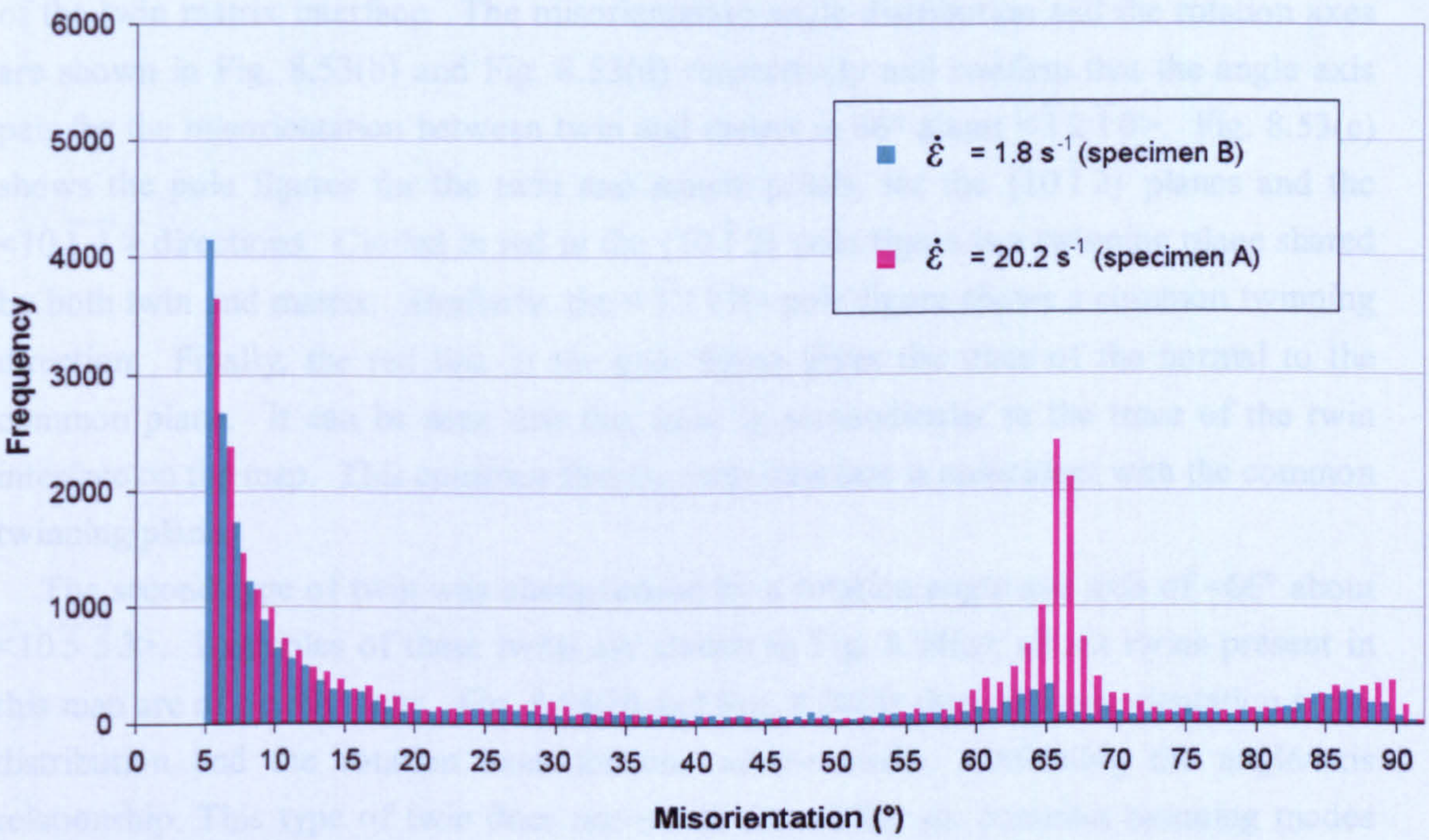

Fig. 8.52 Misorientation angle distributions (>5°) in the α_p grains for the specimens deformed to a strain of approximately $\bar{\varepsilon} = 0.64$ at strains rates of 1.8 and 20.2s^{-1}. The frequencies are for equal volumes of α_p phase.

8.3.3.6 Twinning Modes in the α_p Phase

All of the twins observed at strains of 1.8 and 20.2s^{-1} belonged to one of two types. They could be identified in the EBSD data by the minimum misorientation angle and the corresponding rotation axis of the twinned volume relative to the matrix. One type had a

rotation of approximately 86° about <11$\bar{2}$0>, while the type that accounted for the majority of twins at the strain rate of 20.2s^{-1} had a rotation of approximately 66° about an axis close to <10$\bar{5}$ $\bar{5}$3>. This axis can be pictured as a rotation of the [2$\bar{1}$ $\bar{1}$0] direction towards the c-axis by angle of approximately 17.3°.

The rotation axis and angle for the first type of twin is close to the angle axis pair of 84.78°<11$\bar{2}$0> given by Mironov *et al.* (2006) for the {10$\bar{1}$2}<10$\bar{1}$ $\bar{1}$> tensile twinning mode. This is one of the six commonly reported modes of mechanical twinning in α titanium. The slightly higher rotation angles observed in the present work are probably due to the slight difference in the c/a ratio for the composition of the α_p phase in Timetal 834 compared to commercial purity titanium. Single surface trace analysis conducted on a number of the 86° twins confirmed that this type corresponds to the {10$\bar{1}$2}<10$\bar{1}$ $\bar{1}$> tensile twinning mode. An example of this trace analysis is shown in Fig. 8.53. A thin lenticular twin terminating within an α_p grain can be seen in the orientation map (Fig. 8.53(a)). To study the twin relationship, a subset of pixels was acquired from either side of the twin matrix interface. The misorientation angle distribution and the rotation axes are shown in Fig. 8.53(b) and Fig. 8.53(d) respectively and confirm that the angle axis pair for the misorientation between twin and matrix is 86° about <$\bar{1}$2$\bar{1}$0>. Fig. 8.53(c) shows the pole figures for the twin and matrix pixels, for the {10$\bar{1}$2} planes and the <10$\bar{1}$ $\bar{1}$> directions. Circled in red in the {10$\bar{1}$2} pole figure is a twinning plane shared by both twin and matrix. Similarly, the <$\bar{1}$2$\bar{1}$0> pole figure shows a common twinning direction. Finally, the red line in the pole figure gives the trace of the normal to the common plane. It can be seen that this trace is perpendicular to the trace of the twin interface on the map. This confirms that the twin interface is coincident with the common twinning plane.

The second type of twin was characterised by a rotation angle and axis of ~66° about <10$\bar{5}$ $\bar{5}$3>. Examples of these twins are shown in Fig. 8.54(a); all six twins present in this map are of the 66° type. Fig. 8.54(b) and Fig. 8.54(d) show the misorientation angle distribution and the rotation axes for one of the twins, confirming the angle/axis relationship. This type of twin does not match any of the six common twinning modes listed by Mironov *et al.* (2006). The rotation axes for the reported common twinning modes are either <10$\bar{1}$0> or <11$\bar{2}$0>, both of which lie in the basal plane. The twin/matrix were found to share a {10$\bar{1}$2}, {11$\bar{2}$1}, {10$\bar{1}$1} and {11$\bar{2}$4} plane and a <$\bar{1}$ $\bar{1}$23> direction. However, the traces of these shared low index planes did not coincide with the twin interfaces. This type of twin has been previously reported in hot deformed Timetal 834 by Thomas (2007). An example of this type of twin was presented and single surface trace analysis showed that there was a shared {13$\bar{4}$1} plane, which coincided with the twin interface. In Fig. 8.54(a), the traces of the shared {13$\bar{4}$1} plane have been superimposed on each twin. In the present work it was found that for these and other analysed examples of this type of twin, in most cases, the shared {13$\bar{4}$1} plane

gave at best only an approximation to the twin interface and no other low index planes gave a perfect match. The precise twinning plane and shear direction for these twins remains unresolved and further work is required using TEM or two surface trace analysis to accurately determine these.

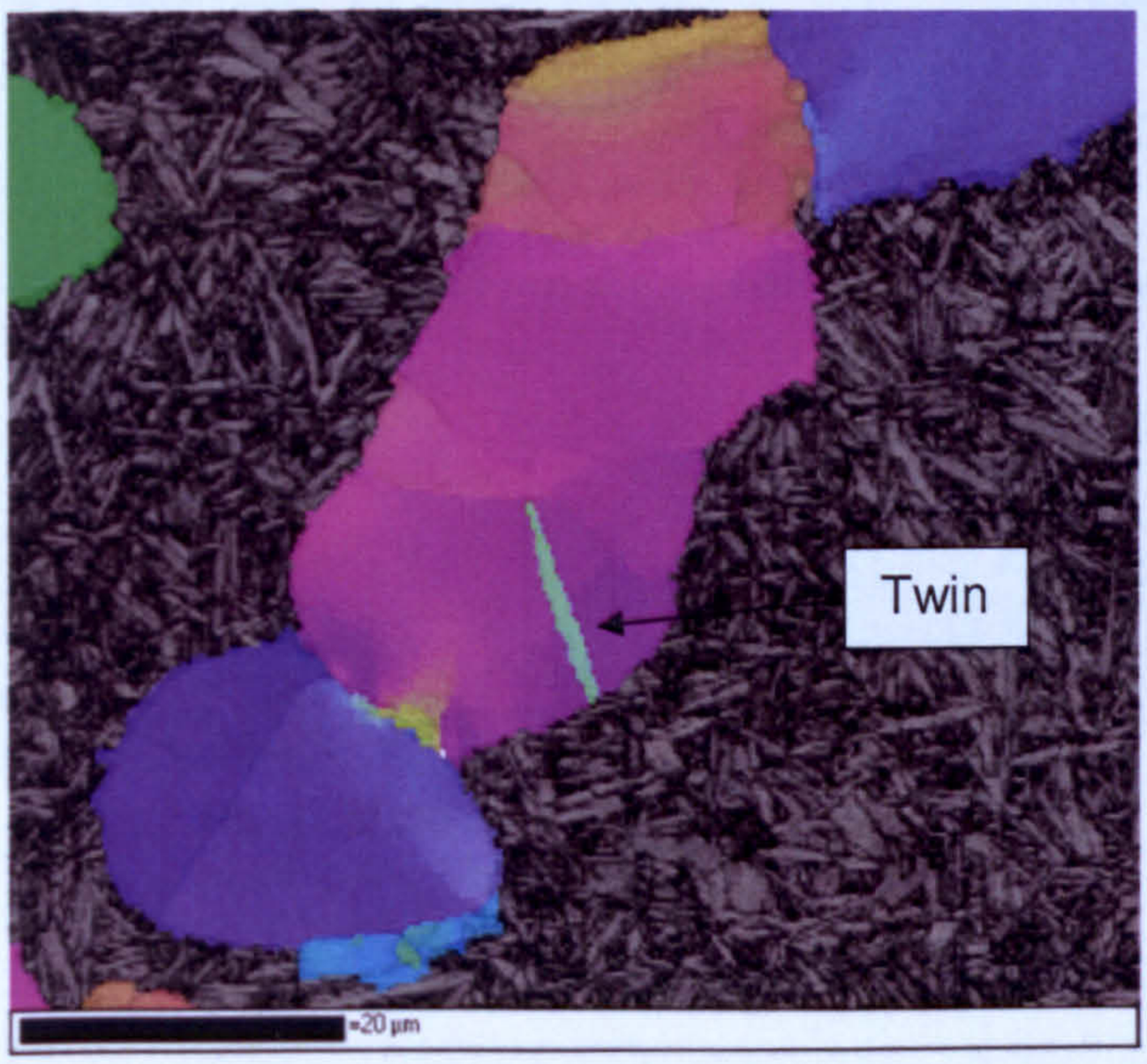

Fig. 8.53 Characterisation of a $\{10\,\bar{1}\,2\}\langle\bar{1}\,2\,\bar{1}\,0\rangle$ twin in an α_p grain: (a) IPF map with band contrast for the α_p grains (twin indicated); (b) misorientation angle distribution for the twin/matrix interface; (c) $\{10\,\bar{1}\,2\}$ and $\langle\bar{1}\,2\,\bar{1}\,0\rangle$ pole figures, showing a common twinning plane and the trace of the plane normal and a common twinning direction; (d) misorientation axes for the twin/matrix interface.

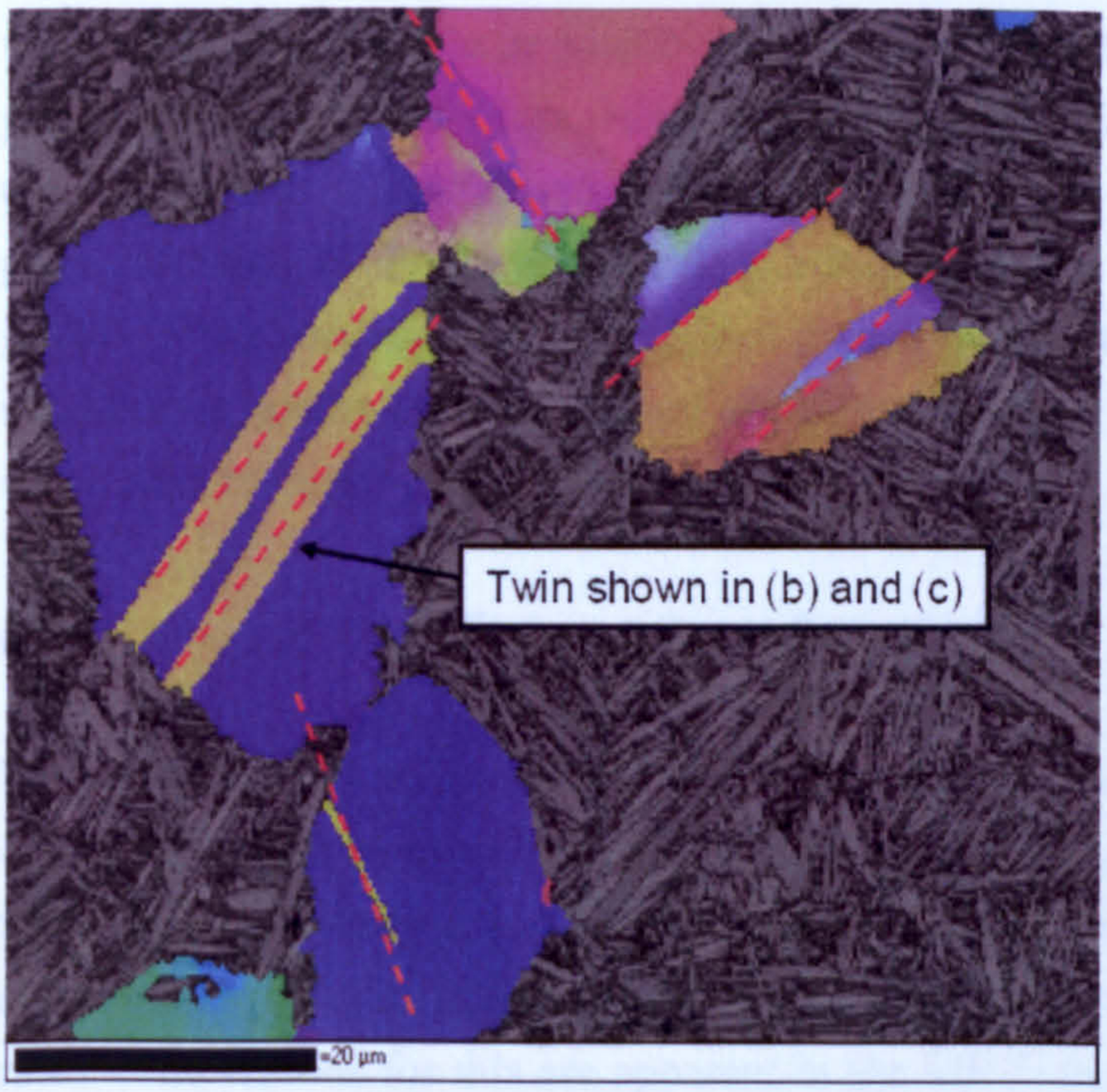

(a)

Traces of the common {13-41} plane in the twin and matrix for each twin.

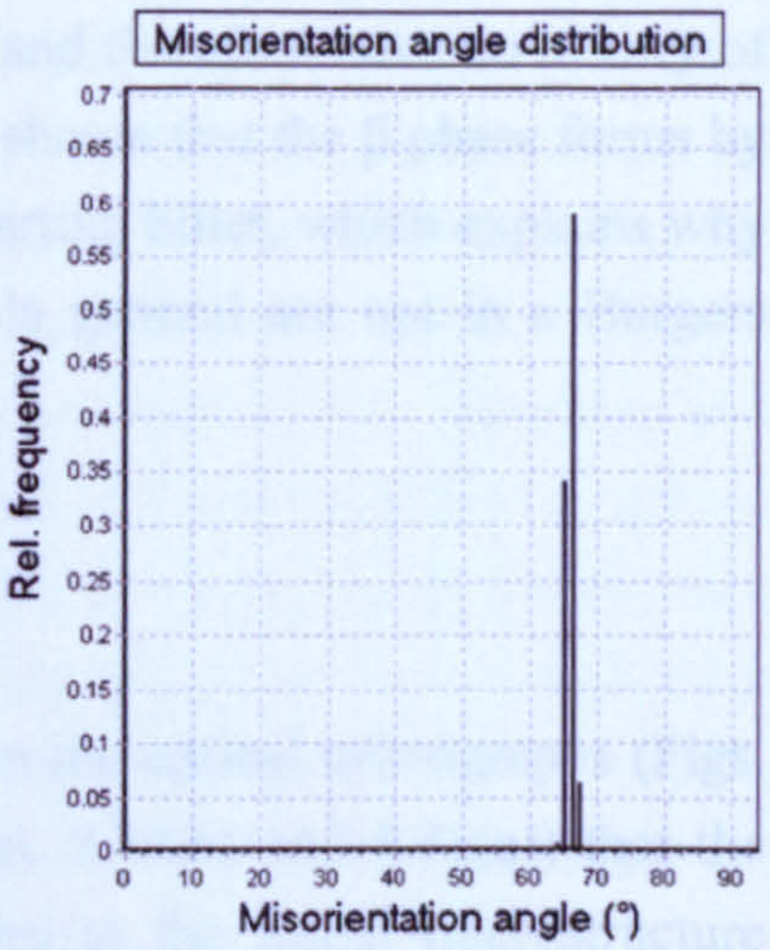

(b)

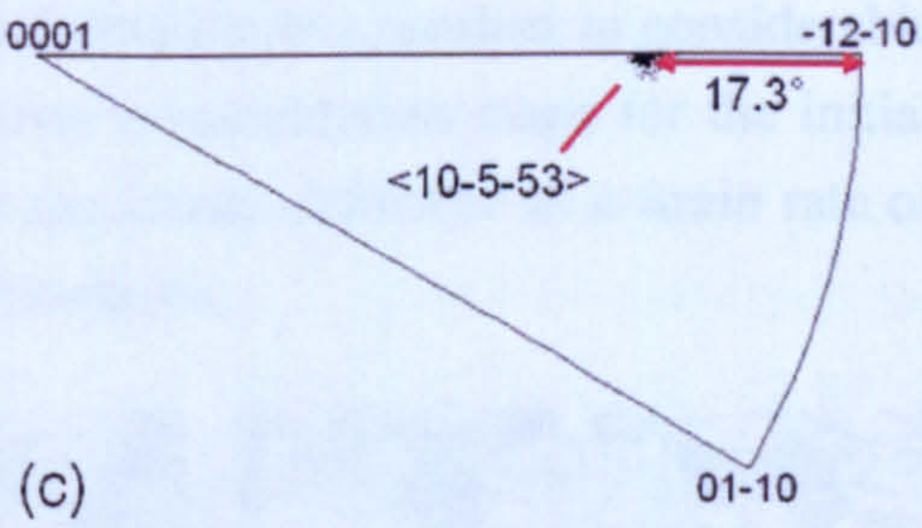

(c)

Fig. 8.54 Map containing six examples of twins in α_p grains which are characterised by a rotation angle and axis between the twin and matrix of ~66° about <10 $\bar{5}$ $\bar{5}$ 3>. (a) IPF map with band contrast for the α_p grains (also shown are the traces of the common {13 $\bar{4}$ 1} plane for each twin/matrix combination); (b) misorientation angle distribution for the indicated twin; (c) misorientation axes for the indicated twin.

8.3.4 Microstructural Evolution in the β Phase

8.3.4.1 Initial Microstructure Specimen

The orientation map for the reconstructed β grains in the initial microstructure specimen (Fig. 8.38(c)) shows that the β grain size is controlled by the pinning of the α_p grains. This means that like the α_p grains, the β grains tend to be non equiaxed and aligned along the billet axis (ND). It can be seen that often several neighboring β grains share similar orientations, with only low angle boundaries (5-15°) between them. Within the β grains

themselves, there is little or no substructure and accumulated misorientations across the β grains are low (typically less than 3°). This initial β microstructure reflects the fact that the β grains are newly formed during the heat treatment and therefore have no history of prior deformation. Previous work (Gey *et al.*, 2000) has shown that the β phase forms by growth of the small amounts of retained β phase in the starting billet, which explains why neighboring grains often have similar orientations and in general are not in a Burgers orientation relation with neighbouring α_p grains.

8.3.4.2 Analysis of the Tests at a Strain Rate of $1.8s^{-1}$

For the specimens deformed at $1.8s^{-1}$, it can be seen from the optical micrographs (Figs. 8.23 and 8.24) and the EBSD band contrast maps (Figs. 8.40(a) and 8.41(a)) that the transformed microstructure is noticeably finer compared to the initial microstructure (Figs. 8.21 and 8.38(a)), despite the $\beta \rightarrow \alpha_s$ transformation occurring under similar cooling rates. The reasons for this are apparent in the EBSD maps for the reconstructed β phase (Figs. 8.40(c) and 8.41(c)), which show that the deformation has resulted in considerable refinement of the β microstructure. Fig. 8.55 shows misorientation maps for the initial microstructure and the two levels of strain for the specimens deformed at a strain rate of $1.8s^{-1}$ to allow a direct comparison of these microstructures.

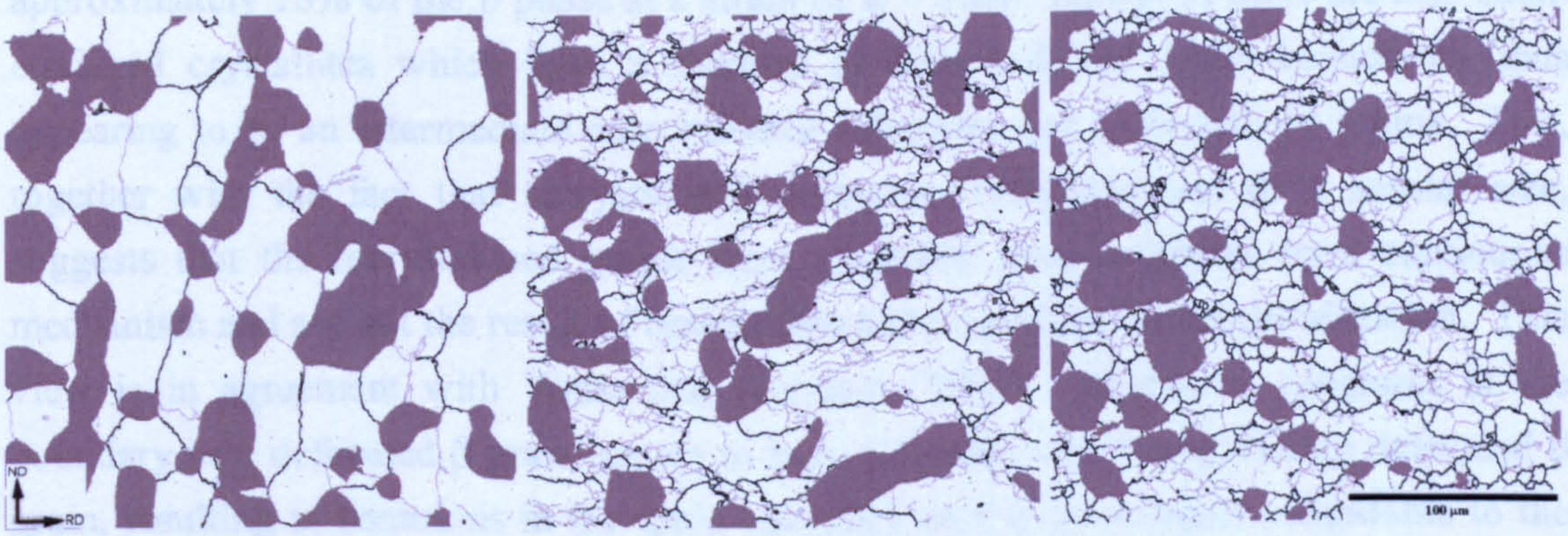

(a) Initial Microstructure (b) $\bar{\varepsilon} = 0.64$ (c) $\bar{\varepsilon} = 1.23$

Fig. 8.55 Misorientation maps for the reconstructed β phase showing the effect of strain for specimens deformed at $\dot{\varepsilon} = 1.8s^{-1}$. Light grey boundaries > 5° and black boundaries > 15°.

The high resolution reconstructed β map for the $\bar{\varepsilon} = 0.64$ test at a strain rate of $1.8s^{-1}$ (Fig 8.40(c)) reveals a mixed microstructure consisting of large deformed β grains, which are pancaked along RD, and smaller more equiaxed grains with high angle grain boundaries. The similarity in grain size between the large pancaked grains and the β grains in the initial microstructure, suggests these correspond to β grains in the initial microstructure which have become deformed. It can be seen from the orientation colouring that the deformed β grains contain gradual accumulated misorientations, indicating that the grains

have undergone significant levels of strain by slip and must contain a high dislocation density. Subboundaries can also be seen in the deformed β grains, which indicates that there has been dynamic recovery (DRE) during deformation. Some of these subboundaries form equiaxed subgrains approximately 10-20 μm in diameter. The subboundaries, subgrains and accumulated misorientations are more concentrated in the vicinity of the β grain boundaries compared to the grain interiors, showing that strain in the large β grains is inhomogenous. In addition, the subboundaries, subgrains and accumulated misorientations show the highest concentrations in the vicinity of α_p grains. This shows that significant strain concentrations develop where the β phase must accommodate the harder α_p grains, adding further to the inhomogenous strain within the β phase. An example of strain concentrated around an α_p grain is shown in Fig. 8.56(a). Similar strain concentrations in the vicinity of α_p grains has been reported previously for β-CEZ by Chaze and Montheillet (1994).

The smaller equiaxed grains with high angle grain boundaries are approximately 10-20μm in diameter. Clearly, high angle grains of this size are not present in the initial microstructure, so these are recrystallised grains which have formed either dynamically or metadynamically. The recrystallised grains tend to be located in the regions of higher strain at β grain boundaries and in the vicinity of α_p grains. The recrystallised grains, defined as small grains bounded completely by high angle boundaries accounted for approximately 18% of the β phase at a strain of $\bar{\varepsilon} = 0.64$. However, there are also small equiaxed crystallites which have a mixture of high and low angle boundaries, thus appearing to be an intermediate case between subgrains and recrystallised grains. This, together with the fact that recrystallised grains and subgrains are of a similar size, suggests that the recrystallised grains form gradually from subgrains by a continuous mechanism and are not the result of typical discontinuous dynamic recrystallisation. This view is in agreement with Weiss and Semiatin (1998). In places, subgrains at the boundary of a deformed β grain appear to have migrated into a neighboring deformed β grain, resulting in serrations in the grain boundary with a wavelength comparable to the subgrain size. This appears to be evidence of strain induced grain boundary migration (SIBM) and may be one mechanism by which small high angle grains can form from subgrains. An example of possible SIBM is indicated in Fig. 8.56(a). SIBM has been reported previously in a β alloy deformed in the α+β phase field by Robertson and McShane (1997).

The high resolution reconstructed β map for the higher strain of $\bar{\varepsilon} = 1.23$ (Fig 8.41(c)), also shows a mixed microstructure of deformed and recrystallised grains. However, the volume fraction of recrystallised grains has increased, accounting for approximately 46% of the β phase. In the remaining deformed β grains, there is a more developed structure of equiaxed subgrains compared to the lower strain. As in the case of the lower strain, the substructure and recrystallised grains are more concentrated at prior β boundaries and at

highly strained regions in the vicinity of α_p grains.

Misorientation angle distributions for misorientations greater than 5° in the reconstructed β phase are shown in Fig. 8.57 for the initial microstructure and the two levels of strain at a strain rate of $1.8s^{-1}$. In Fig. 8.57(a), the data are for an equal volume of β phase, which allows a comparison between the level of boundaries in each specimen as well as the angular distribution. The standard method of displaying misorientation angle distributions in terms of relative frequency is also shown in Fig. 8.57(b). It can be seen from Fig. 8.57(a) that the distribution for the initial microstructure contains far fewer misorientations above 5° compared to the deformed specimens because the β grains are relatively large and contain no substructure. The higher frequency of misorientations between 5° and 15° reflects the fact that neighboring β grains often share similar orientations rather than being randomly orientated. The distribution for the $\bar{\varepsilon} = 0.64$ specimen shows the highest level of low angle boundaries, which are mostly due to the substructure within the large deformed β grains, which form the majority of the β phase at this strain. The increase in higher angle misorientations is mainly the result of the new recrystallised grains. In the distribution for the $\bar{\varepsilon} = 1.23$ specimen, there is a decrease in low angle boundaries and an increase in high angle boundaries due to the increasing volume fraction of recrystallised grains. Fig. 8.57(b) shows that the shape of the distribution is similar for the initial microstructure and both deformed specimens.

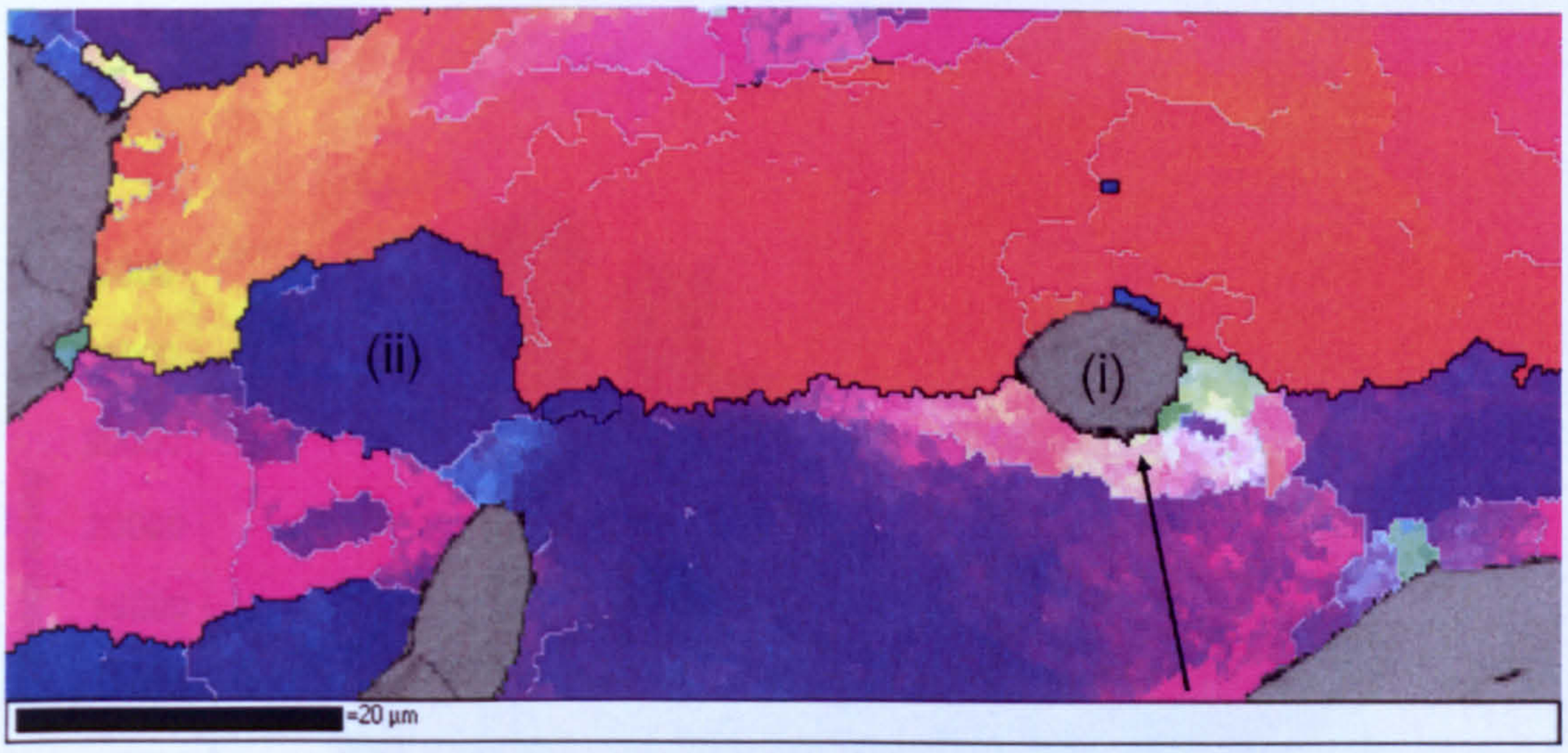

(a)

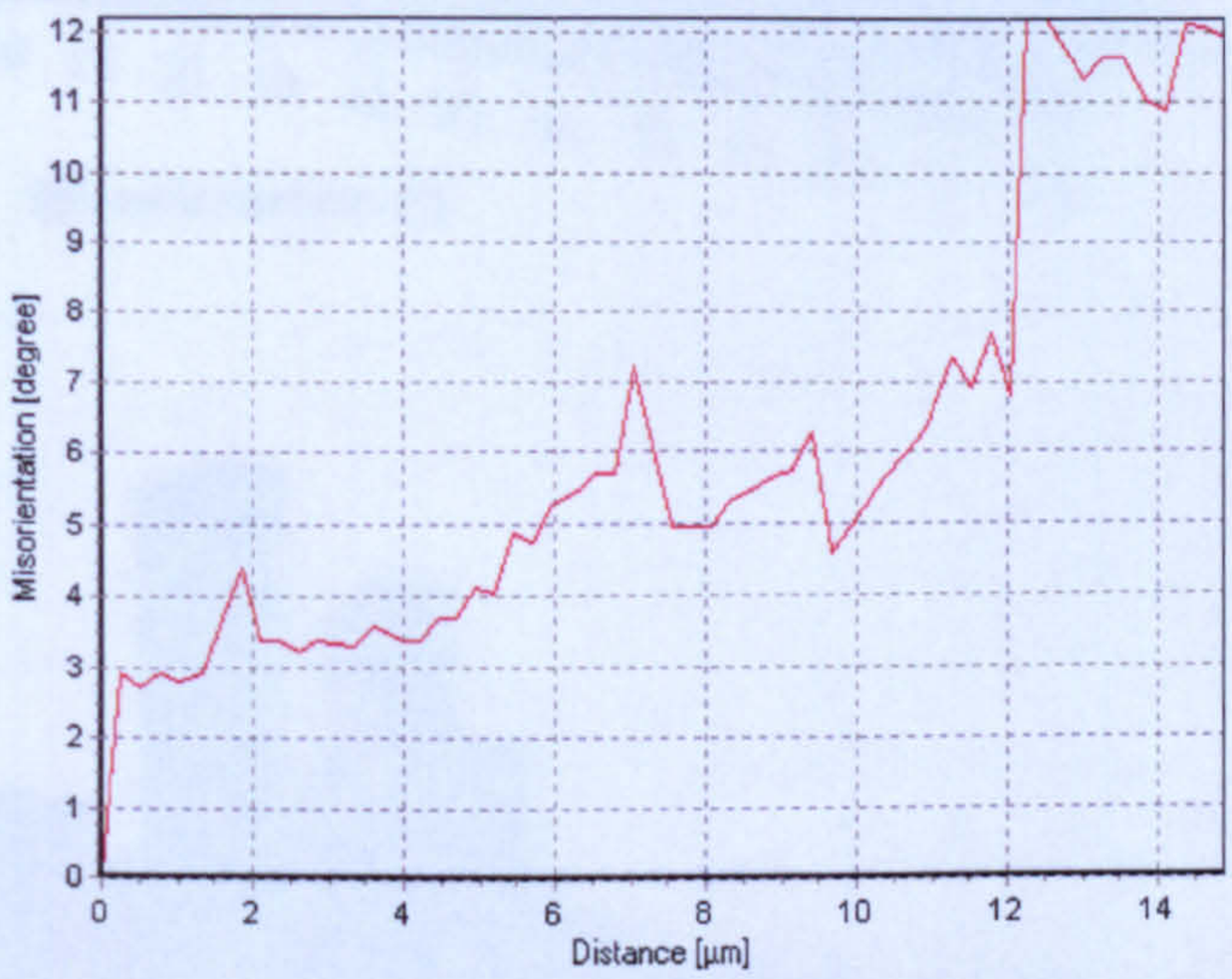

(b)

Fig. 8.56 (a) Part of the reconstructed β phase map for specimen C ($\dot{\varepsilon} = 1.8s^{-1}$, $\bar{\varepsilon} = 0.64$). Label (i) indicates accommodation strains in the β phase surrounding an α_p grain and label (ii) shows possible strain induced boundary migration. The misorientation profile for the arrow on the map is shown in (b).

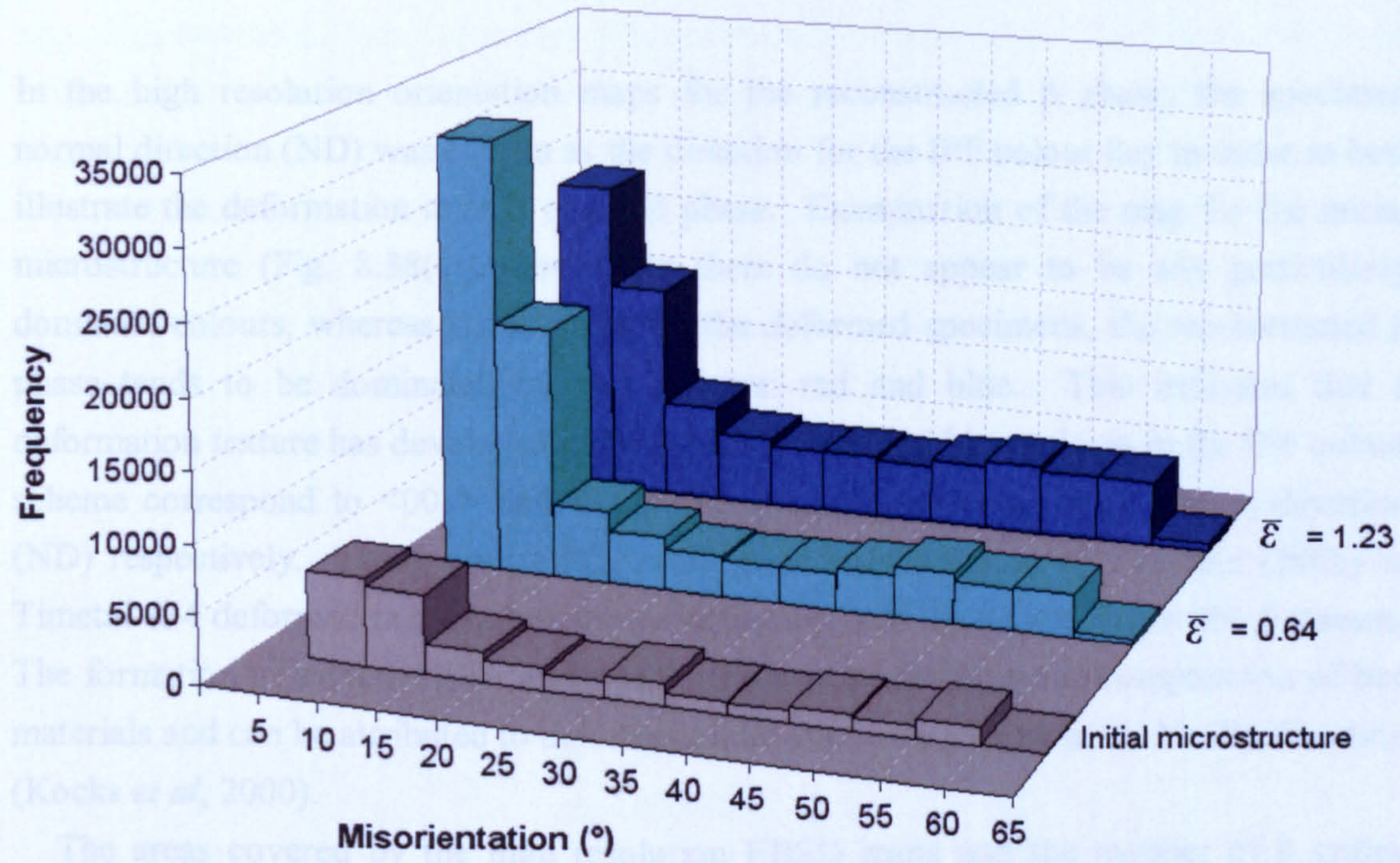

(a)

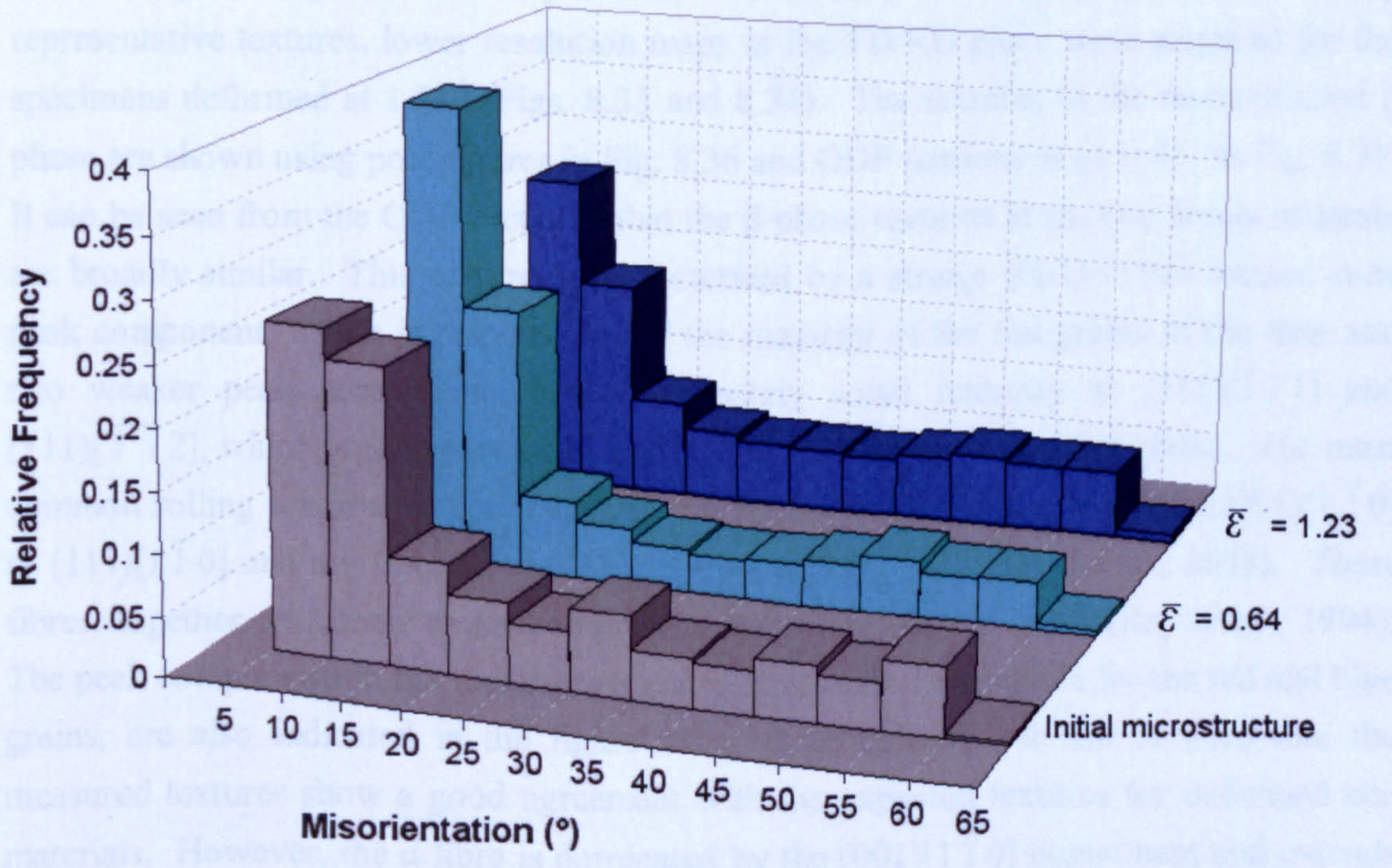

(b)

Fig. 8.57 Misorientation angle distributions (>5°) in the reconstructed β grains for the initial microstructure test (G) and the two tests at a strain rate of $1.8s^{-1}$ (B and C). (a) Absolute frequencies from the EBSD data for an equal volume of β phase. (b) The same data plotted using relative frequencies for each series.

8.3.4.3 Texture Development in the β Phase.

In the high resolution orientation maps for the reconstructed β phase, the specimen normal direction (ND) was chosen as the direction for the IPF colour key in order to best illustrate the deformation texture of the β phase. Examination of the map for the initial microstructure (Fig. 8.38(c)) shows that there do not appear to be any particularly dominant colours, whereas in the maps for the deformed specimens, the reconstructed β phase tends to be dominated by two colours: red and blue. This indicates that a deformation texture has developed in the β phase. Red and blue colours in the IPF colour scheme correspond to <001> and <111> directions close to the compression direction (ND) respectively. These orientations were previously reported by Germain (2005) in Timetal 834 deformed in axisymmetric compression both above and below the β transus. The formation of mixed <100> and <111> fibres is common in the compression of bcc materials and can be attributed to deformation on slip systems with a <111> slip direction (Kocks *et al*, 2000).

The areas covered by the high resolution EBSD maps and the number of β grains which they contain is relatively small. Therefore, to acquire more statistically representative textures, lower resolution maps in the TD/RD plane were acquired for the specimens deformed at $1.8s^{-1}$ (Figs. 8.33 and 8.34). The textures in the reconstructed β phase are shown using pole figures in Fig. 8.36 and ODF sections at $\varphi_2 = 45°$ in Fig. 8.37. It can be seen from the ODF sections, that the β phase textures at the two levels of strain are broadly similar. This texture is characterised by a strong {001}<110> rotated cube peak component, which is responsible for the majority of the red grains in the map and two weaker peak components of approximately equal intensity at $(111)[1\,\bar{2}\,1]$ and $(111)[\bar{1}\,\bar{1}\,2]$, which together are responsible for the majority of the blue grains. The most common rolling textures of bcc metals/alloys are the α fibre extending from $(001)[1\,\bar{1}\,0]$ to $(111)[1\,\bar{1}\,0]$ and a γ fibre from $(111)[1\,\bar{1}\,0]$ to $(111)[\bar{1}\,\bar{1}\,2]$ (Dey *et al.*, 2008). These fibres, together with their major components are shown in Fig. 8.58 (Ray *et al.*, 1994). The peak components in the measured textures, which are responsible for the red and blue grains, are also indicated in the figure using these colours. It can be seen that the measured textures show a good agreement with the expected textures for deformed bcc materials. However, the α fibre is dominated by the $(001)[1\,\bar{1}\,0]$ component and extends with decreasing intensity only as far as $(112)[1\,\bar{1}\,0]$. Similarly, the γ fibre is incomplete and is better described as peak components at {111}<112>.

For the higher level of strain (Fig. 8.37(b)), the texture intensity is stronger and the ODF section is smoother and has a closer correspondence to Fig. 8.58. This indicates that despite the increase in recrystallisation that was observed with an increase in strain, this did not lead to any significant new texture components appearing, nor did it produce a weaker deformation texture.

It can be seen from the low resolution maps in the TD/RD plane, that the major red and blue components are not distributed evenly through the map. There are large regions of either red or blue grains, which are of the order of several millimetres in size. This suggests that the stable component (red or blue) which develops during deformation is dependent on the initial orientation of the β grains and that large texture heterogeneities were present in the initial microstructure and starting billet. These texture heterogeneities are probably related to either the prior β grains or β contained between colonies of α_s lamellae prior to the final α+β forging step during primary working of the billet.

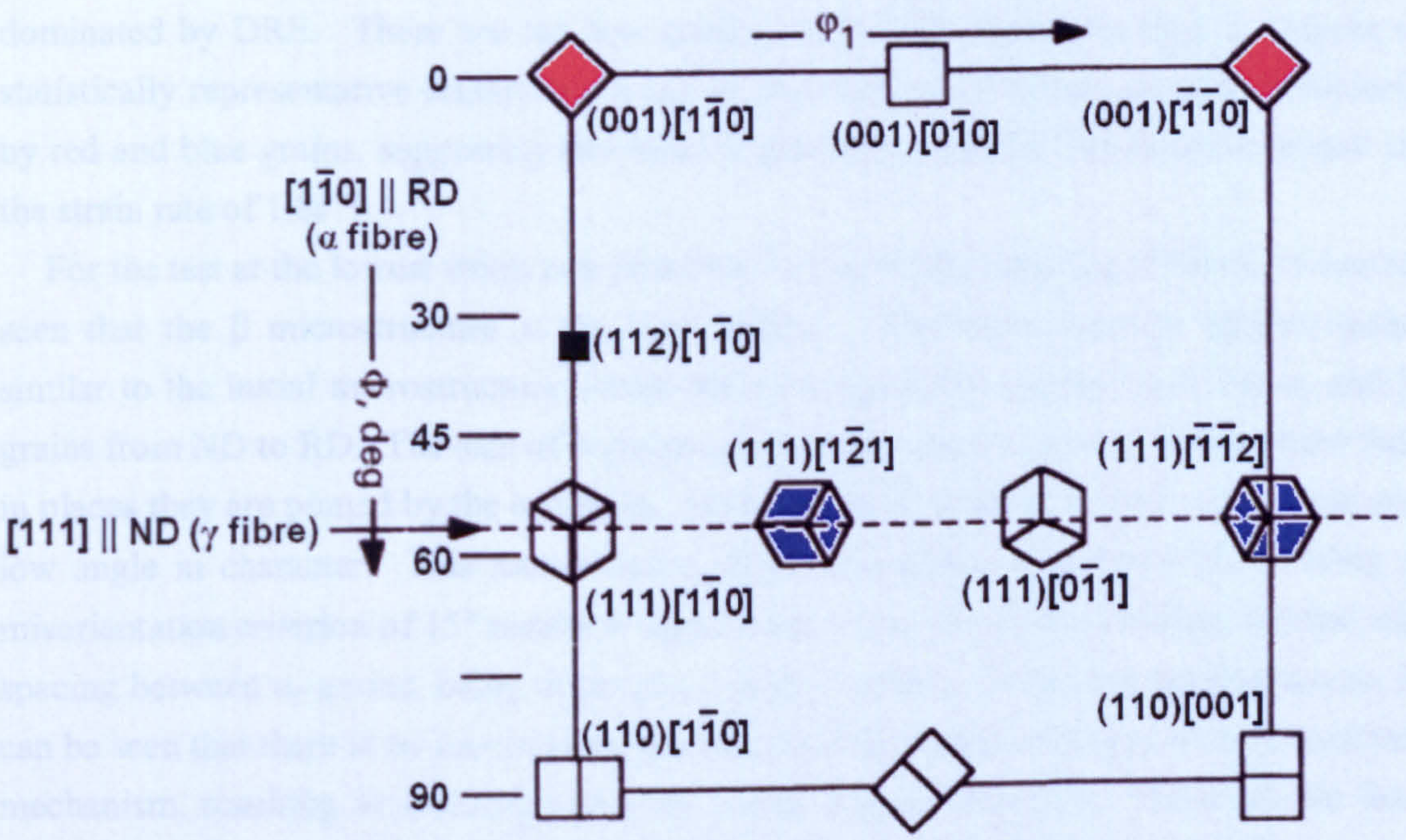

Fig. 8.58 Ideal rolling orientations for rolled bcc metals in the $\phi_2 = 45°$ section of the ODF. The components coloured red and blue are those present in the measured textures and are responsible for the dominance of red and blue grains in the IPF maps for the deformed specimens (adapted from Ray *et al.*, 1994).

8.3.4.4 Analysis of the Tests at the Lower and Higher Strain Rates

Having discussed the microstructural evolution in the β phase at a strain rate of $1.8s^{-1}$, here the effect of the lower and higher strain rates is examined. Fig. 8.59 shows misorientation maps for the initial microstructure and tests at four different strain rates to the same level of strain ($\bar{\varepsilon} = 0.64$), to allow a direct comparison of the microstructures.

For the test at a lower strain rate of $0.18s^{-1}$ (Fig. 8.42(c) and Fig. 8.59(d)), it can be seen that the microstructure shows less refinement compared to the strain rate of $1.8s^{-1}$. The microstructure is again mixed, consisting of large deformed grains pancaked along RD and some smaller equiaxed grains with high angle grain boundaries. As before, the

deformed grains contain accumulated misorientations and subboundaries. However, compared to the strain rate of $1.8s^{-1}$, more of these subboundaries are arranged into equiaxed subgrains, and this subgrain size is noticeably larger. This indicates that the slower deformation has allowed more extensive DRE to occur. The smaller equiaxed grains are similar in size to the subgrains i.e. larger than at $1.8s^{-1}$, but relatively few of these are completely bounded by high angle grain boundaries. From this microstructure, it appears that the more extensive recovery at the slower strain rate reduces the severity of the strain concentrations at prior β boundaries and in the vicinity of α_p grains. This results in less recrystallisation in these areas. Thus at a strain rate of $0.18s^{-1}$, restoration is dominated by DRE. There are too few grains in the high resolution map to acquire a statistically representative texture but it can be seen that the β phase is again dominated by red and blue grains, suggesting that there is probably a similar deformation texture to the strain rate of $1.8s^{-1}$.

For the test at the lowest strain rate of $0.019s^{-1}$ (Fig. 8.43(c) and Fig. 8.59(e)), it can be seen that the β microstructure is the least refined. The microstructure appears quite similar to the initial microstructure except for a change in the alignment of the α_p and β grains from ND to RD. The size of β grains and subgrains has increased to the extent that in places they are pinned by the α_p grains. Many of the boundaries within the β phase are low angle in character. This means that a grain reconstruction in the β phase using a misorientation criterion of 15° results in large areas of the β matrix, extending beyond the spacing between α_p grains, being detected as single 'grains'. From this microstructure, it can be seen that there is no recrystallisation and that DRE is the only operative restoration mechanism, resulting in a homogenous but coarse β grain structure. There are too few grains in the high resolution map to acquire a statistically representative texture but it can be seen that the β phase is again dominated by red and blue grains, suggesting that there is probably a similar deformation texture to the strain rate of $1.8s^{-1}$.

Maps for the reconstructed β phase for the test at the highest strain rate of $20.2s^{-1}$ are shown in Fig. 8.39(c) and Fig. 8.59(b). As was the case for the strain rate of $1.8s^{-1}$, the microstructure is mixed, consisting of deformed β grains containing substructure and more equiaxed recrystallised grains bounded by high angle grain boundaries. However, for the same level of strain, the fraction of the β phase which is recrystallised is much higher: 62% at $20.2s^{-1}$ compared to 18% at $1.8s^{-1}$. The recrystallised grains are also larger than they were for the lower strain rate of $1.8s^{-1}$ and their size appears to have increased to the extent that in places, they have begun to be pinned by the α_p grains. This increase in recrystallised grain size with an increase in the strain rate is the opposite of the expected trend for the size of subgrains and dynamically recrystallised grains, which generally decrease in size with increasing strain rate (Furuhara *et al.*, 2007). A possible explanation for the increase in size may be grain growth of the recrystallised grains during and immediately after deformation before the specimen was quenched. At the

higher strain rate, there would be a greater driving force for the migration of high angle grain boundaries due to the higher level of stored energy in the deformed grains as a result of the reduced time for DRE. This possible explanation is in agreement with the view of Weiss and Semiatin (1998) that the high angle grain boundaries which form by a continuous process, during or after deformation undergo a growth process analogous to metadynamic recrystallisation. As a result of the smaller size difference between recrystallised and deformed grains, it is more difficult to distinguish between them. However, an examination of intragranular misorientations shows a clear difference between the two types of grain. Such a comparison is shown in Fig. 8.60. It can be seen that the profile labeled (i) crosses four recrystallised grains. Within these grains, there are no accumulated misorientations. In contrast, the profile labeled (ii) crosses a deformed β grain and shows significant accumulated misorientations and small abrupt changes in orientation due to low angle subboundaries.

Misorientation angle distributions for misorientations greater than 5° in the reconstructed β phase are shown in Fig. 8.61 for the initial microstructure and the specimens deformed at the four different strain rates to a strain of 0.64. In Fig. 8.61(a), the data are for an equal volume of β phase, which allows a comparison between the level of boundaries in each specimen as well as the angular distribution. The standard means of displaying misorientation angle distributions in terms of relative frequency is also shown in Fig. 8.61(b). It can be seen from Fig. 8.61(b) that the initial microstructure and the specimens deformed at strain rates of 0.019 to $1.8s^{-1}$, have similar misorientation angle distributions in terms of their relative frequency. These are characterised by a high relative frequency of misorientations between 5° and 15° due to subboundaries and reflects the fact that DRE is the dominant restoration mechanism at slower strain rates. In Fig. 8.61(a), it can be seen that in terms of absolute frequencies, only the initial microstructure and $0.019s^{-1}$ specimen have similar absolute values. This reflects the fact that in both of these specimens, the size of the subgrains and grains is controlled by the pinning effect of the α_p grains. As the strain rate increases through $0.18s^{-1}$ to $1.8s^{-1}$, the absolute frequencies increase due to the increasing refinement in the microstructure. The distribution for the $20.2s^{-1}$ specimen is significantly different to the specimens deformed at slower strain rates. In terms of relative frequency, misorientations between 5° and 15° still have the highest frequency, but there is a much higher fraction of high angle boundaries compared to the slower strain rates. This change reflects the fact that the majority of the β phase is now comprised of recrystallised grains.

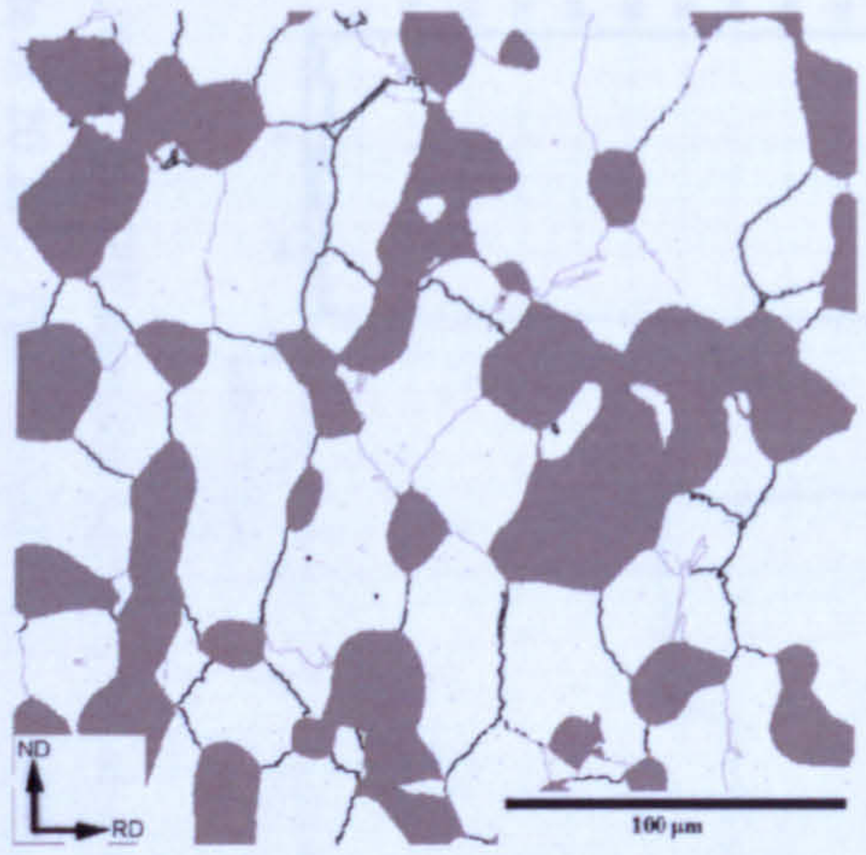

(a) Initial Microstructure

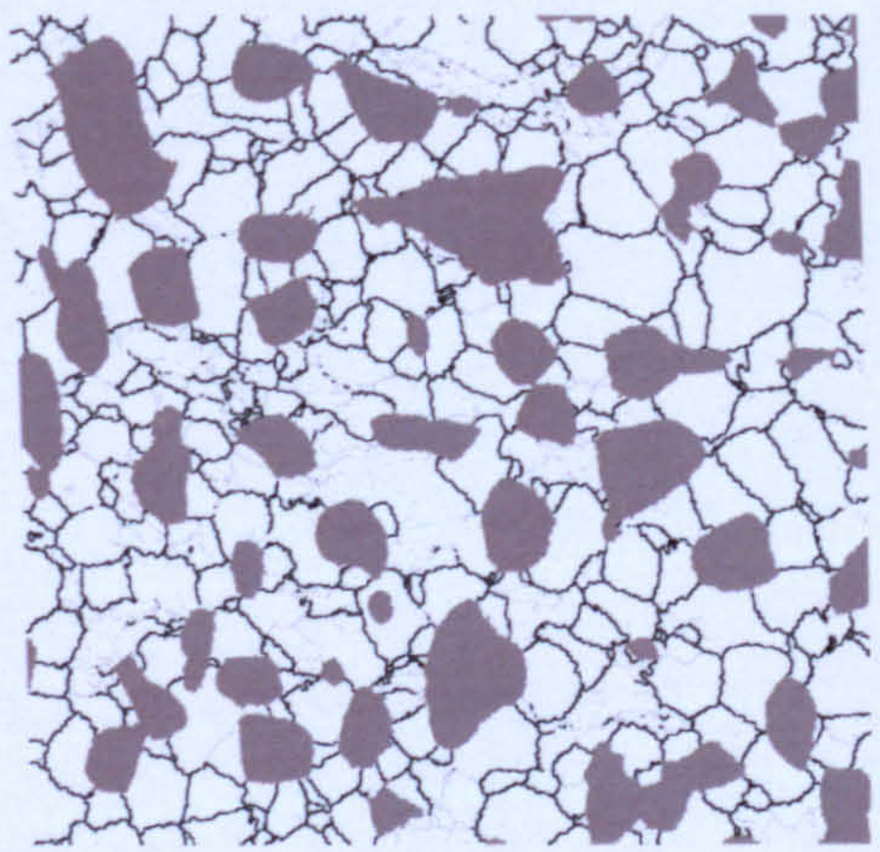

(b) $\dot{\varepsilon} = 20.2\ s^{-1}$

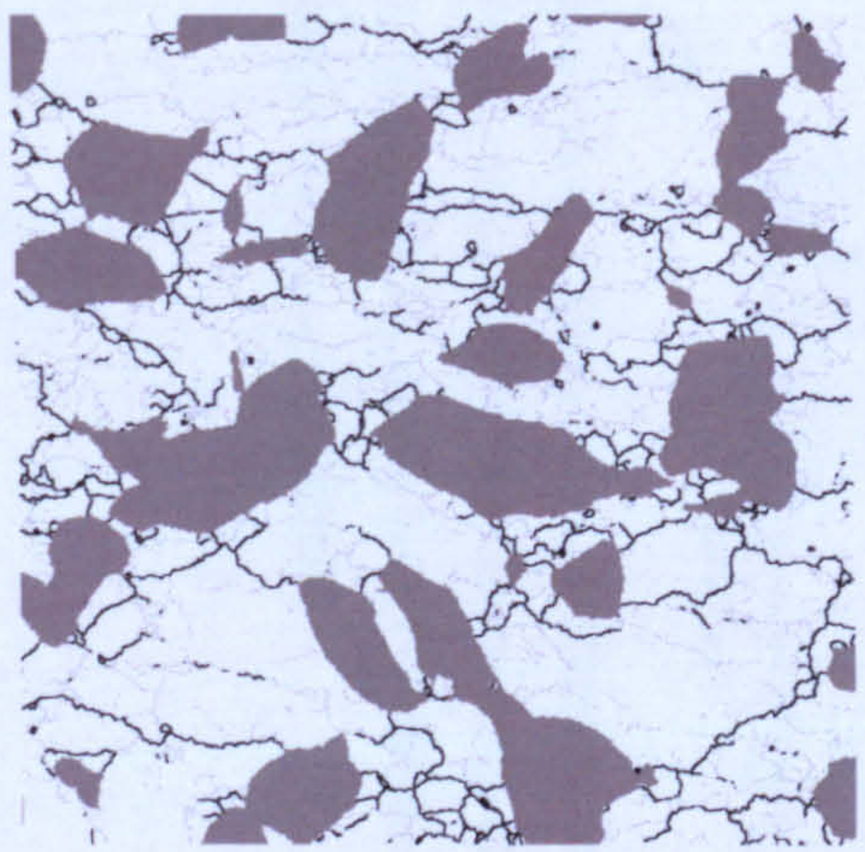

(c) $\dot{\varepsilon} = 1.8\ s^{-1}$

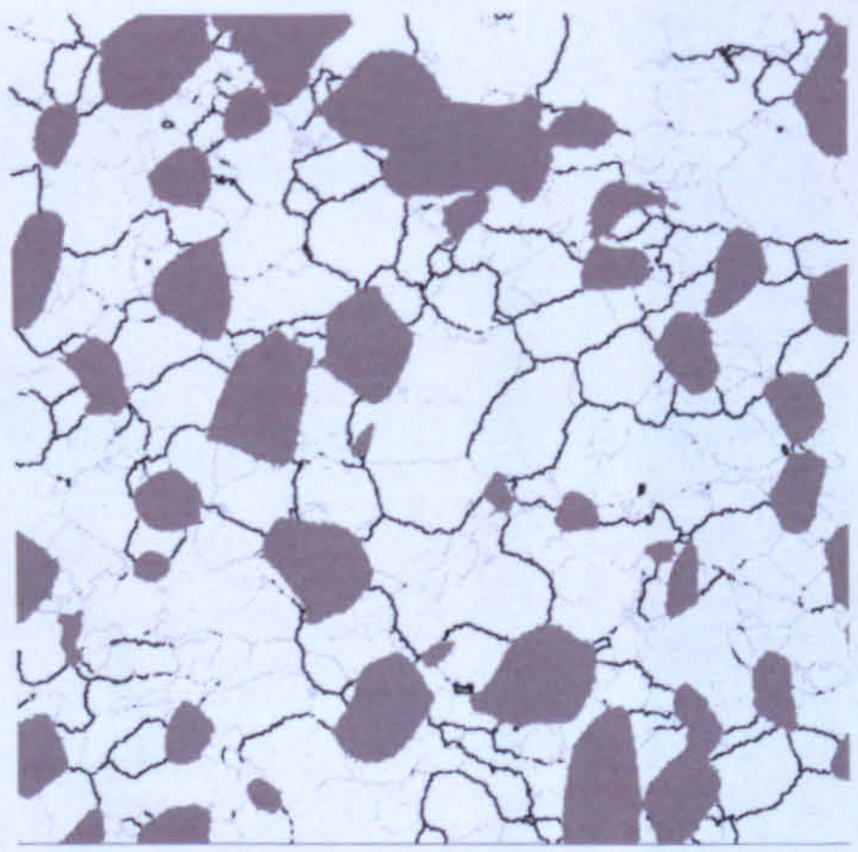

(d) $\dot{\varepsilon} = 0.18\ s^{-1}$

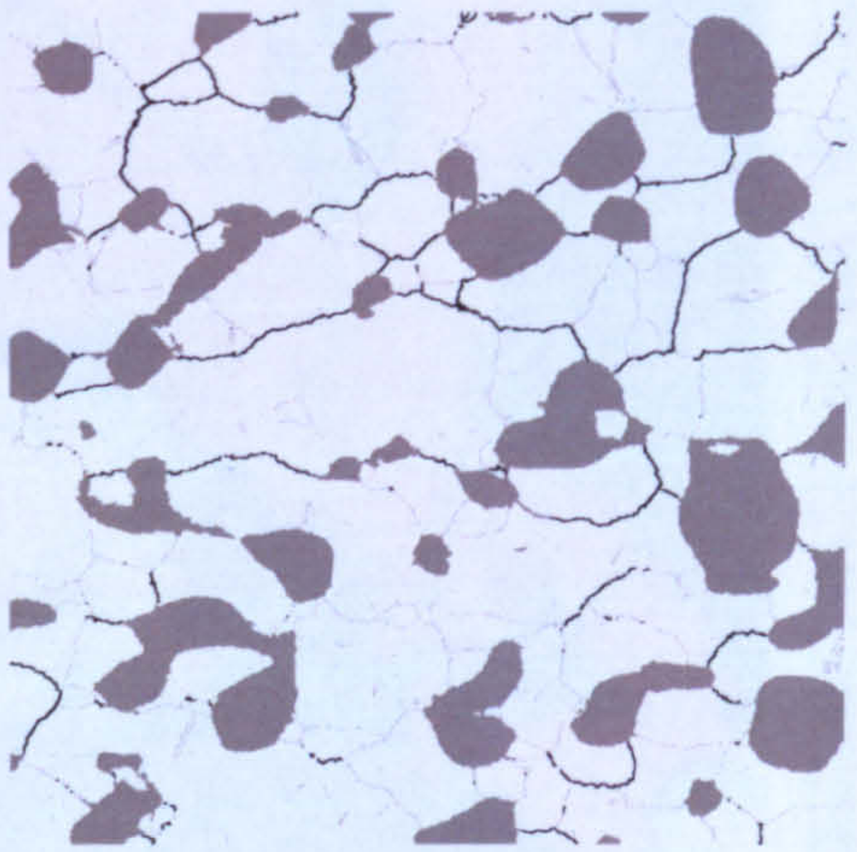

(e) $\dot{\varepsilon} = 0.019\ s^{-1}$

Fig. 8.59 Misorientation maps for the reconstructed β phase showing the effect of strain rate for specimens deformed to $\bar{\varepsilon} = 0.64$. Light grey boundaries > 5° and black boundaries > 15°.

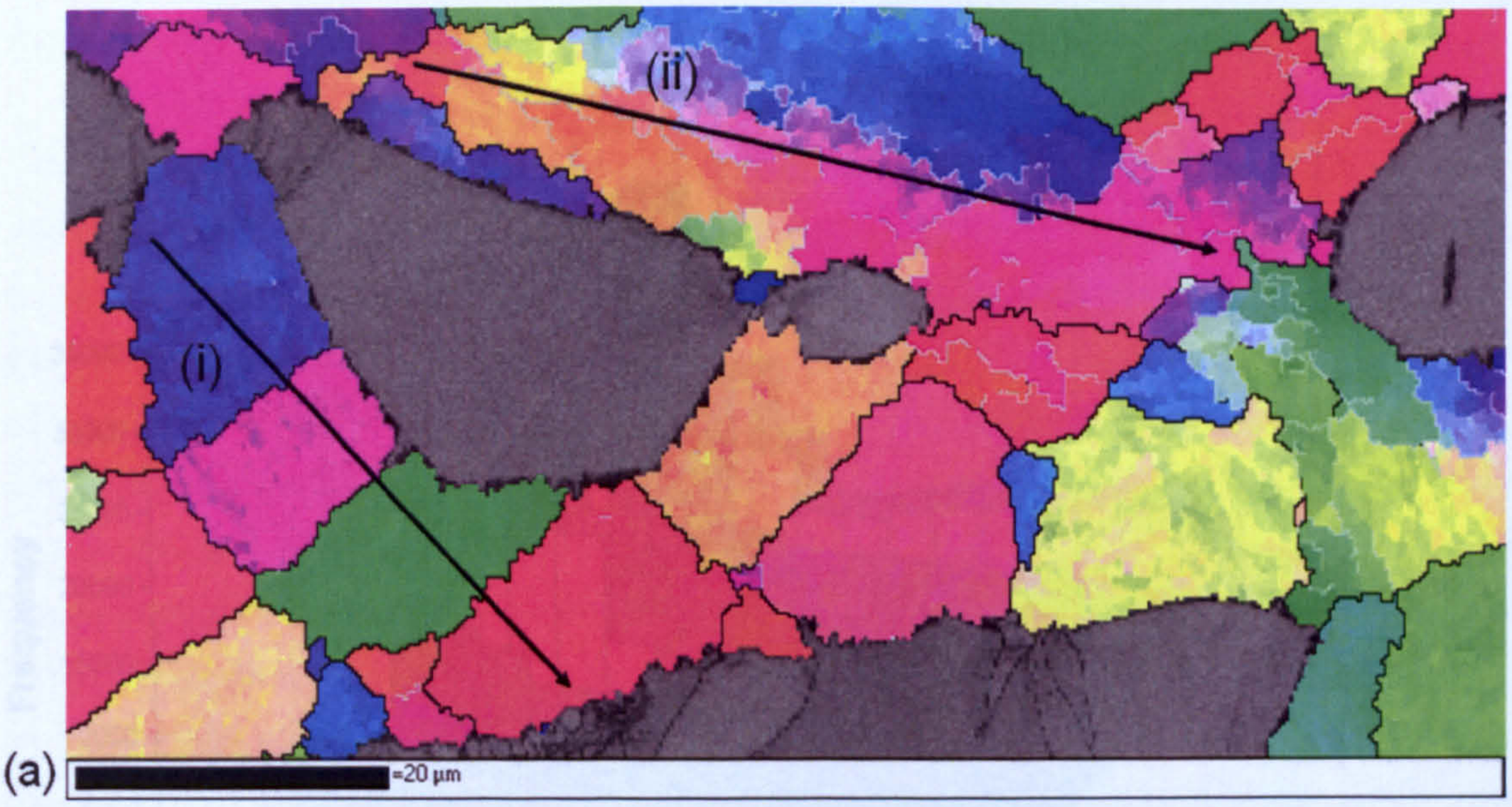

(a)

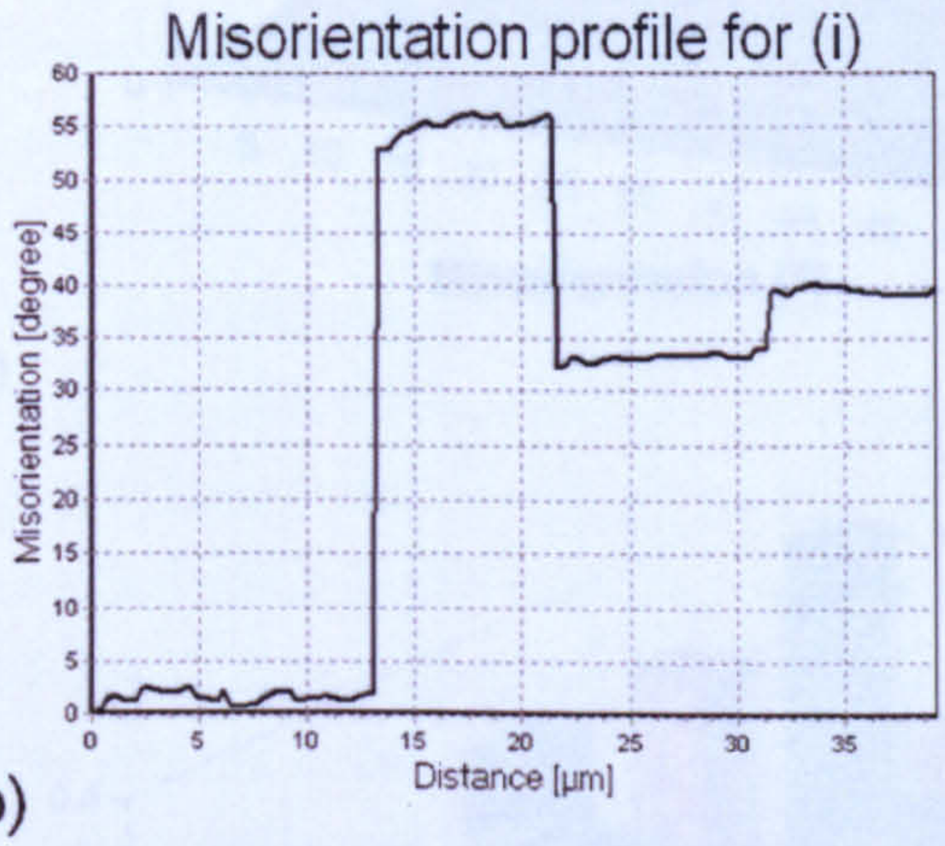

(b)

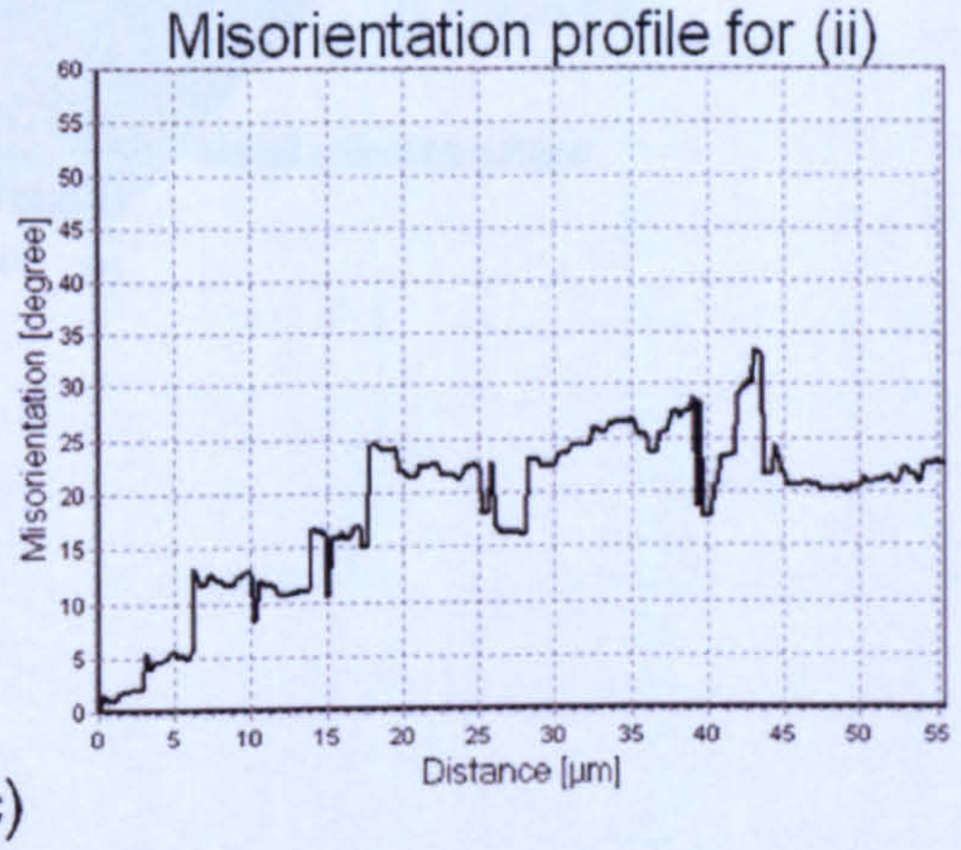

(c)

Fig. 8.60 (a) IPF map for part of the reconstructed β phase in specimen A, deformed at a strain rate of $20.2s^{-1}$. The misorientation profiles for the arrows (i) and (ii) are shown in (b) and (c) respectively. (i) Crosses four recrystallised grains whereas (ii) crosses a heavily deformed grain containing subboundaries and gradual changes in orientation.

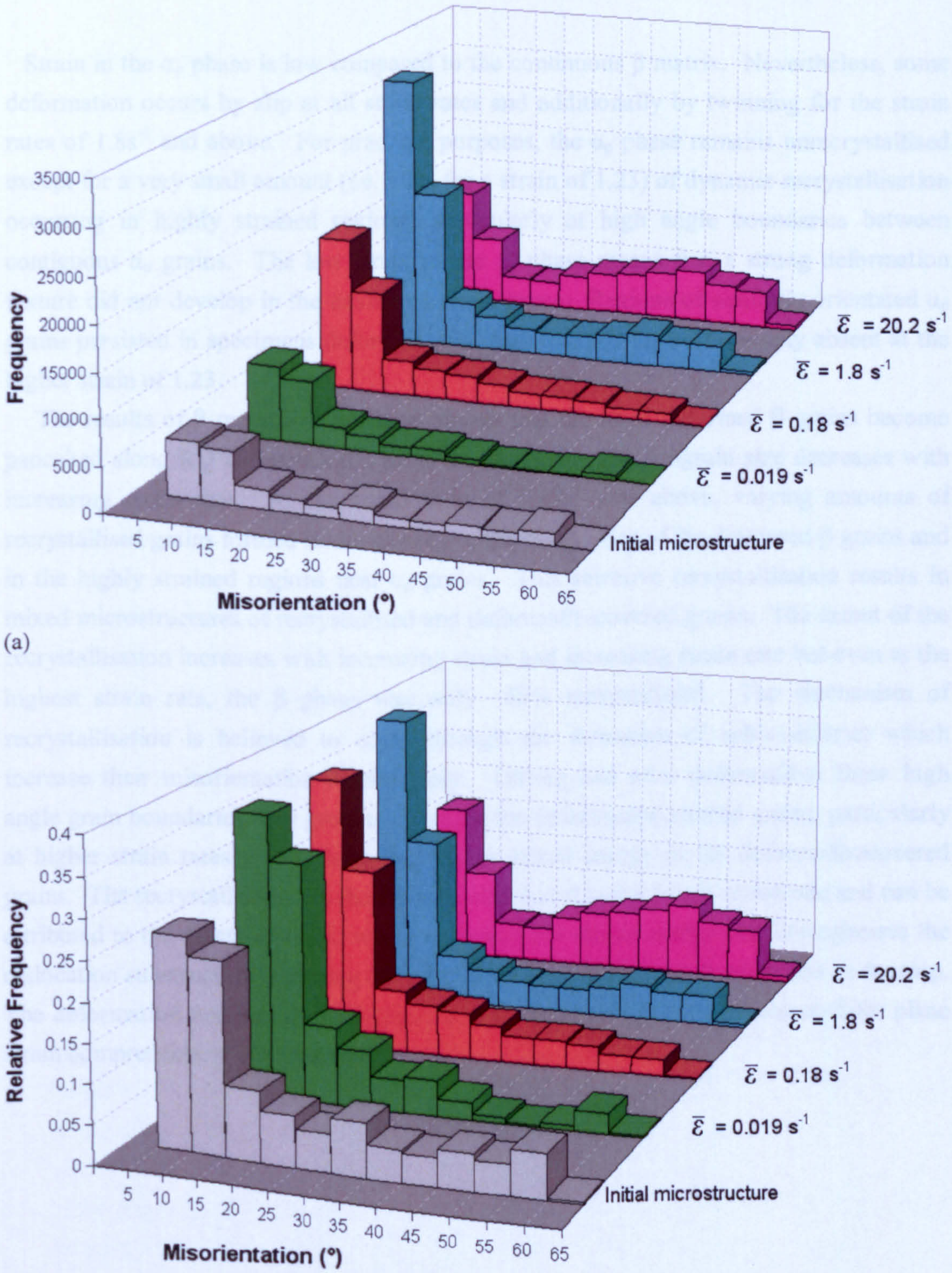

(a)

(b)

Fig. 8.61 Misorientation angle distributions (>5°) in the reconstructed β grains for the initial microstructure test and the four tests deformed to a strain of approximately 0.64 at different strain rates. (a) Absolute frequencies from the EBSD data for an equal volume of β phase. (b) The same data plotted using relative frequencies for each series.

8.3.5 Summary of the Microstructural Evolution During Simulated Secondary Working

Strain in the α_p phase is low compared to the continuous β matrix. Nevertheless, some deformation occurs by slip at all strain rates and additionally by twinning for the strain rates of $1.8s^{-1}$ and above. For practical purposes, the α_p phase remains unrecrystallised except for a very small amount (i.e. <2% for a strain of 1.23) of dynamic recrystallisation occurring in highly strained regions, particularly at high angle boundaries between contiguous α_p grains. The low strain in the α_p phase means that a strong deformation texture did not develop in the examined strain range. Regions of similarly orientated α_p grains persisted in specimens deformed to a strain of 0.63 but were largely absent at the higher strain of 1.23.

The results of β reconstruction have shown that the large deformed β grains become pancaked along RD and develop a subgrain structure. The subgrain size decreases with increasing strain rate. At the strain rates of $0.18s^{-1}$ and above, varying amounts of recrystallised grains formed in the vicinity of the boundaries of the deformed β grains and in the highly strained regions near α_p grains. This selective recrystallisation results in mixed microstructures of recrystallised and deformed/recovered grains. The extent of the recrystallisation increases with increasing strain and increasing strain rate but even at the highest strain rate, the β phase was only ~60% recrystallised. The mechanism of recrystallisation is believed to occur through the formation of subboundaries which increase their misorientation continuously. During and after deformation, these high angle grain boundaries may grow to consume the deformed/recovered grains, particularly at higher strain rates where there is a higher stored energy in the deformed/recovered grains. The recrystallisation in the β phase was absent at the lowest strain rate and can be attributed to the extent of DRE, which decreases the stored energy and homogenises the dislocation substructure, reducing the tendency for small high angle subgrains to develop. The deformation textures in the β phase are in agreement with those expected for plane strain compression of bcc materials.

9 CONCLUSIONS

9.1 EBSD Post-processing

- A computer program has been written that incorporates various EBSD post-processing tasks that are not provided in the standard EBSD software. These are useful for EBSD studies of titanium alloys and other hcp metals.

- The program includes a technique for separating the α_p and α_s phases in an EBSD dataset of a bimodal microstructure. Unlike previous methods, it is based only on information provided in the initial EBSD dataset.

- The technique allows the user to analyse separately the textures of the α_p and α_s phases. It is also an essential step in the reconstruction of the high temperature β phase from the inherited α_s microstructure.

- The technique enables quick and accurate phase separation in microstructures where the α_s phase is in the form of martensite or has a basketweave Widmanstätten morphology. It is less effective for separating α_s that has formed at slower cooling rates, where techniques based on a second image acquired using either optical or scanning electron microscopy may give better results.

- The program includes a technique for automatically reconstructing the orientations of the high temperature β phase from an inherited α_s phase. Unlike previous methods, the procedure reconstructs variants individually making it better suited to the reconstruction of deformed microstructures.

- Tests using a variety of EBSD datasets have shown that the technique is robust and capable of reconstructing β microstructures in a variety of alloys, for both high and low resolution maps and for a range of α_s morphologies.

- More recently, the reconstruction technique has been successfully used by other workers at the University of Sheffield and has proved useful in the analysis of Ti-6Al-4V ingot forging routes, titanium friction stir welds and parts produced by shaped metal deposition using titanium powders.

9.2 Characterisation of a Timetal 834 Billet

- EBSD analysis revealed that the billet contained microtexture heterogeneities (macrozones) throughout the billet cross-section.

- Macrozones are related to prior colonies of aligned α lamellae, which have the same crystallographic orientation and as a result tend to deform and globularise in a similar manner, thus maintaining similar crystallographic orientations in the globularised α_p grains.

- The α phase texture of a typical macrozone is composed of a single hcp component, with varying degrees of spread up to around 30°.

- Macrozones are typically columnar shaped regions elongated along the billet axis. In certain locations of the billet, some macrozones also show a secondary elongation in the transverse plane.

- Macrozones are typically 100-1000μm in diameter in the transverse plane and up to several thousand microns in length.

- There is a strong primary alignment of the macrozones and the α_p grains along the billet axis. However, a secondary alignment in the transverse plane was also observed due to the non equal strains imposed about the billet axis during ingot forging.

- The majority of macrozones can be classed as either axial (c-axis parallel to the billet axis) or transverse (c-axis perpendicular to the billet axis).

- In the centre of the billet cross-section, the global texture was dominated by a fibre-like $\{10\bar{1}0\}$ texture due to a dominance of transverse macrozones. At the edge, there was a greater proportion of axial macrozones which gave rise to an additional (0002) component

- In parts of the billet there was symmetry in the global textures due to the non equal strains imposed about the billet axis.

- The textures in the centre can be explained by considering each forging bite as a plane strain compression, with the texture the net result of a series of plane strain compressions about the billet axis.

- The different textures observed around the edge are more complex and can be attributed to constraint and side spread of material during the different compressions about the billet axis.

9.3 Determination of the β Approach Curve

- The β transus for the billet was estimated to be between 1050°C and 1055°C. The β approach curve was similar to the β approach curves determined previously for two other Timet 834 billets.

9.4 Phase Transformations During Cooling

- The effect of cooling rate on the $\beta \rightarrow \alpha_s$ phase transformation in a bimodal microstructure was investigated for Timetal 834 using a Jominy specimen equipped with thermocouples.

- From the optical, SEM and microhardness results, there was no clear distinction between a diffusional and diffusionless transformation, with an essentially continuous transition in the transformed microstructure from a martensitic transformation at the highest cooling rates to a diffusional transformation at lower cooling rates.

- Microstructures were interpreted as predominantly martensitic at cooling rates higher than approximately 300°C s^{-1} and entirely diffusional (Widmanstätten) below approximately 50°C s^{-1}.

- The transition in the Widmanstätten morphology from basketweave to colony occurred at around 20°C s^{-1}.

- Growth of the α_p grains leading to a significant increase in α_p volume fraction occurred below approximately 20°C s^{-1}. α_p grain growth had a 'feathery' appearance below approximately 15°C s^{-1}.

- Newly nucleated α_{GB} precipitates were observed below approximately 90°C s^{-1}. There was continuous coverage of β boundaries by a combination of α_{GB} and protuberances from α_p grains below approximately 30°C s^{-1}. Growth of α at the grain boundaries became 'feathery' below approximately 15°C s^{-1}. At very slow cooling

rates, α_p grain growth reduces the β/β grain boundary area available for nucleation of α_{GB}.

- Local variant selection was observed for the diffusional transformation at β/β boundaries when adjacent β grains share a common {110} pole. When this occurs, closely orientated α_s variants with (0002) poles aligned with the common {110} pole are preferentially selected on either side of the β/β boundary.

- Local variant selection was observed for the diffusional transformation at α_p/β boundaries when an α_p grains and an adjacent β grain have an orientation relation close to the Burgers relation. When this occurs, the α_s variant that is close to the α_p orientation forms preferentially at the α_p/β boundary.

- The local variant selection occurring at α_p/β boundaries was seen to have a significant effect on the overall α_s texture for cooling rates below approximately 40°C s^{-1}. In regions where the α_p grains are textured i.e. macrozones, this local variant selection increases the frequency of α_s variants which coincide with the main α_p orientation. This leads to a strengthening of the texture within macrozones.

9.5 Simulated Secondary Working Using Plane Strain Compression Tests

- For Timetal 834 at a forging temperature of 1010°C, where the microstructure consists of α_p grains in a continuous β matrix, the overall strain accommodated by the α_p phase is low, with the majority of the strain accommodated by the softer β phase.

- Deformation in the α_p phase is heterogeneous between grains and within the grains themselves.

- Deformation in the α_p occurred by slip at all strain rates and additionally by deformation twinning for the strain rates of $1.8s^{-1}$ and above.

- The majority of the α_p phase remains unrecrystallised even at high strains. However, in some localised areas of high strain, small amounts of dynamic recrystallisation were observed.

- The macrozones present in the billet persist to high plastic strains due to the low strain accommodated by the α_p phase. Macrozones were still present at a strain of 0.63 but were less apparent at the higher strain of 1.23. This indicates that given

sufficient strain, the strength of these texture heterogeneities can be reduced. Secondary working at 1010°C is not an efficient means to remove macrozones.

- A typical closed die forging operation will produce a forging with significant regions that have received relatively low strains due to forging dead zones and thus can be expected to contain regions of similarly orientated α_p grains, which has implications for the fatigue performance of bimodal microstructures produced from forged billet.

- Deformation in the β phase is also heterogeneous due to the accommodation strains imposed by the α_p grains.

- Large deformed β grains become pancaked perpendicular to the compression direction and developed a subgrain structure. The subgrain size decreases with increasing strain rate.

- At the strain rates of $0.18s^{-1}$ and above, varying amounts of recrystallised grains formed in the vicinity of the boundaries of the deformed β grains and in the highly strained regions near α_p grains. This selective recrystallisation results in mixed β microstructures of recrystallised and deformed/recovered grains.

- The extent of recrystallisation increases with increasing strain and increasing strain rate.

- The mechanism of recrystallisation is believed to occur through the formation of subboundaries which increase their misorientation continuously. During and after deformation, these high angle grain boundaries may grow rapidly to consume the deformed/recovered grains, particularly at higher strain rates, where there is a higher stored energy in the deformed/recovered grains.

- The recrystallisation in the β phase was absent at the lowest strain rate examined ($0.019s^{-1}$) and can be attributed to the extent of dynamic recovery, which decreases the stored energy and homogenises the dislocation substructure, reducing the tendency for small high angle subgrains to develop.

- The deformation texture in the β phase consists of an α fibre which is dominated by the $(001)[1\bar{1}0]$ component and peak components belonging to the γ fibre at {111}<112>.

10 FURTHER WORK

9.1 EBSD Post-processing

- At present, for the majority of microstructures, the β reconstruction program achieves a very high level of reconstruction with very few erroneously reconstructed variants. Erroneously reconstructed variants are more common in slower cooled diffusionally transformed α_s microstructures, where there may be a less strict adherence to the Burgers relation and variant selection can result in closely orientated variants on either side of certain β/β boundaries. In these circumstances, the best reconstruction will be a compromise between a high level of reconstructed variants and an acceptable number of erroneously reconstructed variants. This balance is found by varying the tolerance angles used for the reconstruction. To further improve the accuracy of reconstruction in these microstructures, a final manual correction procedure could be added to the program. Erroneously reconstructed variants are usually readily apparent as they tend to be isolated regions having an unexpected orientation within an otherwise correctly reconstructed β grain. It would therefore be a simple procedure to select an erroneously reconstructed variant and cycle through the 5 other potential parent solutions to find the solution which matches the surrounding β grain. Alternatively, if no potential solution gives a close match, then the reconstructed β orientations in the variant in question would be nullified.

9.2 Billet Characterisation

- To develop an increased understanding of the development of macrozones within titanium billets and how forging practise can be optimised to reduce the size and texture strength of these features, it would be useful to analyse the billet at intermediate stages of the ingot forging route as well as the final billet.

- In any future studies, it would be useful if the locations of the axes of intermediate rectangular mults i.e. the major and minor axis of the rectangular cross-section were noted on the final billet.

- The billet characterised in the present study was forged from an ingot using an open die forging press. Timet UK also produce billets using a 4 die rotary forging machine. It would be interesting to study the effect of the different forging routes on the development of macrozones in billets. In particular, the effect of the additional

constraint in the 4 die route that reduces redundant work by preventing side spreading.

- In future analyses of macrozones using EBSD, an EBSD post-processing procedure could be developed to automatically detect macrozones in EBSD datasets using a modified grain detection routine. This would allow statistical information such as the size, shape, orientation and texture of macrozones to be gathered more easily.

9.3 Phase Transformations During Cooling

- Further study of the microstructures in the Jominy specimen using TEM would provide more insight into the nature of the $\beta \rightarrow \alpha$ phase transformation at high cooling rates, where it was difficult to determine the transformation mode through use of optical microscopy and SEM.

9.4 Simulated Secondary Working Using Plane Strain Compression Tests

- Further study of the microstructures in the plane strain compression specimens using TEM would provide more insight into microstructural evolution in the α_p grains. In particular, an analysis of dislocations to determine the active slip systems, a study of the 66° twins to determine the slip plane and direction more accurately and an analysis of the localised areas of recrystallisation.

- Further testing at different temperatures in the $\alpha+\beta$ phase field and above the β transus together with reconstruction of the β microstructures would provide more insight into the dynamic restoration mechanisms in the β phase, particularly the selective recrystallisation that was observed in the present work.

- Further tests followed by a controlled cooling rate designed to simulate the typical cooling rates for an industrial forging. This would provide insight into the static structural changes that occur in the deformed microstructures during cooling.

11 REFERENCES

Ahmed, T., Rack, H.J., 1998, Materials Science and Engineering A, 243, p. 206-211.

Ankem, S., Margolin, H., 1986, Metallurgical Transactions A, 17, p. 2209-2225.

ASTM, 1995, *Standard Test Method for END-Quench Test for Hardenability of Steel*, ASTM Standard A255-89, vol. 1.05, ASTM, Philadelphia, PA, p. 25-42.

Bache, M.R., 2003, International Journal of Fatigue, 25, p. 1079-1087.

Baeslack, W.A., Mullins, F.D., 1982, Journal of Materials Science Letters 1, p.371-373.

Bate, P.S., Blackwell, P.L., Brooks, J.W., 1989, *Sixth World Conference on Titanium*, Eds. Lacombe, P., Tricot, R., Beranger, G., p. 287-292, Les Ulis Cedex, France.

Balasubrahmanyam, V.V., Prasad, Y.V.R.K., 2002, Materials Science and Engineering A, 336, p.150-158.

Baxter G.J., 1991, *Fatigue Damage Accumulation in Titanium Alloy 834*, PhD thesis, The University of Sheffield, UK.

Bescond, C., Lévesque, D., Guénette, J.B., Monchalin, J.P., 2004, *Proceedings of the 16th World Conference on Non Destructive Testing (16 WCNDT)*.

Bhattacharyya, D., Viswanathan, G.B., Denkenberger, R., Furrer, D., Fraser, H.L., 2003, Acta Materialia, 51, p. 4679-4691.

Bhattacharyya, D., Viswanathan, G.B., Fraser, H.L., 2007, Acta Materialia, 55, p. 6765-6778.

Blackmore, M., 2009, *The Effect of Strain Path on the Thermomechanical Processing of Near-α Aerospace Alloy Timetal 834*, PhD Thesis, The University of Sheffield, UK.

Boyer, R.R., 1985, *Titanium and Titanium Alloys*, in *Metals Handbook 9th Ed, Volume 9 Metallography and Microstructures*, ASM.

Bunge, H.J., 1982, *Texture Analysis in Materials Science*, Butterworths, London.

Burgers, W.G., 1934, *Physica,* p. 561-586,Utrecht.

Cayron, C., 2006, Acta Crystallographica.Section A, 62, p. 21-40.

Cayron, C., Artaud, B., and Briottet, L., 2006, Materials Characterization, 57, p. 386-401.

Cervenka, M., 2000, Rolls Royce PLC,
http://www.msm.cam.ac.uk/phase-trans/mphil/Trent1/sld001.htm
(accessed 2005)

Chaussy, F., Driver, J.H., 1994, in *β Titanium* Alloys, Eds. Vassel, A., Eylon, D., Combres, Y., p. 57-64, Editions de la Revue de Metallurgie, Paris.

Chen, C.C. and Coyne, J.E., 1976, Metallurgical Transactions A, 7 (12), p. 1931-1941.

Colas-Ortiz, R., 1983, PhD Thesis, The University of Sheffield, UK.

Daeubler, M.A., Helm, D., Neal, D.F., 1990, *Applications of IMI 834 in Aero Engines - A Collaborative IMI/MTU Programme*, Titanium Development Association, p. 78-87.

Dieter, G.E., 1989, *Mechanical Metallurgy*, SI Metric Edition, McGraw-Hill, New York.

Ding, R., Guo, Z.X., Wilson, A., 2002, Materials Science and Engineering A, 327, p. 233-245.

Dumas, G., Saunier, Y.M., Poirier, F., Wey, E., 1995, *Titanium '95, Proceedings of the 8th World Conference on Titanium*, Eds. Blenkinsop, P.A., Evans, W.J., Flower, H.M., Institute of Materials, London, p. 651-658.

Duncan, R.M., Blenkinsop, P.A., and Goosey, R.E., 1981, *Titanium Alloys*, in *The Development of Gas Turbine Materials,* Ed. Meetham, G.W., Applied Science Publishers, London, p. 63-88.

Evans, W.J., Bache, M.R., 1994, International Journal of Fatigue, 16, p. 443-452.

Eylon, D., Fujishiro, S., Postans, P.J., and Froes, F.H., 1984, *High-Temperature Titanium Alloys – A review*, Journal of Metals, p. 55-62.

Flower, H.M., 1990, Materials Science and Technology, 6, p. 1082-1092.

Foster, S.R., 1981, PhD Thesis, The University of Sheffield, UK.

Fox, S.P., Neal, D.F., 1995, *Titanium '95, Proceedings of the 8th World Conference on Titanium*, Eds. Blenkinsop, P.A., Evans, W.J., Flower, H.M., Institute of Materials, London, p. 628-635.

Furuhara, Y., Toji, T., Maki, T., 2003, *Ti-2003, Science and Technology, Proceedings of the 10th World Conference on Titanium*, Eds. Lütjering, G., and Albrecht, J., p. 1219-1226, Wiley-VCH, Weinheim.

Furuhara, Y., Abe, H., Poorganji, B., Maki, T., 2007, *Ti-2007, Science and Technology, Proceedings of the 11th World Conference on Titanium*, Eds. Nimoni, S., Ikeda, M., Hagiwara, M., Maruyama, K., p. 913-919, The Japan Institute of Metals, Sendai.

Gambogi, J., 2004, *Titanium*, *U.S. Geological Survey Minerals Yearbook*, http://minerals.er.usgs.gov/minerals/pubs/commodity/titanium/titanmyb02.pdf (accessed 1/06/04).

Germain, L., 2005, *Contribution à l'étude des heterogeneities de texture des billettes d'IMI 834*, PhD Thesis, l'Université de Metz, France.

Germain, L., Gey, N., Humbert, M., Bocher, P., Jahazi, M., 2005a, Acta Materialia, 53, p. 3535-3543.

Germain, L., Gey, N., Humbert, M., Hazotte, A., Bocher, P., and Jahazzi, M., 2005b, Acta Materialia, 54, p. 216-222.

Germain L., Gey, N., Humbert, M., 2007, Ultramicroscopy, 107, p.1129-1135.

Gey, N., Humbert, M., Moustahfid, H., 2000, Scripta materialia, 42, p. 525–530.

Gey, N., and Humbert, M.J., 2003, Materials Science and Engineering A, 38, p. 1289-1294.

Ginatta, M.V., 2001, *Economics and Production of Primary Titanium by Electrolytic Winning, Proceedings of Extraction and Processing Division (EPD) of TMS (The Minerals, Metals & Materials Society)*, EPD Congress, TMS Annual Meeting, February 11-15, 2001, p. 13-41.

Glavicic, M.G., Kobryn, P.A., Bieler, T.R., Semiatin, S.L., 2003a, Materials Science and Engineering A, 346, p. 50-59.

Glavicic, M.G., Kobryn, P.A., Bieler, T.R., Semiatin, S.L., 2003b, Materials Science and Engineering A, 351, p. 258-264.

Glavicic, M.G., Kobryn, P.A., Semiatin, S.L., 2004, Materials Science and Engineering A, 385, p.372-376.

Glavicic, M.G., Miller, J.D., Semiatin, S.L., 2005, Materials Science and Engineering A, 346, p.50-59.

Glez, J.C., and Driver, J. J., 2001, Applied Crystallography, 34, p. 280-288.

Goosey, R.E., 1989, *Developments in titanium alloys for aerospace*, Metals and Materials, August, p. 451-454.

Guo, Z.X., Baker, T.N., 1992, Materials Science and Engineering A, 156, p. 63-76.

Han, Y.K., Thompson, R.B., 1997, Metallurgical and Materials Transactions A, 28, p. 91-104.

Harauz, G., 1990, Ultramicroscopy, 33, p. 209-213.

Higginson, R. L., Sellars, C. M., 2003, *Worked Examples in Quantitative Metallography*, Woodhead Publishing Limited, Cambridge.

Hinton, J.S., 2006, PhD Thesis, The University of Sheffield, UK.

Missing pages are unavailable

Lord, J.D., Loveday, M.S., 2001, *Tools and Lubricants for High Temperature Metalworking Laboratory-Scale Tests*, Centre for Materials Measurement and Technology, National Physical Laboratory, Teddington, UK.

Lütjering, G., 1998, Materials Science and Engineering A, 243, p. 32-45.

Lütjering, G., Williams, J.C., 2003, *Titanium*, Springer-Verlag, Berlin.

Lutterotti, L., Mathies, S., and Wenk, H.R., 1999, *Proc. of the 12th International Conference on Textures of Materials (ICOTOM-12) Vol. 1,* NRC Research Press, Montreal, p. 1599.

Male, A.T., Cockcroft, M.G., 1965, Journal of the Institute of Metals, p. 38-46.

Meetham, G.W., Van de Voorde, M.H., 2000, *Materials for High Temperature Engineering Applications*, Springer-Verlag, Berlin.

Mirza, M.S., Sellars, C.M., 2001a, Material Science and Technology, 17, p. 1133-1141.

Mirza, M.S., Sellars, C.M., 2001b, Materials Science and Technology, 17, p. 1142-1148.

Morawiec, A., and Pospiech, J., 1989, Textures Microstruct. 10, p. 211-242.

Moril, K., Mecking, H., Lütjering, G., 1986a, *Strength of Metals and Alloys (ICSMA 7), Proceedings of the 7th International Conference*, V1, p. 251-256, Pergamon Press, Oxford.

Moril, K., Mecking, H., Lütjering, G., Nakayama, Y., 1986b, Scripta Metallurgica, 20, p. 1795-1800.

Moustahfid, H., Humbert, M., Phillipe, M.J., 1997a, Acta Materialia, 45, p. 3785-3790.

Moustahfid, H., Gey, N., Humbert, M., Philippe, M.J., 1997b, Metallurgical and Materials Transactions A, 28, p. 51-61.

Neal, D.F., 1988, *Sixth World Conference on Titanium*, Eds. Lacombe, P., Tricot, R., Beranger, G., p. 253-258, Les Ulis Cedex, France.

Neal, D.F., 2001, *Development of Timetal 834, Conf. Materials Design Approaches and Experiences*, TMS fall meeting, Indianapolis, IN, USA, 4-8 November, 2001, Minerals and Materials Society / AIME, Warrendale, PA.

Oxford Instruments, 2004, *Electron Backscattered Diffraction Explained*, Oxford Instruments Technical Briefing (PDF), http://www.oxinst.com/wps/wcm/resources/file/ebcdd14ee13ed6f/EBSD_Explained.pdf (accessed 2005).

Partridge, P.G., 1967, Metallurgical Reviews, 12, p. 169-194.

Philippart, I., Rack, H.J., 1998, Materials Science and Engineering A, 243, p. 196–200.

Polmear, I.J., 1989, *Light Alloys 2nd Ed*, Edward Arnold, London.

Poths, R.M., Angella, G., Wynne, B.P., Rainforth, W.M., Semiatin, S.L., Beynon, J.H., 2004, Metallurgical and Materials Transactions A, 35, p. 2993-3001.

Ramachandra, C., Singh, A.K., Sarma, G.M.K., 1993, Metallurgical Transactions A, 24, p. 1273-1280.

Randle, V., Engler, O., 2000, *Introduction to Texture Analysis: Macrotexture, Microtexture & Orientation Mapping*, Gordon and Breach Science Publishers, Amsterdam.

Ray, R.K., Jonas, J.J., Hook, R.E., 1994, International Materials Reviews, 39 (4), p. 129-172.

Robertson, D.G., Mcshane, H.B., 1997a, Materials Science and Technology, 13, p. 459-468.

Robertson, D.G., Mcshane, H.B., 1997b, Materials Science and Technology, 13, p. 575-583.

Rolland, P., Dicks, K., Ravel-Chapuis, R., 2002, Microscopy and Microanalysis, 8 (suppl. 2), p. 670-671.

Rollet, A.D., 2005, *Rodrigues Vectors, Quaternions*, http://neon.mems.cmu.edu/rollett/27750.old.Spg05/RFvecs_quats_18Jan05.ppt (accessed 17/10/2007).

Rollet, A.D., and Kalu, P.N., 2005, *Misorientations and grain boundaries*, http://neon.mems.cmu.edu/rollett/27750.old.Spg05/Misorientation_HowTo_17Feb05.ppt (accessed 17/10/2007).

Sastry, S.M.L., Pao, P.S., Sankaran, K.K., 1980, *Titanium '80 - Science and Technology, Proceedings of the Fourth World Conference on Titanium*, Eds. Kimura, H., Izumi, O., p. 873-886, Warrendale, PA, TMS-AIME.

Searles, T., Tiley, J., Tanner, A., Williams, R., Rollins, B., Lee, E., Kar, S., Banerjee, R., Fraser, H.L., 2005, Measurement Science and Technology, 16, p.60–69.

Semiatin, S.L., Lahoti, G.D., 1981, Metallurgical Transactions A, 12, p. 1705-1717.

Sellars, C.M., Sah, J.P., Beynon, J.H., Foster, S.R., 1976, *Report on research work supported by SRC Grant B/RG/1481*, The University of Sheffield,UK.

Semiatin, S.L., Seetharaman, V., Weiss, I., 1999, Materials Science and Engineering A, 263, p. 257-271.

Semiatin, S.L., Knisley, P.N., Fagin, P.N., Zhang, F., and Barker, D.R., 2003, Metallurgical and Materials Transactions A, 34, p. 2377-2386.

Shi, H., McLaren, A.J., Sellars, C.M., Shahani, R., Bolingbroke, R., 1997, Journal of Testing and Evaluation, 25(1), p. 61-73.

Silk, N.J., van der Winden, M.R., 1999, Materials Science & Technology, 12 p. 295-300.

Stanford, N., Bate, P.S, 2004, Acta Materialia, 52, p. 5215-5224.

Stanford, N., Bate, P.S, 2005, Materials Science Forum, V 495-497, PART 1, *Textures of Materials, ICOTOM 14 - Proceedings of the 14th International Conference on Textures of Materials*, p. 669-674.

Struers, *Application Notes – Metallographic Preparation of Titanium*, http://www.struers.com/resources/elements/12/79131/Application%20Notes%20titanium%20English.pdf (accessed 2005).

Sufogulu, H., Gedikli, H., 2002, Tribology International, 35, p. 27-34.

Taylor, G.I., 1938, Journal of the Institute of Metals, 62, p. 307.

Thomas, M.J., Wynne, B.P., Rainforth, W.M., 2005, Materials Characterisation, 55, p. 388-394.

Thomas, M.J., 2007, *The Effect of Thermomechanical Process Parameters on the Microstructure and Crystallographic Texture Evolution of Near-α Aerospace Alloy Timetal 834*, PhD Thesis, The University of Sheffield, UK.

Thompson, R.B., Margetan, F.J., Haldipur, L., Yu, L., Li, A., Panetta, P., and Wasan, H., 2007, Wave Motion, 45, p. 655-674.

Timet, 2000, *Timetal® 834*, http://www.timet.com/pdfs/834.pdf (accessed 2005).

Tukey, J.W., 1977, *Exploratory Data Analysis*, Addison-Wesley.

Vo, P., Jahazi, M., Yue, Bocher, P., 2007, Materials Science and Engineering A, 447 p. 99–110.

Von Mises, R., Angew, Z., 1928, *Math. Mech.*, 8, p. 161.

Wanajara, P., Jahazi, M., Monajati, H., Yue, S., Immarigeon, J.-P., 2005, Materials Science and Engineering A, 396, p.50-60.

Wanjara, P., Jahazi, M., Monajato, H., Yue, S., 2006, Materials Science and Engineering, A416, p.300-311.

Weiss, I., Froes, F.H., 1985, in *Titanium 84, Science and* Technology, Eds. Lütjering, G., Zwicker, U., Bunk, W., p. 499-506, Deutsche Gesellschaft für Metallkunde E>V>, Oberrursel.

Weiss, I., Froes, F.H., Eylon, D., Welsch, G.E., 1986a, Metallurgical Transactions A, 17, p. 1935-1947.

Weiss, I., Welsch, G.E., Froes, F.H., Eylon, D., 1986b, *Strength of Metals and Alloys (ICSMA 7), Proceedings of the 7th International Conference*, V2, p. 1073-1078, Pergamon Press, Oxford.

Weiss, I., Semiatin, S.L., 1998, Materials Science and Engineering A, 243, p. 46-65.

Weiss, I., and Semiatin, S.L., 1999, Materials Science and Engineering A, 263, p. 243-256.

Wilson, A.F., Venkatesh, V., Pather, R., Brooks, J.W., Fox, S.P., 2003, *Ti-2003, Science and Technology, Proceedings of the 10th World Conference on Titanium*, Eds. Lütjering, G., and Albrecht, J., p. 321-328, Wiley-VCH, Weinheim.

Woodfield, A.P., Gorman, M.D., Corderman, R.R., Sutliff, J.A., Yamrom, B., 1995, *Titanium '95, Proceedings of the 8th World Conference on Titanium*, Eds. Blenkinsop, P.A., Evans, W.J., Flower, H.M., Institute of Materials, London, p. 1116-1123.

Zombeck, M.V., 2007, *Handbook of Space Astonomy and Astrophysics*, 3rd Edition, Cambridge University Press, Cambridge.